Ionisation of caesium Rydberg atoms for a mono-chromatic electron source for applications in electron microscopy and spectroscopy

Raphaël Hahn

université PARIS-SACLAY

Source d'électrons monochromatique par l'ionisation d'atomes de Rydberg de césium pour des applications en spectroscopie et en microscopie électronique

Ionisation of caesium Rydberg atoms for a monochromatic electron source for applications in electron microscopy and spectroscopy

Thèse de doctorat de l'université Paris-Saclay

École doctorale n°572, Ondes et Matières (EDOM)
Spécialité de doctorat: Physique
Unité de recherche : Université Paris-Saclay, CNRS, Laboratoire Aimé Cotton, 91405, Orsay, France
Référent : ENS Paris-Saclay

Thèse présentée et soutenue à Paris-Saclay, le 05/03/2021, par

Raphaël HAHN

Composition du Jury

Odile STÉPHAN Professeure, Laboratoire de Physique des Solides (LPS), Université Paris-Saclay	Présidente
Christian BORDAS Directeur de recherche, Institut Lumière Matière (iLM), Université de Lyon	Rapporteur
Arnaud ARBOUET Directeur de recherche, Centre d'élaboration de matériaux et d'études structurales (CEMES), Université de Toulouse	Rapporteur
Matthieu VITEAU Orsay Physics	Examinateur

Direction de la thèse

Daniel COMPARAT Directeur de recherche, CNRS, Laboratoire Aimé Cotton (LAC)	Directeur de thèse

Thèse de doctorat

NNT : 2021UPASP007

Résumé en français

Les sources d'électrons utilisées en microscopie électronique ont une haute brillance mais une haute dispersion en énergie (>250 meV). D'autres types de sources existent, basées sur la photo-ionisation de jets atomiques, remarquables par leur finesse énergétique (quelques meV), mais à faible courant (quelques dizaines de pA au mieux) ce qui interdit leur usage en microscopie. Une source d'électrons générant un courant de 1 nA tout en gardant une faible dispersion en énergie permettrait d'améliorer grandement certaines techniques de microscopie en se débarrassant des aberrations chromatiques dans la colonne, mais aussi de construire un nouvel instrument : HREELM. Cet instrument permettrait, pour la première fois, de coupler des mesures de microscopie électronique à basse énergie (de surface, type LEEM) avec des mesures de spectroscopie de perte d'énergie d'électrons de haute résolution (de type HREELS). Le premier chapitre de cette thèse rappelle l'état de l'art en microscopie électronique et montre comment HREELM permettrait de réaliser des études encore impossibles avec les instruments existants. La réalisation instrumentale de HREELM est détaillée, et converge vers la conclusion que les sources d'électrons existantes ne permettent pas de réaliser HREELM.

Une piste très prometteuse pour obtenir une source d'électron adaptée est de partir d'une source intrinsèquement monochromatique (source en photo-ionisation d'un jet atomique) et d'augmenter la brillance de la source en améliorant le processus d'ionisation des atomes du jet. Ceci peut se faire en excitant les atomes vers des états très excités dits de Rydberg, qui peuvent présenter des taux d'ionisation non-négligeables en champ électrique.

Cette thèse explore à la fois théoriquement et expérimentalement comment les états de Rydberg peuvent être utilisés pour développer une source d'électrons innovante adaptée au projet HREELM, présentée en détail dans le premier chapitre. C'est pourquoi cette thèse contient deux chapitres dédiés à la prédiction de l'énergie et des taux d'ionisation de ces états, tant d'un point de vue théorique (voir chapitre 2) qu'expérimental (voir chapitre 3). Une fois que nous avons vérifié que nous étions capables de prédire quantitativement à la fois l'énergie et le taux d'ionisation de presque n'importe quel état de Rydberg individuel perdu dans la région des spaghettis [1], nous pourrions l'utiliser pour poursuivre l'étude des sources d'électrons, dans les deux chapitres suivants : le chapitre 4 traite des études sur une source d'électrons continue, tandis que le chapitre 5 traite des sources d'électrons pulsées.

De manière un peu plus détaillée, voici le contenu de ces cinq chapitres :

[1] (c'est le surnom des régions de la carte de Stark où les états de Rydberg sont complètement mélangés les uns aux autres et où l'évolution de l'énergie des états semble presque aléatoire).

- Dans le premier chapitre, je donne un rapide aperçu du domaine de la microscopie électronique, en montrant les formidables réalisations des cinquante dernières années, particulièrement les développements récents qui font entrer la spectroscopie d'électrons dans les colonnes de microscopie. Cela m'aidera à introduire l'idée que le projet HREELM comblerait un vide dans la boîte à outils des scientifiques de surface d'aujourd'hui. Les détails de l'instrument HREELM sont ensuite donnés, de la conception de la colonne à l'analyse de l'énergie. Ceci a des conséquences pour la source d'électrons, car une solution nécessite un faisceau continu et intense, alors que l'autre solution nécessite un faisceau d'électrons pulsé avec une faible dispersion temporelle. De plus, je passerai en revue les sources d'électrons utilisées en microscopie électronique, et montrerai comment elles ne sont pas adaptées à HREELM. Cette revue générale de la microscopie électronique est justifiée par le fait qu'une source d'électrons intrinsèquement monochromatique adaptée à une colonne de microscope rendrait non seulement possible la construction de l'instrument HREELM, mais bénéficierait à toutes les techniques existantes qui utilisent des sondes électroniques. La seconde partie de ce premier chapitre sera consacrée à d'autres sources d'électrons existantes, dans le domaine de la physique atomique et moléculaire, caractérisées par leur faible dispersion d'énergie. Les électrons sont dans ce cas extraits d'atomes en jet ou en vapeur, par des radiations laser soigneusement accordées. Cela permettra une analyse détaillée des sources de dispersion d'énergie dans une telle source d'électrons et servira de base à toutes les études ultérieures, car la meilleure compréhension de cette dispersion d'énergie est nécessaire pour la maintenir à son niveau le plus bas. Un point important est que, comme prévu, si nous voulons à la fois un faisceau d'électrons à faible dispersion d'énergie et des courants suffisamment élevés pour les applications, une compréhension détaillée des processus d'excitation et d'ionisation est nécessaire. Les applications de HREELM sont évidentes, mais comme nous l'avons déjà mentionné, les résultats les plus excitants seraient probablement obtenus sur d'autres systèmes, qu'il est presque impossible de prévoir.

- Le deuxième chapitre présente les atomes de Rydberg et la physique de Rydberg en détail, d'un point de vue théorique. En particulier, l'accent est mis sur les méthodes théoriques permettant d'étudier les états de Rydberg dans les champs électriques, car ce sont les réservoirs d'électrons que nous utiliserons. Une méthode en particulier, la méthode de transformation de repère local (LFT) sera expliquée en détail et une dérivation de ses principaux résultats sera donnée. Ceci sera utile pour comprendre les résultats d'un code informatique exploitant cette méthode et fournissant des spectres de photo-absorption d'atomes de métaux alcalins. Ce code est à la base de nos études sur l'ionisation des états de Rydberg, car il donne à la fois l'énergie de ces états, la force relative des dipôles de transition et leur taux d'ionisation.

- Dans le troisième chapitre, je compare les résultats obtenus par le code LFT aux cartes Stark expérimentales. Le dispositif expérimental que j'ai construit de toutes pièces au cours de cette thèse est présenté en détail, et une comparaison quantitative est réalisée pour le césium, sur une large gamme d'énergie. Je trouve que l'accord est excellent dans l'ensemble, et que cette méthode est totalement adaptée aux études d'ionisation requises pour développer notre source d'électrons.

- Dans le quatrième chapitre, je traite de la réalisation d'une source d'électrons à faisceau continu pour HREELM. Je présente d'abord une description de l'ionisation des états de Rydberg dans un champ, et montre comment notre connaissance des atomes de Rydberg peut être utilisée pour minimiser les différents termes de la dispersion d'énergie qui ont été identifiés à la fin du chapitre 1. Ceci m'amène à détailler une tentative expérimentale de mesure de la dispersion énergétique de notre source d'électrons. Le montage a en effet été enrichi d'un spectromètre d'électrons, pour mieux comprendre le lien entre champ électrique d'extraction et dispersion en énergie du faisceau d'électrons produits. Les résultats obtenus m'amènent à proposer deux variantes d'une source d'électrons continue proche de l'optimum, avec des simulations détaillées montrant l'impact des différentes sources de dispersion d'énergie.

- Dans le cinquième chapitre, je me tourne vers la réalisation d'une source d'électrons pulsée. Cela commence par une proposition détaillée d'un schéma de détection pulsé dans HREELM, jusqu'aux détecteurs que nous pourrions utiliser. Il s'agit d'un préliminaire au reste de la discussion sur la source d'électrons pulsés, car ce schéma de détection impose des contraintes à la source d'électrons, notamment en termes d'étalement temporel des impulsions d'électrons. Deux façons d'ioniser les atomes de manière pulsée sont discutées : tout d'abord, il est possible de pulser le laser ionisant, et je présente quelques données expérimentales acquises à Mayence. Comme à la fin du chapitre 1, les sources d'étalement temporel dans une source d'électrons pulsée sont explicitement citées et expliquées. La possibilité de manipuler les paquets d'électrons pour améliorer leur énergie ou leur étalement temporel est étudiée théoriquement, par des simulations et expérimentalement. Ensuite, je montre qu'il est possible de pulser le champ électrique nécessaire au processus d'ionisation, dans un processus d'ionisation innovant (et breveté) appelé ionisation par champ de résonance pulsé de Rydberg. Je présente des données expérimentales acquises à Orsay montrant qu'une expérience de preuve de concept permet d'approcher des impulsions d'électrons d'un étalement temporel de 1 ns.

- Le sixième et dernier chapitre fait office de conclusion et détaille les travaux en cours au Laboratoire Aimé Cotton. Il commence par décrire notre nouveau dispositif expérimental qui nous permettra de réaliser le premier prototype de l'instrument HREELM, ainsi que plusieurs perspectives très prometteuses permettant d'améliorer encore les performances de notre source d'électrons.

Remerciements

Les quelques lignes qui suivent, qui seront probablement les plus lues du manuscrit, rendent compte de l'importance des rencontres que j'ai pu faire et des interactions que j'ai pu avoir dans la conduite de mes travaux ainsi que dans ma vie durant ces 3 dernières années (et demie). Une thèse est un exercice particulier, qui peut être parfois solitaire, mais une bonne thèse de physique expérimentale est toujours, au moins en partie, une réussite collective, et celle-ci ne fait pas exception.

Ce manuscrit reflète les travaux entrepris pendant plus de 3 ans au laboratoire Aimé Cotton, au bâtiment 505 puis au bâtiment 221, mais aussi pendant mes excursions à Mayence et à Fuveau. J'y ai croisé beaucoup de monde, que je veux aujourd'hui remercier. En particulier, je remercie:

Jean-François Roch, **Djamel Benredjem**, **Olivier Dulieu** qui furent successivement directeurs du laboratoire. Mon arrivée a coïncidée avec le départ de Jean-François Roch, que j'ai donc peu connu. On peut penser à un laboratoire comme à un bateau qui navige dans les eaux parfoius troubles de la recherche académique, et qui est mené par un équipage où chacun a sa place, ses compétences et son rôle à jouer. Le LAC était en pleine tempête et Djamel a courageusement tenu la barre dans un moment où personne d'autre n'aurait pu ni voulu la tenir. Ton grand calme et ta diplomatie n'ont malheureusement pas suffit à garder le navire entier. Notre moitié de navire a ensuite trouvé un nouveau capitaine en la personne d'Olivier. Les circonstances particulièrement difficiles de ton mandat (un déménagement pendant une pandémie avec un service administratif en sous-effectif, que demander de plus ?) n'ont pas suffit à ébranler ta motivation. Le laboratoire vogue maintenant plus sereinement vers les eaux de l'UMR, et il ne fait aucun doute que le cap que tu as fixé est le bon.

Pierre Pillet qui fut un temps directeur du laboratoire et directeur de l'équipe à mon arrivée. Merci pour les discussions scientifiques (mais pas que), toujours très riches et ouvertes. Je retiendrais longtemps la maxime d'un bon directeur: "La science c'est important, les gens sont importants, les institutions doivent suivre".

Odile Stéphan, pour avoir acceptée d'être rapportrice de mes travaux dans un premier temps, puis, une fois les consignes de composition de jury bien relues, d'avoir acceptée d'être présidente de mon jury de thèse. J'ai beaucoup apprécié votre enthousiasme pour mes travaux.

Arnaud Arbouet et **Christian Bordas** pour avoir accepté d'être rapporteur de mon épais manuscrit. Merci particulièrement à Arnaud Arbouet de m'avoir fait parvenir une longue liste de coquilles dans la première version du manuscrit. Merci pour vos retours constructifs et enthousiastes qui m'ont redonné confiance en moi au moment ou j'en avais bien besoin. Je vous serai toujours reconnaissant d'avoir fait le déplacement pour ma soutenance, ce qui m'a permis d'avoir une soutenance dans de très bonnes conditions, presques normales.

Matthieu Viteau et **Morgan Réveillard** de la société Orsay Physics, qui m'ont chaleureusement accueuilli à Fuveau pendant une semaine. Je remercie particulièrement Matthieu d'avoir aussi accepté de faire parti de mon jury de thèse, et d'avoir fait le déplacement jusqu'à Orsay. Grâce à vous je suis maintenant bien conscient qu'il existe aussi de la recherche de qualité dans le privé, malgré les contraintes de liberté.

Many thanks to **Gerd Schönhense**, **Sergii Chernov** and **Olena Fedchenko** for the scientific collaboration and the time spent in Mainz. I want to particularly thank Lena for her kindness, her energy and thoughtfulness. I really enjoyed working with you in the lab, and hope that we will meet again in our academic (or else) life.

Pascal, **Daniel**, **Henri**, **Guillaume** et **Lionel**, pour leur bons et loyaux services au bureau d'étude (Pascal) et à la méca. J'ai fait un usage extensif de leurs services pendant ma thèse, et j'étais toujours très bien accueilli quand je poussais la porte. Merci à eux.

Jean-Paul, **Elie**, **Jules** et **Jim**, du service électronique. J'ai intéragi avec chacun d'entre vous à différents degrés mais étais toujours très bien accueilli, même avec mes questions de béotiens.

Jules, j'ai beaucoup aimé la séance de polissage d'électrodes en ta compagnie ! Merci particulièrement à Jean-Paul qui a suivi de près le projet HREELM et a permis qu'il avance rapidement et se conclue avant mon départ. Merci pour ta gentillesse et ta disponibilité.

Jérôme et **Michèle** du service informatique, toujours disponibles (et toujours souriant !) pour dépatouiller mes problèmes de réseau ou d'imprimantes, ce qui m'a économisé quelques crises de nerfs ! Je n'avais jamais vu un chasseur de champignons aussi acharné. Je me souviendrais aussi longtemps de ton goût (?) certain pour les pantalons bariolés...

Bruno Vivan, merci pour tout ! Je garderai énormément de bons souvenirs de cette dernière année, pendant laquelle on a pu intéragir longuement. Ton goût du travail bien fait, parfois jusqu'à l'extrême, et ta passion, forcent le respect. J'ai beaucoup appris sur la mécanique de précision grâce à toi. C'était un vrai plaisir de pouvoir travailler ensemble, et de partager à l'occasion nos dernières trouvailles musicales.

Christine, **Basile** et tous les membres des services administratifs que j'ai connu (beaucoup). Merci à eux deux pour leur bonne humeur à toute épreuve et leur disponibilité. Merci particulièrement à Christine pour ces derniers mois intenses, où ton zèle, ton profesionalisme et ta capacité d'organisation, qui m'ont permis de me concentrer sur ma rédaction et mes manipes. Les "formalités" administratives ont toujours été particulièrement difficiles pour moi, mais tu as tout fait pour tout rendre simple. Merci beaucoup pour tes très nombreux conseils et ton franc-parler !

Daniel Comparat, mon directeur de thèse, pour tout ! La liste serait vraiment très longue des choses que je te dois, mais je tiens à souligner ton incroyable dynamisme, ton énorme curiosité scientifique et ta passion toujours intacte. Ton envie de toucher à tout (de l'antimatière aux sources de particules chargées, des molécules froides au dipole électrique de l'électron) et de ne jamais reculer devant une nouveau projet, ainsi que ta gentillesse, font de toi quelqu'un de très occupé, ce qui m'a aussi appris l'autonomie et l'indépendance, indispensables pour progresser en tant que chercheur. Ton envie de satisfaire tout le monde te met parfois dans des situations difficiles, et t'obligent à travailler d'arrache-pied, ce qui est toujours très impressionant (moi qui croyais que je faisais beaucoup de biblio...). Mais malgré tout ça tu restais très disponibles dans les moments importants, comme la rédaction et la soutenance. Merci pour ta confiance. Tu resteras un modèle pour moi, et si j'arrive un jour à la moitié du scientifique que tu es, j'en serais très fier.

Hans Lignier, nos discussions (où tu parles et j'écoute) étaient un vrai bol d'air et me manqueront énormément. Quel plaisir de disserter sur la chute de Rome, de linguistique, de politique, d'obscures groupes de musique (je n'ai pas oublié Gong !), des exploits de cascadeur de Dennis Hopper et milles autres sujets passionants. Je garde encore précieusement la track-list de Gizzard, merci encore ! J'aurais beaucoup aimé qu'on puisse plus travailler ensemble, tant j'admire ta pédagogie, ta passion et ta gentillesse. Je pense (et j'espère !) que nos routes se recroiseront, au labo, ou dans la rue ;-) Et longue vie au petit Iraj !

Patrick Cheinet, pour ta disponibilité, ta passion, ton entrain dès qu'il s'agit d'expliquer un concept obscure de physique atomique ou un coup d'échec de génie. Nous n'avons malheureusement pas pu aller aux champignons ensemble mais j'ai quand même retenu pas mal de choses de tes leçons exhaustives sur leur cueillette. Et merci pour le vinaigre ;-)

Steven Lepoutre, pour ta gentillesse, ta passion et ta richesse intellectuelle. Les trop rares fois où nous avons pu prendre le temps de discuter resteront des très bons souvenirs. Tu as su me redonner confiance en moi lorsque les recherches infructueuses de post-doc me plombaient le moral. Avec un peu de chance nous nous recroiserons dans nos carrières à venir !

Yan Picard, pour ta sympathie et ton aide pour l'acquisition de données et le partage de tes connaissances nombreuses sur les détecteurs, ça me sera bien utile !

Colin Lopez, avec qui j'ai partagé une manipe en début de thèse, puis un laser et beaucoup de bons moments, particulièrement en fin de thèse. Je me sentais moins seul dans la galère, et tu m'as bien aidé pour la soutenance, merci beaucoup !

Nouari, **Nadia**, **Goulven** (l'autre breton du labo, avec qui je partage ma passion de la trance/techno des années 90), et tous les autres membres du laboratoire, avec qui j'ai pu échanger quelques mots à l'occasion, et qui m'ont toujours bien accueilli.

Thibault, **Ky-Luc**, **Lucas**, ou le club d'échec/escalade local. Vous aurez presque réussir à me convertir à ces deux activités. J'aurai vraiment aimé être plus disponible pour approfondir nos liens. Bon courage pour la suite et j'espère qu'on pourra se recroiser dans les labos ou ailleurs !

Mélissa, **Baptiste**, **Paul**, **Aurélien**, **Fériel**, **Ferdinand**, **Thimothée**, **Pascal**, **Lucile**, **Grégory**, **Debanush**, **Aya** et tous les autres thésards que j'ai pu croiser au laboratoire et ailleurs, pour l'ambiance générale très agréable, loin des divisions, et les quelques sorties et soirées qu'on a pu faire avant qu'une pandémie n'en décide autrement.

Thomas, bon courage pour la suite ! Tu vas avoir la chance d'avoir Daniel pour toi tout seul, essaie juste de lutter contre ses propositions d'utiliser du patafix dans la manipe de métrologie...

Je remercie **Camille Noûs** et tous ceux qui nous rappellent que, à rebours de la tendance, qui s'intensifie, à considérer des individus stars comme parangon de la recherche, la science est une pratique collective, qui tire sa force et sa pertinence de la mise en commun des curiosités et des intransigeances.

Je remercie les syndicats, les gens qui se battent, toutes celles et ceux qui osent encore dire que le monde de la recherche meurt à petit feu, que les étudiant.e.s, travailleurs et travailleuses de la recherche et de l'université souffrent, et que les réformes successives auront bientôt achevé de saccager les libertés académiques au profit d'une vision productiviste et mercantile de l'Université. Merci à celles et ceux qui n'oublient pas que les première victimes, particulièrement lorsque l'université ne peut ouvrir ses portes, sont toujours les plus fragiles, c'est à dire les étudiant.e.s, les précaires et les dégouté.e.s.

Henri, **Clément**, **Erwan**, **Luca** et **Lucile** pour être devenus des amis.

Victor, **Thomas**, **Nicolas**, **Cyril**, **Clément**, la bande du magistère ! Quel plaisir de voir que notre petite troupe perdure malgré la distance et les fins de thèse de chacun ! J'ai hâte qu'on ait tous fini (hein Polese !) et qu'on puisse fêter tout ça. Merci de n'avoir pas coupé les ponts avec le presque-physicien de la bande... Et dans quelques mois on se pourra se mettre d'accord (enfin !) si la neige est meilleure à la Mongie, dans la Chartreuse ou dans les Alpes suisses !

La bande, vous savez pourquoi.

J'aimerais également remercier **Luigi** car sans lui je ne serais pas docteur.

Malika, pour ton amour, ton soutien dans la période la plus difficile de notre vie, pour avoir choisi la vie.

Mes parents, pour votre soutien sans failles depuis toujours, pour votre amour, votre tolérance, pour avoir su cultiver ma curiosité d'enfant et ne m'avoir jamais imposé de voie.

Karen, merci de m'avoir porté à bout de bras, particulièrement à la fin. Tu as accepté beaucoup, et je ne serais jamais arrivé au bout d'un tel travail si tu n'avais pas été là.

À Lalo…

Contents

Physical constants and conversion factors

General constants:	
Speed of Light	$c = 2.997\,924\,58 \times 10^{8}\,\mathrm{m\,s^{-1}}$ (exact)
Planck constant	$h = 6.626\,070\,15 \times 10^{-34}\,\mathrm{J\,Hz^{-1}}$ (exact)
Reduced Planck constant	$\hbar = 1.054\,571\,817 \times 10^{-34}\,\mathrm{J\,s}$ (exact)
Elementary charge	$\mathrm{e} = 1.602\,176\,634 \times 10^{-19}\,\mathrm{C}$ (exact)
Avogadro constant	$\mathcal{N}_A = 6.022\,140\,76 \times 10^{23}\,\mathrm{mol^{-1}}$ (exact)
Electron volt	$\mathrm{eV} = 1.602\,176\,634 \times 10^{-19}\,\mathrm{J}$ (exact)
Unified atomic mass unit	$\mathrm{u} = 1.660\,539\,066\,60(50) \times 10^{-27}\,\mathrm{kg}$
Proton mass	$m_p = 1.672\,621\,923\,69(51) \times 10^{-27}\,\mathrm{kg}$
Caesium standard atomic weight	$m\left(^{133}\mathrm{Cs}\right) = 132.905\,451\,96(6)\mathrm{u}$
Fine-structure constant $e^2/(4\pi\epsilon_0\hbar c)$	$\alpha = 7.297\,352\,569\,3(11) \times 10^{-3}$
Vacuum magnetic permeability $4\pi\alpha\hbar/(e^2c)$	$\mu_0 = 1.256\,637\,062\,12(19) \times 10^{-6}\,\mathrm{N\,A^{-2}}$
Vacuum electric permittivity $1/\mu_0c^2$	$\epsilon_0 = 8.854\,187\,812\,8(13) \times 10^{-12}\,\mathrm{F\,m^{-1}}$
Atomic units:	
Electron mass (atomic unit of mass)	$m_e = 9.109\,383\,701\,5(28) \times 10^{-31}\,\mathrm{kg}$
	$= 5.485\,799\,090\,65(16) \times 10^{-4}\,\mathrm{u}$
Bohr's radius (atomic unit of length)	$a_0 = 5.291\,772\,109\,03(80) \times 10^{-11}\,\mathrm{m}$
Hartree (atomic unit of energy)	$E_h = 4.359\,744\,722\,207\,1(85) \times 10^{-18}\,\mathrm{J}$
	$= 2Ry_\infty \cdot hc$
	$= 27.211\,386\,245\,988(53)\,\mathrm{eV}$
Atomic unit of electric field E_h/ea_0	$F_{au} = 5.142\,206\,747\,63(78) \times 10^{11}\,\mathrm{V\,m^{-1}}$
Rydberg constant	$Ry_\infty = 10\,973\,731.568\,160(21)\,\mathrm{m^{-1}}$
Atomic units for hydrogen:	
Mass	$\mu_e^H = 9.104\,425\,276\,5 \times 10^{-31}\,\mathrm{kg}$
Length	$a_0^H = 5.294\,654\,098\,23 \times 10^{-11}\,\mathrm{m}$
Energy	$E_h^H = 4.357\,371\,623\,417 \times 10^{-18}\,\mathrm{J}$
	$= 2Ry^H hc$
	$= 27.196\,574\,528\,357\,\mathrm{eV}$
Electric field E_h^H/ea_0^H	$F_{au}^H = 5.136\,610\,253\,25 \times 10^{11}\,\mathrm{V\,m^{-1}}$
Rydberg constant	$Ry^H = 10\,967\,758.340\,280\,\mathrm{m^{-1}}$
Atomic units for caesium:	
Mass	$\mu_e^{Cs} = 9.109\,346\,101\,7 \times 10^{-31}\,\mathrm{kg}$
Length	$a_0^{Cs} = 5.291\,793\,951\,44 \times 10^{-11}\,\mathrm{m}$
Energy	$E_h^{Cs} = 4.359\,726\,726\,910\,9 \times 10^{-18}\,\mathrm{J}$
	$= 2Ry^{Cs} \cdot hc$

		$= 27.211\,273\,928\,184\,\text{eV}$
Atomic unit of electric field E_h^{Cs}/ea_0^{Cs}	F_{au}^{Cs}	$= 5.142\,164\,297\,75 \times 10^{11}\,\text{V}\,\text{m}^{-1}$
Rydberg constant	Ry^{Cs}	$= 10\,973\,686.273\,038\,\text{m}^{-1}$
Useful conversions:		
Spectroscopic wave-number	$\overline{\nu}(\text{cm}^{-1})$	$= \frac{10^7}{\lambda(\text{nm})}$
		$= \frac{\nu(\text{MHz})}{29979.2458}$
Linear frequency	$\nu(\text{THz})$	$= \overline{\nu}(\text{cm}^{-1}) * 0.0299792458$
		$= \frac{2.997\,924\,58 \times 10^5}{\lambda(\text{nm})}$
Angular frequency	$\omega(\text{rad}\,\text{s}^{-1})$	$= 2\pi\nu(\text{Hz})$
Wavelength	$\lambda(\text{nm})$	$= \frac{10^7}{\overline{\nu}(\text{cm}^{-1})}$
		$= \frac{2.997\,924\,58 \times 10^5}{\nu(\text{THz})}$

Data comes from the 2018 CODATA recommended values[1] and 2013 IUPAC Technical report[2].

Introduction

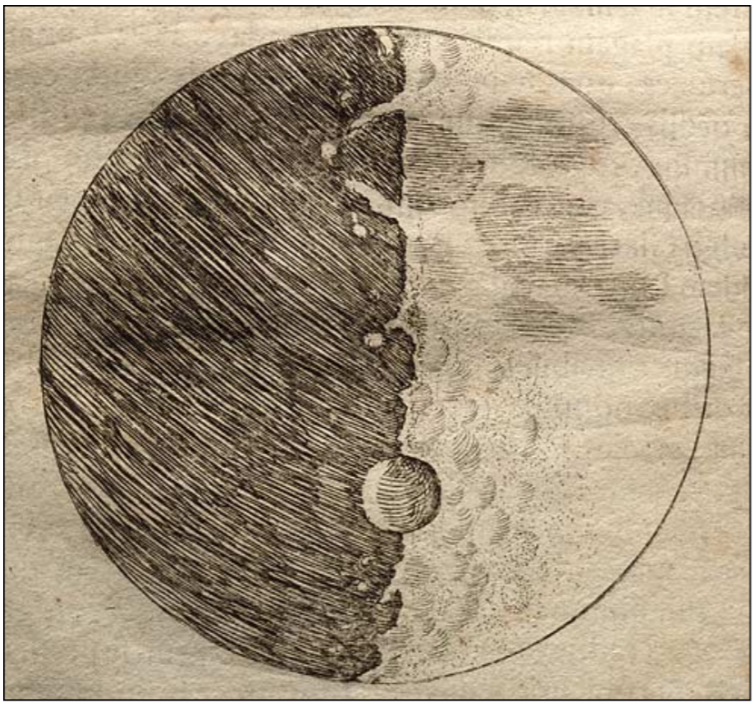

FIGURE 1: Sketch of the surface of the Moon by Galileo, obtained with a recently improved refracting telescope. Reproduced from [1].

On the 30th November of 1609, Galileo Galilei began pointing his recently improved refractive telescope towards the moon, observed its rough surface, and found it to be quite different from the perfect stellar object postulated by Aristotle. It is an improved version of previous instruments (the "Dutch perspective glass"), that were used mostly for military purposes. The report of this observation, among many others, was published in his Starry Messenger (Sidereus Nuncius) and startled debate on the nature of the stellar objects. Shortly after this report, scholars from all over Europe started experimenting and improving the refractive telescope. This led to Newton and his reflective telescope, and to the giant telescopes that are now used every day in observatories around the world. The observation of Galileo is often quoted as the first use of an optical instrument for the observation of the sky, but many scholars performed similar observations before Galileo. Thomas Harriot for example performed both earlier and more precise observations of the moon, but did not distribute his work and communicated it as well as Galileo did. These observations were made possible by a technological improvement: the birth of a novel scientific instrument, the refractive telescope, that was able to surpass the precision of the naked-eye observations of Ticho Brahe.

This historical detour illustrates two main points about science and scientific progress:

- Science is intricately linked to technology, and the development of novel scientific instruments is a strong vector of scientific progress. The biggest progress is furthermore usually not in the direction intended during the development of the instrument.

- Science is a collective process, thus based on communication, and communicating is easier with nice sketches.

Four centuries later, modern science is inseparable from its instruments. Imaging atoms, producing the coldest matter in the universe or observing black holes is now routinely achieved in laboratories. The year 2020 showed that fundamental research (in biology, virology...) could be of paramount importance to the sanitary and political stability worldwide. In particular the study of the COVID-19 virus rests heavily on cryo-electron microscopes (cryo-EM)[2–4], formidable instruments that give access to the detailed structure of proteins without the requirements of protein-crystallisation. Atomic resolution for proteins in the single-particle cryo-EM was obtained very recently[5], concluding almost a century of the development of the electron microscope.

Another direction of the developments of electron microscopes is towards the study of surfaces, interfaces, and bulk materials. The present thesis is a continuation of these developments, through the HREELM project. HREELM stands for high-resolution electron energy loss microscope, and is a scientific collaboration between teams in Laboratoire Aimé Cotton (LAC), in the Institut des Sciences Moléculaires d'Orsay (ISMO) and the Service de Physique de l'Etat condensé (SPEC). The ambition of this project is to develop and construct a new, innovative instrument for the surface science community, that will enable both high-resolution electron spectroscopy and low-energy electron microscopy.

Many techniques already exist in this field to study and analyse the physics and chemistry happening on sample surfaces. A rapid and non-exhaustive sum-up of the dominant techniques and their possibilities is presented in table 1, along with the ambition of the HREELM project.

Technique	Imaging	Δx(nm)	ΔE(meV)	Surface sensitivity
STEM-EELS	Scanning	< 1	5	$\times$
Micro-Raman	Scanning	500	< 1	$\times$
TERS	Scanning	35	< 1	$\sim$
HREELS	$\times$	$\times$	1	✔
LEEM	Full-field	15	250	✔
HREELM	Full-field	20	5	✔

TABLE 1: State of the art of different techniques relevant in surface science and materials analysis (highly non-exhaustive), with spatial resolution (Δx) and energy resolution (ΔE). The quoted values for HREELM show the ambition of the project. STEM-EELS: scanning-transmission electron microscope coupled with electron energy loss spectroscopy; Micro-Raman: Raman spectroscopy coupled to an optical micrscope TERS: tip-enhanced Raman scattering; HREELS: high-resolution electron energy loss spectroscopy and LEEM: low-energy electron microscopy. Surface sensitivity indicated if the technique is particularly sensitive to the surface features.

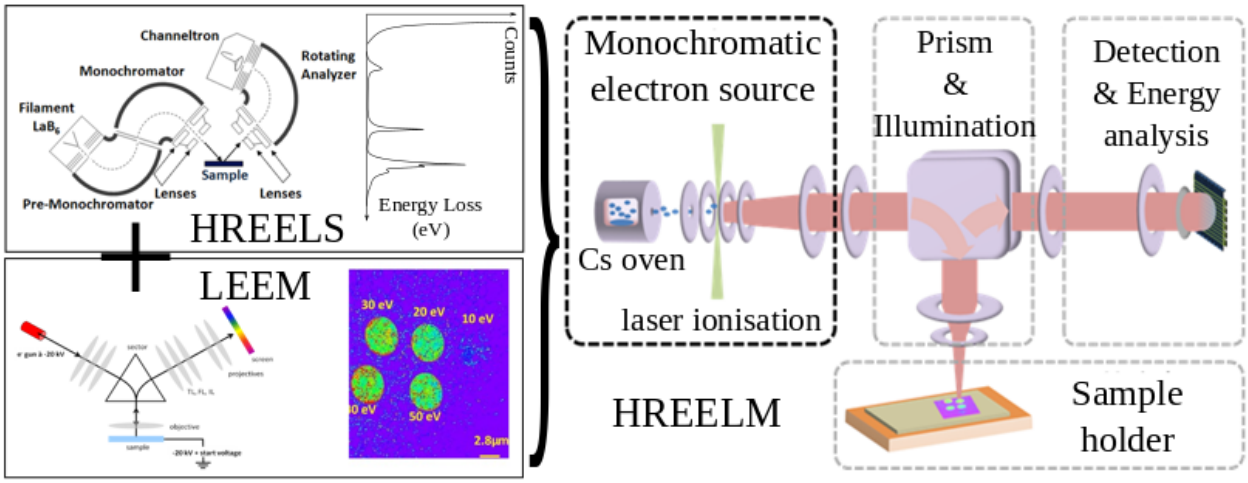

FIGURE 2: Schematic of the HREELM project, combining both the spectroscopic resolution of HREELS and the imagery of LEEM into a single instrument. The HREELM instrument requires a monochromatic electron source, with a caesium oven producing an atomic beam ionised with lasers.

Most of these techniques use electron probes, but TERS and micro-Raman uses photons. Micro-Raman is the combination of a Raman spectrometer and an optical microscope. TERS is modified version of micro-Raman, based on the intensity increase of Raman scattering close to tips. A nanometric-scale tip is scanned on the surface of the sample and the Raman signal is recorded. Using light allows good spectral resolution, but it is currently limited to a few tens of nm concerning the spatial resolution, and it requires scanning. Other relevant techniques are STEM-EELS, HREELS and LEEM. They use electron probes at high-energy for STEM-EELS and low-energy for HREELS and LEEM. STEM-EELS is the combination of two techniques: scanning transmission electron microscopy and electron energy loss spectroscopy in the same instrument. It provides very high spatial resolution, with usually rather poor spectral resolution. It is however a very active field, and recent instrumental improvements now gives access to a very good spectral resolution (5 meV). It is however a bulk-sensitive technique and also requires scanning the electron probe to obtain a microscopic image.

HREELS and LEEM are both sensitive only to the surface of the sample and require no scanning. They use both low-energy electrons impinging on the surface of the sample. In HREELS the electrons are very monchromatic and the energy losses at the contact of the sample are analysed, providing a high-resolution spectroscopic technique. In LEEM, the low-energy electron probe is used to image the surface of the sample, providing microscopy images with good spatial resolution.

Table 1 indicates that there is currently no technique allowing full-field imagery of a surface with the spectroscopic resolution enough for resolving surface phonons and low energy surface plasmons (it demands less than 10 meV spectral resolution).

The main idea of the HREELM project is to combine two mature surface science techniques (HREELS and LEEM) into a single instrument, allowing full-field imagery combined with resolution of low-loss phenomena like surface plasmons and phonons. If it represented schematically on figure 2. This combination should allow the acquisition of a high-resolution image of a sample's surface coupled with a high-resolution spectroscopic analysis, and to correlate microscopy and spectroscopic information with high resolution.

Furthermore, a second acquisition mode should allow to map the dispersion of phonons of the surface at high spectral resolution.

Many studies of physico-chemical systems would greatly benefit from such an instrument. For example, in photovoltaic systems the interaction of charge carriers with surface phonons leads to non-radiative losses, to the detriment of the desired function. Being able to map the vibrational energy losses would therefore help to elucidate and potentially reduce parasitic coupling. The study of ferroelectricity would also greatly benefit from this possibility. Indeed the ferroelectric effect (a long-lasting magnetization) is associated with the generation of a characteristic soft-phonon mode that could be observed and correlated to microscopy contrast features. The study of surface plasmons and surface phonons on nano-scale objects could also greatly benefit from this instrument, as it already benefited from the great improvements of STEM-EELS[6]. Another field of application beyond the advanced analysis of a system is the modification of this system, with real-time monitoring. For example the study of the functionalization of molecular layers on surface by optical or electronic irradiation requires both very high spectroscopic resolution and a spatial resolution of a few nanometers[7].

One of the most crucial elements in the instrumental developments of all techniques involving electron probe is obviously the improvement of the electron probe itself. This is particularly true for HREELS, which benefited from the impressive improvements in electron source monochromation. However, this monochromation decreases the quality of the electron beam, and does not allow high-resolution microscopy like LEEM. Joining these two techniques thus has a strong prerequisite: an novel electron source must be developed, that will have the properties fitted for both spectroscopy and microscopy purposes. The crucial element that allows the realization of HREELM is indeed a highly-monochromatic electron source, very different from the ones usually used in electron microscopy.

Indeed it exists a variety of different electron sources, like tungsten wires or LaB_6 tips, but these create electron beam with large energy spread, in the eV range (0.25 eV for the cold-field electron guns (CFEG)). Close-to-monochromatic electron beams are used in the field of atomic and molecular physics, where the study of electron collisions with atoms or molecules require electrons with very well defined energies. These are created by electron sources based on the photo-ionisation of free atoms. The work achieved during this thesis is an effort to start from these monochromatic electron sources, improve their properties, and make them fit for the HREELM project. In particular they usually lack enough current to be used as a microscopy probe. This low current is a direct consequence of the low efficiency of photo-ionisation, and the associated very high laser power required.

As these electron sources involves the controlled ionisation of atoms, improving their properties requires an in-depth understanding of the physics at play. In particular, this can involve Rydberg states, that are very peculiar, highly excited atomic states. Exciting Rydberg states requires a lot less laser power than photo-ionisation, which could increase the electron current given by these electron sources.

The study of the properties of Rydberg states is an active subject, both fundamental and about their possible applications in quantum communication, quantum simulations or sensing. Rydberg states are very well known in the Laboratoire Aimé Cotton, particularly in the group of Pierre Pillet, continued as the group of Daniel Comparat nowadays. The study of the ionisation of Rybderg states in electric fields is active since the early days

of Rydberg physics, but predicting the precise lifetime of individual strongly-shifted Rydberg is not easy, and very few studies exist on caesium in particular. This constitutes an interesting problem in itself, but is also a preliminary to using these states as the basis for an efficient and innovative electron source.

This thesis thus explores both theoretically and experimentally how this knowledge on Rydberg states can be applied on electron sources, to develop an innovative electron source adapted to the HREELM project, presented in details in the first chapter. This is why this thesis contains two chapters dedicated to the prediction of the energy and ionisation rates of these states, both from a theoretical (see chapter 2) and an experimental point of view (see chapter 3). Once we verified that we were able to predict quantitatively both the energy and the ionisation rate of almost any individual Rydberg state lost in the spaghetti region[2], we could use it to pursue electron source studies, in the following two chapters: chapter 4 deals with studies on a continuous electron source, while chapter 5 deals with pulsed electron sources.

In a bit more details, this is what the five chapters contain:

- In the first chapter I give a rapid overview of the field of EM, with an emphasis on recent developments that bring electron spectroscopy into EM columns, showing the tremendous achievements of the last fifty years. This will help me introduce the idea that the HREELM projet would fill a gap in today's surface scientists toolbox. Details about the HREELM instrument are then given, from the design of the column to the energy analysis. this has consequences for the electron source, as one solution requires a continuous, intense beam, whereas the other solutions requires a pulsed electron beam with low temporal spread. Furthermore, I will review the electron sources used in EM, and show how they are not adapted to HREELM. This broad review of EM is justified by the fact that an intrinsically mono-chromatic electron source adapted to a microscope column would not only make possible the construction of the HREELM instrument, but would benefit all the existing techniques that use electron probes. The second part of this first chapter will be about other existing electrons sources, in the field of atomic and molecular physics, characterised by their low energy spread. The electrons are in this case extracted from free atoms, by carefully tuned laser radiations. This will allow a detailed analysis of the sources of energy spread in such an electron source and serve as a basis for all further studies, as the best understanding of this energy spread is required to keep it at its lowest. An important point in that, as expected, if we want to have both a low-energy spread electron beam and high-enough currents for the applications, a detailed understanding of the atomic laser excitation and of the ionisation process is required.

- The second chapter deals introduce Rydberg atoms and Rydberg physics in some details, from a theoretical point of view. In particular some emphasis is put on theoretical methods to study Rydberg states in electric fields, as these are the reservoir of electrons that we will use. One method in particular, the local-frame transformation method (LFT) will be explained in details and a derivation of its principal results are given. This will be helpful to understand the results of a computer-code exploiting this method and providing photo-absorption spectra of alkali-metal atoms. This

[2]this is the nickname of the regions of the Stark map where Rydberg states are completely mixed with one another and the energy evolution of the states appears almost random.

code is the basis of our studies about the ionisation of Rydberg states, as it gives both the energy of these states, the relative strength of transition dipoles, and their ionisation rate.

- In the third chapter I compare the results obtained by the LFT-code to experimental Stark maps. The experimental set-up that I build from scratch during this thesis is presented in details, and quantitative comparison is achieved for caesium, over a large energy range. I find that the agreement is very good overall, and that this method is totally adapted to the ionisation studies required to develop our electron source.

- In the fourth chapter I deal with the realisation of a continuous beam electron source for HREELM. I first present a description of the ionisation of Rydberg states in a field, and show how our knowledge of Rydberg atoms can be used to minimise the electron spread source identified at the end of chapter 1. This leads me to detail an experimental attempt to measure the electron spread of our electron source. The set-up was enriched with an electron spectrometer, to prove that we understand the energy spread of the produced electron beams. Some results are obtained, that lead me to propose two variations of a close-to-optimal continuous electron source, with detailed simulations showing the impact of the different energy spread sources.

- In the fifth chapter, I turn to the realisation of a pulsed electron source. This starts with a detailed proposition for a pulsed detection scheme in HREELM, down to the detectors that we could use. This is a preliminary to the rest of the pulsed electron source discussion because this detection scheme imposes constraints on the electron source, particularly in terms of time spread of the electron pulses. Two ways of ionising atoms in a pulsed way are discusses: firstly it is possible to pulse the ionising laser, and I present some experimental data acquired in Mainz and analysis. Analogously with the end of chapter 1, the sources of temporal spread in a pulsed electron source are explicitly cited and explained. The possibility to manipulate the electron bunches to improve their energy or temporal spread is studied theoretically, with simulations and experimentally. Secondly I show that it is possible to pulse the electric field required from the ionisation process, in an innovative (and patented) ionisation process called Rydberg pulsed-resonance field-ionisation. I present experimental data acquired in Orsay showing that a proof-of-concept experiment approaches electron pulses of temporal spread 1 ns.

This thesis is written from an instrumentalist point of view, with an emphasis on the definition and use of concepts instead of rigorous and tedious mathematical developments, because it reflects best the work achieved and the results obtained during these 3 years at Laboratoire Aimé Cotton and elsewhere.

References

[1] Galileo Galilei. *Sidereus nuncius*. Apud Thomam Baglionum, 1610. DOI: 10.5479/sil.95438.39088015628597.

[2] Yan Gao et al. “Structure of the RNA-dependent RNA polymerase from COVID-19 virus”. In: *Science* 368.6492 (2020), pp. 779–782. ISSN: 0036-8075. DOI: 10.1126/science.abb7498.

[3] Dora Pinto et al. “Cross-neutralization of SARS-CoV-2 by a human monoclonal SARS-CoV antibody”. In: *Nature* 583.7815 (2020), pp. 290–295. DOI: 10.1038/s41586-020-2349-y.

[4] Daniel Wrapp, Nianshuang Wang, Kizzmekia S. Corbett, Jory A. Goldsmith, Ching-Lin Hsieh, Olubukola Abiona, Barney S. Graham, and Jason S. McLellan. “Cryo-EM structure of the 2019-nCoV spike in the prefusion conformation”. In: *Science* 367.6483 (2020), pp. 1260–1263. ISSN: 0036-8075. DOI: 10.1126/science.abb2507.

[5] Takanori Nakane et al. “Single-particle cryo-EM at atomic resolution”. In: *Nature* (2020). DOI: 10.1038/s41586-020-2829-0.

[6] Hugo Lourenço-Martins. “Experiment and theory of plasmon coupling physics, wave effects and their study by electron spectroscopies”. 2018SACLS284. PhD thesis. 2018. URL: http://www.theses.fr/2018SACLS284/document.

[7] L. Amiaud, J. Houplin, M. Bourdier, V. Humblot, R. Azria, C.-M. Pradier, and A. Lafosse. “Low-energy electron induced resonant loss of aromaticity: consequences on cross-linking in terphenylthiol SAMs”. In: *Phys. Chem. Chem. Phys.* 16 (3 2014), pp. 1050–1059. DOI: 10.1039/C3CP53023J.

Chapter 1

A new electron source for a new instrument

> Nothing tends so much to the advancement of knowledge as the application of a new instrument.
>
> Humphry Davy

1.1 The HREELM project

1.1.1 Scientific context, modern analysis techniques

This section deals with the main techniques that use electrons to perform analysis of materials in bulk or of surfaces nowadays. It is not an exhaustive review but rather a rapid overview, that will bring us to the core of this thesis, that is the HREELM project and in particular the unique electron source that enables its realisation.

Material analysis with an electron probe is a vast scientific field, and many imaging and spectroscopic techniques have been developed and are in daily use since the beginning of the 20th century and the invention of the electron microscope[1–3], and electron spectroscopy[4]. The applications are numerous (in physics, chemistry, biology, materials science, geology...) and the range of different instruments based on electrons probes is large.

The interaction of an electron probe with a sample (in bulk or a surface) depend on a large number of parameters, the landing energy of the electron being the main one. This interaction can be classified either as elastic, inelastic or quasi-elastic scattering, depending on the quantity of energy deposited by the electron in the sample. Elastic scattering means that the electron does not lose any energy. Inelastic scattering concerns electrons that lose energy to electronic excitations, electron-hole pair formation, and other process that spans the 1 eV to 100 eV range, while quasi-inelastic scattering (also often called simply inelastic scattering) concerns other processes that lead to energy deposition less than 1 eV (e.g. phonons or magnons excitations,...). The influence of electron energy on their inelastic mean free-path in matter is shown on figure 1.1. This curve is called universal as its fits well the vast majority of material sample[5]. This diversity of phenomena explains the vast number of spectroscopic and microscopy techniques based on electron probes.

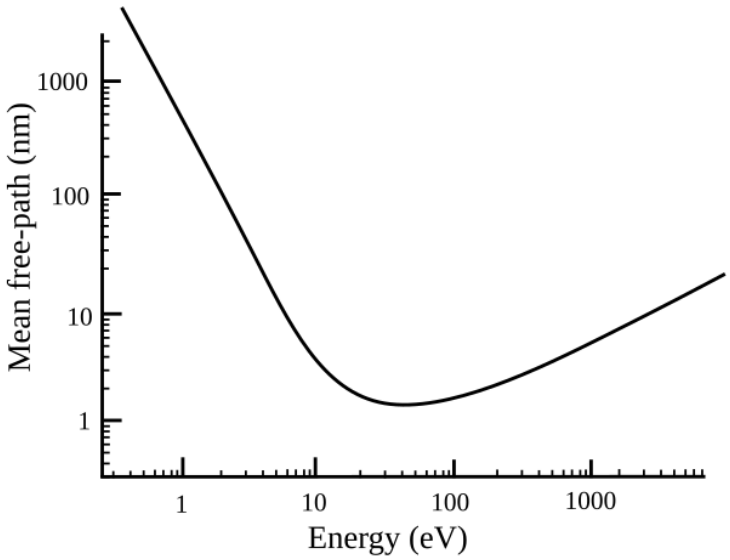

FIGURE 1.1: Universal curve for inelastic mean free path, plotted from formulas found in ref. [5]

Bulk electron microscopy: SEM, CTEM & STEM

Since the early days of quantum mechanics and the recognition that electrons can be described as waves[6], the idea of using electrons as a probe of matter has been developed. For non-relativistic electrons, their wavelength λ can be calculated from h the Planck constant and p the momentum (or directly from its energy, E) as:

$$\lambda(\text{nm}) = \frac{h}{p} = \frac{1.226}{\sqrt{E(\text{eV})}} \tag{1.1}$$

This dependence is to be put along with the Abbe diffraction limit (d) formula for electron microscopes(where θ is the collection angle of electrons):

$$d = \frac{1.2\lambda}{\sin\theta} \tag{1.2}$$

Taking relativistic corrections into account, electrons at 200 keV have a wavelength of 2.5 pm, which gives (for $\theta \approx 10$ mrad) $d \approx 300$ pm, opening up the possibility to resolve atomic distances. This explains the overwhelming use of electron beams in material analysis over photons, because photons of equivalent wavelength (corresponding to X-rays) are difficult to create, to manipulate and have orders of magnitude lower interaction cross-sections than electrons[7]. Furthermore, the electric charge of the electron makes its manipulation much easier, via electric or magnetic fields.

The field of electron microscopy (EM) is vast and in constant evolution. We present here the three main techniques that use high-energy electrons to probe samples: the scanning electron microscope (SEM), the conventional transmission electron microscope (CTEM) and the scanning transmission electron microscope (STEM). The last two form the field of transmission electron microscopy (TEM). The energy unit of choice in this field is the eV because it is defined as the potential energy of an electron in an electric

potential of 1 V. This means that when an electron is created at rest at a potential of 1 keV and travel to a zone of null potential, its kinetic energy is equal to 1 keV. The conversion to SI units is simple: $E(\mathrm{J}) = E(\mathrm{eV}) * e$, with e the electric charge of the electron.

The three main techniques can be schematically described with figure 1.2. This figure represents the irradiation of a sample with a focused high-energy electron beam along with the induced phenomena, the interactions with the condensed matter and the possible electron trajectories. In SEM, a finely focused electron is moved boustrophedonically[1] on the surface of a sample and electrons and photons emitted from the sample are recorded at each position. The movement of the electron probe is done via deflection coils that are synchronised with the recording devices. The diameter of the electron beam at the sample is usually around 1 nm and the electrons have an energy between 1 keV and 30 keV.

A variety of signals can be recorded and analysed at the same time in a SEM, as seen in figure 1.2: Auger electrons, secondary electrons, backscattered electrons, cathodoluminescence, X-ray emissions, transmitted electrons and absorbed electrons. Secondary electrons are historically defined at the electrons emitted with energies below 50 eV. This definition is somewhat arbitrary, especially at low interaction energy. They represent the biggest proportion of the detectable electrons (as seen on figure 1.3). These electrons come from the material itself, so the rate of emission depends greatly on the sample properties. Due to the high-energy needed for electrons to travel from deep inside the sample to the surface, secondary electrons are characteristic of the surface of the sample, from 2 nm to 50 nm depending on the sample.

This means that high-spatial resolution images taken with a SEM usually are secondary-electrons images. However, secondary electrons may come from a variety of different phenomena, and some studies even showed that secondary electrons coming directly from the interaction of the primary incident electron beam with the sample (called SE1 electrons) represent less than 30 % of the total detected secondary electrons[8].

Backscattered electrons are electrons from the primary incident beam that are scattered multiple times by the sample, with each scattering event changing their momentum orientation until they come out of the sample slab. A good proportion of the scattering events can be inelastic so that the energy distribution of backscattered electrons (as seen on figure 1.3) starts at and goes well below the primary beam energy E_0. As the energy of these electrons is significantly higher than the energy of secondary electrons, it is not easy to remove them all from detectors. The topology of the surface sample and the relative orientation of the sample and the detectors are thus crucial parameters of the final image, as clearly demonstrated in figure 1.4.

Auger electrons are electrons emitted during an electronic recombination of excited atoms in the sample. They are highly characteristic of the sample surface composition and can serve to the identification of surface contaminant levels down to a fraction of a monolayer, but require very-high vacuum. Different configurations of lenses and detectors exists and an optimal placement of detectors has to be found for each emission. One of the possible configuration uses only one electron detector for recording both the secondary and the backscattered electrons. The detector is surrounded by a grid whose potential can be positive or negative. When the grid is positively biased (300 V for example), emitted electrons are attracted to it and the collection efficiency is high. When the grid is negatively biased, it is used to select the energy of the detected electrons. This way,

[1] turning like oxen in plowing, forming a raster pattern

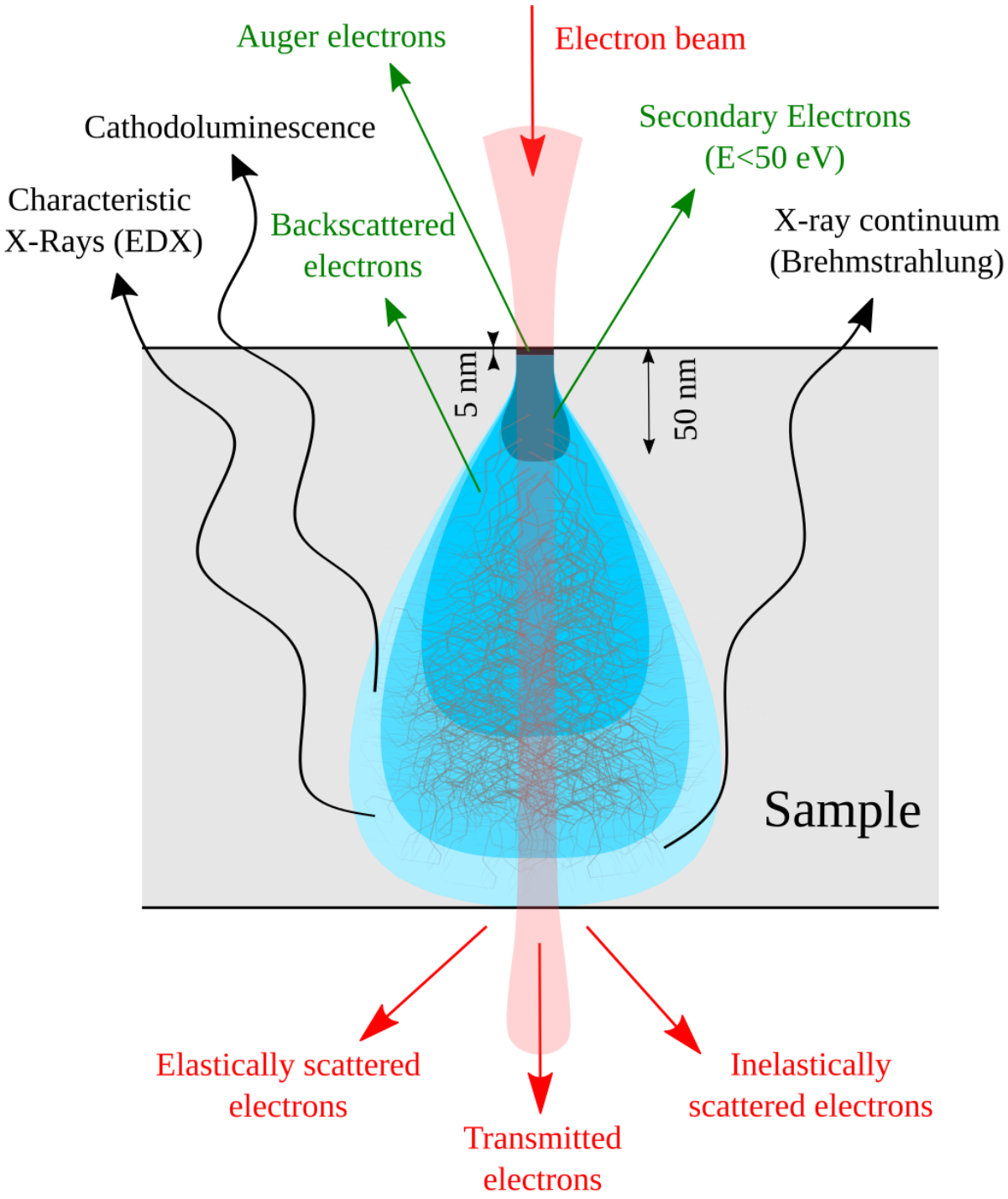

FIGURE 1.2: Schematics of the different interactions and electron trajectories during the illumination of a condensed-matter sample slab with high-energy electrons. The depth of the different interactions is not to scale and varies rapidly with the incident energy of the electron probe. Curved black arrows picture photon emission, green straight arrows depicts upwards electron emission, red straight arrows represents downwards electron emission. Each type of emission comes from a different volume inside the sample, and carries different information.

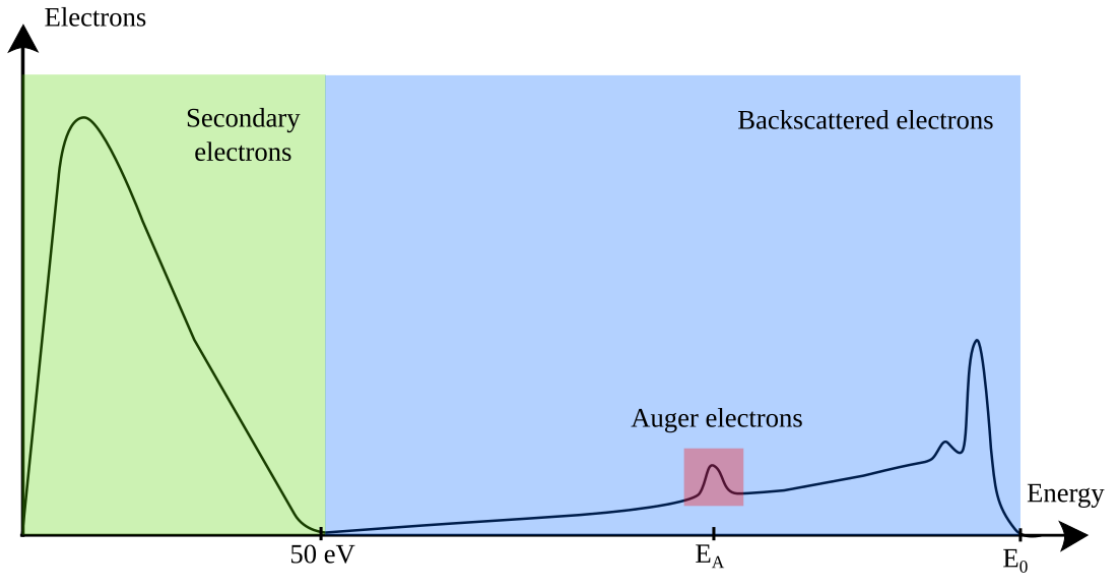

FIGURE 1.3: Schematic energy distribution of the different emitted electrons. E_0 is the primary electron beam energy and E_A is the energy of the Auger electron.

one can chose what kind of electron signal is recorded. Two different images of the same object in these two different settings can be seen on figure 1.4.

Cathodoluminescence is the emission of light following the recombination of electron-hole pairs in samples with an electronic energy gap. The wavelength of this light spans the UV-visible-infrared range, depending on the sample, and can be used to follow crystal growth for example, along with the detection of X-rays by the sample.

The figure 1.2 features, in addition to all the different emissions already presented, transmitted electrons. These electrons can also be used to study, image and characterise a sample, and the instruments that are specifically constructed to do so are called Conventional Transmission Electron Microscope (CTEM) and Scanning Transmission Electron Microscope (STEM). The difference between the two kinds of transmission microscopy is that in CTEM the sample is fixed and illuminated by a large probe and an image of the sample is recorded by a detector larger than the probe, and in STEM the probe is focused on a very small spot ($\approx$ 0.1 nm) and is raster-scanned over the sample surface. These instruments usually go to the high-end of the energy scale, with electrons energy from 30 keV to 1 MeV or even higher. The reason is easy to understand from both figure 1.1 and equation 1.1. Higher energy means a higher proportion of transmitted electrons and a smaller focussed electron probe. Samples that are studied in transmission modes must obviously have a small thickness, from a few nm up to a few hundred nm. Higher energy allows thicker sample but induce more sample damage. Figure 1.2 shows that part of the transmitted electron are scattered by the sample, and a crucial part of STEM instrument is the detection of these electrons. STEM actually features two main modes of detection: bright-field (BF) imaging and annular dark-field (ADF) imaging. Bright-field imaging is performed in STEM by placing a detector in the optical axis of the electron probe. The signal measured in bright-field configuration is coherent, which complicates the interpretation of the observed contrasts. For example, in a crystalline sample where we might expect a diffraction Bragg figure, the focusing of the electron probe actually produces

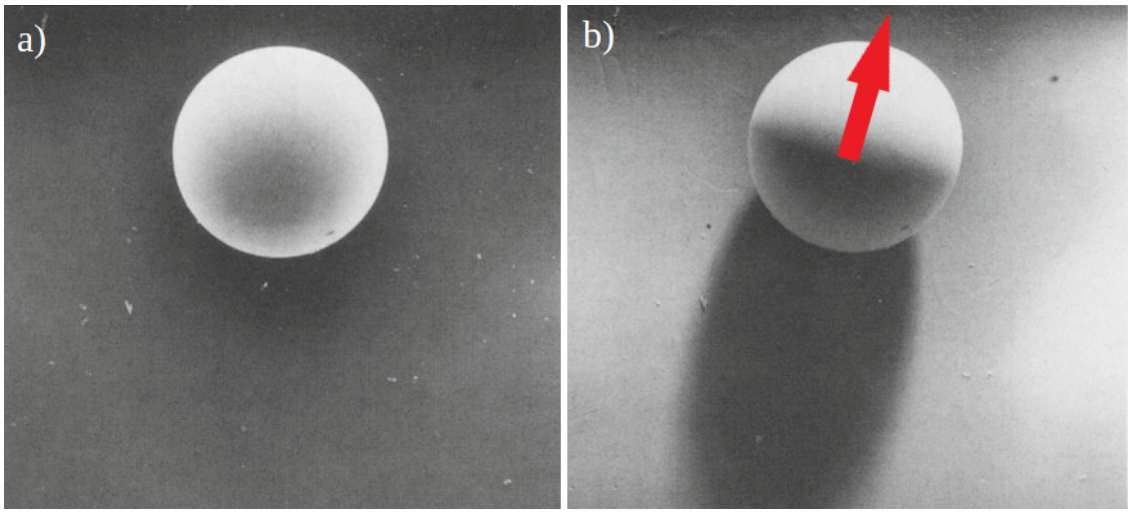

FIGURE 1.4: SEM images of a 1 mm steel ball in two different recording settings. a) Secondary electrons image b) Backscattered electrons image (negatively-biased detector). The red arrow indicates the position of the electron detector. Reproduced from [9].

diffraction circles in a process called convergent electron beam diffraction.

Annular dark-field imaging is unique to STEM and is the most used imaging mode. It consists in detecting the electrons on a disk far from the axis of the probe. This means that a signal is observed only when the probe hits a highly-scattering portion of the sample. In contrast to bright-field imaging, here the signal can be viewed as incoherent, making it easier to interpret.

Nowadays and owing to the recent advances in aberration correction and instrument design, STEM can be considered as the flagship of electron microscopy, with an unrivalled spatial resolution. The resolution of TEM instruments is generally better than SEM, and imaging atoms is now routinely achieved at high electron energies. Two of the main directions of improvements for this technique are now the introduction of high-resolution electron spectroscopy, and lowering the electron energy. The transmission mode indeed allows spectroscopy to be done inside the STEM, by analysing the energy losses of the electrons. More details on this feature can be found in section 1.1.2. Recent advances in STEM design, aberration correction, electron beam monochromation, and in-lens sample location now also allow atomic resolution at low landing energies (down to 40 keV[10]). This is interesting because, as higher-energy electrons can be focused tighter, the induced damages are also bigger, and it makes it hard to image very small (and fragile) features in samples.

These same instrumental developments have also benefited SEM instruments, that extend to low-energy for the same reasons. Low to very-low energy SEM has been successfully developed over the years, characterised by landing energies below 1 keV. The associated techniques are called Scanning Low Energy Electron Microscopy (SLEEM) or Low Voltage Electron Microscopy (LVEM). LVEM has several advantages: higher contrast due to an increase in cross-sections for inelastic and elastic scattering, as well as reduced radiation damage. The trade-off between spatial resolution worsening and instrumental improvements now allow 1.4 nm resolution at 1 kV and even 5 nm resolution at 0.1 kV[10].

The three techniques (SEM, CTEM and STEM) presented above (usually) rely on high

energy electrons, meaning that they can be treated analytically within the first Born approximation i.e. the incident electron wave is taken as a plane wave. We will see in the following section that when the energy of the incident electron is lowered to the eV range, the interactions that take place change and both the simple view and the theoretical treatment are different. Another major difference when lowering the incident electron energy is that the electron probe is no longer sensitive to the bulk of the material (see figure 1.2), but rather only to the first atomic layers, the surface of the sample. This is the realm of low-energy electron microscopy.

Surface electron microscopy:LEEM

Low energy electron microscopy (not to be confused with LVEM[2]) was invented and developed in the late 1950s, and the first prototype was presented at a conference in 1962[11]. This prototype had the peculiarity of taking place in a glass chamber (see the right panel of figure 1.5), but the technique had to wait a proper stainless steal implementation to achieve its first images[12]. Numerous improvements and developments have since made LEEM a central technique in surface analysis, even if the performance in terms of spatial resolution remain inferior to the standard ones for bulk analysis[9].

LEEM allows the acquisition of images of the surface of samples thanks to a low to a very low energy (0 eV to 100 eV) electronic probe. An electron beam is transported from the electron source to the sample at high velocity (5 keV to 20 keV), deflected towards the sample by a beam splitter, then enters a lens called an immersion lens where the electrons are strongly decelerated to an energy called interaction energy. The electron probe illuminates the surface to be imaged homogeneously, on a typical size of 50 µm × 50 µm. The interaction energy corresponds to the potential difference between the starting potential and the sample potential, which (in normal acquisition mode) is higher (more positive) than the starting potential of the electrons. The electrons are thus attracted to the sample, resulting in a strong interaction with the surface.

Some of these electrons are elastically backscattered, accelerated by the immersion lens (called "obective lens" on figure 1.5), pass back through the beam splitter and electrostatic or magnetic optics form an image of the sample on a detector. An image is typically recorded for each value of the interaction energy.

The low velocity of the electrons means that they will interact with the electrons of the sample much longer than in TEM. This removes the validity of the first Born approximation that is used at high energies, which states that when the interaction potential is small against the incident energy, one can model the incident wave by a plane wave. An analysis in terms of partial waves is indeed necessary, meaning that the incident plane wave and the outgoing scattered wave are expanded into spherical harmonics centred at the atom. We call ϕ_l the phase difference between the partial waves. In this framework, and considering only elastic processes, the scattering amplitude is given by[9]:

$$f(\theta, k) = \frac{1}{2ik} \sum_{l=0}^{\infty} (2l+1) \exp(2i\phi_l - 1) P_l \cos(\theta) \tag{1.3}$$

[2]LEEM is a full-field technique while LVEM is a scanning technique

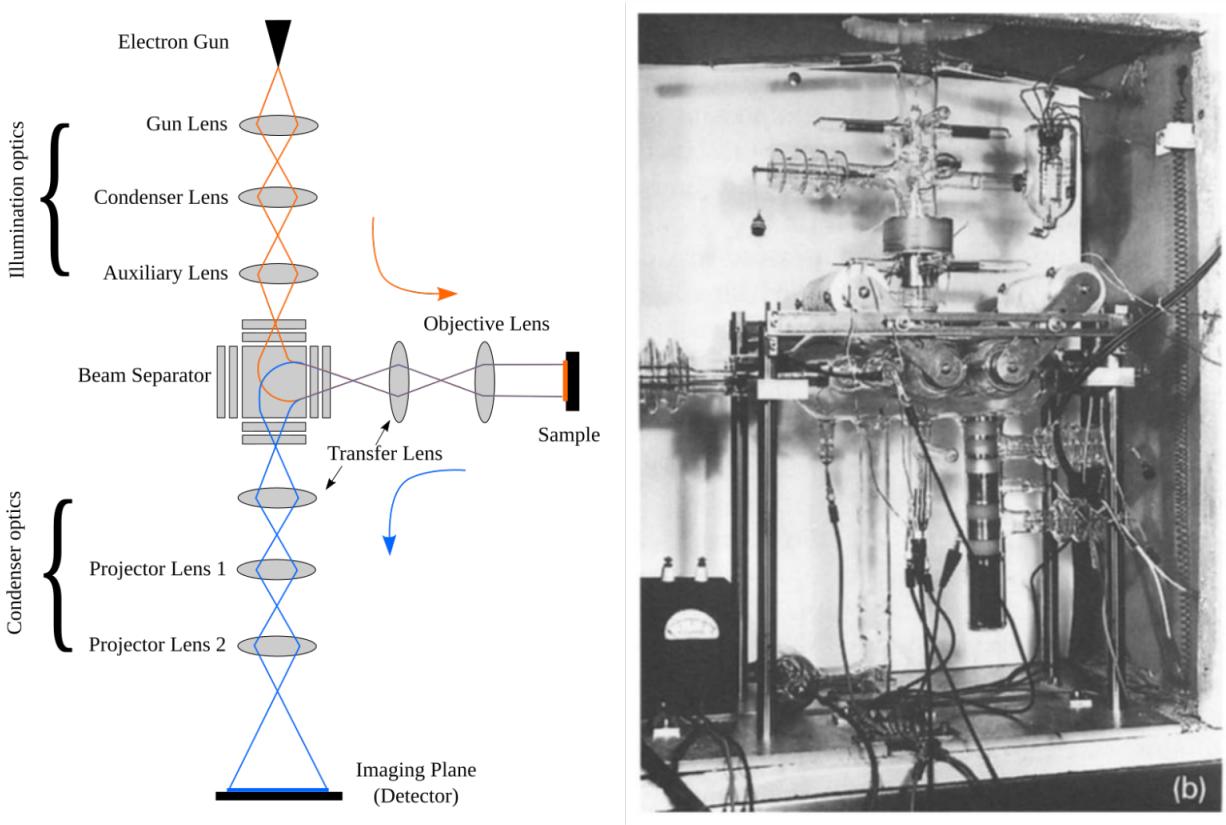

FIGURE 1.5: On the left panel is a typical design of a standard LEEM with a 90° beam separator (a magnetic device that separates electrons going to and coming from the sample). Electrons from electron gun to sample are in orange, electrons from sample to detector are in blue. On the right panel is the first prototype of a low-energy electron microscope presented in 1962 (Reproduced from [12])

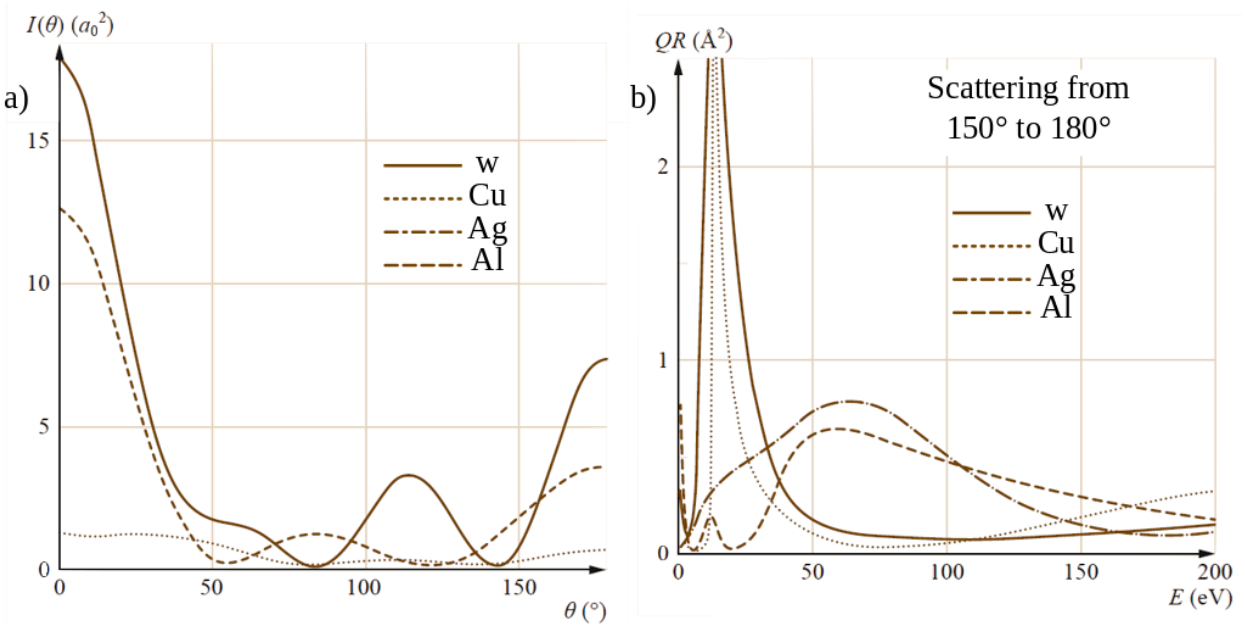

FIGURE 1.6: Intensity of electron scattering of different materials calculated from equation 1.3. a) Angular dependence for 50 eV electrons b) Energy dependence of backscattering into a 30° cone around the backward direction ($\theta = 180°$) (Adapted from [9]).

with k the wavenumber, θ the scattering angle and P_l are Legendre's polynomials. Figure 1.6 shows the angular and energy dependence of the scattering intensity of electrons on different materials.

This figure (panel a) shows that at 50 eV the scattering is dominantly backwards. Panel b shows that the backward scattering is most important at low energy, under 50 eV, and that there can exist a strong energy-dependence of the intensity of scattering, which explains why LEEM images are measured at different interaction energies.

When the interaction energy is set to a negative value, the electrons don't have enough energy to reach the surface of the sample and are mirrored away at long distance. This imaging mode is called mirror electron microscopy (MEM).

LEEM is sensitive to local variations in surface potential, and therefore allows the topology, composition and thickness of samples to be probed over a few nanometres[9]. Typical spatial resolutions today are 15 nm to 20 nm, with a record at 1.5 nm. However, this record is based on aberration corrections and the configuration of the device capable of delivering this resolution is not stable for more than a few minutes[13].

A common complementary technique to a LEEM instrument is to add an optical source that will excite the sample and release electrons, to perform photo-emission electron microscopy (PEEM). The photo-emitted electrons can be analysed in the same way that the reflected electrons in LEEM so the imaging optics are the same as in LEEM. PEEM is thus useful to obtain more information on the sample but also to align the instrument in first installations. When the light source is an X-ray emitter, this technique is called XPEEM.

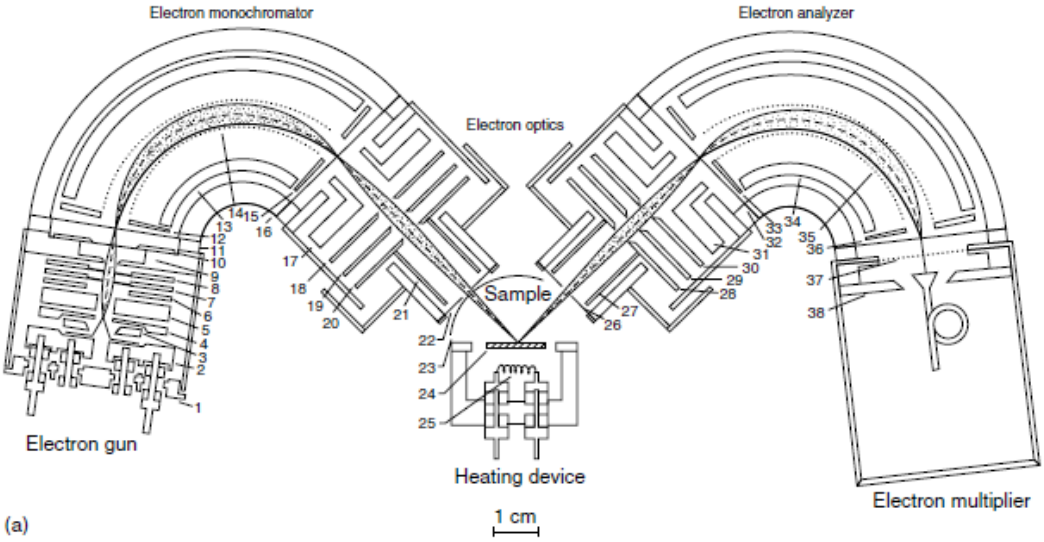

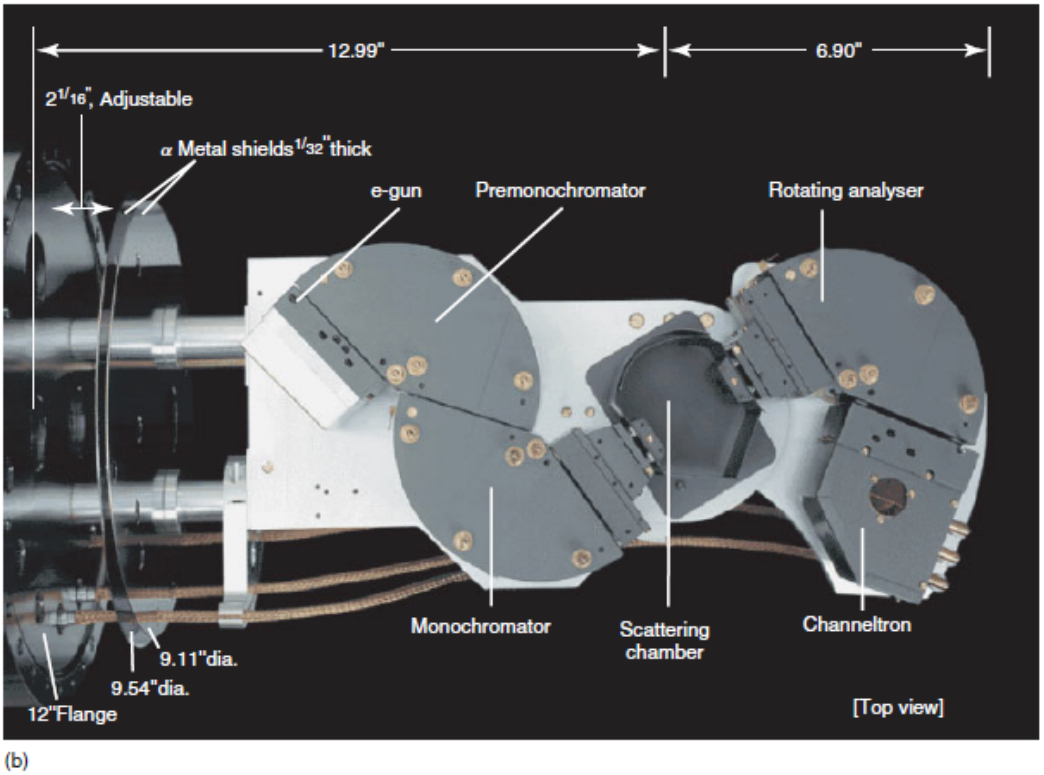

FIGURE 1.7: a) Schematic of a simple pass HREELS instrument. Note the symmetry of the electron monochromator and electron analyser. b) Picture of a modern high resolution electron spectroscope featuring a double-pass monochromator. (Reproduced from [14])

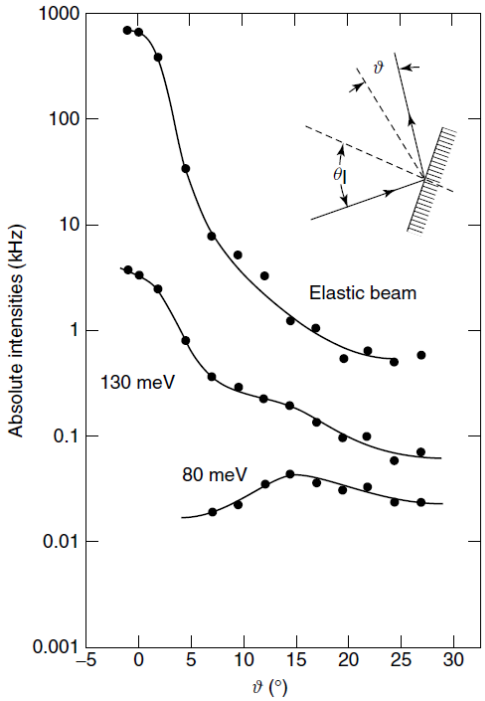

FIGURE 1.8: Angle dependence of the intensity of H vibration modes on a tungsten surface. The 130 meV mode is dipolar, the 80 meV mode is best described by impact scattering. (Reproduced from [15])

High-resolution electron energy loss spectroscopy: HREELS

When low-energy electrons are scattered by a surface, they can also be scattered inelastically, i.e. by changing their energy during the interaction. The beam of electrons scattered by the surface can then be collected by electrostatic or magnetic lenses and enter an analyser, an element that will disperse the electrons according to their energy E_{in} (see section 1.1.3 for details on energy analysis). A position-sensitive detector (or a combination of a simpler detector and an energy selection-slit) can then measure the remaining electron energy E_{out} and one can construct the energy loss spectrum of the surface using the relation:

$$E_{\text{Loss}} = E_{\text{in}} - E_{\text{out}} \tag{1.4}$$

This is the operating principle of High-Resolution Electron Energy Loss Spectroscopy (HREELS). It is a standard technique of surface analysis, developed since the late 1970s[15]. A schematic and a photograph of an actual HREELS instrument are shown on figure 1.7. It uses energy loss to probe the surface of a sample and identify its chemical composition. Indeed, the energy deposited by electrons at 1 eV to 10 eV is of the order of a hundred meV and corresponds to excitations of vibration modes of adsorbed molecules or surface phonons[14].

The inelastic interaction between the incident electron and the surface can be described by two main mechanisms: long-distance dipole scattering, in which the electron is represented by an oscillating field and follows dipole selection rules; and impact scattering, which corresponds to a very short-range interaction and requires full quantum processing. This phenomenon can also be called resonant scattering when the electron remains momentarily trapped on the surface, which can change the shape, energy, and

angular distribution of the resonances[16].

These two mechanisms coexist but have different intensities and especially different incidence angle dependencies, which allows one or the other mechanism to be favoured by varying the angle of incidence of the electron beam. Dipolar scattering is mainly specular, while impact scattering is almost zero in the specular direction[14]. This feature of HREELS is visible in figure 1.8.

In addition to identifying the chemical bonds present on the surface, the dipolar selection rules make it possible to determine the inclination of these bonds and thus the adsorption geometry of the molecules surveyed. The selection rules for impact scattering are more difficult to rationalize, however, we note that molecules diffusing strongly by one mechanism diffuse weakly by the other. This additional angle dependence therefore increases the analytical power of this technique, which explains why the vast majority of spectroscopes allow the rotation of the analyser with respect to the specular direction. The energy losses of the electron beam in contact with the surface therefore depend on: their initial energy, the composition of the surface, the rules for selecting dipole transitions and the angle of impact of the electrons. Modern commercial instruments are capable of spectral resolutions around 1 meV with an electron beam on sample with an energy width less than 0.5 meV[17].

1.1.2 Spectroscopy in an electron microscope

Up to now we presented ways of acquiring images of samples, or spectrum of samples, in different instruments. An obvious direction of improvement for these kind of instruments is to offer both microscopy and spectroscopy information about a sample. In this section we will present the existing instrumental solutions, and show that they do not offer high spectral and spatial resolutions for surfaces.

In the LEEM, the central design element is the beam splitter (see fig. 1.5), which mostly consists of a magnetic prism, i.e. a set of regions with very well controlled magnetic fields oriented perpendicular to the direction of electron propagation. Its role is to separate the electrons going to (incident) and coming from the sample (backscattered). The deflection being due to the Lorentz force effect ($\vec{F} = -e\vec{v} \wedge \vec{B}$, with $\vec{v}$ the electron velocity, $\vec{B}$ the magnetic field), it is not the same for two electrons of different energy. This type of prism rotates the incident beam by a certain angle (45°, 60° and 90° are the most common values), but the exact angle of rotation is dependent on the energy of the electrons (this principle is widely used in magnetic analysers).

This small angular dispersion at the output of the prism is generally compensated by the optics, but can also allow to couple a spectroscopic measurement to LEEM imaging. However, the typical dispersion of the prisms is about 10 µm/eV for electrons of 10 keV[18]. This is not dispersive enough to acquire images with a spectral resolution of the order of 5 meV, which is necessary to map vibrational energy losses, that is one of the motivations of the HREELM project.

Since the 1960s, some transmission microscopes have been able to acquire images from electrons selected according to their energy loss within the sample[19]. In this type of apparatus the spectral resolution is obtained by energy filtering, i.e. a dispersive element is placed between the sample and the detector and a slit is used to select the electrons having the energy at which one wants to acquire an image. This configuration is called serial, because acquiring an image at another energy will require another measurement.

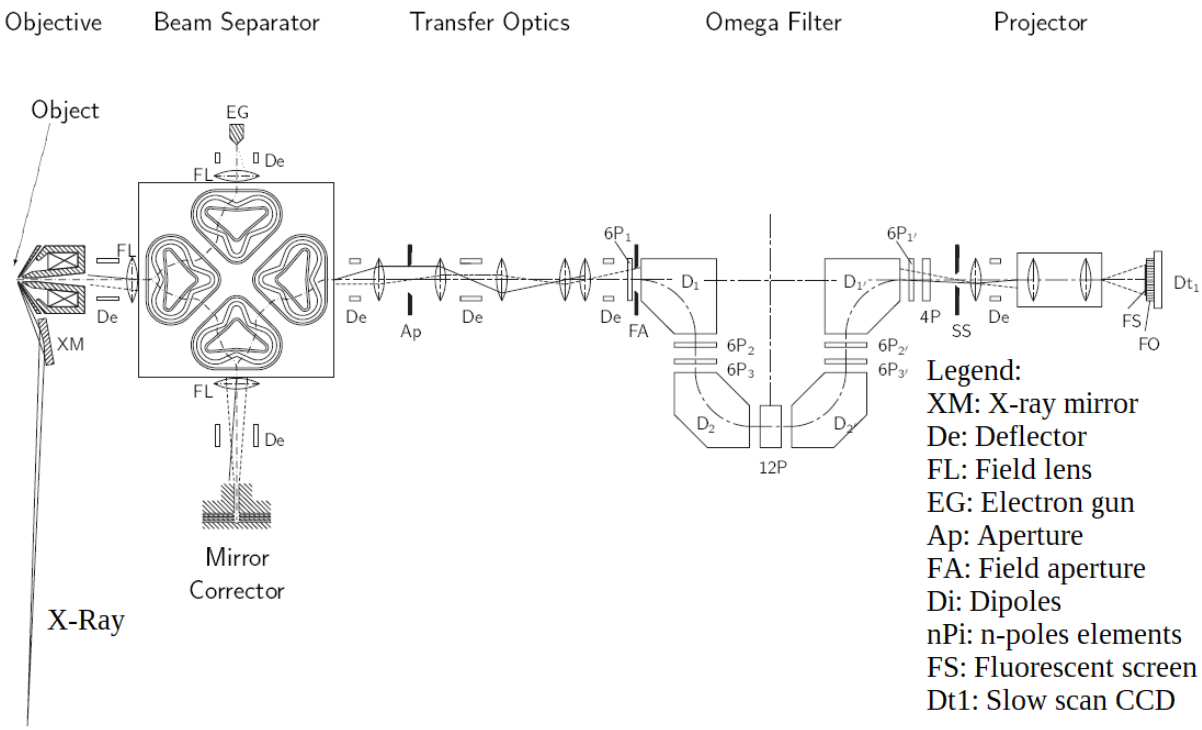

FIGURE 1.9: Design of the SMART instrument installed at the BESSY II Synchrotron. It is aberration corrected and allows high spatial resolution LEEM and XPEEM studies, among other techniques. The sample (object) is placed at the far left, at the focal point of the objective lens. (Reproduced from [23]).

In the parallel configuration, one removes the slit and all the electrons are detected at the same time. The electron dispersion axis then forms the energy axis[20]. This technique is called ESI (for Electron Spectroscopic Imaging) or EFTEM (for Energy Filtering Transmission Electron Microscopy)[21]. The great progress in aberration correction and instrument design has allowed *scanning* transmission microscopes to recently reach spectral resolutions below 5 meV while maintaining spatial resolutions of the order of the nm[22]. However, these instruments are particularly complex and expensive, and are only sensitive to the total thickness of the sample. Moreover, acquiring an energy-resolved image here requires scanning the entire surface point by point, which can result in acquisition times that are too long to be feasible in some applications. Finally, the high energy of transmission microscopy electrons can degrade and damage the sample. Still, these techniques represent an important benchmark for any method that aims to combine excellent imaging and spectroscopy.

Transmission electron microscopy aside, there are other instruments that combine electron microscopy and spectroscopic analysis, in particular with LEEM imagery. One of these instruments is installed at the BESSY synchrotron (for X-rays studies) and is called SMART for "Spectro-Microscopy with aberration correction for relevant techniques". It is a versatile tool that allows, among many other techniques, to perform "energy-filtered" LEEM. Its design can be seen in figure 1.9. For the electronic illumination it uses a standard electron gun without monochromation, meaning that the energy spread of the electron probe is larger than 0.3 eV. Furthermore, in LEEM mode and for symmetry reasons,

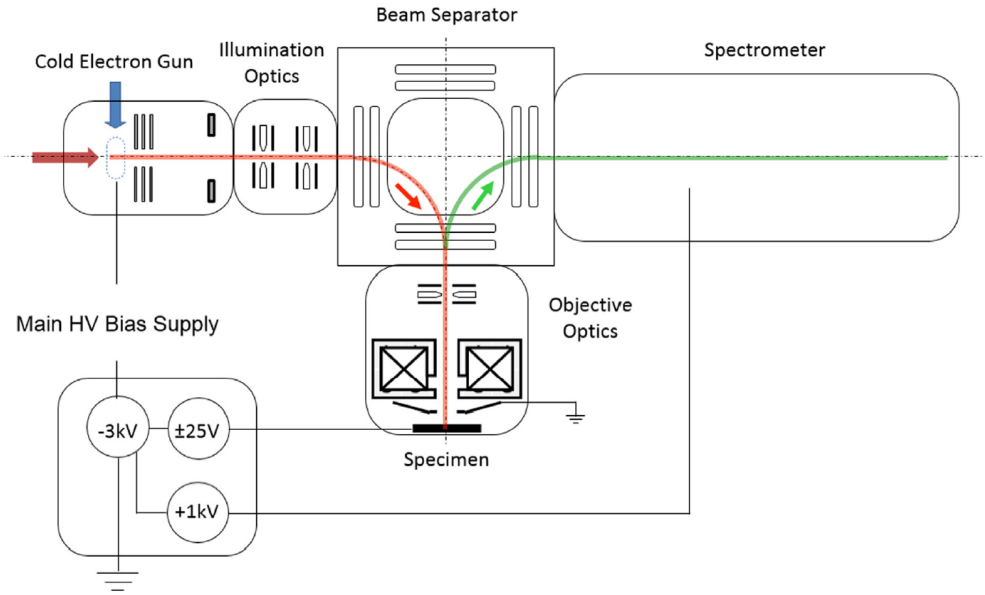

FIGURE 1.10: General design of the HREELM instrument. The large red arrow correspond to neutral Cs atoms, the blue arrow is an ionising laser that produces the electrons, represented in red as they are travelling to the sample and in green when they are coming from the sample to the spectrometer and detector. Reproduced from [24].

the illumination energy has to be the same as the detected energy[23] (the energy that electrons must have to be detected). This means that the LEEM image will be acquired with only elastic electrons, but it also means that the spectroscopic analysis is limited to the photo-emitted electrons. Hence it is not a true energy-filtered LEEM and can't provide an electron energy-loss spectrum.

Ultimately, and despite the strong interest and recent instrumental developments, there is currently **no technique allowing the simultaneous acquisition of high spectral resolution energy loss spectra, imaging with very good spatial resolution and sensitive only to the surface of a sample**. HREELS and LEEM have several important instrumental similarities: the need for ultra-high vacuum, the use of a low energy electron probe, the wide illumination of the sample and the backscattering of electrons (as opposed to a transmission measurement). These instrumental similarities and the additional information on a sample they are able to provide justify the ambition to combine them in a single instrument. In a chapter of the very recent *Springer Handbook of Microscopy* devoted to the implementation of electron energy loss spectroscopy in the LEEM, the author states that[9]:

> *"Obviously, the LEEM instrument will not be able to match [HREELS's] level of technical sophistication"*

The goal of the HREELM project is precisely to achieve this kind of sophistication.

1.1.3 HREELM: a new design for a new kind of electron microscope

From this observation, as well as from the common features noted in section 1.1.2, the idea of combining LEEM and HREELS in one instrument emerged. The HREELM collaboration published a proposition of the design of such an instrument. It is called HREELM for High-Resolution Electron Energy Loss Microscope[24], and we present here its main features. The biggest part of the electron column design was realised by Marian Mankos and Kash Shadman from the Electron Optica company. They performed a full simulation of this column[25] with electron-optical software packages developed by MEBS, Ltd., in particular the SOFEM program (second order finite element method field solver); the PRISM2 program (analytical computation of optical properties and second and third order aberrations of magnetic prisms); and the IMAGE program (Monte Carlo simulations of combined lens aberrations and Coulomb effects).

The design we[3] developed and published can be seen on figure 1.10, and I was particularly involved in the conception of the electron gun and the choice of the detector. This design features an electron source, illumination optics, a beam splitter prism, objective optics, a sample holder, as well as a spectrometer.

It is quite resemblant to a standard LEEM column, with some significant differences. All the lenses are magnetic lenses, except for the immersion lens that is both electric and magnetic. The major differences of this instrument with a LEEM column is the use of a bright, highly monochromatic electron source, and the addition of a high-performance spectrometer, which are both indispensable for high spectral resolution analysis. The development of such an electron source is the core goal of the present thesis and is paramount to the success of the project. Theses elements require to adapt the standard design of a LEEM column, as we will see in section 1.1.3.

As the discussion of the instrument design and operation will involve details about the electron optics, we introduce some elements of understanding about this subject in the following section.

Elements of electron optics

A few basic elements of electron optics are necessary to describe the operation of the device effectively. Clearly, the undulatory character of the electron justifies the very strong analogies existing between the field of photonic optics and electronic optics. This first domain was developed well before the second, which explains the massive use of the vocabulary of photonic optics for electron optics ("lens", "mirror", "image", "ray", or "prism"...). This is not limited to the vocabulary, since many concepts have an equivalent definition in both fields. Thus, the concepts of image plane and diffraction plane are used in the same sense in electron optics and in photonic optics: the image plane is the one-point collection plane of electrons having the same point of creation (regardless of their initial momentum) and the diffraction plane is the one-point collection plane of electrons having the same initial momentum (regardless of their initial position). In an optical system, when the detector is placed in the image plane of the sample, one acquires its real-image, whereas a detector placed in the diffraction plane will acquire its diffraction image, or diffractogram.

[3] the HREELM collaboration

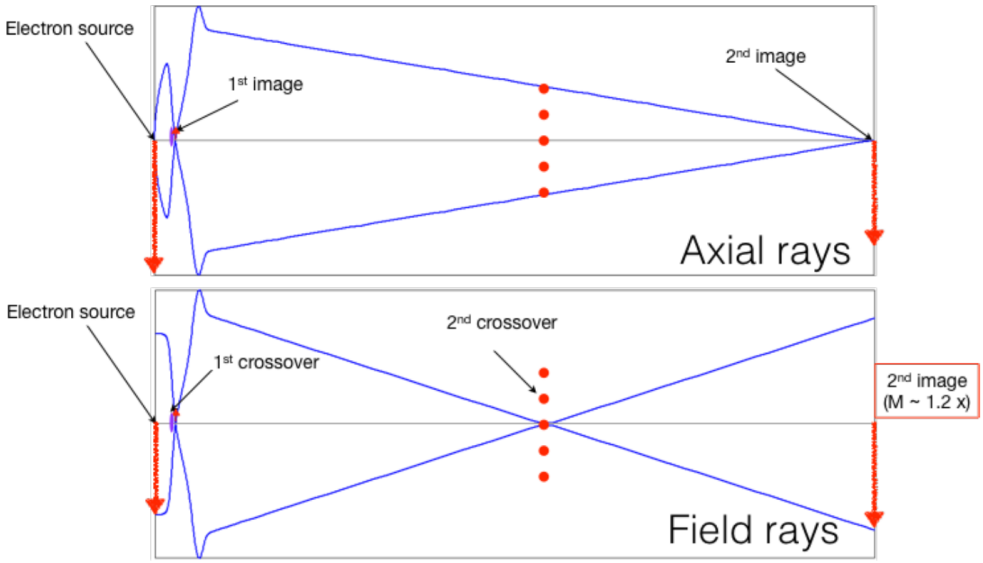

FIGURE 1.11: Ray representation of the effect of two lenses. On the top panel two axial rays are represented, starting from the optical axis with an angle. They cross the optical axis at the first and second image points. On the bottom panel two field rays are represented, starting at a distance from optical axis but with no angle. They cross the optical axis at the first and second crossovers. Arrows represent real-images, lines of dots represent diffraction-images and M is the magnification of the source.

The concept of rays is also very useful in electron optics. Figure 1.11 shows a typical ray construction in the paraxial approximation where only two rays are sufficient to describe the positions of the image planes and diffraction planes in an electron microscope. The paraxial approximation is valid for small angles (<10°) and small displacements from the optical axis and consists in considering that:

$$\sin\theta \approx \theta,\ \tan\theta \approx \theta,\ \cos\theta \approx 1$$

This approximation actually consists in linearising the problem, making two rays a complete basis of all possible electron trajectories. These two rays are usually taken as the field ray and the axial ray: the field ray corresponds to the trajectory of an electron with momentum along the optical axis but having an off-axis initial position (see bottom panel of figure 1.11), while the axial ray corresponds to the trajectory of an electron starting on the optical axis with a momentum oriented off-axis (see top panel of figure 1.11). It is then very simple to locate the image planes and the diffraction planes along the column: when the field ray crosses the optical axis (a point called cross-over), it defines a diffraction plane, while the axial ray crosses the optical axis in the image plane.

In the context of electron microscopy, it is thus essential to determine which plane will be placed on the detector: by placing the image plane of the sample on the detector it will be possible to acquire a real image of the sample (with a certain magnification determined by the optics), while a detector placed in the diffraction plane of the sample will permit the analysis of the momentum distribution of the electrons leaving the surface (this kind of "image" is then called a diffractogram).

The lenses used to manipulate the electron beams are either electrostatic or magnetic,

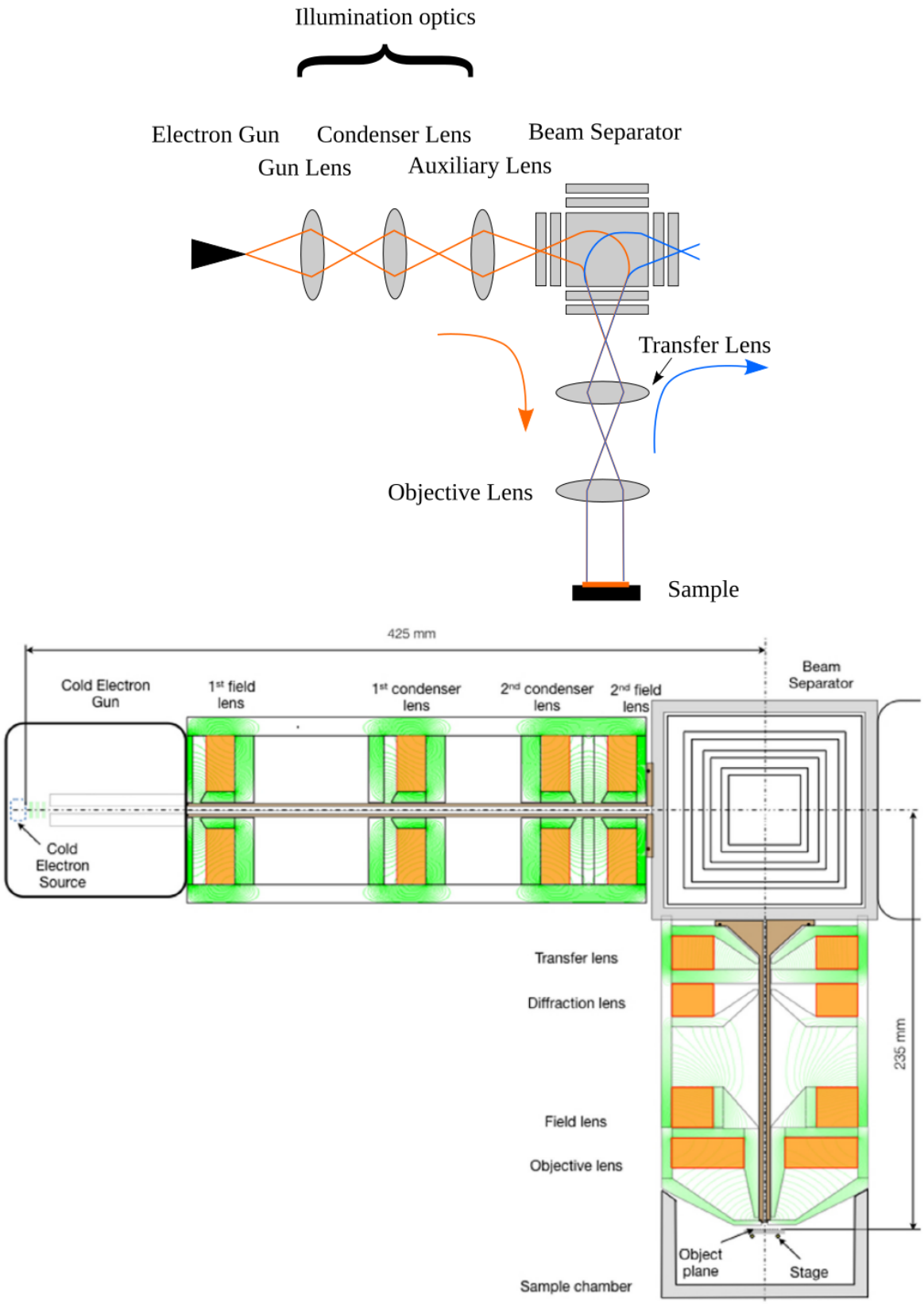

FIGURE 1.12: Design of the HREELM instrument showing its subsystems: an electron gun, illumination optics, a beam splitter prism and objective optics, Reproduced from [25] (bottom panel). The top panel shows a standard LEEM design for comparison. Note the added lens before and after the magnetic sector in the HREELM design.

the former being typically simpler to model and design, the latter typically having better aberration performance. An electrostatic lens is often constructed from three electrodes, the front and back ones kept at the common ground, while the potential of the central one is the free parameter that determines the focal length of the lens. This configuration is called uni-potential or Einzel lens, and it has the advantage of acting as a lens without modifying the beam energy. The shortcomings is that the magnification value of this lens is fixed by distances between the source and the image. A complete control of focal length and magnification without changing the electron energy requires an additional electrode like in the zoom lens that features four electrodes.

The electrodes themselves can be flat (typically 1 mm thin) with a small hole (they are then called aperture electrodes and the resulting lens is an aperture lens), or thick and with a wide aperture giving cylindrical electrodes and a cylindrical lens. A rule of thumb for the comparative properties of these lens is that the apertures lenses are very compact and powerful (very small focal length is easily achievable), but the cylindrical ones have less aberrations due to their smoother effect on the beam angle but can be excessively long for some applications.

Magnetic lenses can be round, or composed of pairs of identical quadrupoles, rotated from one another by 90°. See section 4.2.1 for details on magnetic quadrupole lenses. It is important to note that, just as in photonic optics, when an electron beam is focused at the center of a lens, this lens has no effect on the collimation of that beam. This principle is widely used in instruments design and in particular in HREELM.

As we saw earlier, the prism of the LEEM is intrinsically a dispersive element. For application in an electron microscope, the different field regions inside the prism are therefore optimized (in terms of size, field intensity, spacing between zones) to deflect the electron beam at a pre-determined angle, minimizing its dispersion and adapting the lens effects to the rest of the column. The effect of an optimized magnetic prism is then simply described by considering two distinct planes, the slit plane and the achromatic plane (see figure 1.13). The achromatic plane corresponds to the image plane of a beam for which the dispersion of the prism is almost zero, whereas the dispersion will be maximal (but low, about 10 µm/eV) for electrons whose image plane corresponds to the slit plane. Thus to keep the real image or the diffraction image of the sample intact (free of dispersion), it should be placed in the achromatic plane of the prism.

This short introduction of the relevant terms and concepts will now be used to describe the working principle of the newly design HREELM instrument.

Working principle of the HREELM

In HREELM, high-resolution microscopic images are acquired at each loss-energy. This requires that the electron probe has a zero angle of incidence on the surface, so this imposes a design similar to standard LEEM instruments. This resemblance is evident from figure 1.12, where a standard LEEM optics and the HREELM optics are compared.

The measuring principle of the HREELM instrument is as follows: the electrons emitted by the source are accelerated and collimated by the illumination optics in the magnetic prism, which deflects it by 90°. The objective optics then illuminates the sample by placing the source diffraction image in the sample plane. The sample is placed in an immersion lens that strongly decelerates the incident electrons to illuminate the sample with low-energy electrons (0 eV to 10 eV). This type of lens is a central element of the LEEM

technique and is designed so that the sample is placed inside the lens itself, allowing very good collection of the scattered electrons. These backscattered electrons are re-accelerated by the immersion lens and transported into the magnetic prism which then deflects them towards the spectrometer. The spectrometer performs the energy analysis and an image (real image or diffraction image, depending on the selected measuring mode) is placed on the detector, along with an analysis of energy losses.

As we already saw, the design of HREELM has LEEM as a starting point, to which we add a monochromatic electron source and an energy analyser, but also 3 additional lenses: 1 illumination lens and 2 objective lenses. Indeed, in the standard operation of a LEEM column, the objective optics (often composed of a single lens) allow only one mode, which corresponds to placing the image of the sample in the achromatic plane of the prism to keep the high spatial resolution of the microscope. A measurement of the diffractogram (or diffraction image) of a sample is always possible by modifying the post-prism optics, but the diffraction plane of the sample is then necessarily placed in the slit plane of the magnetic prism, i.e. in the dispersive plane. This dispersion considerably reduces the spectral resolution obtained on the diffractograms, so we had to adapt the design to circumvent this effect. Therefore, two different measurement modes are provided in HREELM: the image mode and the diffraction mode.

In image mode, the objective lenses are optimized to place the real-image of the sample in the achromatic plane of the magnetic prism, which is the standard functioning of LEEM.

In diffraction mode, the image of the sample is placed in the slit plane of the prism so the diffraction image is placed in its achromatic plane, which guarantees minimal dispersion. These two modes are compared on figure 1.13, with the image mode on top and the diffraction mode on bottom.

The optical simulation program that were used to optimize the column assumes a straight optical axis so in the simulation code the achromatic plane is at the center of the prism but in the real instrument it is located at the 45° symmetry plane (see the dotted blue "achromatic plane" on figure 1.13). Thus the electron trajectories are depicted on figure 1.13 in blue lines without rotation (as simulated) and with a manual 90° rotation (corresponding to the physical behaviour).

The swap between the image mode and the diffraction mode must be achieved without modifying the illuminating conditions of the sample i.e. without modifying the objective lens. This illumination is achieved by placing the diffraction image of the source in the sample plane, because the diffraction image of the source is expected to be closer to a top-hat distribution than the real image (probably closer to a Gaussian distribution), and hence more uniform. Keeping this illumination the same between the two modes requires one additional lenses between the electron source and the prism (the 2^{nd} condenser lens is used only in the diffraction mode), and two additional lenses between the prism and the specimen (the diffraction lens is used only in the diffraction mode).

The diffraction lens is placed at the location of a source image with low magnification to have no impact on the incident electrons and thus not change the sample illumination, and send the diffraction image of the sample into the achromatic plane of the prism.

In both modes, the prism transfer the electrons into the spectrometer, that will allow the analysis in terms of energy losses, and thus the coupling between a spectroscopic and a microscopic measurement.

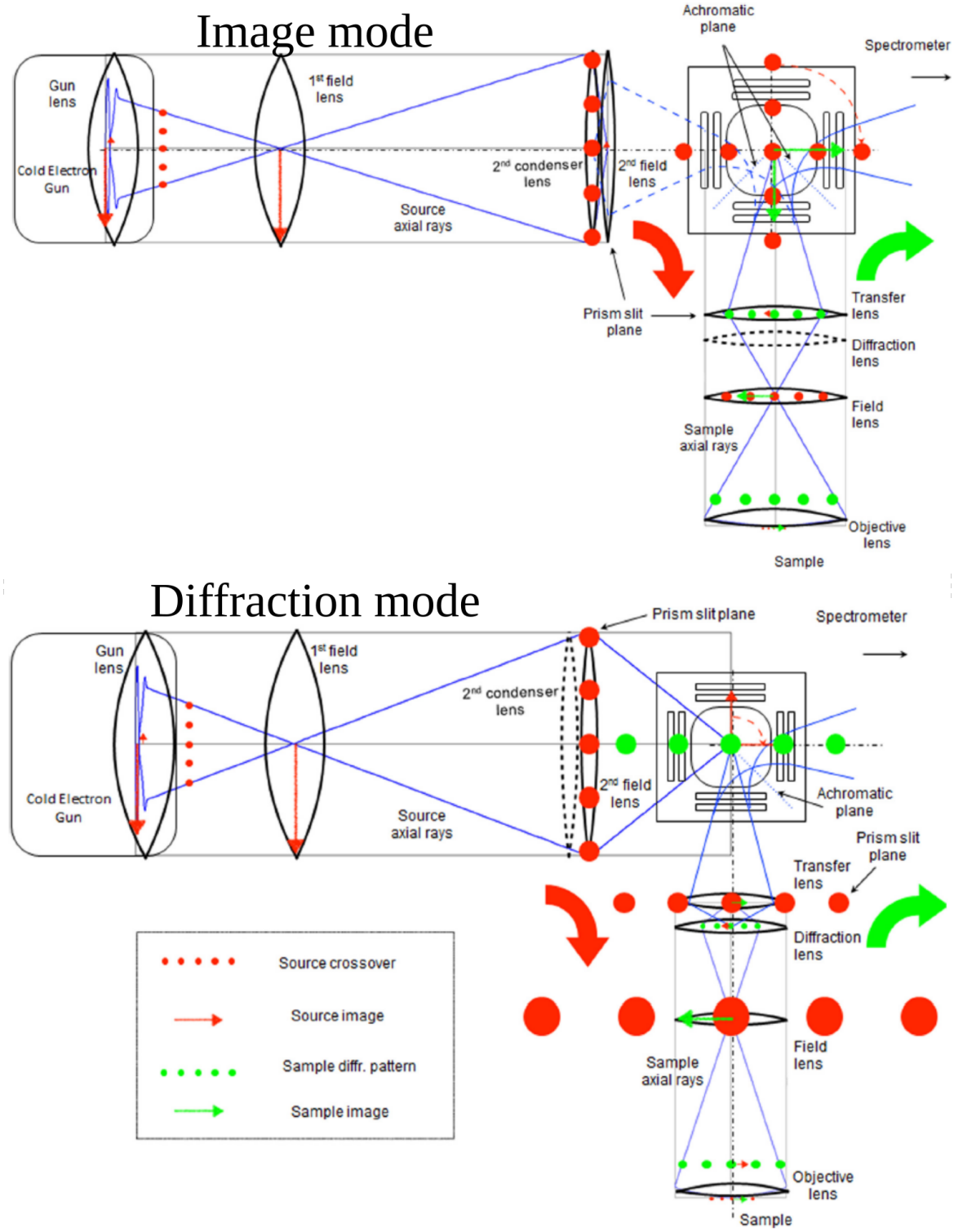

FIGURE 1.13: Representation of the optics of the HREELM in Image mode (top) and in Diffraction mode (bottom). Blue lines are the electron trajectories. Red (green) elements are for incident (backscattered) electrons, respectively. Small coloured arrows represent real-images, coloured lines of dots represent diffraction-images from the source or the sample, in scale with the actual magnification throughout the column. Big coloured arrows depicts the rotation of the beam due to the prism. Trajectories and patterns are represented *with and without the rotating effect* of the prism for clarity of lens roles. Reproduced from [25].

Energy analysis in HREELM

There are two different kinds of spectrometer that offer the high resolution and can be coupled with our design: a time-of-flight spectrometer (TOF) or a dispersive analyser, for an example a hemispherical analysers (HSA). Schematics of these two different energy analysis can be seen on figure 1.14.

In a TOF spectrometer the energy analysis is performed by flying electrons at low energy, the drift energy, in a field-free tube of length L with a precisely known starting time (set to 0). The arrival time τ of the electron (or time-of-flight) then gives its energy E_d via the formula:

$$E_d = \frac{L^2 m_e}{2\tau^2} \tag{1.5}$$

which can be compared with the energy of electrons arriving at the sample. The difference in energy can then be attributed to energy losses at the surface of the sample (see equation 1.4), and a spectrum of energy losses can be reconstructed. The energy resolution dE on a time-sensitive detector with a temporal resolution of $d\tau$ is then given by:

$$\frac{dE}{d\tau} = -2\left(2\sqrt{\frac{E_d^3}{m_e}}\right)/L \tag{1.6}$$

With a DLD from Surface Concepts ($d\tau \approx 150\,\text{ps}$)[26], we can thus achieve 5 meV energy resolution with a drift energy of 9 eV in a 1 m-long drift tube, making ToF analysis suitable for HREELM. The spectral range[4] can go easily up to 6 eV. Increasing this range would decrease the acquisition rate (at 3 eV the electron has a ToF of 1 µs that already limits the acquisition rate to 1 MHz), necessary to avoid bunches overlap (see figure 1.14), thus increasing the measurement time to keep the same statistics. One could also increase the spectral range by decreasing the energy resolution i.e. increasing the drift energy to a few tens of eV. A detailed example of how we could implement a ToF acquisition sequence in HREELM is presented in section 5.1.5. In that case, the electron source must be able to produce electrons in a pulsed way, with a very low temporal dispersion (not more than 150 ps).

A parallel hemispherical analyser is composed of an entrance slit, a region of deflection and a position-sensitive detector. The incoming beam of electrons is collimated on the slit, that selects a part of the beam, which is then deflected by a magnetic field onto the detector. Usually the deflection is around 180° from the slit (hence the name of this analyser). The entrance slit is useful to ensure that the electron beam's initial size is small in comparison with the final spot on the detector. This way we make sure that the size of the electron spot on the detector comes from the energy spread induced by the interaction with the sample (i.e. energy losses) and not from an initial position spread. The temporal precision that was necessary for the ToF analysis is thus translated here to a spatial precision, because the energy scale is "projected" onto the spatial dimension and not on time. The width of the entrance slit w actually defines the energy resolution ΔE of such an instrument:

$$\Delta E = wE/2R \tag{1.7}$$

[4] the size in eV of the acquired spectra

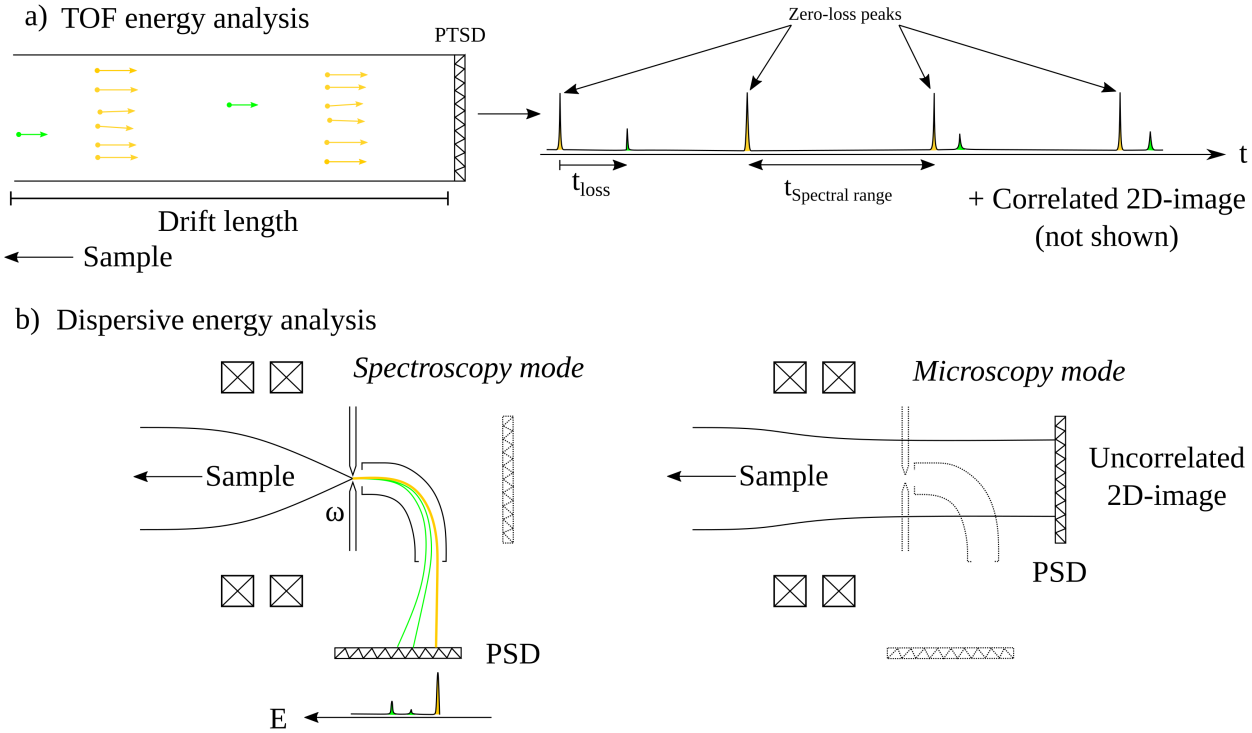

FIGURE 1.14: Schematics of the two proposed energy measurement for HREELM. a) TOF energy analysis, requiring a pulsed electron source and a high-performance position-and-time-sensitive detector (PTSD), retrieves the energy loss spectrum from time delays between electrons. Electrons in yellow are elastically scattered while green electrons are inelastically scattered. b) Dispersive energy analysis requires either two position-sensitive detectors (PSD), and two acquisition modes: spectroscopy and microscopy as represented here; or one detector and scanning the sample in one-dimension (not represented here, see text). In the represented case, the energy loss spectrum is directly acquired from the electron position after deflection, which is turned off in microscopy mode. The deflection angle represented here is 90° but other angle are possible.

where E is the pass energy and R is the radius of the hemisphere. A 5 meV energy resolution can be obtained with an energy selecting-slit width of 200 µm, an energy of 25 eV and a radius of 50 cm. Such a small pass energy means that a strong electrostatic deceleration to bring electrons from the transport energy (3 keV in the published design of HREELM[24]) to 25 eV (ratio of 120) is necessary. As this deceleration follows Liouville's conservation theorem, it results in the growth of the beam dimensions and divergence. Indeed, we have:

$$M\sqrt{E}\sin(\alpha) = \text{constant} \tag{1.8}$$

where M is the magnification of the beam and α is the divergence semi-angle of the beam. If the beam is kept collinear during the deceleration, this gives a beam size multiplied by 11. To minimize the current loss at the slit, the initial beam size must thus be around 50 µm at the transport energy[27]. A real advantage of this technique is that the energy analysis can be performed continuously, and does not require a pulsed electron source. The maximum value of the spectral range is fixed by the spectrometer geometry so the only way to increase it without decreasing the energy resolution is to increase the physical dimensions of the analyser (in analogy to ToF analysis where we could increase the temporal dimension of the analysis with a longer drift tube or a lower drift energy), which is not practical. As obvious from equation 1.7, we can increase the spectral resolution by reducing the slit width. This reduces the current on the detector by a factor that can be around 100[5], so such an energy analyser requires a higher source current than the ToF spectrometer. Furthermore, the coupling of a very small slit to an electronic microscope column can represent a real design challenge, particularly with the strong deceleration imposed by the low pass energy.

Finally and most importantly for HREELM, with a dispersive energy analyser the energy scale is projected to a spatial dimension (whereas the ToF spectrometer "projects" the energy scale on the time dimension). This is particularly problematic if we want to acquire an image of the sample, as information about the starting point and the energy of the electron are scrambled in one direction of space. This demands the adaptation of the acquisition sequence:

- either we measure the image in one dimension along with the energy losses, and scan the other dimension
- or we perform two different acquisitions, of the sample's image and of the energy losses, as described on figure 1.14. This demands two detectors, increases acquisition time and removes the possibility to precisely correlate the LEEM contrast with the energy losses, forming what we call a correlated image.

The first version of this measurement scheme is favoured because it allows the acquisition of spectroscopy enriched images (correlated images), but it introduce other experimental difficulties as it requires scanning one dimension.

Both solutions of spectrometers are possible, and both impose strong constraints on the electron source. In both cases the energy spread of the electron beam must be below 5 meV to achieve the expected spectral resolution. For a ToF analyser, the electron source must provide very short electron pulses (around 150 ps). For an HSA, the electron source must be intense, typically ten times more intense than in ToF, because of the current losses

[5] this values depends on a lot of experimental parameters and is to be adjusted for each measurement to reach the desired intensity/resolution ratio

at the entrance slit of the spectrometer. Considering that a HREELS spectrum with a decent signal over noise ratio can be constructed with 1×10^3 inelastic electrons and that we want to acquire a full spectrum for each pixel of the image (say an image of 512*512 pixels, so 2.6×10^5 pixels), this gives us 2.6×10^8 inelastic electrons to acquire to consider a measurement complete. This number can be multiplied by 10 to account for the elastic/inelastic electrons, and by 10 again to account for the absorbed/scattered electrons ratio. If a measurement takes 1 minute, this requires at least 70 pA of electron current. It is thus reasonable to consider that a current of 100 pA is enough for ToF energy analysis, and that a HSA requires around 1 nA of current.

These constraints form the basis of the research directions followed during this thesis, to elaborate an electron source fitted for this ambitious experimental project. The design presented in this section should allow, for the first time, to acquire either low-energy electron microscopy images or diffractograms coupled with energy loss analysis at high spectral resolution. In addition to the obvious interest of being able to correlate spectroscopic and in-situ microscopy measurements, the ToF energy analysis version of this design allows to realize an advanced function of transmission microscopy instruments, energy-filtered imaging, without the usually associated instrumental heaviness (see section 1.1.2). In fact, in a single acquisition, a spectroscopic-rich image is recovered, which can be transformed into energy-filtered imagery by post-acquisition processing. This special feature of ToF energy analysis (not present in one version of the HSA energy analysis because of the sequential acquisition of spectroscopy and microscopy, but still possible at the cost of scanning one dimension of the sample) makes it the preferred energy analysis for HREELM, but the associated additional requirements on the electron source should incite us to keep both solutions in mind. At the core of this instrument in the electron source. In the next section we present existing sources in microscopy and spectroscopy, and explain why these are not adapted to HREELM.

Section summary

The HREELM project

This section was the occasion to present the HREELM project in the context of electron microscopy, that has the ambition to construct a novel instrument for surface sciences enabling high-resolution imaging similar to LEEM combined with high-resolution energy-loss spectroscopy (HREELS). This would be the reunion of two well established technique into a unique instrument, that would provide simultaneous, in-situ chemical analysis and electronic imagery. Some very-high-end electron microscopes already allow electron energy loss spectroscopy, but mostly with poor energy resolution (at the exception of one kind of instrument of the Nion company[28,29]). Furthermore, these electron microscopes use high-energy electrons, in transmission mode.
HREELM would on the other hand allow simultaneously surface microscopy and spectroscopy, with very-low energy electrons. The applications would be numerous, both fundamental as a way to relate the formation of contrast in LEEM with chemical structure; and very applicative as a high-performance material analysis for biology, chemistry, physics or geology, for example.
The electron column design is realised and published, based on a standard LEEM design with some modifications: the addition of pre- and post-prism lenses, to allow two different acquisition modes: the image mode and the diffraction mode. Some design choices still need to be made, especially for the energy analysis. We have two possibilities: continuous energy analysis, or pulsed energy analysis; both with advantages and drawbacks, but this choice will have a strong influence on the rest of the design and particularly on the electron source, at the heart of this instrument. In particular ToF-energy analysis is more ambitious in terms of final instrumental feature, but is also more demanding on the electron source because of the required temporal precision. The requirements for the electron source are summed-up in the following table:

Spectrometer	ToF	HSA
Source	Pulsed	Continuous
Flux	10 pA to 100 pA	$\geqslant 1$ nA
Energy spread	$\lesssim 5$ meV	$\lesssim 5$ meV
Temporal spread	$\lesssim 150$ ps	...
Minimal spot size	...	$\lesssim 50$ µm
Brightness (at 100 keV)[a]	1.4×10^4 A cm^{-2} sr^{-1}	1.4×10^4 A cm^{-2} sr^{-1}

[a] see next section for the detail of the estimation

1.2 Electron sources in microscopy and spectroscopy

An indispensable part of any electron microscope is obviously the electron source. The scientific and technological fields using electrons as tools for analysis or modification

of matter being plethoric, there are a large number of different types of sources, with varied properties. We present here the electron sources usual in electron microscopy, their principle of operation and their characteristics, to conclude as to the possibility of using them in the context of the HREELM project with the help of the requirements summed-up at the end of last section. An important distinction is to be made between electron sources and electron guns. We define the electron source as the material providing the electrons as well as the ionisation process that extract the electrons from the material. The electron gun is a crucial part of any electron microscope, and is composed of the electron source, plus the electrodes that allow the coupling between the source and the rest of the column. For example, in PEEM the sample can be considered as an electron source, but not an electron gun. The following section is devoted to the analysis of electron sources, but we should keep in mind that the final properties of the electron beam that is effectively used in instruments also strongly depends on the properties of the electron gun.

1.2.1 Key concepts for performance evaluation

A preliminary to the presentation of the usual sources in electron microscopy is the definition of the important quantities to be evaluated. To effectively describe the performance of an electron source, we analyse the characteristics of the electron beam that we can extract from it with several concepts: the emitted current I, the energy spread ΔE, the transverse emittance ϵ, the brightness β and the reduced brightness β_{red}.

These concepts can have different definitions and uses among the different fields in which they are used, so we must cautiously compare different sources. We thus provide general definitions of these concepts for coherence and ease of understanding but they may be unsatisfactory for some readers. An effective analogy here is the concept of the size of the beam, that can have various definition (its FWHM, the size that encloses 90% of the beam, its waist...), depending on the application and the context.

The emitted current is defined as the electron flux in the beam, often expressed in pA, nA or µA. The energy spread of the source is defined as the full width at half maximum (FWHM) of the total electron energy histogram, expressed in eV or meV. The emittance of a beam is a measure of the average spread in particle positions and momenta i.e. the phase-space volume of the particle ensemble. The emittance of a beam can be decomposed in the transverse emittance and the longitudinal emittance, considering the axis of the electron beam. It is tightly linked to the concept of luminosity in accelerator physics.

The transverse emittance ϵ_T then corresponds to the effective volume of transverse phase space occupied by the electrons in the beam:

$$\epsilon_T = A\Omega \tag{1.9}$$

with $A = \Delta x \Delta y$ the beam cross-section (Δx and Δy are spatial extension of the beam in the two transverse directions) and $\Omega = \Delta x' \Delta y'$ the transverse speed dispersion (with $\Delta x'$ and $\Delta y'$ the velocity component of the beam in the two transverse directions). For the brightness β (often expressed in $\mathrm{A\,cm^{-2}\,sr^{-1}}$) we adopt the convenient definition:

$$\beta = \frac{I}{A\Omega} = \frac{I}{\epsilon_T} \tag{1.10}$$

Conceptually it represents the density of electrons in phase-space. This quantity is interesting because, at constant beam energy[6] and under geometrical optical conditions (i.e. without diffraction, inter-particle interactions and under the paraxial approximation) it is preserved at any plane in an electron microscope column[9]. It is a direct consequence of Liouville's theorem, that states that the phase-space volume is conserved under Hamiltonian evolution (with independent particles).

This conservation property makes it possible, based on knowledge of the area of interaction with the sample, the maximum angle of incidence (defined by the spherical aberrations of the column and constrained by apertures) and the current required to acquire an image in a reasonable time, to define a minimum brightness of the electron source to be used. Thus, microscopy techniques (such as scanning transmission electron microscopy) based on an electron probe focused on 0.1 nm, with an angle limit of 10 mrad (limited by spherical aberrations in the column) and a minimum current of 25 pA require a brightness of about 1×10^9 A cm^{-2} sr^{-1}[9].

Since LEEM is a wide illumination technique (the electron probe is typically collimated on 10 µm to 100 µm), the required brightness for HREELM is lower than for STEM. However the illumination of the sample must be achieved by a near collimated beam, so the maximum acceptable divergence angle is lower than in STEM. Simulations from the Electron Optica company show that in the published HREELM prototype design, a beam with diameter $d = 100$ µm with a divergence semi-angle of $\alpha = 0.58$ mrad (1 meV in the transverse direction at longitudinal energy of 3 keV) allows a 10 nm resolution with a field-of-view of 100 µm[25], so we can consider that $\alpha = 0.1$ mrad and $d = 50$ µm for safety. The required brightness (with 1 nA) at 3 keV is 4×10^2 A/cm^2/sr. Using the conservation of the reduced brightness (see footnote 6), the required brightness is thus:

$$\beta_{100\,\mathrm{keV}} = \frac{100}{3}\beta_{3\,\mathrm{keV}} = 1.35 \times 10^4\ \mathrm{A/cm^2/sr} \tag{1.11}$$

In the following we will see that this value is well in reach for common sources in microscopy.

1.2.2 Standard sources in microscopy and spectroscopy

Thermoionic sources

The most classic type of electron source is the thermoionic source. In these sources a material (typically a Tungsten tip, or a single crystal of LaB_6 or CeB_6) is heated to a high temperature (about 1800 K or even higher)[31], which greatly reduces the work-function of the materials. At these temperatures, the conduction electrons in the material (called the cathode) have enough kinetic energy to overcome the barrier of ionisation. As detailed on figure 1.15, an electric field is usually applied to the sample by keeping the anode at a positive potential, to extract the already formed electrons but has little influence on the emission efficiency. This means that to control the current emitted by the source, one must change the temperature of the emitting material, which can take a long time.

[6] when the electron energy E changes along the column, it is advisable to introduce the reduced brightness β_{red} as $\beta_{red} = \beta/E$. This new quantity (also conserved under geometric optical conditions) is more adequate when an electron beam is accelerated or decelerated along the column (like in LEEM).

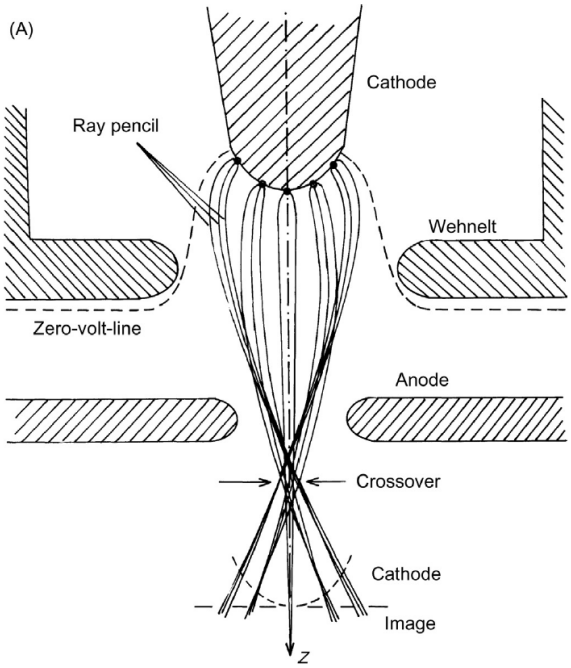

FIGURE 1.15: Thermoionic source in the triode configuration. The cathode thermally emits electrons, the wehnelt defines the zero-line, controls the current and focuses the electrons before the anode, that applies the electric field necessary to extract the electrons to the column. (Reproduced from [30])

This is the reason why these emitters are used in a triode configuration, as depicted on figure 1.15. In this configuration, a third electrode is added between the cathode and the anode, and is called the wehnelt. The wehnelt is kept at a negative potential and regulates the emitted current by shifting the zero-volt line on the cathode, without changing the temperature of the cathode or the potential of the anode. Another effect of the wehnelt is to strongly focus the electrons at the anode so that they don't hit it. One can use a single crystal (faces $\langle 111 \rangle$ or $\langle 310 \rangle$) in order to favour the emission from one of the faces and thus improve the directionality of the source and its brightness. This kind of source is rather robust and only needs a secondary vacuum to work, but is not very bright (see the table 1.1 for a quantitative comparison between all common sources in electron microscopy).

Field-assisted sources

Field-assisted sources use tunnelling to extract electrons from a very sharp tip. A very strong electric field (about 1×10^9 V/m) is applied to the tip of a specific material (see figure 1.16) to lower its potential barrier, and electrons can then escape in vacuum by tunnelling. The field is adjusted so that the barrier is lowered sufficiently (allowing electrons to tunnel into the vacuum) only in a very small solid angle. Thus the emission is very localized (at the tip, over a diameter of a few hundred nanometres), and very directional (a few degrees of solid angles), which makes it a very bright source. The temperature of the cathode material depends on the expected performance of the source, and can vary from 300 K to 1800 K[31]. The higher the temperature, the higher the emission current but also the higher the energy spread of the electron beam. When the emitter is heated

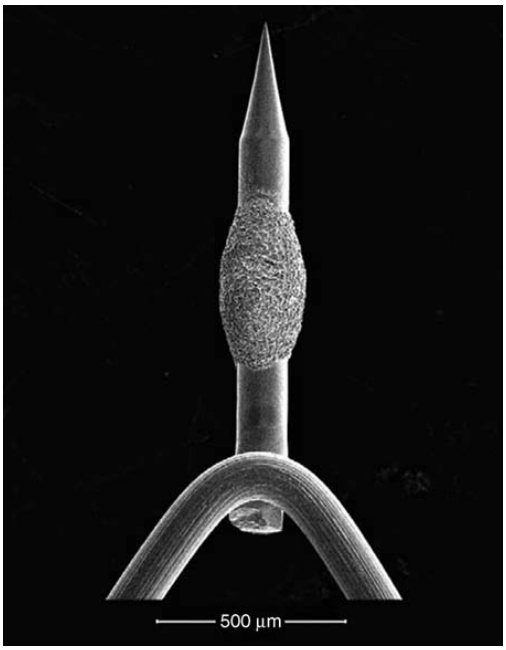

FIGURE 1.16: Electron microscope image of a ZrO/W tip showing the ZrO_2 reservoir. This constitutes the cathode in Schottky-type electron guns. (Reproduced from [31])

and in a strong field, the emission process is then a complex combination between thermoionic and field-assisted emission, also called the Schottky effect. This effect is present in a lot of materials, but the most common implementation of this type of source, sometimes simply called the Schottky source, is where the emitting material is a complex of ZrO on the surface of a Tungsten (W) tip, which is heated to high-temperatures, under a moderate electric field. This emitting layer is rapidly degraded by electron emission, and the quality of the emission is highly dependant on the quality of the oxide layer. This requires heating the tip, so that the emitting layer reconstitutes itself from a reservoir of ZrO_2, which diffuses on the surface of the tip. The sensitivity of the emission quality to the surface state of the tip thus requires a very good vacuum and a very regular thermal cleaning ("flash").

Performances of different types of electron sources used in electron microscopy are gathered in the table 1.1. The cold-field electron guns (CFEG) (with a cathode at 300 K) notably produce electron beams with the smallest energy spread, down to 0.25 eV. This value is however much higher than the spectral resolutions routinely achieved in electron spectroscopy, as discussed previously (on the order of 5 meV, even less than 0.5 meV for the record values[32]). This means that in order to obtain meaningful results in terms of spectroscopy, the electron source must be monochromated.

The scientific field of field-assisted emitters is still very active and recent progress has shown that new kinds of materials can also achieve very good properties in an electron source. For example, carbon nanotubes[33], carbon cone nanotips[34], and graphene[35] have shown very promising brightness values, but are still in the development phase, and the available data shows no improvement in terms of energy spread in comparison to the state-of-the-art CFEG.

On the contrary, some other tip-based electron sources showed very low energy spread, but lack stability and reliability. For example an electron source using a 80 K single Pt

Properties / Sources	Thermoionic (W)	Thermoionic (LaB_6)	Schottky (ZrO on W)	CFEG (W)	TPES (see caption)	For HREELM
Brightness β at 100 keV ($A\,cm^{-2}\,sr^{-1}$)	10^5	10^6	$10^7 - 10^8$	10^9	3×10^2 [7]	1.4×10^4
Energy spread ΔE (meV)	800	600	600	250	2-10	$\lesssim 5$
Vacuum (Pa)	10^{-3}	10^{-4}	10^{-7}	1×10^{-8}	1×10^{-7}	$<10^{-6}$
Current (µA)	100	50	80	10	$10^{-6} - 10^{-4}$	1×10^{-3}
Lifetime	80 h	1000 h	> 1 year	> 1 year	> 1 year	> 1 year
Apparent diameter (µm)	30	10	0.05	0.005	50-200	≤ 100

TABLE 1.1: Typical performances of electron sources used in electron microscopy, along with the requirements for HREELM. The brightness is given at 100 keV because it is the standard value in EM, but HREELM operates around 3 keV, mainly due to the availability of cheap voltage supplies with mV stability. Sources from the photoionisation of atoms (TPES for threshold-photoionisation electron sources) are introduced in section 1.3.1 but shown here for comparison.

atom as an emitter has shown an energy spread of 64 meV with indications that further cooling down to liquid helium temperature would give around 20 meV of energy spread[36]. Negative electron affinity photocathodes also showed energy spread around 50 meV[37] at room temperature, and about 10 meV at cryogenic temperatures[38], but none of these two techniques are sufficiently mature to be used in microscopy, despite their very good energy spread performances.

Monochromators

From the list of available electron sources in microscopy, and their energy spread (see table 1.1), it appears that spectroscopy with electrons is condemned to poor spectral resolution, around 0.2 eV at best. In this section we will see how it is possible to improve this number by several orders of magnitude.

The key to obtaining spectroscopically usable electron beams (i.e. with an energy spread less than the typical line widths of interest) is the monochromator. This type of apparatus selects electrons with a well-defined energy and filters all electrons whose energy do not fit in its bandwidth. In a monochromator, a dispersive element will transform the energy spread of an electron beam in spatial dispersion. A slit is then used to select the part of the beam with the chosen energy. There are different types of dispersive elements that can play this role (see figure 1.17), such as:

- magnetic sectors
- electrostatic or magnetic deflectors (alpha or omega filters)
- Wien filters

A Wien filter is a zone in space in which an electric field F and a magnetic field B are arranged perpendicularly so as to disturb the trajectories of the electrons according to

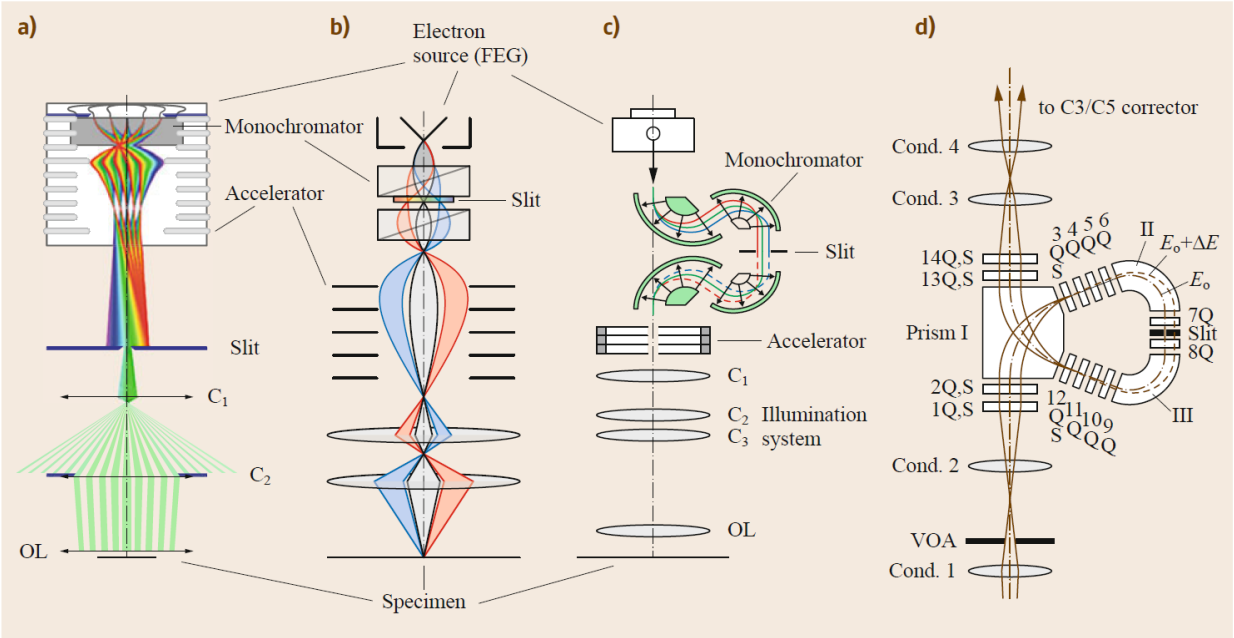

FIGURE 1.17: Four different implementations of monochromators in commercial electron microscopy columns. Trajectories of electrons with different energies are represented in different colors. a) Single Wien filter (FEI) b) Double Wien filter (JEOL) c) Electrostatic Omega filter (Libra Zeiss) d) Magnetic Alpha filter (NION). (Reproduced from[9])

their energy (and therefore their axial speed v). The total force can be written as $F_{Wien} = e(F + vB)$. By fine-tuning the field amplitudes, it is possible to let a certain electron velocity v_0 unperturbed by the fields, i.e. $F_{Wien} = e(F_0 + v_0 B_0) \simeq 0$. This means that the action of the electric field (independent of the axial speed of the electron) perfectly compensates for the action of the magnetic field (which is proportional to the speed of the electron) only for the electrons with velocity v_0. Other electrons with different energies spiral one way or another and the amplitude of this movement can be traced back to the initial axial kinetic energy.

Monochromators are indispensable for any application of electron spectroscopy and have been present in these instruments since the 1960s[39], usually both before and after the sample. They are then called monochromator and analyser, respectively (see figure 1.7), but are the same instruments. For very high resolution measurements, a second monochromator can be added, allowing measured resolutions better than 1 meV[20]. As presented in section 1.1.2, state of the art electron microscopes also implement monochromators, in various forms (see figure 1.17). The particularity of monochromators used in microscopy is that they retain the column's axiality (for mechanical stability reasons, since an axial column is less sensitive to vibrations than a right-angle column).

These instruments have spectral resolutions on the order of 20 meV to 100 meV[40–43], with the exception of the instrument manufactured by the company Nion, which reaches spectral resolutions better than 5 meV at 30 keV[29]. This is made possible by placing the monochromator and the analyser in series on the same power supply, and measuring the current on both sides of the energy selection slot. Thus, no matter what energy is selected by the monochromator, it will not change the position of the spectrum on the detector[22]. Furthermore, measuring the current on the slit allows to retro-act on the high voltage

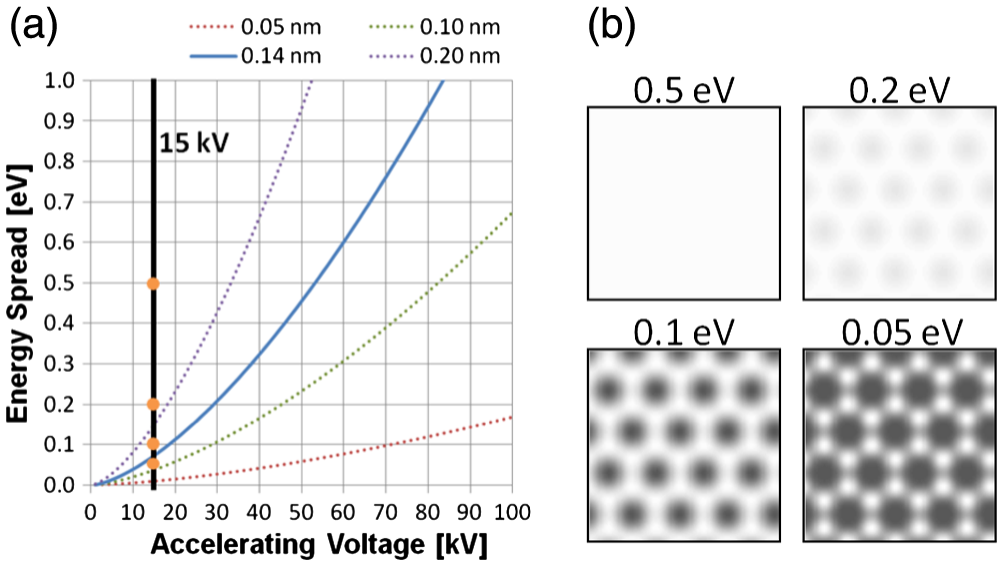

FIGURE 1.18: Simulations on the effect of the energy spread of the electron probe on the achievable spatial resolution in function of the electron potential. a) Lowest energy spread for 0.05 nm, 0.1 nm, 0.14 nm and 0.2 nm resolutions, in function of the acceleration voltage. b) Simulated images of graphene at 15 kV with the four values of energy spread indicated by orange dots on the a) curve, clearly showing the detrimental effect of energy spread on the image resolution. (Reproduced from [45])

power supply in order to keep the center of the beam in the center of the slit and thus keep a high current with a very good spectral resolution. The monochromator allowing this resolution is in "alpha"[8] configuration (see figure 1.17 d)), which has the particularity of having the energy selection slit in the middle of the electron path, the other half of the monochromator simply serving to cancel the dispersion induced by the first half[44]. This configuration is essential to maintain the brilliance of the source in the rest of the device.

The very low energy spread of the electron probe is essential for the spectroscopic resolution, but also for imaging properties. This is due to the presence of chromatic aberrations in the column, that lead to different focus to electrons with a different energy. A recent study has proven that a monochromated electron source is essential in a STEM to lower its working potential down to 15 kV while keeping atomic resolution. In particular, simulations with a reasonable amount of chromatic aberrations (see figure 1.18) show that the best electron sources used in microscopy are unable to provide an electron beam with a sufficiently low energy spread to perform low-energy electron microscopy at atomic resolution[45]. This lead to a very promising use of monochromatic electrons sources, because high-potential electron microscopes suffer from electron-induced sample damage, due to knock-on displacement i.e. crystalline defect induced by high-energy electrons. As an illustration, the very recent obtained atomic resolution in cryo-EM is also due to a lower electron energy spread than before (0.3 eV instead of 0.7 eV)[46] and even lower energy spread would surely benefit the technique even further.

Monochromators are therefore an essential part of electron spectroscopy and an increasingly essential one of modern electron microscopes, allowing impressive performances to be achieved. It is to note that in a microscopy application, monochromators

[8] this names comes from the shape of the monochromator, resembling the Greek letter α

have the disadvantage of transforming an important part of the longitudinal emittance i.e. the momentum dispersion in the optical axis of the beam into transverse emittance, which decreases its brightness. Furthermore, the flux reduction inherent to the operation of monochromators (they do not reduce the dispersion of electrons in the beam, but filter out a large part of it) may also be too large to obtain reasonable acquisition times.

All this makes the motivation for the development of other types of electron sources, which should be intrinsically monochromatic, rather strong. Indeed, the instrumental heaviness and the cost of these instruments make Egerton[20] say in his 2011 book:

> *"Instead of a monochromator, it would be attractive to have a high-brightness electron source with low-energy width"*

In particular, the success of the HREELM project strongly depends on a new, monochromatic and bright electron source. The ambition being to surpass state-of-the-art microscopy sources by two orders of magnitude (in terms of energy spread), such a goal can be achieved only by drastically changing the approach to electron production.

Section summary

Electron sources in microscopy and spectroscopy

In this section I have reviewed the existing sources in electron microscopy and spectroscopy. These electrons sources are not adapted to the construction of HREELM, mainly due to their high energy spread. It is possible to reduce this energy spread with monochromators, as is done in HREELS, but the imaging conditions of HREELM makes this solution not usable in our case. More elaborate implementation of electron beam monochromation is possible and used in a few state-of-the-art microscopes, but they are extremely expensive and technologically really involved. The cause of the large energy spread in existing electron sources is the material source from which these electrons are extracted: macroscopic materials, involving very-high electric fields, introducing irreversible energy spread at the emission point of these electrons sources. This analysis clearly indicate that we should look elsewhere to find an appropriate electron source.

1.3 Electron sources from the ionisation of atoms

An inspiration for a new approach to electron sources can be found in electron attachment spectroscopy. Indeed this spectroscopy probes the energy levels of free molecules, so it requires at least equal precision on the energy of the electrons[47]. As most of the molecular lines probed by electron impact have an intrinsic width on the order of the meV, this spectroscopy requires an electron source with very low energy spread[48].

The electron sources developed for this application differ greatly in principle from the sources seen above. They originate from atomic physics (as opposed to the condensed matter physics of filaments and nano-tips) and are based on laser or synchrotron radiation ionization of effusive or laser-cooled atoms. Since the material from which the electrons

are extracted is much simpler (a free atom compared to a macroscopic solid), this allows a very advanced control of the ionization process, and thus a very good control of the characteristics that directly result from this process. In particular the ionisation process is a crucial aspect of these sources, which can involve highly-excited states of the atoms, i.e. Rydberg states (details on Rydberg states can be found in section 2.1). The atoms that are used in these electron sources are usually alkali metals, alkaline-earth atoms, or rare-gas atoms.

1.3.1 Low energy spread photoionisation electron sources

While the most important property for the sources used in electron microscopy is the brightness of the source, in gas phase electron spectroscopy the electron sources are fully optimised to produce electrons with the lowest possible energy spread[9].

In these sources the electrons are created from the photoionisation of free flying atoms, either in an atomic beam or in a vapour. As can be seen on figure 1.19, depending on the particular kind of electron spectroscopy (either electron attachment spectroscopy or electron scattering studies) the experiments have typically two different configurations: for laser photoelectron attachment (LPA) studies the electrons are produced directly in the vicinity of a sample beam (the target), while for scattering studies they are ionised in a separate chamber, formed into a beam, and collide with the sample in another chamber. This last configuration can thus be described as having an electron source coupled to an analysis chamber.

The pioneer electron source of this kind was developed in 1974 and provided less than 1 pA of usable electron beam, with an energy width of 6 meV[50]. Several years afterwards an improved version of the set-up showed a current of 2 pA with an energy width of 5 meV[53]. Since then a lot of set-ups were built according to this principle[51], the best reported properties being a current of 50 pA − 90 pA with an energy width of 4.5 meV[54][10]. To achieve these performances, it is essential to identify and evaluate all the phenomena at the origin of the energy spread of the electrons (see section 1.4).

The properties of these sources are rarely described in terms of brightness, because it is not an important quantity in spectroscopy. Using the reported values of Ref. [54] for the beam diameter, maximum current and electron velocity (less than 0.1 meV excess energy isotropically distributed[54]), I can estimate the brightness of these sources from equation 1.10:

$$\beta = \frac{I}{A\Omega} = \frac{90\,\mathrm{pA}}{\left(\frac{\pi \times 120\,\mu\mathrm{m}^2}{4}\right)(\pi\alpha^2)} \tag{1.12}$$

with α the semi-angle, that can be approximated in the case of an acceleration to 100 keV (for the purpose of the comparison with other sources) by $\alpha = \sqrt{\frac{0.1\,\mathrm{meV}}{100\,\mathrm{keV}}} = 0.03\,\mathrm{mrad}$.

[9] other fields might have other constraints as, for example, low-energy electron diffraction studies focus on electron sources with the shortest possible electron pulses with the highest temporal coherence[49]

[10] The lowest reported values of energy spread (as low as 20 µeV with a current below 0.05 pA[55]) come from LPA set-ups and can't be directly compared with the formation of an electron beam. These experiments sometimes also show higher currents, up to 200 pA[56], with less energy spread than in scattering experiments. This can be explained by the fact that ionic space-charge have a lower detrimental effect in LPA than in scattering studies.

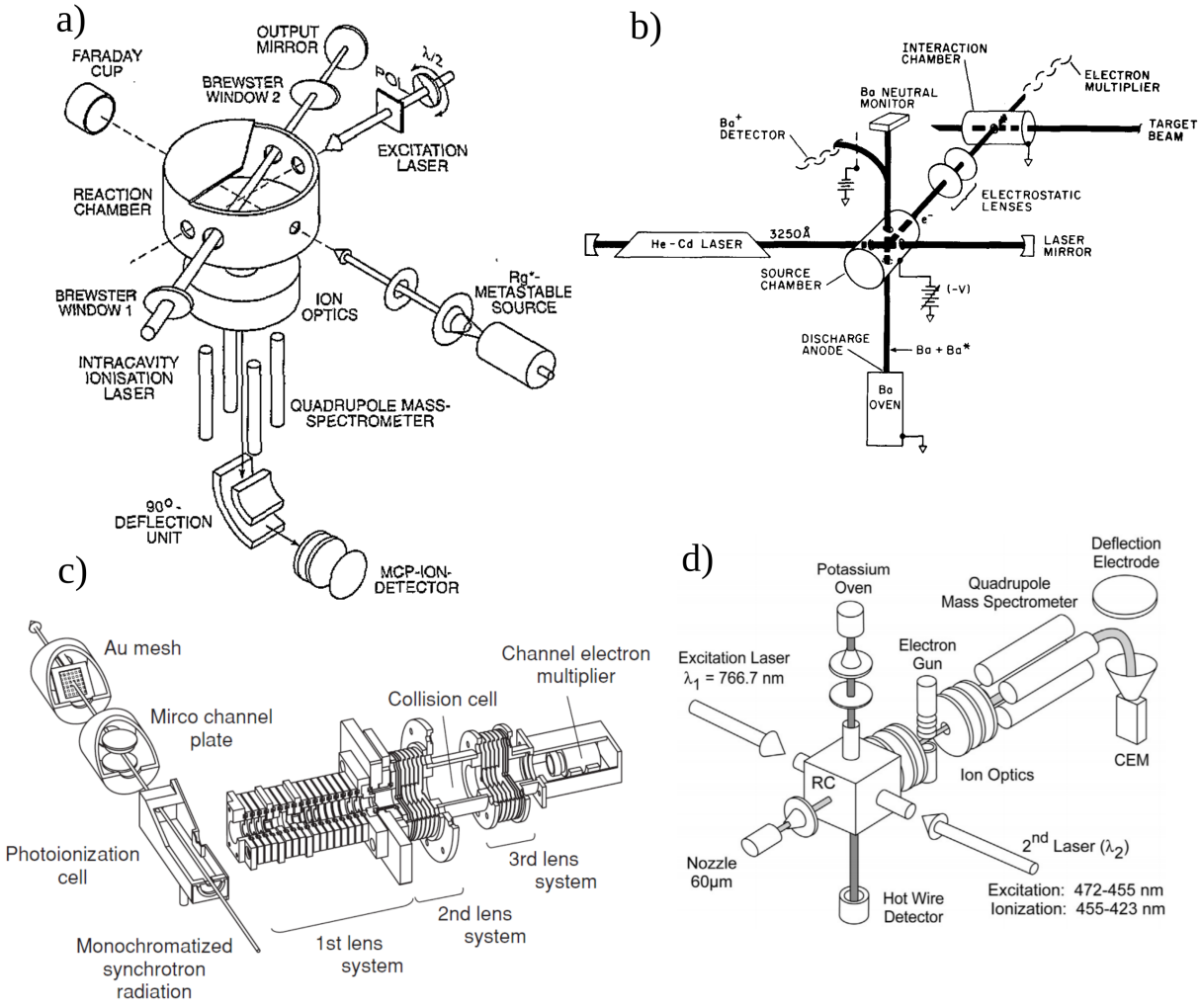

FIGURE 1.19: Examples of the set-ups of four electronic gas-phase spectroscopy experiments. Electrons are created directly in contact with the target in a) and d) to perform attachment studies, while electron beams are directed to a reaction chamber in b) and c) to conduct electron scattering studies. Photo-ionisation is done by a laser in a), b), d) and by XUV radiation in c). The source of electrons is: a) a metastable argon beam. (Reproduced from [48]); b) a Ba beam ([50]); c) an argon vapour ([51]); d) a potassium beam ([52])

This gives:

$$\beta_{100\,\mathrm{keV}} \approx 3 \times 10^2\,\mathrm{A/cm^2/sr} \tag{1.13}$$

which is very modest, and between one or two orders of magnitude too small for HREELM (see table 1.1.3).

1.3.2 Precision spectroscopy with electrons

I finish this overview of electron sources with the presentation of precision spectroscopy involving electron beam with a low to very low energy spread. They are not *stricto sensu* electron sources but nevertheless provide good insight into controlled ionisation.

Spectroscopy of atoms or small molecules can be done simply by scanning the wavelength of a laser and analysing the energy of the electrons produced when the laser interacts with a stream of atoms or molecules. When the wavelength of the laser (or other light source) corresponds to an energy at least higher than the ionization energy of the system under study, there is a certain probability that a photon absorption leads to an electron being released and detected. The ejected electron then carries the spectroscopic information of the ionised system. The basic equation of this technique is the conservation of energy applied to the ionization process by an above-threshold laser:

$$E_{ion} = h\nu - IE - E_{el} \tag{1.14}$$

Where E_{ion} is the internal energy of the created ion, $h\nu$ is the energy of the incident photon, IE is the ionisation energy of the neutral particle and E_{el} is the kinetic energy of the photo-electron. When the energy of the ionizing radiation $h\nu$ is very close to the ionization threshold of the system, it is called threshold photo-electron spectroscopy (TPES).

The spectroscopic resolution of these techniques therefore depends directly on the ability to accurately analyse the energy of the emitted electrons E_{el}, but also on the initial dispersion of these electrons ΔE_{el}. This is why many efforts have been made in this field to minimize as much as possible the energy dispersion of the electrons created by the photo-ionization of atoms or molecules in a jet. These efforts have led in part to the Pulsed Field Ionization-Zero Electron Kinetic Energy spectroscopy (PFI-ZEKE) in which the measurement makes clever use of electric field pulses and delays to reduce the initial energy spread of the electrons and thus improve the spectral resolution. This spectroscopy is based on the fact that, below the threshold, it is possible to excite Rydberg atoms, that will ionize with virtually no kinetic energy transfer to the electron. By delaying the extraction of the electrons, we let the fastest electrons (the ones that acquired some kinetic energy) travel freely and crash onto the walls of the chamber, and then extract only the ones with zero kinetic energy.

These experiments have thus shown that one way to reduce the energy spread of the electrons is, instead of using a light source with an energy above the threshold (as in standard photo-ionization), to identify and excite an unstable Rydberg state. In an electron source perspective, this means that the ionization of a Rydberg atom can be done with $E_{el} \simeq 0$, i.e. near-zero energy spread for the emitted electrons. This would also mean, naively, a near-zero emittance (because of the near-zero momenta of the electrons) and thus high brightness (see equation 1.10). More details on the directionality of the photo-electron can be found in section 4.1.2.

Section summary

Electron sources from the ionisation of atoms

In this section we have seen that, in contrast with usual electron sources for electron microscopy, there exists electron sources that provide electron beams with small enough energy spread for an application in HREELM. These sources use atomic beams or vapours as electron reservoirs, and extract them with photo-ionisation under very low extracting fields. Under the right circumstances this can create electrons with very low energy spread (1 meV or even better for electron attachments experiments where the electrons are created directly in contact with the target[48,55], and around 2 meV to 5 meV for electron beams formed by these sources for scattering experiments[54,57]), but usually with lower current (200 pA at best[56]) and brightness than what is required for HREELM.

1.4 Where does the electron energy spread come from?

These last examples of electron sources have shown that it is possible to produce electron beam with very low energy spread ΔE. The requirement for that is of course to correctly identify, and then cancel the possible sources of energy spread. This is what I do in this section. I identify five main sources of energy spread within an electron source from atoms:

1. The kinetic energy acquired by the electrons during the ionization process
2. The difference in electrical potential along the ionization zone
3. The initial velocity (temperature) dispersion of the atoms to be ionized
4. The interaction between electrons
5. The "parasitic" effects

Each point is developed in the following, from their origin, to the estimated impact of the energy spread, and possible solutions.

1.4.1 Ionisation process

Origin

This first point has already been mentioned in the context of photoelectron spectroscopy (see section 1.3.2). In photo-ionisation, the electron acquires energy from the ionising radiation. The difference between the energy of the ionizing photon and the ionization threshold is redistributed between the ion and the electron according to the mass ratios (1.8×10^3 for hydrogen and 2.42×10^5 for caesium). As the ionisation radiation can have a non-negligible linewidth, this gives different energy to different electrons. Furthermore, the energy is distributed in different directions. In photoionisation, the polarization of the incident radiation then plays an important role in the electron initial momentum.

Solution

A simple solution to minimize this term in the case of photoionization is to tune the ionizing wavelength exactly to the ionization threshold, to minimize the excess energy. We have seen also that it is possible to excite Rydberg states which then ionize with zero kinetic energy of the electron. We present experimental results supporting these considerations in section 5.2. Using another experimental set-up, allowing indirect measurement of the release energy of the electron during photoionisation, we confirmed that some Stark-shifted Rydberg states release their electrons with undetectable kick-energy (with a detection limit at 1 meV)[58].

More details on these processes (photoionisation and Rydberg ionisation) can be found in section 4.1.1.

1.4.2 Potential difference across the ionisation zone

The difference in electric potential across the ionisation volume is usually the main source of energy spread in electron sources. This actually is composed of two terms: the effect of the extracting field, and the potential induced by the ions created during the ionisation. These two effects are very different but directly influence the electric potential in the ionisation zone, which motivates that they are grouped under the same global effect. As the electric potential is changed in space, and that the ionization zone always has a certain spatial extent (for example a sphere of diameter Δz), this creates energy spread as the electron are extracted.

Extracting field - Origin

The first term comes from the presence of an electric field (along z) $\vec{F}$, that induces an electric potential difference for two electrons located on both sides of the ionization zone. These two electrons then have a difference in energy ΔE of:

$$\Delta E = \|\vec{F}\|\Delta z \tag{1.15}$$

Extracting field - Solution

The solution to reduce this energy spread is therefore either to reduce the size of the ionization zone Δz or to reduce the field F. Decreasing the size of the zone requires focusing the laser or ionizing light source, which is usually done down to 10 µm to 100 µm but not below, to maintain sufficient current. The value of the extracting electric field is therefore the main parameter determining the energy spread of the electrons, and typical very low values of 1 V/m to 10 V/m are used in practice[50,51,59,60]. Using equation 1.15 we can estimate that in these conditions:

$$\Delta E = 100\,\mu\text{m} * 1\,\text{V/m} = 0.1\,\text{meV} \tag{1.16}$$

However, using very low extracting field will lead to a positive charge accumulation in the ionisation region. Indeed, the electrons will be extracted in a few ns (under 1 V/cm they are 220 µm away from their starting point after 50 ns), while the ions (particularly caesium ions) will need 25 µs to reach the same distance from the origin.

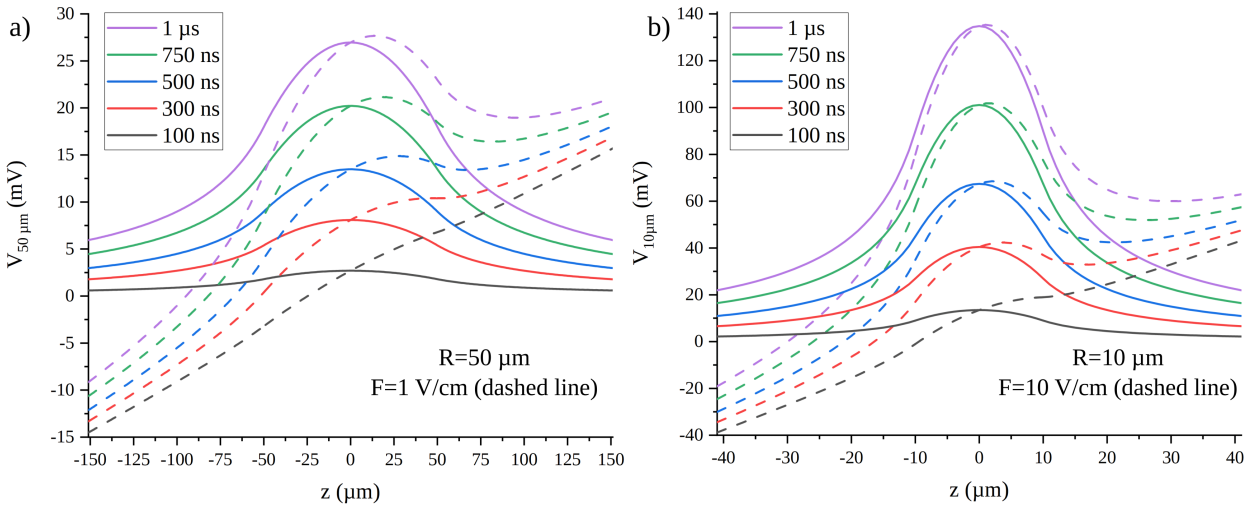

FIGURE 1.20: a) Electric potential at a distance z from the origin due to a charged solid sphere of radius $R = 50\,\mu m$ (solid line), with five different charge densities ρ corresponding to five different durations of charge accumulation (1 µs in pink, 750 ns in green, 500 ns in blue, 300 ns in red and 100 ns in black) at a current of 100 pA. In dashed line is the sum of this potential with the potential gradient (i.e. extracted electric field) of $1\,V/cm$ b) Same but with $R = 10\,\mu m$ (solid line) and $F = 10\,V/cm$.

Ionic space-charge - Origin

The production of ions concomitant to the production of electrons (as well as the inertia of the ions with respect to the electrons) leads to an accumulation of positive charges in the ionization zone, with the volumetric charge density ρ. This accumulation leads to an additional electric potential difference as a function of time and position, that is called ionic space-charge.

A first approach for the evaluation of this effect is to consider standing charges forming a sphere around the origin. This would correspond to a photo-ionisation source with a very-low extracting field and cold atoms with no initial velocity, such that the formed ions stay in the ionisation region. The electric potential at distance r from the origin in a solid sphere of radius R of continuous charge density has the expression:

$$V_R^{r<R}(r) = \frac{\rho}{2\epsilon_0}\left(R^2 - \frac{r^2}{3}\right) \tag{1.17}$$

and outside the sphere the potential is:

$$V_R^{r>R}(r) = \frac{\rho R^3}{3\epsilon_0 r} \tag{1.18}$$

and is plotted against r with $R = 50\,\mu m$ on figure 1.20 (a) (solid lines) and with $R = 10\,\mu m$ on panel b)(solid lines), with five different values of ρ corresponding to five different charge accumulation time. The current is chosen to be 100 pA, so 1 µs accumulation means 625 ions, 500 ns is around 312 ions and 100 ns accumulation amounts to 62.5 ions on average. It is clear that the influence of these ions is not negligible at the level of energy spread that we want, with potential shifts around 10 mV already after only 500 ns.

The plot with $R = 10\,\mu m$ clearly puts a lower limit on the ionisation zone, to limit the detrimental energy spread due to ionic space-charge. To limit this influence to 5 meV in a sphere of radius 30 µm, this gives a maximum ionic charge of $Q = 3.34 \times 10^{-17}\,C$, corresponding to 208 ions. At a current of 100 pA, this number of ions is produced in 334 ns. Thus the low energy spread requirement induces a limit to the number of ions that can accumulate in the ionisation region, that is reached quite rapidly under normal circumstances.

To go further in the analysis, it is important to consider the geometry of ionisation i.e. the relative orientation of the atomic beam, the laser beams and the extracting field. Indeed in this case the sphere of radius will gradually evolve into a cylinder starting from the ionisation zone and towards the direction imposed by the atomic initial velocity and by the extracting field. In terms of geometry there are roughly two possibilities (neutral beam can be either perpendicular or parallel to the ionisation axis) but most published electron source adopted a perpendicular orientation[50,60,61] (see figure 1.19). This perpendicular arrangement has the advantage of minimising pollution by the neutral beam of the rest of the experiment. The other way to arrange beams, where the neutral beam is along the electron propagation axis (z axis), features an ion-induced potential difference along the principal component of the electric field. Detailed simulations involving the influence of ionic space-charge in both configurations show that (see section 4.4) the increase in energy spread is comparable in both cases (without compensation).

In an orthogonal set-up, Monte-Carlo simulations have given the relation (with ΔE the FWHM of the electron energy distribution):

$$\Delta E \approx 15.6\,\mu eV/pA \tag{1.19}$$

for uncompensated ionic space charge effect[61].

Clearly, if we want to provide an electron beam of 1 nA with $\Delta E < 5\,meV$, something must be done to prevent the accumulation of ions at the ionisation zone, either by passively removing them (passive clearing), apply an additional field along the ionisation zone (compensating) or actively removing the ions (clearing).

Ionic space-charge - Solutions

Passive clearing is one way to remove the ions from the ionisation zone by relying solely on the inertia of the ions and/or on the extracting field. It requires appropriate choice of atomic velocity (amplitude and orientation) and electric field and can be used in both pulsed or continuous electron source. An ion with an initial velocity v_0 (in the direction of the field) accelerated by a static field of amplitude F attains the distance r_F after τ:

$$r_F = \frac{qF}{2m_{ion}}\tau^2 + v_0\tau \tag{1.20}$$

Imagining a caesium atom at rest when it is ionised under an electric field of $F = 10\,V/cm$, the resulting ion will take 525 ns to be 100 µm away from its ionisation point. A neutral effusive beam of caesium from an oven at 400 K will have a mean velocity in its propagation direction of 274 m/s ($\frac{1}{2}m_{Cs}v = \frac{3}{2}k_BT$). If this velocity is in the opposite direction of the field, the ions will experience a back-and-forth trajectory, first driven by their inertia and then by the acceleration of the field. They will need 1.02 µs to be at 100 µm of

the origin, meaning that the density of ions will be the double in the ionisation region. With low extracting fields and a high-inertia ion like caesium, passive clearing is thus not enough to guaranties that the energy spread induced by the ions will be less than 5 meV, particularly if we lower the electric field.

Compensation and active clearing are more involving and correspond best respectively to continuous and pulsed electron source.

Field compensation along the electron propagation axis in the perpendicular configuration has been proven to work well, but in a compensated electron source providing 30 pA with an energy spread of 2 meV, ionic space charge still account for around 1 meV energy width[52]. A fundamental limit to compensation comes from the fact that they originate from charges, whose field can't be compensated perfectly by external fields.

This approach corresponds best to a continuous electron source simply because the compensation must be done in a stationary situation (in terms of ion density in the ionisation zone), and can thus efficiently be coupled with an appropriate passive clearing strategy.

However, I note that maybe additional field are not required to allow good compensation. Indeed the potential shift induced by the ion space charge in the parallel configuration is the same at both end of the ionisation zone (i.e. $V_{shift}(z) = V_{shift}(-z)$), but is maximum between the center of the ionisation zone (i.e. the origin) and the edges as seen on figure 1.20. This is different from the potential gap due to the extracting field where electrons at the center of the ionisation zone are created at a mean potential between electrons created at both ends of the ionisation zone. Figure 1.20 a) features the total potential in the case of an extracting field of 10 V/cm (in dashed line) to underline the different spatial dependence of these two potential differences (extracting field and ionic space-charge).

On the left panel (b) of this figure I plot the same curves in the case of a charged sphere of radius 10 µm and under a field of 10 V/cm. This shows that the extracting electric field seems to have a compensating effect on the space-charge of the ions.

To further study the possible space-charge/field compensation, I then plot on figure 1.21 the potential difference at the center and at the edge of the ionisation zone, in function of the radius R of the ionisation zone. It can easily be calculated in function of the charge Q (equal to $\rho\frac{4}{3}\pi R^3$):

$$\Delta V(R) = V_R(0) - V_R(R) = \frac{Q}{8\epsilon_0\pi R} \tag{1.21}$$

I also plot the sum of this potential difference with electric fields of 1 V/cm and 10 V/cm. The potential difference for these curves is the difference at the center and the high-field edge of the ionisation zone ($z = +R$). It clearly shows that the electric field can indeed compensate in part the detrimental effect of positive charge accumulation, and even after 750 ns, a charged sphere of 20 µm under an electric field of 10 V/cm shows no potential difference between the center and its edge. This "natural" compensation between ionic space-charge and extracting electric field needs careful design and tuning, but could be a viable approach in combination with passive clearing in a continuous beam electron source.

It should be clear however that other points in the ionisation zone have different potential. To obtain a good estimation of the total energy spread induced by the combination of ionic space-charge and extracting field, detailed simulations with space-charge effects

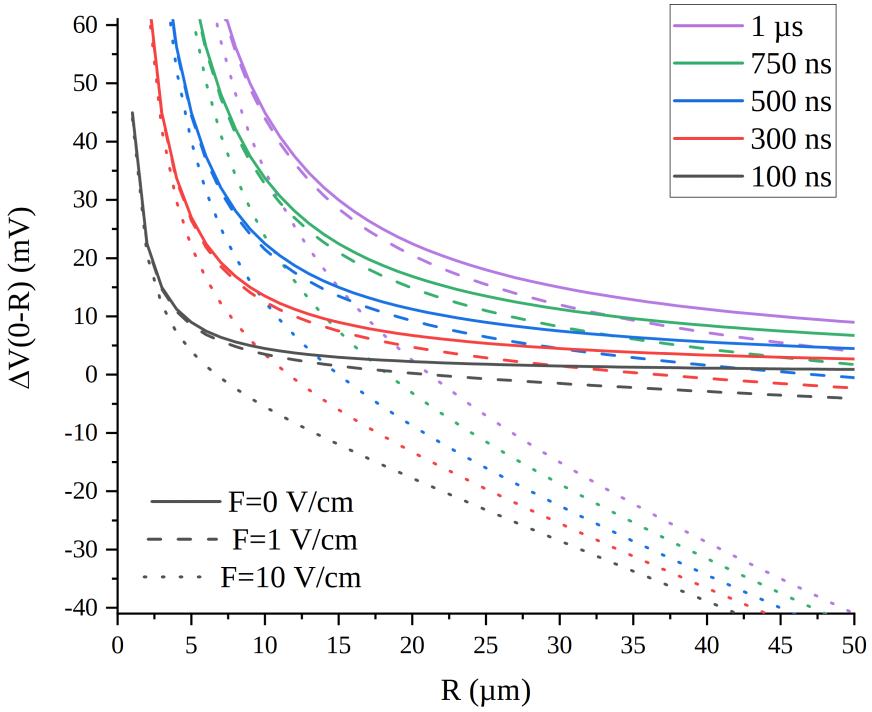

FIGURE 1.21: Voltage difference in the case of a variable radius R of the ionisation zone with an electron current of 100 pA after variable charge accumulation time, under fields of 0 V/cm (solid lines), 1 V/cm (dashed lines) and 10 V/cm (point lines), between electrons created at the centre of the ionisation zone and at the edge of it in each case.

are required, particularly when the dynamics of the system is considered (the ionic velocity, charge accumulation...). Such simulations are presented in various configurations in section 4.4.4.

The active clearing approach to the ionic space-charge problem is to limit the charge accumulation in the ionization zone by pulsed electric fields. It requires to divide the working time of the source into production/clearance cycles, thus making it adapted only to pulsed electron sources. The pulsed electric field activated during a clearance cycle removes the residuals ions formed by the previous ionisation period. In the case of a high-repetition rate, low current electron source, this clearing can also occur only one every n production cycles, to optimise the quality/quantity of produced electrons.

Active clearing requires pulsed fields of high-amplitude to be effective, and to keep a low cleaning duty cycle. For example, a 23.5 ns pulse of 5 kV/cm brings caesium ions initially at rest 100 µm away from their starting point. For ions with a starting velocity of 274 m/s in the opposite direction, this pulse needs to be at least 24.3 ns long. This shows that the initial atomic velocity/initial temperature is not dominant in the required clearing time, but instead that the mass of the ion and the intensity of the electric field pulse are preponderant. Building on the estimation of the level of detrimental ion numbers (attained in 334 ns, but lowered to 300 ns for safety), a clearing time of 30 ns would represent only 10% of the electron production time. We can thus safely say that active clearing is viable in an pulsed electron source, at least from a pure duty cycle/efficiency point of view, but it is a bit involved experimentally as it demands pulsing high voltage very rapidly.

Active clearing can also be used in "continuous" beam electron sources, where the

electron production is stopped and the ions are removed for 3.4 µs every 2.7 µs[48]. This allows the creation of electron beams with very low energy spread and removes the constraint of pulsing high fields, but significantly decreases the maximum producible current (reported below 1 pA[48]).

Overall the initial electric potential differences, coming from an applied extracting field or from ion space-charge are the most critical points and there is a compromise to be found in the electric field amplitude, the size of the ionisation zone and the electron current to be able to go down to the meV range.

1.4.3 Initial atomic temperature

Origin

Another potential source of energy spread is the initial temperature of the neutral atoms that will get ionised. This will create Doppler broadening of the ionising linewidth, and some of the initial kinetic energy of the atom will be transferred to the ion and the electron.

Solution

The obvious way to reduce the effect of the temperature of the target on the energy spread is to reduce the temperature of the target. It can be reduced easily by using neutral atom jets, or even supersonic jets (see figure 1.19) because the transverse degrees of freedom of the atoms are cooled down.

Some electron sources go beyond and use laser cooling techniques to minimize this term, with the idea of producing "cold electrons" from cold atoms. Laser cooling is a set of techniques that allows to trap and/or cool the external degrees of freedom of neutral atoms[62–65], and allows to reach limit temperatures of a few tens of µK for Doppler cooling, and a few nK for more advanced techniques (Sisyphus cooling, evaporative cooling...). About a third of the stable elements in the periodic table have been cooled in this way since the end of the 1980s[66].

This is how sources of charged particles (ions and electrons) from cold atoms emerged from the end of the 2000s[67,68], and especially in the early 2010s. Several groups have implemented this kind of source, and some examples are visible on the figure 1.22.

These electron sources are therefore based on a first step of cooling and trapping atoms, then ionization in several laser steps (via a Rydberg state or directly above the ionization threshold) and finally electron extraction, each of these steps can be performed continuously or in a pulsed manner[71].

The typical implementation uses alkali metal atoms cooled in a 3-dimensional magneto-optical trap between two electrodes creating an electric field.

The contribution of pre-ionisation laser cooling on the optical properties (brightness, emittance) of the sources is very important for ion beams. Indeed, the initial momentum (before acceleration by an electric field) of the ion is almost entirely determined by the initial momentum of the neutral atom, so reducing the initial temperature of the atoms mechanically reduces the initial temperature of the ions; and thus the associated emittance. This explains why sources of ions from cold atoms are already the subject of semi-industrial applications in ion beam microscopy[72,73]. For electron sources, the improvements is not so straightforward.

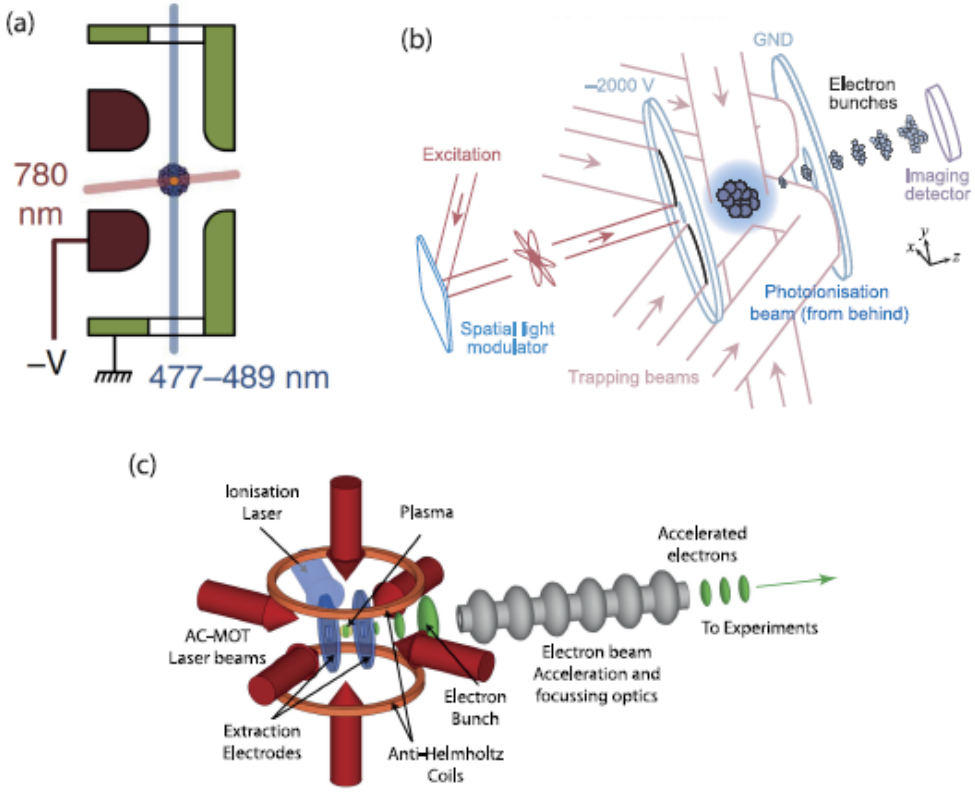

FIGURE 1.22: Some examples of electron sources from cold atoms. a) design from ref. [49] with Rb atoms, for rapid switching of the acceleration field b) from ref. [69] adapted for arbitrary transverse beam shaping c) based on an AC-MOT, used to produce short electron bunches, from ref. [70]

Indeed the fundamental difference between an ion and an electron is that in an electric field, the kinetic energy of the former is a non-negligible term of its total mechanical energy. Thus, reducing the kinetic energy spread of the ions significantly reduces the energy spread. An electron and an ion acquire the same amount of electric potential energy (in absolute value) when the pair is created at rest (neglecting any momentum kick from the ionisation process, dealt with in section 4.1.1) at a potential V: $E_{pot} = eV$. This potential energy will, after an acceleration from $\pm V$ to 0 V, translate into additional kinetic energy:

$$E_{kin}^{pot} = \frac{1}{2} m_e \left(v_e^{pot}\right)^2 = \frac{1}{2} m_{ion} \left(v_{ion}^{pot}\right)^2 \tag{1.22}$$

And so the ratio of the velocity amplitude coming solely from the initial potential energy is

$$\frac{v_e^{add}}{v_{ion}^{add}} = \sqrt{\frac{m_{ion}}{m_e}} \approx 492 \text{ for Cs} \tag{1.23}$$

This means that an electron will have an additional velocity 492 times bigger than the velocity added to the ion. Thus the spread in initial kinetic energy (the temperature), has 492 times less influence (for caesium ions) on the final electron speed dispersion than on that of the ions. Considering an atomic cloud whose center of mass is at rest in the laboratory frame of reference, the initial velocity dispersion of the atoms that leads to

1 meV of final electron energy spread is

$$\Delta v_{1\,\mathrm{meV}} = \frac{1}{2}\sqrt{\frac{2\cdot 10^{-3}e}{m_e}} \approx 18\,800\,\mathrm{m/s} \text{ for electrons} \tag{1.24}$$

when it is only 38 m/s for caesium ions.

Comparing this figure with typical gas phase atom velocities at room temperature (a few hundred m/s), we conclude that the cold atom/cold ion analogy is correct, but the cold atom/cold electron analogy is misleading. It is not enough to cool atoms to get cold electrons, because the dominant terms of the energy spread are not directly linked to the initial atomic temperature, but instead to energy potential differences and energy due to the ionisation process.

To summarize, in an ion beam (formed by the ionisation of a neutral atomic beam) the total energy spread depends on the initial kinetic energy spread. For electrons, the initial neutral kinetic energy spread (due to thermal agitation at room temperature) is generally negligible compared to the potential spread dispersion.

In the currently existing electron sources from cold atoms, the energy spread is at least three times higher than the usual sources in microscopy[71,74], which are already far from being monochromatic. This is the direct consequence of the strong electric extraction fields that they use (around 1 kV/cm to 10 kV/cm), the moderate size of the ionization zone (typically around 200 µm)[74] and of equation 1.15. The current implementations of these kind of sources use large electric fields because they are used in ultra-fast electron diffraction studies, where the extraction needs to be ultra-fast to preserve their high temporal and spatial coherence[49,71]. In order to use these in our application, we need to lower the energy spread by using a lower extracting field.

1.4.4 Electron-electron interactions

Origin

The fourth point is the Coulombic interactions between electrons. I separate it from the interactions with the space charge of the ions because it is not active only in the ionisation zone but from the ionisation to the detector.

Electron-electron interaction's detrimental effects on electron beams have different names in the literature, and some names are sometimes used in different meanings, depending on the sub-field in which it is used. We follow here the nomenclature of the reference [30], separating the interactions between electrons into space-charge effects and the Boersch effect, which can be further decomposed into the energetic Boersch effect and the spatial Boersch effect. The space charge interaction between electrons is a global Coulomb interaction along the column depending on the mean charge density. It depends strongly on the number of crossovers, current and energy of the electrons[75]. This interaction decreases brightness (by increasing emittance) but when the emittance increases linearly with the charge density, this growth is reversible. However, it does not increase the energy spread[76]. This effect has been the subject of many studies (and a very detailed treatment can be found in chapter 7 of Ref. [31]).

The precise measurements of electron beam properties throughout the development of electron guns has revealed that the interactions between electrons can not be fully

explained by global space-charge effects[77]. Among the discrepancies, the broadening of the energy and spatial distributions are called the energetic Boersch effect and the spatial Boersch effect, respectively. Contrary to space-charge (i.e. mean field) effects, these are the results of pair-interaction between electrons, in a stochastic way.

The spatial Boersch effect, also called "trajectory displacement" or Loeffler effect, represents a lateral shift of the electron position due to the pair interaction. Contrary to the space-charge effects, this is not a reversible evolution and this effect actually decreases the brightness of the source, but does not increase the energy spread.

The energetic Boersch effect is the broadening of the energy distribution of the electrons due to stochastic pair interactions between electrons. It is closely related to the probability of formation of an electron in direct proximity to another electron, which would induce strong Coulombic repulsion and thus a heating of the translational degrees of freedom of electrons. This effect is also called DIH for "Disorder-induced Heating" in the field of ultracold plasmas[78].

This effect is particularly important for sources in photoionization, but an interesting effect of Rydberg physics can limit the amplitude of DIH: the dipole blockade effect.

Solution

Dipole blockade occurs when (at least two) neutral atoms are close to each other, and one of them is excited to a Rydberg level. Because two Rydberg states have a strong interaction, this shifts the resonant frequency to excite the second ground atom to a Rydberg state. In the case of a spectrally narrow excitation radiation, this shift can be large enough to bring the second ground atom transition to the Rydberg state out of resonance with the laser. In the absence of electric field, the Van der Walls interaction between two Rydberg states is proportional to $1/r^6$ (r being the distance between these atoms), the probability to excite two very-close Rydberg atoms is thus small. In an electron source based on the formation of Rydberg states as intermediate states, the probability to create electrons very close to each other is thus equally small. The radius of dipole blockade in an atomic sample can be as large as 10 µm for Rydberg states around 80[79]. Using this feature of Rydberg atoms was indeed proposed for a photo-ion source from the ionisation of Rydberg atoms as a way to reduce the disorder-induced heating or energetic Boersch effect[80].

The energy spread due to pair interaction (or energetic Boersch effect) is present not only in the ionisation region but also all along the column. Boersch effects are by their stochastic nature not compensable, so one must use these simple design rules to limit their influence on the final energy spread and brightness of the electron beam:

- Avoiding crossovers, points where the average inter-electron distance gets small.
- Transporting the electrons at high energy. As a rule-of-thumb a higher acceleration always decreases the Coulomb effects. The reason is that as electrons go faster, they spend less time in the column, so they are less sensible to deteriorating interactions. So in cases where the energy of the electrons has to be low in certain part of the instrument (at the sample in a LEEM for example), it is better to transport them at high energy, decelerate and then re-accelerates them than to transport them at the required low energy.

- Limit the current of the source, with a beam-limiting aperture for example. When the crucial point of the electron source is its energy spread then it is preferable to limit the current to the minimal value.

In our design of the HREELM column, simulations have shown that at a current of 1 nA, electron-electron interactions has negligible influence on the final energy spread of the electron beam[24].

1.4.5 Parasitic effects

The "parasitic" effects (the fifth point) include contributions from uncontrolled oscillating electric and magnetic fields, power supply instabilities, and all sources of energy spread that are not calculable or easily controllable. The ionisation zone must be very well shielded from uncontrolled electric fields by being remote from the vacuum chamber surfaces, avoiding as much as possible insulating elements (whose electric potential is not easily controllable) close to the electrons and stabilising the power supplies to the electrodes. In HREELM, the working potential is 3 kV so voltage-supplies with stability and precision around 10^{-6} are required. This value of working potential has been chosen partly because of the relatively cheap voltage supplies with this level of stability (e.g. at ISEG company). Keeping the same energy resolution at higher working potential would significantly increase the price of such an instrument. Any oscillating or uncontrolled constant magnetic field[11] must be eliminated by several layers of μ-metal shielding[12] in the zones were the electron are slow. An important source of parasitic energy spread is the differential surface potential drifts between different parts of the apparatus, especially the electron source and the sample. The surface potentials are greatly influenced by the deposited layers, especially with caesium which is the most electro-positive stable element. Covering electrodes with colloidal graphite can improve the stability of surface potentials (even with alkali metal coverage), that have shown to be around 1 meV/h, low enough to allow below 5 meV electron spectroscopy[54,59].

For applications requiring an electron source with very low energy dispersion, the best possible control of these five points is essential.

[11] constant magnetic fields such as the Earth's magnetic field do not induce energy spread[61]

[12] An alloy of nickel, iron and molybdenum having a very high magnetic permeability, that "traps" magnetic fields

Section summary

Electron sources from the ionisation of atoms

In this section I have detailed all the possible sources of energy spread in an electron source from the ionisation of atoms, and have regrouped them in five different points. To be able to produce monochromatic electron sources, a good control of these five points is required: the cold atom/cold ion analogy is correct, but the cold atom/cold electron analogy is misleading. I have summed-up these energy spread sources and the possible solution for each of these points in the following table:

Sources of energy spread	Estimation of ΔE	Remedy
Ionisation process	a few meV for above-threshold photoionisation	Rydberg field-ionisation
Potential difference	$F\Delta z$	very low extracting field small ionisation region
Ion space-charge	15.6 meV/nA	active/passive clearing compensation, low I
Atomic temperature	$<$1 meV	no need
Boersch effect	a few meV	good column design low I
Parasitic effects	a few meV	shielding stable electric supplies

Designing and constructing the electron source of HREELM (either the continuous version or the pulsed version) will require the best control of all these points.

1.5 Conclusion on the electron source for HREELM

The HREELM project is ambitious, and at the heart of this ambition lies the promise of an electron source that is able to produce an electron beam with an energy spread less than 5 meV, at a current sufficient to allow spectroscopic cartography of a sample while keeping a brightness high-enough for low-energy electron imaging (see table 1.1.3).

From the above presentation of existing electrons sources and the very-low maximal energy spread of the electron beam that we need, two general possibilities arise for the electron source in HREELM. The first possibility is to follow the path of modern state-of-the-art STEM instruments and to rely on the monochromation of a bright microscopy source. This would demand the same instrumental efforts and would result in a very expensive instrument (recent high-end STEM cost between 5 M€ and 10 M€). The second possibility is to adapt the techniques developed in atomic physics for the spectroscopy of atoms and molecules to the world of microscopy, so as to develop a highly-monochromatic electron source from the ionisation of free atoms. This thesis explores the second possibility. It thus encompasses two main goals, with different ranges.

The first goal is almost a purely technological one, that is to construct the electron source best adapted to the requirements of the HREELM project, enabling its unique possibilities. The second goal, with further reaching possible consequences, is to explore in details how the peculiar properties of Rydberg atoms can be used to improve electron and ion sources.

These two goals are not completely independent, but there is no simple logical relation between them i.e. each one can be achieved without the other one. Indeed, the HREELM project could in principle adapt the techniques that allow highly sophisticated STEM instruments to reach 5 meV spectral resolution to low-energy electron microscopy. The first goal would then be achieved, but not the second one.

One of the great potential advantages of electron sources from the ionization of free atoms is the ability to easily generate spin-polarized electron beams[81]. The spin polarisation of the photo-electrons can be explained by the transfer of the ionising laser polarisation to the ejected electron via the spin-orbit interaction, or the so-called Fano effect[82]. This would enable the microscopy of magnetic domain walls[83] or the observation of atomic steps in magnetic thin films[84], with the low-energy spread characteristic of these sources.

It it important to note that the introduction of an intrinsically low-energy spread electron source to the electron microscopy community would have advantages beyond the realisation of the HREELM project, as it would suppress the effect of chromatic aberrations that limit most of the electron microscopes nowadays.

There is a strongly dividing line in terms of design, ion space charge, analysing instrument and detection scheme, that is the question of whether the source should be continuous or pulsed. This choice has heavy consequences on the instrument as a whole, but also on the operation of the electron source and the solutions that we can apply to try to limit the energy spread. As an example, if we decide to use a HSA for the analysis, then we need higher primary current because of its slit, and this has deep impacts on the kind of Rydberg states we would ionise or on the higher ion space charge that it would create. On the other hand, ToF analysis requires a very precise temporal resolution of the electrons, as well as a region of very-low energy flight, that requires extra care on the magnetic shielding.

Chapters 4 and 5 present the experimental efforts of the present work in both directions, starting with the continuous electron source, and followed by the pulsed-electron source. A preliminary to these studies is the theoretical description of Rydberg atoms under an electric field, that is introduced in the next chapter, chapter 2. This theory gives us access to Stark maps of Rydberg atoms that we test against experiments in chapter 3.

References

[1] E. Brüche. "Elektronenstrahl und Gasentladung". In: *Annalen der Physik* 408.4 (1933), pp. 377–403. ISSN: 00033804. DOI: 10.1002/andp.19334080402.

[2] M. Knoll and E. Ruska. "Das Elektronenmikroskop". In: *Zeitschrift fr Physik* 79.9-10 (1932), p. 699. ISSN: 1434-6001. DOI: 10.1007/BF01330526.

[3] Manfred Baron von Ardenne. *Elektronen-Übermikroskopie*. Berlin, Heidelberg: Springer Berlin Heidelberg, 1940. ISBN: 978-3-642-47103-2. DOI: 10.1007/978-3-642-47348-7.

[4] J. Hillier and R. F. Baker. "Microanalysis by Means of Electrons". In: *Journal of Applied Physics* 15.9 (1944), pp. 663–675. ISSN: 0021-8979. DOI: 10.1063/1.1707491.

[5] M. P. Seah and W. A. Dench. "Quantitative electron spectroscopy of surfaces: A standard data base for electron inelastic mean free paths in solids". In: *Surface and Interface Analysis* 1.1 (1979), pp. 2–11. ISSN: 0142-2421. DOI: 10.1002/sia.740010103.

[6] Louis De Broglie. "Recherches sur la théorie des Quanta". Theses. Migration - université en cours d'affectation, Nov. 1924. URL: https://tel.archives-ouvertes.fr/tel-00006807.

[7] John C. H. Spence. "Outrunning damage: Electrons vs X-rays-timescales and mechanisms". In: *Structural dynamics (Melville, N.Y.)* 4.4 (2017), p. 044027. ISSN: 2329-7778. DOI: 10.1063/1.4984606.

[8] R. P. Apkarian. "Conditions required for detection of specimen-specific SE-I secondary electrons in an analytical SEM". In: *Journal of microscopy* 154.Pt 2 (1989), pp. 177–188. DOI: 10.1111/j.1365-2818.1989.tb00580.x.

[9] Peter W. Hawkes and John C. H. Spence. *Springer Handbook of Microscopy*. Cham: Springer International Publishing, 2019. ISBN: 978-3-030-00068-4. DOI: 10.1007/978-3-030-00069-1.

[10] David C. Bell and Natasha Erdman, eds. *Low Voltage Electron Microscopy*. Chichester, UK: John Wiley & Sons, Ltd, 2012. DOI: 10.1002/9781118498514.

[11] Academic Press Inc., ed. *Fifth International Congress for Electron Microscopy*. Elsevier, 1962. ISBN: 9781483227955.

[12] E. Bauer. "Surface electron microscopy: the first thirty years". In: *Surface Science* 299-300 (1994), pp. 102–115. ISSN: 00396028. DOI: 10.1016/0039-6028(94)90649-1.

[13] S. M. Schramm, S. J. van der Molen, and R. M. Tromp. "Intrinsic instability of aberration-corrected electron microscopes". In: *Physical review letters* 109.16 (2012), p. 163901. ISSN: 0031-9007. DOI: 10.1103/PhysRevLett.109.163901.

[14] R. Bruce King, ed. *High Resolution Electron Energy-Loss Spectroscopy: Encyclopedia of inorganic chemistry*. 2. ed., new and completely rev. Chichester: Wiley, 2005.

[15] H. Ibach and D. L. Mills. *Electron Energy Loss Spectroscopy and Surface Vibrations*. Elsevier, 1982. DOI: 10.1016/c2013-0-10894-x.

[16] Larry L. Kesmodel. "High-Resolution Electron Energy Loss Spectroscopy (HREELS)". In: *Encyclopedia of Surface and Colloid Science*, 2015, pp. 3038–3045.

[17] LK Technologies. *ELS5000-Brochure*. URL: http://www.lktech.com/documents/ELS5000-brochure.pdf (visited on 06/10/2020).

[18] Y. Fujikawa, T. Sakurai, and R. M. Tromp. "Surface plasmon microscopy using an energy-filtered low energy electron microscope". In: *Physical review letters* 100.12 (2008), p. 126803. ISSN: 0031-9007. DOI: 10.1103/PhysRevLett.100.126803.

[19] Lucien Henry. "Filtrage magnétique des vitesses en microscopie électronique". In: *Bulletin de la Société française de Minéralogie et de Cristallographie* 88.2 (1965), pp. 172–198. ISSN: 0037-9328. DOI: 10.3406/bulmi.1965.5833.

[20] R. F. Egerton. *Electron Energy-Loss Spectroscopy in the Electron Microscope*. Boston, MA: Springer US, 2011. ISBN: 978-1-4419-9582-7. DOI: 10.1007/978-1-4419-9583-4.

[21] C. Colliex. "From a physicist's toy to an indispensable analytical tool in many fields of science: A personal view of the leading contribution of Ondrej Krivanek to the spectacular successes of EELS spectroscopy in the electron microscope". In: *Ultramicroscopy* 180 (2017). ISSN: 03043991. DOI: 10.1016/j.ultramic.2016.11.007.

[22] T. C. Lovejoy, G. J. Corbin, N. Dellby, N. Johnson, M. V. Hoffman, A. Mittelberger, and O. L. Krivanek. "Progress in Ultra-High Energy Resolution EELS". In: *Microscopy and Microanalysis* 25.S2 (2019), pp. 628–629. ISSN: 1431-9276. DOI: 10.1017/S1431927619003878.

[23] R. Wichtendahl et al. "SMART: An Aberration-Corrected XPEEM/LEEM with Energy Filter". In: *Surface Review and Letters* 05.06 (1998), pp. 1249–1256. ISSN: 0218-625X. DOI: 10.1142/S0218625X98001584.

[24] Marian Mankos, Khashayar Shadman, Raphaël Hahn, Yan J. Picard, Daniel Comparat, Olena Fedchenko, Gerd Schönhense, Lionel Amiaud, Anne Lafosse, and Nick Barrett. "Design for a high resolution electron energy loss microscope". In: *Ultramicroscopy* 207 (2019), p. 112848. ISSN: 03043991. DOI: 10.1016/j.ultramic.2019.112848.

[25] M. Mankos and K. Shadman. *Electron Optics Design*. Technical Report for HREELM Project. Electron Optica, Inc., 2018.

[26] Surface Concept GmbH. *Delayline Detectors*. URL: https://www.surface-concept.com/downloads/info/delaylinedetectors.pdf (visited on 06/06/2020).

[27] K. Medjanik et al. "Progress in HAXPES performance combining full field k-imaging with time of flight recording". In: *Journal of synchrotron radiation* 26.Pt 6 (2019), pp. 1996–2012. DOI: 10.1107/S1600577519012773.

[28] F. S. Hage, D. M. Kepaptsoglou, Q. M. Ramasse, and L. J. Allen. "Phonon Spectroscopy at Atomic Resolution". In: *Physical Review Letters* 122.1 (2019). ISSN: 0031-9007. DOI: 10.1103/PhysRevLett.122.016103.

[29] O. L. Krivanek et al. "Progress in ultrahigh energy resolution EELS". In: *Ultramicroscopy* 203 (2019), pp. 60–67. ISSN: 03043991. DOI: 10.1016/j.ultramic.2018.12.006.

[30] P. W. Hawkes and E. Kasper, eds. *Principles of electron optics*. Second edition. London: Elsevier/AP Academic Press an imprint of Elsevier, 2018. ISBN: 978-0-08-102256-6. DOI: 10.1016/B978-0-08-102256-6.00041-9.

[31] Jon Orloff. *Handbook of charged particle optics*. 2nd ed. Boca Raton: CRC Press/Taylor & Francis, 2009. ISBN: 1420045547.

[32] Harald Ibach, Martin Balden, and Sieghart Lehwald. "Recent advances in electron energy loss spectroscopy of surface vibrations". In: *Journal of the Chemical Society, Faraday Transactions* 92.23 (1996), p. 4771. ISSN: 0956-5000. DOI: 10.1039/FT9969204771.

[33] Niels de Jonge, Yann Lamy, Koen Schoots, and Tjerk H. Oosterkamp. "High brightness electron beam from a multi-walled carbon nanotube". In: *Nature* 420.6914 (2002), pp. 393–395. DOI: 10.1038/nature01233.

[34] S. Mamishin, Y. Kubo, R. Cours, M. Monthioux, and F. Houdellier. "200 keV cold field emission source using carbon cone nanotip: Application to scanning transmission electron microscopy". In: *Ultramicroscopy* 182 (2017), pp. 303–307. ISSN: 03043991. DOI: 10.1016/j.ultramic.2017.07.018.

[35] Xiuyuan Shao and Anjam Khursheed. "A Review Paper on "Graphene Field Emission for Electron Microscopy"". In: *Applied Sciences* 8.6 (2018), p. 868. DOI: 10.3390/app8060868.

[36] S. T. Purcell, Vu Thien Binh, and N. Garcia. "64 meV measured energy dispersion from cold field emission nanotips". In: *Applied Physics Letters* 67.3 (1995), pp. 436–438. ISSN: 0003-6951. DOI: 10.1063/1.114624.

[37] Aaron W. Baum, William E. Spicer, Roger Fabian W. Pease, Kenneth A. Costello, and Verle W. Aebi. "Negative electron affinity photocathodes as high-performance electron sources: Part 2: Energy spectrum measurements". In: *Proc. SPIE* 2550 (1995), pp. 189–196. DOI: 10.1117/12.221430.

[38] D. A. Orlov. "Ultra-Cold Electron Beams for the Heidelberg TSR and CSR". In: *AIP Conference Proceedings*. AIP, 2005, pp. 478–487. DOI: 10.1063/1.2190155.

[39] H. Boersch, J. Geiger, and W. Stickel. "Das Auflsungsvermgen des elektrostatisch-magnetischen Energieanalysators fr schnelle Elektronen". In: *Zeitschrift fr Physik* 180.4 (1964), pp. 415–424. ISSN: 1434-6001. DOI: 10.1007/BF01380526.

[40] Stephan Uhlemann and Max Haider. "Experimental set-up of a purely electrostatic monochromator for high resolution and analytical purposes of a 200 kV TEM". In: *Microscopy and Microanalysis* 8.S02 (2002), pp. 584–585. ISSN: 1431-9276. DOI: 10.1017/S1431927602105861.

[41] P. C. Tiemeijer, J. H. A van Lin, B. H. Freitag, and A. F. de Jong. "Monochromized 200 kV (S)TEM". In: *Microscopy and Microanalysis* 8.S02 (2002), pp. 70–71. ISSN: 1431-9276. DOI: 10.1017/S143192760210184X.

[42] E. Essers, G. Benner, T. Mandler, S. Meyer, D. Mittmann, M. Schnell, and R. Höschen. "Energy resolution of an Omega-type monochromator and imaging properties of the MANDOLINE filter". In: *Ultramicroscopy* 110.8 (2010), pp. 971–980. ISSN: 03043991. DOI: 10.1016/j.ultramic.2010.02.009.

[43] Terauchi, Tanaka, Tsuno, and Ishida. "Development of a high energy resolution electron energy-loss spectroscopy microscope". In: *Journal of microscopy* 194.1 (1999), pp. 203–209. DOI: 10.1046/j.1365-2818.1999.00450.x.

[44] O. L. Krivanek, J. P. Ursin, N. J. Bacon, G. J. Corbin, N. Dellby, P. Hrncirik, M. F. Murfitt, C. S. Own, and Z. S. Szilagyi. "High-energy-resolution monochromator for aberration-corrected scanning transmission electron microscopy/electron energy-loss spectroscopy". In: *Philosophical transactions. Series A, Mathematical, physical, and engineering sciences* 367.1903 (2009), pp. 3683–3697. DOI: 10.1098/rsta.2009.0087.

[45] Shigeyuki Morishita, Masaki Mukai, Kazu Suenaga, and Hidetaka Sawada. "Atomic Resolution Imaging at an Ultralow Accelerating Voltage by a Monochromatic Transmission Electron Microscope". In: *Physical review letters* 117.15 (2016), p. 153004. ISSN: 0031-9007. DOI: 10.1103/PhysRevLett.117.153004.

[46] Takanori Nakane et al. "Single-particle cryo-EM at atomic resolution". In: *Nature* (2020). DOI: 10.1038/s41586-020-2829-0.

[47] David Field, Stuart L. Lunt, and Jean-Pierre Ziesel. "The Quantum World of Cold Electron Collisions". In: *Accounts of Chemical Research* 34.4 (2001), pp. 291–298. ISSN: 0001-4842. DOI: 10.1021/ar0000962.

[48] D. Klar, M-W Ruf, and H. Hotop. "A tunable laser-atomic beam photoelectron source with sub-milli-electron-volt resolution: design, operation and application to threshold electron attachment studies". In: *Journal of Physics B: Atomic and Molecular Physics* 5.10 (1994), pp. 1248–1261. ISSN: 0022-3700. DOI: 10.1088/0957-0233/5/10/010.

[49] W. J. Engelen, M. A. van der Heijden, D. J. Bakker, E. J. D. Vredenbregt, and O. J. Luiten. "High-coherence electron bunches produced by femtosecond photoionization". In: *Nature Communications* 4 (2013), p. 1693. ISSN: 2041-1723. DOI: 10.1038/ncomms2700.

[50] A. C. Gallagher and G. York. "A photoionization source of monoenergetic electrons". In: *Review of Scientific Instruments* 45.5 (1974), pp. 662–668. ISSN: 0034-6748. DOI: 10.1063/1.1686709.

[51] M. Kurokawa, M. Kitajima, K. Toyoshima, T. Odagiri, H. Kato, H. Kawahara, M. Hoshino, H. Tanaka, and K. Ito. "Threshold photoelectron source for the study of low-energy electron scattering: Total cross section for electron scattering from krypton in the energy range from 14 meV to 20 eV". In: *Physical Review A* 82.6 (2010), p. 593. ISSN: 1050-2947. DOI: 10.1103/PhysRevA.82.062707.

[52] S. Barsotti, I. I. Fabrikant, M.-W. Ruf, and H. Hotop. "High resolution low-energy electron attachment to molecular clusters of sulfur dioxide". In: *International Journal of Mass Spectrometry* 365-366 (2014), pp. 301–310. ISSN: 13873806. DOI: 10.1016/j.ijms.2013.12.029.

[53] R. E. Kennerly, R. J. van Brunt, and A. C. Gallagher. "High-resolution measurement of the helium 1s2s2S2 resonance profile". In: *Physical Review A* 23.5 (1981), pp. 2430–2442. ISSN: 1050-2947. DOI: 10.1103/PhysRevA.23.2430.

[54] K. Franz, T. H. Hoffmann, J. Bömmels, A. Gopalan, G. Sauter, W. Meyer, M. Allan, M.-W. Ruf, and H. Hotop. "Low-lying resonances in electron-argon scattering: Measurements at 5−meV resolution and comparison with theory". In: *Physical Review A* 78.1 (2008), p. 1. ISSN: 1050-2947. DOI: 10.1103/PhysRevA.78.012712.

[55] A. Schramm, J. M. Weber, J. Kreil, D. Klar, M.-W. Ruf, and H. Hotop. "Laser Photoelectron Attachment to Molecules in a Skimmed Supersonic Beam: Diagnostics of Weak Electric Fields and Attachment Cross Sections Down to 20 μeV". In: *Physical Review Letters* 81.4 (1998), pp. 778–781. ISSN: 0031-9007. DOI: 10.1103/PhysRevLett.81.778.

[56] M. Keil, T. Kolling, K. Bergmann, and W. Meyer. "Dissociative attachment of low-energy electrons to vibrationally excited Na_2 molecules using a photoelectron source". In: *The European Physical Journal D* 7.1 (1999), pp. 55–64. ISSN: 1434-6060. DOI: 10.1007/s100530050347.

[57] M. Braun, S. Marienfeld, M-W Ruf, and H. Hotop. "High-resolution electron attachment to the molecules CCl_4 and SF_6 over extended energy ranges with the (EX)LPA method". In: *Journal of Physics B: Atomic, Molecular and Optical Physics* 42.12 (2009), p. 125202. ISSN: 0953-4075. DOI: 10.1088/0953-4075/42/12/125202.

[58] R. Hahn, A. Trimeche, C. Lopez, D. Comparat, and Y. J. Picard. *Cesium Rydberg states ionization study by 3-D ion-electron correlation*. 2021.

[59] J. Bömmels, K. Franz, T. H. Hoffmann, A. Gopalan, O. Zatsarinny, K. Bartschat, M.-W. Ruf, and H. Hotop. "Low-lying resonances in electron-neon scattering: Measurements at 4 meV resolution and comparison with theory". In: *Physical Review A* 71.1 (2005), p. 1. ISSN: 1050-2947. DOI: 10.1103/PhysRevA.71.012704.

[60] A. Gopalan, J. Bömmels, S. Götte, A. Landwehr, K. Franz, M.-W. Ruf, H. Hotop, and K. Bartschat. "A novel electron scattering apparatus combining a laser photoelectron source and a triply differentially pumped supersonic beam target: Characterization and results for the $He^-(1s2s^2)$ resonance". In: *The European Physical Journal D - Atomic, Molecular and Optical Physics* 22.1 (2003), pp. 17–29. ISSN: 1434-6060. DOI: 10.1140/epjd/e2002-00219-7.

[61] J. Bömmels, E. Leber, A. Gopalan, J. M. Weber, S. Barsotti, M.-W. Ruf, and H. Hotop. "Energy broadening due to photoion space charge in a high resolution laser photoelectron source". In: *Review of Scientific Instruments* 72.11 (2001), pp. 4098–4105. ISSN: 0034-6748. DOI: 10.1063/1.1412861.

[62] Ertmer, Blatt, Hall, and Zhu. "Laser manipulation of atomic beam velocities: Demonstration of stopped atoms and velocity reversal". In: *Physical review letters* 54.10 (1985), pp. 996–999. DOI: 10.1103/PhysRevLett.54.996.

[63] William D. Phillips, John V. Prodan, and Harold J. Metcalf. "Laser cooling and electromagnetic trapping of neutral atoms". In: *Journal of the Optical Society of America B* 2.11 (1985), p. 1751. ISSN: 0740-3224. DOI: 10.1364/josab.2.001751.

[64] David J. Wineland and Wayne M. Itano. "Laser Cooling". In: *Journal of the Optical Society of America B* 40.6 (1987), pp. 34–40. ISSN: 0740-3224. DOI: 10.1063/1.881076.

[65] A. Aspect, E. Arimondo, R. Kaiser, N. Vansteenkiste, and C. Cohen-Tannoudji. "Laser cooling below the one-photon recoil energy by velocity-selective coherent population trapping: theoretical analysis". In: *Journal of the Optical Society of America B* 6.11 (1989), p. 2112. ISSN: 0740-3224. DOI: 10.1364/JOSAB.6.002112.

[66] J. Dalibard. *Une brève histoire des atomes froids: Cours au Collège de France: Atomes et lumière en équilibre thermique*. 2015. URL: https://www.college-de-france.fr/site/jean-dalibard/course-2015-05-20-09h30.htm.

[67] B. J. Claessens, S. B. van der Geer, G. Taban, E. J. D. Vredenbregt, and O. J. Luiten. "Ultracold electron source". In: *Physical review letters* 95.16 (2005), p. 164801. ISSN: 1079-7114. DOI: 10.1103/PhysRevLett.95.164801.

[68] B. J. Claessens, M. P. Reijnders, G. Taban, O. J. Luiten, and E. J. D. Vredenbregt. "Cold electron and ion beams generated from trapped atoms". In: *Physics of Plasmas* 14.9 (2007), p. 093101. ISSN: 0375-9601. DOI: 10.1063/1.2771518.

[69] A. J. McCulloch, D. V. Sheludko, S. D. Saliba, S. C. Bell, M. Junker, K. A. Nugent, and R. E. Scholten. "Arbitrarily shaped high-coherence electron bunches from cold atoms". In: *Nature Physics* 7.10 (2011), pp. 785–788. ISSN: 1745-2473. DOI: 10.1038/nphys2052.

[70] G. Xia, M. Harvey, A. J. Murray, L. Bellan, W. Bertsche, R. B. Appleby, O. Mete, and S. Chattopadhyay. "An ultracold low emittance electron source". In: *Journal of Instrumentation* 9.06 (2014), P06011–P06011. ISSN: 1367-2630. DOI: 10.1088/1748-0221/9/06/P06011.

[71] Andrew J. McCulloch, Ben M. Sparkes, and Robert E. Scholten. "Cold electron sources using laser-cooled atoms". In: *Journal of Physics B: Atomic, Molecular and Optical Physics* 49.16 (2016), p. 164004. ISSN: 0953-4075. DOI: 10.1088/0953-4075/49/16/164004.

[72] M. Viteau et al. "Ion microscopy based on laser-cooled cesium atoms". In: *Ultramicroscopy* 164 (2016), pp. 70–77. ISSN: 03043991. DOI: 10.1016/j.ultramic.2015.12.007.

[73] Brenton J. Knuffman, Adam V. Steele, Jon Orloff, and Jabez J. McClelland. "Nanoscale focused ion beam from laser-cooled lithium atoms". In: *New Journal of Physics* 13.10 (2011), p. 103035. ISSN: 1367-2630. DOI: 10.1088/1367-2630/13/10/103035.

[74] J. G. H. Franssen, J. M. Kromwijk, E. J. D. Vredenbregt, and O. J. Luiten. "Energy spread of ultracold electron bunches extracted from a laser cooled gas". In: *Journal of Physics B: Atomic, Molecular and Optical Physics* 51.3 (2018), p. 035007. ISSN: 0953-4075. DOI: 10.1088/1361-6455/aa9954.

[75] M. S. Bronsgeest, J. E. Barth, G. A. Schwind, L. W. Swanson, and P. Kruit. "Extracting the Boersch effect contribution from experimental energy spread measurements for Schottky electron emitters". In: *Journal of Vacuum Science & Technology B: Microelectronics and Nanometer Structures* 25.6 (2007), p. 2049. ISSN: 10711023. DOI: 10.1116/1.2794067.

[76] D. J. Thompson, D. Murphy, R. W. Speirs, R. M. W. van Bijnen, A. J. McCulloch, R. E. Scholten, and B. M. Sparkes. "Suppression of emittance growth using a shaped cold atom electron and ion source". In: *Physical review letters* 117.19 (2016), p. 193202. ISSN: 1079-7114. DOI: 10.1103/PhysRevLett.117.193202.

[77] H. Boersch. "Experimentelle Bestimmung der Energieverteilung in thermisch ausgelsten Elektronenstrahlen". In: *Zeitschrift fr Physik* 139.2 (1954), pp. 115–146. ISSN: 1434-6001. DOI: 10.1007/BF01375256.

[78] S. G. Kuzmin and T. M. O'Neil. "Numerical simulation of ultracold plasmas". In: *Physics of Plasmas* 9.9 (2002), pp. 3743–3751. ISSN: 0375-9601. DOI: 10.1063/1.1497166.

[79] E. Urban, T. A. Johnson, T. Henage, L. Isenhower, D. D. Yavuz, T. G. Walker, and M. Saffman. "Observation of Rydberg blockade between two atoms". In: *Nature Physics* 5.2 (2009), pp. 110–114. ISSN: 1745-2473. DOI: 10.1038/nphys1178.

[80] D. Murphy, R. E. Scholten, and B. M. Sparkes. "Increasing the Brightness of Cold Ion Beams by Suppressing Disorder-Induced Heating with Rydberg Blockade". In: *Physical review letters* 115.21 (2015), p. 214802. ISSN: 1079-7114. DOI: 10.1103/PhysRevLett.115.214802.

[81] R. Mollenkamp and U. Heinzmann. "A source of highly spin-polarised slow electrons based on the 'Fano effect' on caesium atoms". In: *Review of Scientific Instruments* 15.6 (1982), pp. 692–696. ISSN: 0034-6748. DOI: 10.1088/0022-3735/15/6/020.

[82] U. Fano. "Spin Orientation of Photoelectrons Ejected by Circularly Polarized Light". In: *Physical Review* 178.1 (1969), pp. 131–136. ISSN: 0031-899X. DOI: 10.1103/PhysRev.178.131.

[83] Chao Zhou, Gong Chen, Jia Xu, Jianhui Liang, Kai Liu, Andreas K. Schmid, and Yizheng Wu. "Magnetic domain wall contrast under zero domain contrast conditions in spin polarized low energy electron microscopy". In: *Ultramicroscopy* 200 (2019), pp. 132–138. ISSN: 03043991. DOI: 10.1016/j.ultramic.2019.02.026.

[84] MacCallum Robertson, Yizheng Wu, Andreas K. Schmid, and Gong Chen. "Observation of surface step bunch induced perpendicular magnetic anisotropy using spin-polarized low energy electron microscopy". In: *Ultramicroscopy* 200 (2019), pp. 180–183. ISSN: 03043991. DOI: 10.1016/j.ultramic.2019.02.025.

Chapter 2

Rydberg atoms and Stark effect

> The miracle of the appropriateness of the language of mathematics for the formulation of the laws of physics is a wonderful gift which we neither understand nor deserve.
>
> Eugene Paul Wigner

In this chapter I will introduce the theoretical background relevant to the study of Rydberg atoms, from basic elements of Rydberg physics to an elaborate method to predict their energies and ionisation rates in an electric field. This is a necessary material to have in mind to use these particular atomic states for the elaboration of a high-performance electron source for the HREELM project. This discussion starts with a short introduction to Rydberg atoms (section 2.1), followed by a discussion of the quantum defect theory applied to alkali metal atoms (section 2.2), that will give some insights into the behaviour of the valence electron in these elements, as well as a derivation of the Rydberg formula from scattering theory. I follow in section 2.3 with the introduction of the problem of the hydrogen atom under an electric field, which will help me establish the tools and concepts to treat alkali metal atoms. This treatment can be achieved in numerous ways, but I insist in section 2.4 on the matrix diagonalization method, as well as the local frame-transformation method. This last method will be used throughout the rest of this work, as a basis for all our Rydberg ionisation studies in chapter 3, 4 and 5.

In the rest of this manuscript, I use the following notations: ω for angular frequencies (usually expressed in s^{-1}), ν for linear frequencies (in THz for transitions, and in MHz for shifts or state linewidths), $\bar{\nu}$ for spectroscopic wavenumbers (in cm^{-1}), and λ for wavelengths (in nm). These are linked to the energy by the following formulas: $E = h\nu(\mathrm{Hz}) = \frac{hc}{\lambda(nm)} = \hbar\omega(s^{-1}) = 100hc\bar{\nu}(cm^{-1})$. All wavelengths are expressed in vacuum. Many formulas are given in atomic units, and the conversion to SI units must take into account the context of the formula, i.e. if the atom is hydrogen or caesium. This distinction comes from the fact that the Hartree atomic units correspond to an atom with a virtually infinitely massive core, thus the reduced mass of the two-body problem is $\mu = \frac{m_e m_{Core}}{m_e + m_{Core}} = m_e$. The atomic units of length (the Bohr radius), energy (the Hartree)

and electric field are thus respectively:

$$a_0 = \frac{4\pi\epsilon_0\hbar^2}{m_e e^2}$$
$$E_h = \frac{\hbar^2}{m_e a_0^2} = 2Ry$$
$$F_{au} = \frac{E_h}{e a_0}$$

In this system of units, the Schrödinger equation for one electron is universal and given by equation 2.6. The atomic units for hydrogen or caesium are obtained by replacing m_e by $\mu_H = \frac{m_e m_p}{m_e+m_p}$ and $\mu_{Cs} = \frac{m_e m(^{133}\mathrm{Cs})}{m_e + m(^{133}\mathrm{Cs})}$ respectively. Conversion factors to SI units for these systems are given at the beginning of this document.

2.1 Elements of Rydberg physics

The alkali metal atoms have the peculiarity of having a closed-shell electronic configuration, with one extra electron. This makes them similar to hydrogen atoms in some aspects, where the proton is replaced with a big positively charged core and a single electron orbits around this core (see figure 2.1). This allows the description of the atom as a one electron state, with the usual quantum numbers n, l, m_l and m_s. Relativistic corrections lift the degeneracy of states with same n but different l, and electron spin-orbit coupling and the Darwin term lift the degeneracy of states of same l but different m_l, resulting in the fine structure of the atom. In large atoms (in caesium in particular), this is further complicated by hyperfine splitting, which is the interaction between the electron orbital moment and the nuclear dipole moment.

As the principal quantum number n of the one-electron state gets higher, this one electron state view becomes more and more accurate, and we call these high-n states the Rydberg states. An empirical formula for the energy levels of Rydberg states was devised as early as 1889[1,2]:

$$E(n) = \frac{-Ry}{(n-\delta_l)^2} \tag{2.1}$$

It gives the energy of a given level from the principal quantum number n as well as the quantum defect δ_l. A derivation of this formula will be given in section 2.2. As the spatial extension of the electronic wave function expands radially as n^2, these states can quickly exhibit sizes several orders of magnitude larger than ground-state atoms (the geometric cross-section is proportional to the radius squared so it evolves with n^4), as can be seen schematically on figure 2.1.

The spatial extension is not the only property that scales up with powers of n: their long radiative lifetimes ($\propto n^3$), strong and tunable long-distance (Van der Walls) interactions ($\propto n^{11}$), and sensitivity to electric fields (their polarizability rises as n^7) offer a very rich and complex physics. This last scaling means that the same electric field will induce an energy shift more than 6 orders of magnitude stronger on a $n = 80$ state than on a $n = 15$ state.

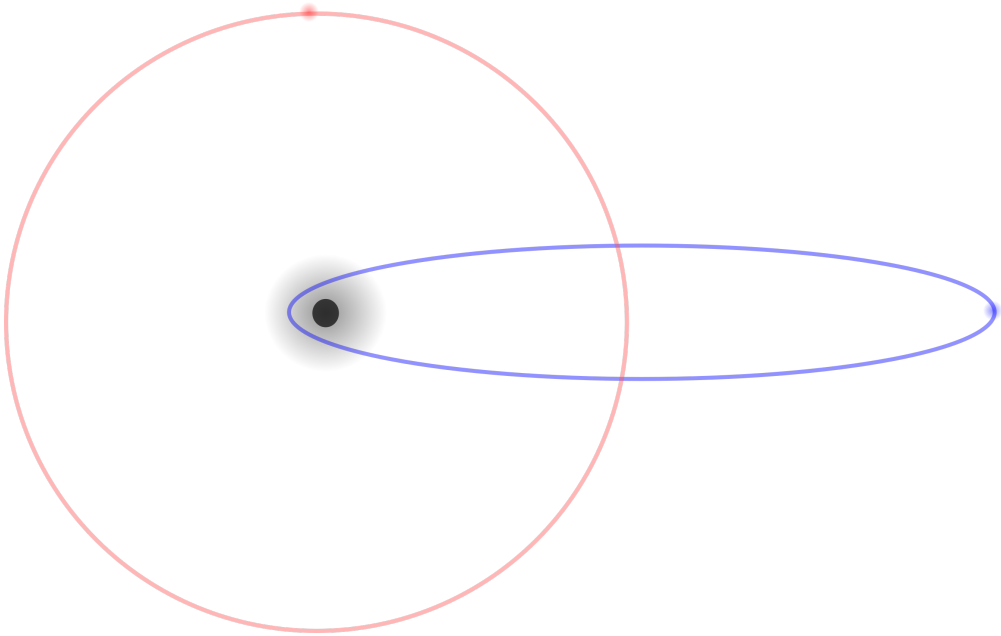

FIGURE 2.1: Schematic view of the classical orbit of the outer electron in a Rydberg atom (with high n number), showing the large extent of the outer electron. In black is the ion core, the grey cloud represents the closed-shell electrons. The blue orbit corresponds to a low l level, while the red orbit correspond to a high-l level ($l \approx n - 1$), so-called circular state.

For these reasons, Rydberg atoms are often attributed "exaggerated properties", quoting the reference book on that matter[3]. The actual frontier between "regular" atoms and Rydberg atoms is not firm however, and depends on the specific properties and conditions at play. Rydberg atoms with principal quantum number around 40 to 60 are routinely used in laboratories, but states with n over 1000 have been studied[4].

The effect of an external electric field $\vec{F}$ on a Rydberg atom can be treated with the Stark Hamiltonian $\mathcal{H}_{Stark} = -\vec{d}.\vec{F}$ with $\vec{d}$ the electric dipole moment of the system exposed the field. This additional term in the electron potential lowers the ionisation threshold energy of the atom to $E_F = -2\sqrt{F}$ in the direction of the electric field. In fact the field F_{ion} at which a given Rydberg states of principal quantum number n ionizes can be approximated[1] (in atomic units) by:

$$F_{ion} = \frac{1}{16n^4} \tag{2.2}$$

This will be analysed more precisely in sections 4.1.2, but it is important to note that Rydberg states ionise around a given electric field value.

On top of lowering the ionisation threshold, the electric field also shifts the energy of Rydberg states, an effect called the Stark shift. A Stark map, showing the evolution of the individual Rydberg states in an increasing electric field can be seen on figure 2.2, featuring the field F_{ion} as a dashed blue line.

This energy shift can be positive or negative, depending on the state. When it is negative, it means that the laser radiation to excite it from the ground state will shift towards lower frequencies, i.e. towards the red part of the spectrum. Thus states with a negative

[1] this formula neglects Stark-shift of the states

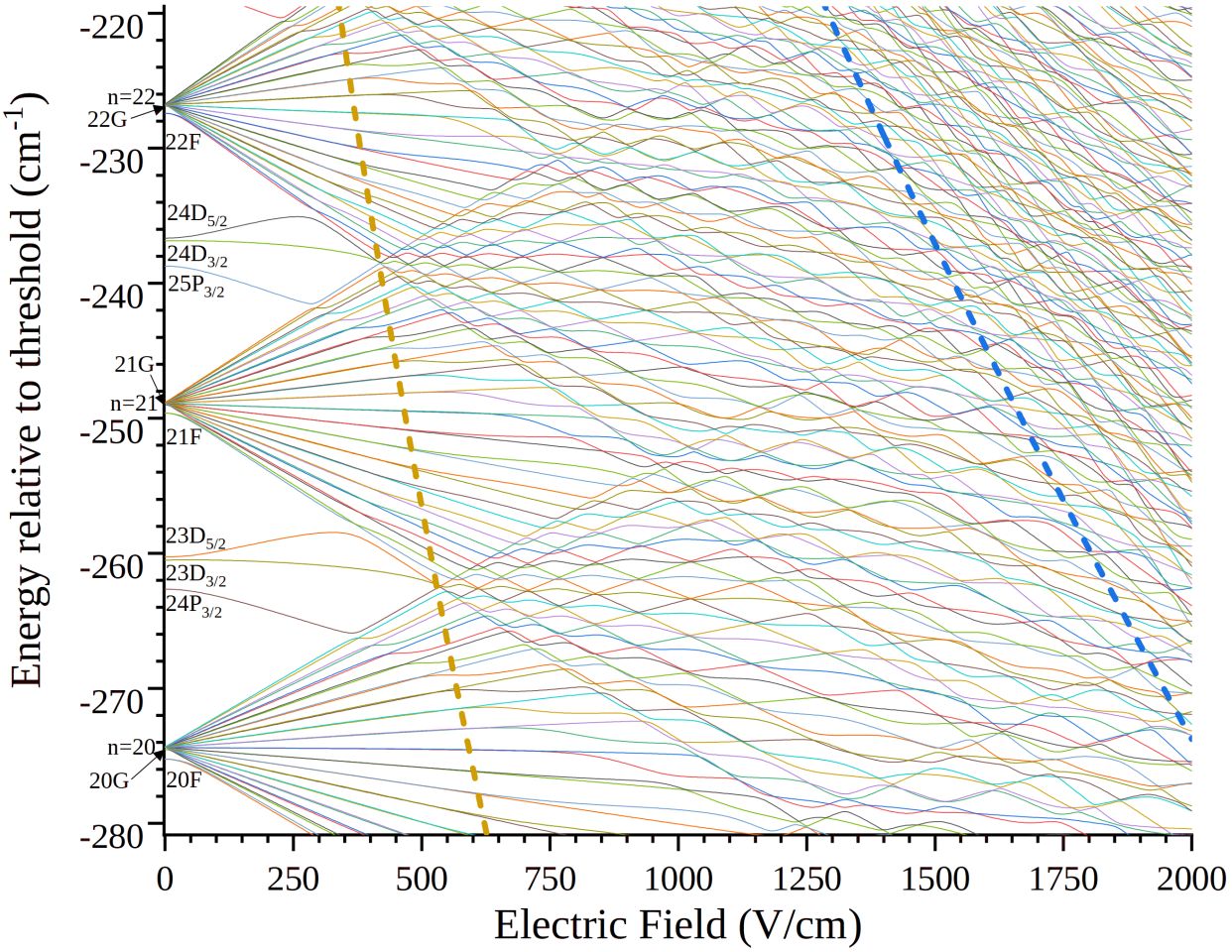

FIGURE 2.2: Computed Stark map of caesium around $n = 25$, between 0 and 2000 V/cm, with $|m_l| = 0$. Low l states ($l < 3$) are explicitly labelled, the others form the manifolds of indicated principal quantum number n. In blue dashed line is the classical ionisation threshold ($F = \frac{1}{16n^4}$), and in orange is the Inglis-Teller limit ($\frac{1}{3n^5}$) where the manifolds of different n start to mix, and marks the entry of the "spaghetti" region of the Stark map.

Stark shift are called "red states", and states with a positive Stark shift are called "blue states". Seeing the Stark effect as the orientation of the electric dipole $\vec{d}$ in the electric field, this means that red-states have their dipole oriented along the electric field. In other words, their Rydberg electron density is higher in the direction of the lowered potential. This means that theses states have a higher probability of ionising, because their excited electron is mostly close to the barrier, where the tunnelling probability is the higher.

"Blue states" will, following the same reasoning, have longer lifetimes regarding tunnelling ionisation. The Stark shift amplitude is proportional to the electric dipole of the state, and as the electric dipole amplitude evolves as n^2, the maximum Stark shift observed in Rydberg states can be large in comparison with the Stark shifts of the ground state, that are usually negligible. This energy shift also gives rise to state mixing, particularly after the Inglis-Teller limit where manifolds of different n mix (see the orange dashed line on figure 2.2) and new quantum numbers must be defined (see section 2.3). In most atoms this mixing complicates the energy level structure and makes the energy level prediction very difficult. However, alkali metal atoms are simple enough so that it is possible to predict precisely the energy levels of Rydberg states and their evolution under the action of electric fields, as further explored in section 2.4.

2.2 Quantum defect theory in alkali metal atoms

Before introducing methods to compute the effect of electric fields on the energy levels, I introduce the basic tools to describe the energy levels without an electric field. We already saw the Rydberg energy levels formula in equation 2.1, but I present here its derivation from scattering theory, giving us additional physical insight.

In an alkali metal Rydberg atom, characterised by a large principal quantum number n, the outer electron is far enough from the other electrons constituting the closed-shell ionic core that all these influences (the electron-core interactions) can be summed up in a potential depending only on the distance to the core, $V(r)$. This gives (in atomic units) the non relativistic time-independent Schrödinger equation:

$$E\Psi_{nlm}(\vec{r}) = \left(-\frac{1}{2}\nabla_r^2 + V(r)\right)\Psi_{nlm}(\vec{r}) \tag{2.3}$$

whose solutions are in the form

$$\Psi_{nlm}(\vec{r}) = \Psi_{nlm}(r,\theta,\phi) = \frac{u_{nl}(r)}{r}Y_{lm}(\theta,\phi) \tag{2.4}$$

where $Y_{lm}(\theta,\phi)$ is a spherical harmonic. With the use of an appropriate model potential for $V(r)$ (see equation 2.23 for an example), it is possible to numerically solve this equation for $u_{nl}(r)$ and get the energy levels of Rydberg states. However, the quantum defects approach provides more physical insights.

I plot on figure 2.3 the potential $V(r)$ for caesium and compare it the potential in hydrogen ($-1/r$). This allow me to define the distance r_0 where both these potentials are equivalent. Thus in an alkali-metal atom, for a large portion of space where $r > r_0$, the interaction with the core is very close to a pure $^{-1}/_{r}$ potential. This interaction and the

centrifugal term (in atomic units) gives:

$$V(r)^{r>r_0} = \frac{l(l+1)}{2r^2} - \frac{1}{r} \tag{2.5}$$

Thus the radial Schrödinger equation for $r > r_0$ can be written as:

$$\left(-\frac{1}{2}\frac{d^2}{dr^2} + \frac{l(l+1)}{2r^2} - \frac{1}{r} - E_{nl}\right) u_{nl}(r) = 0 \tag{2.6}$$

This is a second order linear equation so all its solutions can be written as a linear combination of any two linearly independent solutions. These base solutions for $E_{nl} = \epsilon$ are called $f_{\epsilon l}$ and $g_{\epsilon l}$ and can have various forms. We treat only bound state in the following, so we take ϵ as the negative energy $\epsilon = -1/2\nu^2$, with ν the effective quantum number (defined as positive). A usual choice is to take the following asymptotic forms, with D a parameter dependent on ν and l whose value is not important here:

$$f_{\epsilon l}(r)^{r>r_0} = \sqrt{\frac{\nu}{\pi}}\left(\frac{\sin(\pi(\nu-l))\exp r/\nu}{Dr^\nu} - \frac{\cos(\pi(\nu-l))Dr^\nu}{\exp^{r/\nu}}\right) \tag{2.7}$$

$$g_{\epsilon l}(r)^{r>r_0} = -\sqrt{\frac{\nu}{\pi}}\left(\frac{\cos(\pi(\nu-l))\exp r/\nu}{Dr^\nu} + \frac{\sin(\pi(\nu-l))Dr^\nu}{\exp^{r/\nu}}\right) \tag{2.8}$$

$f_{\epsilon l}$ is called the physical solution, or *regular* solution, because it obeys the boundary conditions for the pure Coulomb potential. $g_{\epsilon l}$ is the *irregular* solution because it is a solution for the pure Coulomb potential but with an unphysical boundary condition. For further use of these functions, we set $g_{\epsilon l}$ with a 90° phase lag behind $f_{\epsilon l}$.

These two functions ($f_{\epsilon l}$ and $g_{\epsilon l}$) serve as basis for the solutions of equation 2.6, that can be written as[5]:

$$u_{nl}^{r>r_0}(r) = \mathcal{N}\left(f_l(r) - \tan\mu_l g_l(r)\right) \tag{2.9}$$

Here $\mathcal{N}$ is a normalization constant and μ_l in the phase shift for the lth partial wave[2] (as in scattering theory). The interpretation of such a decomposition is quite straightforward: the term μ_l effectively mixes the pure Coulomb solution with the irregular solution due to the complicated core potential. Here we introduced δ_l, the quantum defect, as $\delta_l = \mu_l/\pi$.

Inserting eqs. 2.7 and 2.8 into eq. 2.9 gives:

$$u_{nl}^{r>r_0}(r) = \frac{\mathcal{N}'}{\cos(\pi\delta_l)}\left(\frac{\sin\left(\pi(\nu-l+\delta_l)\right)\exp\left(r/\nu\right)}{Dr^\nu} - \frac{\cos\left(\pi(\nu-l+\delta_l)\right)Dr^\nu}{\exp\left(r/\nu\right)}\right) \tag{2.10}$$

Since ν is defined as positive, this equation features a diverging term ($\exp(r/\nu)$) that must be eliminated. The only way to achieve that is to make the pre-factor $\sin(\pi(\nu-l+\delta_l))$ vanish. This condition gives:

$$\pi\left(\nu - l + \delta_l\right) = \pi z,\ z \in \mathbb{Z} \tag{2.11}$$

[2] in some references μ is called δ, but I reserve δ for the quantum defects

We can now define the principal quantum number n as $n = z + l$ and recall that $\epsilon = -1/2\nu^2$. The energy formula gives:

$$\epsilon_{nl} = -\frac{1}{2(n-\delta_l)^2} \tag{2.12}$$

This equation is given in atomic units, and the introduction of the Rydberg constant Ry converts to SI units and gives the well-known Rydberg energy formula :

$$E(n) = \frac{-Ry}{(n-\delta_l)^2} = \frac{-Ry}{n^{*2}} \tag{2.13}$$

This is therefore a derivation of equation 2.1. This formula is very close to the well-known hydrogen state formula, the two differences being the presence of δ_l and the different value of Ry. The Rydberg constant is indeed specific to each element, requiring a subscript when considering a particular element (for hydrogen it is called Ry_H and for caesium we use Ry_{Cs}). The universal Rydberg constant Ry_∞ is thus defined as the Rydberg constant for an infinitely heavy core

The physical meaning of the quantum defect is clear from the above derivation, as the influence of the finite-size core on the outer electron, similar to a phase shift of $\mu_l = \pi\delta_l$ at each revolution around the core. The bigger this phase-shift, the bigger the value of δ_l.

The subscript indicates that is depends strongly on the value of orbital quantum number l, but it is almost independent of n for $n \gtrapprox 10$. The values of quantum defects and of the Rydberg constant are obtained by fitting of a slightly modified formula (the Ritz formula, that generalizes eq. 2.13 to spectroscopic data, the precision from these measurements making the Rydberg constant one of the most accurately known physical constant across all physics[3].

Section summary

Quantum defect theory in alkali metal atoms

In this section I have introduced the quantum defect theory for alkali metal atoms and derived the Rydberg formula. The main lesson of this derivation is that the quantum defect δ_l, introduced to fit the energy levels with $E = -\frac{Ry}{(n-\delta_l)^2}$, can also be understood as a phase shift on the valence electron introduced at each recursion around the ion core by the departure from a pure Coulomb potential. Thus the quantum defect can be seen as a measure of the perturbation of the ion core on each specific Rydberg state. We have seen that each l-level has a specific quantum defect value, and that it does not depend on n passed $n \gtrapprox 10$.

[3] even though it was recently shifted by over 6 σ as a result of progress in the resolution of the proton radius puzzle

2.3 Stark effect on Rydberg states: hydrogen

Now that we know how to describe the energy levels of Rydberg atoms, I can introduce an electric field and see how this will be modified. As a first step I study the Stark effect on the Rydberg states of hydrogen, neglecting the fine and hyperfine structures. When a hydrogen atom is placed in a static electric field $\vec{F} = F\vec{e_z}$, the potential in which its electron evolves (at distance r from the core) changes from $V(r) = -\frac{1}{r}$ to:

$$V(r,z) = -\frac{1}{r} + Fz$$

The first order Stark effect lifts the degeneracy of the l levels (composed of m_l sub-levels), so l is no longer a good quantum number but m_l is.

It is common to express the problem in terms of parabolic coordinates ξ and η as it is fully separable in this representation:

$$\xi = r + z = r(1 + \cos\theta) \tag{2.14}$$
$$\eta = r - z = r(1 - \cos\theta) \tag{2.15}$$
$$\phi = \tan(y/x)^{-1} \tag{2.16}$$

As the (negative) field is lowering the ionisation threshold in the $+z$ direction, this means that the motion of the electron is bound in the η direction and the electron can escape in the ξ direction (visible at high r on figure 2.3). The advantage of using parabolic coordinates is apparent here because the solution wave-function to the Schrödinger equation can be written as a product (hence separable):

$$\psi^F_{\epsilon n_1 m_l} = \psi^F_{\epsilon\beta m_l}(\xi,\eta,\phi) = \frac{\exp(im_l\phi)}{\sqrt{2\pi}}\Xi^F_\beta(\xi)\mathrm{Y}^F_\beta(\eta) \tag{2.17}$$

Here ϵ is the electron energy with respect to the ionisation threshold when $F = 0$. The resulting Schrödinger equations (in the notation of Ref. [6]) are:

$$\left[\frac{d^2}{d\xi^2} + \left[-\frac{m_l^2-1}{4\xi^2} + \frac{\beta}{\xi} + \frac{\epsilon}{2} - \frac{F\xi}{4}\right]\right]\sqrt{\xi}\Xi^F_\beta(\xi) = 0, \tag{2.18}$$
$$\left[\frac{d^2}{d\eta^2} + \left[-\frac{m_l^2-1}{4\eta^2} + \frac{1-\beta}{\eta} + \frac{\epsilon}{2} + \frac{F\eta}{4}\right]\right]\sqrt{\eta}\mathrm{Y}^F_\beta(\eta) = 0 \tag{2.19}$$

One thing to note about these equations is that m_l appears squared, so it means states with the same absolute value of m_l will be energy-degenerate, in a direct consequence of the Kramers degeneracy theorem[7].

The actual form of Ξ^F_β and Y^F_β feature two new quantum numbers n_1 and n_2 (called the parabolic quantum numbers, equal to the number of nodes in Ξ^F_β and Y^F_β, respectively), as well as the usual n and m_l (remember that l is no longer a good quantum number). They obey the rule:

$$n_1 + n_2 + |m_l| + 1 = n \tag{2.20}$$

This means that giving n_1, n_2, m_l, and n is redundant. To remove this redundancy

Region	Core region	Coulomb region	Coulomb-Stark region
System	Complicated potential	Similar to field-free H	Similar to H under E-field
Potential	$V_l(r)$	$1/r$	$1/r + Fz$
Q. numbers	ε, l, m	ε, l, m	ε, β, m
Coordinates	Spherical coordinates	Spherical coordinates	Parabolic coordinates
Wave-functions	Unknown wave-functions	H wave-function: $\psi_{\varepsilon lm}(r,\theta,\phi)$ Regular: $f_{\varepsilon l}$ Irregular: $g_{\varepsilon l}$ Cs wave-function: $\Psi_{\varepsilon lm}(r,\theta,\phi)$	$\psi^F_{\varepsilon\beta m}(\xi,\eta,\phi)$ and $\chi^F_{\varepsilon\beta m}(\xi,\eta,\phi)$) (H)-Regular: $\Xi^F_\beta(\xi)$, $Y^F_\beta(\eta)$ (H)–Irregular: $Y^F_\beta(\eta)$

$U^{\varepsilon m}_{\beta l}$

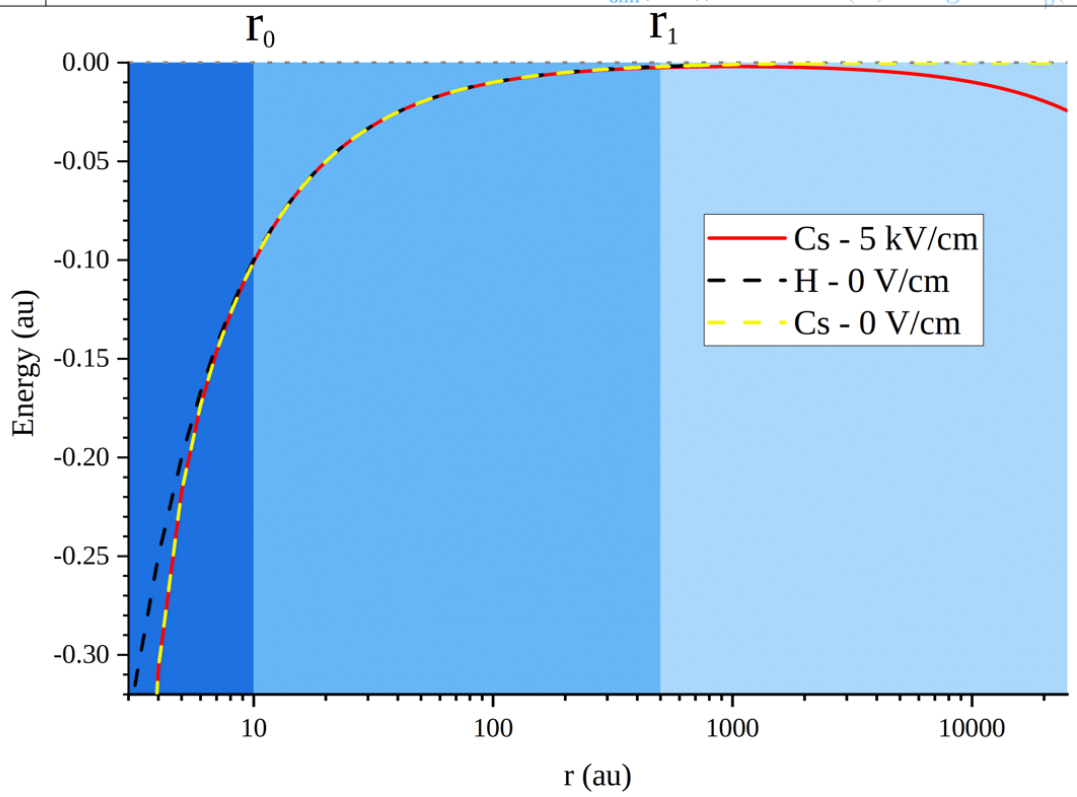

FIGURE 2.3: Log-linear plot of the field-free atomic potential (in atomic units) in function of its distance r to the ionic core experienced by the valence electron of a caesium atom (yellow dashes) compared to the Hydrogen case (black dash). For $r > r_0$ these are similar. Also shown is the caesium potential under an electric field of $-5\,\mathrm{kV/cm}$ oriented along r (red solid line), which is similar to field-free caesium for $r < r_0$, to field-free hydrogen for $r_0 < r < r_1$ and to the (not shown) Stark potential of hydrogen for $r > r_1$. On top of the plots are indicated the potential in each region, the good quantum numbers, the wave-functions for hydrogen and caesium and the transfer matrix $\underline{U}$ that converts spherical wave-functions into parabolic wave-functions.

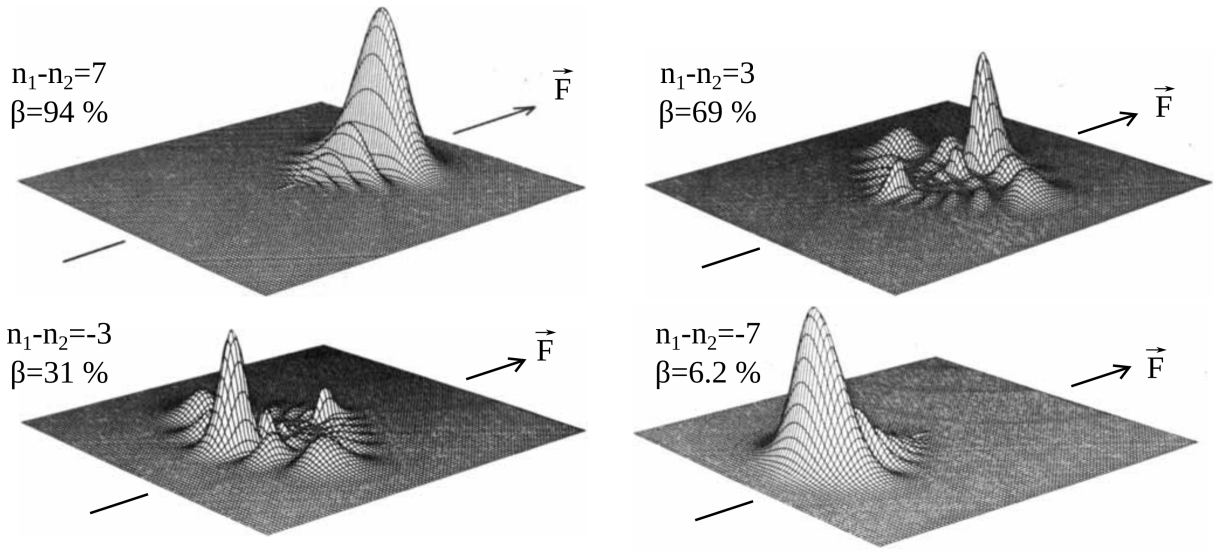

FIGURE 2.4: Representation of the charge distribution along the electric field $\vec{F}$ for 4 of the 8 different combinations of $n_1 - n_2$ for the states $n = 8$, $m_l = 0$. It clearly shows that β quantifies the charge orientation along the field. The real wave function are paraboloid of these shapes around the electric field axis. Adapted from [8]

in the following we label the states with the parameter β, that is the charge separation parameter. It is linked to the quantum numbers along:

$$\beta = \frac{1}{2} + \frac{n_1 - n_2}{2n} \tag{2.21}$$

This parameter actually depends on ϵ, F, and m_l and represents the fractional charge of the bounded electron in the ξ (up-field) and η (down-field) directions. It is a good quantum number for this problem, and has the advantage over n_1 and n_2 of not depending on the particular choice of parabolic coordinates. Figure 2.4 clearly illustrates the physical meaning of this quantum number as a charge separation along the field axis. If we take a look back, the only difference between equations 2.18 and 2.19 is the sign of the electric field term, and that β is changed to $1 - \beta$.

To establish the energy levels of hydrogen it is common to first compute Ξ_β^F and Υ_β^F with a null-electric field, and then add the electric field as a perturbation[3]. The first-order perturbation gives:

$$\epsilon(n, \beta) = -\frac{1}{2n^2} + 3n^2 \left(\beta - \frac{1}{2}\right) F \tag{2.22}$$

This means that hydrogen features a linear Stark shift, and thus that the Stark effect can be regarded as the orientation of a permanent electric dipole (given by $\beta - \frac{1}{2}$) in the electric field. The dipolar behaviour is apparent in figure 2.4. This also means for example that for states with $|m_l| = 1$ and the same $n = 8$ (called a multiplicity), the degeneracy of the 7 states will be lifted, with slopes of the linear Stark shift spanning from -72 to $+72$ by increments of 24. Some states, that have $\beta = 1/2$ (a symmetric charge distribution, i.e. no dipolar moment) will experience only a second-order Stark shift.

The use of perturbation theory to acquire the parabolic wave-functions means that

we are once again limited to moderate field values. To go further we can include higher order perturbations terms, but when approaching the field ionisation limit we must resort to more elaborate techniques, that will be introduced in section 2.4.2. It is to note that even for hydrogen, DC-Stark effect is by no means a completely-solved problem, and recent progress has brought new methods with increased precision.[9–11] In the following section we will see how we can use the results obtained in this section and apply them to alkali metal atoms like caesium.

Section summary

Stark effect on Rydberg states: hydrogen

In this section I have presented an analytic derivation of the Stark effect on Rydberg states of Hydrogen. It relies on the parabolic reformulation of the problem, and the introduction of new quantum numbers: n_1, n_2. The Stark shift is found to be linear for states of the same n-manifolds, that can be interpreted as the orientation of dipolar moment (characterised by the charge separation parameter β) in the electric field. In first order perturbation theory the Stark shift of the states is given by $\frac{3}{2}n^2\left(\beta - \frac{1}{2}\right)F$. Some states, with $\beta = 1/2$ feature no linear Stark shift, and second-order perturbation theory is required to obtain their Stark shift. Using perturbation theory implies that this view breaks down at high-field values, so more elaborate methods need to be devised.

2.4 Stark effect on Rydberg states: alkali metal atoms

In nonhydrogenic atoms, the problem of the Stark effect constitutes a difficult problem to tackle and we focus here on the case of alkali metal atoms, which constitute an already simplified version of the problem thanks to their unique valence electron. The way to simplify the problem of an alkali metal atom under an electric field is to devise regions of space where different approximations are valid (see figure 2.3). We start by considering the potential of the ionic core. Here the term 'core' means the atomic nucleus with its closed-shell electrons. This core is positively charged, has a finite spatial extension and a complex structure, as well as a non-negligible polarizability α_c. This creates a departure from a pure Coulomb potential. The dynamics of the outer electron close to the ionic core constitutes a complex many-body problem, complicated by the application of an external field.

However, at very short range, the external electric fields attainable in the laboratory are usually negligible in comparison with the core potential (see the comparison in figure 2.3), so it can be neglected for the treatment of the core. The core-potential $V_l(r)$ experienced by the electron can then be expressed as a parametric fitted potential[12]:

$$V_l(r) = -\frac{1}{r}\left(1 - \exp^{-a_1 r} - r\left(a_3 + a_4 r\right)\exp^{-a_2 r}\right) - \frac{\alpha_c}{2r^4}\left(1 - \exp^{-(r/r_c)^6}\right) \tag{2.23}$$

The parameter r_c cuts the non-physical behaviour of the r^{-4} potential at the origin and the value of the four a_i ($i = 1, 2, 3, 4$) parameters are l-dependent. A graphic comparison with a pure Coulomb potential for a p-state can be found in the low-r region of figure 2.3. This plot clearly features three different regions, delimited by two values of r called r_0 and r_1. Obviously r_0 and r_1 are not precisely defined but useful orders of magnitude are typically a few bohrs for r_0 (atomic unit of distance) and r_1 is chosen so that:

$$r_0 \ll r_1 \ll \frac{1}{\sqrt{F}}$$

The region of very low values of r, from the origin to r_0 is the core region, constituting a complex problem. Between r_0 and r_1 is the Coulomb region where both the electric field and the many-body character are weak. This means that the problem is, to a very good approximation, similar to a pure Coulomb potential. From r_1 to infinity, i.e. in the Coulomb-Stark region, the Stark shift is not negligible any more, but the core potential is very similar to the Coulomb potential, so that the problem is similar to an hydrogen atom under an electric field. The Schrödinger equation featuring the model potential of equation 2.23 can be solved numerically to obtain energy levels, but it does not provide as much information as an approximate analytic theory.

Many different methods have been devised over the years to obtain Stark shifts and Stark maps in alkali metal atoms. We will rapidly review two of them (the matrix diagonalization method (MD) and the local frame transformation method (LFT)), focusing on the accuracy of predicted energy levels at a given electric field, and the way of determining the lifetime of states in each method.

2.4.1 Matrix diagonalization

The most straightforward way to treat the problem of energy levels of alkali metal atoms under an electric field is the diagonalization of the Stark Hamiltonian[13]. It is the method implemented in the code "Alkali Rydberg Calculator" which is a Python library for computing properties of Rydberg states of alkali metal atoms[14]. It starts with the expression of the Hamiltonian of the atom under an DC-electric field in function of the zero-field Hamiltonian $\mathcal{H}_0$:

$$\mathcal{H}_{Stark} = \mathcal{H}_0 + F\hat{z} \tag{2.24}$$

This Hamiltonian can be diagonalised in the zero-field eigenstates basis set (taken as $|nlm_l\rangle$ or $|njm_j\rangle$ without and with the spin-orbit interaction respectively), giving new eigenstates with corresponding Stark shifts. The electric field mixes states with the rule $\Delta m_l = 0$ and $\Delta l = \pm 1$, and l is no longer a good quantum number but m_l still is.

This method provides energy levels and state mixing up to a good precision at low field but is rapidly limited by the necessity to include more and more basis states as the electric field goes up. Furthermore, the method includes only bound states, so states near the ionisation limit are not well described and no insight into ionisation rates can be obtained.

One way to improve the description of ionisation is the complex absorbing potential method. The starting point is the addition of a complex term $-i\eta\hat{W}$ to the atomic Hamiltonian $\hat{\mathcal{H}}$, giving a non-hermitian Hamiltonian $\hat{\mathcal{H}}_{CAP} = \hat{\mathcal{H}} - i\eta\hat{W}$. Several expressions

have been used for $\hat{W}$, such as $\hat{W} = \hat{r}^6$[15], a Heaviside function[16] or a combination of these two[17].

In the usual implementation, $\hat{W}$ has no adjustable parameter and the parameter η has to be evaluated for each resonance at each value of the electric field. It is also possible to parametrize $\hat{W}$ with $r_{cut-off}(F)$, that will represent a radial cut-off of the complex potential depending on the electric field, so that η can have the same value in a whole region of the spectrum, thus reducing the computational needs[17]. This radius is typically taken as the saddle point in the Stark Hamiltonian of the atom:

$$r_{cut-off}(F) = \frac{1}{\sqrt{F}}$$

The direct interpretation of the effect of the complex potential $-i\eta\hat{W}$ is the absorption of the outgoing wave at long range, giving its name to this method[18]. The eigenvalues ϵ_c of the complex Hamiltonian can be expressed with the real eigenvalues ϵ_r in the form:

$$\epsilon_c = \epsilon_r - i\frac{\Gamma}{2}$$

In this relation Γ is the ionisation rate of the considered state. This method has shown good agreement with experimental results, even above the classical ionisation threshold, for energy levels as well as for ionisation rates[17,19].

A similar approach to this method is the introduction of complex rotation into the description of the atom under an electric field. It consists in the substitution of complex operators for position and momentum in the Hamiltonian along $\hat{r} \leftarrow \hat{r} \times \exp(i\theta)$ and $\hat{p} \leftarrow \hat{p} \times \exp(-i\theta)$, with θ a free-parameter that needs to be determined for a certain range of resonances. This transformation results in a non-Hermitian Hamiltonian featuring complex eigenvalues, that can be used to obtain energy levels and ionization rates[20].

In particular it transforms a scattering state (with terms like $\exp(i\vec{k}\cdot\vec{r})$) into a bound state with a boundary condition (typically $\exp(-2k\sin\theta r)$). As the eigenfunctions are square-integrable and vanish asymptotically, the ionisation rate can be found by diagonalization of the non-Hermitian Hamiltonian matrix.

During the course of this work I used the matrix diagonalization method only occasionally, but relied heavily on another method, implemented by F. Robicheaux in a code at our disposal. In the next section I introduce the main ideas of this method and derive its main results.

2.4.2 Local frame transformation theory

A number of other methods have been described and used for the computation of energy levels and photoionisation spectra of alkali metal atoms, but we won't attempt to give an exhaustive review of all: **R**-matrix theories associated with complex rotation[21], multichannel incoherent Landau-Zener model[22], complex eigenvalue Schrödinger equation[23], B-spline-based coordinate rotation method[24] or operator perturbation theory[25] are examples of the many different approaches in the literature. In this section, we will focus instead on an approach called the Local Frame Transformation (LFT) theory, that sometimes also holds the name of its main initiator, David A. Harmin[6,26,27][4].

[4] Even though it should probably be called Fano-Harmin theory[28,29]

This method fully exploits the core/short/long range separation presented in figure 2.3. In a nutshell, the long-range is treated as an hydrogen atom, in parabolic coordinates, and we replace the complicated dynamics of the electron in the non-Coulomb core potential (at short range) by a number (the quantum defect) that quantifies the deviation to a pure Coulomb potential. Transfer matrices from spherical to parabolic coordinates are used to correlate the wave-functions of the different regions. As far as the long-range dynamics is concerned, this constructs an accurate description.

Local-frame transformation in hydrogen

As this description entirely rests on the hydrogen treatment, I first derive the meaningful quantities in this simple case, and then apply the corrections necessary to account for the differences between hydrogen and alkali metal atoms.

I introduce the Hamiltonian of a neutral hydrogen atom in an electric field F along the z axis as:

$$\mathcal{H} = -\frac{1}{2}\nabla_r^2 - \frac{1}{r} + Fz \tag{2.25}$$

The Stark term Fz has a cylindrical symmetry and is negligible below r_0, and the first two terms have spherical symmetries. Thus the short range ($r < r_0$) has spherical symmetry while the long range ($r > r_0$) has only cylindrical symmetry (around the z axis imposed by the electric field).

We recall from section 2.3 that $\psi^F_{\epsilon\beta m}$ is the regular wave-function associated with this Hamiltonian, in parabolic coordinates. At zero field, each discrete stable ($\epsilon < 0$) Rydberg level has its energy depending only on n, and has n^2 degenerate wave-functions $\psi_{\epsilon lm}$[5] naturally expressed in spherical coordinates, but these wave-functions can be also expressed in parabolic coordinates. Thus we have the transformations[30]:

$$\psi^{F=0}_{\epsilon\beta m} = \sum_{l=m}^{n-1} U^{\epsilon m}_{\beta l}\psi_{\epsilon lm} \tag{2.26}$$

As ϵ is a good quantum number, we can write the following energy normalization[6]:

$$\int \psi^F_{\epsilon'\beta m}\psi^F_{\epsilon\beta m}d\tau = \delta(\epsilon' - \epsilon) \tag{2.27}$$

with δ the Dirac function. This condition can also be written as an energy-dependent normalisation factor $N^F_{\epsilon\beta m}$ in $\psi^F_{\epsilon\beta m}$[6]. This normalisation factor depends on the behaviour of the wave-functions at large r (where the Stark field is important), but we are most interested in the coordinate transformation (between spherical and parabolic) at small r. This means that we would like to express the transformation matrix $\underline{U}^{\epsilon}_{\beta}$ (all underlined quantities are matrices) without the influence of the long-range details. To do that, I now consider only the "energy-normalised" wave-functions (normalised by the energy-dependent factor $N^F_{\epsilon\beta m}$), with an electric field and in parabolic coordinates: $\psi^F_{\epsilon\beta m}/N^F_{\epsilon\beta m}$ and without electric field in spherical coordinates: $\psi_{\epsilon lm}/N_{\epsilon lm}$. We also use the fact that, since we removed any long-distance deviation due to the electric field, at $r \leq r_1$, $\psi^F_{\epsilon\beta m}/N^F_{\epsilon\beta m} \approx \psi^{F=0}_{\epsilon lm}/N^{F=0}_{\epsilon lm}$.

[5] in the following we use ϵ instead of n and m for either m_l or m_j

This helps us write the extension at any field F of the transformation relations from equation 2.26, that holds only at $r < r_1$[6]:

$$\frac{\psi^F_{\epsilon\beta m}}{N^F_{\epsilon\beta m}} = \sum_{l=m}^{n-1} a^{\epsilon m}_{\beta l} \left(\frac{\psi_{\epsilon l m}}{N_{\epsilon l}} \right) \tag{2.28}$$

$$\psi^F_{\epsilon\beta m} = \sum_{l=m}^{n-1} \left[a^{\epsilon m}_{\beta l} \frac{N^F_{\epsilon\beta m}}{N_{\epsilon l m}} \right] \psi_{\epsilon l m} = \sum_{l=m}^{n-1} U^{\epsilon m}_{\beta l} \psi_{\epsilon l m} \tag{2.29}$$

$$\psi_{\epsilon l m} = \sum_{\beta} \left(U^{-1} \right)^{\epsilon m}_{l\beta} \psi^F_{\epsilon\beta m} \tag{2.30}$$

The coefficients a are purely geometrical, and can be seen as a projection of $\psi^{F=0}_{\epsilon\beta m}$ onto the associated Legendre polynomials $P^m_l(\cos\theta)$[28]. They depend on F only via the values of β, as we put $F = 0$ to compute their values. I note here that the third relation explicitly postulates the existence of the inverse transformation $\left(\underline{U}^{-1}\right)^{\epsilon}_{\beta}$ to go from parabolic to spherical coordinates. This is not fully justified, and will introduce some errors in the theory, as explained in section 2.4.3.

Application to photo-ionisation: hydrogen

The transformation between spherical and parabolic coordinates established in equations 2.28, 2.29,2.30 will help establish the photo-ionisation cross-section under an electric field. I start with the cross-section for the absorption of a photon of energy $\omega = \epsilon + 1/2$ from the ground state of hydrogen $|g\rangle$, given by the incoherent sum over all independent continuum channels (characterised by their value of β)[6]:

$$\sigma^F(\epsilon) = (4\pi^2\alpha)\hbar\omega \sum_{\beta} |\langle \psi^F_{\epsilon\beta m} | \hat{r} | g \rangle|^2 \tag{2.31}$$

with α the fine-structure constant and $\hat{r}$ the appropriate operator (i.e. $\hat{r} = r\cos\theta$ for π polarisation and $\hat{r} = r\sin\theta\exp(\pm i\phi)/\sqrt{2}$ for $\sigma^{\pm}$ polarisation). As the spatial expansion of the state $|g\rangle$ is located around the origin, we can safely use the transformation of equation 2.29 to expand the parabolic functions $\psi^F_{\epsilon\beta m}$ into spherical functions $\psi_{\epsilon l m}$:

$$\langle \psi^F_{\epsilon\beta m} | \hat{r} | g \rangle = \sum_{l=m}^{\infty} U^{\epsilon m}_{\beta l} \langle \psi_{\epsilon l m} | \hat{r} | g \rangle \tag{2.32}$$

The ground state has $l = 0$ so the dipole selection rule of $\Delta l = \pm 1$ suppress all terms but the $l = 1$ one, and we have[26]:

$$\sigma^F(\epsilon) = (4\pi^2\alpha)\hbar\omega |\langle \psi_{\epsilon 1 m} | \hat{r} | g \rangle|^2 \sum_{\beta}^{\infty} \left(U^{\epsilon m}_{\beta 1} \right)^2 = \sigma^{F=0}(\epsilon) \sum_{\beta}^{\infty} \left(U^{\epsilon m}_{\beta 1} \right)^2 \tag{2.33}$$

[6]This transformation is allowed in this range because the spherical and parabolic wave-functions are solutions to the same Schrödinger equation

with $\sigma^{F=0}(\epsilon)$ the zero-field photoabsorption cross section of this transition. The remaining term contains all the field-dependent modulation of the cross-section, determined by the mixing of spherical channels with open parabolic channels. In eq. 2.33 it is written for a single photon absorption from the ground state, but in most experiments the transition towards the ionising state will be done in at least two steps, thus involving an intermediate p state.

A generalization to two-steps ionisation involving l and l' levels (the intermediate and ionising states respectively) requires the introduction of the energy-dependent modulating factor matrix $\underline{H}^F$ that will be responsible for the shape of the photo-ionisation spectrum, and whose elements are given by $H^F_{l'l}$:

$$H^F_{l'l}(\epsilon) = \langle \psi_{\epsilon l' m'} | \underline{H}^F | \psi_{\epsilon l m} \rangle = \delta_{m'm} \sum_{\beta} U^{\epsilon m'}_{\beta l'} U^{\epsilon m}_{\beta l} \tag{2.34}$$

This factor stems from the fact that, with $F \neq 0$, the $|\psi_{\epsilon l m}\rangle$ states (see equation 2.29) are not orthonormal because the field F mixes different l-channels, so that overlaps between $|\psi_l\rangle$ and $|\psi_{l'}\rangle$ are non-zero. In other words, in the normalisation condition of the $|\psi_{\epsilon l m}\rangle$ states, the $\delta_{ll'}$ term is replaced by $\left[(\underline{H}^F)^{-1}\right]_{l'l}$:

$$\langle \psi_{\epsilon' l' m'} | \psi_{\epsilon l m} \rangle = \left[(\underline{H}^F)^{-1}\right]_{l'l} \delta_{m'm} \delta(\epsilon' - \epsilon) \tag{2.35}$$

In hydrogen, $\underline{H}^F = \underline{D}^F$ where $\underline{D}^F$ is the density-of-states matrix that represents the ability of the outer field to absorb the photo-electron[26]. Indeed, during the photo-ionisation of an atom, the spherical wavefunction of the ejected electron is redistributed over a range of field-dependent, parabolic open channels, and the information about these channels is comprised of $\underline{D}^F$. As the axial symmetry around z is conserved, m stays a good quantum number so that $\langle \psi_m | \psi_{m'} \rangle = \delta_{mm'}$. Thus we can express the field-dependent generalized form of the hydrogenic photo-ionisation cross-section[6]:

$$\sigma^F(\epsilon) = (4\pi^2\alpha)\hbar\omega \sum_{l'l} \frac{\langle \psi_i | \hat{r} | \psi_{l'} \rangle \langle \psi_l | \hat{r} | \psi_i \rangle}{\langle \psi_{\epsilon' l' m} | \psi_{\epsilon l m} \rangle} = \sum_{l'l} \sigma^{F=0}_{l'l}(\epsilon) H^F_{l'l}(\epsilon) \tag{2.36}$$

where $|\psi_i\rangle$ is an intermediate state still localised where the Stark effect in negligible, and the transition from the ground state to this state is saturated.

This result is remarkable, as it clearly shows that the modulation of the spectrum from the electric field will come only from the final state, and not on the initial state. Informations about the initial state and the strength of the particular transitions between states will be included solely in $\underline{\sigma}^{F=0}(\epsilon)$.

Application to photo-ionisation: alkali metals

The results on hydrogen will be very useful to extend the theory to alkali metal atoms. The Stark-Hamiltonian for an alkali metal atom can indeed be written:

$$\mathcal{H} = -\frac{1}{2}\nabla^2_r + V_s(r) - \frac{1}{r} + Fz \tag{2.37}$$

where $V_s(r)$ was null for hydrogen (see 2.25) and is equal to $V_l(r) + 1/r$ for an alkali metal. $V_s(r)$ is thus a spherically symmetric potential, that is negligible above r_0 (as shown on figure 2.3). This means that the Hamiltonian for an alkali-metal atom has the same symmetries that for hydrogen, and the same transformations between spherical and parabolic coordinates can be applied.

Let $\Psi_{\epsilon lm}^{r_0<r<r_1}$ be the electronic wave-function for an alkali-metal atom in the Coulomb region (see figure 2.3) after the absorption of a photon. We can write it in function of the energy-normalized hydrogenic spherical regular $f_{\epsilon l}$ and irregular functions $g_{\epsilon l}$ (see section 2.2)[7]

$$\Psi_{\epsilon lm}^{r_0<r<r_1}(r,\theta,\phi) = \cos\delta_l \left(f_{\epsilon l}(r) - \tan\delta_l g_{\epsilon l}(r)\right) Y_{lm}(\theta,\phi) \tag{2.38}$$

Explicit spherical harmonics give:

$$\Psi_{\epsilon lm}^{r_0<r<r_1}(r,\theta,\phi) = \left[\frac{\exp(im\phi)}{\sqrt{2\pi}}\right] P_{lm}\cos\theta \left(\cos\delta_l f_{\epsilon l}(r) - \sin\delta_l g_{\epsilon l}(r)\right) \tag{2.39}$$

The influence of the ion core on this wave-function is completely described by the values of δ_l (and thus of δ_l the quantum defects). We now must establish the link to the outer region (the Coulomb-Stark region, in parabolic coordinates) with the help of the derivation on hydrogen. As $\Psi_{\epsilon lm}^{r_0<r<r_1}(r,\theta,\phi)$ is energy normalised we can apply the same transformation between spherical and parabolic coordinates. We recall here (see equation 2.17 and figure 2.3) that $\Xi_\beta^F(\xi)$ is the hydrogenic regular parabolic eigenfunction in the ξ direction while $\mathrm{Y}_\beta^F(\eta)$ is the hydrogenic regular parabolic eigenfunction in the η direction. We define also $\overline{\mathrm{Y}}_\beta^F(\eta)$ as the hydrogenic *irregular* parabolic eigenfunction in the η direction. This irregular function has a certain phase shift to Y_β^F and in the high η limit this phase shift is called the asymptotic phase shift γ_β^F.

We recall the hydrogenic energy-normalised total wave-function in parabolic coordinates: the regular is taken as $\psi_{\epsilon\beta m}^F$ (defined in equation 2.17) and the irregular as $\chi_{\epsilon\beta m}^F$. We define the latter as:

$$\chi_{\epsilon\beta m}^F(\xi,\eta,\phi) = \frac{\exp(im\phi)}{\sqrt{2\pi}} \Xi_{\epsilon\beta m}^F(\xi)\overline{\mathrm{Y}}_{\epsilon\beta m}^F(\eta) \tag{2.40}$$

Energy normalisation and "continuum-normalisation" of these functions have the following consequences[6]:

$$\langle\psi_{\epsilon'\beta'm'}^F|\psi_{\epsilon\beta m}^F\rangle = \langle\chi_{\epsilon'\beta'm'}^F|\chi_{\epsilon\beta m}^F\rangle = \delta(\epsilon'-\epsilon)\delta_{\beta'\beta}\delta_{m'm} \tag{2.41}$$

$$\langle\psi_{\epsilon'\beta'm'}^F|\chi_{\epsilon\beta m}^F\rangle = \langle\chi_{\epsilon'\beta'm'}^F|\psi_{\epsilon\beta m}^F\rangle = \cos\left(\gamma_\beta^F\right)\delta(\epsilon'-\epsilon)\delta_{\beta'\beta}\delta_{m'm} \tag{2.42}$$

We continue with the reformulation of equation 2.25 in the Coulomb region (where $r_0 < r < r_1$), where the Stark term is negligible, as:

$$\left[\epsilon + \frac{1}{2}\nabla_r^2 + \frac{1}{r}\right]\Psi = V_s(r)\Psi \tag{2.43}$$

[7] note that the definition is different but close to equation 2.9

This clearly shows that $V_s(r)$ can be treated as an inhomogeneity[8] in the Schrödinger equation. These kinds of differential equation can be solved using the appropriate Green's function $\mathcal{G}_C(r,r')$ (equation 4.107 in ref. [31]), that solves the particular equation:

$$\left[\epsilon + \frac{1}{2}\nabla_r^2 + \frac{1}{r}\right]\mathcal{G}_C(r,r') = \delta(r-r') \tag{2.44}$$

This equation is not enough to uniquely define a Green's function in this range, but the boundary condition that we put at $r = 0$ ($f_{\epsilon l} = 0$ and $g_{\epsilon l}$ with $\pi/2$ phase lag behind $f_{\epsilon l}$) fixes the value of the Green's function uniquely. This means that the Green's function in parabolic and spherical coordinates are the same ($\mathcal{G}_C(r,\theta,\phi) \equiv \mathcal{G}_C(\xi,\eta,\phi)$) in the Coulomb region.

These Green's functions can be expressed in function of $f_{\epsilon l}$ and $g_{\epsilon l}$ and in function of $\psi^F_{\epsilon\beta m}$ and $\chi^F_{\epsilon\beta m}$ respectively. This leads[6] to the following relations between the parabolic and spherical eigenfunctions, analogous to equations 2.29 and 2.30 :

$$\psi^F_{\epsilon\beta m}(\vec{r}) = \sum_l U^{\epsilon m}_{\beta l} f_{\epsilon l}(\vec{r}) \tag{2.45}$$

$$\chi^F_{\epsilon\beta m}(\vec{r}) = \sum_l \sin\left(\gamma^F_\beta\right)\left({}^t U^{\epsilon m}_{\beta l}\right)^{-1} g_{\epsilon l}(\vec{r}) \tag{2.46}$$

This gives also:

$$f_{\epsilon l}(\vec{r}) = \sum_\beta \left(\underline{U}^{\epsilon m}_{l\beta}\right)^{-1} \psi^F_{\epsilon\beta m}(\vec{r}) \tag{2.47}$$

$$g_{\epsilon l}(\vec{r}) = \sum_\beta {}^t\underline{U}^{\epsilon m}_{l\beta} \csc\left(\gamma^F_\beta\right) \chi^F_{\epsilon\beta m}(\vec{r}) \tag{2.48}$$

Combining equations 2.39, 2.47 and 2.48 we have this expression of the alkali wavefunction valid for $r > r_1$:

$$\Psi_{\epsilon lm}(\vec{r}) = \left[\frac{\exp(im\phi)}{\sqrt{2\pi}}\right] P_{lm}\cos\theta \sum_\beta \Xi^F_\beta(\xi)\left[\cos\delta_l (U^{-1})^{\epsilon m}_{l\beta} \Upsilon^F_\beta(\eta) - \left(\sin\delta_l\, {}^t U^{\epsilon m}_\beta \csc\gamma^F_\beta\right)\overline{\Upsilon}^F_\beta(\eta)\right] \tag{2.49}$$

Once again we need to orthonormalize the set of the $\Psi_{\epsilon lm}$ functions. This is done with the help of the fact that the Ξ^F_β functions are orthogonal and with equations 2.41 and 2.42:

$$\langle \Psi_{\epsilon' l' m'} | \Psi_{\epsilon lm}\rangle = \left(\cos\delta_l - \sin\delta_l \sum_\beta U^{\epsilon m}_{\beta l'} \cot\left(\gamma^F_\beta\right) U^{\epsilon m}_{\beta l}\right)\left(\sum_\beta U^{\epsilon m}_{\beta l'} U^{\epsilon m}_{\beta l}\right) \tag{2.50}$$

We can define another matrix quantity $\underline{h}^F$, analogous to $\underline{H}^F$, whose elements are defined as:

$$h^F_{l'l} = \sum_\beta U^{\epsilon m}_{\beta l'} U^{\epsilon m}_{\beta l} \cot(\gamma^F_\beta) \tag{2.51}$$

[8] a non-zero second term in a differential equation

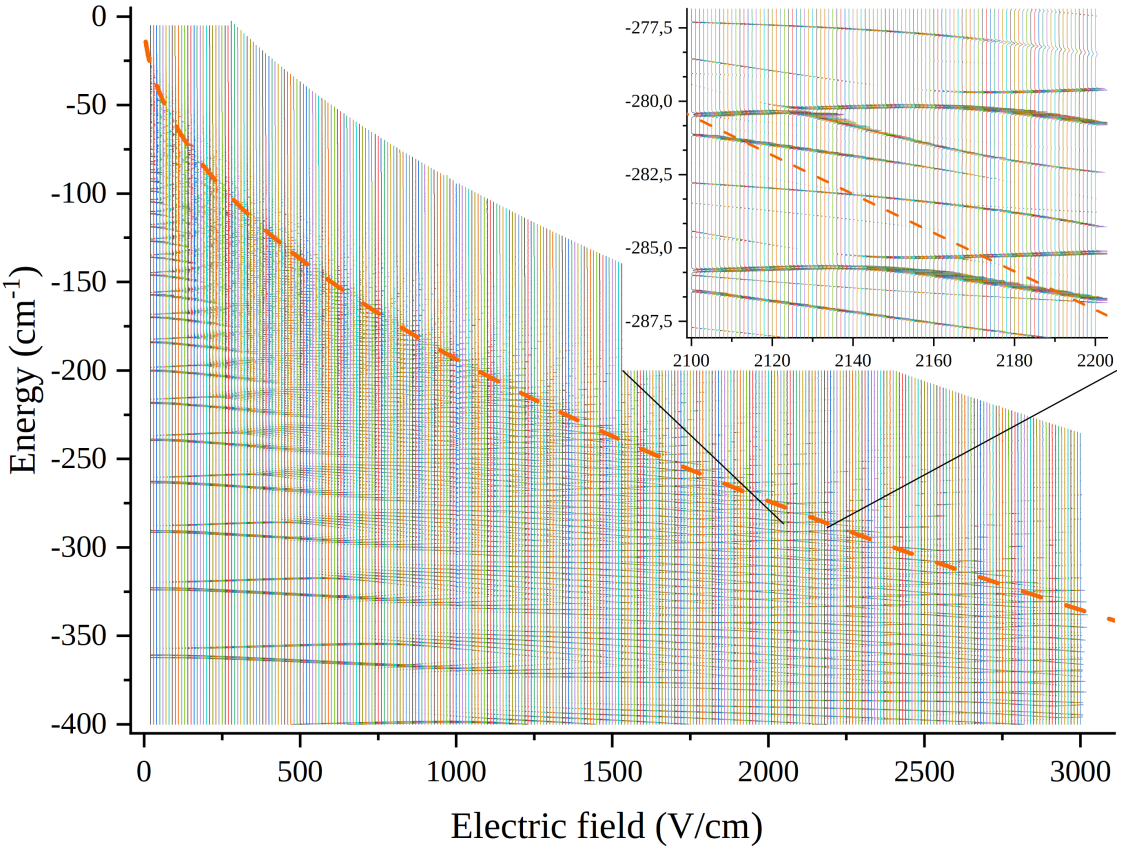

FIGURE 2.5: Stark map of caesium from individual photoabsorption spectra computed with our implementation of the LFT theory. The channels included in this calculation correspond to the absorption of a photon with polarisation π from the $7S$ state. Each spectra (with a different color) is computed at one electric field value, and its horizontal position indicates the value of the electric field. The dashed orange line is the classical ionisation threshold. Parameters are chosen to go $100\,\mathrm{cm}^{-1}$ higher than this limit all over the negative energy range. The inset shows a more detailed Stark map in the vicinity of the classical ionisation threshold. Ionisation rates of individual levels can be extracted from the width of the lines.

An important point to realise is that the sum of equation 2.51 is over all the *open parabolic channels* characterised by values of $\beta < 1$. Equation 2.51 allows the reformulation of equation 2.50 in terms of the density of state matrix, for alkali:

$$\underline{D}^F = \langle \Psi' | \Psi \rangle^{-1} = \{ \left(\cos \underline{\delta}_l - \sin \underline{\delta}_l \underline{h}^F \right) \left(\underline{H}^F \right)^{-1} \left(\cos \underline{\delta}_l - \underline{h}^F \sin \underline{\delta}_l \right) + \sin \underline{\delta}_l \underline{H}^F \sin \underline{\delta}_l \}^{-1} \tag{2.52}$$

with the curly brackets indicating a matrix, and $\underline{\delta}_l$ diagonal matrices with quantum defects. Finally we arrive to the photo-ionisation cross-section for an alkali-metal atom, constructed as a generalisation of the hydrogen result:

$$\sigma^F(\epsilon) = \sum_{l'l} D^F_{l'l} \sigma^{F=0}_{l'l}(\epsilon) \tag{2.53}$$

From that expression, it is possible to compute photoabsorption spectrum at any given

field, even above the classical ionisation threshold (but it is restricted to $\epsilon < 0$). An example of such a computation is visible on figure 2.5, where a Stark map of caesium is reconstructed from multiple calculations at different field amplitudes, from $-400\,\mathrm{cm}^{-1}$ to $+100\,\mathrm{cm}^{-1}$ over the classical ionisation threshold. This figure shows that the theory gives the shift in energy of the Rydberg states in function of the electric field (the Stark shift), but also the ionisation rate of individual atoms, thanks to the linewidth of the peaks present in the spectra. The description of the states included in this calculations involves the spin-orbit coupling (see section 3.1.3), and include all states with $m_j = 3/2$.

The framework of LFT is applicable to any atom because all the specific information about an atom is included in the zero-field parameters $\sigma_{ll'}$ and δ_l. This approach is in fact very general, and has also been applied to more complex problems like the influence of an electric field on two valence electrons atoms[32,33], noble gases[34] or molecular hydrogen[35]. Its accuracy is overall remarkable, considering its computational low-cost.

2.4.3 Generalized local frame transformation

Over the years the improvements in the accuracy of Stark spectroscopy and photo-ionisation microscopy[9] showed non-negligible discrepancy between the predicted and measured energies, up to 1000 ppm[21,33]. This called for a revaluation of LFT core hypotheses, what was done in the beginning of the 2010s.

A careful look on LFT[37–39], showed that when the field is low, it does not conserve the angular momentum because it considers only physical, open channels (with $\beta < 1$). This could then decrease the precision of the theory when describing states with high-l components. This was resolved[29] by extending the sum in 2.49 to the limit $\beta \to \infty$. A clear source of errors comes from the assertion that there always exists an inverse transformation to match the regular spherical function (with a well-defined l number) to the regular parabolic eigenfunction, as defined in equation 2.30. This is further used in the LFT theory to define Green's functions in spherical and parabolic coordinates in the Coulomb region, that are supposedly uniquely defined. Ultimately, this assumption gives a way to map irregular function's from spherical to parabolic coordinates. However, this assumption is false and the inverse transformation U^{-1} does not always exist[40].

Another way to understand these errors is that even if the external field is low in the Coulomb region, it is enough to mix different l-states, which makes the matching of spherical and parabolic irregular functions approximate[40]. In order to improve its accuracy, the theory was reformulated in the Lippmann-Schwinger formalism, as the generalized local frame transformation (GLFT) theory[29]. Figure 2.6 shows a comparison of LFT and GLFT with a full numerical calculation for a photo-absorption spectrum in Na under a 4 kV/cm electric field. It clearly demonstrates the improvement from LFT, with an accuracy around 50 times better. Aside from the improved accuracy, this theory lays a systematic pathway to improve the initial LFT theory, and can be applied to other problems such as ultra-long Rydberg molecules[41] or easily include relativistic and spin-orbit corrections[29].

The code that I used for the computation of all Stark spectra (presented in figure 2.5 and beyond) was written by Francis Robicheaux, and implements the standard LFT theory with quantum defects inputs, with the addition of spin-orbit interactions, but without

[9] a technique that allows direct visualisation of the expanding wavefunction of an emitted electron[36]. It gives access to differential cross sections, that can easily be compared with computed values in the theory.

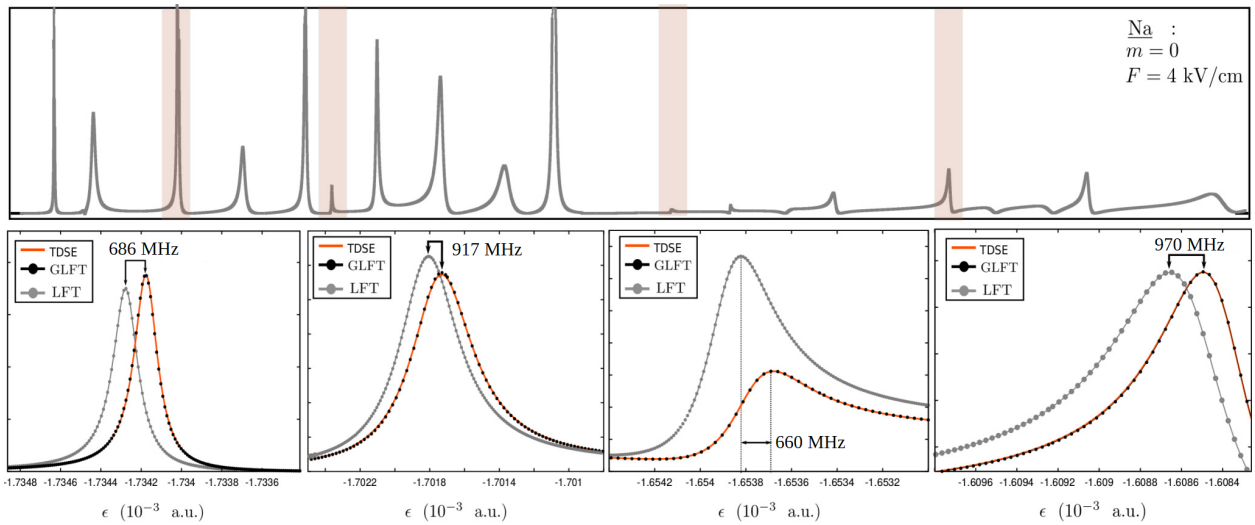

FIGURE 2.6: Calculated photo-absorption spectra from Na under a 4 kV/cm electric field, from ref. [29] comparing LFT theory (gray dots) with their GLFT (black dots) as well as a full numerical calculation (Time-dependent Schrödinger Equation (TDSE)) (orange solid line) for reference. It shows that the LFT theory has errors in the 500 MHz to 1000 MHz range, while GLFT's errors are in the 0 MHz to 20 MHz range.

the input from zero-field photoabsorption cross-sections. I modified it slightly to increase the dimensions of internal vectors and matrices (to increase the energy range) and to actualise the values of quantum defects to higher accuracy.

Section summary

Stark effect on Rydberg states: alkali metals

In this section I have presented two of the main methods to treat the Stark effect in alkali metal atoms: the matrix diagonalisation method and the LFT theory. I insisted on the latter, which is based on the space-separation possible in the Coulomb-Stark problem. I presented a derivation of the main results, showing how we can construct a full photo-absorption Stark map from just a set of quantum defects and field-free cross-sections, with the help of the formula:

$$\sigma^F(\epsilon) = \sum_{l'l} D^F_{l'l} \sigma^{F=0}_{l'l}(\epsilon) \tag{2.54}$$

In this formula, $\underline{D^F}$ is the density of state matrix that contains all field-dependent spectral information. This theory will be the basis for all the experimental and theoretical investigations, thanks to its ability to predict precise energy levels around the ionisation threshold, as well as ionisation rate in the form of spectral linewidth. I finally presented some new developments of the theory, that should expand its usability and usefulness even more.

2.5 Conclusion on the theoretical treatment of Stark effect on Rydberg atoms

In this chapter I introduced the theoretical treatment of the effect of an electric field on Rydberg states of hydrogen and of alkali metal atoms. I provided a derivation for the well-known Rydberg formula, showing that it gives a good physical insight into the meaning of quantum defects, that represent the phase-shift acquired by the outer electron at each revolution around the ionic core. This led me to the different methods based on the quantum defect theory that can be used to obtain precise energies and ionisation rates of strongly Stark-shifted Rydberg states. In particular I insisted on the local-frame transformation method, that provides photo-ionisation spectra from quantum defects and field-free photo-absorption cross sections, even well over the classical ionisation threshold.

To the best of our knowledge, no extensive study has yet compared the results of this theory to experimental data in caesium, at least to the level of precision needed for our purpose. In the next chapter I present such a study, whose purpose is to verify the energy-precision of this theoretical method. The LFT theory predicts not only the energy levels of highly-Stark-shifted Rydberg states, but provides a full spectrum. This means that the energy levels can also be attributed linewidth (and thus lifetimes or ionisation rates), and transition amplitudes. Being able to predict the value of these two quantities is also very important in the context of the realisation of a new electron source, because we need intense transitions and rapidly ionising states. In the next chapter I will thus also present some semi-quantitative comparison between experimental and theoretical (LFT) ionisation rates and transition intensities.

References

[1] J. R. Rydberg. "XXXIV. On the structure of the line-spectra of the chemical elements". In: *The London, Edinburgh, and Dublin Philosophical Magazine and Journal of Science* 29.179 (1890), pp. 331–337. ISSN: 1941-5982. DOI: 10.1080/14786449008619945.

[2] H. Kayser and C. Runge. "Ueber die Spectren der Alkalien". In: *Annalen der Physik und Chemie* 277.10 (1890), pp. 302–320. ISSN: 00033804. DOI: 10.1002/andp.18902771010.

[3] Thomas F. Gallagher. *Rydberg atoms*. Cambridge monographs on atomic, molecular and chemical physics. Cambridge University press, 1994. ISBN: 0521021669.

[4] M. T. Frey, S. B. Hill, K. A. Smith, F. B. Dunning, and I. I. Fabrikant. "Studies of electron-molecule scattering at microelectronvolt energies using very-high-n Rydberg atoms". In: *AIP Conference Proceedings* 360.1 (1996), pp. 815–824. DOI: 10.1063/1.49796. URL: https://aip.scitation.org/doi/abs/10.1063/1.49796.

[5] Matthew T. Eiles. "Trilobites, butterflies, and other exotic specimens of long-range Rydberg molecules". In: *J. Phys. B: At. Mol. Opt. Phys.* 11 (2019). DOI: 10.1088/1361-6455/ab19ca.

[6] D. A. Harmin. "Theory of the Nonhydrogenic Stark Effect". In: *Physical review letters* 49.2 (1982), pp. 128–131. ISSN: 0031-9007. DOI: 10.1103/PhysRevLett.49.128.

[7] H. A. Kramers. "Théorie générale de la rotation paramagnétique dans les cristaux". In: *Proceedings of the Royal Netherlands Academy of Arts and Sciences* 33.6-10 (1930), pp. 959–972. URL: https://www.dwc.knaw.nl/DL/publications/PU00014621.pdf.

[8] Daniel Kleppner, Michael G. Littman, and Myron L. Zimmerman. "Highly Excited Atoms". In: *Scientific American* 244.5 (1981), pp. 130–149. ISSN: 0036-8733. DOI: 10.1038/scientificamerican0581-130.

[9] C. Y. Lin and Y. K. Ho. "Complex scaling in Lagrange-mesh calculations for Stark shifts and widths of the screened Coulomb potential". In: *Journal of Physics B: Atomic, Molecular and Optical Physics* 44.17 (2011), p. 175001. ISSN: 0953-4075. DOI: 10.1088/0953-4075/44/17/175001.

[10] L. Fernández-Menchero and H. P. Summers. "Stark effect in neutral hydrogen by direct integration of the Hamiltonian in parabolic coordinates". In: *Physical Review A* 88.2 (2013), p. 345. ISSN: 1050-2947. DOI: 10.1103/PhysRevA.88.022509.

[11] F. M. Fernández and J. Garcia. "Highly accurate calculation of the resonances in the Stark effect in hydrogen". In: *Applied Mathematics and Computation* 317 (2018), pp. 101–108. ISSN: 00963003. DOI: 10.1016/j.amc.2017.08.050.

[12] M. Marinescu, H. R. Sadeghpour, and A. Dalgarno. "Dispersion coefficients for alkali-metal dimers". In: *Physical Review A* 49.2 (1994), pp. 982–988. ISSN: 1050-2947. DOI: 10.1103/PhysRevA.49.982.

[13] M. L. Zimmerman, M. G. Littman, Mi. M. Kash, and D. Kleppner. "Stark structure of the Rydberg states of alkali-metal atoms". In: *Phys. Rev. A* 20 (6 Dec. 1979), pp. 2251–2275. DOI: 10.1103/PhysRevA.20.2251.

[14] N. Šibalić, J. D. Pritchard, K. J. Weatherill, and C. S. Adams. "ARC: An open-source library for calculating properties of alkali Rydberg atoms". In: *Computer Physics Communications* 220.319 (2017). DOI: 10.1016/j.cpc.2017.06.015.

[15] S. Sahoo and Y. K. Ho. "The complex absorbing potential method (CAP) to study the Stark effect in hydrogen and lithium". In: *Journal of Physics B: Atomic, Molecular and Optical Physics* 33.12 (2000), pp. 2195–2206. ISSN: 0953-4075. DOI: 10.1088/0953-4075/33/12/303.

[16] U. V. Riss and H.-D. Meyer. "Calculation of resonance energies and widths using the complex absorbing potential method". In: *Journal of Physics B: Atomic, Molecular and Optical Physics* 26.23 (1993), pp. 4503–4535. ISSN: 0953-4075. DOI: 10.1088/0953-4075/26/23/021.

[17] J. Grimmel, M. Stecker, M. Kaiser, F. Karlewski, L. Torralbo-Campo, A. Günther, and J. Fortágh. "Ionization spectra of highly Stark shifted rubidium Rydberg states". In: *Physical Review A* 96.1 (2017). ISSN: 1050-2947. DOI: 10.1103/PhysRevA.96.013427.

[18] R. Kosloff and D. Kosloff. "Absorbing boundaries for wave propagation problems". In: *Journal of Computational Physics* 63.2 (1986), pp. 363–376. ISSN: 00219991. DOI: 10.1016/0021-9991(86)90199-3.

[19] Markus Stecker, Raphael Nold, Lea-Marina Steinert, Jens Grimmel, David Petrosyan, József Fortágh, and Andreas Günther. "Controlling the Dipole Blockade and Ionization Rate of Rydberg Atoms in Strong Electric Fields". In: *Physical Review Letters* 125.10 (2020). ISSN: 0031-9007. DOI: 10.1103/PhysRevLett.125.103602.

[20] W. P. Reinhardt. "Complex Coordinates in the Theory of Atomic and Molecular Structure and Dynamics". In: *Annual Review of Physical Chemistry* 33.1 (1982), pp. 223–255. ISSN: 0066-426X. DOI: 10.1146/annurev.pc.33.100182.001255.

[21] G. D. Stevens, C.-H. Iu, T. Bergeman, H. J. Metcalf, I. Seipp, K. T. Taylor, and D. Delande. "Precision measurements on lithium atoms in an electric field compared with R-matrix and other Stark theories". In: *Physical Review A* 53.3 (1996), pp. 1349–1366. ISSN: 1050-2947. DOI: 10.1103/PhysRevA.53.1349.

[22] M. Førre and J. P. Hansen. "Selective-field-ionization dynamics of a lithium m=2 Rydberg state: Landau-Zener model versus quantal approach". In: *Physical Review A* 67.5 (2003), p. 043404. ISSN: 1050-2947. DOI: 10.1103/PhysRevA.67.053402.

[23] S. I. Themelis and C. A. Nicolaides. "Complex energies and the polyelectronic Stark problem: II. The Li n = 4 levels for weak and strong fields". In: *Journal of Physics B: Atomic, Molecular and Optical Physics* 34.14 (2001), pp. 2905–2925. ISSN: 0953-4075. DOI: 10.1088/0953-4075/34/14/311.

[24] H.-Y. Meng, Y.-X. Zhang, S. Kang, T.-Y. Shi, and M.-S. Zhan. "Theoretical complex Stark energies of lithium by a complex scaling plus the B-spline approach". In: *Journal of Physics B: Atomic, Molecular and Optical Physics* 41.15 (2008), p. 155003. ISSN: 0953-4075. DOI: 10.1088/0953-4075/41/15/155003.

[25] A. A. Kuznetsova, A. V. Glushkov, A. V. Ignatenko, A. A. Svinarenko, and V. B. Ternovsky. "Spectroscopy of Multielectron Atomic Systems in a DC Electric Field". In: *Quantum Systems in Physics, Chemistry and Biology - Theory, Interpretation, and Results*. Vol. 78. Advances in Quantum Chemistry. Elsevier, 2019, pp. 287–306. ISBN: 9780128160848. DOI: 10.1016/bs.aiq.2018.06.005.

[26] D. A. Harmin. "Theory of the Stark effect". In: *Physical Review A* 26.5 (1982), pp. 2656–2681. ISSN: 1050-2947. DOI: 10.1103/PhysRevA.26.2656.

[27] D. A. Harmin. "Analytical study of quasidiscrete Stark levels in Rydberg atoms". In: *Physical Review A* 30.5 (1984), pp. 2413–2428. ISSN: 1050-2947. DOI: 10.1103/PhysRevA.30.2413.

[28] U. Fano. "Stark effect of nonhydrogenic Rydberg spectra". In: *Physical Review A* 24.1 (1981), pp. 619–622. ISSN: 1050-2947. DOI: 10.1103/PhysRevA.24.619.

[29] P. Giannakeas, C. H. Greene, and F. Robicheaux. "Generalized local frame transformation theory for excited species in external fields". In: *Physical Review A* 94.1 (2016). ISSN: 1050-2947. DOI: 10.1103/PhysRevA.94.013419.

[30] David R. Herrick. "Sum rules and expansion formula for Stark radiative transitions in the hydrogen atom". In: *Physical review. A, General physics* 12.5 (1975), pp. 1949–1953. ISSN: 0556-2791. DOI: 10.1103/PhysRevA.12.1949.

[31] Harald Friedrich. *Theoretical atomic physics*. 3rd ed. Berlin and New York: Springer, 2005. ISBN: 354025644X.

[32] F. Robicheaux, C. Wesdorp, and L. D. Noordam. "Strongly perturbed Stark states and electron correlation in Ba". In: *Physical Review A* 60.2 (1999), pp. 1420–1428. ISSN: 1050-2947. DOI: 10.1103/PhysRevA.60.1420.

[33] M. Grütter, O. Zehnder, T. P. Softley, and F. Merkt. "Spectroscopic study and multichannel quantum defect theory analysis of the Stark effect in Rydberg states of neon". In: *Journal of Physics B: Atomic, Molecular and Optical Physics* 41.11 (2008), p. 115001. ISSN: 0953-4075. DOI: 10.1088/0953-4075/41/11/115001.

[34] H. Fielding and T. P. Softley. "Observation of the Stark effect in autoionizing Rydberg states of Ar with a multichannel quantum-defect analysis". In: *Journal of Physics A: Mathematical and Theoretical* 25.20 (1992), pp. 4125–4139. ISSN: 0034-4885. DOI: 10.1088/0953-4075/25/20/010.

[35] K. Sakimoto. "Influence of electric fields on highly excited states of H_2 : quantum-defect-theory approach". In: *Journal of Physics A: Mathematical and Theoretical* 22.17 (1989), pp. 2727–2739. ISSN: 0034-4885. DOI: 10.1088/0953-4075/22/17/011.

[36] C. Nicole, H. L. Offerhaus, M. J. J. Vrakking, F. Lépine, and Ch Bordas. "Photoionization microscopy". In: *Physical review letters* 88.13 (2002), p. 133001. DOI: 10.1103/PhysRevLett.88.133001.

[37] L. B. Zhao, I. I. Fabrikant, M. L. Du, and C. Bordas. "Test of the Stark-effect theory using photoionization microscopy". In: *Physical Review A* 86.5 (2012), p. 1045. ISSN: 1050-2947. DOI: 10.1103/PhysRevA.86.053413.

[38] P. Giannakeas, F. Robicheaux, and C. H. Greene. "Photoionization microscopy in terms of local frame transformation theory". In: *Physical Review A* 91.4 (2015). ISSN: 1050-2947. DOI: 10.1103/PhysRevA.91.043424.

[39] L. B. Zhao, I. I. Fabrikant, and M. L. Du. "Reply to "Comment on 'Test of the Stark-effect theory using photoionization microscopy' "". In: *Physical Review A* 91.6 (2015), p. 967. ISSN: 1050-2947. DOI: 10.1103/PhysRevA.91.067402.

[40] V. G. Ushakov, V. I. Osherov, and E. S. Medvedev. "Analytical S -matrix derivation in the theory of the nonhydrogenic Stark effect". In: *Journal of Physics A: Mathematical and Theoretical* 52.38 (2019), p. 385302. ISSN: 0034-4885. DOI: 10.1088/1751-8121/ab2efa.

[41] P. Giannakeas, M. T. Eiles, F. Robicheaux, and Rost J.-M. *Generalized local frame transformation theory for ultralong-range Rydberg molecules*. 2020. arXiv: 2005.10246 [quant-ph]. URL: https://arxiv.org/abs/2005.10246.

Chapter 3

Experimental Stark maps

> There's no reason to be agnostic about ideas that are dramatically incompatible with everything we know about modern science.
>
> Sean M. Carroll

In the last chapter we have seen ways to calculate the effect of electric fields on the energy levels of Rydberg states, and even to gain insights into their ionisation from the LFT theory. In this chapter we will experimentally confirm the precision of this theory both for the prediction of the position of strongly Stark shifted Rydberg states as well as for their ionisation rates.

We begin with the presentation of the experimental set-up that has been used for the acquisition of experimental Stark maps. Its purpose is to form Rydberg atoms from neutral caesium atoms and detect produced electrons while scanning an ionising laser. This set-up (entirely designed, and built during this thesis) allows us to compare the LFT computation with experimental values, and to confirm the utility of this theoretical method into our application.

3.1 Experimental set-up for the acquisition of Stark map

The experimental set-up is composed of four principal components: the electrodes, the caesium oven, the lasers and the spectrometer. In this chapter we ignore the role of the spectrometer, that will be dealt with in detail in chapter 4, but we must keep in mind that the presented images feature the detection (x) horizontal axis as a projection of the (z) energy axis in the ionisation zone. Figure 3.1 shows a cut of the electron source featuring the other three parts.

3.1.1 Electrodes

The five electrodes are based on the published HREELM design[1], and a planar cut can be found in figure 3.2. Each electrode has a number that will be used throughout this section. These electrodes consists of disk of stainless steal separated by rings made of PEEK[1]. All electrodes have a thickness of 1 mm except electrode number 5 that is thicker.

[1] An organic polymer adapted for ultra-high vacuum and a good electric isolator

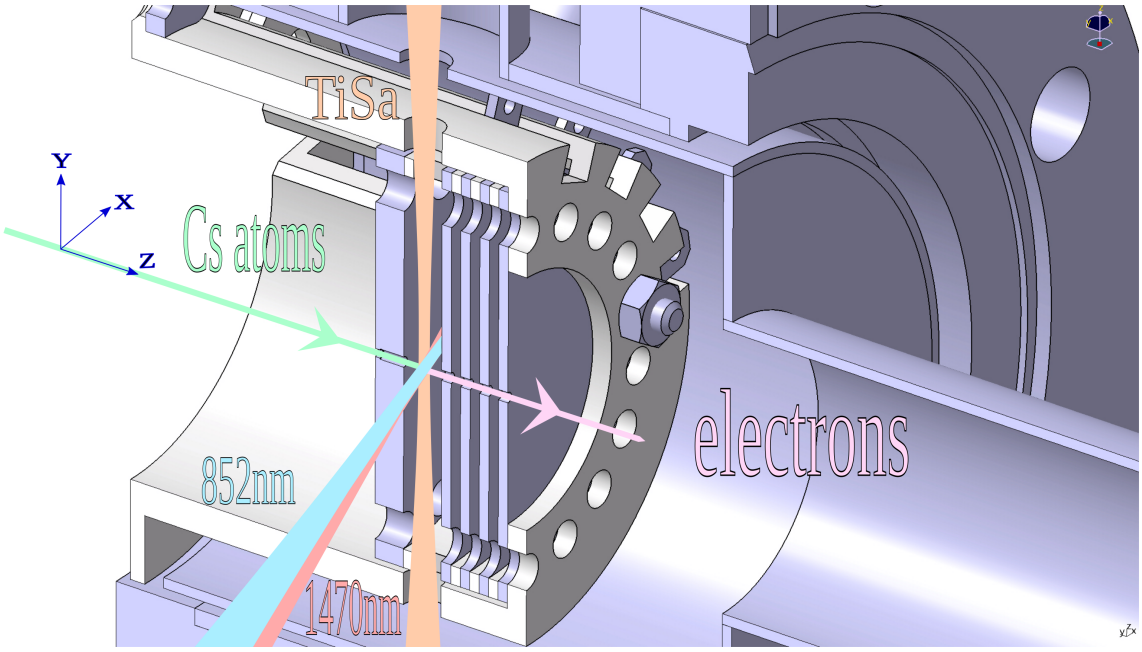

FIGURE 3.1: Mechanical setup of the electron source featuring the electrodes and the three lasers: the 852 nm, the 1470 nm and the Ti:sapphire laser (Ti:Sa), as well as the neutral caesium atoms beam and the produced electron beam.

This electrode also has smaller inner diameter at its left end, that is used to align the electrodes when they are mounted. Indeed, a rod of diameter 1 mm with a 0.8 mm diameter head is inserted into the inner bores of the electrodes and their are fixed on the mounting PEEK piece. This ensures a common central axis on the electrodes. The spacing between electrodes is realized by precisely cut PEEK rings.

Electrodes 1 and 5 determine the electric field in the ionisation zone (the extracting field) and the starting potential of the electrons, while electrodes 2 and 3 can be freely adjusted to tune the focus of the electron beam. Electrode 4 is kept at ground-potential so that electrons reach their final speed at the end of the electrode stack and are not sensible to further ground-potential parts (like vacuum chamber walls, or screws).

All electrodes are held at potentials in range $-2\,\mathrm{kV}$ to $1\,\mathrm{kV}$ with ISEG voltage supplies with less than 7 mV rms ripple. To produce an electric field with an appropriate sign, electrode 5 must always be at a lower potential than all the other electrodes. Typical values in our studies are given in the caption of figure 3.2).

The neutral caesium beam crosses the ionising lasers at the center of electrodes 5 and 1, as depicted on figure 3.1. Electrons are created at a potential $V_{in} \approx \frac{V_5+V_1}{2}$. This value determines the kinetic energy of the electrons from electrode 4 to the detector.

The precise determination of the starting electric field is trickier because of the holes in the electrodes, as well as a possible mechanical variation of the distance between electrodes 1 and 5 from the supposed 4 mm. The naïve value would be $F = \frac{(V_5-V_1)}{0.4}\mathrm{V/cm}$, but the simulation presented in figure 3.2 gives a field of $-2164\,\mathrm{V/cm}$ at the center of the electrodes, instead of the naïve value of $-2175\,\mathrm{V/cm}$. We will see in section 3.2 how we can refine the actual starting electric field with the help of theoretical calculations.

For further discussion of the experimental set-up we need to provide a frame of reference: we define the electron optical axis as Z, from the electron source to the detector,

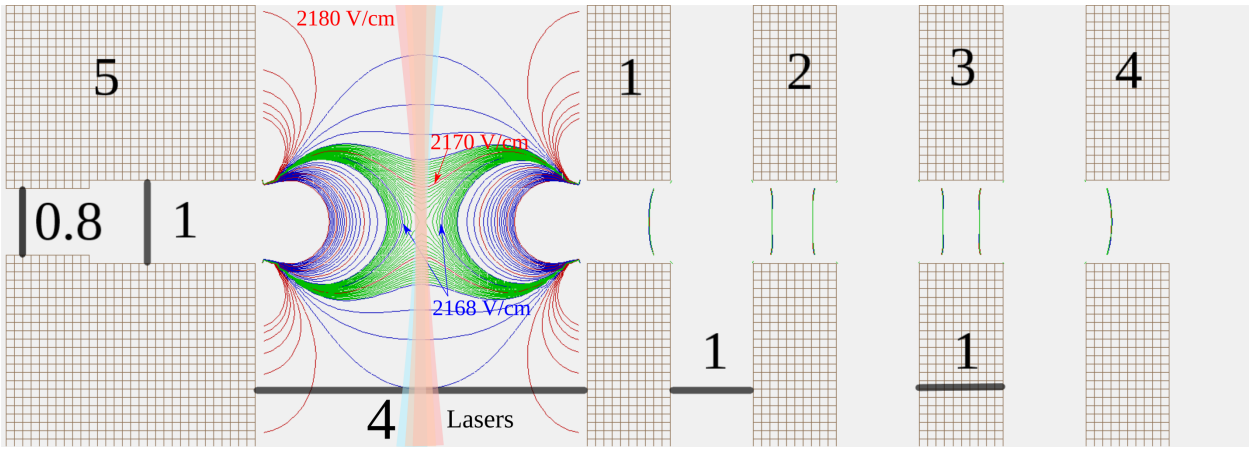

FIGURE 3.2: Planar cut of the electrodes in the set-up, reproduced in the Simion software, with laser beams superimposed. Numbers on electrodes are their names, while distances between electrodes and inner diameters are indicated in mm. Field lines are represented for potentials equal to $V_5 = -1870\,\mathrm{V}$, $V_1 = -1000\,\mathrm{V}$, $V_2 = V_4 = 0\,\mathrm{V}$ and $V_3 = -1300\,\mathrm{V}$. Red lines are separated by $10\,\mathrm{V/cm}$, blue lines are every $2\,\mathrm{V/cm}$ and green lines are separated by $0.2\,\mathrm{V/cm}$. .

along with the direct orthogonal X and Y directions. The electric field created by electrodes 5 and 1 is thus oriented along Z, as this is the revolution axis. This first frame of reference is depicted on figure 3.1, and is further called the blue frame of reference.

After the electrodes we placed three pairs of electrostatic deflectors, two pairs acting in the Y direction while the middle pair acts on the X direction. These are essential to correct the misalignment of the electrodes relative to the optical axis of set-up. Each pair is composed of two half-cylinder (cut in length) of stainless steal, put at the same potential amplitude but with opposite sign. This deflects the beam of electrons efficiently, and a few V are usually enough to correct misalignments. Having two pairs acting in the same direction, separated from a non-zero distance, allows us to correct the angle as well as the position of the beam, while a single pair can only correct an angle.

3.1.2 Caesium oven

In our set-up the electrons are produced from the ionisation of an atomic beam of caesium. This atomic beam originates from a standard effusive oven, as can be seen on figure 3.3. This figure features a photograph of our caesium oven as well as a schematic of its different parts. The important part is the inner tube, that creates the caesium beam. This tube is in alumina, but we also used copper, and stainless steal tubes on this set-up, as well as other materials on another set-up. This tube is mechanically held by the copper gasket that separates the caesium reservoir from the rest of the vacuum chamber. This allows the other end of the tube to be very close to the electrodes, without mechanical support in this area of high voltage. However, it requires that the length of the alumina tube is precisely chosen so that if fits with the gasket-electrode distance.

The caesium reservoir is heated to temperatures around 100 °C, which creates a dense vapour on top of the liquid lump of caesium. The atoms in this vapour collide with the walls of the chamber, stick to it, re-condensate and drops or are scattered away. Some of

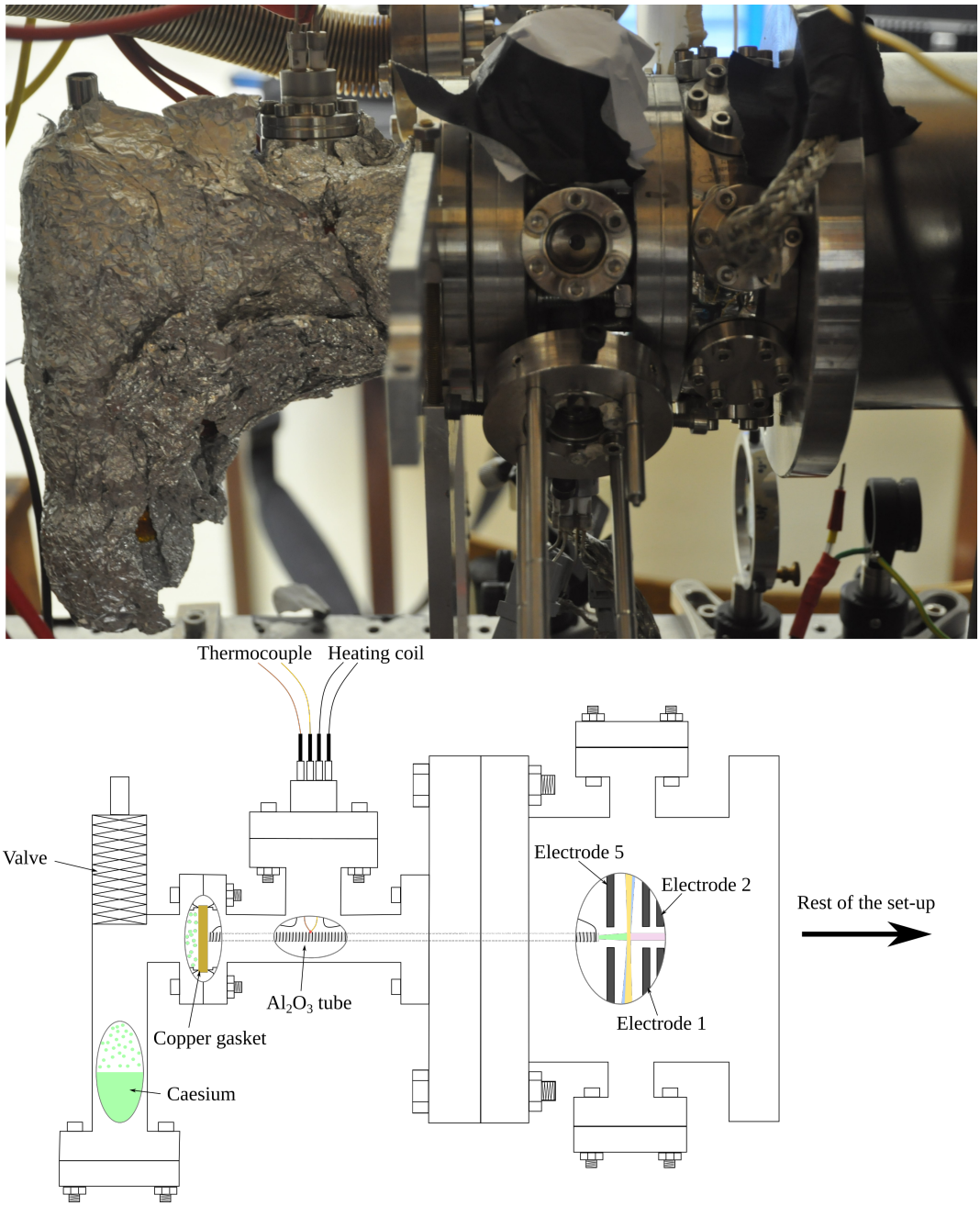

FIGURE 3.3: Photograph and schematic of our caesium oven (inner parts are shown through open ellipsis). A lump of caesium is placed in the CF16 tube on the left. A heating band is wrapped around the tube and covered with aluminium foil to improve the isolation of the heating part and allow higher temperature with less heat diffusion. The area of the liquid caesium is separated from the rest of the chamber by a small tube in Al_2O_3 plugged in a copper disk that plays the role of a gasket as well as the mechanical support for the tube. A valve is used to isolate the caesium from the rest of the experiment, both to easily refurbish the oven when empty and to protect the caesium when the set-up is vented. The inner tube in alumina is heated by a separate heating coil, and its temperature is monitored by a K-type thermocouple. Atoms are driven directly to the center of the electrodes by the inner tube.

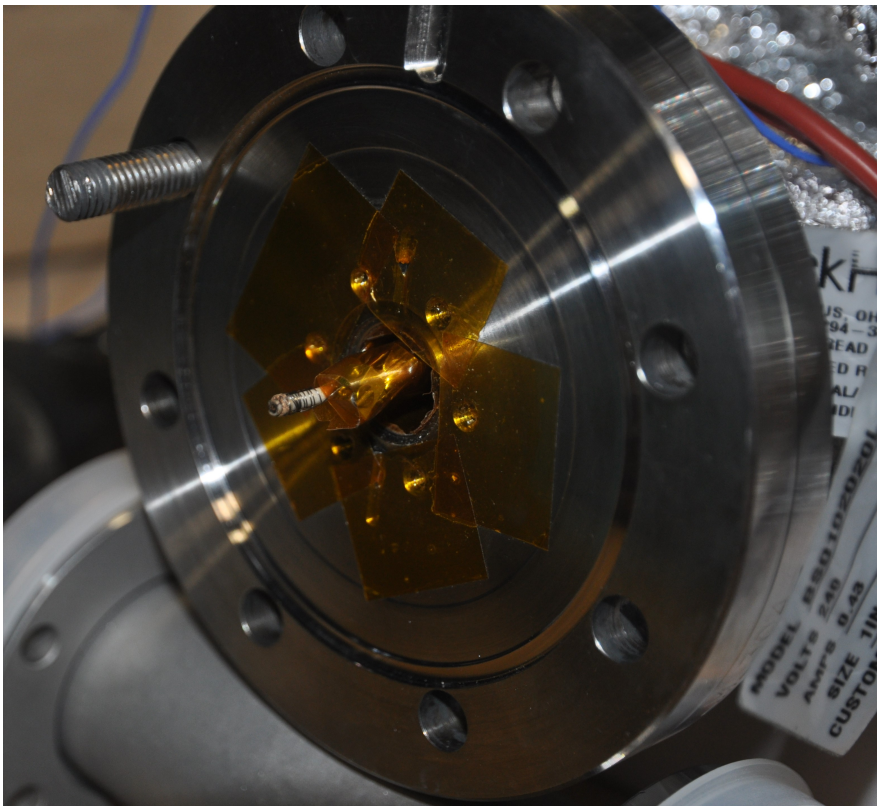

FIGURE 3.4: Photograph of the dismounted inner tube of the caesium oven. This end normally arrives at the back of electrode 5. We can see the heating wire finely coiled and isolated on top by patches of Kapton tapes. At the end of the tube the heating wire is fixed with Thorseal to keep it in place and avoid uncoiling.

these atoms have their velocity oriented along the opening of the inner tube and make their way to the other side of this tube. The end of the tube stops a few mm away from the back of electrode 5 (see figure 3.1), so atoms that exit the tube are directly flying in the center of the electrodes.

A difficult aspect to realize experimentally an efficient caesium oven is to have the temperature of the tube higher than the temperature of the caesium reservoir. It is important because otherwise the caesium atoms could re-condensate in the tube and clog it. This implies that the tube needs to be heated separately from the caesium reservoir. When the inner tube is in metal, this means that heating can be applied only with a non-conducting material. However, heating coils are always in slightly conductive metal (simply because they use Joule effect to heat). They can then be covered in an isolating material like a ceramic to allow heating a conductive material, but this creates additional mechanical constraints. In particular, the minimum curvature we can apply to these heating coils tends to be a lot higher than the required curvature to fit the inner tube. In addition to the heating wire we need a temperature measurement directly on the tube. This is achieved here by a very small K-type thermocouple that is glued on the tube around its center.

This is one of the reason we decided to use a non-conductive tube in Al_2O_3, to be able to use simple and very cheap resistive heating coil to heat the tube under vacuum. The additional reason for this choice is that alumina is one of the only easily available material

that caesium does not rapidly reduce. On figure 3.4 we can see the dismounted inner tube, with its resistive heating coil. Obviously, good care must be taken when coiling this conductive wire around the tube so that no shortage happens, that would result in cold areas of the tube. The coiling must also be quite dense and regular, because alumina is a poor heat conductor and we want to minimize temperature gradient inside the tube. A downside of alumina is its fragility, particularly with this length and small diameter. Extreme care was necessary to assemble the whole apparatus without breaking this tube, or dismantle the heating coils.

Various materials have been tested during this work, and at one point I even constructed a totally dedicated set-up to perform oven studies, with the possibility to heat the tube at temperature around 1000 °C. However, the peculiar properties of caesium (very high reactivity towards oxidation from water or air traces, formation of dimers at high temperature[2,3], very high sticking coefficients on most surfaces, increased sticking coefficients with the presence of oxygen[4,5]...) give rise to sometimes surprising behaviour[6]. The associated oven performances are thus hard to predict from simple considerations, and often not easily repeatable. This makes definitive conclusions on the oven, and definitive ways to improve its emission quite hard to draw. As a result, these studies were not conclusive, and are still going on in our laboratory, in collaboration with the Orsay Physics company that is specialised in focussed ion beam technologies.

I also performed an extensive literature search to seek a material with the smallest caesium sticking coefficient. Indeed caesium has the tendency to stick on every surface, thanks to its very low work function (the lowest of all elements), which leads to decreased values of flux and brightness. A direction of improvement for effusive ovens is thus to replace the tube material by an appropriate material that is able to minimise caesium sticking. I found several promising candidate materials:

- Nickel, that is one of the rare metal that is chemically inert towards caesium[6]. Several nickel-based alloys were also considered like Inconel, an alloy used in nuclear reactors.

- Coatings materials that are used in alkali-metal vapor cells to enhance the coherence time of spin-polarised states. The rationale being that if the alkali-metal atoms don't decohere at the contact with the coated-surface, the atoms don't interact strongly enough to stick to the surface. In other words, long coherence times is a sign that chemisorption (i.e. sticking) is strongly suppressed. The standard coating is paraffin[7], a straight-line alkane, allowing up to 10000 collisions before decoherence. Alkene-based coatings have proven extension of coherence time of at least two orders of magnitude, up to the order of 1 min[8,9]. However, these materials are fragile and not stable at the temperature that we use to vaporize the caesium (paraffin can be used up to 80 °C while alkene-based coatings are limited to below 40 °C))[2]. Octadecyltrichlorosilane (OTS) is a less effective coating[10] but that is stable up to 170 °C[11]. It resembles paraffin with the addition of a silicon head group. This head group increases the strength of the bond with the surface, that explains the higher stability. A short but very recent review on these coatings can be found in Ref. [12].

[2]It is unclear whether a high temperature caesium vapour would condensate on a colder surface with exceptionally small sticking coefficient...

- Various oxides: Al_2O_3[13], ZrO_2...

Instead of passively minimising sticking of caesium, one can also actively remove adsorbed caesium atoms not only with higher surface temperature but with light. This technique is called light-induced atomic desorption (LIAD) and is also widely used on alkali-metal glass cells, including coated-ones[14]. The adaptation of this technique to our context could then take the form of a glass tube, allowing the injection of laser light through the tube. The experimental set-up dedicated to oven studies was thus designed to allow easy injection of light in the glass tube.

The tube of the effusive oven can also advantageously be replaced by an array of silicon capillaries, or even by an array of cascaded capillaries[15]. The smallest angular spread at the output is obtained in cascaded capillaries, at the cost of approximately 97.5% of the atoms.

This work on caesium ovens is motivated by the fact that caesium oven are known to create caesium beams with poor properties compared to gas-phase theories, in terms of atomic flux and output divergence[16]. Improving the quality of our caesium beam will be required to achieve a high current electron source, and a lot of different improving directions have been presented and some of them are currently under investigation. LIAD is particularly promising. In the meantime, the caesium oven implementation described before was reliable enough to provide a caesium beam stable and intense enough for all our measurements.

3.1.3 Lasers and excitation pathways

Now that we have an atomic beam of caesium between electrodes that produce electric fields, the ionisation process only lacks the required energy to pull the electrons from the flying caesium atoms. This energy will be brought in the form of photons, coming from different lasers.

For caesium the full electron configuration is $1s^2 2s^2 2p^6 3s^2 3p^6 4s^2 3d^{10} 4p^6 5s^2 4d^{10} 5p^6 6s^1 \equiv$ [Xe]$6s^1$ but the ground state is simply designated by the spectroscopic term $6S_{1/2}$ (electrons up to the $5p$ orbitals, forming the closed-shell, are implicit). The subscript indicates the fine structure splitting that results from the coupling between the spin angular momentum $\vec{S}$ and the orbital angular momentum $\vec{L}$ to form the total electronic angular momentum $\vec{J}$ along:

$$\vec{J} = \vec{L} + \vec{S} \tag{3.1}$$

For states that exhibit orbital momentum of $L = 1$ (e.g. the first excited state $6P$ in caesium), the fine splitting splits the degenerate states into two groups labelled $nP_{1/2}$ and $nP_{3/2}$. For atoms with non-zero nuclear spins $\vec{I}$, the hyperfine splitting splits these groups even further, the interaction being described as the formation of the total angular momentum $\vec{F}$, along:

$$\vec{F} = \vec{J} + \vec{I} \tag{3.2}$$

In caesium, the nuclear momentum I has an amplitude of $7/2$ so it means that the ground state $6S_{1/2}$ couples to this moment to gives states with $F = 3$ and $F = 4$. The energy separation of these two states is exact as it is used in the current definition of the second. Figures 3.1 (and 4.12) feature the electrodes, as well as the lasers essential to the excitation and ionisation of the neutral beam. In this work we used a three-step ionisation

(summarised in figure 3.5), with three different continuous wave lasers: the 852 nm, the 1470 nm and the Ti:sapphire laser (Ti:Sa).

The first laser is a Toptica DL Pro 852 nm controlled by a Toptica DLC Pro. It emits photons that couple the ground state $6S_{1/2}^{F=4}$ to the first excited state $6P_{3/2}^{F=5}$. The precise value for this transition can be found on figure 3.10. This first transition has the advantage of being a closed transition. This means that atoms that absorbs a photon to the excited $6P_{3/2}^{F=5}$ level have only one relaxation path authorised by dipolar selection rules ($\Delta L = \pm 1$, $\Delta F = 0, \pm 1$), toward the $6S_{1/2}^{F=4}$ state. This is an advantage over other excitation pathways that could leak to other states, resulting in a lower overall ionisation efficiency. Its frequency is stabilised via the traditional saturated absorption technique on a caesium cell.

The second step to the state $7S_{1/2}^{F=4}$ is assured by a 1470 nm photon emitted by a DFB Butterfly from Toptica controlled by a LIR 110/SC110, also stabilised externally via the absorption of caesium vapour excited by the 852 nm laser.

The third step is the absorption of a photon from the Ti:Sa laser to a Rydberg state or to a continuum state. This laser is the SolsTiS from MSquared, pumped by a 25 W Millenia eV 532 nm from Spectra physics. It is controlled via a dedicated software on a computer, and its frequency is monitored and controlled directly by a wavelength meter and a computer. We use a HighFinesse WS8 wavelength meter, that has an absolute precision of 2 MHz and a relative precision of 0.5 MHz. The high performance of the control system of the MSquared laser allows us to very easily scan the wavelength of the laser over a large range, as well as to precisely tune the wavelength at an arbitrary value between 720 nm and 900 nm. It is however very sensible to back-scattered light, and its locking stability is not enough to stay locked more than a few hours. Another important aspect of this system is its ease of use, as it is fully controllable from a single web page. This laser is split into two experimental set-ups: this one and the one, presented in ref. [17], that allows spatially-correlated coincidence detection of electrons and ions from the photoionisation of caesium atoms. This separation allows us to measure data from both set-ups simultaneously, with the exact same laser frequency but different polarization. I note here that the polarisation of the ionising laser has a direct influence on the relative intensities of the different peaks, so we control it to match the experimental polarisation to the ones used in the LFT calculations to select parabolic channels to include.

The intensity of the 852 nm and the 1470 nm lasers largely saturates the related transitions. However when the intensity of a laser is too high, the light shifts the energy of the states, which can decrease the coupling efficiency to the last state. This is why we add filters to each of the lasers path to optimise the electron current on the detectors. We don't control the polarisation of these two first lasers because we easily saturate the transitions. However the last optical step is very sensitive to the polarisation of the Ti:Sa, so we have a half wave-plate that allows us to use perpendicular or parallel polarisation for the last photon step.

Figure 3.5 shows a Stark map constructed from spectrum computed with the theory described in section 2.4.2. The four low energy electronic states ($6S_{1/2}, 6P_{3/2}, 7S_{1/2}$ and $8S_{1/2}$) are represented as coloured horizontal lines because their Stark shift is negligible in this field range. Two types of photon-induced ionisation are represented and used throughout this work (852 nm-794.6 nm-794.6 nm or 852 nm-1470 nm-(Ti:Sa)).

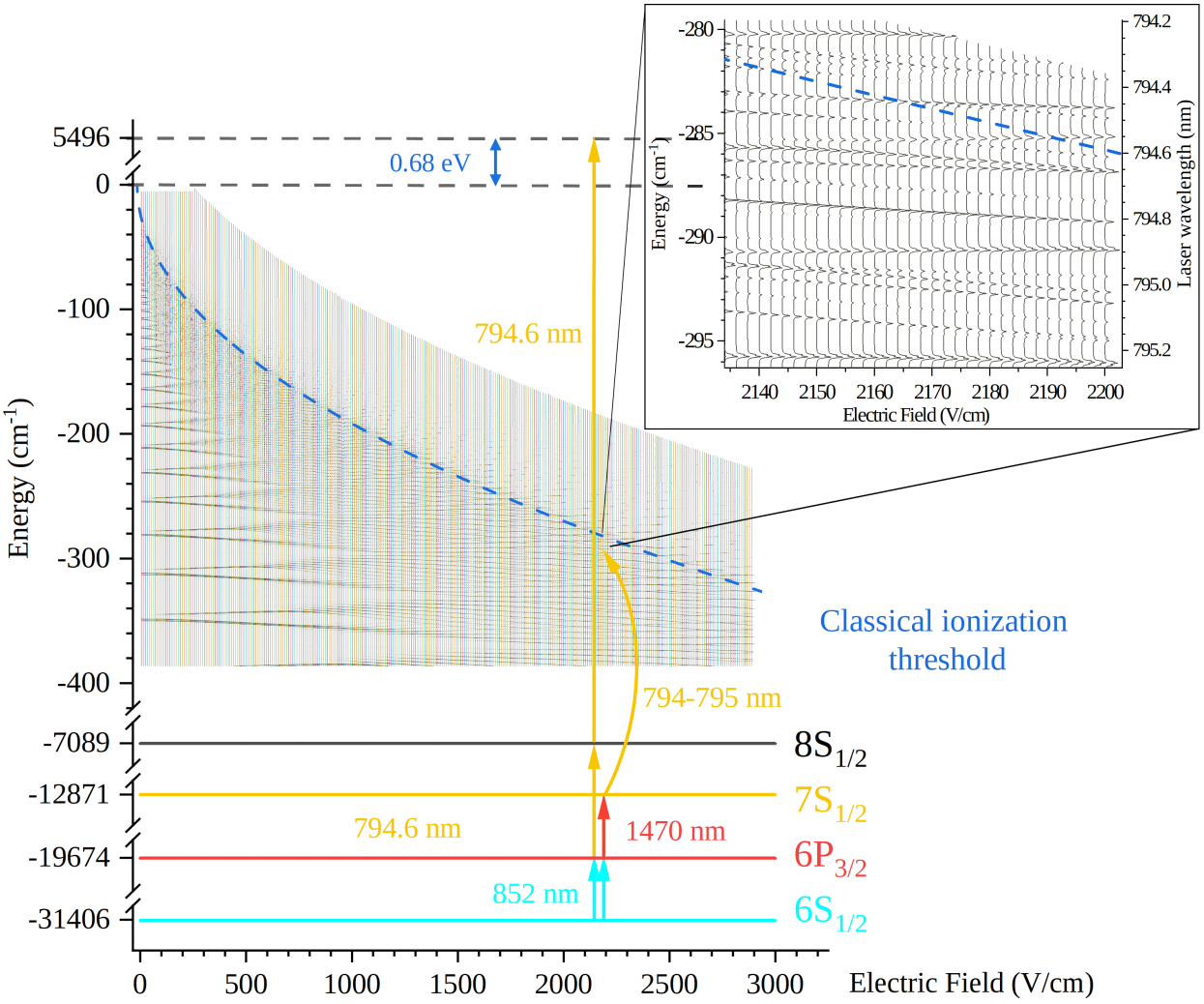

FIGURE 3.5: Stark map of Rydberg states in caesium from the field-free ionisation energy to 400 cm^{-1} below this value and from 0 V/cm to 3000 V/cm with a focus (in caption) on the ionisation paths at 2170 V/cm used in this work and the classical ionisation threshold represented in blue. Arrows represent one photon absorption. The two ionisation paths at 2170 V/cm are represented by two series of consecutive arrows, straight arrows depicting a fixed energy of the associated photon and curved arrows representing tunable photon energy. The ionisation path on the left is above-threshold photoionisation with excess energy (orange double arrow) of 0.68 eV relative to the zero-field threshold and of 0.72 eV relative to the Stark-shifted threshold. The ionisation path on the right corresponds to the excitation of an ionising Rydberg state around the classical ionisation threshold.

Section summary

Experimental set-up

In this section I have presented the experimental set-up that I built and used during this thesis. An important part is the caesium oven, that contains liquid caesium heated to around 370 K separated from the rest of the set-up by a long, heated tube. The material of this tube determines the properties of the oven, and I installed an alumina tube, that is one of the few materials chemically inert to caesium. This oven forms a neutral caesium beam between electrodes that apply a static electric field. 3 lasers (the 852 nm for $6S_{1/2} \rightarrow 6P_{3/2}$, 1470 nm for $6P_{3/2} \rightarrow 7S_{1/2}$ and the Ti:Sa for $7S_{1/2} \rightarrow Ry$ transitions) are aligned and tuned to excite then neutral atoms into Rydberg states, and ionise them into an electron beam that is extracted and focused towards the detector.

3.2 Experiments and theory interplay

In this section I present results of experiments where we scanned the frequency of the last ionising laser (Ti:Sa) and collected the electron signal in correlation with the scanned frequency. The electric field is around $-2170\,\mathrm{V/cm}$[3] and the scan range is chosen to be around the shifted ionisation threshold. These measurements allow us to calibrate the distance between electrodes 5 and 1, and to verify the accuracy of the LFT code (in terms of energy and ionisation rates predictions) over a large range of energy .

3.2.1 Electron signal optimisation

Looking at figure 3.2, we see that our electrode geometry creates not one value but a range of different electric fields in the vicinity of the lasers so the value of the electric field at which the excitation/ionisation occurs depends not only the values of V_5 and V_1 but also on the precise position of the lasers. This means that if we don't control the precise position of the lasers relative to the field line, we will lack precision on the acquired Stark maps. We thus developed a technique to position the lasers more precisely at the center of the electrodes.

We used two different methods to ensure that we positioned the lasers at the center of the electrodes: one is based on the ionisation of Rydberg atoms, and one is based on photo-ionisation. The latter method relies on the fact that our (detection) horizontal axis corresponds to the energy axis z in the ionisation region (thanks to the spectrometer presented further in chapter 4). This means that if the lasers are perfectly centred between the electrodes, the potential at which electrons are created is $V_{in} \simeq \frac{V_1+V_5}{2}$, thus increasing the electric field by changing V_1 and V_5 but keeping the average potential $\frac{V_1+V_5}{2}$ constant does not move the electron spot on the detectors. However, if the lasers are not aligned at the centre of the electrodes then changing the potentials also changes the starting potential of the electrons, thus requiring the modification of the spectrometer current to keep the

[3] This value has no particular justification and is historical

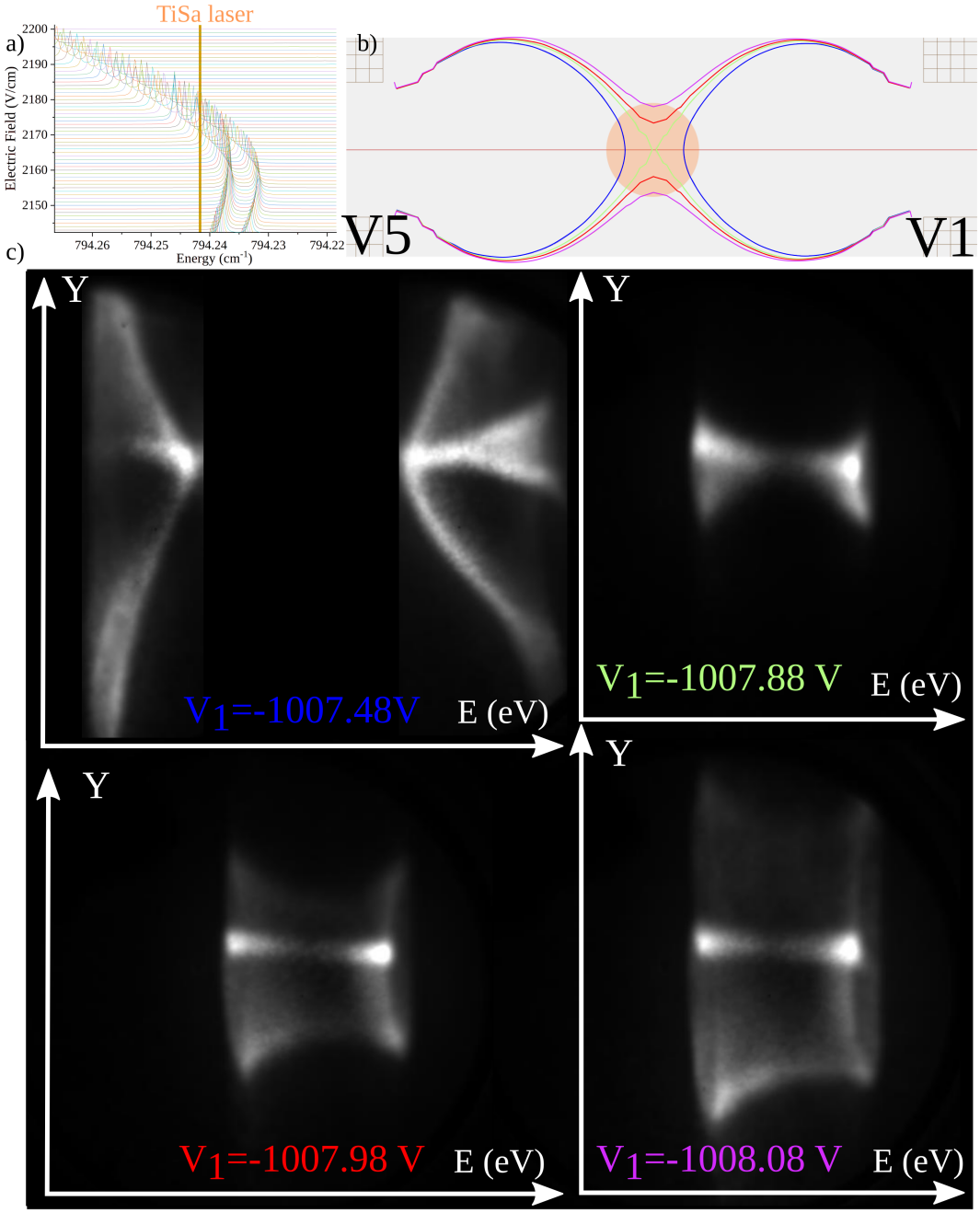

FIGURE 3.6: a) Zoom on the Stark map showing the studied state b) Zoom on electrodes showing laser spot (not on scale) and electric field lines corresponding to the resonant electric field with four different values of V_1 c) Shape of the electron spot in Rydberg field-ionisation depending on the electric field shape. Four different shapes are presented, corresponding to four different values of V_1. In all shapes $V_5 = -1881.26\,\mathrm{V}$ and the wavelength of the Ti:Sa laser is tuned at 794.241 65 nm. It is defocused. The first shape ($V_1 = -1007.48\,\mathrm{V}$, in blue) is reconstructed from two different images because it presents two different ionisation zones (the same electric field present in two different zones) that are at different potentials, thus requiring different spectrometer tuning to arrive on the detectors. Increasing $|V_1|$ moves the resonant electric field value from on-axis symmetric round sheets to a separation away from axis in the center of the electrodes.

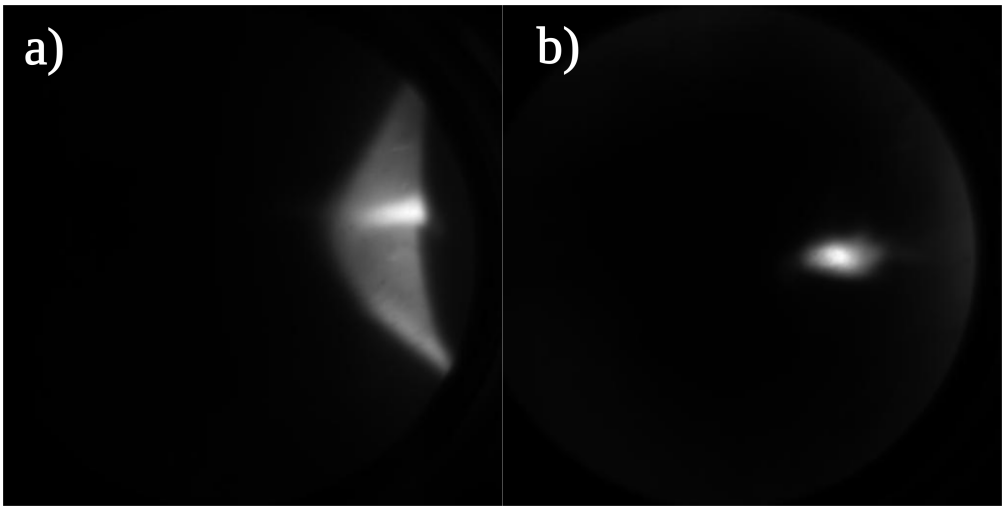

FIGURE 3.7: Electron spots from the ionisation of a short-lived Rydberg state under an electric field of $-2170\,\mathrm{V/cm}$ from a large ionising laser spot (a) and a focused laser spot (b).

electrons on the detectors. This revealed in practice to be a fastidious and not very precise way to center the lasers, mainly due to optical mounting and electric supply hysteresis.

The other method is based on the fact that Rydberg atoms have a very definite value of electric field where they can be excited and ionised (see figure 2.5 for example). This property creates ionisation zones that map the electric field distribution. If we defocus the lasers to irradiate a large part of the space between electrodes, we can visualise on the detectors the shape of the electric field lines. I recall that the electron spectrometer projects the z axis of the ionisation zone into the x axis of the detector. Thus the image that we see can be viewed as a picture of the ionisation zone from the side (in the same perspective as in figure 3.2, allowing direct electric field lines comparisons). This is shown on figure 3.6, where, depending on the value of V_1, the electron are created at different places between the electrodes. The laser wavelength is kept constant at 794.241 65 nm so that the Rydberg states are created at the same value of the electric field, but the actual position of these electric field values will depend on the specific potential applied to V1 and V5. We see clearly on figure 3.6 that the electric field lines corresponding to the resonant excitation and ionisation of the Rydberg atoms are first located around two pseudo-paraboloids centred on axis and oriented away from each other, towards the closest electrode[17]. When we decrease the value of V_1 (making it closer to V_5) these electric field line move closer to each other towards the center of the electrodes until they split and separate radially around the axis.

These experiments thus reveal a very clear visualisation of the electric field lines, which gives us a precise way to center the lasers. Indeed we can progressively focus the lasers, and adjust their position to optimise the electron signal coming from the center of the observed shapes, as shown on figure 3.7. Comparing the observed shapes with Simion simulations gives us a very good estimation of the position of the lasers and thus an increased precision in the determination of the electric field value. This will allow a higher precision in our experimental Stark maps.

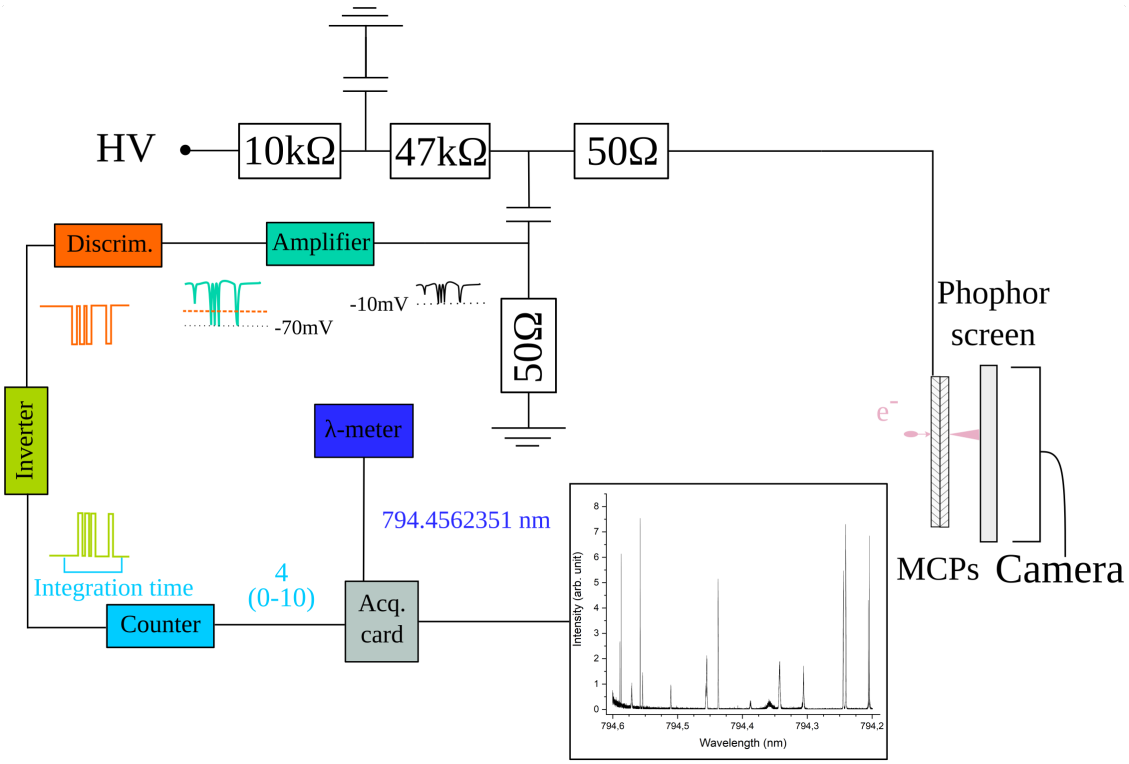

FIGURE 3.8: Experimental set-up for scans acquisition, with details on the electronics that transform the raw multi-channel plate (MCPs) low negative signal to a measurable voltage for an acquisition card ("acq. card") linked to a lambda-meter. The laser is scanned and the continuous wavelength measurement is directly correlated to the electron counter that integrates the signal on the MCP over a small time window, retrieving the inserted scan. "HV" is the high-voltage supply, "Discrim." is the discriminator with an adjustable threshold (orange dashed line). Condensers are 2 nF.

3.2.2 Acquisition of Stark spectra

Specific acquisition set-up had to be installed for the acquisition of these Stark maps, as represented schematically on figure 3.8. The electron signal is generated from the MCP's signal: the high-voltage is supplied through a simple decoupling electronic circuit that allows a read-out of the detected particles. As an electron hits the MCP, it triggers an avalanche that draws electrons from the voltage supply, and that is visible on the voltage in the form of a short negative spike. This spike can be amplified, discriminated, turned into a numeric signal, inverted, and finally integrated over a chosen period of time to represent the electron flux on the detector. A conjoint acquisition with the frequency (or wavelength) measurement gives immediately a photo-*ionisation* spectrum at a given electric field.

The low-lifetime of these Rydberg states means that their excitation will be followed by electron emission and collection, allowing a direct comparison with the photo-*absorption* spectra computed with LFT theory. Furthermore, the actual lifetime of the states τ can be inferred from the linewidth Γ of the peaks. Indeed, we have the relation $\tau(\mu s) = {}^{1}/_{\Gamma(\times 10^{-6} s^{-1})} = \frac{1}{2\pi\Delta\nu(\mathrm{MHz})}$.

	$F1$		$F2$	
	Tab.	Exp.	Tab.	Exp.
$\nu(\alpha 1)$ (THz)	377.2924943	377.2924365	377.2924933	377.2924491
$\nu(\alpha 2)$ (THz)	377.2933708	377.2933187	377.2933698	377.2933251
$\Delta\nu(\alpha)$ (MHz)	876.5	878.4	876.5	876.0
$\Delta\nu_{Tab.-Exp.}(\alpha 1)$ (MHz)	57.8		44.2	
$\Delta\nu_{Tab.-Exp.}(\alpha 2)$ (MHz)	55.9		44.7	

TABLE 3.1: Experimental ("Exp.") and tabulated ("Tab.") (see figure 3.10) values of the transition energy of peaks $\alpha 1$ and $\alpha 2$ at both values of the electric field F. $\Delta\nu(\alpha) = \nu(\alpha 1) - \nu(\alpha 2)$. The tabulated values take the Stark effect of the $8S$ state into account.

The lambdameter gives us access to the instantaneous value of the absolute wavenumber $\overline{\nu}_{abs}$ of the Ti:Sa, in cm^{-1}, while the LFT calculations are in wavenumbers relative to the field-free ionisation threshold. $\overline{\nu}_{abs}$ can be converted into a relative wavenumber to the field-free ionisation threshold $\overline{\nu}_{rel}$ ($\overline{\nu}_{thres} = 31406.4677325\mathrm{cm}^{-1}$[18]) by a simple subtraction. Indeed as can be seen on figure 3.5, this laser couples atoms in the $7S_{1/2}^{F=4}$ state of energy (wavenumber) $\overline{\nu}_{7S}$ to an ionising Rydberg state. This means that the relative energy axis $\overline{\nu}_{rel}$ can be obtained by $\overline{\nu}_{rel} = \overline{\nu}_{7S} + \overline{\nu}_{abs} - \overline{\nu}_{thres}$. The value of $\overline{\nu}_{7S}$ is calculated from the NIST atomic levels database[18] and corrected for the hyperfine structure[19], giving:

$$\overline{\nu}_{rel}(\mathrm{cm}^{-1}) = (18535.5286 + 0.0318614)_{(7S_{F=4})} + \overline{\nu}_{abs}(\mathrm{cm}^{-1}) - (31406.4677325)_{thres} \quad (3.3)$$

$$\overline{\nu}_{rel}(\mathrm{cm}^{-1}) = \overline{\nu}_{abs}(\mathrm{cm}^{-1}) - 12870.9072711 \quad (3.4)$$

3.2.3 Direct comparison with LFT theory

We acquired ionisation scans at two different field values with $V_1 = -1000.90\,\mathrm{V}$, $V_5 = -1880.81\,\mathrm{V}$ and $V_1 = -1006.88\,\mathrm{V}$, $V_5 = -1875.79\,\mathrm{V}$, with $\lambda_{Ti:Sa}$ spanning from 794.2 nm to 794.6 nm, that can be found on figure 3.9. I first analyse the observed peaks, to separate genuine Rydberg field-ionisation peaks from other observed peaks (that will be absent from our LFT calculation) to allow comparison of experiments with LFT theory.

Indeed looking at figure 3.9 we see that several experimental peaks (labelled δ, $\alpha 1$ and $\alpha 2$) are totally absent from the theoretical spectra. This is an indication that there are other ways to climb the energy ladder to ionisation when the Ti:Sa is in our range. For example, when the Ti:Sa laser emits photons with a wavelength of 794.606 nm, atoms in the first excited state ($6P_{3/2}^{F=5}$) can absorb one to the $8S_{1/2}$ state. From there another Ti:Sa photon brings enough energy to ionise the atoms with an excess kinetic energy of 0.72 eV (under 2170 V/cm), corresponding to the δ peak[17], whose foot we see on figure 3.9. The presence of the $8S_{1/2}$ state also explains the origin of two very fine and intense peaks fount at 794.587 26 nm(and 794.589 08 nm respectively labelled $\alpha 2$ and $\alpha 1$ on figure 3.9. Their origin is evident if we calculate the equivalent wavenumber of one two-photon absorption from the Ti:Sa and the 852 nm laser. It is done graphically on figure 3.10. This figure indicates that these two peaks correspond to a two-photon absorption process: one photon from the 852 nm laser close to resonance to the $6P_{3/2}$ state and another photon from

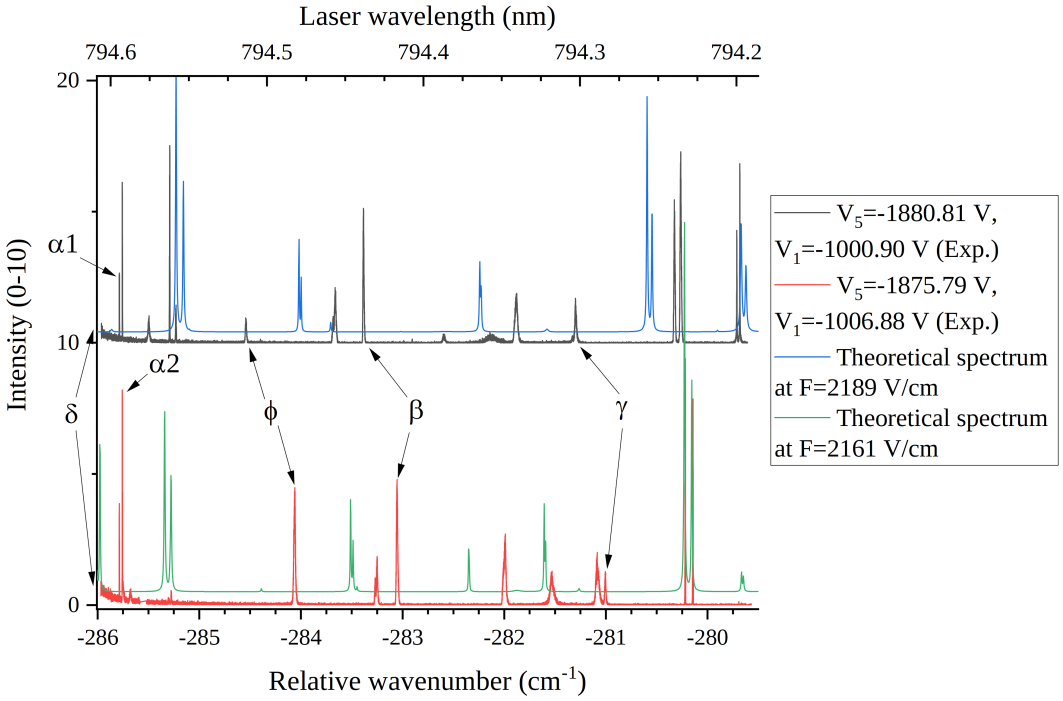

FIGURE 3.9: Experimental Rydberg field-ionisation scans in the vicinity of the ionisation threshold at two different values of V_1 and V_5 (black and red), showing numerous peaks with different width. The intensity scale (in arbitrary units) goes from 0 to 10. Each experimental spectra is accompanied by the theoretical spectrum calculated for the electric field predicted by Simion with an electrode spacing of 4 mm (green and blue), showing poor agreement. The experimental peaks labelled $\alpha 1$, $\alpha 2$ and δ (whose foot is visible) are absent from calculations because they come from the $8S$ state (see figure 3.10 for the detailed attribution). The peaks β, γ and ϕ are labelled here for further discussion.

the Ti:Sa laser excite the ground state $6S_{1/2}^{F=3}$ to the $8S_{1/2}^{F=3}$ and $8S_{1/2}^{F=4}$ states respectively. A further absorption of a photon ionises these states with excess energy.

These two peaks are very interesting for us because they allow a direct calibration of our data by comparing their experimental energy and the tabulated value indicated on figure 3.10. As these states involve the $8S$ state, the exact value of the transitions must include corrections due to the Stark effect on this state. An estimation with ARC shows that the Stark effect on the $8S$ state amounts to -22 MHz at $F \approx 2145$ V/cm ($F1$) and -23 MHz at $F \approx 2170$ V/cm ($F2$). Theses values are found in table 3.1, allowing a comparison between expected and found values. The first comment is that the agreement between experimental and tabulated data for the energy difference between these peaks ($\Delta\alpha$) is very good, confirming the attribution of these peaks. Another interesting aspect is the coherence of the discrepancies $\Delta_{Tab.-Exp.}\alpha 1$ and $\Delta_{Tab.-Exp.}\alpha 2$. As the experimental data relies on fitting peaks of width bigger than 150 MHz, the reported values are to be understood with an uncertainty of at least ± 10 MHz. This is thus a clear indication that our experimental data are shifted of approximately -50 MHz. We believe that this shift comes from a calibration error of our lambdameter. In the following, all experimental data are thus shifted by +50 MHz to account for this calibration problem. Apart from the aforementioned peaks, all the other peaks are due to resonant Rydberg field-ionisation

and we can now compare it to the Stark maps given by our LFT calculation.

3.2.4 Refining comparison between experiments and LFT theory

Ascertaining the actual experimental electric field

The first crude comparison shown on figure 3.9 relied on estimation of the electric field applied during our measurements from the known values of V_1 and V_5 and Simion simulations (already used to center the lasers in section 3.2.1). This estimation yields fields of $F1 = 2188.66\,\mathrm{V/cm}$ and $F2 = 2161.30\,\mathrm{V/cm}$ at the center of the electrodes respectively. The agreement between theory and experiment is visibly quite poor. However, before drawing definitive conclusions on the accuracy of the LFT method, we must first be certain that we compare the calculations with the actual electric field value in our experiments. Here we illustrate the sensitivity of the simulated electric field at the center of V1 and V5 to the precise distance L between these electrodes: for the same voltage difference of 870 V, $L = 3.99\,\mathrm{mm}$ gives $F = 2180.45\,\mathrm{V/cm}$, $L = 4.00\,\mathrm{mm}$ gives $F = 2175\,\mathrm{V/cm}$ and $L = 4.01\,\mathrm{mm}$ gives $F = 2169.58\,\mathrm{V/cm}$. Comparing this field amplitude to the sensitivity of the Rydberg states to the electric field (see for example inset on figure 2.5), we understand that directly comparing calculated positions with experimental ones (taking the field given by the simulation) may grossly overestimate the inaccuracy of the LFT theory. This is why we must first use the comparison of computed and experimental data to retrieve the actual electric field in our experiment (i. e. optimising the value of the electric field), and then we can critically ascertain the accuracy of the theoretical method. Using two sets of values for V_1 and V_5 (i.e. two different electric fields) imposes another constraint on the optimisation, because even if the actual distance between the electrodes is different from what we suppose (and thus that the value of the electric field varies from what we predict from the simulation), at least the **electric field difference** between the two different measurements should be approximately the same, within our experimental precision. This guaranties that we are indeed optimising the distance between the electrodes and not simply introducing an *ad-hoc* scaling to the LFT theory to better fit the data.

Results of this optimisation are found on figure 3.11. For both sets of potentials, I compare the experimental peak position to the theoretical one. When two peaks are not experimentally resolved I put the same experimental value to compare to both peaks. The plotted quantities are the sum of the squared differences[4], showing very clearly optimal values for the electric field in both cases being $F1 = 2171.9\,\mathrm{V/cm}$ and $F = 2144.1\,\mathrm{V/cm}$ (black curves on both panel of figure 3.11). However, when analysing the remaining errors (or residuals) shown on figure 3.12, I found that, at the minimum of the error curve, a single peak around $-283.3\,\mathrm{cm}^{-1}$ at $F1$ (and around $-283.0\,\mathrm{cm}^{-1}$ at $F2$), i.e. the β peak, is responsible for 77% (72%) of the total error, while 15 (14) peaks amount to only 23% (28%) of the total error. Removing this peak from the optimisations showed novel optimum values (see red curves on both panels of figure 3.11) at $F1 = 2172.3\,\mathrm{V/cm}$ and $F2 = 2144.8\,\mathrm{V/cm}$. This procedure was performed a second time to remove the

[4] this sum is done without any particular width-related weight, which could be a way to improve the quality of the fit, because very fine peaks are compared with very wide ones even though the uncertainty about the fitted position is not equivalent

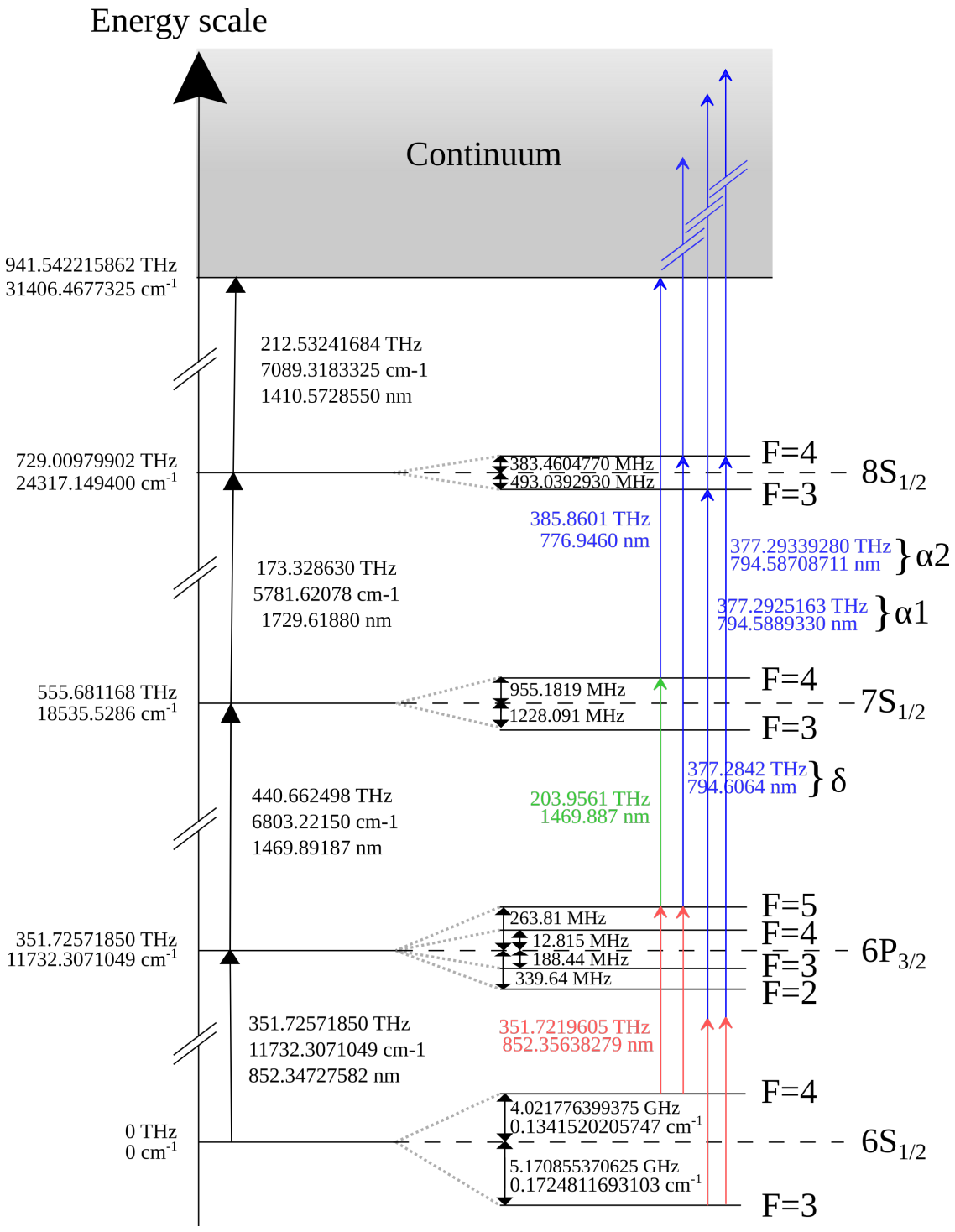

FIGURE 3.10: Energy levels of caesium, showing the hyperfine structure of all relevant states, with detailed absolute energies values and transition values. Coloured arrows depicts photons, with the color depending on the laser that emitted it. Values come from references [18–21] and ref. [20] is favoured in case of conflicts. All source of peaks present in figure 3.9 are explicitly represented here by series of arrows.

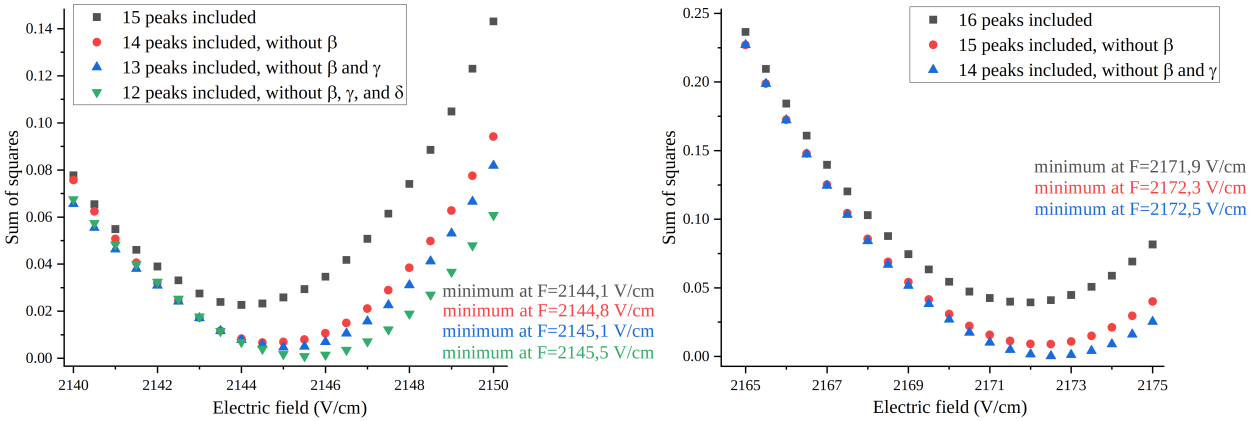

FIGURE 3.11: Results of the optimisation of the electric field value using experimental peak positions and LFT theory as a reference. Two optimisations are done around each field values of 2145 V/cm ($F1$, left panel) and 2170 V/cm ($F2$, right panel), with all observed peaks (in black) and without the most problematic peaks (red, blue and green). The plotted quantities are the sum of the squared differences between experimental and predicted values.

second most problematic peak (the γ peak), that is responsible for 91% of the remaining error at 2172.3 V/cm (see blue curves on both panels with the novel optimum at $F1 = 2172.5$ V/cm and $F2 = 2145.1$ V/cm) and even a third time at $F1$ to remove the ϕ peak, yielding a final optimum value at $F2 = 2145.5$ V/cm. Further investigation on these particular peaks showed a pronounced and unsolvable discrepancy between experiments and theory (see section 3.2.4), this is why I remove them from the optimisation to ascertain the electric field, to improve the precision of this optimisation.

Keeping the optimised value of $F1 = 2172.5$ V/cm and $F2 = 2145.5$ V/cm, and comparing these to the originally Simion simulated values of $F1 = 2188.66$ V/cm and $F2 = 2161.30$ V/cm, this gives correcting factors for the electric field of respectively 0.99262 and 0.99269. The proximity of these factors strongly suggests that the observed discrepancies are effectively primarily due to a deviation of the distance between electrodes V1 and V5 from their supposedly known values. This translates into a correcting factor to the distance between electrodes that is directly introduced in the Simion software via the "Scale" parameter in the ion optics workbench. It effectively modifies all lengths in the simulation, but the distance between these two electrodes is the most sensible length so we adapt the overall scales to fit this one as best as possible. A mean factor of 0.99265 for the fields means that the actual distance between the electrodes is likely to be around 4.030 mm instead of 4.000 mm.

The influence of quantum defects

As stated in section 2.4.2, the LFT code needs a set of quantum defects as input. We searched in the literature for the most recent values and assembled a set of quantum defects for caesium. This set can be seen in table 3.2, along with other values used in a popular code (ARC[22]). The different coefficients found in table 3.2 for one kind of state correspond to the coefficients in the extended Ritz formula, which is a more precise version of the Rydberg formula, particularly adapted to fit the ionisation energy E_I and

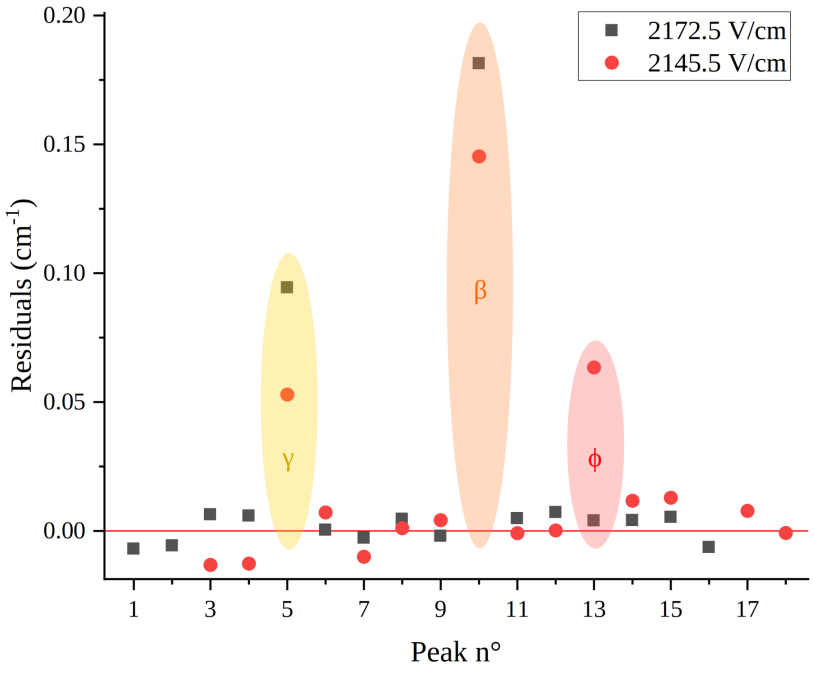

FIGURE 3.12: Plot of residuals after the optimisation presented on figure 3.11 for both values of electric field. It clearly justifies removing peaks β, γ (and ϕ for the optimisation at $F1$) to improve the precision of the optimisation. Peaks are numbered with increasing wavelength, keeping the same number for the same state over both value of electric field.

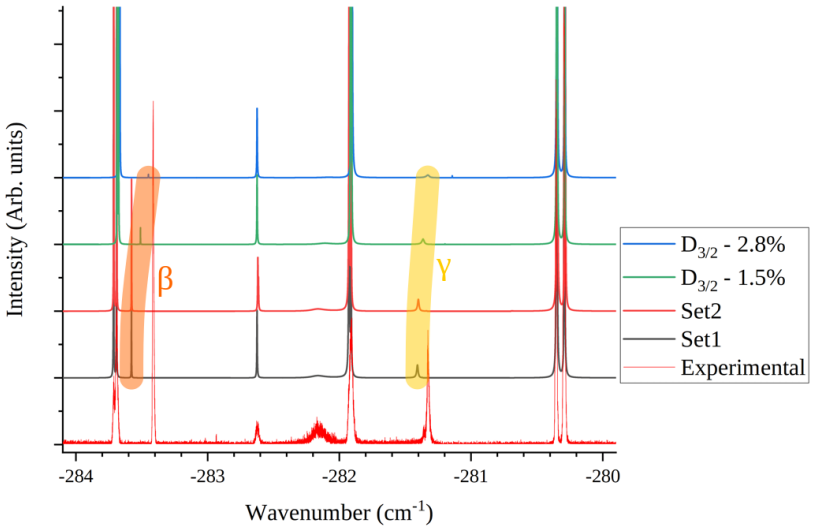

FIGURE 3.13: Photo-absorption spectra with several sets of quantum defects and with experimental data. The orange (yellow) zone features the β (γ) peak, which are the biggest discrepancies between theory and experiments. Peaks β and γ show clearly a high sensitivity to quantum defects of $D_{3/2}$ states, . See table 3.2 for details on the meaning of "Set1" and "Set2". "$D_{3/2}$ - 1.5%" and "$D_{3/2}$ - 2.8%" indicates quantum defects constructed from the "Set1" set with the $D_{3/2}$ value changed by 1.5% and 2.8% respectively.

TABLE 3.2: Sets of quantum defects used in our code ("Set1") and used in a popular code for Rydberg atoms ("Set2"). In "Set1" the value for the $nF_{7/2}$ states is constructed from the value for $nF_{5/2}$ of ref. [24] and the typical difference found in ref. [25].

States	δ_0	δ_2	δ_4	δ_6	δ_8	Ref.
$nS_{1/2}$						
Set1	4.0493532	0.2391	0.06	11	-209	[23]
Set2	4.04935665	0.2377037	0.255401	0.00378		[24]
$nP_{1/2}$						
Set1	3.5915871	0.36273				[23]
Set2	3.5915895	0.360926	0.41905	0.64388		[24]
$nP_{3/2}$						
Set1	3.5590676	0.37469				[23]
Set2	3.5589599	0.392469	-0.67431	22.3531		[26]
$nD_{3/2}$						
Set1	2.475462	0.009320	-0.43498	-0.76358	-18.0061	[26]
Set2	2.475462	0.009320	-0.43498	-0.76358	-18.0061	[26]
$nD_{5/2}$						
Set1	2.4663144	0.01381	-0.392	-1.9		[23]
Set2	2.46631524	0.013577	-0.37457	-2.1867		[24]
$nF_{5/2}$						
Set1	0.03341424	-0.198674	0.28953	-0.2601		[24]
Set2	0.03341424	-0.198674	0.28953	-0.2601		[24]
$nF_{7/2}$						
Set1	0.03355924	-0.198674	0.28953	-0.2601		[24]+[25]
Set2	0.03341424	-0.198674	0.28953	-0.2601		[24]
$nG_{7/2}$						
Set1	0.00703865	-0.049252	0.01291			[24]
Set2	0.00703865	-0.049252	0.01291			[24]
$nG_{9/2}$						
Set1	0.00703865	-0.049252	0.01291			[24]
Set2	0					

the quantum defects to experimental spectral lines[23]:

$$\overline{\nu}_{nlj} = \frac{E_I}{hc} - \frac{Ry_{Cs}}{\left(n - \delta_{lj}(n)\right)^2} \tag{3.5}$$

$$\delta_{lj}(n) = \delta_{0,lj}(n) + \frac{\delta_{2,lj}}{\left(n - \delta_{lj}(n)\right)^2} + \frac{\delta_{4,lj}}{\left(n - \delta_{lj}(n)\right)^4} + \dots \tag{3.6}$$

Our set ("Set1") was constructed primarily from the values of ref. [23], but as this reference presents no values for the $D_{3/2}$ and F or G states, we used older references to fill the gaps[24–26]. These older references use a modified version of the Ritz formula, that is not compatible with eq. 3.5. We thus use the quantum defects values directly, but check afterwards the influence of these values on the results.

The spectra with the two different sets are almost equivalent at our level of precision, with shifts between peaks in the range 0 MHz to 250 MHz. To further investigate the unexplained large discrepancies of the LFT theory with two particular peaks (see peaks β and γ on figure 3.14), and especially the possible detrimental influence of the quantum defects from the modified Ritz formula, I also performed calculations with modified values of $\delta(D_{3/2})$, $\delta(F)$ and $\delta(G)$. Results of all these calculations can be found on figure 3.13.

Changing values for F and G states up to 15% gave no changes in the spectra, so we can safely assume that the reported discrepancies are not attributable to errors in $\delta(F)$ or $\delta(G)$. On the contrary, the quantum defect of the $D_{3/2}$ state has obviously more influence on the presented spectrum, particularly on the position of the problematic peaks and almost none on other peaks. The amplitude of the change in $\delta(D_{3/2})$ required to shift the peak β close to the experimental value is large (around 3%), which is not compatible with the quantum defect error bars (which are on the order of 0.1%)[26]. Thus I can safely conclude that the pronounced discrepancies can't be fully explained by an error in the quantum defects. This is however a clear indication that the states corresponding to the two poorly described peaks (β and γ) have a large $D_{3/2}$ component, that we can relate to the already mentioned shortcomings of the LFT theory, especially towards high-l states[27] (see section 2.4.3).

Conclusion of the precision of LFT-predicted energies

We can now visualise the experimental scans superposed with the theoretical ones, as shown on figure 3.14. It confirms that the LFT theory can be used with confidence to predict the energy position of these highly-shifted peaks. At $F = 2172.5\,\mathrm{V/cm}$, the mean error over the 14 best peaks is 142 MHz, while at $F = 2145.5\,\mathrm{V/cm}$ the mean error over the 12 best peaks is 206 MHz.

However, we can't ignore the fact that the β, γ (and ϕ) peaks seem to be particularly poorly described by the theory. The energy of the two peaks have errors of 5.4 GHz and 2.8 GHz at $F = 2172.5\,\mathrm{V/cm}$; and respectively 4.4 GHz, 1.6 GHz (and 1.9 GHz) at $F = 2145.5\,\mathrm{V/cm}$.

3.2.5 States linewidth and ionisation rates

On top of the position prediction (in energy) of the Rydberg states, the LFT theory gives also an estimation of the ionisation rate of the states, via their linewidth[28] (contrary to ARC for example that gives only positions). In this section I evaluate the code accuracy by comparing the ionisation rates given by the theory to the ones extracted from experimental data in the vicinity of the shifted threshold. This verification in alkali metals improves some earlier investigations with rather poor experimental resolution (that were mostly qualitative)[28,29][5] and is very important for all our future investigations on using these states for electron sources. Indeed, being able to accurately predict the ionisation rate of strongly mixed Rydberg states in an electric field is necessary to efficiently use these states to produce a monochromatic electron beam[1] (see section 4.1).

[5] A recent reference (Ref. [30]) presents a comparison of the amplitude and position of the photoionisation peaks in LFT with GLFT and an "exact" calculations in sodium, but neglecting spin-orbit and other relativistic corrections and without experimental data

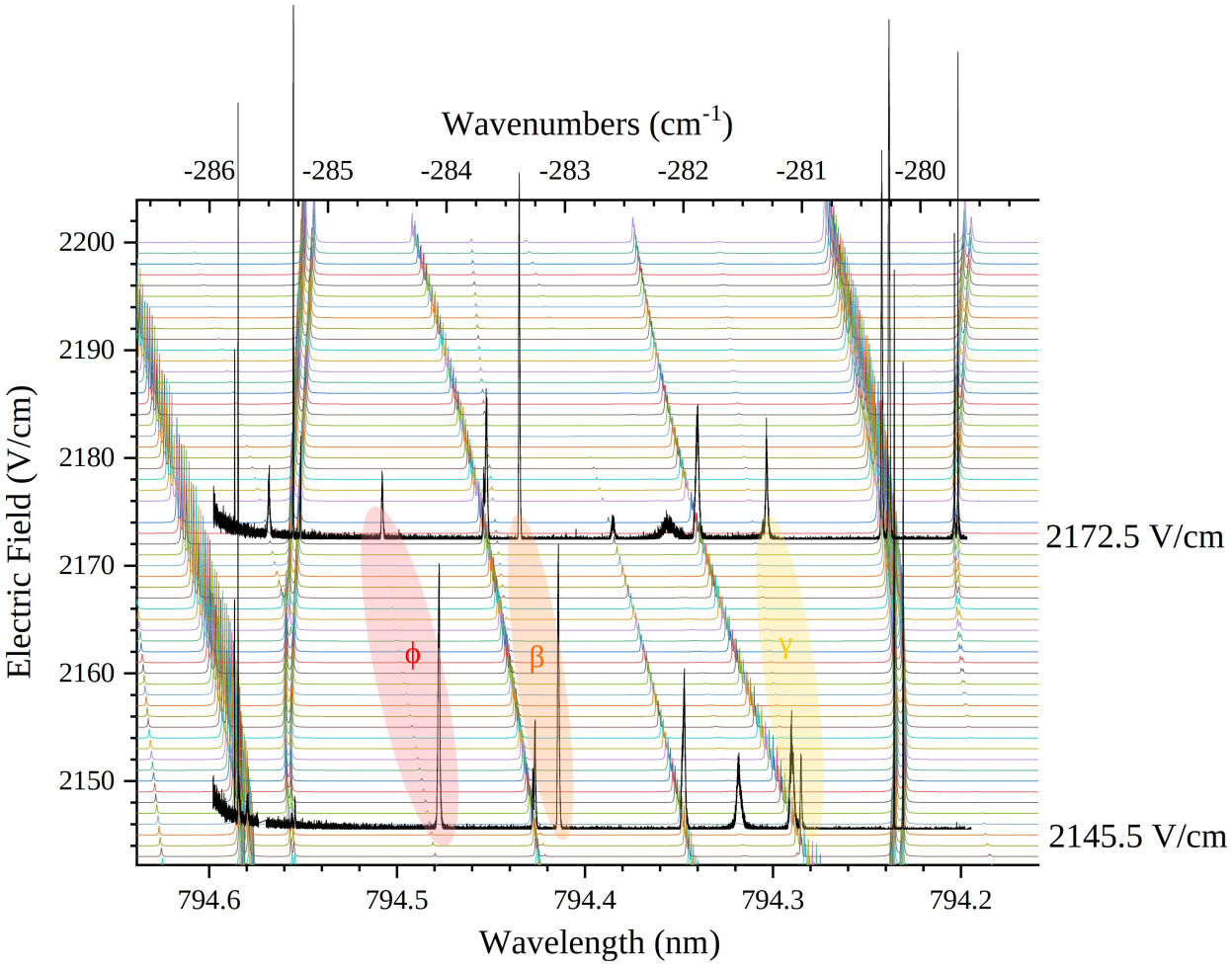

FIGURE 3.14: Superposition of two experimental scans (in black) to series of computed photo-absorption spectra (in colors). The horizontal position is directly given by the lambdameter. Their vertical position (i.e. the electric field) is optimised to minimize the difference with the calculation (see figure 3.11). This value of the electric field in indicated on the right.

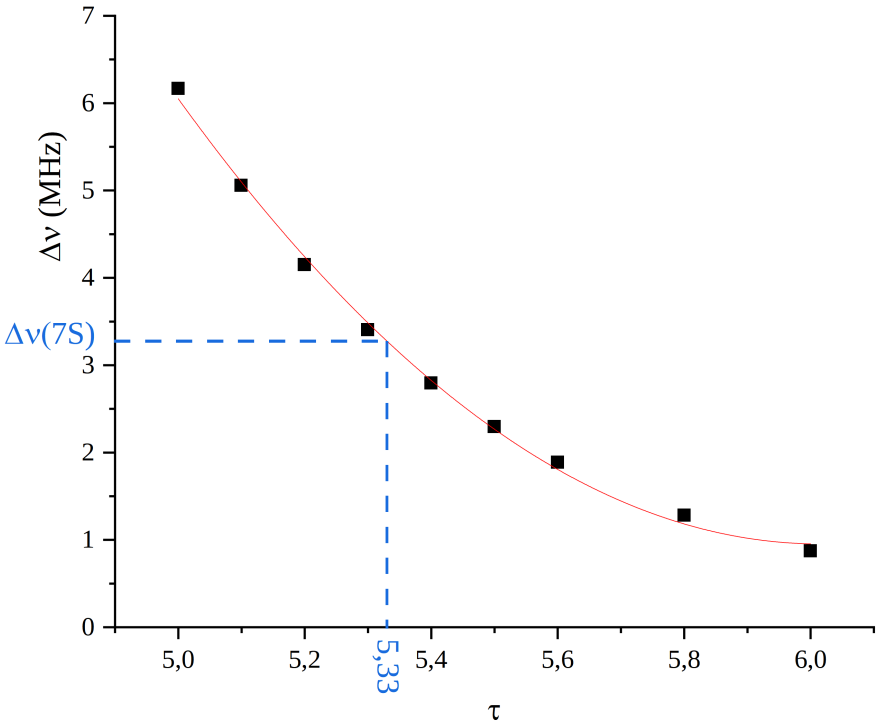

FIGURE 3.15: Computed width of the peak at $\{-280\,\mathrm{cm}^{-1}, 2172.6\,\mathrm{V/cm}\}$ depending on the value of parameter τ. The parabolic fit (in red) guides the eye. τ sets the minimal linewidth for the peak. The appropriate τ, given by the linewidth of the 7S state, is 5.33.

We thus need to compare the computed state linewidths to the experimentally extracted linewidths. The observed linewidths (for example on figure 3.14) can't be directly compared from the spectra, because in each case (theoretical and experimental) there are additional parameters that influence the observed linewidths (such as field inhomogeneities), meaning that the observed linewidth is not directly the state's linewidth Γ_{ion}. In the following sections I thus detail how we can extract this quantity in each case.

Extracting state's linewidth from theoretical data

Our LFT code uses a parameter τ as input, that limits the maximum value that a tunnelling integral can have, thus having a direct influence on the smallest possible linewidths computed peaks can have. The greater this number, the thinnest the observed peaks will be, down to the intrinsic limit of the corresponding state (its "true" linewidth). Decreasing τ will artificially increase the states' linewidth, which can in turn be really useful to limit the number of energy points needed to describe the peak when computing over large energy ranges. This is thus an important parameter to tune, and since it has a direct influence on the observed linewidths, the discussion on computed/experimentally observed linewidth must first consider the choice of τ.

Fundamentally the value of τ adapted to the best description of our experiments depends on the linewidth of our laser, but also mainly on the linewidth of the initial state (the 7S state). Indeed this state has a natural linewidth of $\Delta\nu_{7S} = 3.28\,\mathrm{MHz}$, much larger than the laser linewidth ($\leq 100\,\mathrm{kHz}$), which means that a transition from this state (even towards an infinitely narrow state) will be at least as large. This means that I have to select

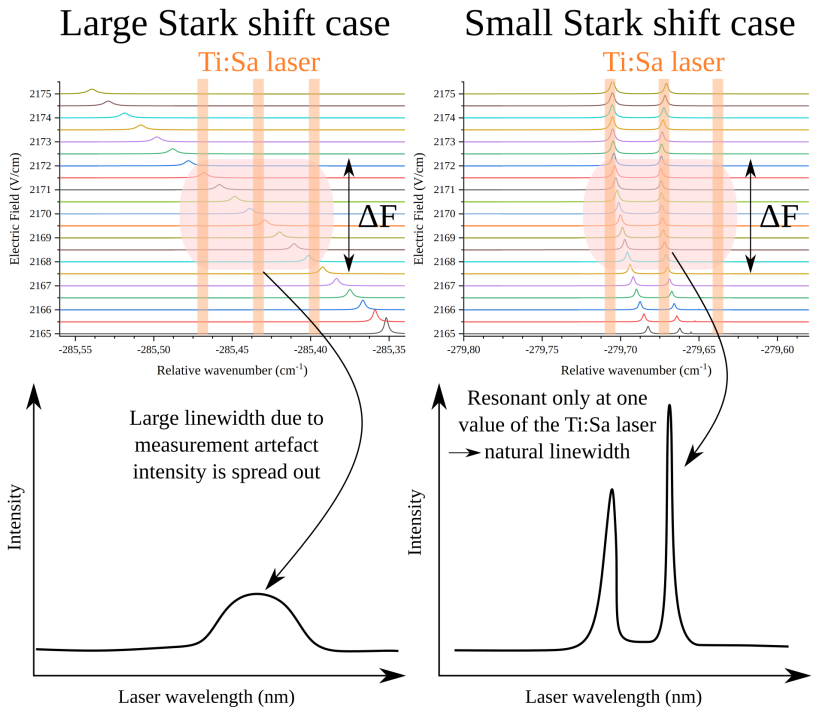

FIGURE 3.16: Schematic illustration of the link between a state's Stark slope and its apparent linewidth and intensity in a set-up like ours. Two states with comparable linewidth appear very different in our set-up because of the different fields present at the same time in the ionisation zone (ΔF), represented in the Stark map by the pale pink area. The scanning laser is represented in pale orange and is to be understood as continuously scanning the energy scale. Both (ΔF and the laser linewidth) are wider than in reality for the sake of clarity.

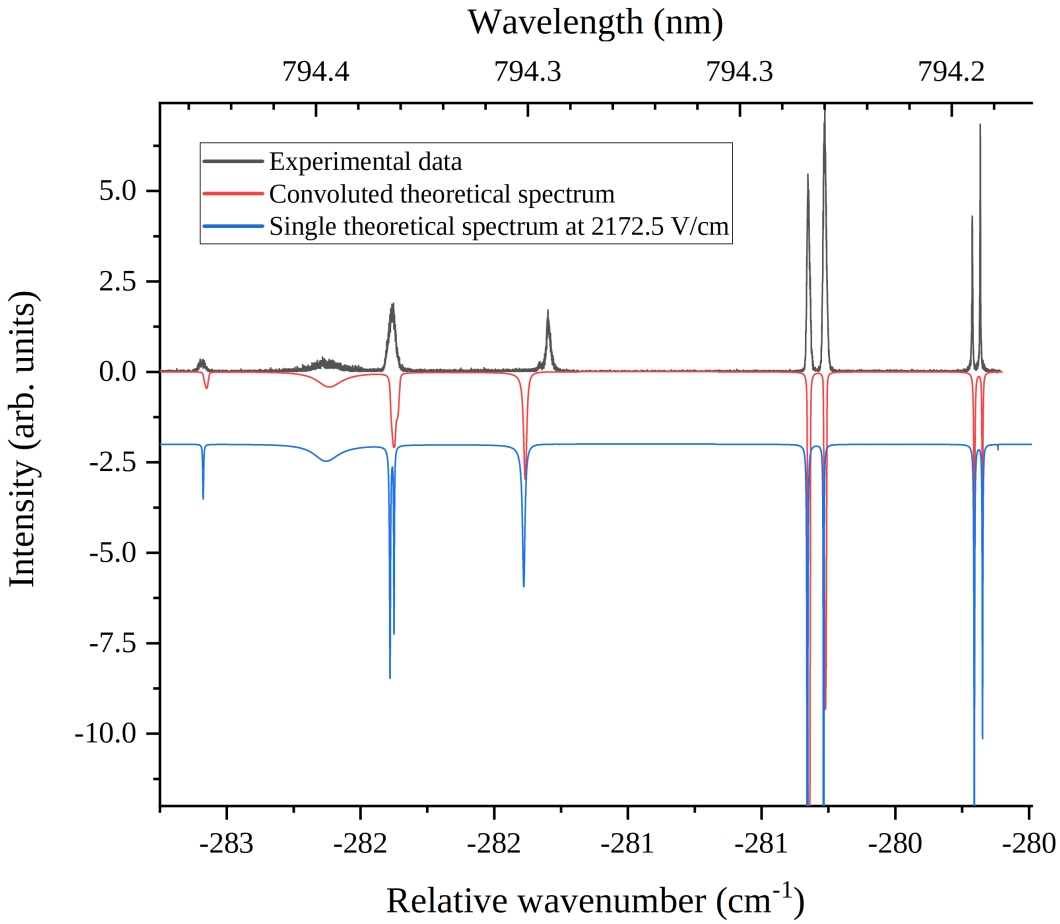

FIGURE 3.17: Comparison of experimental and theoretical linewidths. a) Histogram of the field inhomogeneity ΔF in the laser spot (Gaussian spot with FWHM of 30 µm in all directions). b) LFT-scans used to generate the convoluted theoretical scan. c) Direct comparison between experimental data (in black), a single LFT-scan (in blue, shifted by -2 for clarity) and a convoluted theoretical scan (in red). This convolution accounts for the different electric field values experimentally accessible to atoms. Very good agreement on states' linewidth is observed for all peaks.

a value of τ that gives a minimum state linewidth of 3.28 MHz. The minimal linewidth can also be increased by other effects such as light shifts or power broadening, but this represent an absolute minimal linewidth.

Figure 3.15 shows how I can choose the appropriate value for τ to best describe the experimental data. For that I zoom in on a state that is very thin and I superpose theoretical calculations done with different τ, varying from 5 to 6, and I extract the obtained linewidth. This figure shows that $\tau = 5.33$ is most adapted to our experiments.

Extracting state's linewidth from experimental data

To accurately extract the states linewidths from our experimental data, we have to consider that even when the laser is focused (see section 3.2.1), it spans a certain spatial extension, and thus different electric fields (see figure 3.2). For a state without any Stark shift, all the atoms present in the laser beam will be resonant at the same time (no matter

Peak	$\overline{\nu}^{Exp.}$ (cm^{-}1)	$\overline{\nu}^{Th.}$ (cm^{-}1)	$\Gamma_{exp.}$ (MHz)	$\Gamma_{Th.}^{2172.5}$ (MHz)	$\Gamma_{Th.}^{Conv.}$ (MHz)
1	-285.4967	-285.4879	538	180	385
2	-285.2909	-285.2947	123	8	56
3	-285.2297	-285.2324	207	6	66
4	-284.5408	-284.5426	425	57	237
5	-283.6833	-283.6869	543	9	266
6	-283.6621	-283.6645	567	9	290
7	-283.3845	-283.5638	338	8	148
8	-282.5934	-282.5885	794	108	390
9	-282.1269	-282.1254	3223	3476	3493
10	-281.8821	-281.8896	931	95	653 (unresolved)
10′		-281.8747		333	
11	-281.2974	-281.3898	576	33	385
12	-280.3252	-280.3289	387	30	196
13	-280.2641	-280.2682	420	28	210
14	-279.7121	-279.7048	97	88	88
15	-279.6824	-279.6738	75	73	73

TABLE 3.3: Quantitative comparison between position and linewidth of experimental and theoretical peaks, with and without taking into account the field window ΔF in the laser spot. This clearly shows that the theory predicts accurately the linewidth of the states, provided that ΔF is taken into account. The convoluted theory tends to underestimate the states linewidth, indicating possibly a larger laser spot than used in the convolution

the precise electric field that they feel), but only when the laser is tuned precisely at the resonant frequency. During a frequency scan (as we did), this will result in a very narrow linewidth, that we take as the intrinsic linewidth of the Rydberg state.

On the other hand, a state that has a strong Stark slope will be resonant at different sub-spaces of the laser beam, depending on the precise field value in this sub-space and the laser wavelength. This will result in an artificially large state on our scans, that will need to be deconvoluted to obtain the actual state's linewidth. It will also have an effect on the relative intensities of the states because the number of addressed atoms will be a lot higher for states without any Stark slope. This is illustrated schematically on figure 3.16, where we clearly see the influence of the Stark slope on apparent linewidth and amplitude.

This means that to properly compare experimental and theoretical linewidths it is thus important to estimate the amplitude of the different electric fields accessible to the atoms ΔF (further called the field window); to generate several Stark scans spanning ΔF; and to sum their intensities. This way we can correct both the amplitude and linewidth difference between states with no/strong Stark slopes.

The estimation of the size of the field window is done via Simion simulations, where I create 10^4 electrons at random around the center of the electrodes, following Gaussian distributions of width 30 µm along each direction. This field window corresponds experimentally to the overlap of the three lasers and the caesium beam, so it should be well reproduced by a random Gaussian distribution. I extract the initial field value for each of

these electrons and plot them as an histogram, separating the field values into 60 slab of width 0.02 V/cm, each with its population amplitude. This gives me a field-population normalisation curve, shown on figure 3.17 a).

I then compute 100 LFT scans from 2171.6 V/cm to 2173.6 V/cm (with steps of 0.02 V/cm, shown on figure 3.17 b)) to compare with the experimental scan optimised at 2172.5 V/cm, and add them with the appropriate population normalisation factor. The resulting curve is shown and compared with experimental data on figure 3.17, proving that the theoretical prediction on the states linewidth is quantitatively very good, even for the peaks with strong discrepancies for their energy. This is completed by the quantitative agreement between experimental and theoretical data shown in table 3.3, which underlines the importance of correcting the results from LFT to account for the field-inhomogeneities, particularly to predict apparent linewidth.

The intensity of each peak is good overall but the agreement is not complete, mainly because our code does not contain the field-free transition dipoles necessary to a complete description (see equation 2.53). It gives however a very good indication whether particular states will be visible (or not) in our experiment and thus usable as ionisation pathways for a high-current electron source.

3.3 Conclusion on the experimental and theoretical Stark maps

In this section I presented results of field-ionisation spectra of caesium over a large energy range near the field-shifted ionisation threshold, around 2200 V/cm. These spectra were meticulously compared with LFT calculations, with very good agreement overall, in terms of energy position of photo-ionisation peaks as well as ionisation rates of individual peaks. Individual intensities are less reliable but still give very good qualitative behaviour.

On most peaks the discrepancy between experiments and theory is less than 200 MHz, but some peaks show discrepancies up to 5.4 GHz.

The comparison of experimental data with LFT scans relied on precise determination of the experimental electric field, done via the optimisation of the distance between the electrodes to best fit the data. This optimisation yielded a distance of 4.030 mm instead of 4.000 mm. To improve the accuracy of this optimisation I had to remove several peaks that presented particularly high discrepancy. I then checked if this observed discrepancy could be attributable to errors in quantum defects, but the analysis showed that these errors would have to be significantly larger than plausible to account for the discrepancies between LFT and experimental spectra.

This quantum-defect study however showed a correlation between a state's lack of accuracy and its sensitivity to the quantum defect of $D_{3/2}$ states. The absence of cross-sections inputs makes the relative amplitude of the observed peaks less reliable but does not affect the precision of the predicted energy levels. Updating this code to GLFT would surely provide even higher accuracy, but our LFT code can nevertheless effectively be used to predict energy position of the Rydberg states in a strong electric field, as well as the ionisation rates of these states. This is a very important step in our understanding of Rydberg ionisation, and will be really useful to search for interesting states to use in an electron source. Its accuracy on Stark-shifted energy levels and ionisation rates around

the ionisation threshold is overall very satisfactory and allows a precise choice of ionising Stark-Rydberg state. In the next chapter we will extensively use these Stark maps to present the different ways we can ionise Rydberg atoms, along with the resulting electron beam properties.

References

[1] Marian Mankos, Khashayar Shadman, Raphaël Hahn, Yan J. Picard, Daniel Comparat, Olena Fedchenko, Gerd Schönhense, Lionel Amiaud, Anne Lafosse, and Nick Barrett. "Design for a high resolution electron energy loss microscope". In: *Ultramicroscopy* 207 (2019), p. 112848. ISSN: 03043991. DOI: 10.1016/j.ultramic.2019.112848.

[2] P. P. Sorokin and J. R. Lankard. "Emission Spectra of Alkali–Metal Molecules Observed with a Heat–Pipe Discharge Tube". In: *The Journal of Chemical Physics* 55.8 (1971), pp. 3810–3813. ISSN: 0021-9606. DOI: 10.1063/1.1676665.

[3] D. H. Sarkisyan, A. S. Sarkisyan, and A. K. Yalanusyan. "Thermal dissociation of cesium dimers". In: *Applied Physics B: Lasers and Optics* 66.2 (1998), pp. 241–244. ISSN: 0946-2171. DOI: 10.1007/s003400050382.

[4] J.-L. Desplat and C. A. Papageorgopoulos. "Interaction of cesium and oxygen on W(110)". In: *Surface Science* 92.1 (1980), pp. 97–118. ISSN: 00396028. DOI: 10.1016/0039-6028(80)90246-0.

[5] K. Prince. "Coadsorption of oxygen and caesium on silver (110)". In: *Applied Surface Science* 22-23 (1985), pp. 469–477. ISSN: 01694332. DOI: 10.1016/0169-4332(85)90078-9.

[6] Sofia Cristofaro, Markus Fröschle, Alessandro Mimo, Andrea Rizzolo, Michela de Muri, Marco Barbisan, and Ursel Fantz. "Design and comparison of the Cs ovens for the test facilities ELISE and SPIDER". In: *Review of Scientific Instruments* 90.11 (2019), p. 113504. ISSN: 0034-6748. DOI: 10.1063/1.5128620.

[7] M. A. Bouchiat and J. Brossel. "Relaxation of Optically Pumped Rb Atoms on Paraffin-Coated Walls". In: *Physical Review* 147.1 (1966), pp. 41–54. ISSN: 0031-899X. DOI: 10.1103/PhysRev.147.41.

[8] M. V. Balabas, T. Karaulanov, M. P. Ledbetter, and D. Budker. "Polarized alkali-metal vapor with minute-long transverse spin-relaxation time". In: *Physical review letters* 105.7 (2010), p. 070801. ISSN: 1079-7114. DOI: 10.1103/PhysRevLett.105.070801.

[9] Eric P. Corsini, Todor Karaulanov, Mikhail Balabas, and Dmitry Budker. "Hyperfine frequency shift and Zeeman relaxation in alkali-metal-vapor cells with antirelaxation alkene coating". In: *Physical Review A* 87.2 (2013), p. 9. ISSN: 1050-2947. DOI: 10.1103/PhysRevA.87.022901.

[10] M. A. Hafiz, V. Maurice, R. Chutani, N. Passilly, C. Gorecki, S. Guérandel, E. de Clercq, and R. Boudot. "Characterization of Cs vapor cell coated with octadecyltrichlorosilane using coherent population trapping spectroscopy". In: *Journal of Applied Physics* 117.18 (2015), p. 184901. ISSN: 0021-8979. DOI: 10.1063/1.4919841.

[11] S. J. Seltzer and M. V. Romalis. "High-temperature alkali vapor cells with antirelaxation surface coatings". In: *Journal of Applied Physics* 106.11 (2009), p. 114905. ISSN: 0021-8979. DOI: 10.1063/1.3236649.

[12] Haotian Chi, Wei Quan, Junying Zhang, Lijiang Zhao, and Jiancheng Fang. "Advances in anti-relaxation coatings of alkali-metal vapor cells". In: *Applied Surface Science* 501 (2020), p. 143897. ISSN: 01694332. DOI: 10.1016/j.apsusc.2019.143897.

[13] S. Woetzel, F. Talkenberg, T. Scholtes, R. IJsselsteijn, V. Schultze, and H.-G. Meyer. "Lifetime improvement of micro-fabricated alkali vapor cells by atomic layer deposited wall coatings". In: *Surface and Coatings Technology* 221 (2013), pp. 158–162. ISSN: 02578972. DOI: 10.1016/j.surfcoat.2013.01.044.

[14] E. B. Alexandrov, M. V. Balabas, D. Budker, D. English, D. F. Kimball, C.-H. Li, and V. V. Yashchuk. "Light-induced desorption of alkali-metal atoms from paraffin coating". In: *Physical Review A* 66.4 (2002), p. 9. ISSN: 1050-2947. DOI: 10.1103/PhysRevA.66.042903.

[15] Chao Li, Xiao Chai, Bochao Wei, Jeremy Yang, Anosh Daruwalla, Farrokh Ayazi, and C. Raman. "Cascaded collimator for atomic beams traveling in planar silicon devices". In: *Nature communications* 10.1 (2019), p. 1831. DOI: 10.1038/s41467-019-09647-3.

[16] C. B. Lucas. *Atomic and molecular beams: Production and collimation*. Boca Raton: CRC Press/Taylor & Francis Group, 2014. ISBN: 978-1466561038.

[17] R. Hahn, A. Trimeche, C. Lopez, D. Comparat, and Y. J. Picard. *Cesium Rydberg states ionization study by 3-D ion-electron correlation*. 2021.

[18] A. Kramida, Yu Ralchenko, Reader J., and National Institute of Standards and Technology ASD Team. *NIST Atomic Spectra Database (ver. 5.7.1), [Online]*. URL: https://physics.nist.gov/asd (visited on 06/04/2020).

[19] Guang Yang, Jie Wang, Baodong Yang, and Junmin Wang. "Determination of the hyperfine coupling constant of the cesium $7S_{1/2}$ state". In: *Laser Physics Letters* 13.8 (2016), p. 085702. ISSN: 0022-3700. DOI: 10.1088/1612-2011/13/8/085702.

[20] D. A. Steck. *Cesium D Line Data*. (revision 2.2.1,) Nov. 21, 2019. URL: http://steck.us/alkalidata.

[21] P. Fendel, S. D. Bergeson, Th Udem, and T. W. Hänsch. "Two-photon frequency comb spectroscopy of the 6s-8s transition in cesium". In: *Optics letters* 32.6 (2007), pp. 701–703. ISSN: 0146-9592. DOI: 10.1364/OL.32.000701.

[22] N. Šibalić, J. D. Pritchard, K. J. Weatherill, and C. S. Adams. "ARC: An open-source library for calculating properties of alkali Rydberg atoms". In: *Computer Physics Communications* 220.319 (2017). DOI: 10.1016/j.cpc.2017.06.015.

[23] Johannes Deiglmayr, Holger Herburger, Heiner Saßmannshausen, Paul Jansen, Hansjürg Schmutz, and Frédéric Merkt. "Precision measurement of the ionization energy of Cs I". In: *Physical Review A* 93.1 (2016). ISSN: 1050-2947. DOI: 10.1103/PhysRevA.93.013424.

[24] Weber and Sansonetti. "Accurate energies of nS, nP, nD, nF, and nG levels of neutral cesium". In: *Physical review. A, General physics* 35.11 (1987), pp. 4650–4660. ISSN: 0556-2791. DOI: 10.1103/PhysRevA.35.4650.

[25] P. Goy, J. M. Raimond, G. Vitrant, and S. Haroche. "Millimeter-wave spectroscopy in cesium Rydberg states. Quantum defects, fine- and hyperfine-structure measurements". In: *Physical review. A, General physics* 26.5 (1982), pp. 2733–2742. ISSN: 0556-2791. DOI: 10.1103/PhysRevA.26.2733.

[26] C.-J. Lorenzen and K. Niemax. "Precise quantum defects of nS, nP and nD Levels in Cs I". In: *Zeitschrift fr Physik* 315.2 (1984), pp. 127–133. ISSN: 1434-6001. DOI: 10.1007/BF01419370.

[27] V. G. Ushakov, V. I. Osherov, and E. S. Medvedev. "Analytical S -matrix derivation in the theory of the nonhydrogenic Stark effect". In: *Journal of Physics A: Mathematical and Theoretical* 52.38 (2019), p. 385302. ISSN: 0034-4885. DOI: 10.1088/1751-8121/ab2efa.

[28] F. Robicheaux. "Time- and energy-dependent response of Cs in a strong electric field". In: *Physical Review A* 56.5 (1997), pp. 4032–4037. ISSN: 1050-2947. DOI: 10.1103/PhysRevA.56.4032.

[29] I. Seipp and K. T. Taylor. "The combined R-matrix and complex coordinate method applied to the Stark and Stark diamagnetic Rydberg spectra of Na". In: *Journal of Physics A: Mathematical and Theoretical* 27.13 (1994), pp. 2785–2799. ISSN: 0034-4885. DOI: 10.1088/0953-4075/27/13/009.

[30] P. Giannakeas, C. H. Greene, and F. Robicheaux. "Generalized local frame transformation theory for excited species in external fields". In: *Physical Review A* 94.1 (2016). ISSN: 1050-2947. DOI: 10.1103/PhysRevA.94.013419.

Chapter 4

A continuous electron beam from the ionisation of Rydberg atoms

> I believe that a scientist looking at nonscientific problems is just as dumb as the next guy.
>
> Richard P. Feynman

In the last chapter we have seen that the LFT theory provides very useful Stark maps of Rydberg states in the vicinity of the ionisation threshold, and it compares favourably with experimental data, both for the energy position and the ionisation rates. It also allowed us to deduce the actual distance between our flat electrodes. This work represents the first reported comparison of LFT with experimental data in caesium with this energy resolution, showing that states with strong D-components present the biggest discrepancies on an overall very good agreement. Using LFT-based codes (over matrix diagonalisation based code like the ARC python code[1]) for this energy range is thus a proper way to describe the effect of the electric field on Rydberg state.

In this chapter we will see how we use this code to the production of an electron beam, with the goal of reducing the energy spread of conventional electron sources. This builds up on the previous studies done in this group about such a source. The biggest challenge here is to keep the energy spread of the electron down to a few meV while providing an electron current in the 100 pA-1 nA range. This current is around one order of magnitude higher than what can be provided by threshold photo-ionisation sources, mainly because of the very-low ionisation cross-sections. One way to increase the current is to use a cavity to enhance the ionisation efficiency[2] or to use big laser spots to address a higher number of atoms, allowing (ion) currents up to 5 nA at a cost of brightness[3]. In this chapter, we will see that another way to increase the current is to take advantage of the high transition cross-sections towards Rydberg states.

We saw in section 1.4 that to fulfil the very-low energy spread requirement, it is necessary to use low to very low extracting fields and to reduce the longitudinal size of the ionisation zone, as well as to cope with the ionic space-charge in an efficient way. The most straightforward way to reduce the size of the ionisation zone in a photo-ionisation electron source, is to reduce the size of the ionising laser, by focusing it. This puts a lower bound to the easily achievable size of the ionisation zone, around a few microns.

In this chapter we will see that the peculiar properties of Rydberg atoms might offer another way to reduce the energy spread of continuous photo-ionisation electron sources. The ambition is to reduce the size of the ionisation zone and the associated electron energy

spread, with higher current than standard photo-ionisation sources. Such a source would allow the functioning of the HREELM instrument, opening up new possibilities in surface science.

First we present the different approaches to describe the ionisation of an atom by a laser, and the links of these different approaches to the final electron energy spread. Then I report on an experimental effort to measure the energy spread of such sources in the different ionisation regimes. To analyse the energy spread we use a dedicated electron spectrometer, that had to be adapted and studied in-depth to allow accurate and reliable energy spread measurements. I present measurements of the link between energy spread and extracting electric field in photo-ionisation and discuss the strategies to achieve a very-low energy spread electron source. Two detailed propositions are made, that could be realised and used as electron source for the HREELM project.

4.1 Identification of different ionisation phenomena

We already saw that electrons can be produced from caesium atoms in an electric field via different ionisation phenomena. I introduce here a nomenclature for these phenomena, to clarify their differences. I identify 3 different continuous ionisation phenomena that will be dealt with in this chapter:

- Photoionisation
- Rydberg field-ionisation
- Velocity-induced field ionisation

The separation between these three ionisation mechanisms in partly fundamental, but also context-specific. In particular for us it rests on the fact that the resulting electron energy spread comes from different sources for these three mechanisms. Pulsed ionisation will be introduced and studied in the next chapter.

4.1.1 Photoionisation

Photo-ionisation is the phenomenon that separates an electron from an atom, thanks to a photon whose energy is larger than the ionisation threshold of the atom.It can be understood as a momentum exchange between the photon and the electron, strong enough to overcome the attraction of the electron to the core. This "kick" ejects the electron away from the core, in a direction linked to the electric-field component of the incoming photon. This electron is usually called the photo-electron. Quantum mechanically it can also be described as the coupling between a bound state and the continuum of unbound states, characterised by wave-functions extending well over the Coulomb barrier. This explains why the efficiency of photo-ionisation is usually very low, because the overlaps between these wave-functions are very small quantities, and coupling rates are proportional to these overlaps.

Figure 4.1 shows a Coulomb potential with the definition of the different energies. Photoionisation obviously requires a photon with enough energy to eject the electron from its bound state to the continuum, i.e with a wavelength $\lambda \leq \lambda_0$, with λ_0 the threshold

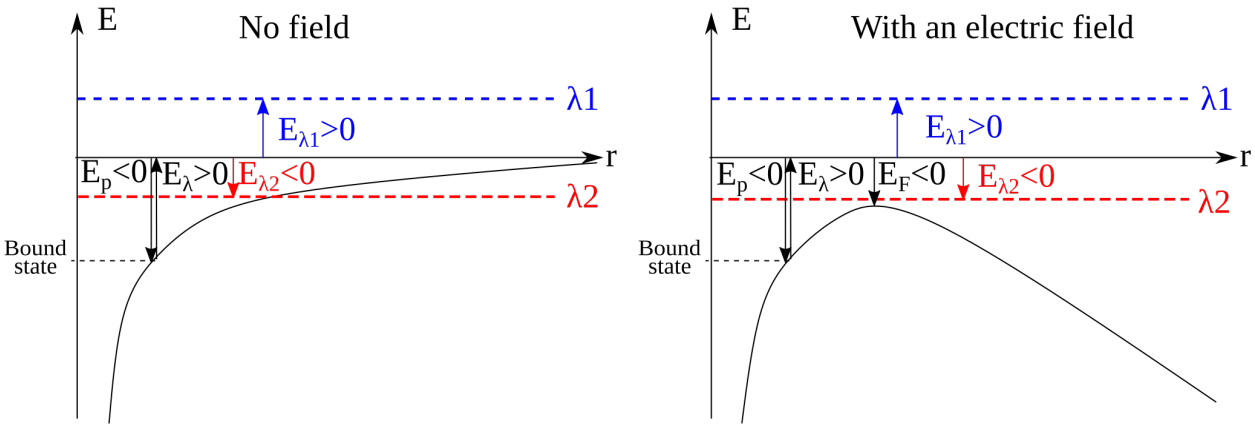

FIGURE 4.1: Schematics of an atomic potential (similar to $^{-1}/_{r}$) without electric field (left panel) and with an electric field (right panel) and definition of the different energies involved in the description of photo-ionisation. The blue excitation level correspond to photo-ionisation without (left panel) or with (right panel) an electric field. The red excitation level corresponds to transition to another bound state without the electric field, and to Rydberg field-ionisation with the electric field.

ionisation wavelength without any electric field and $E_{\lambda 0}$ the associated energy (in atomic units). I call E_λ the photon energy with respect to the field free ionisation threshold:

$$E_\lambda = hc\left(\frac{1}{\lambda} - \frac{1}{\lambda_0}\right) \tag{4.1}$$

This definition implies that field-free photo-ionisation requires $E_\lambda > 0$ and is practical because it does not demand to specify the electron ground state, making comparison between the photoionisation of different bound states easier. The bound state in question (of relative energy $E_p = -|E_{\lambda_0}|$) can be any state of the atom, even its ground state[1].

If we want to simulate the classical trajectory of an electron orbiting around the ion core (without external electric field) during photoionisation, the kinetic energy of the electron E_k is then equal to:

$$E_k = E_\lambda - E_p \tag{4.2}$$

The term E_p is required to take into account the interaction with the ion core. In practice the value of E_λ is known from the experimental laser wavelength and tabulated values for the field-free threshold. Calculating E_p requires the expression of the atomic potential in function of the distance to the core $U(r)$, and an estimation of r. For hydrogen $U(r) = -1/r$, while for alkali metals various parametrised potentials have been devised (see equation 2.23 for an expression for caesium) and can be used effectively to simulate classically this phenomenon[9]. In the following (see section 4.1.2) we see that these simulations can also be used to describe Rydberg field-ionisation.

[1] in this case, λ_0 fall usually in the UV range

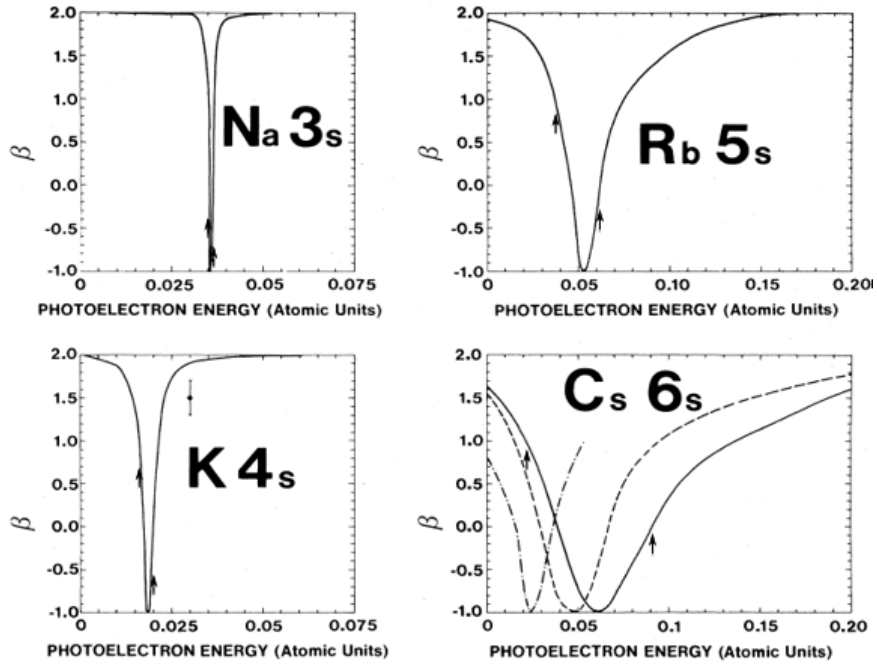

FIGURE 4.2: Photo-electron energy dependence of the asymmetry parameter β for the four heaviest alkali-metal outer ns shells. Different curves for Cs indicate different theoretical methods. The arrows indicate the Cooper minima. Reproduced from [4] with data from [4–8]

Angle dependence of the emission of photoelectrons

The electron starting kinetic energy, or more precisely its starting momentum will be oriented relative to the field-component of the ionising photon. We call θ the angle between the polarisation vector of the incident light and the direction of the outgoing photoelectron. For polarised light, this will produce strongly anisotropic electron ejection: the angular dependence of the photo-ionisation cross-section $\frac{d\sigma}{d\Omega}$ can be estimated with[2][10]:

$$\frac{d\sigma}{d\Omega} = \frac{\sigma}{4\pi}\left(1+\beta\left(\frac{3}{2}\cos^2(\theta)-\frac{1}{2}\right)\right) \tag{4.3}$$

with σ the total cross section for the photo-ionisation of a given sub-shell and β the asymmetry parameter[3]. The value of β is highly non-trivial to pinpoint, as it is energy dependent, and encompasses the effect of all the dynamical aspect of the photo-ionisation, relativistic effects and Cooper minima[4]. The requirement that $\frac{d\sigma}{d\Omega} \geq 0$ however limits β to values between -1 and +2. For hydrogen and in light atoms (i.e. without spin-orbit), with low incident photon energy, one can safely put $\beta = 2$[10,11]. Equations 4.3 then gives:

$$\frac{d\sigma}{d\Omega} = \frac{3\sigma}{4\pi}(\cos\theta)^2 \tag{4.4}$$

[2]This formula is written for linearly polarised light, but can be written in very similar ways for other polarisations or even unpolarised light by appropriate definition of θ[4]

[3]Not to be confused with the charge separation parameter for Rydberg states under an electric field introduced in eq. 2.21

[4]situations where dominant ionisation channels interfere destructively and cancel out

This angular dependence corresponds to the classical result, as well as the quantum mechanical one when considering only $s \rightarrow p$ transitions[4].

Experiments and theoretical results have shown that for alkali atoms, and for caesium in particular, where spin-orbit and other relativistic effects are very strong, it is not a good approximation to take $\beta = 2$, even at low energy[10,12,13]. As an illustration of the non-trivial behaviour of β, its energy dependence for the ground state of the four heaviest alkali metals can be found on figure 4.2. It clearly features large variations from +2 to -1 with the photon energy, centred around the Cooper minimum in each case. The width of the dip increases with the size of the alkali metal atom, as spin-orbit becomes stronger[4].

The departure from $\beta = 2$ is sometimes neglected in the description of photo-ionisation electron sources, usually without too much detrimental effects[9,14]. However, when photo-ionising caesium, taking this factor into account is crucial to understand the momentum distribution.

Amplitude of the photoelectron momentum

The electron ejection momentum amplitude k will obviously depend on the value of E_k, but also on the mass of the ion. Indeed, due to momentum conservation law, the energy transfer will follow from the mass ratio of the electron and the ion. Neglecting the momentum of the photon in the atomic referential, this gives:

$$m_e v_e^{add} = m_{Cs^+} v_{Cs^+}^{add} \tag{4.5}$$

with v_e^{add} and $v_{Cs^+}^{add}$ the additional velocity after the ionisation, once the two particles are well separated and do not interact any more. This can be complemented by the energy conservation for the absorption of the photon. We call E_{exc} the excess energy provided by the ionising photon, giving:

$$E_{exc} = \frac{1}{2} m_{Cs^+} \left(v_{Cs^+}^{add} \right)^2 + \frac{1}{2} m_e \left(v_e^{add} \right)^2 \tag{4.6}$$

The combination of equations 4.5 and 4.6 gives velocities of:

$$v_e^{add} = \sqrt{\frac{2E_{exc}(m_e + m_{Cs^+})}{m_e m_{Cs^+}}} \simeq \sqrt{\frac{2E_{exc}}{m_e}} \tag{4.7}$$

$$v_{Cs^+}^{add} = \frac{m_e}{m_{Cs^+}} v_e^{add} \tag{4.8}$$

This formula is general, with or without electric field, as long as E_{exc} is well defined (and positive). In the absence of an electric field we have simply $E_{exc} = E_\lambda$.

Adding an electric field

Photo-ionisation does not need any external electric-field, but the addition of an electric field F will lower the ionisation threshold of $E_F = -2\sqrt{F}$ in the field direction as can be seen on the right panel of figure 4.1. This will allow the ionisation with $E_\lambda < 0$, as we will see in section 4.1.2.

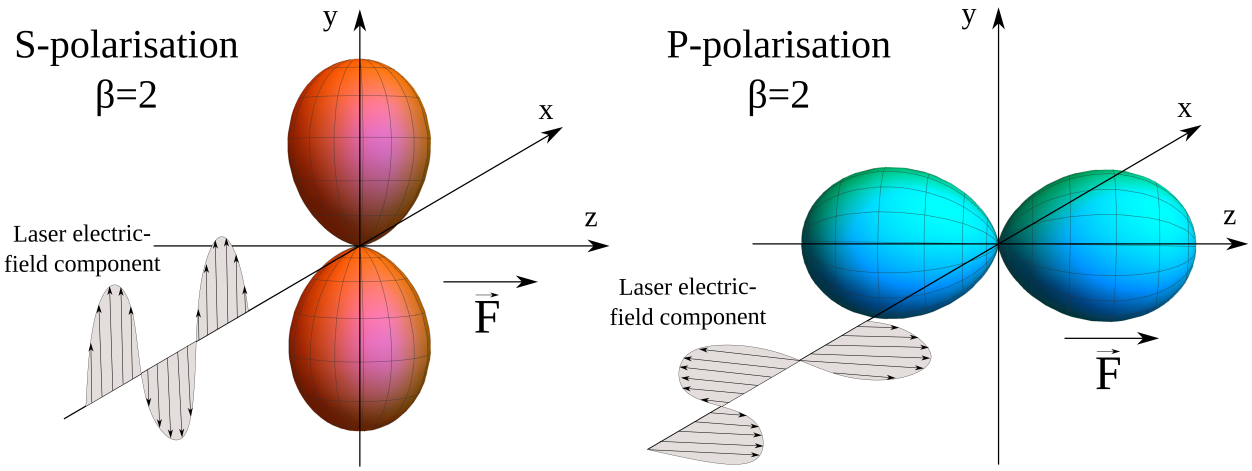

FIGURE 4.3: Angular-dependence of the photo-ionisation in the presence of an electric field oriented along z, with an asymmetry parameter $\beta = 2$ and two different linear polarisation S and P. The laser propagates along the x axis, S-polarisation corresponds to the electric component in the xy plane, P-polarisation corresponds to the electric component in the xz plane.

The formulas 4.7 and 4.8 are still valid, as long as E_{exc} is now defined as:

$$E_{exc} = E_\lambda - E_F \tag{4.9}$$

A numerical application with $E_{exc} = 5\,\text{meV}$ gives $v_e^{add} = 41\,939\,\text{m/s}$ and $v_{Cs^+}^{add} = 0.173\,\text{m/s}$, showing that the conclusions of section 1.4.3 are even more valid with non-negligible ionisation excess energy, i.e. that the initial atomic velocity spread does not play a dominant role on the final electron velocity spread.

Before considering what happens under the field-free threshold, we mention that adding an electric field will break the circular symmetry of the problem, and create a preferred projection axis. This will help us define the polarisation of the ionising laser in an un-ambiguous way. One example of such a definition can be seen on figure 4.3.

In the case of an emission cone oriented primarily along the electric field (for example with an asymmetry parameter $\beta = 2$ and a laser electric field component along the electric field, see right panel of figure 4.3), this will create electrons ejected mainly down-field, and electrons ejected mainly up-field. The latter will then experience the electric field acceleration and if the field is strong enough, turn around toward the down-field regions. This creates sizeable time-delay between the two classes of electrons. We present experimental results showing this behaviour very clearly in section 5.2.

4.1.2 Rydberg field-ionisation

As we already saw, an electric field will open up the possibility to ionise atoms with $E_\lambda < 0$. For the rest of this thesis, this situation is called Rydberg field-ionisation (RFI). We must first note that in the scientific field of Rydberg atoms, the term "field-ionisation" corresponds to a technique to detect Rydberg atoms, where an electric-field is slowly ramped up and any electron signal can be traced back to the presence of a Rydberg state that ionises at this precise field. Our definition of "Rydberg field-ionisation" is a bit more

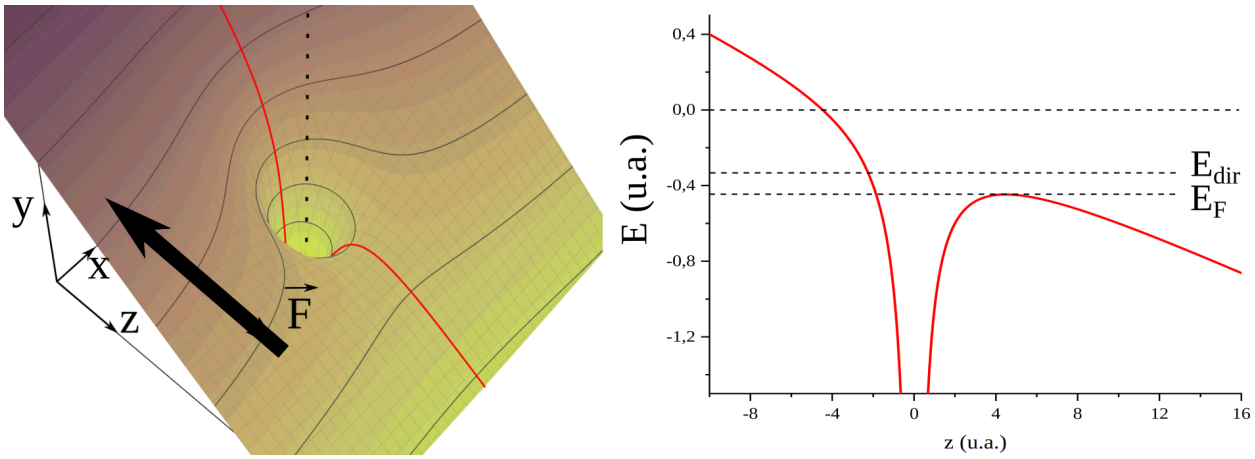

FIGURE 4.4: Combined Coulomb and Stark potential for the outer electron of a Rydberg atom. The left panel shows the potential in a xz plane, and the right plot corresponds to the $x = 0$ profile, giving the Coulomb-Stark potential in function of the distance to the ionic core along the direction of the electric field $\vec{F}$. E_{dir} is the minimum energy of direct ionisation trajectories (see text). E_F is the energy of the saddle-point.

general but encompasses the phenomenon used in this technique, as long as the electric field increase is slow against the lifetime of the Rydberg state.

RFI of hydrogen

Rydberg field-ionisation corresponds to the ionisation of Rydberg states under a static (or slowly changing) electric field. The scans presented in section 3.2 thus correspond to electrons produced by Rydberg-field ionisation. The potential of a Rydberg electron in an electric field can be seen on figure 4.4. It is a combination of the Coulomb field of the ionic core that traps the electron and the electric field that opens this trap towards the high-field region (high z). It features a saddle-point at $E_F = -2\sqrt{F}$ (atomic units are used hereafter).

Ignoring the Stark shift of these states, we can replace E thanks to equation 2.1, which gives:

$$F_{ion} = \frac{1}{16n^{*4}} \tag{4.10}$$

Thus in the classical view, the field F_{ion} corresponds to the ionisation field, that is called the classical threshold field[15].

In general there are two different mechanisms that result in the ionisation of Stark-shifted Rydberg states: tunnelling of the electronic wave-function through the Coulomb-Stark barrier, and coupling to open parabolic channels. The first mechanism is purely quantum mechanical, while the second can be viewed either quantum mechanically as the coupling between different states, or classically, based on calculated trajectories in the potential[15,16].

In hydrogen some states have their electronic wave-function completely in the η coordinates, corresponding to closed parabolic channels. The energy of these states is dominantly in the up-field motion, meaning that the electron will never be able to overcome the Coulomb barrier. We can also state that their coupling to continuum states is weak.

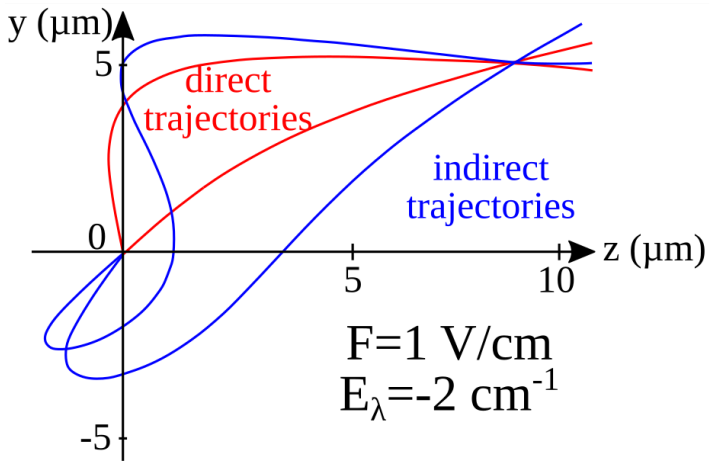

FIGURE 4.5: Classical trajectories (both direct and indirect) in hydrogen under a field of 1 V/cm, with $E_\lambda = -24.8\,\text{meV}$. $E_{\text{dir}} = -59\,\text{meV}$ so direct trajectories are allowed. (Reproduced from [17])

This results in states with energy over E_F that are still stable toward ionisation. Their only path to ionisation is then to tunnel through the barrier.

Classically speaking, we can thus calculate electron trajectories of states with an energy higher than E_F but that can never escape the ion potential. Indeed, depending on the angle γ between the electric field axis and the initial velocity of the electron (see figure 4.6 for the definition of γ), the electron will or won't escape the influence of the core. We note here that the ionisation occurs in the direction of the field, meaning that in the appropriate parabolic coordinates, the open channels are in the ξ coordinate (see section 2.3). We can even define a critical angle γ_c that will determine if the motion of the electron is bound or not, depending on the value of the excess energy E_{exc} and E_F[9]:

$$\gamma_c = 2\arccos\left(\frac{-E_\lambda}{E_F}\right) \tag{4.11}$$

From there we can separate the ionising electron trajectories into direct and indirect trajectories: direct trajectories correspond to electrons escaping the ion potential without crossing the z axis, and electrons following indirect trajectories cross the z axis at least once[17]. Thus just above the saddle-point, almost all trajectories are indirect, whereas at the field-free ionisation threshold most of the trajectories are direct. This separation into direct and indirect trajectories introduces another energy threshold called E_{dir} (see figure 4.4), which corresponds to the energy threshold where direct trajectories start to become allowed. Figure 4.5 features examples of both classical direct and indirect trajectories, where $E_\lambda > E_{\text{dir}}$. Moreover, it is possible to derive: $\kappa = \frac{E_{\text{dir}}}{E_F} \approx 0.775$[17]. We can thus define four regions, depending on the given energy E_λ[17]:

- $E_\lambda < E_F$, this corresponds to completely stable states, where the electron motion is bound. Tunneling ionisation can still occur but the ionisation rates are very low.
- $E_F \leq E_\lambda < E_{\text{dir}}$, the motion is bound along the ξ coordinate if $\gamma < \gamma_c$ and open if $\gamma \geq \gamma_c$, but only indirect trajectories can lead to ionisation

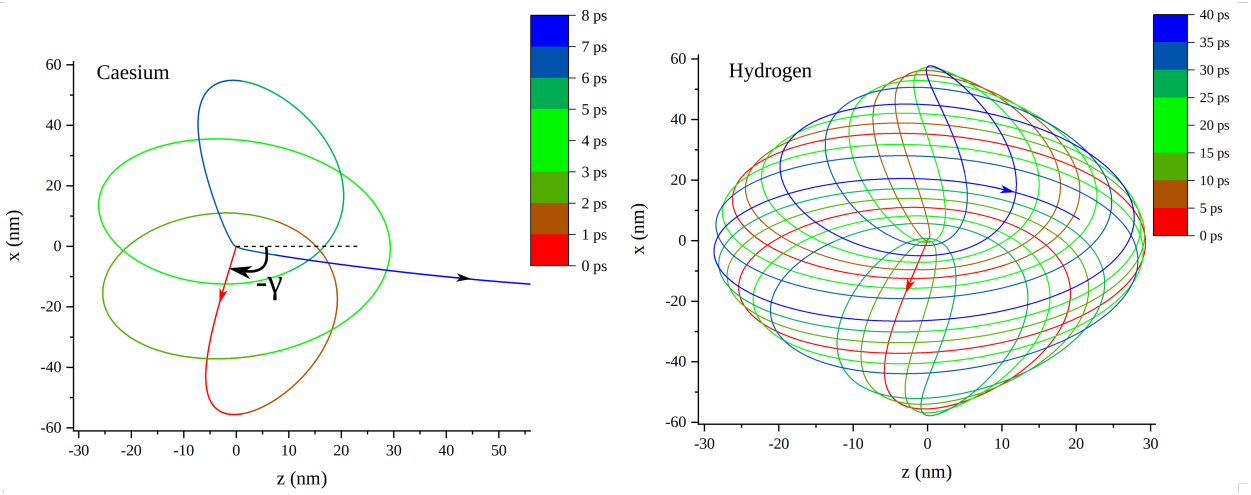

FIGURE 4.6: Classical trajectories in caesium and hydrogen, following the model introduced in ref. [9] for rubidium. Trajectories are computed in General Particle Tracer for the same excess energy ($E_{exc} = 5\,\text{meV}$) and a field of $1.55\,\text{kV/cm}$. The bigger core of caesium deflects the electron into ionisation after a few ps, while the trajectory in hydrogen is completely stable at this time scale.

- $E_{\text{dir}} \leq E_\lambda < 0$, the motion is bound along the ξ coordinate if $\gamma < \gamma_c$ and open if $\gamma \geq \gamma_c$, but both direct and indirect trajectories can lead to ionisation
- $0 \leq E_\lambda$, the motion of the electrode is always open in the ξ coordinate, no matter the value of γ

The hydrogen case gives us an illuminating view on the process of field-ionisation in non-hydrogenic atoms, in contrast. Indeed, the ionic core of a non-hydrogenic atom will couple different parabolic channels, and no state with energy above E_F is stable toward ionisation.

RFI of caesium

In the classical trajectory view, the same simulations, with a potential similar to the one presented in equation 2.23, showed that in a Rubidium atom, there were no closed trajectories at energies above the saddle-point energy[9]. I reproduced these simulations in a caesium atom, and one example of such a scattering event can be seen on figure 4.6. Trajectories starting with $\gamma < \gamma_c$ show recursions in the ion potential until the electron is scattered by the ionic core and escapes to infinity. This departure from the hydrogenic case means that the closed trajectories are coupled to the open trajectories via the interaction of the ion core.

This ionisation process can be analysed as a quenching toward ionisation of stable states by mixing with rapidly ionising states. The high symmetry of hydrogen makes the degeneracy of stable and unstable states possible, as can be seen in any Stark map of hydrogen, where blue (slowly ionising) and red (rapidly ionising) states cross. In non-hydrogenic atoms with lower symmetry this is not possible any more, as evident from the avoided crossings seen on caesium Stark map on figures 2.2 or 3.14. Here states in

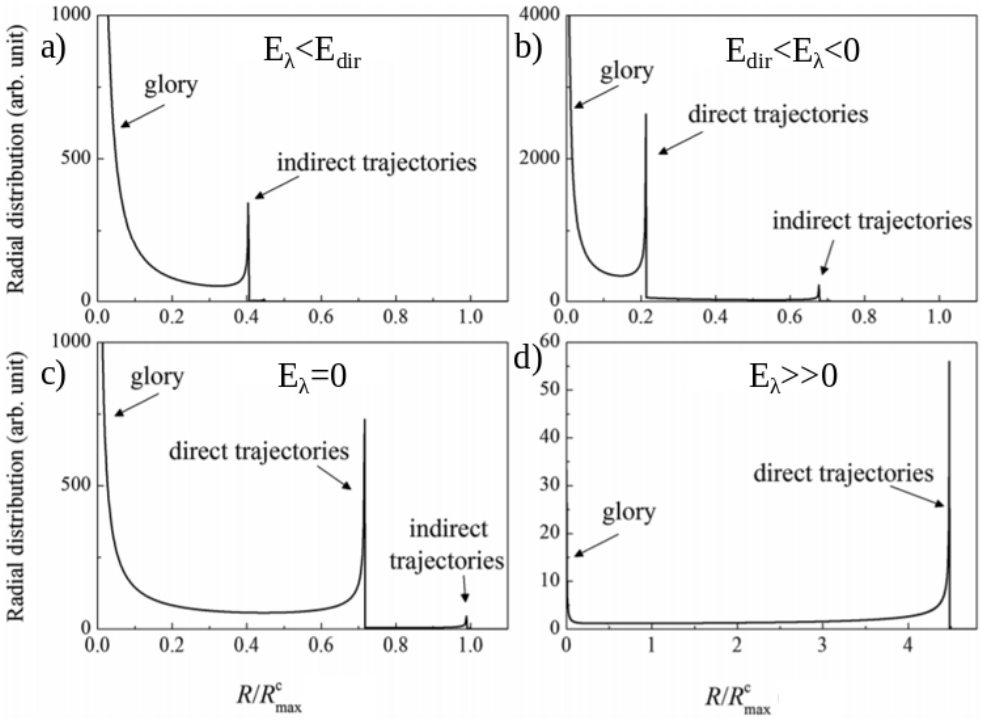

FIGURE 4.7: Dependence of the classical radial distribution of electrons on the value of the ionisation excess energy E_λ, with $E_F < E_\lambda < E_{dir}$ (a), $E_{dir} < E_\lambda < 0$ (b), $E_\lambda = 0$ (c) and $E_\lambda >> 0$ (d). R^c_{max} is the maximum radius of impact. Reproduced from ref. [18]

the energy vicinity of one another can have strong interaction and mixing, due to the perturbation of the ionic core. As already seen in section 2.2 the perturbation of the ionic core on any state can be quantified by the quantum defect of this state. Thus states with high quantum defects will have large avoided crossings on their Stark maps and can experience strong mixing between near-degenerate states. This mixing can happen between stable states and states strongly coupled to the continuum, which explains why some of the avoided crossings abruptly changes the ionisation rates of the avoided states.

Another important aspect of the Rydberg field-ionisation process (for all atoms, provided it is neutral before the ionisation) is that as clearly shown on figure 4.4, the electron can escape only in the direction of the electric field (the ξ parabolic coordinate), whereas in photo-ionisation the excess energy transforms partly into electron momentum directed up-field (see figure 4.3).

On top of that, the precise shape of the Coulomb-Stark potential near the saddle-point in this direction is bottleneck-like. The lasting interaction of the ejected electron and the ionic core creates a force towards the z axis and further reduces the emittance of the created electrons. This is called the glory effect, by analogy with classical optics[18,19], and can be seen very clearly on figure 4.7. The result of this effect is the formation of an intense electron spot on axis on a detector placed at high distance in the direction perpendicular to the electric field. Figure 4.7 shows clearly that for a negative E_λ (i.e. for RFI as I have defined it), the glory part of the electron flux is largely dominant. Contrary to intuition, this effect is still effective in photo-ionisation (when $E_\lambda > 0$), even with high excess energy ($E_\lambda \simeq 0.5\,$eV) even though it is not dominant any more[19] (see panel d) of figure 4.7).

We see here the interesting aspect of the direct/indirect trajectories separation, because these different groups of electrons will have different radial distributions on the detector. The advantageous behaviour to lower the electron emittance is thus to ionise atoms with $E_\lambda < E_{\text{dir}}$, where the glory component is the most dominant in the electron radial distribution. It has been demonstrated experimentally that electron beams from Rydberg field-ionisation have lower transverse temperature than predicted from isotropic emission[9,20]. These two effects (emission directionality and glory effect) directly decrease the emittance of the electron beam and increase the imaging capabilities of these electrons.

In terms of ionisation efficiency this method is typically orders of magnitude higher than photo-ionisation because the laser couples a low energy state to an actual semi-bound state, so the orbital overlap is considerably higher. The transition dipole from the $7S_{1/2}$ state to the Rydberg state $50P_{3/2}$ at $F = 10\,\text{V/cm}$ is given by ARC to be equal to $\mu_{7S\to 50P} = 0.003\,\text{ea}_0$[5]. From the well-known two-level model we can approximate the excitation efficiency from the $7S$ state to a Rydberg state ρ_{ee} as:

$$\rho_{ee} = \frac{\Omega^2}{\Gamma_{Spec.}^2 + 2\Omega^2} \tag{4.12}$$

with Ω the Rabi frequency of the transition and $\Gamma_{Spec.}$ the transition linewidth. Here $\Gamma_{Spec.} = \Gamma_{7S} + \Gamma_{Ry} + \Gamma_{Laser}$, and $\Gamma_{7S} = 21 \times 10^{-6}\,\text{s}^{-1}$. Target states for us have low-lifetime, and have $\Gamma_{Ry} \approx 1 \times 10^8\,\text{s}^{-1}$ to $1 \times 10^9\,\text{s}^{-1}$ (see section 4.1.5). The width of the laser can be neglected as $\Gamma_{Laser} < 2\pi \cdot 10^6 \text{s}^{-1}$. We also have:

$$\Omega = \frac{\mu F_{Laser}}{\hbar} \tag{4.13}$$

with F_{laser} the electric field amplitude of the laser radiation, that is given by:

$$F_{laser} = \sqrt{\frac{4P_{laser}}{\epsilon_0 c \pi w_{laser}^2}} \tag{4.14}$$

with P_{laser} the laser power (in W) and w_{laser} its waist. Combining all these equations gives:

$$\rho_{ee} = \frac{4\mu^2 P^2}{\Gamma^2 \epsilon_0 \pi c w_{laser}^2 \hbar^2 + 8\mu^2 P^2} \tag{4.15}$$

Laser power of 1 W focused on 30 µm ($w_{laser} = 15\,\mu\text{m}$) is almost enough to saturate the transition as we have $\rho_{ee} = 0.47$ for $\Gamma_{Ry} = 1 \times 10^8\,\text{s}^{-1}$, but $\rho_{ee} = 0.1$ for $\Gamma_{Ry} = 1 \times 10^9\,\text{s}^{-1}$. This shows that it is reasonable, given the laser at our disposal, to expect good excitation of the Rydberg states.

[5]This value does not take into account possible deviations from the statistical ratio between magnetic sub-levels, due to the presence of Cooper minima. In particular, strong discrepancy with experiment appears when comparing cross-sections in caesium from $6P_{1/2}$ and $6P_{3/2}$[21–23]

We can also use the following formula for the field free excitation cross-section of a Rydberg state of principal quantum number n[24]:

$$\sigma_{Ry}^{F=0}(n) = \frac{\sigma_{PI}}{\Gamma_{Spec.}^{F=0} n^3} \tag{4.16}$$

with σ_{PI} the threshold photo-ionisation cross-section and $\Gamma_{Spec.}^{F=0}$ the width of the field-free transition. In the absence of an electric field the target Rydberg state is very thin (the linewidth of Rydberg states evolves as $\frac{1}{n^3}$, and $\Gamma_{Spec.}^{F=0} \approx \Gamma_{7s}$). For $n = 50$ in particular, this gives:

$$\frac{\sigma_{Ry}^{F=0}}{\sigma_{PI}} = 1.6 \times 10^4 \tag{4.17}$$

To estimate the impact of the electric field on this ratio, I use the ratio $r_{n=50}(F) = \frac{\sigma_{Ry}^{F}}{\sigma_{Ry}^{F=0}}$ given by our LFT code (see chapter 2). At $F = 50\,\mathrm{V/cm}$, I find $r_{n=50}(F) = 9.8\%$, and thus we have:

$$\frac{\sigma_{Ry}^{F=50\,\mathrm{V/cm}}}{\sigma_{PI}} = 1.5 \times 10^3 \tag{4.18}$$

This value is a useful estimation, but depends strongly on the particular state that we excite. In the interesting region (i.e. the spaghetti region, over the classical ionisation threshold), the excitation efficiency of a particular state varies strongly with the electric field and its coupling to other states. Again, the Stark maps obtained with our LFT code help us choose an intense state and maximise the conversion efficiency towards the Rydberg states, and thus the ionisation efficiency.

4.1.3 Velocity-induced field-ionisation

A variant of Rydberg field-ionisation is the Rydberg velocity-induced field-ionisation (VIFI)(it has also been called "selective field ionisation"[25] or "forced-field ionisation"[26]). This describes the same kind of Rydberg states under a static electric field, but here we consider a Rydberg atom with a non-negligible velocity in an electric-field *gradient*. This means that the excitation to the Rydberg state is done at a certain electric field, where its ionisation rate is typically low. Its velocity (coming from the inertia of the neutral atom from an effusive beam) makes the Rydberg atom move in the electric field gradient, experiencing a rising (or decreasing) electric field, depending on the sign of the gradient.

Under the right conditions, a relatively stable Rydberg state is excited over a large zone, moves along its initial velocity to a higher electric field region where its ionisation rate increases, and ionises in the spatial slab where the electric field correspond to a large ionisation rate[28]. This abrupt change of ionisation rate typically happens because of an avoided crossing with a state with high ionisation rate, as explained in the previous section. Such a mechanism becomes really interesting with a Rydberg state such as the one presented on figure 4.8. Indeed on the left panel of this figure a Stark map is shown where an individual Rydberg state evolves in the increasing electric field by becoming wider. This means that its lifetime decreases with the increasing electric field. We can

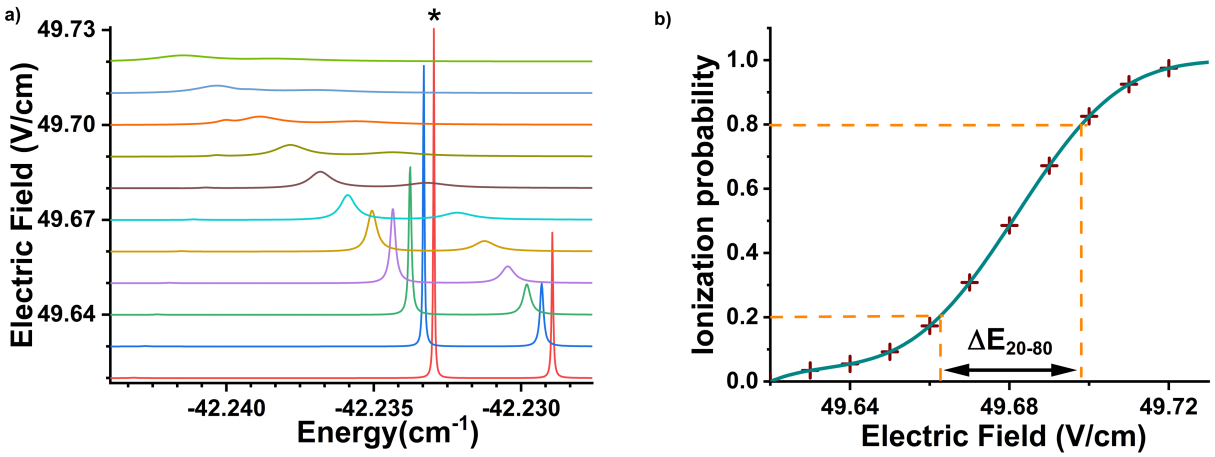

FIGURE 4.8: a) LFT-Photoabsorption spectra for P-polarized light from an s state in presence of an electric field. The horizontal axis is the binding energy (E_λ). The star indicates the state that is considered in the text and in panel b. b) Ionization probability of an atom in the star-marked state with a velocity of 274 m/s as a function of the electric field. Crosses are the state bandwidth extracted from a), the line is an interpolation of this data. Reproduced from [27].

actually calculate the ionisation probability in function of the electric field $F(z)$[26]:

$$P[F(z)] = 1 - \exp\left(-\frac{1}{vF'}\int_{F_0}^{F(z)} \Gamma(\tilde{F})d\tilde{F}\right) \tag{4.19}$$

v is the velocity of the neutral atom in the direction of the electric field gradient, hence the name of this ionisation process. From the Stark map on the left panel of figure 4.8, we can construct the shape of $\Gamma(F)$ from a fit at each electric field value. It is very well fitted by a 2-degree polynomial, which allows easy integration of equation 4.19, and a common velocity for a neutral atomic beam of caesium ($v = 274\,\mathrm{m/s}$) yields the shape of $P[F(z)]$ visible on the right panel of figure 4.8. If we consider 60% of the electrons created after excitation of this Rydberg state at 49.62 V/cm, these are created in an electric field interval named ΔE_{20-80}. Here $\Delta E_{20-80} \approx 0.036\,\mathrm{V/cm}$, which can be translated to an spatial slab by dividing by the electric field gradient F'. Thus the size of the ionisation zone Δz will be determined by:

$$\Delta z = \frac{\Delta E_{20-80}}{F'} \tag{4.20}$$

This changes the situation from photo-ionisation or Rydberg-field ionisation and has obvious consequences in terms of electron energy spread.

In the next section I describe the influence of each of these ionisation phenomena in terms of energy spread.

4.1.4 Links to the ionisation size

To make the link between the ionisation process and the resulting energy spread of the electron beam, we must first recall the possible sources of energy spread in our electron

source from section 1.4, in particular the point about potential differences across the ionisation zone. We repeat here equation 1.15:

$$\Delta E = \|\vec{F}\|\Delta z \tag{4.21}$$

This is true for all ionisation phenomena, but the difference comes from the size of the ionisation zone in the electric field direction Δz, and the possible ways to decrease this size in each case:

- For photo-ionisation, the size of the ionisation zone is defined simply by the spatial overlap between the laser and the atomic beam (or other laser beams in the case of a multi-photon ionisation). This means that this size can't become smaller than a few µm in the strongest focused beams[2,3]. Focussing the ionising laser this small then requires an intense flux of neutral atoms to keep an acceptable electron current. For a typical focused-infra-red laser spot of 30 µm, an electric field of 50 V/cm gives $\Delta E = 150$ meV.

- For Rydberg field-ionisation, the situation is close because the ionisation takes place where the Rydberg states are excited, i.e. in the laser/atomic beam overlap. However, in the case of a strong field gradient and a state with a relatively small linewidth, the resonance condition on the electric field can allow the excitation only in a portion of the laser beam. But a too small linewidth and the state will have non-negligible lifetime, which can create in turn (due to the atomic velocity) a bigger ionisation zone than the initial excitation zone. This clearly requires a detailed modelling to see what are the conditions for Rydberg field-ionisation to actually decrease the energy spread in comparison to photo-ionisation. Such a model is presented in section 4.1.5.

- In the case of Rydberg velocity-induced field-ionisation, it depends on the electric field gradient, the velocity of the neutral atom and the behaviour of the Rydberg state in an increasing electric field. As shown on the right panel of figure 4.8, the ionisation zone can be traced back to a certain electric field change. This means that the actual spatial extension of the ionisation zone depends on the electric field gradient, as described by equation 4.20. Combining this equation with equation 4.21 gives:

  $$\Delta E = \frac{F}{F'}\Delta E_{20-80} \tag{4.22}$$

  In this particular case, we have $\Delta E_{20-80} = 0.036$ V/cm, so a moderate field gradient of $F' = 100$ (V/cm)/cm gives $\Delta z = 3.6$ µm. With an electric field of 50 V/cm, we have $\Delta E = 18$ meV.

Rydberg-field ionisation relies on a lot of different parameters to produce an effectively smaller ionisation size than photo-ionisation, particularly the choice of the Rydberg state (ionisation rate, Stark slope, ...) and field parameters. In the next section I provide a simple model able to predict the values of these parameters optimised to minimise the electron energy spread.

4.1.5 Modelling the energy spread with Rydberg-field ionisation

In the case of Rydberg-field ionisation there are three factors that influence the size of the ionisation zone (for an atomic beam parallel to the electron beam):

1. The curvature of the electric field lines. It is responsible for the fact that an equi-field line will span out a large range of different electric potentials. We refer to the induced energy-spread as $\Delta V_{Curvature}$.
2. The spectral width of the ionising radiation and the Stark effect. This gives rise to a *range* of resonant electric-field value, thus enlarging the ionisation zone. The resulting energy spread is ΔV_{Stark}.
3. The lifetime of the excited Rydberg state, that increases the ionisation zone from the excitation zone, in relation with the atomic beam velocity. In the following it is called $\Delta V_{Lifetime}$

The role of the field lines curvature: $\Delta V_{curvature}$

This source of energy spread simply comes from the fact that electric field lines are curved, while equipotentials line are not. In the case of cylindrically symmetric fields it is possible to derive relations to calculate the potential $V(r,z)$ at distance r from the axis (at height z) as well as the potential on axis at height z, from only the potential on axis $V(0,0)$ and its derivatives[29]:

$$V(r,z) = V(0,z) - \frac{r^2}{4}V^{(2)}(0,z) + \frac{r^4}{64}V^{(4)}(0,z) - \frac{r^6}{2304}V^{(6)}(0,z) \tag{4.23}$$

$$V(0,z) = V(0,0) + V'z + \frac{V^{(2)}(0,0)z^2}{2} + \frac{V^{(3)}(0,0)z^3}{6} + \frac{V^{(4)}(0,0)z^4}{24} + \frac{V^{(5)}(0,0)z^5}{120} + \frac{V^{(6)}(0,0)z^6}{720} \tag{4.24}$$

where the $'$ sign and numbers in brackets imply derivatives against z. Equation 4.24 is simply the Taylor expansion on z and is valid only for small values of z. In the case of electric fields with pure gradient (i.e. with $V^{(\geq 3)} = 0$), two electrons, one created on axis at height $z = 0$ and the other created at a distance r from axis and height z would have a potential difference $\Delta V(r,z)$ of:

$$\Delta V(r,z) = V(r,z) - V(0,0) = V'(0,0)z + V^{(2)}(0,0)\left(\frac{z^2}{2} - \frac{r^2}{4}\right) \tag{4.25}$$

We can replace $V'(0,0)$ by $-F_0$ and $V^{(2)}(0,0)$ by $-F'$ for the sake of clarity. To get a sensible estimation of this potential difference during Rydberg-field ionisation, we must use the fact that Rydberg atoms (and thus electrons) will be created at the same norm of the electric field. This norm can be written as:

$$||F(r,z)|| = \sqrt{\left(\frac{-\partial V(r,z)}{\partial r}\right)^2 + \left(\frac{-\partial V(r,z)}{\partial z}\right)^2} \tag{4.26}$$

For small z and r, the condition $||F(r_1, z_1)|| = ||F_0||$ gives:

$$z_1 \to -\frac{F_0}{F'} - \sqrt{\frac{F_0^2}{F'^2} - \frac{r^2}{4}} \tag{4.27}$$

Inserting equation 4.27 into equation 4.25 gives:

$$\Delta V(r_1, z_1) = -F_0 \left[-\frac{F_0}{F'} - \sqrt{\frac{F_0^2}{(F')^2} - \frac{r^2}{4}} - \right] - F' \left[\frac{1}{2} \left(-\frac{F_0}{F'} - \sqrt{\frac{F_0^2}{(F')^2} - \frac{r^2}{4}} \right)^2 + \frac{r^2}{4} \right] \tag{4.28}$$

which easily simplifies to:

$$\Delta V(r_1, z_1) = \Delta V_{Curvature} = \frac{-3r^2}{8} F' \tag{4.29}$$

We thus have obtained a analytic estimation of the energy spread induced by the curvature of the electric field $\Delta V_{Curvature}$, in the case of a pure electric field gradient.

The influence of the state's lifetime: $\Delta V_{Lifetime}$

This second term is straight-forward to evaluate and simply comes from the fact that the excited Rydberg states have a finite lifetime $1/\Gamma_{Ry}$ (we recall that $\Gamma_{Ry} = 2\pi\Delta\nu$). This means that they will take a non-negligible time to ionise once they are excited. As usual, the resulting energy spread comes from the fact that the ionisation zone has a larger spatial extension than the excitation zone. It involves the velocity of the atom along the electric field axis v and, in a collinear configuration, can be evaluated as:

$$\Delta V_{Lifetime} = F\Delta z_{additional} = F\frac{v}{\Gamma_{Ry}} \tag{4.30}$$

The effect of spatial resonance: ΔV_{Stark}

The size of the excitation slab also increases due to the fact that the targeted Rydberg transitions have a finite spectral width of $\Gamma_{Spectral}/2\pi$, and a finite Stark shift. This linewidth is the sum of the intrinsic linewidth of the "ground" state for this transition (Γ_{7s}) and the intrinsic linewidth of the target Rydberg state Γ_{Ry}:

$$\Gamma_{Spectral} = \Gamma_{7s} + \Gamma_{Ry} \tag{4.31}$$

This creates a certain "energy slab" where the transition might occur. This energy slab will be translated into an electric field slab by the Stark shift of the Rydberg state. As already seen in section 2.4, Rydberg states with parabolic quantum numbers n, k have linear Stark shifts (in atomic units) of $\frac{3}{2}nkF$[24]. As k goes from $-n$ to n, their Stark slope goes from $-\frac{3n^2}{2}$ to $\frac{3n^2}{2}$. For the estimation of ΔV_{Stark} I take the mean value of the amplitude of the Stark slope as $\frac{3n^2}{4}$. This Stark slope translates the energy slab into an electric field slab, which in turn can be translated to a spatial slab by the field gradient F'. The resonance conditions are thus fulfilled on a spatial slab of size given by the ratio of the

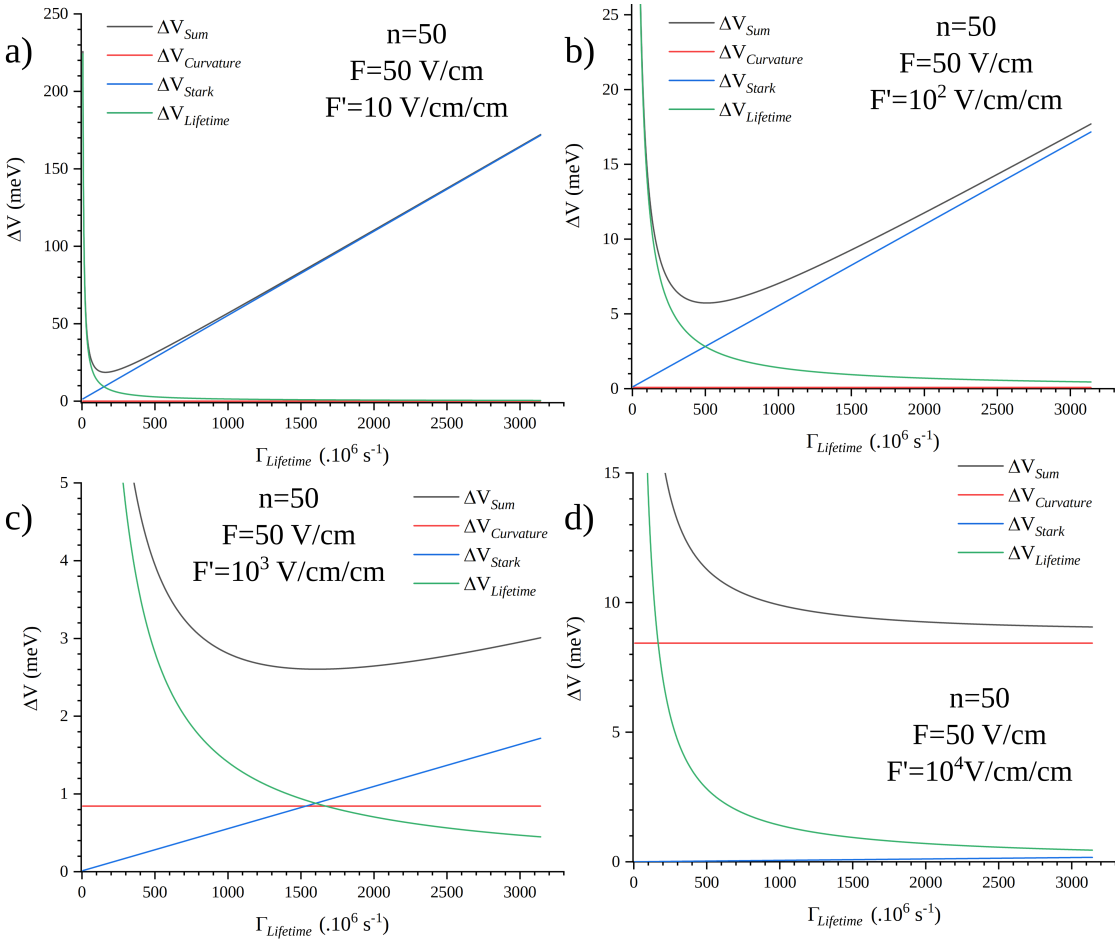

FIGURE 4.9: Energy spread specific to Rydberg field-ionisation including ΔV_{Stark} (see eq. 4.32), $\Delta V_{Lifetime}$ (see eq. 4.30), and $\Delta V_{Curvature}$ (see eq. 4.29) for $v = 274\,\mathrm{m/s}$, $r = 15\,\mu\mathrm{m}$, $n = 50$, $F = \frac{1}{16n^4}$ and for four values of F': $10\,\mathrm{V/cm/cm}$ (a), $100\,\mathrm{V/cm/cm}$ (b), $1 \times 10^3\,\mathrm{V/cm/cm}$ (c) and $1 \times 10^4\,\mathrm{V/cm/cm}$ (d).

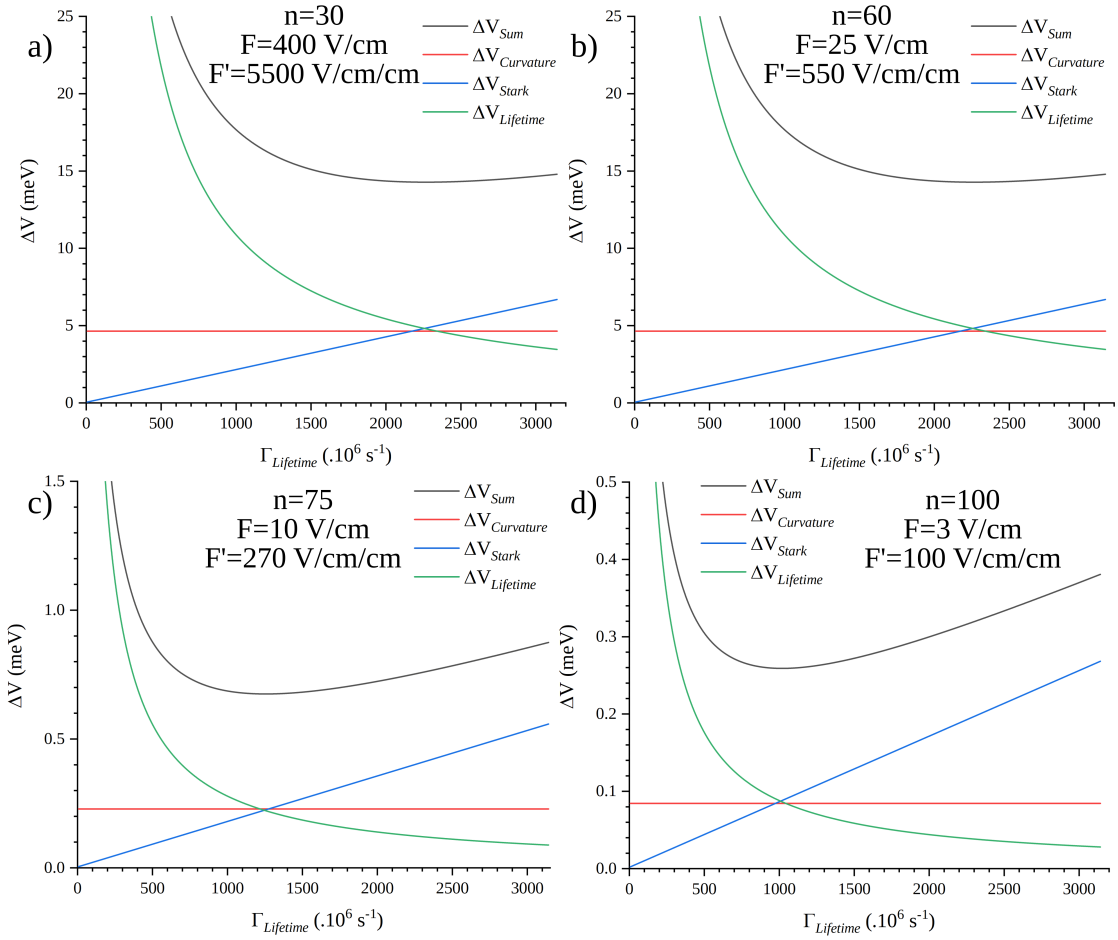

FIGURE 4.10: Energy spread specific to Rydberg field-ionisation along the model presented in section 4.1.5, including ΔV_{Stark} (see eq. 4.32, $\Delta V_{Lifetime}$ (see eq. 4.30, and $\Delta V_{Curvature}$ (see eq. 4.29 for $n = 30$ (a), $n = 60$ (b), $n = 75$ (c), $n = 100$ (d), $v = 274\,\mathrm{m/s}$, $r = 15\,\mu\mathrm{m}$ and $F = \frac{1}{16n^4}$. In each case the value of the field gradient is optimised to lower the energy spread, given n.

spectral width, the Stark slope and F', so $\Delta z_{Stark} = \frac{2\Gamma_{Spectral}}{3\pi F' n^2}$, and we have:

$$\Delta V_{Stark} = F\Delta z_{Stark} = F\frac{2\Gamma_{Spectral}}{3\pi F' n^2} \tag{4.32}$$

Parameter optimisation

We can simplify these expressions by replacing F with $1/16n^4$ because we will ionise Rydberg atoms near the classical ionisation threshold, and take reasonable values for $v = 274\,\mathrm{m/s}$ and $r = 15\,\mu\mathrm{m}$. This gives us only two parameters left for optimization, n and F'. To see the overall effect we define ΔV_{Sum} as $\Delta V_{Sum} = \Delta V_{Stark} + \Delta V_{Lifetime} + \Delta V_{Stark}$, and we can plot the evolution of ΔV_{Sum} in function of Γ_{Ry}.

As a first look into this optimisation, I fix $n = 50$, and plot ΔV_{Sum} for different values of F'. This value of n corresponds to an ionisation field of $50\,\mathrm{V/cm}$. The results for $F' = 10\,\mathrm{V/cm/cm}$, $10^2\,\mathrm{V/cm/cm}$, $10^3\,\mathrm{V/cm/cm}$ and $10^4\,\mathrm{V/cm/cm}$ can be seen on figure 4.9. This figure clearly shows that the electric field gradient is a very important parameter

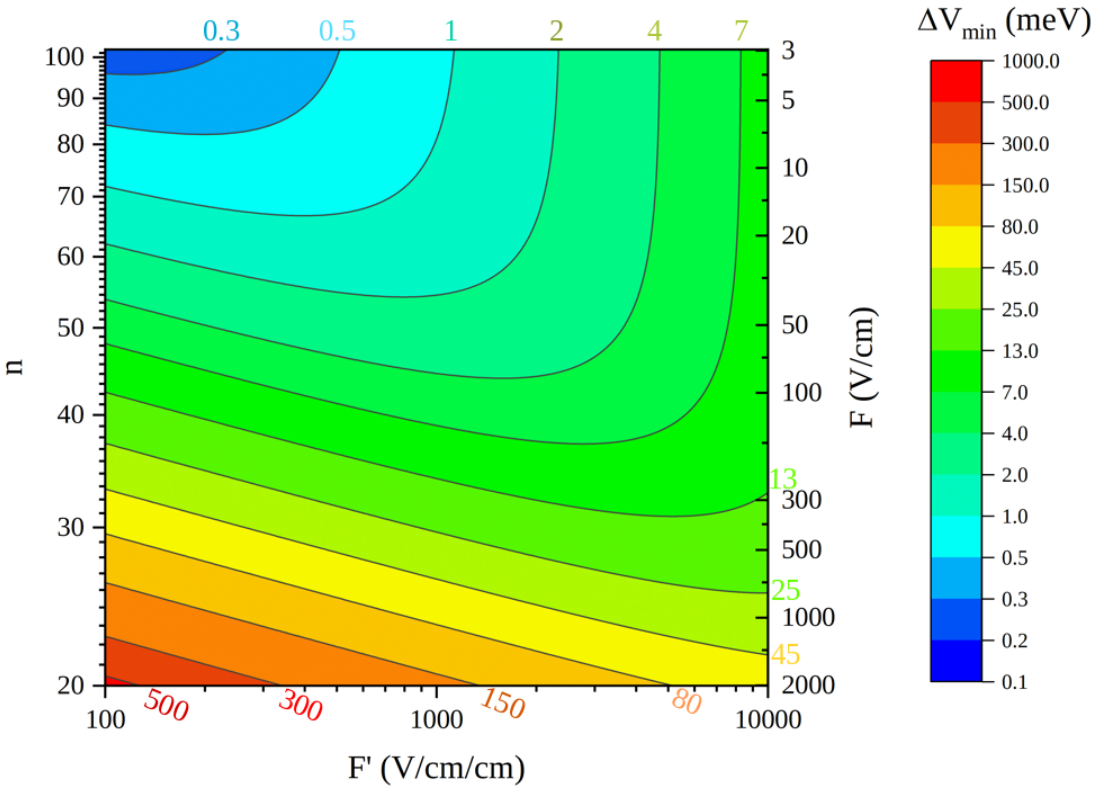

FIGURE 4.11: Optimisation plot of ΔV_{Sum} (in log-log scale) for the parameters n and F' and with the optimal value of $\Gamma_{Lifetime}$ (resulting in $\Delta V_{Sum} = \Delta V_{min}$, see eq. 4.34). The right axis is the field corresponding to the value of n, given the formula 2.2. The colours represent the sum of energy spread induced by the three different mechanisms at play in RFI. Contour lines are lines of constant energy spread.

to determine the lowest possible energy spread attainable in RFI. Panel c) shows a promising value of the total energy spread due to RFI around lower than 3 meV, for $F' = 10^3$ V/cm/cm. For lower values of F' the energy spread is dominated by the ΔV_{Stark} term, i.e. a large ionisation zone due to loose resonant-constraints, and for larger F' the curvature of the equipotential lines become too large.

To underline the role of n, I plot four energy spread curves with optimised values of F' on figure 4.10 for $n = 30$, $n = 60$, $n = 75$ and $n = 100$. The best value of F' is usually the one that brings the three energy spread sources at the same level. This figure shows that the highest n we choose, the smallest the expected energy spread, provided by the hypothesis of the model are still fulfilled.

I can go a little bit further by consistently choosing the optimised value of $\Gamma_{Lifetime} = \Gamma_{Opt}$, that minimises ΔV_{Sum}. I thus have:

$$\frac{\partial \Delta V_{Sum}}{\partial \Gamma_{Lifetime}} \left(\Gamma_{Opt}, n, F'\right) = 0 \tag{4.33}$$

$$\Delta V_{Sum} \left(\Gamma_{Opt}, n, F'\right) = \Delta V_{min} \left(n, F'\right) \tag{4.34}$$

I have removed the $\Gamma_{Lifetime}$ dependence and can now plot the optimisation map of

ΔV_{Sum} for the two parameters n and F', as shown on figure 4.11. This shows that an energy spread lower than 5 meV requires Rydberg states with principal quantum numbers of at least $n = 50$, or higher, and field gradients lower than 5000 V/cm/cm. The heat-map does not show a lower bound to the energy spread, and we might conclude that the bigger the principal quantum number the better, but at very-high n ($n \geq 80$), other problems arise. In particular it might be hard to find a Rydberg state that is sufficiently isolated from others to have the expected behaviour and not leak towards other ionisation channels that might be slower. Exciting these states selectively would also demand a very good control of electric field lines and a small laser linewidth. Finally, it is based on the optimal value of $\Gamma_{Lifetime}$, which might be hard to find in actual Stark maps.

However, this heat-map gives us confidence that RFI is able to produce very monochromatic electron beams, provided that we find an appropriate combination of field, field gradient and Rydberg state.

Here we see the advantage of using a very heavy atom like caesium, because of its low velocity in beams. This relatively low velocity decreases the importance of the $\Delta V_{Lifetime}$ term, because atoms have a bigger time window to ionise before the ionisation region becomes too big. For lighter and hence faster atoms, $\Delta V_{Lifetime}$ would be bigger, potentially requiring pre-ionisation cooling in the longitudinal direction. Detailed simulations on the impact of this lower velocity on the ionic space-charge are needed, but, as stated in section 1.4.2, it is very specific to the relative orientation of lasers, atomic beam and electron beam as well as the chosen method to account for the accumulation of ions in the ionisation region (active/passive clearing, compensating). Examples of such simulations can be found in section 4.4.4.

It is clear that the energy spread of the electron beam will depend strongly on the chosen ionisation process, but also on the field configuration, the field gradient, and other parameters. At the core of this thesis was the intention to demonstrate that using Rydberg atoms is a way to improve the properties of electron sources based on the ionisation of atoms, via Rydberg-field ionisation or the more elaborate velocity-induced field-ionisation. This demands a fine comprehension of the different processes, and the links between these processes and the energy spread source as listed in section 1.4.

Section summary

Identification of different ionisation phenomena

In this section I presented the three different ionisation phenomena that could be used in our continuous electron source:

- Photo-ionisation: when the ionising radiation (usually a laser) brings the electron energy over the field-free ionisation threshold. In most cases, the electron is then ejected preferentially in the direction of the electric field component of the laser polarisation, but atoms with strong spin-orbit coupling can show different angular modulation of their photo-ionisation cross-section.
- Rydberg field-ionisation: when, under an electric field, the atom is excited to a strongly shifted Rydberg state that is coupled to the continuum and releases the electron primarily in the direction of the electric field. Hydrogen, due to its high symmetry, has stable states in this energy region but for alkali-metals all the states above the field-shifted threshold ionise rapidly.
- Velocity-induced field-ionisation: when an alkali-metal atom is excited to a relatively stable Rydberg state under a given electric field and, due to its initial velocity, it travels to a region where the field is enough to ionise it. This technique makes heavy use of the rapidly changing ionisation rates found in caesium.

Each of these phenomena has a different efficiency (RFI and VIFI involve the excitation of Rydberg states, which produce orders of magnitude more electron current than photo-ionisation) and a different link to energy spread, that we can estimate from a simple modelling of the ionisation zone, in the hypothesis of a pure gradient electric field. This was done especially for Rydberg field-ionisation, where I studied the optimal choices for the properties of the Rydberg state (n, $\Gamma_{Lifetime}$) and the field gradient F'. The energy spread is calculated as the sum of three terms, $\Delta V_{Curvature}$, ΔV_{Stark} and $\Delta V_{Lifetime}$.
Rydberg field-ionisation has the potential to improve the brightness of the photo-ionisation sources to our desired level for two main reasons: the higher current obtained by saturation of the Rydberg transitions, and the electron emission directionality due to the combined effect of the electric field and the electron-ion core interaction.
The energy spreads calculated here come in addition to the energy spread due to ionic space-charge, but this study shows that a good choice of parameters could already provide a very-low energy spread along with the high current associated with Rydberg states excitation. It is also evident that for energy spread lower than 5 meV the Rydberg states should be with high principal quantum number n in the range $50 - 100$, with field gradient lower than 5000 V/cm/cm.
In addition to these results, we recall that this model does not take into consideration the presence of other states that could be resonant in the focus of the laser. This needs a detailed study on Stark maps to ensure that the state is isolated enough (particularly as n gets high) and that the field gradient is low enough to ensure that only one Stark-shifted state is resonant.

Now that we have explicitly introduced three different ionisation phenomena for producing a continuous electron beam, we need to compare the electron energy spread that they will produce. For that, we need a way to measure the energy spread of the electron beams that we produce with one of these methods. The next section deals with the addition of an electron spectrometer to the experimental set-up already described in chapter 3, to experimentally study these ionisation mechanisms and the resulting energy spread.

4.2 Installation of a high-resolution spectrometer

Studying the characteristics of the created electron beam requires a dedicated experimental set-up. Its purpose is to form Rydberg atoms from neutral caesium atoms, to ionise these states to form an electron beam, and to analyse the properties of this electron beam, in particular its energy spread. It is the extension of the set-up presented in 3.1, modified to allow energy spread measurements. In this section I thus present the main component of the energy spread measurements, the Gatan electron spectrometer. A schematic representation of all parts of the set-up can be found on figure 4.12.

4.2.1 The Gatan 666 electron spectrometer

The most important part of the experimental design is the energy analyser. Indeed, the property that we want to investigate in relation to the different ionisation phenomena is the total energy spread of the resulting electron beam. The published HREELM design requires an energy spread less than 5 meV on an electron energy of 3 keV, representing a ratio of $\approx 10^{-6}$. We already saw that such a large energy resolution over nominal energy ratio is attainable only by state-of-the-art HMAs[6]. Investing resources into such an instrument without the certainty that it will be used in the final HREELM instrument was deemed unreasonable. We reached out[7] to the team of, at that time, M. Christian Colliex at *Laboratoire de Physique du Solide*, specialized in EELS in STEM. They gave us a high-performance energy analyser: the Gatan 666 Parallel Electron Energy Loss Spectrometer (PEELS).

In this section we retrieve information about the functioning of this instrument from the literature[30–32] and a patent covering its invention[33]. This was not an easy task, but a particularly important one, as only a deep understanding of this instrument could ensure a proper implementation on our set-up, as well as an optimised usage, required to attain a very high energy resolution.

For the sake of simplicity and in a first analysis we consider the incoming electrons as emitted by a point-like source in front of the entrance slit, with a finite energy spread that we want to measure. As the source is point-like, it hardly makes sense to attribute a diffraction plane. However we can define a "chromatic image plane" where electrons from different starting angle but with the same longitudinal kinetic energy are gathered in a point (see figure 4.14). An optimal tuning of this instrument places a sharp chromatic image on the detectors.

[6] ToF analysis being incompatible with a continuous electron beam
[7] This was done before I arrived at LAC

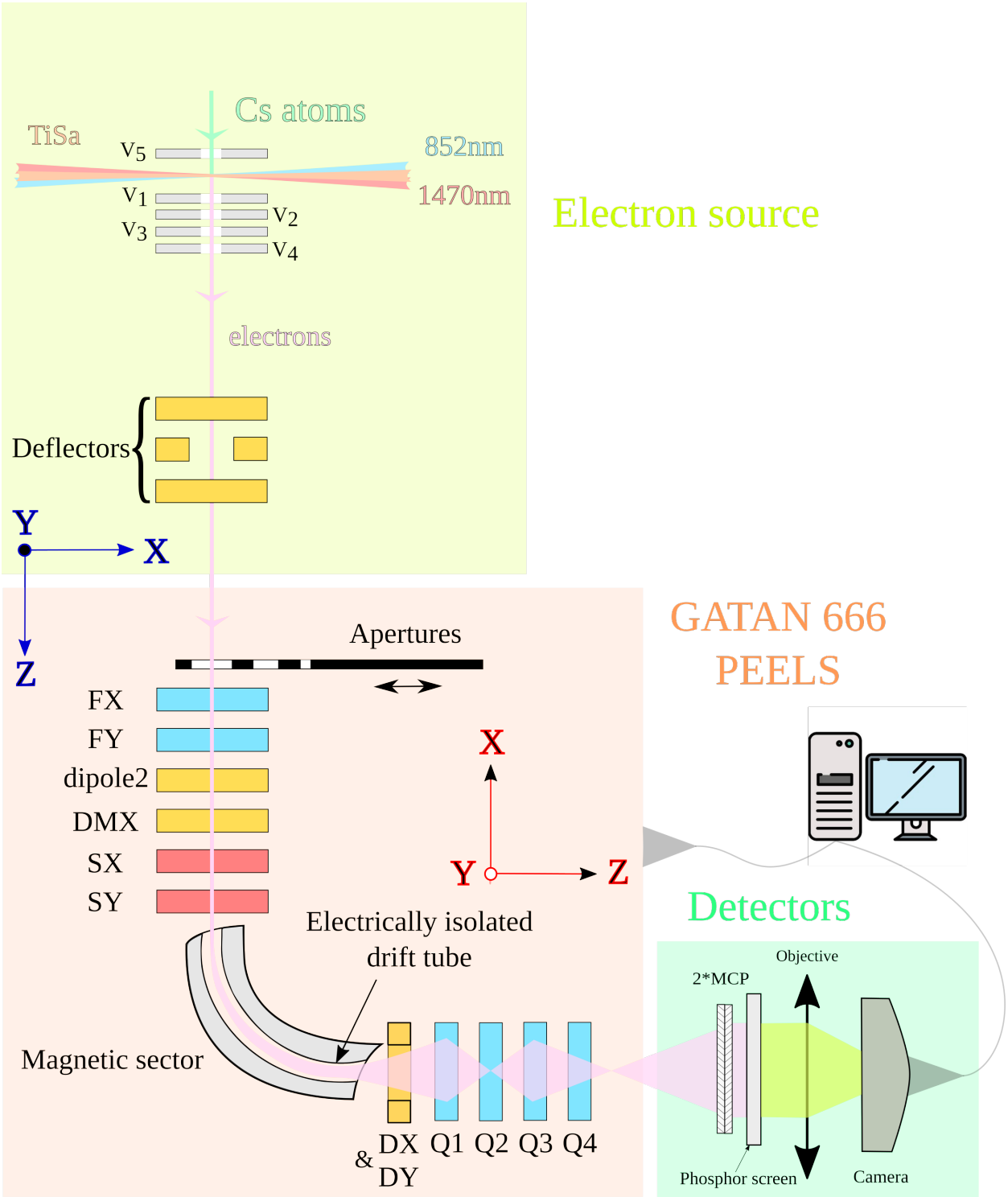

FIGURE 4.12: Schematic of the experimental set-up, containing the electron source, the Gatan 666 photo-electron energy loss spectrometer (PEELS) and the detectors. The blue frame of reference is for elements before the magnetic sector, while elements after the sector are referenced in the red frame. See text for detailed explanation of specific parts.

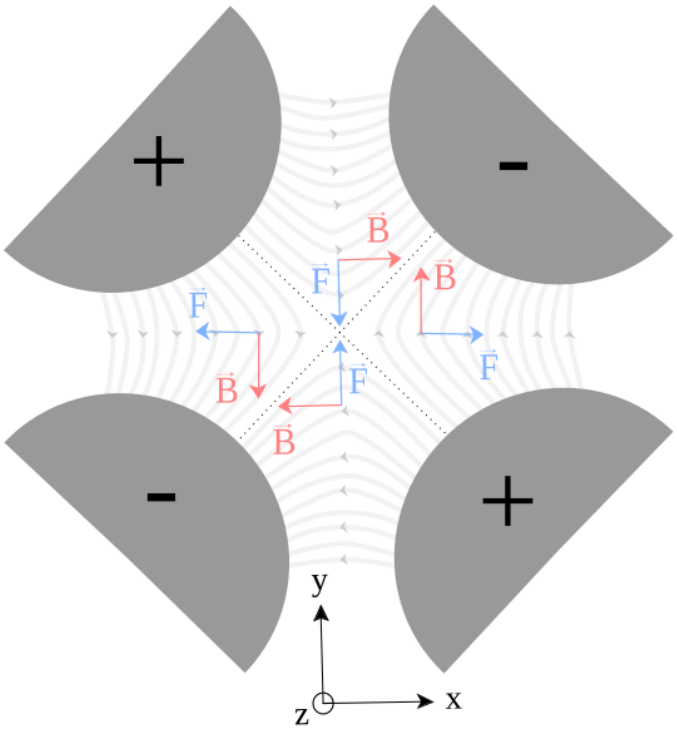

FIGURE 4.13: Schematic of the magnetic fields (in red) in a quadrupole magnetic lens, plus the force (in blue) exerted on electrons travelling in the z direction (outside the plan towards the reader). The dark grey area are cuts of the magnetic yoke that serve as magnetic poles. This configuration focus in the y direction and defocus in the x direction.

This instrument is a fully magnetic electron spectrometer and was developed as an add-on to TEM columns[30], allowing to perform EELS inside the transmission microscope (see section 1.1.2). Its parallel design means that all electrons are transmitted so that a full spectrum can be recorded at once (i.e. there is no exit slit). Its functioning relies heavily on the peculiar behaviour of quadrupole magnetic lenses. For the clarity of the discussion I now detail the functioning of these lenses.

Quadrupole magnetic lenses

Quadrupoles are composed of four rods of a magnetic material (the yokes) individually surrounded by an electrical coil. The four coils are plugged serially with alternating rotation direction so that the magnetic yokes create magnetic fields with equal amplitudes, but opposing parity with their neighbours (see figure 4.13).

The field lines created by this arrangement can be seen on figure 4.13. From that it is easy to understand how to retrieve a lens-like behaviour. Indeed when an electron is situated in the center of the horizontal (x) axis but slightly above the center in the vertical (y) axis, it feels a horizontal magnetic field, and the induced Lorentz force pushes it downwards (in our example), towards the center. The same happens for electrons positioned below the horizontal axis as it is pushed upwards, toward the center.

Electrons on the horizontal axis but away from the vertical axis also feel the Lorentz force but with an opposite sign, and are pushed away from the center. This means that a single magnetic quadrupole actually focuses in one axis and defocuses in the other

axis. The same quadrupole with opposite polarity will then focus in the horizontal direction and defocus in the vertical direction. A proper lens thus has to feature at least two quadrupole elements to be able to focus a beam in both directions.

Working principle of the Gatan 666 spectrometer

The central part of this instrument is the magnetic sector, that is a composed of two flat curved electromagnets in opposition so as to create a adjustable perpendicular magnetic field (see figure 4.12). This is the dispersive element, that separate the electrons in function of their incoming energy.

As the magnetic sector curves the optical axis, and for the sake of clarity in the discussion, we define a new frame of reference (called "red") for the last part of the set-up. The Z axis is still the optical axis, but the X and Y are rotated (see figure 4.12). This rotation is essential so that the electrons momenta are always primarily in the Z direction, that the red XZ plane is the dispersion plane, and the XY plane is always orthogonal to the electron propagation. All references to X and Y before the magnetic sector are to be understood in the blue frame, while the red frame deals with X and Y after the sector.

Before the magnetic sector are four beam-shaping elements (two quadrupoles: FX, FY and two sextupoles: SX, SY) and two dipoles (called DMX and $dipole2$) for beam deflection in the Y and X direction, respectively. After the sector there is another dipole for beam deflection in each direction (DX and DY) as well as four quadrupoles ($Q1$, $Q2$, $Q3$, $Q4$) whose roles are described hereafter. An aperture is placed at the entrance of the whole spectrometer to restrain the acceptance angle. This aperture is circular and features three different diameters, 1 mm, 2 mm or 3 mm. It is also possible to remove it completely from the beam for full acceptance.

The spectrometer does not have the same effect in the XZ and in the YZ planes (see figure 4.14). In the XZ plane (the dispersion plane), the magnetic sector and the post-sector quadrupoles must place the chromatic image plane of the electron source at the surface of the detector, with the appropriate magnification. The overall role of the post-sector quadrupoles is to increase the dispersion of the energy spectrum by magnifying in the X direction. This magnification actually defines the final energy resolution attainable by the instrument. In the XY plane, the optics of the spectrometer must spread the dispersed spectrum in the Y direction on the detector but keep the Y component of the beam small enough to fit on the detector. The main reason for that is to reduce the damage on the detector induced by a two finely focused electron beam.

This means that the size of the spot in the X direction represents the energy spread of the electron source, and a typical measurement will feature a vertical line of finite horizontal spread. We detail here the roles of the pre-sector elements:

- FX and FY are quadrupole lenses that allow pre-deflection focusing. The instrument is designed and works at best with a virtual source 10 cm to 15 cm in front of its aperture, so the optimal operation mode here is a slight defocus.
- DMX and $dipole2$ are magnetic dipoles that can be used to deflect the electron beam is the X and Y direction respectively.
- SX and SY are hexapoles that can be used to correct spherical aberrations, and to restore the shape of the final spot on the detector back to a vertical line.

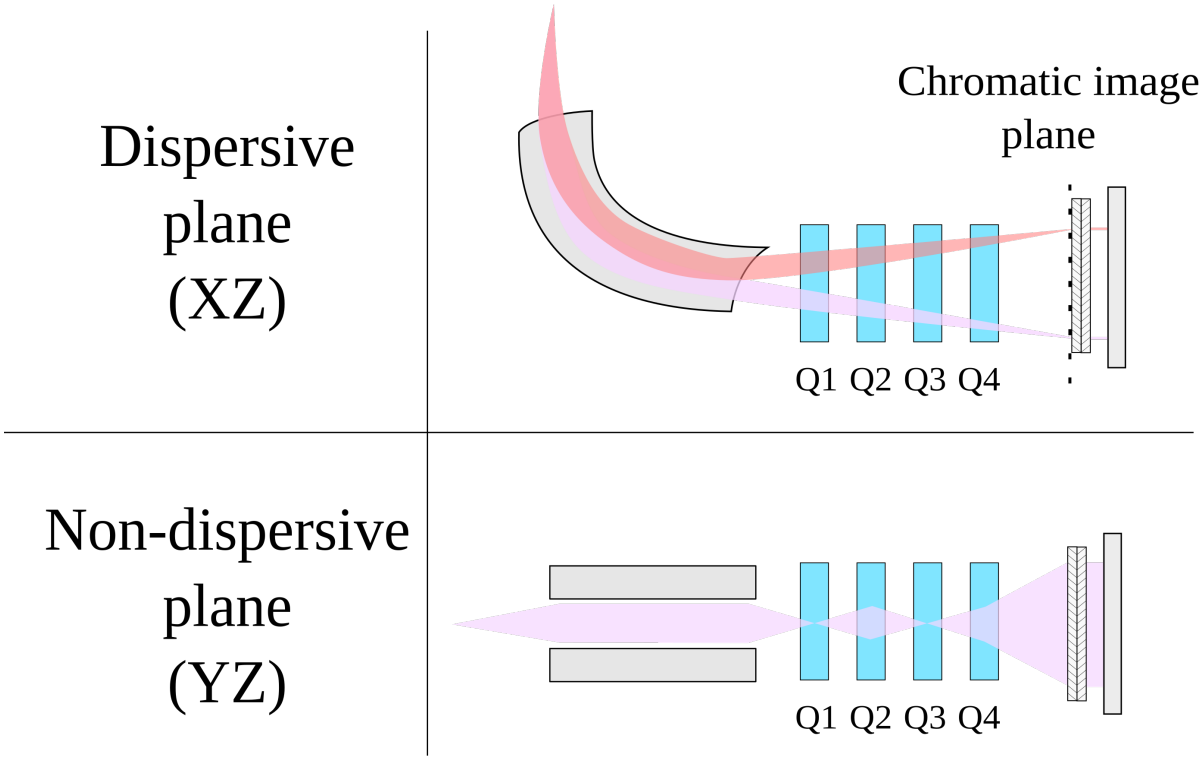

FIGURE 4.14: Schematic of the electron trajectories inside the Gatan 666 PEELS in XZ and YZ plane, under optimal tuning of post-sector quadrupoles. Note that we are in the red frame of reference here (see figure 4.12). In the top image the two colours corresponds to electrons with different longitudinal energy, showing the transformation of this energy difference to a lateral displacement on the detector.

The magnetic sector deflects the electron beam at a 90° angle. The shape of the two opposing electro magnets is optimised so that the resulting magnetic field has a different role in each direction (described in details further). In the X direction, the angle of the magnetic sector relative to the optical axis can be adjusted by an external screw to correct aberrations. The exit angle and the distances between the quadrupoles is chosen to focus the electron beam somewhere between $Q1$ and $Q2$.

An important feature of all lenses is that when an electron beam is focused at the center of a lens, this lens has no effect on the collimation of that beam. In the case of quadrupole lenses, an electron beam can be focused only in one direction at the center of the lens, so it will affect only the other direction. This gives a very practical way to prevent defocusing in one direction when focusing in the other direction.

In particular here, in the Y direction the magnetic sector focuses the electron beam at the center of $Q1$ (see figure 4.14), so that this quadrupole can have an effect on the X component on the beam without changing the position on the crossover on the Y axis (as already explained in section 1.1.3). This principle is used to ensure independent focusing in the dispersion plane and in the non-dispersive plane. The quadrupoles $Q1$, $Q2$, $Q3$ and $Q4$ are then tuned to achieve the required dispersion.

The magnetic sector itself has a dispersion of 5 µm/eV and the quadrupoles can increase this to 10 mm/eV[33]. The post-sector elements thus have different roles (at least this is the way this instruments should work, as it is designed):

- DX and DY are dipole magnets that are used to deflect the beam in the X and Y direction, respectively.
- $Q1$ has an effect only in the X direction and primarily determines the focus of the energy spectrum on the detector.
- $Q2$ is the first quadrupole acting on the Y direction. It should reproduce the crossover in the Y direction on $Q3$.
- $Q3$ affects only the X direction and controls the energy dispersion increase, i.e. the magnification of the spectrum in the X axis.
- $Q4$ is supposed to adjust the size of the spectrum in the Y direction so that it spans the entire detector. It also has en effect on the X component.

This arrangement means that $Q1$ and $Q3$ can be adjusted without any modification on the non-dispersive plane electron trajectories, $Q3$ tuning the energy dispersion while $Q1$ finely adjusts the spectrum's focus on the detector. An important feature of the spectrometer is the so called "drift tube" in which the electrons travel inside the magnetic sector. It is electrically isolated from the rest of the spectrometer, which has two main uses: by connecting it to a picoammeter (and turning off the magnetic field so that the electrons crash on its surface) we can measure the total electron current; and also it is possible to apply a potential to this tube that will modify the potential difference of the electrons to their surroundings. In other words, it is possible to modulate the kinetic energy of the electrons inside the dispersive element. As the dispersion angle depends primarily on the kinetic energy, an electron with 1 keV kinetic energy with a 0 V drift-tube potential will be deflected the same way as a 999 eV electron under a drift tube potential of 1 V.

The Gatan 666 PEELS was designed as an add-on to a TEM column, to enable a spectroscopic analysis addition to transmission microscopy. This means that it is intended to

work with high-energy electrons (of $\approx 100\,\text{keV}$). Thus the specifications about its performance on low-energy electrons are not to be taken at face value. In particular it is hard to ensure that the ratio $\frac{\Delta E}{E}$ stays around 10^{-5} when analysing 1 keV electrons. The position of the crossovers at the exit of the magnetic sector are also susceptible to vary with the electron energy. In the next section I will detail the implementation of this instrument in our particular set-up, as well as the experimental investigation about its actual functioning at low energy.

4.2.2 Implementation and control of the spectrometer

The ambition with this instrument is to be able to measure energy spreads around 10 meV. This requires an optimal use of the Gatan 666 PEELS, based on an in-depth understanding of its functioning. In particular I needed to verify that the spectrometer actually works as intended, and that the information that I gathered on its functioning at high energy still applies to low-energy electrons.

One of the first thing I did to adapt this instrument from high-energy electrons to low-energy electrons was to remove the heavy lead enclosure that protected the operators from high-energy radiations emitted during the deflection of high-energy electrons (a phenomenon heavily used in synchrotrons). With low-energy electrons this protection is no longer necessary but its weight makes it cumbersome to manipulate and place the spectrometer on an optical table so we removed it completely from the instrument. However, low-energy electrons are very sensitive to external magnetic fields, so a μ-metal external shield was designed and added around the spectrometer.

Another preliminary modification was to change and grease the internal o-rings of the spectrometer. Indeed all of our first experiments with the spectrometer were plagued by bad vacuum conditions, so we had to check the airtightness of every o-ring. We found several of them that were in bad shape (as can be seen on figure 4.15), so we replaced and grease them.

The Gatan 666 is driven by a custom version of the proprietary DigitalMicrograph (Dm) software developed by the Gatan company. It is designed as a base software to control any electron microscope, EELS systems and CCD cameras, as well as to acquire, manipulate, display and analyse the data. The adaptation to a particular instrument is done via plug-ins and scripts that can easily be implemented in Dm. We received the instrument with a partially adapted version of Dm, that had been modified by M. Marcel Tencé from LPS to control the 666 PEELS system[34]. Before using the spectrometer, I needed to adapt and complete the control of the spectrometer.

The instrument came with a custom electric supply, controlled by Dm and supplying stabilised electric current to the electro-magnets of FX, FY, SX, SY, $Q1$, $Q2$, $Q3$, $Q4$, DX, $dipole2$, DMX and DY. We installed a detector at its end, composed of a stack of 2 micro-channel plates (MCPs) on top of a P43 type phosphor screen from Hamamatsu. MCPs are arrays of microscopic channels tilted from the optical axis, that amplify the electron signal. The front side of the first plate is kept at ground and the back-side of the second plate is placed at high positive potential (usually around 1.5 kV for us). When electrons hit the surface of the first MCP with enough energy, it triggers a burst of secondary electrons (around 1000 per electron) that are attracted to the high positive potential of the second MCP and hit its surface. The two MCPs have their channels arranged in chevron from one another so that there are no clear path from incoming electron through the MCP stack.

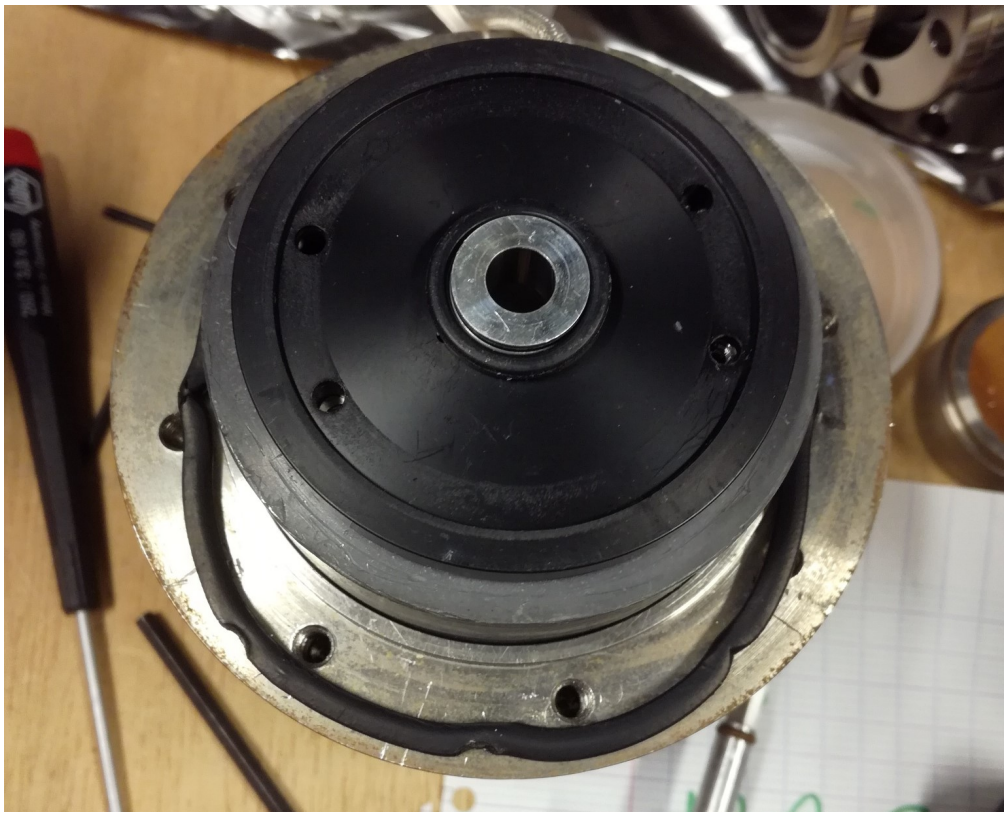

FIGURE 4.15: Photograph of a disassembled part of the spectrometer, showing a damaged o-ring.

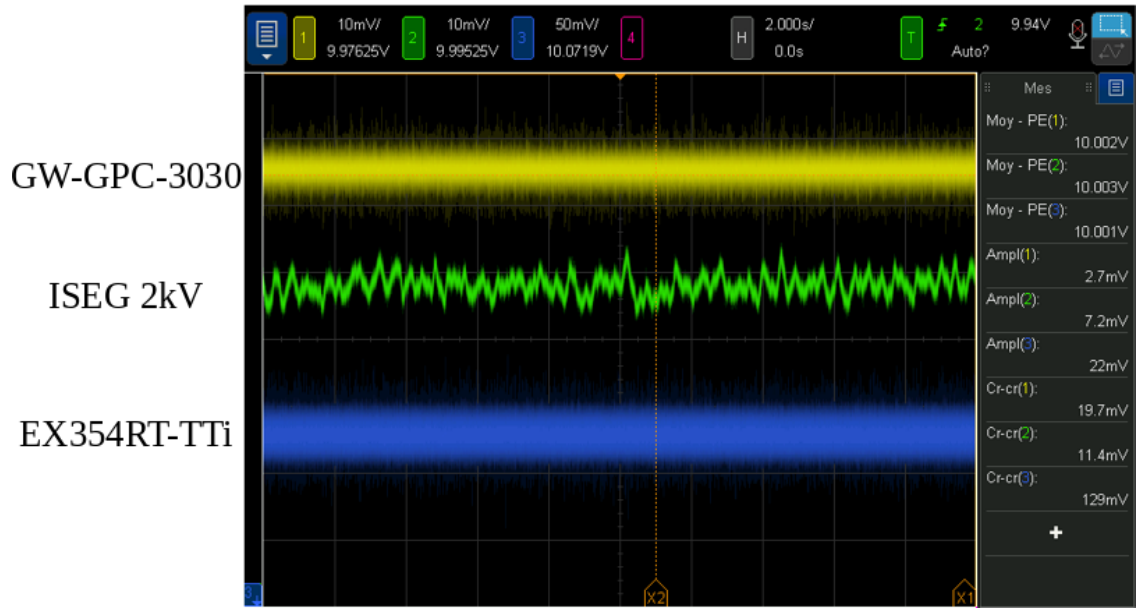

FIGURE 4.16: Long-term stability of 3 voltage supplies at our disposal, whose names are given on the left side of the figure. It shows that the ISEG ripple time scale is longer than the other two, and compatible with high energy-resolution (< 5 meV) provided that the acquisition time is less than 1 s. Note the different voltage amplitude scale for the first two (10 mV/unit) and the third (50 mV/unit)

FIGURE 4.17: Electron trajectories simulated in the Simion software under low extracting field ($F_{extr.} = -99.8\,\mathrm{V/cm}$, created by $V_5 = -1460\,\mathrm{V}$ and $V_1 = -1420\,\mathrm{V}$) and optimal tuning of potentials 2 and 3 ($V_2 = -400\,\mathrm{V}$ and $V_3 = -1119\,\mathrm{V}$). Note the crossover ten centimetres away from the output of the electron source, corresponding to a virtual source a few centimetres in front of the apertures of the spectrometer. This configuration corresponds to the circled data point in figure 4.18.

The second MCP will multiply the electron flux by another factor ≈ 1000, giving a substantial electron flux on the phosphor screen. This screen is covered with electroluminescent material that emits photons when it is hit by electrons, in the inverse process responsible for the photo-electric effect. It rests on a quartz window that can be used as an interface between the inside and the outside of the vacuum chamber. Outside the chamber, a 45°-angle mirror and a camera objective projects the image of the phosphor screen surface to the chip of a CCD camera that is connected to a computer. This CCD camera is a ANDOR DV437 and it can be controlled directly from the software that controls the spectrometer. The stack composed of two MCPs and a phosphor screen coupled to a camera forms a classical electron detector.

Voltage and current supplies for the spectrometer

We tested the stability of different voltage supplies for the deflectors that are outside of the spectrometer. The results can be seen on figure 4.16. From this test we see that the ISEG are the best voltage supply to use for our electrodes and our deflectors. Indeed they have low-noise and a ripple temporal scale around 1 s, which is longer than a typical exposure time of the camera (usually less than 100 ms). This is why we use the high-voltage ISEG units for our deflectors, for voltages around $\pm 15\,\mathrm{V}$.

We also checked the stability of the custom current supply (that supplies the current for magnetic quadrupoles and dipole inside the spectrometer) and verified that they have a ripple less than 1 µA, too low to me measured with available multimeters.

Choosing the potentials of electrodes 2 & 3

We saw in section 3.1.1 that electrodes 1 and 5 determine the starting potential V_{in} and the extraction electric field $F_{extr.}$, and electrode 4 determines the electron acceleration at the

end of the electron source. In this study we worked at $V_{in} \approx 1400\,\mathrm{V}$, which is an arbitrary but practical value, because it is high enough for electrons to be detected at the MCPs kept at ground, but high electric fields ($F_{extr.} > 2500\,\mathrm{V/cm}$) can still be applied with 2 kV voltage supplies for electrodes 1 and 5. This leaves electrodes 2 and 3 freely adjustable, so their role is to shape the electron beam in the optimal configuration for the spectrometer.

The spectrometer is designed to work best with a virtual source at 10 cm to 15 cm in front of the magnetic sector. This means that the potential of electrodes 2 and 3 must be tuned to put a crossover of the electron beam a few centimetres in front of the apertures, as is shown in figure 4.17. This figure shows a simulation of the electrodes configuration in the Simion software, where the potential of electrodes 2 and 3 are optimised to create a crossover of the electron source several centimetres after the end of electrode 4.

I performed this optimisation at different values of the extracting field, and for two different electron starting potential values ($V_{in} = -1440\,\mathrm{V}$ and $V_{in} = -1000\,\mathrm{V}$), and the results can be found on figure 4.18.

As we have no direct access to the actual collimation of the electron beam in front of the spectrometer, we must rely on these simulations to appropriately tune the potentials V_2 and V_3. An interesting behaviour appears when we study the optimal values of V_2 and V_3 in function of the extracting electric field $F_{extr.}$. The results of systematic optimisation can be found on figure 4.18, showing very clearly that there exist two separate areas of equilibrium. As a general rule, there are always two combinations of V_2 and V_3 that focus the beam at a given point, but these two points can either be located on a closed ellipsis or in two different branches of an open ellipsis[35].

Figure 4.18 indicates that for both values of the potential, depending on the field value, these two optimal configurations can either be close to each other, or far away. Panel b) shows that, for potentials around $-1440\,\mathrm{V}$, above $-1300\,\mathrm{V/cm}$ (in absolute value) the equilibrium points are arranged in concentric ellipsis with a bigger length the higher the field, centred around $(V_2 = -900\,\mathrm{V}; V_3 = -550\,\mathrm{V})$. Lowering (in absolute value) the fields leads to a singularity and the equilibrium points jump. For fields lower than $-1300\,\mathrm{V/cm}$ the equilibrium points are separated in two lines: one is around $V_3 = 3500\,\mathrm{V}$ and is not shown, while the other (shown in figure 4.18) has a small positive slope around the point $(V_2 = 0\,\mathrm{V}, V_3 = -1200\,\mathrm{V})$. In very low extracting electric fields ($-0.5\,\mathrm{V/cm}$) the ellipsis forms again from the two branches around about the same point that at high fields.

Panel a) of figure 4.18 shows that at a potential of $-1\,\mathrm{kV}$, the situation is very similar. At high fields (above $-1500\,\mathrm{V/cm}$) the ellipsis is centred around $V_2 = -500\,\mathrm{V}, V_3 = -500\,\mathrm{V}$ and opens abruptly in two distinct branches around $-500\,\mathrm{V/cm}$: one at very high V_3 and the other at very low V_3, close to the lower limit. With decreasing fields the two branches move closer to each other and merge below $-10\,\mathrm{V/cm}$ into a closed ellipsis.

This makes a clear distinction between high (closed ellipsis), medium (open branches) and low electric fields (closed ellipsis) for the amplitude of excitation of electrodes 2 and 3. We will see in section 4.3.5 that this has consequences on the achievable energy resolution of the electron spectrometer, because in certain potential/field configurations, focusing requires high potential on V2 and/or V3, not only available with our voltage supplies. To sum up, figure 4.18 demonstrates that the tuning of V_2 and V_3 heavily depends on the value of the starting potential and of the extracting field, and are in turn a crucial parameter for the electron energy measurement.

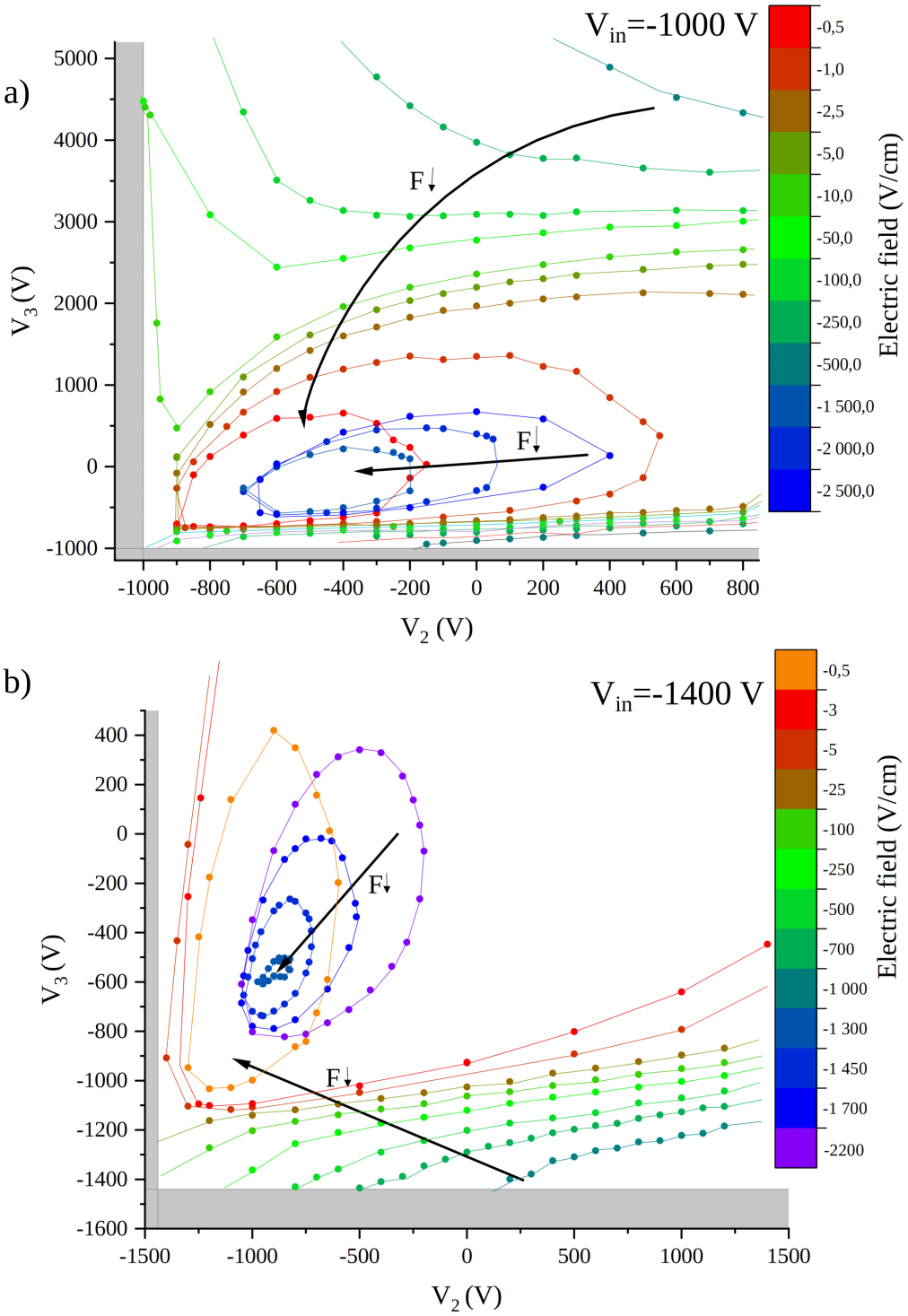

FIGURE 4.18: Optimised values for the potential on electrode 2 and 3, in function of the extracting electric field (indicated in colors). The coloured lines are manually added to guide the eye. The values come from simulations in Simion, with a starting potential of $V_{in} = -1000\,\mathrm{V}$ (a) and $V_{in} = -1440\,\mathrm{V}$ (b), and $V_4 = 0\,\mathrm{V}$. V_1 and V_5 impose the value of the electric field while staying symmetric around $-1000\,\mathrm{V}$ (a) or $-1440\,\mathrm{V}$ (b), which limits the possible values of V_2 and V_3 to not reflect the electrons (unavailable values are indicated by grey shaded areas). Black arrows guide the eye through the evolution of ellipsis when lowering the extracting electric field. See text for detailed analysis of the obtained shapes.

Current in magnetic sector and starting potential

During our test measurements with the spectrometer, we found that the sextupoles SX and SY had barely any effect on the shape of the electron spot. This is why we used the custom high-stability current supply normally supplying SX to supply the magnetic sector itself. This allows us to control the current in the sector from the same software as the other parts of the spectrometer, with added stability in comparison with common laboratory current supplies.

The required magnetic field to fit the curve radius of the electrons (called the cyclotron radius R_c) to the tube radius (i.e. allowing electrons to pass through the spectrometer) B_{pass} is called the passing field and depends only on their velocity v:

$$B_{pass} = \frac{m_e v}{eR_c} \tag{4.35}$$

We can relate this field to the kinetic energy of the electrons E_k by using $E_k = \frac{1}{2} m_e v^2$:

$$B_{pass} = \frac{\sqrt{2m_e}}{eR_c}\sqrt{E_k} \tag{4.36}$$

The electron kinetic energy (in eV) is, to a very good approximation, given by the starting potential of the electrons V_{in} (see section 1.4.3). This relation between the electrons starting potential and the passing field (or the current in the sector's coils) is experimentally verified on figure 4.19, showing a very good square-root fit. This demonstrates proportionality between the current in the coils and the resulting magnetic field, and that the electron velocity in the optical axis is indeed determined by the starting potential.

Hysteresis in magnetic materials

During the course of our work with this instrument it became clear that the different magnetic elements (sector and multipoles) showed strong hysteresis. This is a well known fact, that magnetic materials tend to retain a residual magnetisation even after the current is off. This decreases the repeatability of experiments because the same flow of current in the electro-magnets will create a different magnetic field. To prevent this I wrote a dedicated script in Dm, that removes any residual magnetisation in all the magnetic elements at once. When activated, this script brings the current flowing to all magnetic elements to zero in a series of alternating signs steps. At each step, the current amplitude is divided by 2, and the sign of the current is alternated. The number of steps is chosen so that the last step's amplitude is negligible. This results in a gradual removal in all residual magnetic fields and improve greatly the reproducibility of measurements. We activate this script regularly, several times a day when actively using the spectrometer.

An important part of using the spectrometer is to properly align the electron beam, so that the quadrupoles will have a proper quadrupolar behaviour. The procedure to align the electron beam in the spectrometer can be found in annex 6.3.2.

Controlling the current flow in magnetic elements

The Dm software that control the electron spectrometer gives us access to a value for the excitation of each element (called Q_i for the post-sector quadrupoles), but it has no

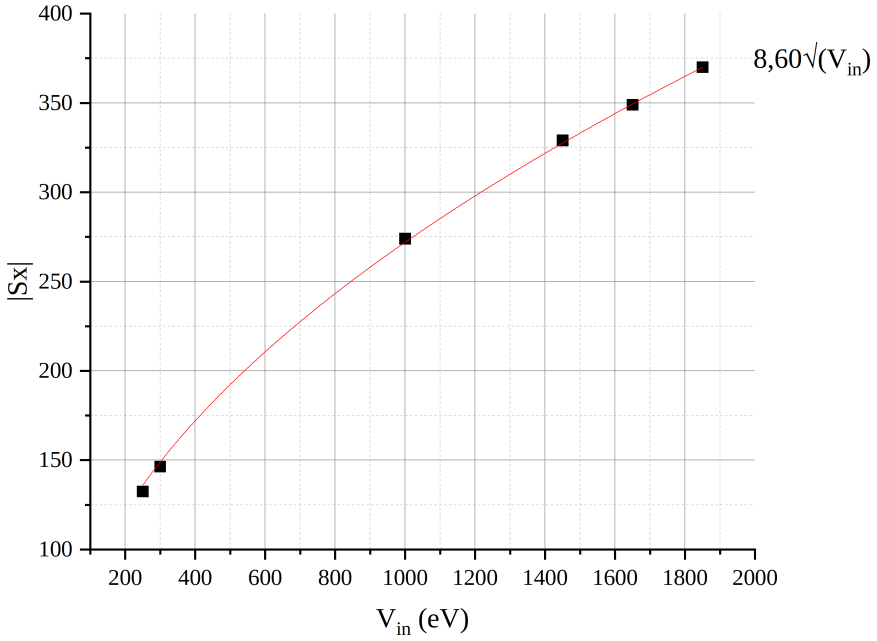

FIGURE 4.19: Link between the starting potential of the electrons V_{in} (i.e. their kinetic energy) and the tuning of the magnetic sector to pass the energy (expressed as Sx because it is supplied by the custom current supply previously used to supply the Sx hexapole). The very good square-root fit demonstrates the applicability of equation 4.36.

physical sense. One annoying fact is the offset from the actual excitation, meaning that $Q_i = 0$ does not shut off the element.

The first step to improve the control of the spectrometer is to retrieve the actual electric current that corresponds to the displayed values of Q_i. For that we measure the current with an ammeter in line with each element, check the linearity, and retrieve these relations:

$$I_i = Q_i * \beta_i + I_{i0} \tag{4.37}$$

with

Element	β_i	I_{i0}
Q1	-1.30124	8.65582
Q2	1.27253	84.5468
Q3	-0.993093	0.646503
Q4	-1.02	-2.3766

The hypothesis of a linearity between I and Q is very reasonable, and supported by figure 4.19. Indeed it features a perfect fit for a square-root relation between the internal Dm parameter and the effect on the electrons. By analogy with a quadrupole (see equation 4.39) where the square-root relation between the electron energy and the effect of the magnetic field intensity is transparent, this proves that there is a very good linearity between internal Dm parameters, output current of the custom current supply and magnetic field intensities.

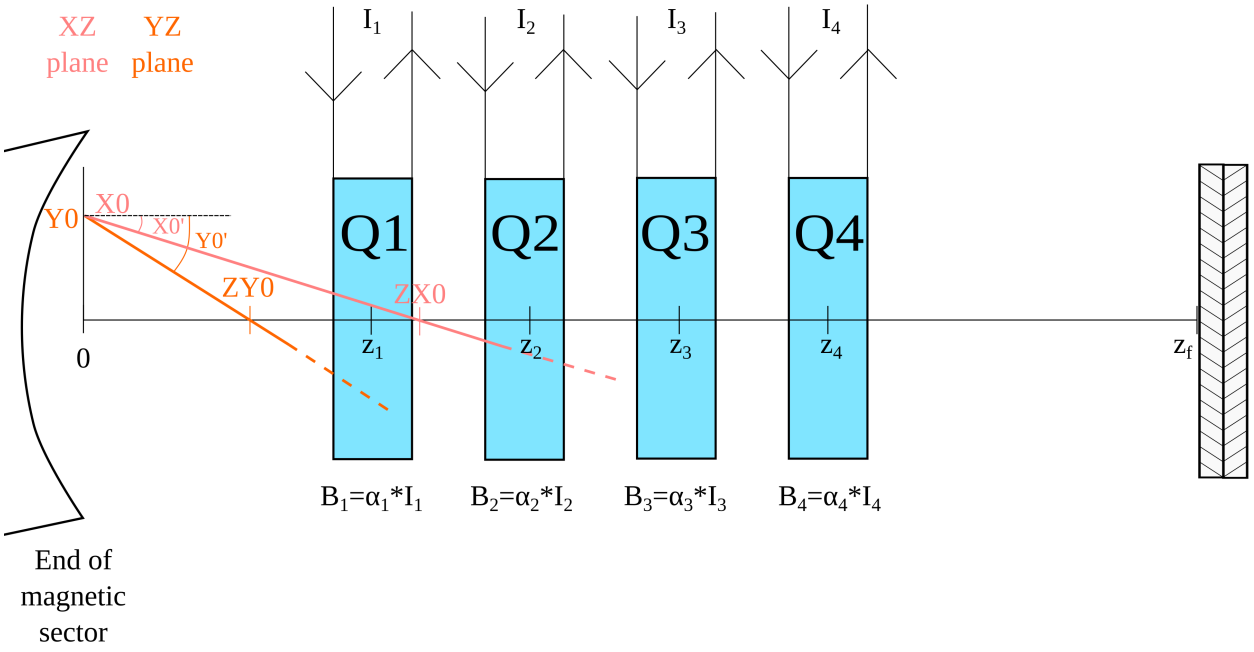

FIGURE 4.20: Definition of the parameters used in the model. Both the YZ plane (red) and the XZ plane (pink) are represented, for the sake of brevity. $Y0$ and $X0$ represent $Y(0)$ and $X(0)$.

These relations are very practical and I wrote a script to control the spectrometer directly with the current. I note that the sign of the current is arbitrary here as we don't have access to the inner coil of the magnetic quadrupoles.

4.2.3 Retro-engineering of the Gatan 666 PEELS

Modelling the effect of the post-sector quadrupoles

To perform an optimal tuning of the post-sector quadrupoles, I modelled their effect on an electron beam via matrix electron optics as depicted on figure 4.20. Indeed the action of a quadrupole (and any standard microscope element in the paraxial approximation) on an electron beam can be represented by a matrix multiplication.

This model is based on the linearisation already introduced in section 1.1.3. The electron beam envelope at any position on the z axis is thus simply described by the position and momentum of a representative particle. It can be expressed as a four-element vector $\underline{E}(z)$, in the axial/field ray basis:

$$\underline{E}(z) = \begin{pmatrix} X(z) \\ X'(z) \\ Y(z) \\ Y'(z) \end{pmatrix} \tag{4.38}$$

X and Y are positions on the x and y axis, and X' and Y' are angles relative to the z axis. In the following we replace the angles by crossover position on the z axis (see figure 4.20) because it is more practical to discuss, but the calculations are still done in terms of angles.

The documentation about the Gatan 666 PEELS indicate that the curvature of the exit plane is chosen to focus the beam on Q1 in the YZ plane and between Q1 and Q2 in the XZ plane (see figure 4.14), but as we work at quite a different electron energy, we make the conservation assumption that the positions of these crossovers are unknown. They are called $ZY0$ and $ZX0$ respectively (see figure 4.20).

I introduce now the matrices $\underline{Q}_i$ with $i = 1,2,3,4$ that represent the effect of the four post-sector quadrupoles of length L[36]:

$$\underline{Q}_i = \begin{pmatrix} \cos\left[\sqrt{K_i(L)}\right] & \frac{\sin\left[\sqrt{K_i(L)}L\right]}{\sqrt{K_i(L)}} & 0 & 0 \\ -\sqrt{K_i(L)}\sin\left[\sqrt{K_i(L)}\right] & \cos\left[\sqrt{K_i(L)}\right] & 0 & 0 \\ 0 & 0 & \cosh\left[\sqrt{K_i(L)}\right] & \frac{\sinh\left[\sqrt{K_i(L)}L\right]}{\sqrt{K_i(L)}} \\ 0 & 0 & \sqrt{K_i(L)}\sinh\left[\sqrt{K_i(L)}\right] & \cosh\left[\sqrt{K_i(L)}\right] \end{pmatrix} \tag{4.39}$$

with K_i defined as:

$$K_i = \frac{eB_i}{m_e L\sqrt{\frac{2eV_{in}}{m_e}}} \tag{4.40}$$

Here B_i is the amplitude of the magnetic field inside the quadrupole Qi (in Tesla), eV_{in} is the kinetic energy of the electrons inside the quadrupole, that is kept constant in the post-sector region. All other quantities are in SI units.

Note that these matrices are block-diagonal, so I could also write 2*2 matrices $\underline{Q}X_i$ and $\underline{Q}Y_i$ without any loss of information. Here we have $\sqrt{K_i(L)} \ll 1$ so the cosine term can be developed as $1 - \frac{|K_i(L)|}{2}$ and the hyperbolic cosine can be developed as $1 + \frac{|K_i(L)|}{2}$. This is the reflection of the fact, already introduced in 1.1.3, that magnetic quadrupole have an opposite effect on each transverse component of an electron beam.

As I don't know the actual values of the B_i quantities, I express them in terms of experimentally accessible physical quantities, i.e. the electric current I_i flowing through the magnetic coils. I assume proportionality between these quantities (which has been verified in the previous section):

$$B_i = \alpha_i \times I_i \tag{4.41}$$

In-between each of these quadrupoles are regions of free flight for the electrons (see figure 4.14). These regions must be introduced in the optical treatment because their length has a direct influence on the coordinates of the electrons. A region of free flight of length z_0 is described via the matrix $\underline{T}[z_0]$:

$$\underline{T}[z_0] = \begin{pmatrix} 1 & z_0 & 0 & 0 \\ 0 & 1 & 0 & 0 \\ 0 & 0 & 1 & z_0 \\ 0 & 0 & 0 & 1 \end{pmatrix} \tag{4.42}$$

From the previous definitions, noting z_i the central position of the quadrupole Qi (see figure 4.14), we can write the matrix of the final electron beam (at the position of the

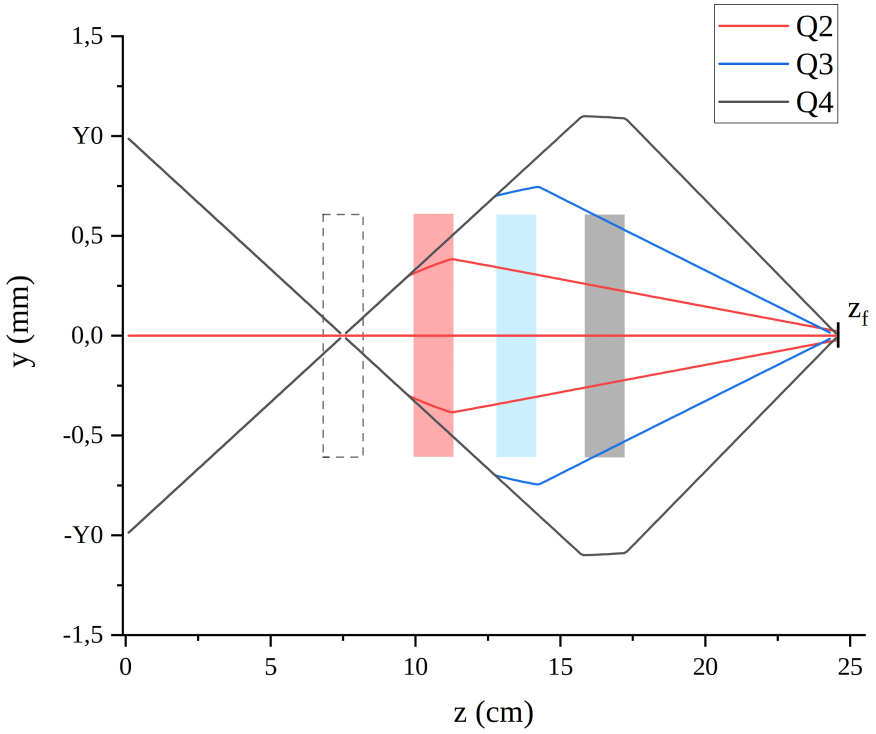

FIGURE 4.21: Simulations of the effect of Q2, Q3 and Q4 in the YZ plane (Q1 is shown in dashed line as it has no effect in this plane) on electrons starting at $y = \pm Y0$. We use $Y0 = Y(0) = 1\,\text{mm}$ to draw the trajectories. $ZY0$ is put equal to z_1 (see text). We simulate the trajectories for each quadrupole independently (with the others shut off), and in each case we adjust the value of B_i, $(i = 2,3,4)$ to focus the beam at $z = z_f$. The drawn trajectories corresponds to fields of $B_2 = -5.7\,\text{mT}$, $B_3 = -3.5\,\text{mT}$, $B_4 = -3.2\,\text{mT}$.

detector z_f) $\underline{E}(z_f)$:

$$\underline{E}(z_f) = \underline{Tf}\left[z_f - (z_4 + {}^{L}/_{2})\right] \cdot \underline{Q}_4 \cdot \underline{Tf}\left[z_4 - z_3 - L\right] \cdot \underline{Q}_3 \cdot \underline{Tf}\left[z_3 - z_2 - L\right] \cdot \underline{Q}_2 \cdot \underline{Tf}\left[z_2 - z_1 - L\right] \cdot \underline{Q}_1 \cdot \underline{Tf}\left[z_1 - {}^{L}/_{2}\right] \cdot \underline{E}(0) \quad (4.43)$$

This model enables us to see the effect of each quadrupole, and to seek for optimal configuration for their excitations. To be completely operational however, this needs to be adapted to our particular set-up. Values for the different unknown parameters must be chosen carefully to fit the actual behaviour of the instrument as best as possible.

Fitting the model in the YZ plane

As shown on figure 4.14, there are 15 parameters to fit: α_i $(i = 1,2,3,4)$, z_i $(i = 1,2,3,4)$, z_f, L_i $(i = 1,2,3,4)$, $ZX0$ and $ZY0$. Such a large parameter space would require massive amount of experimental data and a clever fit procedure to obtain meaningful results.

I thus first try to reduce this space by assuming reasonable values for some parameters. From a simple physical inspection we assume that the quadrupoles are of the same length L, and equidistant (distance d) from each other. This reduces the number of parameters to 10, because $z_2 = z_1 + d$, $z_3 = z_1 + 2d$ and $z_4 = z_1 + 3d$. We also measure

that $z_f \approx 24.5\,\text{cm}$, $z_1 \approx 7.5\,\text{cm}$, $d \approx 3\,\text{cm}$, $L \approx 1.5\,\text{cm}$. This reduces the parameter space further to 6 parameters: the 4 α_i, $ZX0$ and $ZY0$.

We recall that $ZX0$ and $ZY0$ are ways to describe the collimation of the beam at the output of the magnetic sector in the XZ and the YZ planes. From the technical literature of the spectrometer we expect $ZY0 = z_1$ and $z_1 < ZX0 < z_2$.

As we saw in section 4.2.1, there is a very simple way to verify if the beam effectively is focused on Q1 in the YZ plane: Q1 should have no effect on this beam component, no matter the strength of its excitation. We verified experimentally that, at $V_{in} = 1445\,\text{eV}$, Q1 has no effect on the Y component of the electron beam, contrary to Q2, Q3 an Q4, so that we can safely assume that $ZY0 = z_1$.

Now that we know the "initial" conditions in the YZ plane (that the beam is focused on Q1), we can use it to determine the values of α_2, α_3 and α_4 with experimental data, in this 3-parameters space.

One way to determine the α_i ($i = 2, 3, 4$) is to find the values of I_i that focus the beam on the detector, both in the simulation and experimentally. This way the comparison with the simulation is much easier, because it does not depend on the unknown experimental values of the initial beam size (i.e. the values of $Y0$ and $X0$). Results from the simulations are shown on figure 4.21, giving us the values of B_i.

The same procedure done on the experimental set-up (with only one quadrupole activated at the same time) gives us $Q_2 = -93.98$ ($I_2 = -35.04\,\text{mA}$), $Q_3 = 6.92$ ($I_3 = -6.23\,\text{mA}$) and $Q_4 = 29.66$ ($I_4 = -32.63\,\text{mA}$). On top of the one quadrupole configuration, we also acquired couples of values for cross-excited quadrupoles. I thus have 9 sets of experimental data points, which gives us a first estimation of the α_i ($i = 2, 3, 4$): $\alpha_2 \approx 0.2$, $\alpha_3 \approx 0.6$ and $\alpha_4 \approx 0.1$.

I note here that there is an unresolved ambiguity in the effect of Q2, Q3 and Q4 and the sign of the α_i. Indeed they have the same sign, but the definition of I_i and the possible 90° rotation between the quadrupoles prevent us from drawing too much conclusions about the same polarity of the α. I can make one remark though: as I know that the cross-over in the YZ plane is in Q1, the only way to have a second crossover on the detectors is to focus the beam (because the quadrupoles are placed after the first crossover). Thus the values for $Q_i (i = 2, 3, 4)$ corresponding to a crossover at $z = z_f$ correspond to a *focussing* effect of these quadrupoles in the YZ plane. As already stated in section 1.1.3, quadrupoles have opposite effect on orthogonal directions. This means that Q2, Q3 and Q4 will "defocus" the electron beam in the XZ plane under the same tuning that makes them focus the beam in the XZ plane. This gives a focusing action in the XZ plane for a positive current in the Qi ($i = 2, 3, 4$) (which will be important for the final fit).

Fitting the model in the XZ plane

Now I use this same procedure, but in the XZ plane. Here the difficulty is that I don't know the value of $ZX0$, since experimentally all quadrupoles have an effect on the XZ plane. But now that I have the sign of the α_i ($i = 2, 3, 4$), I can use this fact to put boundaries on the value of $ZX0$.

Indeed I know that Q2, Q3 and Q4 have a focusing effect on the XZ plane when $I > 0$. These considerations, together with the experimental values of $Q_2 = -61.14$ ($I_2 = 6.74\,\text{mA}$), $Q_3 = -2.06$ ($I_3 = 2.69\,\text{mA}$) and $Q_4 = -22.42$ ($I_4 = 20.49\,\text{mA}$) to focus (one at a time) on the detector in the XZ plane, tells us that these elements must also focus

the electron beam in the XZ plane to put a crossover on the detector. This is only possible if $0 < ZX0 < z_2$ or if $z_f < ZX0$ (if $z_2 < ZX0 < z_f$, the only way to focus on the detector with one active quadrupole is to defocus in either one of Q2, Q3 or Q4.).

Furthermore, the estimated values of the B_i ($i = 2, 3, 4$) in this case are $B_2 = 1.35\,\mathrm{mT}$, $B_3 = 1.61\,\mathrm{mT}$ and $B_4 = 2.05\,\mathrm{mT}$. This amplitude increase is only compatible with $ZX0 > z_f$. I performed a fit on the XZ plane, with only Q2, Q3 and Q4 "activated", searching for the optimal value of $ZX0$ with the previously estimated values of the α_i ($i = 2, 3, 4$) and experimental values of Q_i ($i = 2, 3, 4$) in 9 focusing configurations, and the procedure gave unambiguously $ZX0 \gg z_f$. This corresponds to a practically collimated beam (for the same electron energy) at the exit of the sector. This is in contradiction with the published description of the Gatan 666 PEELS, but it is probably due to the lower electron energy (here at 1.5 keV) than devised for.

With this value of $ZX0$, I performed an overall fit with both XZ and YZ datasets, and found these results: I also recall the value of the other parameters:

TABLE 4.1: Fitted values for the simulation of post-sector quadrupoles

Parameter	α_1	α_2	α_3	α_4	$ZX0$
Fitted value	0.067	0.163	0.542	0.098	80 cm

TABLE 4.2: Other parameters for the simulation of post-sector quadrupoles

Parameter	z_1	z_2	z_3	z_4	z_f	$ZY0$	L
Value	7.5	10.5	13.5	16.5	24.5 cm	7.5 cm	1.5 cm

At the end of this fitting sequence I tested different values for z_f, d, or L, but did not find any improvement on the residuals of the fit.

4.2.4 Optimal tuning of quadrupoles

Now that we have a simulation that is adjusted to experimental values, we can use it to obtain optimal values of Q_i, to help us retrieve the most from the Gatan 666 spectrometer.

The test simulation uses three initial points at $z = 0$, from which three electrons emerge with different velocity directions. The procedure for an optimal tuning of the quadrupoles to retrieve the kind of trajectories presented in figure 4.14 is as follows:

- Tune Q2 to focus the electron beam in the YZ plane on Q3
- Tune Q1 in the XZ plane to form a diffraction image at $z = z_f$
- Tune Q3 to obtain the desired zoom in the XZ plane
- Tune Q4 to correct for the zoom in the YZ if the electron spot is too large for the detector

I wrote a script that does this automatically, given a desired zoom in the XZ and YZ directions. The simulated trajectories can be found on figure 4.22. The first step is quite straightforward (tune Q2 to have a crossover on Q3), and we can verify that the value

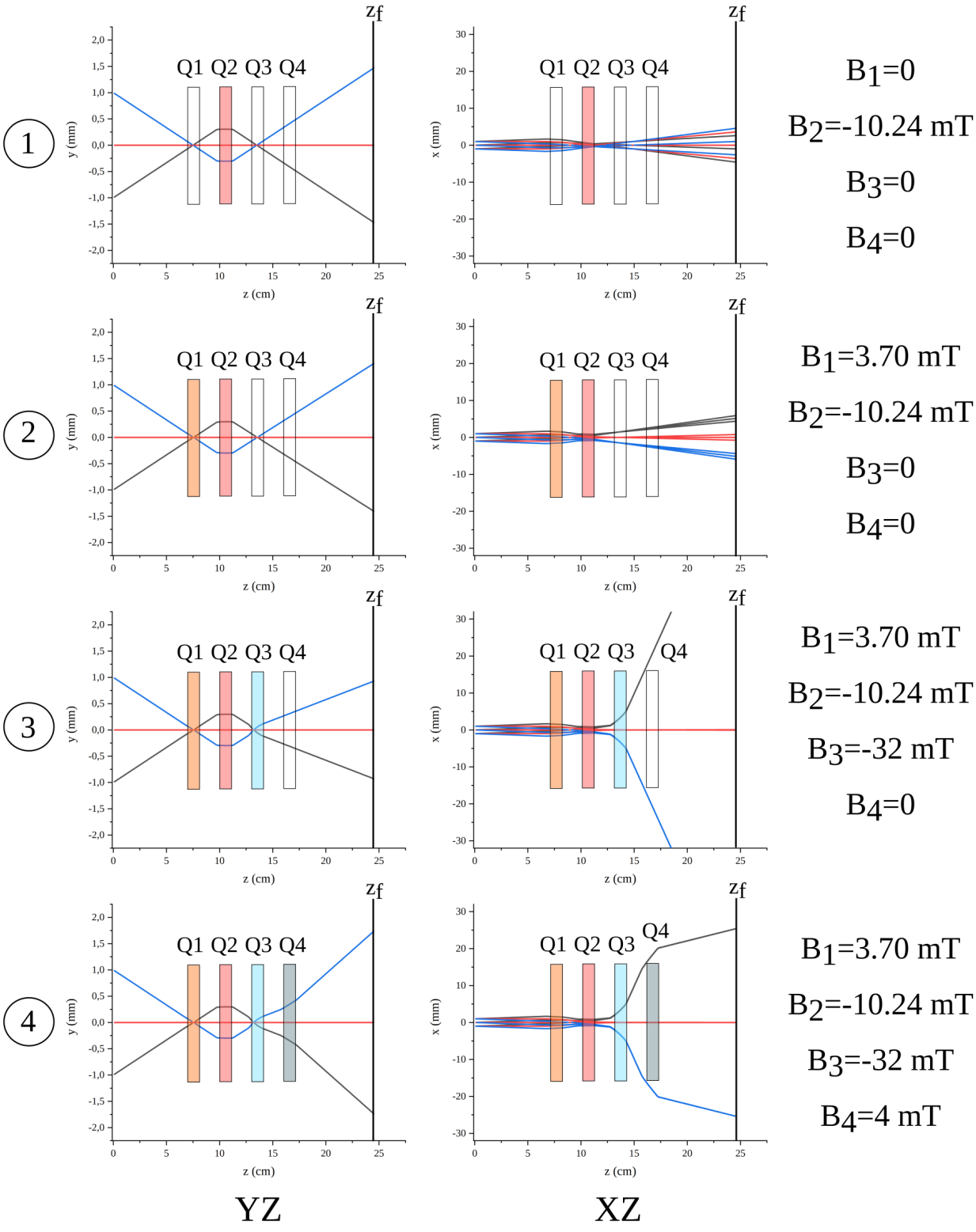

FIGURE 4.22: Sequence of tuning with the simulation for optimised values of the B_i, ($i = 1, 2, 3, 4$). The trajectories with the same colour have the same electron momentum orientation. These four steps (1. Q2 focus on Q3 2. Q1 forms the image in plane XZ 3. Q3 increases the dispersion in plane XZ 4. Q4 increases the image size in plane YZ) require some back and forth fine-tuning to have the best results in the final trajectories, because Q1, Q3 and Q4 act on the same plane. B_1 in particular is optimised at the end to have the sharpest diffraction pattern, but this optimisation is small in comparison with its value, and we present trajectories with the final values for all B_i instead of the "chronological" ones.

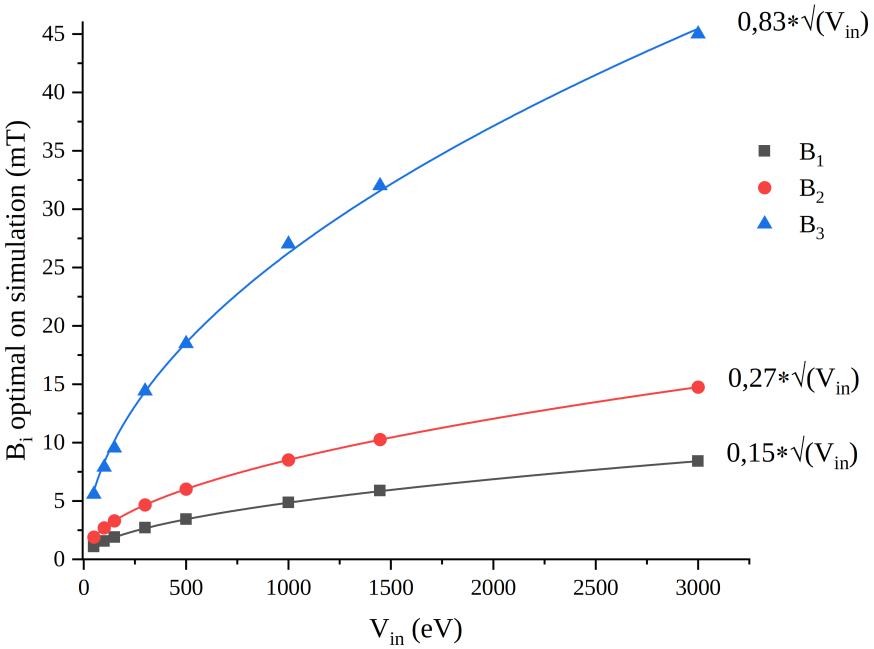

FIGURE 4.23: Values for the simulated optimal values of B_1, B_2 ans B_3 in function of the energy of the electrons (V_{in}). They are fitted to a square-root function of V_{in}. B_1 and B_2 are unambiguous as they have strict tuning criteria, but B_3 (and B_4) is more loose as it depends on the arbitrary zoom value in the XZ and YZ directions.

of B_2 is appropriate by checking if Q3 has any effect on the YZ component of the beam. The simulation gives $B_2 = -10.24\,\text{mT}$, and we find an experimental value for B_2 around $-10.4\,\text{mT}$.

Experimentally, a proper chromatic image is obtained on the detector for values of B_1 around 3.7 mT. We found the best results in terms of zoom with values of B_3 around $-32\,\text{mT}$, and $B_4 \approx 4\,\text{mT}$.

We found overall a very good agreement between the simulation and the experiments, and the model allows us to reach the optimal settings very easily, rendering the best resolution that the Gatan 666 PEELS can offer in this context.

We thus tested different values for the energy of the electrons, and in each case we give the optimal values for the B_i ($i = 1, 2, 3, 4$). Q4 is a bit special because it mainly deals with the electron spot size in YZ, that depends also on the extracting fields and experimental conditions. The optimal values for B_i ($i = 1, 2, 3$) are depicted on figure 4.23, as well as a square-root fit for each quadrupole. This curves is very useful as a reference for the experimental tuning of the B_i over a wide range of energies.

There are two other quadrupole lenses in the spectrometer, before the magnetic sector, called FX and FY. These quadrupoles are used to change the shape of the final electron spot, and are adjusted to keep the spot as a vertical line.

This ends our description of the experimental set-up that we will use to excite Rydberg atoms, create an electron beam and measure its energy spread. One of the goal of this study is to verify that the electron energy spread is dominated by the value of the extracting electric field, and to compare the obtained energy spread when using photo-ionisation and Rydberg field-ionisation. This would help us identify appropriate conditions for the electron source in HREELM.

Section summary

Installation of a high-resolution spectrometer

In this section I detailed a big part of my experimental work, the installation and adaptation of an electron spectrometer to our set-up: fixing its airtightness, selecting appropriate supplies, interfacing its control with the detection software, writing helpful scripts and so on. A lot of efforts went into the understanding of its functioning, both in theory and in practice. A kind of retro-engineering procedure, based on matrix optics, was needed to ensure that we fully understand its behaviour and are able to use it optimally. This procedure succeeded and, thanks to that, we were able to determine optimal tuning of post-sector quadrupoles in various starting kinetic energies.

4.3 Results of the electron energy spread measurements

The performance of a spectrometer can be expressed in terms of the ratio between the electron energy and the energy resolution, which is usually constant over a range of energies. This means that one way to improve the absolute energy resolution of an electron spectrometer (our Gatan 666 in particular) is to reduce the kinetic energy of the electrons. On the other hand, lower energy electrons are much more sensitive to residual magnetic fields and uncontrolled potentials inside the instrument. Most of the results we present are taken around $V_{in} = -1.5\,\text{keV}$, but we also studied the impact of V_{in} on the performance of our energy spread measuring set-up.

The typical raw data that we acquire is shown in figure 4.24. The detectors are placed behind the spectrometer, that disperses electrons in the horizontal direction. This figure shows an increase of the electron spot size in that direction with an increasing extracting electric field. It is an obvious consequence of the formula presented in equation 1.15, that shows that the energy spread of the electron beam increases linearly with the intensity of the electric field. The last images show clipped electron spots because of internal collision with the inner tube in the magnetic sector. This limits the spectral range of one measurement, but corresponds to several eV so it is not an issue for us.

In these studies we use the electrically-isolated drift tube to calibrate the energy scale. This calibration is very easy, fast, and can even be done during an actual measurement. The idea is to apply a time-dependent square potential to the drift tube, from potential $-V_{dt}$ to V_{dt}. This way, a continuous beam of electrons will create two well separated lines on the detector, with the spacing between the line directly correlated to the energy spacing $2V_{dt}$.

We record this image (examples can be seen on figure 4.25), and use the known energy separation (i.e. the applied potential amplitude) to calculate the energy dispersion D^E_{isp} in eV/pixel (or meV/pixel). I then fit the horizontal profile of the vertical line with a gaussian fit (or lorentzian fit, depending on the shape of the peak) and extract its full-width at half-maximum (FWHM) Δx. The energy spread ΔE is then given by:

$$\Delta E = D^E_{isp} \Delta x \tag{4.44}$$

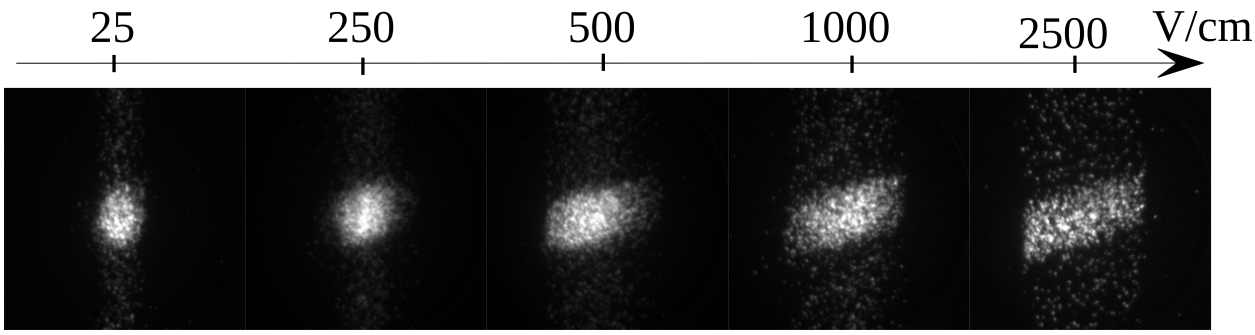

FIGURE 4.24: Electron spot with increasing electric field in V/cm. The horizontal spot size represents the electron energy spread, revealed by the magnetic sector. The last images are clipped and represent the maximum energy width than can pass through the spectrometer at once.

We note that a proper tuning in the XZ plane gives clean gaussian profiles, whereas a lorentzian fit is more appropriate when the focus is not done properly. This is a purely empirical remark, and the quality of the fit needs to be checked before concluding on the observed energy spread.

When the vertical lines are straight enough, the horizontal profile is constructed from the whole picture, but when the lines are too curved we take the profile over a smaller region. This is done cautiously, as this can underestimate the actual energy spread. The idea is that this must not filter out parts of the energy distribution, so we take the profile only on parallel lines, over the center of the line. We present two cases on figure 4.25, that shows a situation where a selective horizontal profile is acceptable, and one case where it is not.

As can be seen on the left image of figure 4.25, we have two peaks that we can fit, and the fit does not give the same results in terms of width. This difference is due to a combination of homogeneous broadening of the MCPs, phosphor screen and camera detection, and a differential sensitivity of the MCPs. In other words, the peak is wider as it becomes more intense, and the intensity depends on the position where this beam hits the detectors, so the width of the peak depends on the position of the beam on the detector. This effect was more and more obvious as we went along with the measurements, because the MCPs started to be damaged in the center where the electron beam was most of the time, sometimes even over-focussed.

Here it should be clear that this width is entirely a detection artefact, and the real energy spread of the electron beam will always be smaller than what we can measure from the fit. This is why the energy spread values are taken from the thinner peak in all the following.

4.3.1 Highest resolution at 1.5 keV

We did measurements to establish the highest attainable resolution on our spectrometer, with the help of the optimised quadrupoles. Resolution has different definitions, but here we give it in terms of Sparrow criteria, meaning that the resolution is given as the smallest energy difference between two discernible gaussian peaks[37]. Here it means that the resulting profile from two peaks separated exactly by the resolution will have a

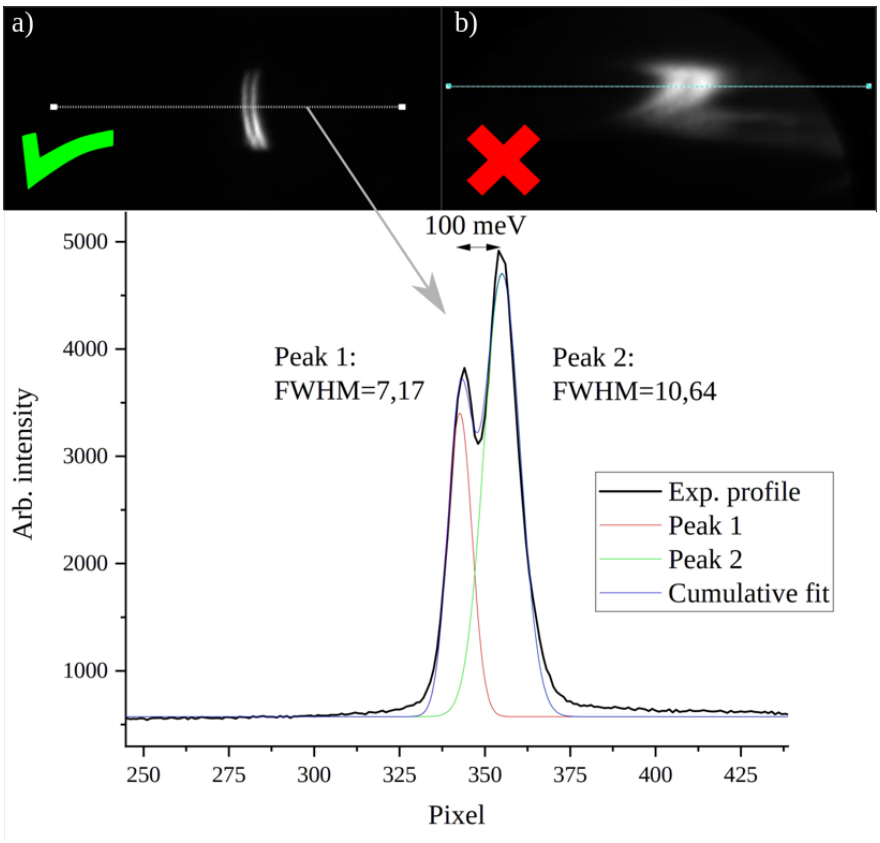

FIGURE 4.25: Two different experimental images acquired under different tuning of the spectrometer, showing well separated peaks (a) and non-separated (b) from the rectangular drift-tube potential, with a pictogram indicating if a partial horizontal profile can be advised in this case. For both measurements the energy separation is 100 meV, and the two lines are clearly distinguishable. On the bottom of this figure is the resulting horizontal profile of case a), with a gaussian fit of the two peaks, showing different widths for each peak.

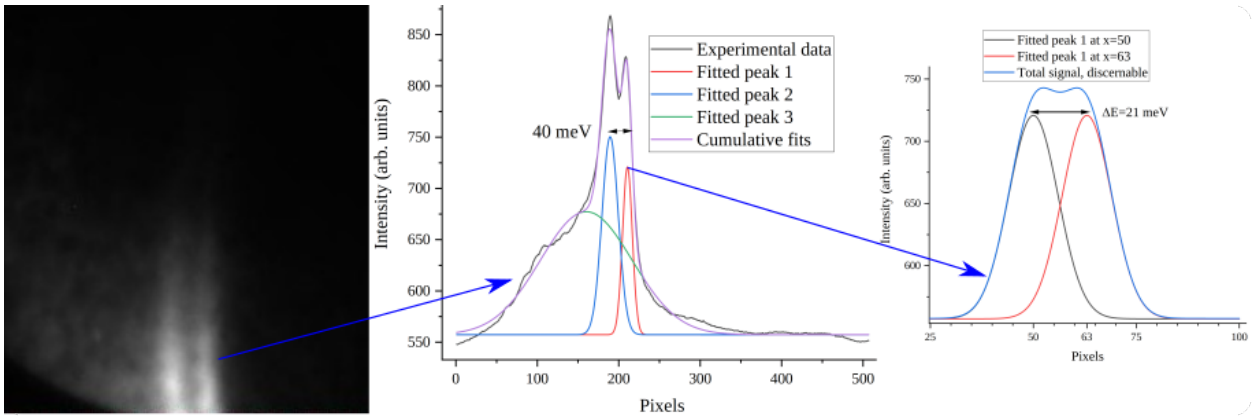

FIGURE 4.26: Energy resolution analysis at 180 eV showing experimental image on the left, a full image horizontal profile showing bad focusing with two well-defined peaks. These peaks are separated by 40 meV with an adjustable two-step potential. The shape of the thinnest peak is extracted and copied twice plotted in the right plot, with an x-distance to make the two peaks appear in the cumulative shape. This analysis yields 21 meV of energy resolution.

saddle-like shape. We take the measurement presented on figure 4.25 and extrapolate the resolution to be around 60 meV.

The value of 60 meV for the close-to-optimal resolution at an energy of 1.5 keV gives a ratio of 4×10^{-5}. This is quite close from the value of 1×10^{-5} quoted in the literature. We are not certain that this value is the lowest value that we could measure, because it could also be the actual value of the electron spread of the beam that we used as a reference for the experimental peak. Indeed this measurement was done with photo-ionisation electrons, under an electric field of 12 V/cm. Equation 4.21 and an ionisation zone of 50 µm already gives the value of 60 meV of dispersion, so we cannot conclude that we obtained the final resolution of our instrument, because the electron source spread itself could be larger.

We performed additional experiments at lower potential (around 180 eV, electric field of 1.8 V/cm), to see the influence of the nominal energy to the energy resolution of our spectrometer. Results can be seen on figure 4.26, clearly showing non-optimal focusing. However, we can safely derive a value for the highest resolution attainable under these circumstances around 21 meV, showing $^{\Delta E}/_{E} = 1.2 \times 10^{-4}$. Electron trajectories simulation showed that in this field configuration the optimal values for V_2 and V_3 were experimentally unattainable, thus decreasing the $^{\Delta E}/_{E}$ ratio.

4.3.2 The effect of the extracting electric field in photo-ionisation

This motivated us to study the influence of the electric field on the measured energy dispersion, first to confirm that equation 4.21 applies and to see if the low limit for measurement could be extrapolated from this data.

This study was done with photo-ionisation of the caesium atoms, and the results are presented in figure 4.27. Given that we obtained 60 meV at 1.5 keV, we lowered the starting potential to have electrons around 1 keV, to see if the resolution improved (as the ratio $^{\Delta E}/_{E}$ is supposedly constant).

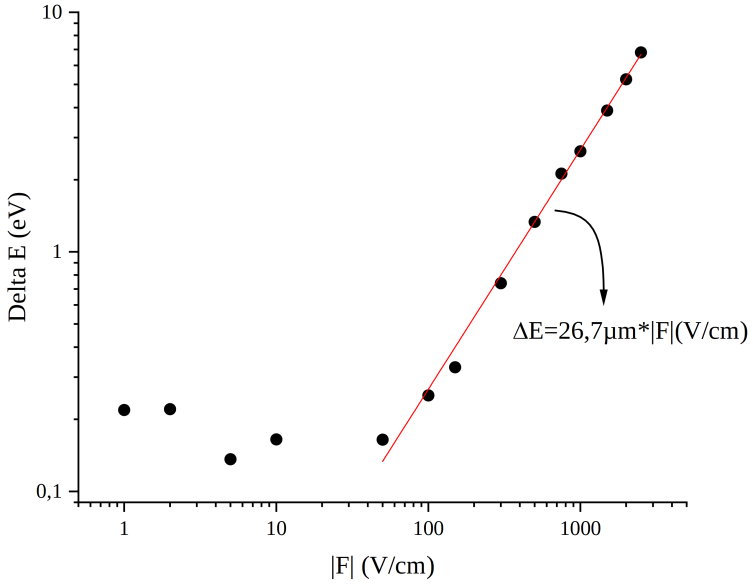

FIGURE 4.27: Experimental values of the energy spread for a photo-ionisation electron beam at 1 keV, with increasing extracting electric field strength, in log scales. This features a very good linearity at high fields, proving the applicability of equation 4.21. This linear behaviour breaks down around 50 V/cm (or around 150 meV) and lower values of the electric field do not give systematic lower energy spread. The fit at high fields gives us an estimate for the ionisation zone of 27 µm

The data presented on figure 4.27 clearly shows that the energy spread is higher than 135 meV at best, no matter the electric field amplitude. This is in contradiction with the expected behaviour of very low spread from very low electric fields. Furthermore, it is surprising that the lowest measured energy spread (i.e. the energy resolution) at 1 keV is more than twice the resolution at 1.5 keV, contrary to the intuition that $\Delta E/E$ is constant. This discrepancies will be further discussed in section 4.3.5, but we attribute the relatively higher measured energy spread to instrumental limitations, and not to an actual electron energy spread limitation.

4.3.3 Rydberg ionisation versus photoionisation

An important study with the functioning apparatus was to compare the energy spread of a photo-ionisation source, and a Rydberg ionisation source. For these measurements we put the potential of electrode 5 at -1883 V, electrode 1 at -1012 V, creating an electric field of ≈ -2170 V/cm at the center of the electrodes. We put $V_2 = -350$ V and $V_3 = -400$ V to have a good crossover in front of the spectrometer.

The lasers are centred with the method presented in section 3.2.1. The images presented on figure 3.7 represent an electron current around 60 pA on the inner tube, whereas tuning the Ti:Sa laser to 787.238 nm to directly photo-ionise creates 5 pA at best. In terms of electron current, Rydberg field-ionisation is clearly superior, and other configurations of lasers and Rydberg states gave us up to 500 pA.

However, in this particular set-up, the energy analysis shows no improvement in terms of energy spread, in comparison with the photo-ionisation case. This is simply

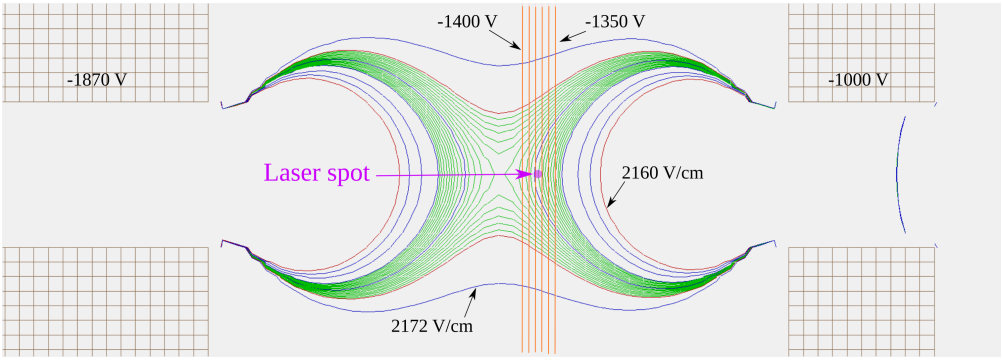

FIGURE 4.28: Planar cut of the electrodes already presented on figure 3.2. On top of the equi-field lines (red lines every 10 V/cm, blue lines every 2 V/cm, green lines every 0.2 V/cm) we added equipotential lines in orange, separated by 10 V. A pink disk of radius 30 µm indicates the approximate ionisation zone. This clearly shows the strong curvature of equi-field lines in comparison with equipotential lines.

because, as stated in section 4.1.4, the only way to do better at a given electric field, is to have a smaller ionisation zone than the ionising laser spot. In the case of Rydberg field-ionisation, it can be achieved if the electric field resonance condition imposes an ionisation zone smaller than the laser spot. We will see in the next section why it is not the case here.

4.3.4 Field inhomogeneity in published electrodes design

If we take a look on the electric potential created by the electrodes, presented on figure 4.28, it is apparent that the equipotential lines (in orange) are vertical, straight in the XY plane, while the equi-field lines are highly curved (see the red, blue and green curves). This means that one electric field value will span out to a large range of electric potentials.

In terms of energy this means that the electrons created on a certain equi-field line (due to selective excitation of ionising Rydberg states) will have very different starting potential, and thus a large energy spread at the end of the acceleration zone. This explains why this electrode design is not adapted to produce very low energy spread with Rydberg field ionisation. The model presented in section 4.1.5 is therefore not valid here, because the term $\Delta V_{Curvature}$ is greatly under estimated. Indeed, the obtained result ($\Delta V_{Curvature} = \frac{-3r^2}{8}F'$) is very dependent on the assumption that the field gradient is constant over the ionisation zone, so that we can ignore higher terms in the decomposition of the electric field over z and r. This condition is actually not fulfilled in our electrodes, and the highly-curved field lines visible on figure 4.28 come from higher order terms. As an illustration of this high-order behaviour of aperture electrodes, we took data from the Simion software of our actual electrode configuration and tried to find the appropriate values of F, F' and F'' to reconstruct the lines in a pure gradient configuration ($F'' = 0$ as in the derivation of equation 4.29) or even with non-zero F''. Examples of the obtained lines can be seen on figure 4.29, showing that the simulated field lines in our experimental electrode configuration (middle panel) do not resemble a "pure gradient" situation (top panel) but shows instead similarities with high-F'' situations (bottom panel). This clearly demonstrates that the derivation of $\Delta V_{Curvature}$ is not directly applicable to our electrodes

but represent rather a minimum value for the influence of the curved electric equi-field lines.

From there, we can improve the model and re-derive $\Delta V_{Curvature}$ from eq. 4.25, without making the assumption that $V^{(\geq 3)} = 0$. This would give us a better estimation of the energy spread in situations with highly-curved field lines, but these would only show higher energy spread than the pure gradient situations. The other approach is to try to fit the experimental electrode configuration to this idealised case, an idea that we explore in section 4.4.1.

4.3.5 Additional experimental limitations

During the course of the energy spread measurements it became clear that the electrodes were fixed in a somewhat inappropriate manner (see section 3.1.1). This assembly does not guarantee that the electrodes are very concentric, nor very parallel. This creates some experimental issues that made our efforts tedious, and limited the range of possible electric field configuration. Indeed in some cases (in particular when electrode 3 was at high potential amplitude), the electron beam was completely unaligned with the rest of the instrument and the deflectors had to correct large angles. Figure 4.18 shows that in some electric field configuration it is required to put high potential on V3, which in turn has some detrimental effect on the measurement precision.

As an example, we wanted to measure the influence of the electric field amplitude on the energy spread of the electron beam at a central potential of 1.8 kV. At very low electric field, the Simion analysis for the V_2 and V_3 appropriate potentials gives values of $V_2 = -400$ V and $V_3 = -1220$ V (see figure 4.17), to have a virtual source about 10 cm in front of the spectrometer. This high-excitation of electrode 3 induced a large displacement of the electron beam that we could not correct efficiently with the deflectors. Thus we had to fall back a not so proper configuration to be able to place the electron beam at the center of the quadrupoles. This non-optimal tuning of electrode 3 lowers the precision of the instrument, and we could not measure any dispersion lower than 280 meV under these conditions, even with very low electric fields.

The first version of this set-up had no deflectors between the source and the spectrometer's entrance, and it was not possible to achieve any measurement because of that. We thus modified it by inserting deflectors between the source and the spectrometer, that allowed us to correct the misalignment of the electrodes.

However this correction was not always possible in the field configurations with the highest deviation from the optical axis, as these deflectors were not designed to correct large angles. We can see on figure 4.30 the clear correlation between the voltage on electrode 3 and the required deflection on the first deflector. This means that the field/potential configurations that require a high voltage on electrode 3 for proper tuning (as seen on figure 4.18) also require high deflection. These high-angles most probably induce aberrations and non-paraxial trajectories in the spectrometer, decreasing the precision of measurement on the energy spread. Indeed the spectrometer relies on well defined and controlled electron trajectories to measure energy, and any deviation from the expected trajectories will directly decrease the precision of measurement.

Another related issue that limits the range of accessible parameters (mainly the starting potential of the electrons), is the inefficient magnetic shielding of the apparatus. This was particularly true in the electron source region where the μ-metal shielding has to be

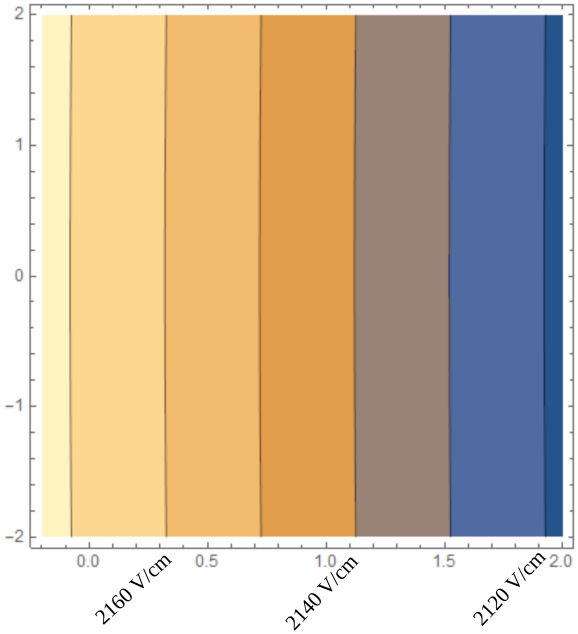

Example of a "pure gradient" configuration. Electric field lines with F=2168 V/cm F'=-250 V/cm/cm F''=0 V/(cm)$^{-3}$

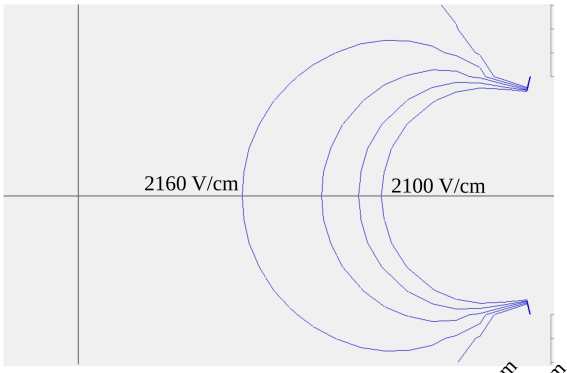

Actual electrode configuration in the Simion software. Line every 20 V/cm

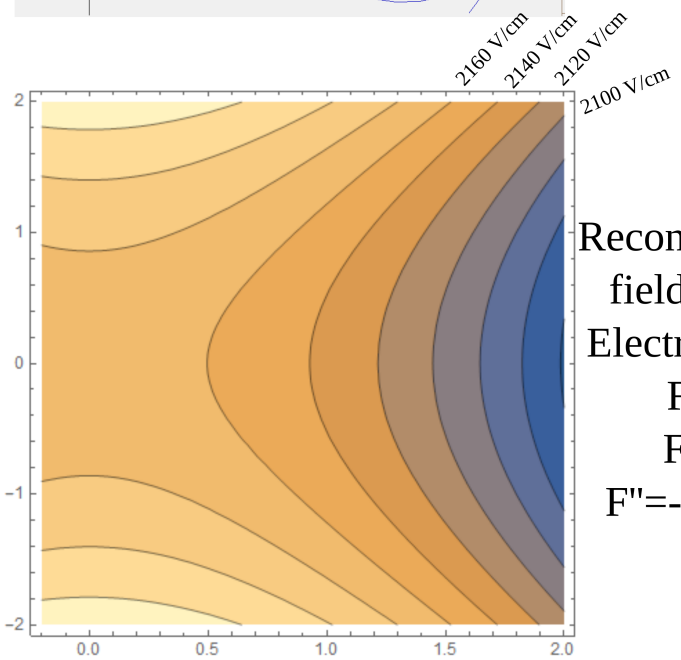

Reconstruction of actual field-lines with F''≠0 Electric field lines with F=2168 V/cm F'=0 V/cm/cm F''=-650000 V/(cm)$^{-3}$

FIGURE 4.29: Comparison of actual equi-field lines in our experiment as simulated in the Simion software (also shown on figure 4.28) (middle), with lines coming from a "pure-gradient" field $F'' = 0$ (top) and coming from optimising the value of F'' to best fit the actual lines (bottom). Clearly a "pure-gradient" model does not hold, and the curvature of the field lines is due to the influence of high order terms, initially neglected.

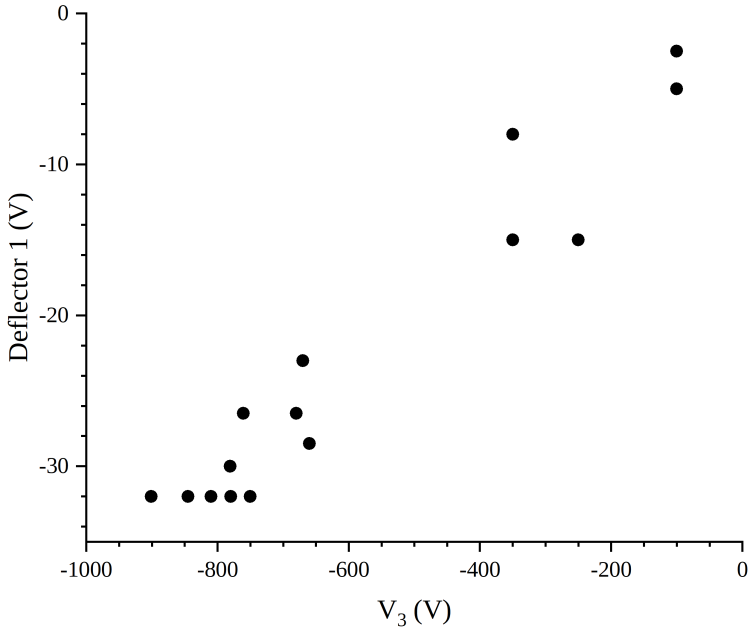

FIGURE 4.30: Evolution of the required deflection with the voltage on electrode 3, showing a clear correlation between these two values. The deflection potential saturates at -32 V because it was the highest possible value of the stabilised-voltage supply that we used.

modified to incorporate the deflectors. This resulted in a non-optimal shielding, and a simple magnetic optical post held at 10 cm outside of the vacuum chamber had visible effect on the electron spot at the detectors. This also explains why the energy resolution/energy ratio $\Delta E/E$ is not constant over the whole energy scale, and is particularly low at energies below 1 keV. This is also one possible reason why we could not measure very low energy spread at very low extracting electric fields. Indeed when the electrons are created under a low extracting field, they are not strongly accelerated, spend some time in the electron source where the shielding is inefficient and accumulate influence of the external magnetic field that is detrimental to the proper energy measurement.

Overall we realised that the energy spread measurement with the Gatan 666 PEELS is not very straightforward, and that a very good knowledge of the whole apparatus is required to be able to retrieve genuine data on our electron beam. This explains why it took approximately a year between the installation of the spectrometer on our set-up and the first reliable results. This allowed us to fully understand the functioning of the spectrometer, and to identify crucial points for a proper measurement. The actual set-up was not able to perform definitive experiments on the link between Rydberg forced-field ionisation and the electron energy spread, but we clearly understood what was in the way of such measurements and can envision a new version of this set-up that could give interesting data on this problem.

Section summary

Results of the electron energy spread measurements

This section contained results of energy spread measurements obtained with the electron spectrometer. We determined the optimal energy resolution of this instrument to be 60 meV at 1.5 keV, giving a ratio of 4×10^{-5}. Lowering the energy to 180 eV gave a value of extrapolated resolution of 21 meV (but with non-optimal electron focusing, indicating higher energy spread), far from the optimal value if the ratio were constant. Studies on the influence of the electric extracting field on the energy spread at an energy of 1 keV showed a departure from proportionality at low field values. As the experimental limit of the energy spread was higher than the lowest resolution obtained at higher energy, I concluded that this lower bound comes from inappropriate focusing of the electron beam in the spectrometer, due to inadequate energy/field combination. Experiments on Rydberg field-ionisation also revealed a critical issue of using aperture electrodes to apply the electric field: the induced field-curvature is much more intense than what can be predicted from a back-of-the-envelope gradient estimation. Thus the use of resonant space-field conditions for the ionisation of Rydberg atoms needs to be associated with controlled, flat equi-potential and equi-field lines, thoroughly simulated in an appropriate software.

4.4 Propositions for a highly-monochromatic electron source

4.4.1 A better electrode design for improved control of electric field lines

Now that we have a better understanding of the sources of energy spread in Rydberg field-ionisation electron beams, we can envision an optimal configuration of atomic beams, laser and potential/field lines. This is what we do in this section, with two different propositions. The only difference between these propositions is the direction of the neutral atomic beam in relation to the electron optical axis.

The important part of these propositions is the need to shape the electric field lines to control their curvature. This is impossible to do with only two electrodes influencing the field lines at the center. Indeed this gives only two degrees of freedom, that are used to fix the potential and the electric field at the center, but all other quantities are fixed and determined by these two potentials, plus the geometry. For an improved control of the gradient of the electric field and higher order terms we need new degrees of freedom. One way to achieve that is to increase the inner bore of the central electrodes to increase the influence of the further two electrodes. Such an electrode configuration can be found on figure 4.31, where four electrodes have strong influence on the field lines at the center. This brings two new degrees of freedom, that can be used to shape the field lines to some degree.

One efficient way to shape the electric field lines is to use the potential decomposition presented in equation 4.23, that allows to express the potential at any point from

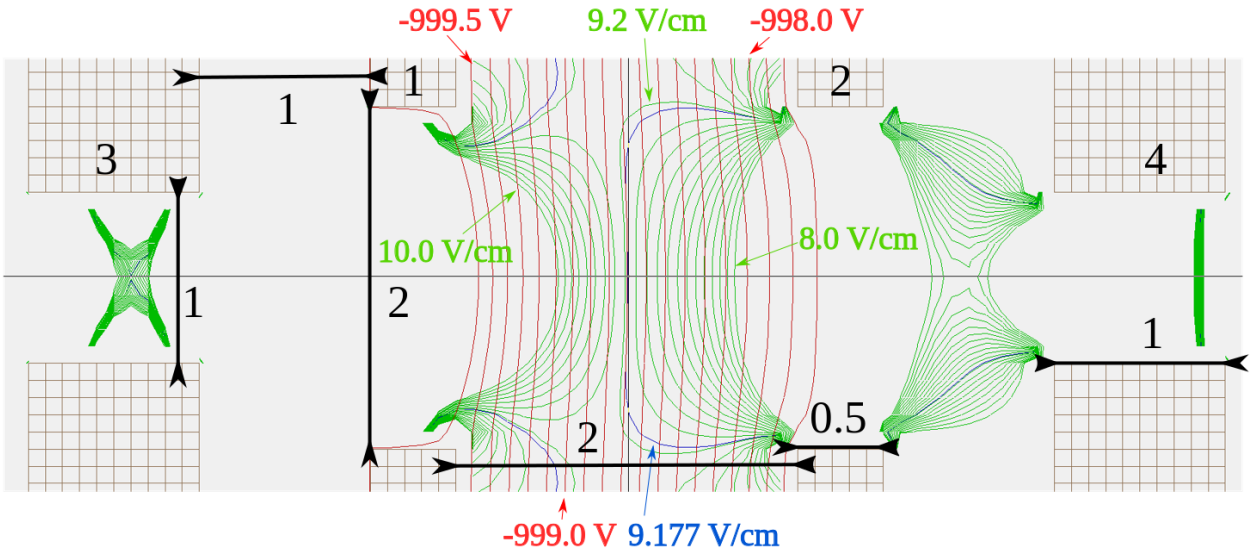

FIGURE 4.31: Planar cut of an electrode design that allows shaping of electric field lines with four electrodes. Here electrode 1 is at −999.43 V, electrode 2 is at −1001.28 V, electrode 3 at −994.9 V and electrode 4 at −1002.36 V. Black numbers close to arrows are distances in mm. Green lines are equi-field lines, every 0.2 V/cm. Blue line is the equi-field line at 9.177 V/cm. Red lines are equi-potential lines, every 0.1 V. This configuration shows flat potential and field lines at the origin.

the potential on axis, for example for points on electrodes. First we choose a value for the potential (i.e. final electron energy) and the electric field values at the center of the electrodes. We use Mathematica to visualize the resulting 3D-electric field and to tune the electric field gradient and its gradient to achieve close-to-flat lines. When appropriate values are found, we calculate the corresponding potential at the position of the electrodes, then we use these potentials in the Simion software to check the electric field lines. This procedure gives good results, as can be seen on figure 4.31, where we were able to obtain both flat potential and field lines at the origin. This minimizes the energy spread term $\Delta V_{Curvature}$.

4.4.2 Proposition 1: RFI with orthogonal atomic and electron beams

This first proposition for an improved set-up starts with orthogonal beams, as depicted on figure 4.32, and uses the ionisation process described as Rydberg-field ionisation (RFI). The crucial aspect of this process (see section 4.1.4) is the possibility to create electron/ion pairs in small regions, thanks to the field-resonant condition.

The first two lasers (852 nm and 1470 nm) are focused to beam sizes around 30 µm in all directions, and cross a neutral caesium atomic beam with a width in the x direction of 100 µm at the center of electrodes designed to have a full control of the potential, the electric field and the electric field gradient. The intensity of the lasers is enough to saturate the transitions and produced high-density of atoms in their $7S$ state. The ionising laser propagates along the x direction and is cylindrically focused to a beam size of 5 µm in the z direction and 30 µm in the y direction. The electric field must be very low, not bigger than 10 V/cm, to keep the energy spread below 10 meV. The field configuration should

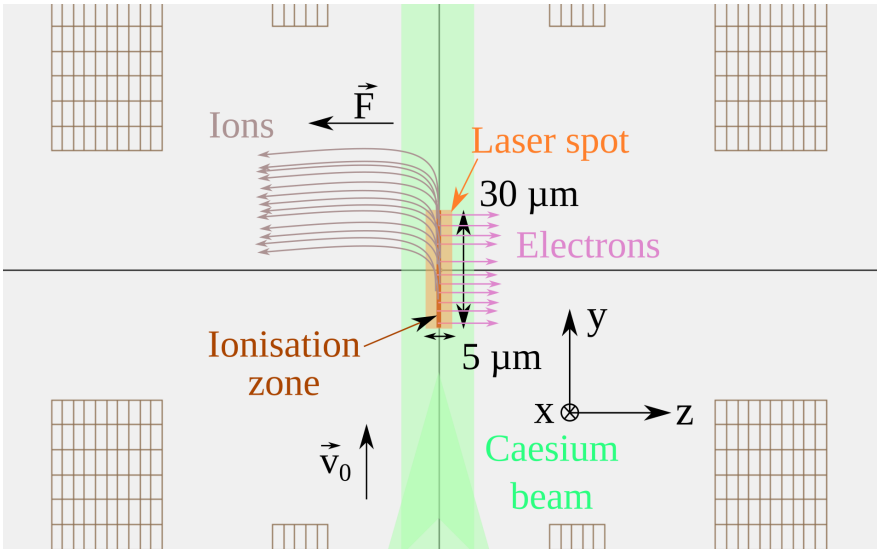

FIGURE 4.32: Schematics of the proposition 1, featuring RFI with orthogonal beams in Simion, with the caesium beam (in green), the laser spot (5 µm*30 µm)(in orange) and the ionisation zone (in brown), not at scale. The initial atomic velocity oriented along y pulls the created ions out of the optical axis.

be tuned to have flat equi-field and equi-potential lines as in figure 4.31 to minimize $\Delta V_{Curvature}$. The ionising laser is precisely tuned to excite a rapidly ionising state at this field value, which is both sufficiently fine and isolated to ensure a good spatial selection.

Such a state can be found on figure 4.33. It is intense and relatively isolated from other states. Its remarkable properties are the result of the mixing of 6 states in a close vicinity, resulting in a very rapid change in its coupling to the continuum.

If we look at the electric field corresponding to the star on figure 4.33, i.e. 9.177 V/cm at $-17.7692\,\mathrm{cm}^{-1}$, here the state can be fitted by a Lorentzian width of $5.57 \times 10^{-4}\,\mathrm{cm}^{-1}$ or 16.7 MHz. This gives a Γ_{Ry} of $1.05 \times 10^{8}\,\mathrm{s}^{-1}$ and is equivalent to a lifetime of 9.53 ns.

We can now estimate the energy spread resulting from the ionisation of this state in the electrode configuration shown on figure 4.31. Although we are in the context of RFI, the model presented in section 4.1.5 does not apply fully, because of the perpendicular orientation of the neutral and electron beams. This means that the atomic velocity is oriented primarily along equi-potentials lines, so even a large ionisation zone in that direction (from a long lifetime) does not increase the energy spread of the resulting electron beam. We can thus safely neglect $\Delta V_{Lifetime}$. From the parameter optimisation presented in section 4.1.5, we can see that neglecting $\Delta V_{Lifetime}$ opens up the possibility to use states with long-lifetime, as this term was dominant at small $\Gamma_{Lifetime}$. This will allow ionisation of thin states, and thus a more stringent spatial selection.

For the estimation of the energy spread due to different starting potential (ΔV_{Stark} and $\Delta V_{Curvature}$) I rely on the field simulation in Simion to relate a field range (the range of different fields where the electrons will be created) to a potential range (that will be transformed into a kinetic energy spread down the column). To estimate the field range ΔF (due to the spectral width of the transition $\Delta\overline{\nu}_{Spec.} = \left(\Gamma_{7s} + \Gamma_{Ry}\right)/2\pi$ and the state's

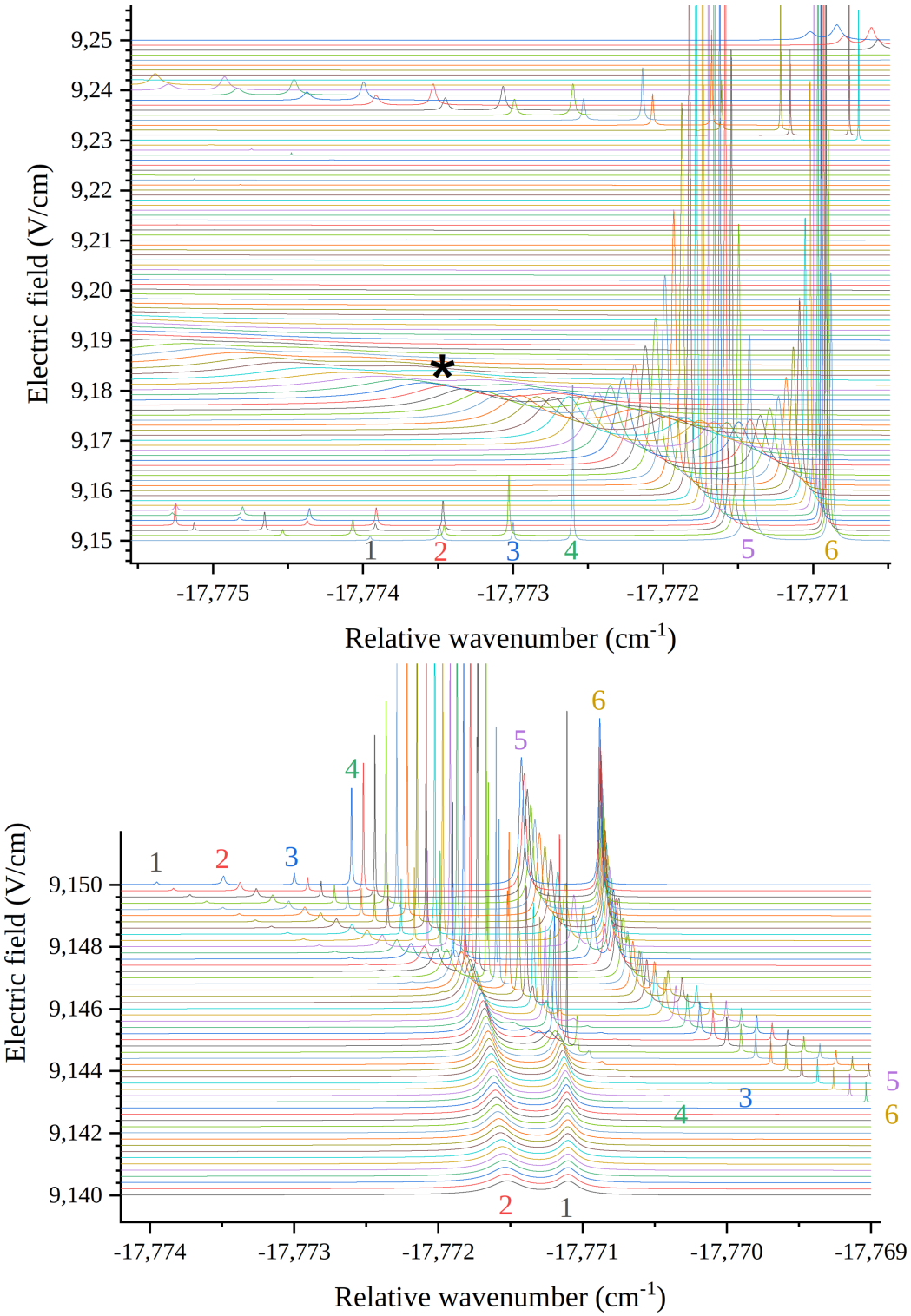

FIGURE 4.33: Stark maps of a state that could be used in a monochromatic Rydberg-field ionisation electron source. The top panel shows the state evolving rapidly into a rapidly ionising state, from an intense and thin state. The star denotes the state's position at a field of 9.177 V/cm where its width indicate an ionising rate of $1.05 \times 10^8\,\mathrm{s}^{-1}$. It is relatively isolated from other states. The bottom panel shows the 6-state Stark mixing occurring at lower fields in higher field resolution (one plot every 2×10^{-4} V/cm, that explains the rapid evolution of the state's coupling to the continuum.

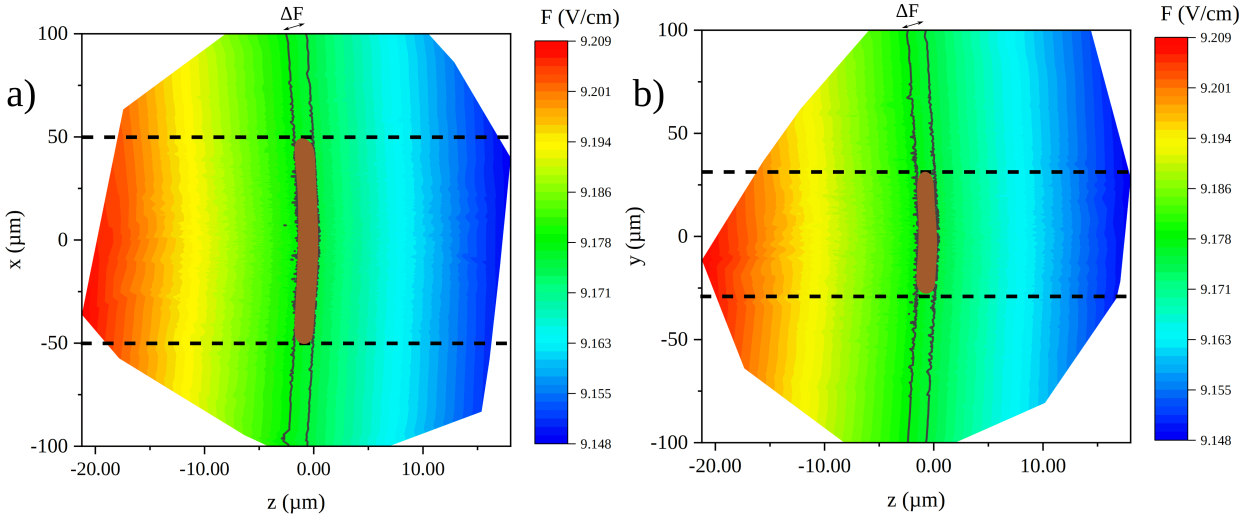

FIGURE 4.34: Results of the resonant conditions on the starting location of electron-ion pairs in a simulation of the excitation of the state presented on figure 4.33 in the field configuration presented on figure 4.31. Particles are generated at random in the laser spot region (see figure 4.32), and their starting field is analysed for the three dimensions (x and z in panel a), z and y in panel b)). The resonant condition ($\Delta F = 1.33\,\mathrm{mV/cm}$) makes the ionisation zone (in brown) very small in the field (z) direction ($\Delta z \approx 1.8\,\mu\mathrm{m}$), and longer in the orthogonal directions where it is limited by the laser waist (30 µm in the y direction and the atomic beam waist in the x direction (100 µm)).

Stark slope $\frac{d\overline{\nu}}{dF}$) I use:

$$\Delta F = \Delta\overline{\nu}_{Spec.} / \left(\frac{d\overline{\nu}}{dF}\right) \tag{4.45}$$

From figure 4.33 I can estimate the Stark slope of this state to be $\frac{d\overline{\nu}}{dF} = 0.5\,\mathrm{cm}^{-1}/(\mathrm{V/cm})$, and its linewidth $\Delta\nu = 20.0\,\mathrm{MHz}$, which gives:

$$\Delta F = \frac{6.67 \times 10^{-4}}{0.5} = 1.33\,\mathrm{mV/cm} \tag{4.46}$$

To relate this field range to the potential range, I simulate a large number of pair creations around the origin of my simulation, and select only the electrons and ions created at the field value of $9.177\,\mathrm{V/cm} \pm 1.33\,\mathrm{mV/cm}$ as can be seen on figure 4.34. This shows how the spatial selection inherent to RFI acts, by selecting only the atoms that experience the field resonant with the laser. The small linewidth of the state chosen here (thanks to the orthogonal arrangement) makes the spatial selection very stringent. The resulting size of the ionisation zone in the z direction is 1.8 µm.

I then check the starting potential for each of these selected pairs, and I find that the determination of the starting potential distribution is limited by the simulation's grid resolution, which is at 1 mV. I can thus conclude that the energy spread (FWHM of the energy distribution) from differential starting potential would be less than 2 meV.

The effect of the ionic space-charge and electron-electron interactions will be dealt with in details in section 4.4.4, and we will see that in this configuration the energy

spread should be kept under 5 meV. Provided the potentials are supplied with a stability of 1×10^{-6} (less than 1 mV ripple at 1 kV), this source could potentially produce an appropriate electron beam for HREELM.

I note that the presence of ions will also surely influence the electric field lines and possibly alter their flatness, but a more detailed investigation would be needed to evaluate precisely this influence. For a continuous production of electrons, the density of ions will rapidly arrive at a stationary value, so this influence (shifting the field-lines for example) may be compensated for by slightly changing the electrode potentials or the wavelength of the ionising laser. The precise electric-field value to excite this state should of course be tuned experimentally in function of the field experimental inhomogeneities, and whether it gives better results to increase the lifetime of the state (excite the state at a point where its Γ is smaller) in order to tighten the spatial selection. The electric fields of 10 V/cm is enough to efficiently extract the electrons and this configuration could very well represent a viable option for HREELM. Simulations on the published HREELM design showed good compatibility with this extraction field[27].

Concerning the current, the ionisation zone would represent only a thin (but rather long) slice of surface S of the atomic beam (see figure 4.32), meaning that only a small portion of the total neutral atomic beam would be excited and ionised. That would require a dense atomic beam to produce enough electrons: the density of neutral ground atoms $d_{Cs}^{prop.1}$ to produce a continuous beam of $I = 100\,\text{pA}$ is:

$$d_{Cs}^{prop.1} = \frac{I}{e\gamma^{Tot} S v_0} \tag{4.47}$$

with γ^{Tot} a global ionisation efficiency from the ground state coefficient. To estimate γ^{Tot} I define:

$$N^{el} = N^{7S}\gamma^{ION} \tag{4.48}$$
$$N^{7S} = N^{6P}\gamma^{1470} \tag{4.49}$$
$$N^{6P} = N^{6S}\gamma^{852} \tag{4.50}$$

with N being the stationary number of electrons, atoms in the $7S$, the $6P$ or the $6S$ state in the ionisation zone, and γ the conversion efficiency between these different states, $\gamma^{Tot} = \gamma^{ION} * \gamma^{1470} * \gamma^{852}$ and $N^{el} = \gamma_{Tot} N^{6S}$, which make the link between the electron density and the ground state atomic density. Taking reasonable values for $\gamma^{852} = \gamma^{1470} = 0.5$[8], γ^{ION} (0.1, see the estimation in section 4.1.2) and $S = 1.8\,\mu\text{m} * 100\,\mu\text{m}$ (Δz given by the resonant condition and Δx given by the neutral beam width), I finally have:

$$d_{Cs}^{prop.1} = \frac{100 \times 10^{-12}}{e * 0.5 * 0.5 * 0.1 * 1.8 * 100 * 10^{-12} * 274} = 5 \times 10^{11}\,\text{cm}^{-3} \tag{4.51}$$

This calculated required atomic densities is in the upper end of most reported values for densities in collimated neutral caesium beams: $10^9\text{cm}^{-3} - 10^{11}\text{cm}^{-3}$[39], 10^{10}cm^{-3}[40],

[8] Coherent-transfer methods could allow a better efficiency, as already demonstrated in a cold electron source[38]

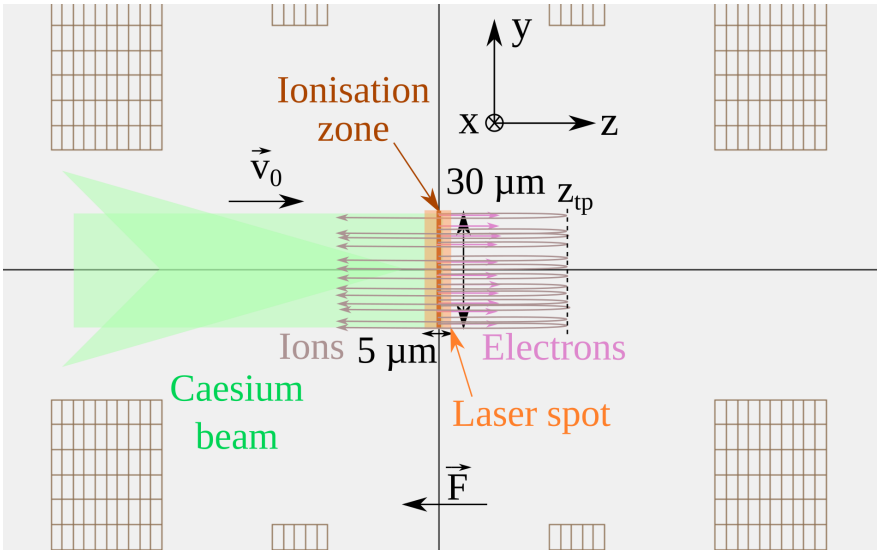

FIGURE 4.35: Schematics of the proposition 2 in the Simion electrode simulation, featuring RFI with collinear beams, with the caesium beam (in green), the laser spot (in orange) and the ionisation zone (in brown), not at scale. The initial velocity oriented along z creates a turning-point for the ions down the electron beam represented at $z = z_{tp}$

$3 \times 10^{13}\,\mathrm{cm}^{-3}$[41] (a surprisingly high value). This justifies the caesium oven studies reported in section 3.1.2 to lower the angular spread of the produced beam and thus increase its density at the laser intersection.

4.4.3 Proposition 2: RFI with collinear atomic and electron beams

The second proposition uses the same state and the same electric field/potentials. The main difference is that the neutral beam is now parallel to the electron axis, as shown on figure 4.35.

This orientation changes mainly two things: the density of ions in the ionisation zone and the overlap between the atomic beam and the ionising laser beam[9]. The first effect will be dealt with in details in section 4.4.4, and I focus on the second effect here. Orienting the atomic beam along the electron axis would indeed increase the intersection between the atomic beam and the ionisation zone, and thus require a less dense atomic beam to produce enough electrons. Indeed the very small ionisation zone ($\Delta z = 1.8\,\mu\mathrm{m}$) in the previous proposition comes from a stringent spatial selection of RFI. In the collinear configuration a larger portion of the atomic beam will be in the resonant region (see figure 4.35) because, with a neutral beam of waist 100 µm in the x direction, the overlap is the bigger rectangle $S = 100 \times 30 \times 10^{-12}\mathrm{m}^{-2}$. The required atomic density is now:

$$d_{Cs}^{prop.2} = 3 \times 10^{10}\,\mathrm{cm}^{-3} \tag{4.52}$$

[9]It would also mean that the neutral caesium beam is oriented towards the rest of the electron column, which could cause caesium pollution. This can be avoided with a retractable on-axis cold finger placed at the center of the beam-separating prism (where the electrons don't pass)

while following the same strict resonant criteria, thus relaxing the conditions on the atomic beam density without increasing the energy spread due to the extracting field[10].

In this collinear configuration the velocity of the ions v_0 is oriented along the electric field principal component. This means that the electric field will reflect these ions back to the direction where the neutral atoms came from. The position of the turning-point of the ions is given by $z_{tp} = \frac{m_{ions} v_0^2}{2 q_{ions} F}$, which gives 56 µm in our configuration (see figure 4.35).

I note in passing that the collinear orientation allows a variant of this proposition, that would be to use velocity-induced field-ionisation (VIFI) instead of RFI. In the VIFI mechanism, the target Rydberg state must be excited where it is the most intense and stable, and the velocity of the atom will drive it to higher electric field regions, where it will rapidly ionise. Looking at the Stark map on figure 4.33, we see that the chosen state (5) is the most stable and intense at a field of 9.155 V/cm. In the hypothesis that we excite it at this field, we can calculate the ionisation probability $P[F(z)]$ from equation 4.19, and the procedure introduced in section 4.1.3. We take an atomic velocity of 274 m/s, typical for caesium effusive beams. This gives us the shape of $\Gamma(F)$, visible on figure 4.36, along with the shape of $P[F(z)]$. This plot shows that for the state 5 excited around 9.155 V/cm, 68.27% of the ionisation occur in a field slab of $\Delta F_{2\sigma} = 0.0115$ V/cm, which corresponds to twice the standard deviation of a Gaussian peak. The FWHM is given by $1.18 \times \Delta F_{2\sigma} = 0.0135$ V/cm which, in our field configuration, corresponds to a slab of 7 µm and a potential difference of 6.4 mV.

It is apparent from equation 4.19 that the initial velocity of the ions plays a large role on the size of the ionisation zone, and in the density of ions in the ionisation zone. Increasing the velocity will increase the size of the ionisation zone and the resulting energy spread but does not change the ion density until the velocity is low enough for the ions to be directly removed from the ionisation zone by the electric field. I note that VIFI with this state could produce much smaller ionisation zone in a higher field gradient[25], but I don't detail it as it would need an entirely different electrode set-up.

The proposition 2 thus rests on RFI with stringent resonant condition as it gives a lower energy spread.

Thus the two propositions (1 and 2) will differ in the influence of the ionic space-charge, and the atomic density required for the same electron current (by a factor of 17). I have already analysed the density difference, and I can now study the ionic space-charge differences.

4.4.4 Simulating the performance of electron sources

I performed accurate particle simulations of the extraction of the electrons in the presence of the ions, to evaluate the impact of the photo-ions and the inter-electron interactions on the resulting electron energy spread in the two proposed configurations and in some

[10] There is indeed a slight increase in the energy spread as the velocity of atoms in now oriented along the electric field, and atoms at $v_0 = 274$ m/s with an ionisation rate of $\Gamma_{Ry} = 1.05 \times 10^8$ s^{-1} are excited on 1.8 µm but ionise in 2.6 µm. This would normally increase the energy spread in comparison to prop. 1. However, for the simplicity of the comparison between props. 1 and 2, I keep the same value of Δz. We must keep in mind that, in this collinear configuration, the model introduced in section 4.1.5 shows that the optimal value for Γ_{Ry} is around 1×10^9 m^{-1} (see figure 4.10 c)). Experimentally this would simply mean to address the state at a slightly higher electric field and retrieve the same energy spread as in prop. 1

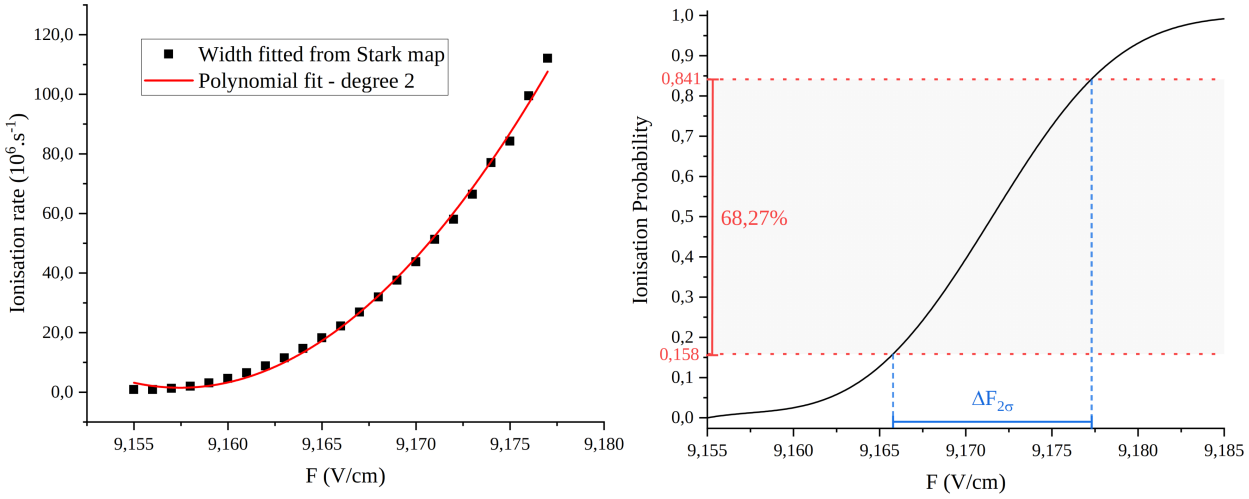

FIGURE 4.36: Determination of the electric field slab in the case of VIFI. The left panel presents the evolution of the ionisation rate of the state 5 presented in figure 4.33 in an increasing electric field. Values are extracted from the Stark map and fitted by a 2-degree polynomial. The right panel uses this fit to calculate the ionisation probability from equation 4.19 in function of the electric field, at $v = 274\,\mathrm{m/s}$ and in the electric field configuration presented on figure 4.31. From that we obtain an estimation of the resulting ionising field spread $\Delta F_{2\sigma}$ which entails 68.27% of the distribution. The FWHM of a Gaussian peak is then given by $1.18 \times \Delta F_{2\sigma}$.

variations of these propositions. I used the General Particle Tracer[42,43] code to simulate the trajectories of 3120 pairs of ions and electrons created almost at rest at random positions (but not closer than 1 µm from another particle) in a 5 µs time interval. This corresponds to an electron current of 100 pA[11]. Table 4.3 shows the 12 performed simulations and the tested parameters, with the impact on the potential difference energy and the inter-particle-related energy spread and potential shift.

These simulations show the performance of the sources described in sections 4.4.2 and 4.4.3 taking into account all the dominant sources to the energy spread as described in section 1.4 (comparing simulations n°5 and n°6 for proposition 1 and n°7 and n°8 for proposition 2). I can thus safely assume that the resulting electron energy spread is close to what an experimental realisation would give. The comparison between all simulations are done in details on figures 4.37, 4.38 and 4.39. These simulations also allow to compare my propositions with an hypothetical cold atom electron source using RFI ($|v_0| = 0$, with the simulations n°9, n°10). Simulations n°1, n°2, n°3 and n°4 show the impact of using RFI to lower the ionisation zone size in the field direction Δz from 7 µm to 2 µm, in comparison to a situation close to threshold-photoionisation (n°3 and n°4) and the VIFI variant of proposition 2 (n°1 and n°2).

It clearly shows that reducing the size Δz of the ionisation zone (with RFI for example) reduces the potential difference term (from 5.5 meV to 1.8 meV), but also increases the impact of inter-particle interactions (IPI: electrons-electrons interaction, space-charge

[11] for some cases, the computer code stalled around 3 µs, so I stopped the particle creation at 2 µs, thus reducing the number of simulated pairs down to 1248 but conserving the same current. Figure 4.38 shows that stationary state is attained before 1 µs so this only reduces the statistics but still captures the essential behaviour

N°	Beams	Δz(µm)	$\lvert v_0 \rvert_{mean}$ (m/s)	IPI	ΔV_{shift} (mV)	ΔE (meV)
1 (VIFI)	$\parallel$	7	274	ON	-22	8.1
2 (VIFI)	$\parallel$	7	274	OFF	0	5.5
3 (Phot.)	$\perp$	7	274	ON	-14	7.6
4 (Phot.)	$\perp$	7	274	OFF	0	5.5
5 (prop. 1)	$\perp$	2	274	ON	-14	7.6
6 (prop. 1)	$\perp$	2	274	OFF	0	1.8
7 (prop. 2)	$\parallel$	2	274	ON	-22	3.7
8 (prop. 2)	$\parallel$	2	274	OFF	0	1.8
9	-	2	0	ON	-24	4.7
10	-	2	0	OFF	0	1.8
11	-	7	0	ON	-24	5.8
12	-	7	0	OFF	0	5.5

TABLE 4.3: Sum-up of the performed GPT simulations, showing explicitly the tested parameters in each case and the resulting potential shift and energy spread. These simulations allows to test three parameters: the relative orientation of the neutral atom and the electron beam, the ionisation zone extension in the field direction (Δz), and the mean amplitude of the initial atomic velocity ($|v_0|$). To test the effect of these parameters on the ionic space-charge and disorder-induced heating (see sections 1.4.2 and 1.4.4), I must simulate all these cases with and without interparticle interactions (IPI).

effect of the ions and stochastic electron-ion interaction). This increase is the biggest when the atomic beam is orthogonal to the z axis (simulations 5,6), featuring 5.8 meV of additional energy spread due to the IPI, where a parallel beam (simulations 7,8) feature only 1.9 meV of additional energy spread. I interpret this high value of added energy spread in the case of an orthogonal beam as mainly due to ionic space-charge, along the y axis. As the beam has an extent of 30 µm in the y direction, the electric field induced by the ion accumulation at positive y induces a potential difference on the electrons, depending on their initial y value.

In a bigger ionisation zone ($\Delta z = 7$ µm), the difference in the impact of IPI is smaller (and inverted), with 2.1 meV and 2.6 meV additional energy spread for orthogonal and parallel beams respectively. This can be explained by the fact that increasing the Δz size of the ionisation zone decreases the density along other coordinates, particularly along y (because the current is kept the same). This thus reduces the effect of ionic space-charge along y and decrease the associated energy spread. However, the fact that ions travel back and forth in the ionisation region probably increases the stochastic ion-electron interaction, leading to an increased energy spread in the parallel configuration than in the orthogonal configuration.

The lowest energy spread in the six simulations with IPI is 3.7 meV and is obtained with a small ionisation zone in the z direction ($\Delta z = 2$ µm), parallel beams and an atomic beam velocity of 274 m/s (simulation n°7). The same parameters but with cold atoms ($v = 0$ m/s) (simulation n°9) gives an energy spread of 4.7 meV. This shows that the back-and-forth movement of the ions actually removes 1 meV from the energy spread (24% of the total energy spread). This can be explained by the fact that, once the stationary state is attained, the electrons are created in-between two cylinders of charged ions (the ones

travelling towards $+z$ and the ones travelling towards $-z$). This situation is probably more favourable in terms of detrimental ion space-charge than when electrons are created at the end of an ion cylinder (like in the cold atom case where no ion travels towards the $+z$ axis).

Figure 4.37 shows the transverse positions of electrons after extraction, that is directly related to the emittance of the electron source. Very clearly we see the increase in emittance due to inter-electron Coulomb repulsion (as stated in section 1.4.4), that increases the transverse cross-section of the electron beam in all simulations where interparticle interactions are activated. Without interactions the transverse emittance is $\epsilon_T = 2.52 \times 10^4\,\mu m^2\,(m/s)^2$ and $\epsilon_T = 4.92 \times 10^3\,\mu m^2\,(m/s)^2$ while it becomes, for propositions 1 & 2 (simulations n°5-8), $8.08 \times 10^{12}\,\mu m^2\,(m/s)^2$ and $1.17 \times 10^{14}\,\mu m^2\,(m/s)^2$, respectively. The fact that ions are travelling back and forth in the ionisation region in the parallel configuration with initial atomic velocity along z leads to an emittance growth 74 times bigger than in the orthogonal configuration (proposition 1). This increased emittance comes in part from the electron-electron (reversible) repulsion, but also in part from the Loeffler effect (irreversible, see section 1.4.4). The electron-electron repulsion should be very similar in both cases so the factor of 74 comes mainly from increases electron-ion interactions. Quantifying the reversible/irreversible fraction of this emittance increase would require further analysis. Another noticeable feature is the lowest spot size in the y axis than in the x axis, showing that the ions have a slight focusing role in the y axis.

Figure 4.37 also clearly shows that in the orthogonal configurations (simulations n°3 and n°5) the ionic space-charge displaces the electron beam off-axis, at $y = +120\,\mu m$ in the direction of the initial atomic velocity. This is explained easily by the initial velocity of atoms in the $+y$ direction that leads to the accumulation of ions in the positive y region, that steer the electron beam toward positive y. It is an important effect to have in mind, that could potentially induce beam displacement in the column. This would thus need to be corrected in an actual source, probably best with a mechanical correction to the angle between the electron source and the rest of the column.

Figure 4.38 shows the dynamics in the electron energies for all simulations, showing the energy spread due to starting potential differences, the energy spread due to interparticle interactions (both additional starting potential differences due to ionic space-charge and disorder-induced heating, see sections 1.4.2 and 1.4.4), as well as the evolutions of these energies over time. Clearly in the case of active inter-particle interactions there is a transient evolution during 1 µs towards a stationary state, due to the slow accumulation of ions in the ionisation zone. This evolution lowers the final absolute electron kinetic energy (shifts the starting electron potential of ΔV_{shift}) by 14 meV, 22 meV or 24 meV depending on the different parameters (see table 4.3). Once in the stationary state, we can analyse the energy spread without IPI and with IPI. This inter-particle related additional energy spread comes mainly from disorder-induced heating (as shown by other simulations with only space-charge interactions that don't show additional energy spread[12]).

This figure shows clearly that, depending on the beam orientations, Δz and v_0, but with the same electron current, the energy spread due to disorder-induced heating will add from 0.3 meV (simulation n°11) to 5.8 meV (simulation n°5) to the electron energy

[12] in GPT, there is the function *spacecharge3Dclassic* that entails all interparticle interactions, and the *spacecharge3Dmesh* that entails only space-charge interactions. All the presented simulations are thus done with *spacecharge3Dclassic* with an *xaccuracy* of 7 and a *taccuracy* of 9

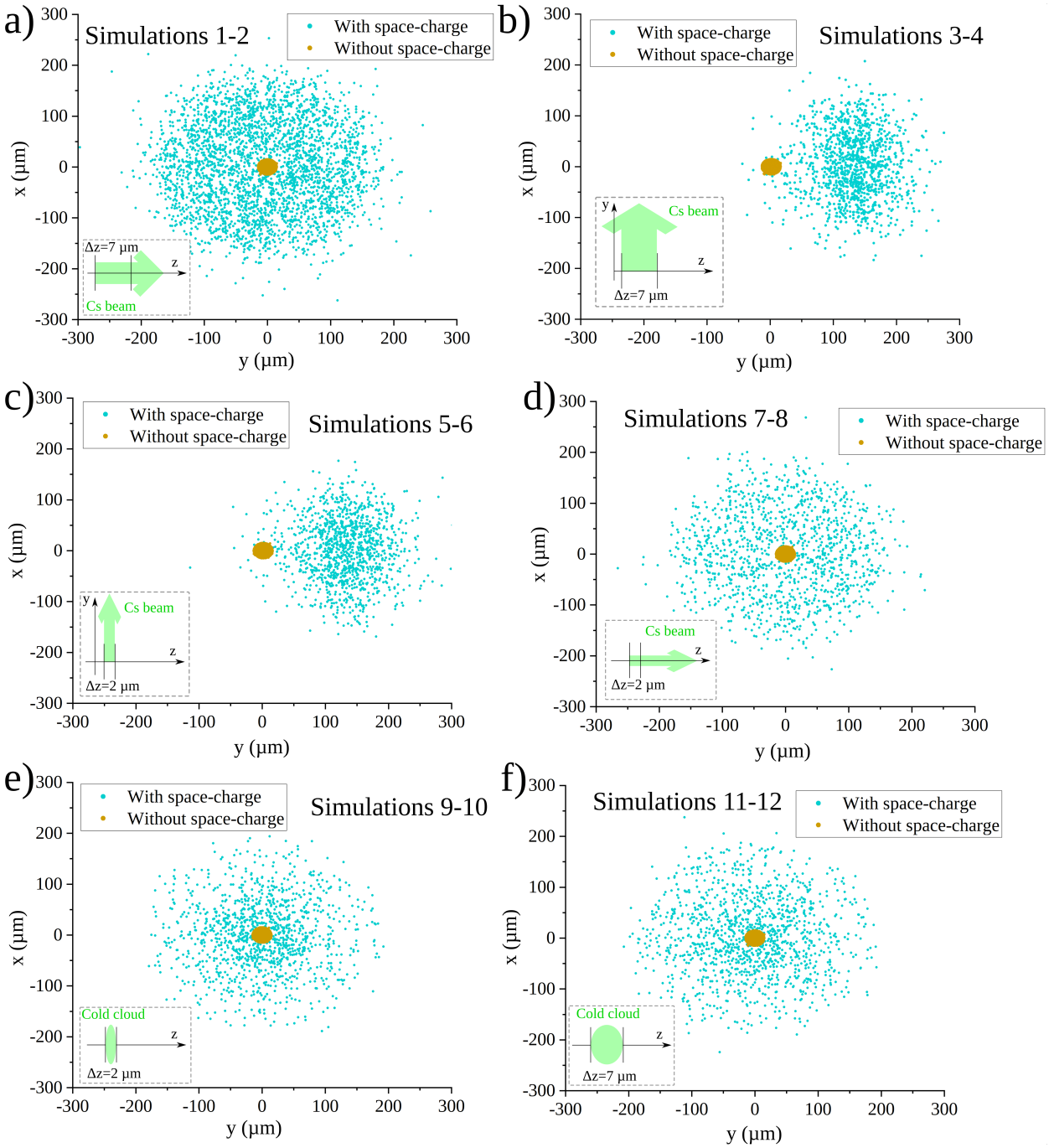

FIGURE 4.37: Transverse electron positions after extraction in the GPT simulations under a static field of 9.17 V/cm and a current of 100 pA (see text for rest of parameters), showing the impact of interparticle interactions in each case, for the simulations detailed in table 4.3 a) Simulations n°1-2 b) 3-4 c) 5-6 (Proposition 1) d) 7-8 (Proposition 2) e) 9-10 f) 11-12. A schematic on each panel recalls the important parameters (orientation and velocity of the neutral beam, size of the ionisation zone in z).

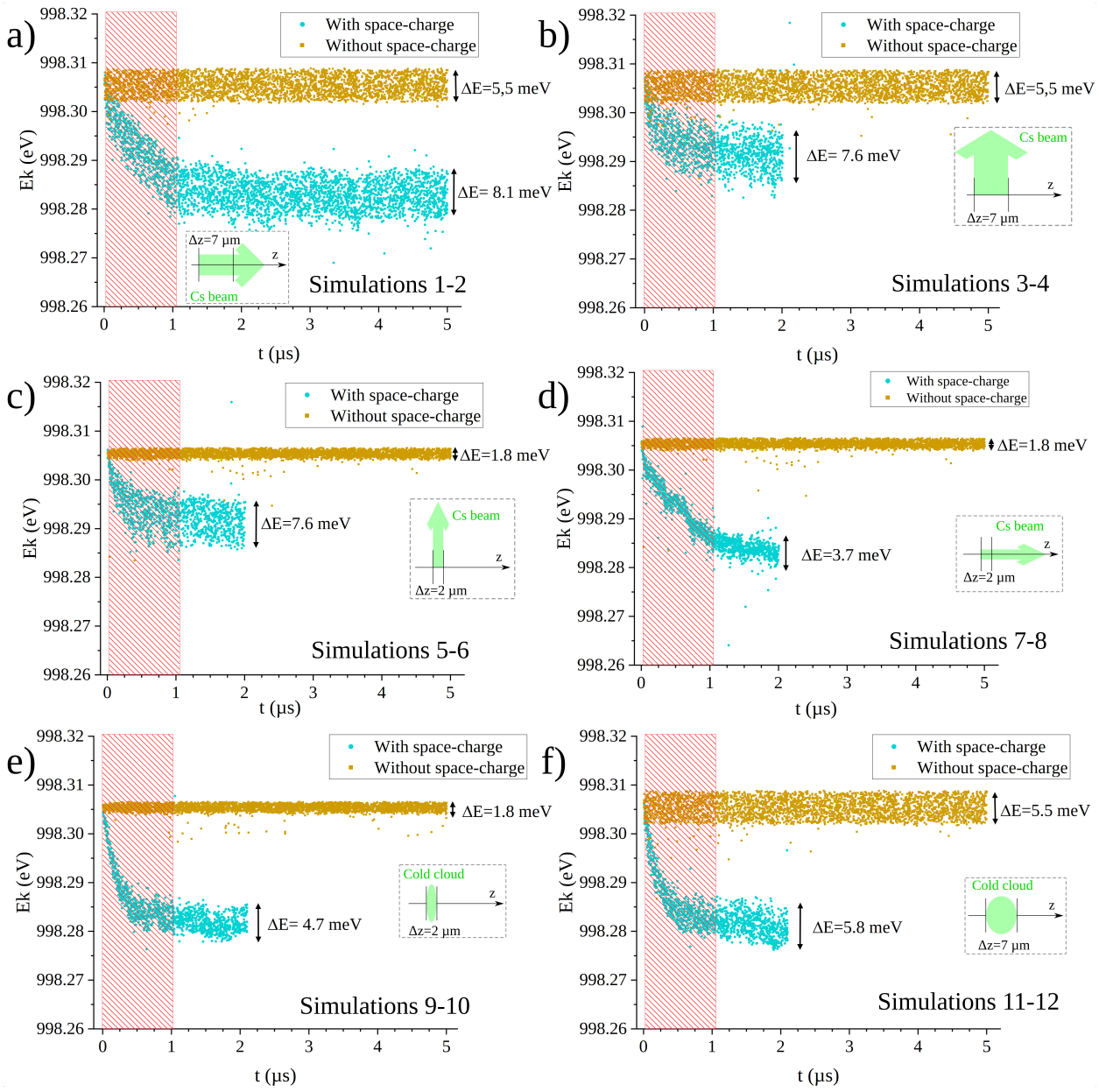

FIGURE 4.38: Dynamics of the electrons creation in the GPT simulations under a static field of 9.17 V/cm and a current of 100 pA (see text for rest of parameters), showing the impact of interparticle interactions in each case, for the simulations detailed in table 4.3. a) Simulations n°1-2 b) 3-4 c) 5-6 (Proposition 1) d) 7-8 (Proposition 2) e) 9-10 f) 11-12. A schematic on each panel recalls the important parameters (orientation and velocity of the neutral beam, size of the ionisation zone in z).

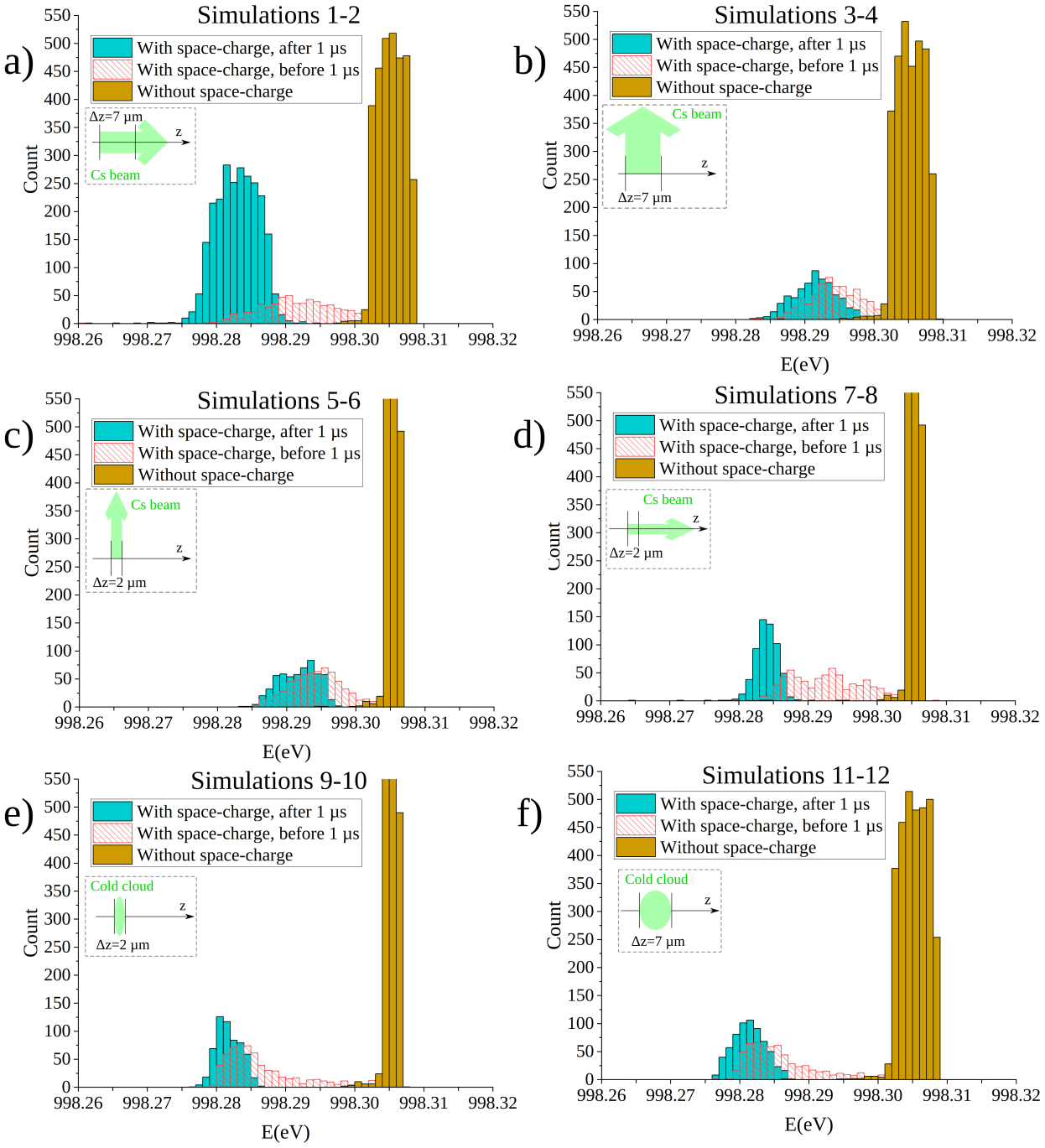

FIGURE 4.39: Electron energies after extraction in the GPT simulations, under a static field of 9.17 V/cm and a current of 100 pA (see text for rest of parameters), showing the impact of interparticle interactions in each case, for the simulations detailed in table 4.3. a) Simulations n°1-2 b) 3-4 c) 5-6 (Proposition 1) d) 7-8 (Proposition 2) e) 9-10 f) 11-12. The most probable energies without space-charge in c) d) e) are not shown entirely and go up to 1800 counts. A schematic on each panel recalls the important parameters (orientation and velocity of the neutral beam, size of the ionisation zone in z).

spread. This illustrates the fact that these simulations are essential to accurately predict the energy spread of an electron source.

Figure 4.39 shows the final electron energy in all configuration with and without inter-particle interactions. We see clearly what was already underlined in figure 4.38, that the lowest energy spread is attained with an ionisation zone of 2 µm with an initial velocity of the ions on the z axis. Comparing with the simulations with atoms at rest (n°9, 10, 11 and 12), we see that ionising atoms in a beam is better in terms of IPI (both for the potential shift and the additional energy spread) than ionising cold atoms.

Section summary

A continuous electron source for HREELM

In this section I built up on the acquired knowledge on the different ionisation phenomena and their links to the resulting electron energy spread presented before to propose a 4-electrodes configuration that allows a better control over the field and potential curvature lines in the extraction zone; and two sets of experimental conditions providing estimated energy spread of 3.7 meV (1.9 meV from IPI and 1.8 meV from initial potential differences) and 7.6 meV (5.8 meV from IPI and 1.8 meV from initial potential differences). These two propositions differ from their collinear/orthogonal (respectively) configuration of the neutral atom and electron beams. The usually dominant energy spread sources were investigated and estimated: field inhomogeneities, ion-induced space charge potential shift and disorder-induced heating (stochastic interactions between electrons and with ions). Simulations including detailed inter-particle calculations show a time-dependent energy shift that is stationary after 1 µs. I conclude that the orthogonal configuration induces 3 times more added energy spread and 74 less emittance growth, but also a potentially detrimental off-axis beam shift. This could be circumvented by proper corrective deflection or even the introduction of an controllable angle between the source electron axis and the rest of the set-up. The parallel configuration, with a small ionisation zone of $\Delta z = 2\,\mu m$ shows the smallest energy spread (3.7 meV) of the six tested configurations.
I thus proposed a set of experimental conditions that could be used as an electron source for HREELM. It is based on an existing Rydberg state ionised under 9.17 V/cm with a stringent resonant-field condition, giving an ionisation zone extension in the field direction of 1.8 µm. It also requires a neutral beam density of $3 \times 10^{10}\,cm^{-3}$ to achieve 100 pA, 17 times less dense than to achieve the same current in an orthogonal configuration.

4.5 Conclusion on the monochromatic electron source

In this chapter I have presented the experimental efforts to produce and study a monochromatic continuous beam electron source. The presentation of the experimental set-up with the Gatan electron spectrometer showed how we adapted this instrument to our experiments, to experimentally test our ideas on the realisation of such a source. A further

investigation of the different ionisation processes allowed a clear distinction between photo-ionisation, Rydberg-field ionisation and velocity-induced field ionisation, as well as a detailed modelling on the energy spread in the case of Rydberg-field ionisation. An increased electron current and electron emission directionality strongly favours RFI as the method of choice for our purpose.

Experimental limitations in the energy spread measurements were clearly identified, but we nevertheless demonstrated a very good control of the Gatan spectrometer in an electron energy range outside its specifications. We also demonstrated the production of an electron beam at 1.5 keV with less than 60 meV energy spread in photo-ionisation, and current above 500 pA in Rydberg-field ionisation (with the laser at 794.241 65 nm under a field of 2170 V/cm). The results obtained on the experimental set-up confirmed the modelling to a certain extent, and really underlined the importance of a very good control of the electric field curvature in the ionisation zone. In particular it showed that the standard aperture lenses configuration is not compatible with a monochromatic electron beam from Rydberg-field ionisation or velocity-induced ionisation, because of the very-high field curvature induced by the small apertures.

From there I proposed a new electrode design to allow an improved control on the field configuration, a set of potentials that would create a flat potential/field lines configuration, as well as one particularly interesting Rydberg state. This state, in this field configuration, in this electrode design, could be ionised by either Rydberg-field ionisation or velocity-induced ionisation and create a monochromatic electron beam, in both collinear or orthogonal atomic/electron beams configurations. Simulations with GPT in either case show that the total energy spread will be less than 10 meV at 100 pA, even 3.7 meV for the parallel configuration, making it a potential electron source for the HREELM project.

This gives us a clear roadmap for the future of these continuous beam studies, for improving the energy-measuring set-up and confirming the low energy spread that we predict.

During the course of this work, I also spent some time to work on an implementation of the ideas presented this chapter on an ion source. This work took place at the Orsay Physics company in the south of France (one week of presence there), where I provided calculations and insights from *Laboratoire Aimé Cotton*. This is largely covered by industrial secret and not presented here, but the main idea is to reverse the polarity of the whole source to make it a monochromatic caesium ion source[40]. The direct application is in the field of focused ion-beam (FIB) microscopy which is a rapidly developing technique, widely used in the semi-conductor industry, for nano-lithography and material analysis. The very high mass of Cs^+ ions (compared to electrons) means that laser cooling the neutral Cs atoms will directly improve the energy spread of the ion source. The advantage of an ion source with very low energy spread is a better control of the impact energy, reduced chromatic aberrations but most importantly the possibility to lower down the final focus size of the ion beam. Usual ion sources are limited to 5 nm spot sizes, but ion sources from laser-cooled atoms have shown spot sizes around 2 nm[44] opening-up new possibilities in terms of surface ion microscopy, nanofabrication, and miniaturisation of semi-conductors.

References

[1] N. Šibalić, J. D. Pritchard, K. J. Weatherill, and C. S. Adams. "ARC: An open-source library for calculating properties of alkali Rydberg atoms". In: *Computer Physics Communications* 220.319 (2017). DOI: 10.1016/j.cpc.2017.06.015.

[2] G. ten Haaf, S. H. W. Wouters, P. H. A. Mutsaers, and E. J. D. Vredenbregt. "Cavity-enhanced photoionization of an ultracold rubidium beam for application in focused ion beams". In: *Physical Review A* 96.5 (2017). ISSN: 1050-2947. DOI: 10.1103/PhysRevA.96.053412.

[3] B. Knuffman, A. V. Steele, and J. J. McClelland. "Cold atomic beam ion source for focused ion beam applications". In: *Journal of Applied Physics* 114.4 (2013), p. 044303. ISSN: 0021-8979. DOI: 10.1063/1.4816248.

[4] Steven T. Manson and Anthony F. Starace. "Photoelectron angular distributions: energy dependence for s subshells". In: *Reviews of Modern Physics* 54.2 (1982), pp. 389–405. ISSN: 0034-6861. DOI: 10.1103/RevModPhys.54.389.

[5] Warren Ong and Steven T. Manson. "Photoelectron angular distributions for the outer shell of the alkali-metal atoms". In: *Phys. Rev. A* 20 (6 1979), pp. 2364–2369. DOI: 10.1103/PhysRevA.20.2364. URL: https://link.aps.org/doi/10.1103/PhysRevA.20.2364.

[6] Milton A. Chaffee. "The Angular Distribution of Photoelectrons Ejected by Polarized Ultraviolet Light in Potassium Vapor". In: *Phys. Rev.* 37 (10 1931), pp. 1233–1237. DOI: 10.1103/PhysRev.37.1233. URL: https://link.aps.org/doi/10.1103/PhysRev.37.1233.

[7] Keh-Ning Huang and Anthony F. Starace. "Ab initio treatment of final-state spin-orbit interactions: Photoionization of the 6*s* electron in cesium". In: *Phys. Rev. A* 19 (6 1979), pp. 2335–2346. DOI: 10.1103/PhysRevA.19.2335. URL: https://link.aps.org/doi/10.1103/PhysRevA.19.2335.

[8] G V Marr. "The effect of spin-orbit interaction on the angular distribution of photoelectrons from alkali atoms". In: *Journal of Physics B: Atomic and Molecular Physics* 7.3 (1974), pp. L47–L50. DOI: 10.1088/0022-3700/7/3/015. URL: https://doi.org/10.1088%2F0022-3700%2F7%2F3%2F015.

[9] W. J. Engelen, E. J. D. Vredenbregt, and O.J. Luiten. "Analytical model of an isolated single-atom electron source". In: *Ultramicroscopy* 147 (2014), pp. 61–69. ISSN: 03043991. DOI: 10.1016/j.ultramic.2014.07.001.

[10] Scofield. "Angular and polarization correlations in photoionization and radiative recombination". In: *Physical review. A, General physics* 40.6 (1989), pp. 3054–3060. ISSN: 0556-2791. DOI: 10.1103/PhysRevA.40.3054.

[11] Anthony Starace. "Photoionization of Atoms". In: *Springer Handbook of Atomic, Molecular, and Optical Physics*. Ed. by Gordon Drake. Vol. 102. New York, NY: Springer New York, 2006, pp. 379–390. ISBN: 0142196355. DOI: 10.1007/978-0-387-26308-3_24.

[12] Pindzola. "Photoelectron angular distributions for excited ns subshells of cesium". In: *Physical review. A, General physics* 32.3 (1985), pp. 1883–1884. ISSN: 0556-2791. DOI: 10.1103/PhysRevA.32.1883.

[13] Cuéllar, Compton, Carman, and Feigerle. "Photoelectron angular distributions for ns (n=8-12) subshells of cesium: Relativistic effects". In: *Physical review letters* 65.2 (1990), pp. 163–166. ISSN: 1079-7114. DOI: 10.1103/PhysRevLett.65.163.

[14] O. Fedchenko, S. Chernov, G. Schönhense, R. Hahn, and D. Comparat. "Narrow-band pulsed electron source based on near-threshold photoionization of Cs in a magneto-optical trap". In: *Physical Review A* 101.1 (2020). ISSN: 1050-2947. DOI: 10.1103/PhysRevA.101.013424.

[15] M. L. Zimmerman, M. G. Littman, Mi. M. Kash, and D. Kleppner. "Stark structure of the Rydberg states of alkali-metal atoms". In: *Phys. Rev. A* 20 (6 Dec. 1979), pp. 2251–2275. DOI: 10.1103/PhysRevA.20.2251.

[16] F. Robicheaux. "Time- and energy-dependent response of Cs in a strong electric field". In: *Physical Review A* 56.5 (1997), pp. 4032–4037. ISSN: 1050-2947. DOI: 10.1103/PhysRevA.56.4032.

[17] Ch. Bordas, F. Lépine, C. Nicole, and M. J. J. Vrakking. "Semiclassical description of photoionization microscopy". In: *Physical Review A* 68.1 (2003), p. 1463. ISSN: 2469-9926. DOI: 10.1103/PhysRevA.68.012709.

[18] T. Barillot et al. "Influence of long-range Coulomb interaction in velocity map imaging". In: *The Journal of Chemical Physics* 147.1 (2017), p. 013929. ISSN: 0021-9606. DOI: 10.1063/1.4982616.

[19] S. Cohen, P. Kalaitzis, S. Danakas, F. Lépine, and C. Bordas. "Photodetachment and photoionization rainbows and glories". In: *Journal of Physics B: Atomic, Molecular and Optical Physics* 50.6 (2017), p. 065002. ISSN: 0953-4075. DOI: 10.1088/1361-6455/aa5c5e.

[20] R. W. Speirs, A. J. McCulloch, B. M. Sparkes, and R. E. Scholten. "Identification of competing ionization processes in the generation of ultrafast electron bunches from cold-atom electron sources". In: *Physical Review A* 95.5 (2017). ISSN: 1050-2947. DOI: 10.1103/PhysRevA.95.053408.

[21] E. Fermi. "Über das Intensittsverhltnis der Dublettkomponenten der Alkalien". In: *Zeitschrift fr Physik* 59.9-10 (1930), pp. 680–686. ISSN: 1434-6001. DOI: 10.1007/BF01344810.

[22] J. M. Raimond, M. Gross, C. Fabre, S. Haroche, and H. H. Stroke. "Laser measurement of intensity ratio anomalies in principal series doublets of caesium Rydberg states: Does the D 1 line vanish?" In: *Journal of Physics B: Atomic and Molecular Physics* 11.24 (1978), pp. L765–L771. ISSN: 0022-3700. DOI: 10.1088/0022-3700/11/24/004.

[23] Jacek Migdalek and Yong-Ki Kim. "Core polarization and oscillator strength ratio anomaly in potassium, rubidium and caesium". In: *Laser Physics Letters* 31.9 (1998), pp. 1947–1960. ISSN: 0022-3700. DOI: 10.1088/0953-4075/31/9/011.

[24] Thomas F. Gallagher. *Rydberg atoms*. Cambridge monographs on atomic, molecular and chemical physics. Cambridge University press, 1994. ISBN: 0521021669.

[25] A. J. McCulloch, R. W. Speirs, J. Grimmel, B. M. Sparkes, D. Comparat, and R. E. Scholten. "Field ionization of Rydberg atoms for high-brightness electron and ion beams". In: *Physical Review A* 95.6 (2017), p. 101. ISSN: 1050-2947. DOI: 10.1103/PhysRevA.95.063845.

[26] E. Moufarej, M. Vielle-Grosjean, G. Khalili, A. J. McCulloch, F. Robicheaux, Y. J. Picard, and D. Comparat. "Forced field ionization of Rydberg states for the production of monochromatic beams". In: *Physical Review A* 95.4 (2017). ISSN: 1050-2947. DOI: 10.1103/PhysRevA.95.043409.

[27] Marian Mankos, Khashayar Shadman, Raphaël Hahn, Yan J. Picard, Daniel Comparat, Olena Fedchenko, Gerd Schönhense, Lionel Amiaud, Anne Lafosse, and Nick Barrett. "Design for a high resolution electron energy loss microscope". In: *Ultramicroscopy* 207 (2019), p. 112848. ISSN: 03043991. DOI: 10.1016/j.ultramic.2019.112848.

[28] L. Kime et al. "High-flux monochromatic ion and electron beams based on laser-cooled atoms". In: *Physical Review A* 88.3 (2013), p. 159. ISSN: 1050-2947. DOI: 10.1103/PhysRevA.88.033424.

[29] Jon Orloff. *Handbook of charged particle optics*. 2nd ed. Boca Raton: CRC Press/Taylor & Francis, 2009. ISBN: 1420045547.

[30] O. L. Krivanek, C. C. Ahn, and R. B. Keeney. "Parallel detection electron spectrometer using quadrupole lenses". In: *Ultramicroscopy* 22.1-4 (1987), pp. 103–115. ISSN: 03043991. DOI: 10.1016/0304-3991(87)90054-4.

[31] R. F. Egerton, Y.-Y. Yang, and S. C. Cheng. "Characterization and use of the Gatan 666 parallel-recording electron energy-loss spectrometer". In: *Ultramicroscopy* 48.3 (1993), pp. 239–250. ISSN: 03043991. DOI: 10.1016/0304-3991(93)90098-I.

[32] C. Colliex. "From a physicist's toy to an indispensable analytical tool in many fields of science: A personal view of the leading contribution of Ondrej Krivanek to the spectacular successes of EELS spectroscopy in the electron microscope". In: *Ultramicroscopy* 180 (2017). ISSN: 03043991. DOI: 10.1016/j.ultramic.2016.11.007.

[33] Ondrej L. Krivanek. "Parallel-detection electron energy-loss spectrometer". Patent n°4743756. Aug. 10, 1987. URL: https://patents.justia.com/patent/4743756.

[34] A. Gloter, A. Douiri, M. Tencé, and C. Colliex. "Improving energy resolution of EELS spectra: an alternative to the monochromator solution". In: *Ultramicroscopy* 96.3-4 (2003), pp. 385–400. ISSN: 03043991. DOI: 10.1016/S0304-3991(03)00103-7.

[35] Omer Sise, Nimet Okumus, Melike Ulu, and Mevlut Dogan. "Computer simulation of electrostatic aperture lens systems for electron spectroscopy". In: *Journal of Electron Spectroscopy and Related Phenomena* 175.1-3 (2009), pp. 76–86. ISSN: 03682048. DOI: 10.1016/j.elspec.2009.08.004.

[36] Robert L. Gluckstern and Ronald F. Holsinger. "Variable strength focussing with permanent magnet quadrupoles". In: *Nuclear Instruments and Methods in Physics Research* 187.1 (1981), pp. 119–126. ISSN: 0167-5087. DOI: https://doi.org/10.1016/0029-554X(81)90478-X.

[37] P. W. Hawkes and J. C. H. Spence. *Science of microscopy*. New York: Springer, 2007. ISBN: 0387252967.

[38] B. M. Sparkes, D. Murphy, R. J. Taylor, R. W. Speirs, A. J. McCulloch, and R. E. Scholten. "Stimulated Raman adiabatic passage for improved performance of a cold-atom electron and ion source". In: *Physical Review A* 94.2 (2016). ISSN: 1050-2947. DOI: 10.1103/PhysRevA.94.023404.

[39] Sofia Cristofaro, Markus Fröschle, Alessandro Mimo, Andrea Rizzolo, Michela de Muri, Marco Barbisan, and Ursel Fantz. "Design and comparison of the Cs ovens for the test facilities ELISE and SPIDER". In: *Review of Scientific Instruments* 90.11 (2019), p. 113504. ISSN: 0034-6748. DOI: 10.1063/1.5128620.

[40] M. Viteau et al. "Ion microscopy based on laser-cooled cesium atoms". In: *Ultramicroscopy* 164 (2016), pp. 70–77. ISSN: 03043991. DOI: 10.1016/j.ultramic.2015.12.007.

[41] Vladislav Gerginov and Carol E. Tanner. "Fluorescence of a highly collimated atomic cesium beam: Theory and experiment". In: *Optics Communications* 222.1-6 (2003), pp. 17–28. ISSN: 00304018. DOI: 10.1016/S0030-4018(03)01505-0.

[42] S.B. van der Geer and M.J. de Loos. *Pulsar Physics and the General Particle Tracer (GPT) code*. 2018. URL: http://www.pulsar.nl/gpt/.

[43] S.B. van der Geer, O.J. Luiten, M.J. de Loos, G. Pöplau, and U. van Rienen. "3D space-charge model for GPT simulations of high brightness electron bunches". In: *Institute of Physics Conference Series* 175 (2005).

[44] A. V. Steele, A. Schwarzkopf, J. J. McClelland, and B. Knuffman. "High-brightness Cs focused ion beam from a cold-atomic-beam ion source". In: *Nano Futures* 1.1 (2017), p. 015005. ISSN: 2399-1984. DOI: 10.1088/2399-1984/aa6a48. (Visited on 06/07/2017).

Chapter 5

Pulsed electron source

> If the human brain were so simple that we could understand it, we would be so simple that we couldn't.
>
> Emerson Pugh

In the previous chapter I discussed the continuous beam electron source, from the different continuous ionisation phenomena to our attempts to measure an improvement in the energy spread compatible with the HREELM ambitions. I detailed the implementation of a spectrometer on our set-up, and showed that our electron source can already provide an electron beam with $^{\Delta E}/_{E} < 4 \times 10^{-5}$ at $E = 1.5\,\text{keV}$. I showed that this set-up had to be improved to be able to go further into the demonstration of lower energy spreads. However, a continuous electron beam is not the only choice for the HREELM project. Time-of-flight (ToF) energy analysis is a widely-used, high-precision method to measure electrons energy spectra, and it is very possible that it will be implemented in the final HREELM design (see section 1.1.3). As the energy analysis is a very important aspect of the design of this instrument, the electron source obviously needs to be adapted to its functioning. This is why during my thesis I also explored how we could provide a pulsed electron source fitted to the pulsed energy analysis. In this chapter I discuss the pulsed version of the electron source that should be compatible with the time-of-flight energy analysis in HREELM. I present experimental work done in Laboratoire Aimé Cotton, as well as experiments done in Johannes Gutenberg University in Mainz in the group of Prof. Dr. Schönhense, supported by various simulations and conceptual work revolving around the pulsed electron source.

I won't review the field of pulsed electron sources as I have done for continuous electron sources in section 1.2, mainly because these sources are developed towards different goals. In the field of time-resolved microscopy for example, where electron creation must be pulsed, the cathode is replaced by a photo-cathode. In this technique, the production of electrons is done by an ultra-short laser pulse focused on a material (the cathode). This typically produces ultra-short coherent pulses of electrons, but at the cost of a large energy spread[1]. This method is again not particularly adapted to the HREELM project, so an innovative electron source must be devised.

I start this chapter with a section (5.1) devoted to time-of-flight energy measurements. Its use in mass spectrometry is first presented to introduce the important concepts of TOF

[1] very recent results show that cooling a single crystal of copper ionised at threshold can give electrons with an energy spread of 11.5 meV but this is still far from being applicable in an instrument[1]

analysis: natural bunching, space-focusing and energy-focusing. This helps me describe a possible implementation of time-of-flight energy measurement in the HREELM instrument, in particular the consequences for the electron source, the detection scheme, and the possible detectors. I follow in section 5.2 with the presentation of a pulsed electron source from a pulsed-laser, based on simulations and experimental data from the group of Prof. Dr. Schönhense. I then present, in section 5.3, some ideas and simulations about the manipulation of electron bunches to improve their quality. Finally I introduce the concept of Rydberg pulsed-resonance field-ionisation in section 5.4, showing experimental results obtained in LAC.

5.1 Time-of-flight energy measurement in HREELM

5.1.1 Typical implementation of a ToF energy measurement

The principle of time-of-flight energy measurements is that electrons with different energy will, under the right conditions, arrive at different times on a time-sensitive detector. Measuring the temporal spectrum of arriving electrons can then give access to the energy spectrum of these electrons. A typical set-up schematic is presented on figure 5.1. For a ToF energy measurement to be precise, the time of birth of all measured particles needs to be lower than the time resolution of the detectors. On top of that, the precision of a ToF measurement relies on precise tuning of the experimental conditions to make sure that the ToF of an electron is maximally correlated with its initial energy. In this section I present the main things to have in mind for a proper ToF-energy measurement.

5.1.2 Natural bunching

A field that extensively use time-of-fight energy measurements is the field of mass spectrometry (ToF-MS). Its low cost, very wide mass range and its ability to capture a complete mass spectrum at each ionisation event makes its a central detection method in modern mass spectrometry[2]. The principle of measurement is the following: the sample to analyse is ionised (either positively or negatively) and put to the gas phase by different techniques, depending on the sample. These charged particles are then accelerated by electric fields to a known and precisely determined energy. Then these particles enter a field-free region called the drift region, or drift tube, where they fly freely at the velocity determined by their mass/charge ratio and the given electric potential energy. This drift region ends with a time sensitive detector that records the time of arrival of the charged particle. As the starting energy, the time of departure and the distance to fly is the same for all charged particles, only the mass/charge ratio changes their time of arrival at the detector. Thus by recording hits on the detector in function of time, a mass spectrum of the sample is directly obtained.

In the context of mass-spectrometry, the interesting figure is indeed the mass of the particles, so it is very important that the time $\mathcal{T}(z_0, v_0)$ a particle hits the detector is primarily (if not entirely) determined by its mass m. In particular this means that its initial position z_0 in the accelerating field, or its initial velocity v_0 should not play a role in its

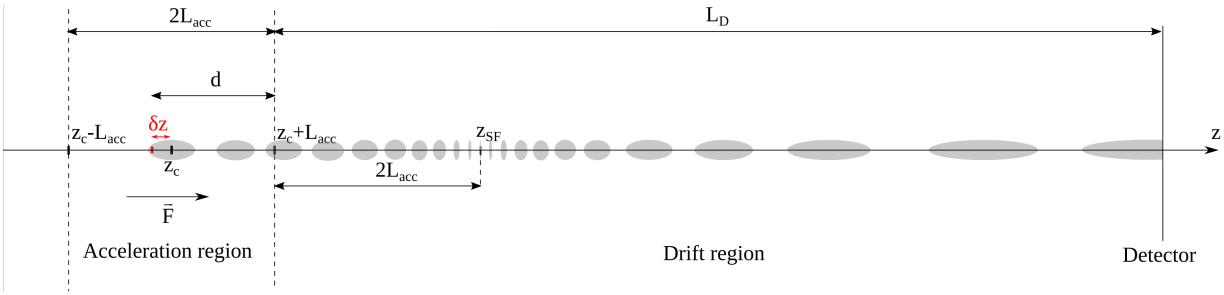

FIGURE 5.1: Typical implementation of a ToF energy measurement. A bunch of charged particles is created with a spatial extension in an accelerating zone, then enter a field-free drift zone and have different arrival time on the detector depending on its initial energy. The grey ellipses represent the electron bunch at different times after its emission, and feature the natural bunching at $z = z_{SF}$ explained in section 5.1.2.

arrival time. Mathematically we can write these two conditions as:

$$\text{ToF-MS conditions} \begin{cases} \frac{\partial \mathcal{T}(z_0,v_0)}{\partial z_0} & = 0 \\ \frac{\partial \mathcal{T}(z_0,v_0)}{\partial v_0} & = 0 \end{cases} \tag{5.1}$$

the first condition is typically called space focusing the spectrometer, while the second condition is called energy focusing[3]. These two conditions realised at the same time would mean an absolute resolution for a mass spectrometer. However, these two conditions cannot be completely fulfilled at the same time and depend strongly on the particular initial spread in velocity and position, as well as the design of the apparatus.

Let us consider a cloud of particles of charge q created at rest around $z = z_c$, immersed in an electric field of amplitude F oriented along the z axis so that the particles are attracted to high z values. This electric field spans out from $z = z_c - L_{acc}$ to $z = z_c + L_{acc}$, as can be seen on figure 5.1. A particle created in this cloud at $z = z_0 = z_c + \delta z$ (δz can be positive or negative) takes a time $t_{L_{acc}}(\delta z)$ to reach the end of the accelerating zone at $z = z_c + L_{acc}$:

$$t_{L_{acc}}(\delta z) = \sqrt{\frac{(L_{acc} - \delta z)2m}{qF}} \tag{5.2}$$

and enters a field free drift zone. I now define $d = L_{acc} - \delta z$. The time at which the particle reach any position z in the drift zone is thus:

$$t(z) = t_{L_{acc}} + z/v(t_{L_{acc}}) = \sqrt{\frac{m}{qF}}\left[\sqrt{2d} + \frac{z}{\sqrt{2d}}\right] \tag{5.3}$$

If we differentiate this equation, we obtain:

$$\frac{\partial t(z)}{\partial d} = \sqrt{\frac{m}{qF}}\left[\frac{\sqrt{2}}{2}\frac{1}{\sqrt{d}} - \frac{z}{2\sqrt{2}d^{3/2}}\right] \tag{5.4}$$

Thus we obtain the position of natural space focusing with:

$$\frac{\partial t(z_{sf})}{\partial d} = 0 \Rightarrow z_{sf} = 2d \approx 2L_{acc} \tag{5.5}$$

This results means that, in an acceleration/drift-zone configuration where the size of the ionisation zone is small against the acceleration distance, the particles created at the back of the ionisation zone will be accelerated longer than the particles created at the front of the ionisation zone, and will catch up always at twice the acceleration distance. This is remarkable as this does not depend on the size of the ionisation zone or the strength of the accelerating field, providing the zone is small against L_{acc}.

In mass spectrometry, it was soon understood that the best way to achieve space focusing is to add another region of acceleration before the drift region, to be able to position the point of natural space-focusing on the detectors, in a configuration since called Wiley-McLaren[4].

In the context of energy measurement, where all particles have the same mass and the interesting information is contained in the initial velocity/energy spread, ToF measurements need only to be space focussed, and as far as possible from velocity focusing. This changes the optimal conditions:

$$\text{ToF energy measurement conditions} \begin{cases} \frac{\partial \mathcal{T}(z_0,v_0)}{\partial z_0} & = 0 \\ \frac{\partial \mathcal{T}(z_0,v_0)}{\partial v_0} & \neq 0 \end{cases} \tag{5.6}$$

In HREELM (as in any other electron spectroscopy), we are interested only in the difference in energy of the electrons as they're scattered by the sample. So the condition of space focusing is best achieved by placing the sample *orthogonal* to the direction of electron propagation, making the initial δz close to 0. This is sometimes referred to as the requirement to put the sample at an isochrone surface[5]. This is fortunately the case in the chosen design for HREELM, so in that regard the ToF energy analysis is fully compatible with the design presented in section 1.1.3.

5.1.3 Imaging with high temporal resolution

HREELS is normally conducted with a continuous beam and requires only position sensible detection, due to the magnetic deflection that is normally used to analyse the energy (see section 1.1.1). Conducting HREELS via a ToF energy analysis would be a unprecedented experimental realisation, even if low-resolution TOF-EELS has already been achieved in an electron microscope[6].

Combining the imagery and the spectroscopic requirements of HREELM on one detector is not a trivial task: the detectors should have the high spatial resolution required by the LEEM imagery as well as a very high temporal resolutions compatible with the high energy resolution of HREELS. The other challenge is the high measurement rate and the resulting large amount of data to encode and transfer. We thus must make the best choice in the large amount of different electron detectors available nowadays.

As already stated, in a ToF spectrometer the energy resolution can be calculated from[5]:

$$\frac{dE}{dt} = -\frac{2}{L_D}\sqrt{2\frac{E_d^3}{m_e}} \tag{5.7}$$

with E_d the drift energy, L_D the drift length before the detectors and dt the time-resolution of the detector. The ambition to resolve phonon-bands in HREELM gives us a value of $dE = 5\,\text{meV}$. It is possible to attain this very low value with $L_D = 1\,\text{m}$, $E_d = 9\,\text{eV}$ and $dt = 150\,\text{ps}$. These already demanding experimental conditions mean that this value of temporal resolution represents an upper limit. At a drift energy of 9 eV, an elastically scattered electron would travel for 562 ns inside the drift region. An energy-loss spectrum range of 5 eV would increase this time to 843 ns[2]. This means that recording a spectrum from 0 eV to 5 eV energy loss will take 281 ns, or that the maximum measurement rate of spectra is around 3.5 MHz (otherwise the spectra would overlap).

I have given exemplary values in section 1.1.3 for the detector temporal resolution (150 ps), the rate of spectra acquisition 3.5 MHz, the quantity of inelastic electrons per spectra (1×10^3) and the total duration of a measurement, that correspond to a reasonable compromise. This also depend on the acquisition set-up, because the rate of 3.5 MHz is in the upper range of state-of-the-art time to digital converters in very-high temporal resolution modes[7]. As the possible value of the different experimental parameters have more degrees of freedom than constraints, in the following I propose a measurement scheme with commercial detectors, that should be able to acquire the full amount of data in 10 min. We will then derive the requirements for the pulsed electron source. Some back and forth might be required to adjust the actual measurement conditions, but this proposition should give us a working starting point.

5.1.4 Proposed detection: MCP+Timepix

This detection scheme is designed not to be the limiting factor of the measurement. This limiting factor should be the electron source, as its properties are still subject to development and improvement. The requirements are summed-up in table 5.1, along with some existing solutions. There are two values for the rate of detection, one for the binning (i.e. temporal resolution) and one for the image acquisition. Indeed there exist no perfect detector for our application, so we consider some hybrid solutions, using MCPs as providers of precise timestamps, that can be correlated with the image given by the other detector. This requires a good acquisition system and careful encoding of data, as well as some timestamps from the image detector, otherwise it is impossible to correlate the information. The requirements for the image acquisition rate comes from the fact that the proposed measurement is at a 3.5 MHz rate, but with 100 pA it corresponds to an average of 4 electrons for the imagery (all electrons hitting the detectors) and 0.4 for the spectroscopy (only inelastic electrons, one tenth of scattered electrons).

Delay-line detectors are arrays of crossed-wires that give arrival time and position of charged particles. The arrival time of the particle is deduced from an average of the signal on different wires, and the position of the particle is deduced from the delays between the signals on different wires (acting as coordinate axis). Modern DLDs allow very good temporal resolution with a good pixel number, but the spectra acquisition rate

[2] this 5 eV span gives a spectral range of 1000 with the energy resolution of 5 meV

Detector \ Requirements	Pixel number	Binning resolution	Binning rate	Image rate	Ref.
	$\geq 500 * 500$	$\leq 150\,ps$	$\geq 3.5\,MHz$	$\geq 14\,Mhits/s$ multi-hits	-
Timepix 3	$256 * 256$	$1.56\,ns$	$85\,MHz$	$85\,MHz$	[8]
MCP+Phosphor screen+CCD	$1000 * 1000$	$\approx 50\,ps$	$\leq 1\,MHz$	$1\,kHz$ whole image	-
DLD	$\approx 700 * 700$	$\approx 150\,ps$	$\leq 5\,MHz$	No multi-hits	[5]
MCP+4 Timepix 3	$512 * 512$	$\leq 50\,ps$	$> 400\,kHz$	$> 10\,kHz$	[9]
Timepix 4	$512 * 448$	$195\,ps$	$2.5\,GHz$	$2.5\,GHz$	[8]

TABLE 5.1: Requirements for the detector in HREELM, as well as the corresponding properties of different available hybrid detectors. DLD: delay-line detector. Image rate means the rate to acquire a full 2D image. The Timepix 4 properties are indicated but this detector is still in the test phase.

envisioned in HREELM ($> 3.5\,MHz$) is in the upper range of DLD reading times. Furthermore the acquisition rate for the image of the sample is the same, but with a higher electron count. Indeed, the elastic peak is always the most intense feature, and is usually in proportion 1:10 against the inelastic electrons. This means that the detector must tolerate multi-hits during the time window corresponding to elastic electrons, and DLDs don't tolerate multi-hits.

The usual combination of MCPs+Phosphor screen+CCD camera is also not compatible with the quoted rates and temporal resolution: a very good time resolution can be retrieved from the MCPs signals, but the read-out time of the CCD camera will limit greatly the measurement rate. Furthermore, at such high rates it is not possible to correlate the image given by the CCD to the temporal information given by the MCPs because typical timestamps from CCD cameras are in the ms range.

The Timepix chip is a high-performance detector based on the Medipix chip[10]. These consists in a slab of semi-conductor material (like silicon) positioned on a pixelated current read-out[11]. Incoming particles create a trail of electron-hole pairs in the semiconductor slab, which can be measured by the complementary metal oxide semiconductor (CMOS)-based chip. Detectors of the Medipix/Timepix family have applications in numerous fields, from biology to antique restoration and from medicine to cosmic rays detection[10]. Medipix (the version of this detector optimised for high-count acquisition) have also already been successfully used in TEM[12] and LEEM[13,14], showing such promising properties that the authors declared[13]:

> *We expect Medipix to become the standard detector for LEEM and PEEM, because of its many advantages.*

The main advantages of the Medipix/Timepix family is its very high maximum count rate, its imagery with close to zero noise and its pixel by pixel integrated time-of-arrival measurement (only for Timepix).

The Timepix chips are optimised to obtain high-temporal resolutions, around 1.6 ns for the Timepix 3 version. This value is a poorer than the best temporal resolution found in detectors nowadays (particularly in MCPs and DLDs), but here it is for each pixel of the chip, and this tolerates large amount of multi-hits. Indeed, each pixel of the detector contains a pre-amplifier, a discriminator with adjustable threshold and a 14-bit counter. It has a specific mode for ToF measurements, where each event is internally referred to an external trigger signal. The Timepix 3 is "3-side buttable" chip, meaning that it has three free sides, allowing the formation of a bigger sensible surface area by fitting 2 or 4 of these chips seamlessly.

The current version of these detectors are Medipix 3 and Timepix 3, each version improving the properties of the chips. The new version of the Timepix chip, the Timepix 4, is currently in its testing phase, but as can be seen in table 5.1, this new version would greatly improve the properties of the chip, in particular in terms of temporal resolution (*8), size (*3.5) and readout bandwith (*22).

In the context of ToF-HREELM measurements, four Timepix 3 chips would create a square of 512*512 pixels, perfect for the imagery. However, the ToF measurements would require a better temporal resolution than offered by the bare Timepix 3 (1.56 ns). This is why I propose to add a pair of MCPs in front of the four chips, paired with a high-resolution time-to-digital-converter (TDC)[3], that would give access to a possibly very precise time of arrival. The time of arrival measured by the Timepix chips is then very useful to correlate the precise time of arrival on the MCPs and the precise position on the Timepix chip. The dimension of a pixel in the Timepix 3 is $55\,\mu m * 55\,\mu m$, so the MCPs would not be detrimental to the spatial resolution (and sub-pixel spatial resolution ($\approx 10\,\mu m$) can be obtained by centroid techniques). The MCP assembly also acts as an electron amplifier, that is essential because of the relatively low energy of the detected electrons and the high threshold of the Timepix. This detection scheme was already used and applied to ion-ion coincidence imaging[9], and we would extend its applications to the simultaneous acquisition of LEEM images and HREELS spectra. We thus follow here the impressive results presented in ref. [9] and envision a detector composed of a pair of 40 mm MCPs stacked on a quad-Timepix 3 chip. When the Timepix 4 will become available, its higher temporal resolution and bigger size would advantageously replace the four-Timepix 3 assembly.

5.1.5 Proposition of a detection sequence

I presented the preferred detectors for ToF-HREELM, I now turn to the measurement sequence. A schematic can be found on figure 5.2. Every 285 ns an electron bunch of ≈ 40 electrons with a temporal and energy spread respectively ≤ 5 meV and ≤ 150 ps impinges on the sample and is reflected back towards the drift region and the detector. In each spectra, on average, the Timepix chips measure the precise position and approximate arrival time of 4 particles (elastic and inelastic electrons) and the MCPs increase the detection limit and give time resolution in the 50 ps time scale. The main point of this measurement scheme is to obtain a good statistics for the imagery with elastic electrons, while triggering the time of arrival/energy loss measurement only for the interesting electrons, i.e. the inelastic electrons. TDCs typically need a non negligible delay to be available for

[3] such an acquisition system is already in place in our laboratory, giving temporal resolution around 75 ps[15]

detection again, in the order of 5 ns[7]. Thus for very intense loss bands the dead-time of the TDC might decrease the apparent intensity, as some electrons would not trigger the TDC (multi-hits), but this can easily be adapted in acquisition parameters.

This utilisation of the detectors presented in section 5.1.4 gives a rate for spectral acquisition of 3.5 MHz, that the Timepix architecture can easily accommodate, and given the 0.4 average "STOP" signal per spectra received by the TDC, it stays well within the acquisition rate of most high-performance TDC[7].

5.1.6 Requirements for the electron source

The choice of a ToF energy measurement in HREELM implies obviously a pulsed electron source, with additional constraints on the properties of the electron source, in particular in terms of pulse length. In this section we analyse these additional constraints, in the hypothesis of the detection scheme proposed in section 5.1.5.

Equation 5.7 is the basis for our discussion of ToF energy analysis. It supposes that the electron pulse duration is negligible against dt given by the detector. Given that the proposed acquisition scheme allows temporal resolution on the order of 50 ps at best, it is very demanding in terms of electron pulse length. In the following we keep the goal of a temporal resolution of 150 ps, but this limitation is assumed to come from the electron pulse length rather than from the actual detection limit.

We can verify that the electron time spread on the sample will not be affected by their energy spread: supposing static electric field along the column of length $L = 660\,\text{mm}$, electron bunches created during a time window Δt_i with an energy spread of ΔE in the electron gun will arrive at the sample (see figure 1.12) with a time spread of $\Delta t_s \approx \Delta t_i + L/\left(\frac{2(E+\Delta E)}{m_e}\right)$. A transport energy of 3 keV and 5 meV energy spread gives completely negligible energy spread-induced time spreads of 20 fs[4].

In terms of time spread, measuring the energy losses in HREELM via ToF-analysis requires the creation of electron bunches not longer than 150 ps. In the end of section 5.1.3 I alluded to the acquisition rate/electron per pulse/measurement duration compromise. For a measurement to be considered complete, I obtained the value of 2.6×10^8 detected inelastic electrons. To trace back the electron current needed to achieve this detection rate, this number has to be multiplied by ten to account for the proportion of elastically/inelastically scattered electrons. Another tenfold multiplication is required to account for the absorption of the electron probe by the sample.

Supposing a detection efficiency of one, this gives us a total number of 2.6×10^{10} electrons impinging on the sample. Producing this quantity over 10 minutes is equivalent to a continuous current of 7 pA to acquire a full image with a high-resolution energy loss spectrum in each pixel. In terms of electrons per pulse, this gives us in average 4 electron per measured spectra (0.4 inelastic ones), so around 40 electrons (a charge of 6 aC) per 150 ps pulse, along the energy spread requirements of not more than 5 meV energy spread. This very low charge in each pulse means that space-charge time and space expansion of the pulse will be negligible[16].

Now that I derived the requirements for the electron source from a realistic acquisition scheme, I turn to the different ways to realise the pulsed electron source for ToF-HREELM.

[4]This is expected, because otherwise it would mean that we are able to measure an energy difference of 1.7×10^{-6}

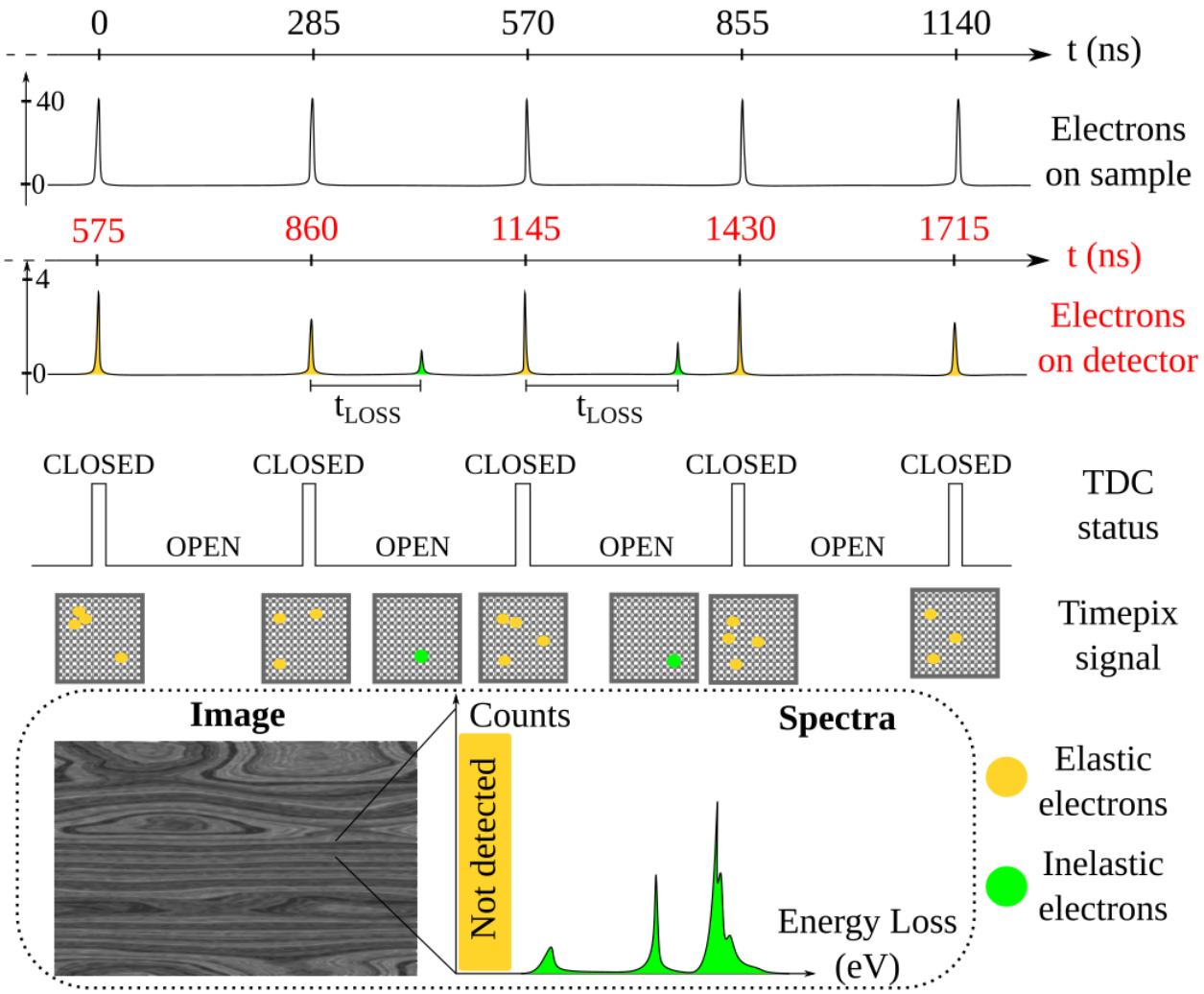

FIGURE 5.2: Proposed measurement sequence of ToF-HREELM allowing high resolution imaging and spectroscopy. "TDC": Time-to-digital converter. We take 575 ns as the travel time for elastically scattered electrons from the sample to the detector. On average 4 electrons attain the detectors per spectra (see section 5.1.6). The TDC is closed at the end of each spectra for read-out and open just after the elastic electrons to trigger only for inelastic electrons. The resulting image contains all electrons, but the spectra contain only inelastically scattered electrons to save TDC time.

Section summary

ToF energy measurement in HREELM

In this section I have introduced the time-of-flight energy analysis in the context of the HREELM project. An introduction to ToF energy analysis, to the concepts of space and velocity focusing led to a description of a probable implementation of ToF analysis in HREELM. An important point is the detection associated with ToF analysis, because it requires spatial, temporal resolution at a high rate. I propose to use a combination of MCPs and Timepix, that have all the required characteristics. Based on this proposition, I propose a detailed measurement sequence for HREELM in the pulsed mode. This helps us define the requirements for the electron source, in terms of energy spread, current, and temporal spread: less than 5 meV, more than 7 pA and less than 150 ps, at a repetition rate of at least 3.5 MHz.

5.2 Pulsed ionisation: pulsing the laser

To create a monochromatic pulsed electron source, a simple way would be to start from a monochromatic continuous electron source and chop the signal to create short electron bunches. This was achieved for example by focusing an electron beam in an electromagnetic cavity that swept the beam at very high frequencies on a tightly closed slit[6]. This creates electron bunches of a few ps duration, but with increased energy spread (up to 4.6 eV, for a measurement resolution of 12 eV)) due to the large non-linearities in the cavity[6]. Other methods exist but instead of starting from a continuous electron source in the following we study the possibilities to create electron bunches from the ionisation of free atoms in a magneto-optical trap or in an effusive beam.

5.2.1 Pulsed-photoionisation

Fundamentally the ionisation process of an atom excited by a pulsed-laser is very similar with a continuous beam laser. Thus we can use the nomenclature introduced in section 4.1 to describe the ionisation of atoms with pulsed-lasers. An important difference comes from the fact that pulsed lasers have larger frequency bandwidth than continuous beam lasers

Photo-cathodes aside (because of their large energy spread), several experiments have already shown that it is possible to create electron bunch with very promising properties by ionising cooled atoms with a pulsed-laser[17,18]. Electron bunch containing 1×10^3 electrons per pulse, with a measured pulse duration of 25 ps were created from the pulsed ionisation of laser cooled Rubidium atoms[16]. However these were created under high extracting fields (8 kV/cm) and energy spread measurement showed over 50 eV of energy spread[19]. The atoms are laser-cooled in a magneto-optical trap, then the trapping laser are turned off for some time (around 1 µs), along with the trapping magnetic fields (for 1 ms). The cold atoms are first excited to an intermediate state by a µs- or ns-time scale laser pulse to ensure good conversion, and then ionised by a very short laser pulse (in the fs-ps time scale).

Using such short laser pulses means that the corresponding frequency bandwidth will be very large. Indeed, Gaussian transform limited pulses of duration 100 fs (FWHM) and wavelength 760 nm have a spectral width of 8.5 nm (18.2 meV, 4.41 THz or 147 cm^{-1}). For pulses around 10 ps (FWHM) the corresponding Gaussian spectral width is 85 pm (44.1 GHz, 0.182 meV or 1.47 cm^{-1}). This has the direct consequence that such large bandwidth makes impossible the excitation and ionisation of unique, specific Rydberg states in the spaghetti region (where ionisation rates are non-negligible).

Once again, there is no reference evoking electron pulses adapted to the requirements derived in section 5.1.6, combining very short duration (less than 150 ps) and very small energy spread (less than 5 meV). In order to produce such an electron source, and along the same logic as with the energy spread in section 4.1.4, we must look into the different sources of time spread during the formation of a pulsed train of electrons.

5.2.2 Factors influencing pulse duration

When measuring the pulse length of an electron bunch created by a laser pulse[5], five different processes characterised by five different durations τ_i can influence the pulse duration:

1. τ_L is the duration of the ionising laser pulse. When several laser pulses are used to ionise the atom in a multi-photon process, τ_L is the smallest value from all laser pulse durations[20]. It can thus easily be under 100 ps.

2. τ_{ion} is the time it takes the electron to escape the ion potential, or simply the duration of ionisation. In the case of above threshold photo-ionisation it is very short (< 1 ps), but in the case of under-threshold tunnelling it can be very long, in the µs range. We can use the model introduced in section 4.1.2 to estimate this time.

3. $\tau_{\Delta E}$ is the time arrival difference from the source to the sample due to the energy spread of the electron bunch. Details on this quantity can be found in section 5.1.2, but for $\Delta E \approx 5$ meV it is completely negligible.

4. τ_{SC} is the pulse lengthening due to space-charge forces inside the electron bunch. For us it will always be negligible as the electron number in each pulse is very low (pulse charges of 6 aC)[16].

5. τ_{mom} is the time spread associated with an initial momentum (k) orientation dispersion of the electron bunch. Figure 5.3 illustrates what is intended by τ_{mom}.

   It is the delay of arrival between electrons ejected in the $+z$ direction and in the $-z$ direction, and can be estimated (as an upper limit) as the time it takes an electron ejected in the low field direction (in the $-z$ direction) to travel back to the ionisation point (pictured in red on figure 5.3). It depends obviously on the intensity of the electric field at this point (F_0, assuming a relatively homogeneous electric field). In the case of a particularly anisotropic emission with non-negligible release velocity v_0, this spread can be large enough to actually split the temporal width of all the

[5] assuming no time spread due to the detection like jitters in the synchronisation

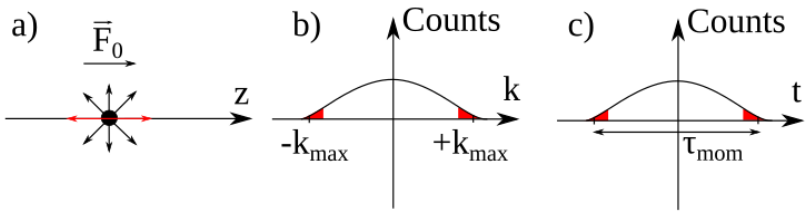

FIGURE 5.3: Schematics of the role of the dispersion of the electron initial momentum on their arrival time dispersion a)-b) Initial momentum distribution for isotropic emission, emission on axis is represented in red c) Arrival time distribution, showing extreme values for the electrons ejected on axis (in red).

electrons into two well separated peaks. The separation is then given by:

$$\tau_{\text{mom}} = \frac{2v_0 m_e}{eF_0} \tag{5.8}$$

where $v_0 = \sqrt{\frac{2E_{exc}}{m_e}} = \sqrt{\frac{2\left(E_\lambda + 2E_{au}\sqrt{F/F_{au}}\right)}{me}}$. We thus have:

$$\tau_{\text{mom}} = \frac{2\sqrt{m_e}}{eF_0}\sqrt{2(E_\lambda + 2E_{au}\sqrt{F/F_{au}}} \tag{5.9}$$

Contrary to $\tau_{\Delta E}$ it is non-zero even for electrons having exactly the same energy (i.e. momentum amplitude), as it is the different *orientations* of the momenta that induce the arrival delay.

I note that the condition of space-focusing (see equation 5.6), when not fulfilled, should contribute to the final time spread. It does, but since in this case the initial position of the electron determines its drift energy, the time spread associated with the spatial dispersion is included in $\tau_{\Delta E}$ (because the spatial dispersion is the dominant term in the energy spread). That is why I don't define a specific τ_i for this position spread.

From these five values, the hardest to predict and usually the dominant term is τ_{ion}. It can vary over 8 or 9 orders of magnitude, depending on the tuning of the ionising laser, or more precisely on the excess energy of the outer electron after absorption of the ionising photon. This excess energy E_{exc} is usually defined relative to the field-shifted ionisation energy E_I^F (see section 4.1 for their definition). For our purpose we will consider that electrons excited with a large positive excess energy will experience negligible ionisation time. In reality there is a strong distinction between electrons with $E_{exc} > |E_F|$ that are effectively emitted in $\tau_{ion} \ll 1$ ps and electrons with an excess energy $0 > E_{exc} \gtrsim E_F$ that can take up to 50 ps to effectively escape the ion potential (see figure 4.6 that shows a 14 ps delay between excitation and ionisation, or experimental data in references [16, 21, 22]). However these figure are negligible against the time spread measured and analysed in the following.

When E_{exc} is close to zero or negative, Rydberg states are populated, and depending on the particular coupling of these states to the continuum, τ_{ion} can be in the ns or the µs time range. The evolution of τ_{ion} from negligible values (well above the field-shifted

threshold) to very large values (under the field-shifted threshold) is continuous, so appropriate states with $\tau_{ion} < 1$ ns can be found by carefully looking into LFT Stark maps, for example on figure 4.33.

An important point to realise is that the simulations presented above are valid in the classical view of ionisation. Comparison with experimental data show good agreement overall[16,18,22,23], but this model cannot account for highly quantum behaviour at the base of velocity-induced Rydberg field-ionisation for example. The classical description is accurate because of the wide bandwidth (small pulse duration) of the lasers used in these experiments, that excite a very large number of different Stark-shifted Rydberg states, thus creating a wave-packet that is not far from the classical electron described in these simulations[22]. For excess energy around 0 (i.e. for states near the field-shifted ionisation threshold) and small bandwidth lasers the situation is more complex and the method presented in section 4.1.3 is more reliable than wave-packet analysis. Indeed the intricacy of the Stark mixing of quantum states can result in orders of magnitude ionisation rate change over almost no change in the ionisation energy or electric field (see figure 4.36 for example).

On top of the time spread, we must not forget that the requirement for HREELM in terms of energy spread (≤ 5 meV) is still present for the pulsed electron source. An important step forward for pulsed electron sources from atoms is thus the ability to deliver these electron bunches with very low energy spread. This can be done primarily by decreasing the value of the electric field. In the next section we present results of such an electron source where the extracting electric field is orders of magnitude lower than in all previously reported pulsed electron sources.

5.2.3 Experimental set-up in Mainz

In this section I will present the experimental set-up and the experiments done in the group of Prof. Schönhense in JGU Mainz. I personally participated in the analysis of experimental data (for the theoretical analysis of the ionisation process and with extensive simulations) acquired in the first version of this set-up, that are presented in reference [24][6]. During two one week-visits in Mainz, I helped in the transformation of this set-up to perform time-dependent manipulation of the electron bunches and analysed the new data acquired with the new version of the set-up.

The set-up, shown on figure 5.4, is composed of a standard 3D magneto-optical trap in anti-Helmholtz configuration, a caesium dispenser, and lasers adapted to the magneto-optical cooling and trapping of caesium atoms. Optical access to the MOT is granted for two additional lasers, the 1470 nm laser and the Ti:Sa.

The caesium atoms are cooled down to around 150 µK and ionised via the same pathway as in experiments presented in chapter 3 (852 nm-1470 nm-Ti:Sa). The first excitation step is assured here by the same laser that performs the radiative cooling. The biggest difference is that the Ti:Sa is now a fs-pulse laser. The polarisation of this laser is an important parameter and can be modified by a half-wave plate to be either parallel to the electric field direction (z axis) or orthogonal (see figure 5.6 d)). The pulse duration of the Ti:Sa is around 100 fs, and its FWHM bandwidth was measured to be around 24 meV. Interferential filters can be added to reduce the bandwidth of this laser down to 4 meV,

[6] they were acquired before I was involved in the collaboration

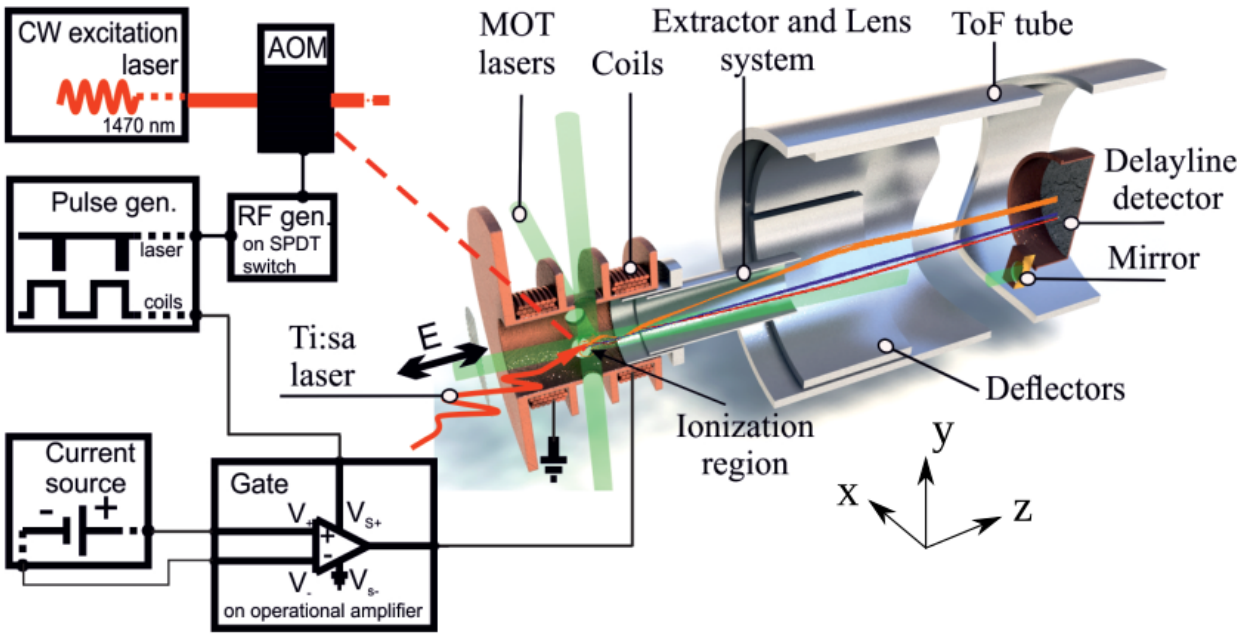

FIGURE 5.4: Schematic view of the complete set-up installed in Mainz. It contains a 3D-MOT whose magnetic field can be shut down for 1 ms, an ionising fs-pulsed Ti:Sa, a continuous 1470 nm laser beam pulsed by an acousto-optic modulator, a magnetically shielded drift tube and time-position sensitive detectors.

corresponding roughly to pulse length of 600 fs, thus still negligible against the time precision of our detector.

The cooling/ionisation zone is placed in a low electric field around 2 V/cm. The way the chamber is designed and the potential are applied does not allow precise determination of the actual electric field, that needs to be deduced from experimental data.

The fact that very low extracting field are used has one major consequence: the electrons are very sensitive to magnetic fields. This has two consequences in terms of experimental design, that a magnetic shielding around the ionisation area and along the electron path is mandatory, and that the magnetic fields used for trapping the atoms must be removed before the ionisation. In another experiment, exciting lasers and magnetic fields were shut down for 5 ms[17] to have negligible effect on the extracted electrons. In this particular set-up, where the extracting electric field is lower, experiments have shown that 4 ms were required for the magnetic fields to have negligible impact on low energy electrons[24,25].

Once the electron leave the extraction region they enter a 0.8 m-long drift tube that allows the temporal separation of electron with different energies. At the end of this drift tube the electrons hits the detector that is composed of two MCPs stacked on a delay-line detector (DLD). This detector has a time resolution of 200 ps. The distance between the ionisation region and the detectors is approximately 0.8 m, the drift tube is kept at ground, and the starting potential E_{in} is around 15 eV.

A sum-up of the acquisition sequence is presented on figure 5.5. The MOT is charged for 5 ms and data is acquired for 1 ms every 9 ms. The DLD is synchronised with the 80 MHz trigger signal from the Ti:Sa, and the intensity is small enough (but still around

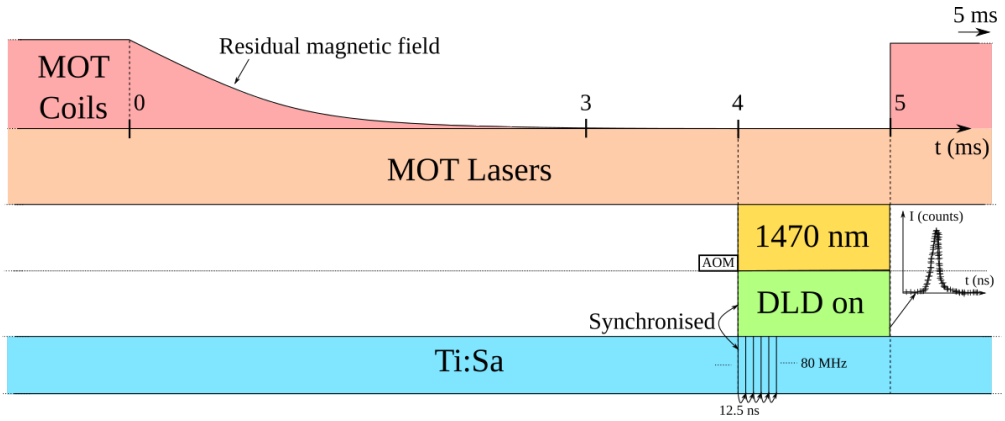

FIGURE 5.5: Schematic view of the experimental sequence for the production and ToF measurement of electron bunches. Less than one electron per Ti:Sa laser pulse (one fs-laser shot every 12.5 ns) is detected by the DLD+MCPs detector, and a ToF spectrum is reconstructed from many different measurement cycles.

100 mW) to avoid two electrons per laser pulse because DLD don't deal well with multi-hits. Thus a ToF spectrum is constructed from a large number of different ionising pulses.

In these measurements, the initial electron bunch is created with an energy spread associated with the size of the ionisation zone and the extraction field but also with the excess energy of the ionising laser. This energy spread will induce a time spread on the detector $\tau_{\Delta E}$. The ionisation and extraction of the electron itself will take a time τ_{ion}, and the time-signal is further enlarge by the asymmetry of the initial momentum distribution, inducing a delay τ_{mom} between electrons ejected with their velocity oriented in the $+z$ direction and electrons with their initial velocity oriented along the $-z$ direction. All other sources of delay are negligible in the presented peaks.

5.2.4 Raw data on pulsed photo-ionisation

The ToF data acquired on the set-up in Mainz by Olena Fedchenko and Sergueï Chernov can be seen on figure 5.6. It features data with laser pulses of $\Delta\omega = 4$ meV bandwidth[7], s- and p-polarized light, and three different central energy of the laser, corresponding to negative mean excess energy, null, or positive mean excess energy. The electric field is around 2 V/cm so the field-shift of the ionisation threshold is around $E_F = -1$ meV.

The first thing to remark about the experimental data is the difference in electron intensity for the different photon energy (775 nm, 777 nm, 779 nm) of the laser. Indeed the exposition time were the same in each case (1 s), so any intensity difference comes from the ionisation process and the collection efficiency. It is very clear from figure 5.6 that the electron intensity is around ten times higher when the laser is tuned at-threshold, compared to above-threshold or below-threshold ionisation. We also see that above-threshold ionisation features two clearly resolved peaks with p-polarisation. The central value of time of flight (measured relative to the trigger of the ionisation laser, see figure 5.5) is 4.9 ns, with a FWHM of 922 ps for s-polarisation threshold ionisation. The two peaks in

[7] Data with $\omega = 24$ meV was also acquired and published in ref. [24], but for the sake of brevity I don't reproduce them here

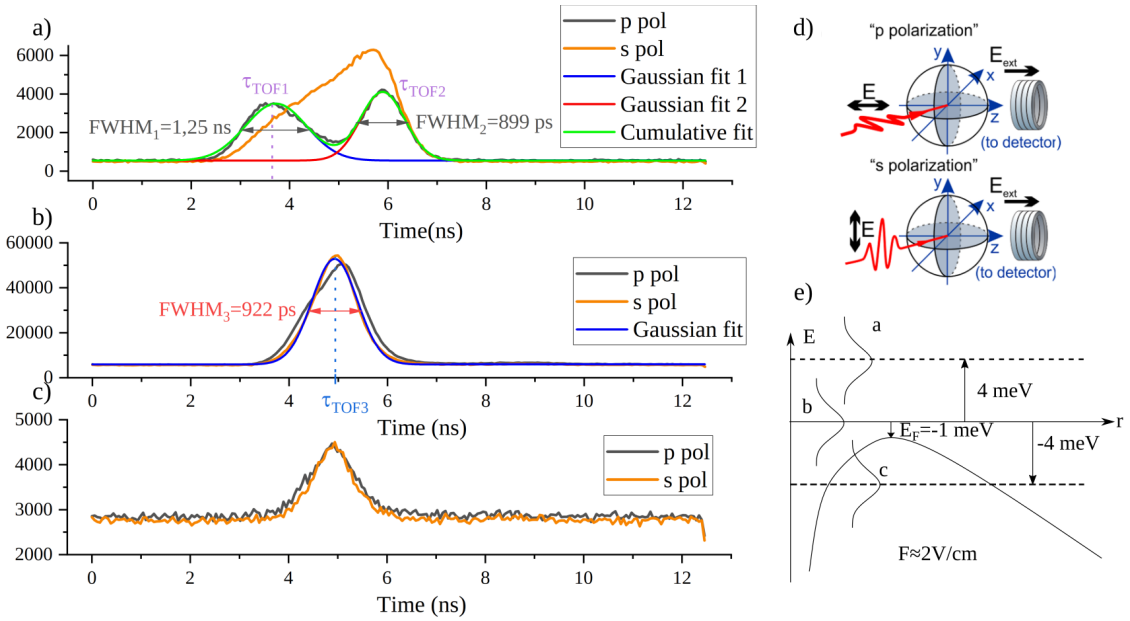

FIGURE 5.6: a)-c) Experimental data on pulsed ionisation of laser cooled caesium atoms, showing the impact of laser polarisation and laser central tuning (i.e. excess energy) on the time-of-arrival of created electrons, with Gaussian fit of the data and explicit FWHM. Note the different intensity scales. These data are acquired with $\Delta\omega = 4$ meV laser bandwidth: above-threshold ionisation (a), threshold ionisation (b) and below-threshold ionisation (c)). d) Definition of the polarisation of the ionisation laser relative to the electric field orientation. e) Schematic of the atomic potential showing the three photon energies. I did not participate in the acquisition of this data but on the analysis and interpretation. Reproduced from [24]

above-threshold ionisation are fitted to ToFs of 3.7 ns and 5.9 ns, with FWHM of 1.25 ns and 899 ps respectively.

For all three cases, p-polarisation measurements show more spread in arrival times than s-polarisation measurements. This spread is stronger as the excess energy gets bigger.

5.2.5 Analysis of raw data

The central value of $\tau_{ToF3} = 4.9$ ns has to be understood as modulo 12.5 ns as it synchronised with the Ti:Sa but without common timestamps, so it is not the actual time-of-flight of electrons since the ionisation. This is a pity, but a proper absolute ToF measurement would require 200 ps timing precision over around 500 ns, which is not possible on the Mainz set-up.

The three different laser wavelengths correspond to three different ionisation regimes: at 775 nm the excitation leads to photo-ionisation (as described in section 4.1), at 777 nm there is a mix between photo-ionisation and Rydberg field-ionisation, and below the threshold at 779 nm there is mainly the slow ionisation of Rydberg states by tunnelling and some rests of Rydberg-field ionisation.

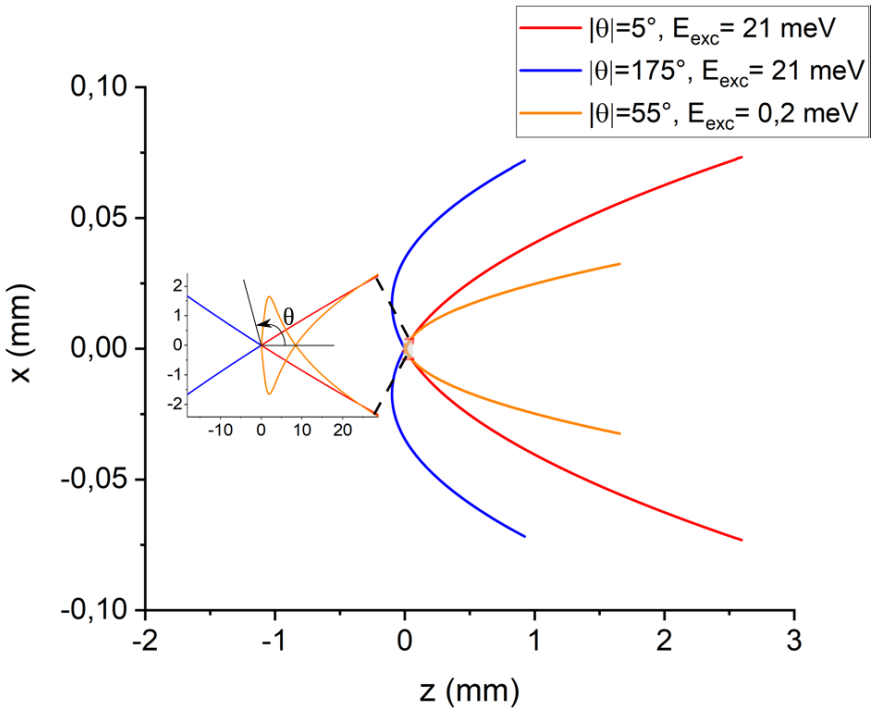

FIGURE 5.7: GPT-simulated trajectories of electrons in three different starting parameters: above-threshold ionisation forwards (in red) or backwards (in blue) and just above threshold field-ionisation (in orange). The excess energy E_{exc} is calculated for an electric field of 2 V/cm. The inset has axes in µm. The simulations ends at 10 ns, showing a clear advance of the red electron, followed by the orange and lastly the blue electron. This explains the three different values of ToF visible on figure 5.6.

This interpretation is fully consistent with the different intensity differences between the three sets of data. Indeed, the intense signal at 777 nm comes from the efficient resonant excitation of Rydberg states around the threshold, that give orders of magnitude higher cross-section than well-above threshold excitation. The relatively low intensity of the peaks in the data at 779 nm comes from the tail of the laser that still excites some rapidly ionising Rydberg states. The intensity of the background is four or five times higher than the background at 775 nm, because the laser excites mainly slowly ionising Rydberg states, so the electrons are not particularly synchronised with the laser pulse.

The influence of the laser polarisation on the shape of the peaks can also be well understood, and fits this interpretation: above threshold, the electrons are ejected depending on the laser electric-field orientation. This orientation is given by the expression of the differential cross-section in photo-ionisation[26] already cited in section 4.1.1:

$$\frac{d\sigma}{d\Omega} = \left(\frac{\sigma}{4\pi}\right) \frac{\left[1+\beta(3\cos^2(\theta)-1)\right]}{2} \tag{5.10}$$

In this formula θ is the angle relative to the electric field (see figure 5.7). In the literature I did not find any measurement of the asymmetry parameter β for the photo-ionisation from the $7s$ state of caesium, only a theoretical one[27]. This reference ([27]) gives two possible values for β when E_{exc} is close to 0, that are around 1.85. For simplicity I thus take the value of $\beta = 2$ in the following. The spatial shape of the emission by photo-ionisation will be the shape of the $\cos^2$ term, leading to an "8" shape in the field direction for s-polarisation and a "∞" shape for p-polarisation (see figure 4.3). This fits very well with the presented data, because the photo-ionisation electrons in the case of p-polarisation are separated in two well resolved peaks. Their ToF delay $\Delta\tau = \tau_{ToF2} - \tau_{ToF1} = 2.2$ ns is attributed to τ_{mom}, i.e. the time it takes for the electrons ejected towards the back of the experiments to be accelerated towards the front and pass its starting point. As already presented, this delay depends only on the electric field value at the ionisation point, and equation 5.9 gives us a good measure of this otherwise not well known electric field: with $E_\lambda = 4$ meV, I find $F_0 = 1.9$ V/cm. This separation into two peaks was predicted in other photo-ionisation electron sources but this is the first time it is actually observed, thanks to the very low extraction field that we used[16,28].

To determine the value of the field more precisely, I performed simulations in the Simion modelling of the actual experiments, taking the $\cos^2$ shape of the initial momentum distribution and the field inhomogeneity into account, and the results can be seen on figure 5.8. They were done with $E_{exc} = 19$ meV and were compared with other data taken with this excess energy ($\tau_{ToF2} - \tau_{ToF1} = 5.0$ ns, see [24]), and yield the same electric field value ($F_0 = 1.9$ V/cm) as the one obtained at $E_{exc} = 4$ meV, making us very confident on the estimation of the electric field via this technique. On the same figure 5.8 (right panel) we can see simulation results that show that the delay between the two peaks ($\Delta\tau_{\text{mom}}$) depends only the excess energy and the value of the extracting field, and not on the drift length or the accelerating length (once above the first 50 mm).

As mentioned in section 5.2.2, the detected pulse length is not a direct measurement of the time or energy spread, but rather a convolution of different temporal spread. To ease the analysis, I draw on figure 5.9 the sum of these two terms, the time spread before the drift (τ_0, composed of τ_{SC}, τ_L, τ_{ion} and τ_{mom}) and the time spread due to the energy spread $\tau_{\Delta E}$. They are added in the worst case scenario, meaning that the slowest electron is also delayed by τ_0.

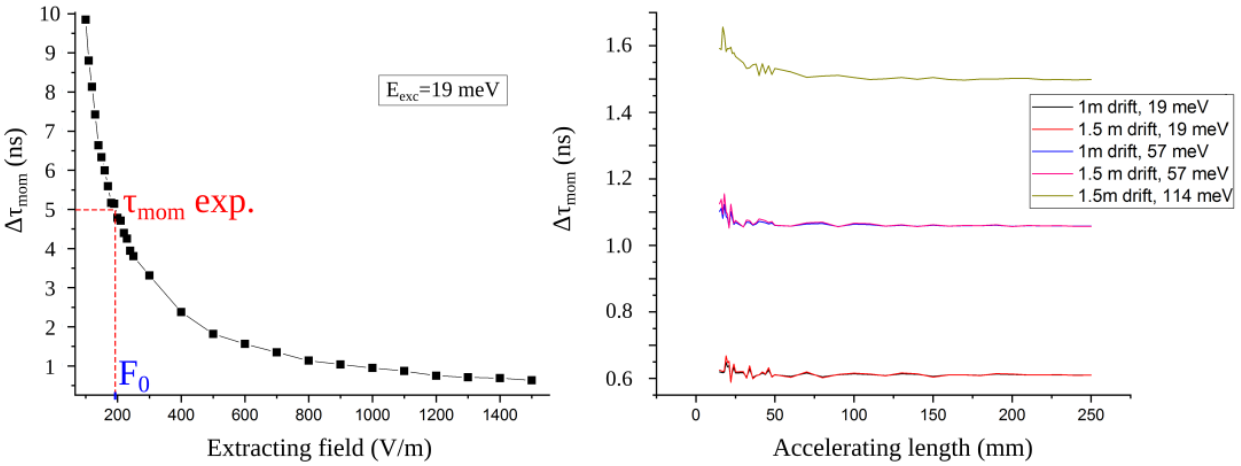

FIGURE 5.8: Simulation of the difference in arrival time at the detector ($\Delta\tau_{\text{mom}}$) for two electrons created with a positive large excess energy of $E_{exc} = 19\,\text{meV}$ (photoionisation) with opposite initial velocity along the acceleration axis. The experimental value of $\Delta\tau = 5.0\,\text{ns}$ gives a starting field of $1.9\,\text{V/cm}$. The influence of the extracting field on τ_{mom} is shown on the left panel. The right panel shows τ_{mom} with various changing parameters: drift length, accelerating length and E_{exc}. The drift length or the accelerating length have no influence (after 50 mm) on τ_{mom}, but the excess energy dominates the value of τ_{mom}, as expected.

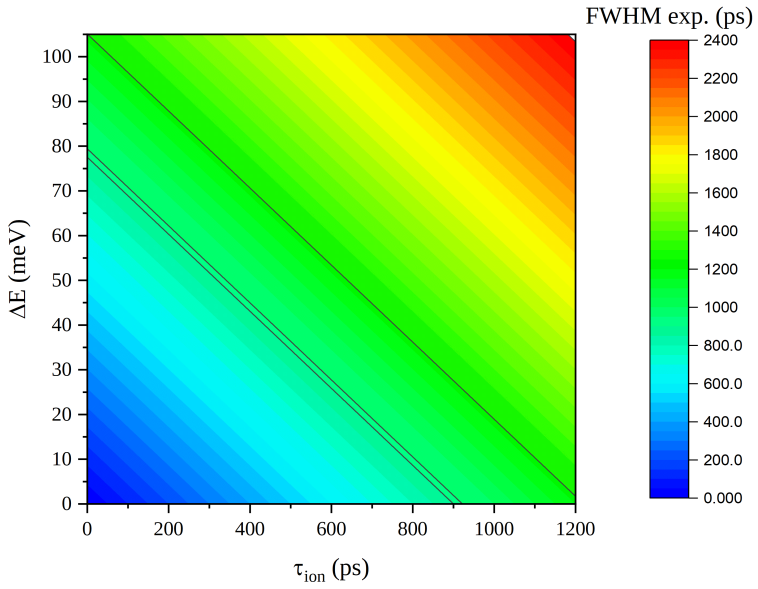

FIGURE 5.9: Map to relate the experimental measured temporal spread (FWHM,in colors) to the electron bunch emission duration (τ_{ion}) and its energy spread (ΔE) for a drift length of 0.8 m at a drift energy of 15 eV. Lines of constant time spread of 899 ps, 922 ps and 1.22 ns are represented, corresponding to the observed time spread in photo-ionisation and RFI. Reasonable energy spread of 24 meV for RFI (see text) gives an ionisation time of 650 ps.

Data of photo-ionisation is easy to analyse: the fact that electrons emitted towards the detectors are separated from electrons emitted backwards makes the FWHM of the ToF peak presented in figure 5.6 a)(FWHM$_1$ corresponds to electrons emitted forward, and FWHM$_2$ correspond to electrons emitted backward) a good measure of their energy spread. Indeed, of the 5 different τ_i: τ_L, τ_{ion}[8] and τ_{SC} are negligible and τ_{mom} is big enough to actually separate the peak in two different peaks; the only term left to explain the value of FWHM$_2$ is thus $\tau_{\Delta E}$.There is however a surprising fact: FWHM$_2$<FWHM$_1$, contrary to the intuition that electrons ejected backwards will be more spread out in time (because of the back-and-forth movement) than electrons ejected forward. One explanation could be that this movement has an temporal focusing effect, like in a reflectron, a device used in ToF-MS to diminish the temporal spread of ions with different kinetic energy[29]. This forms a temporal focusing point down the column, and the detected bunch length is lower than expected, but the energy spread is the same. I did not manage to reproduce these precise temporal spread in the simulations however, indicating a discrepancy between the simulated geometry and the actual geometry.

In the perspective of an electron source for HREELM, the best ionisation condition is obviously at-threshold field-ionisation, in s-polarisation (figure 5.6 b), in orange). The measured FWHM is 922 ps, but I tried to analyse in detail what constitutes this time spread. From the five identified possible delays, I can safely neglect τ_L, τ_{SC} and τ_{mom} (see section 4.1.2 on the forward emission in Rydberg field-ionisation). The measured temporal spread is thus the sum of τ_{ion} and $\tau_{\Delta E}$:

$$\text{FWHM}_3 = \tau_{ion} + \tau_{\Delta_E} \tag{5.11}$$

As the photon pulse is large enough to populate many different Rydberg states, with different ionisation time scales, it is difficult to estimate τ_{ion} *ab-initio*. We can estimate the initial energy spread to 24 meV from the electric field of 2 V/cm and the ionisation zone of size 1 µm (20 meV), plus the excess energy from the ionising laser (4 meV). Figure 5.9 gives the sum of τ_{ion} and τ_{Δ_E}, which, with $\Delta E = 24$ meV gives $\tau_{ion} = 650$ ps.

[8] this data correspond to photo-ionisation, with negligible τ_{ion}

Section summary

Pulsed ionisation: pulsing the laser

In this section I explored the formation of an appropriate electron source for HREELM based on the pulsed photo-ionisation of laser-cooled atoms, first theoretically and then with experimental data from the experiment in Mainz. Using ultra-short laser pulses implies large bandwidth, which implies semi-classical behaviour of the photo-electron and poor selection of ionised states.
The experimental data was acquired with 4 meV laser bandwidth, and the Tof analysis revealed two distinct behaviour corresponding to photo-ionisation and RFI. In photoionisation the electrons are ejected along the polarisation axis. When these coincide with the electric field axis, and the amplitude of the electric field is low enough, the time-resolved electron signal feature very clearly two different peaks, corresponding to electron ejected forward and backward. This is a confirmation of the description of photo-ionisation given in section 4.1.1. This observation was possible only due to the very low extracting field used in these experiments.
RFI is also studied, but as the laser bandwidth is too wide, the result is a mean of the behaviour of all high-lying Rydberg states. The double peak in the temporal spread is no longer present, which confirms the directional emission introduced in section 4.1.2. The ToF analysis gives a maximum energy spread of 80 meV for these electron bunches (for an hypothetical null τ_{ion}), but a realistic energy spread estimation gives 24 meV for $\tau_{ion} = 650$ ps.
These experiments clearly demonstrate that ionising with a fs-laser does not give fs-electron pulse, and that the spectral width of the laser are detrimental to the time and energy definition of the resulting electron bunches. We did not measure the current here but it is expected to be very low, too low for applications in HREELM.

5.3 Time-dependent manipulation of electron bunches

One possible direction of improvement for these electron bunches, to reduce their temporal and/or energy spread, would be to manipulate these bunches once they are formed. In this section I present some theoretical results on what can be done as time-dependent manipulation of electron bunches, as well as an experimental attempt to modify the Mainz set-up to allow these time-dependent modifications.

5.3.1 Time dependent extraction

Before considering what can be done to improve the quality of the electron bunches, we must first consider how we can create this bunch, i.e. what are the different time-dependent ways to extract electrons from the ionisation region. Indeed, as our discussion of energy spread in electron source in section 1.4 and equation 1.15 relied on a static extracting field and considering that this source of energy spread is almost always the dominant one in electron sources, it can be tempting to use time-dependent extraction

fields. We will see what are the different possibilities of this time-dependent extraction, and their impact on the bunches properties (energy spread, time spread).

I introduce a nomenclature to separate and clarify all the different possibilities. This classification relies on the timing between the ionisation process and the pulsed extracting field. There are 4 different timing possibilities that are called: pulsed extraction, delayed extraction, interrupted extraction and static extraction. We define four moments in time:

- t_{IN} and t_{OUT} correspond to the moment that the first electron appears during the ionisation process and the first moment an electron escapes the extraction zone (where the extracting field is applied), respectively.
- t_0 and t_1 correspond to the moment the extracting pulse rises[9] and falls, respectively.

The time sequence of these moments will determine in which case we are in, as seen on figure 5.10. The four different cases are thus defined by:

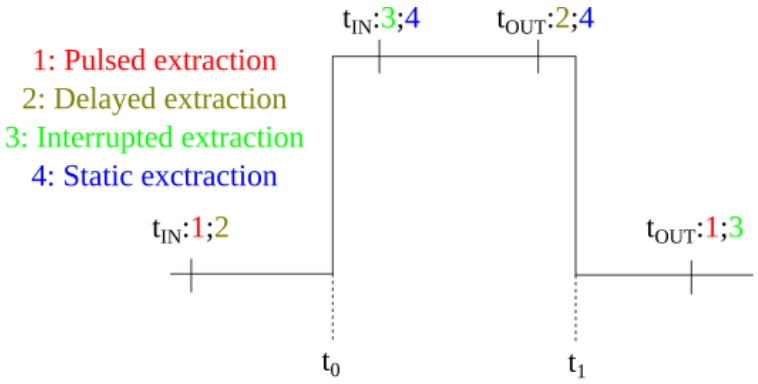

FIGURE 5.10: Four different time sequence of time-dependent extraction, depending on the timing of t_{IN}, t_{OUT}, t_1 and t_0. t_{IN} is the time of the first electron and t_{OUT} is the time an electron exits the ionisation zone.

1. $t_{IN} < t_0$ and $t_{OUT} > t_1$ corresponds to *pulsed extraction*, because the pulse of electric field rises and fall while electrons are in the ionisation zone.
2. $t_{IN} < t_0$ and $t_{OUT} < t_1$ corresponds to *delayed extraction*, because there is a delay between the creation of electrons and the beginning of the extraction pulse.
3. $t_{IN} > t_0$ and $t_{OUT} > t_1$ corresponds to *interrupted extraction*, because electrons are created in the extracting field but this field is turned off before electrons leave the ionisation zone.
4. $t_{IN} > t_0$ and $t_{OUT} < t_1$ is equivalent to static extraction, already studied in chapter 3.

We detail these three kinds of time-dependent extraction in the following.

[9] "rise" refers to the amplitude of the field, but with electrons it will be more negative when risen

Pulsed extraction

The main idea behind pulsed-extraction is that if the field is turned on and off before any electron exits the ionisation zone, they will all experience the same accelerating field (during the same amount of time), independently of their initial position and the associated energy spread will be null. The field F_1 is turn on at $t = t_0$ and off at $t = t_1$ while the whole electron bunch is in the field region, as shown on figure 5.11. I call v_0 the mean

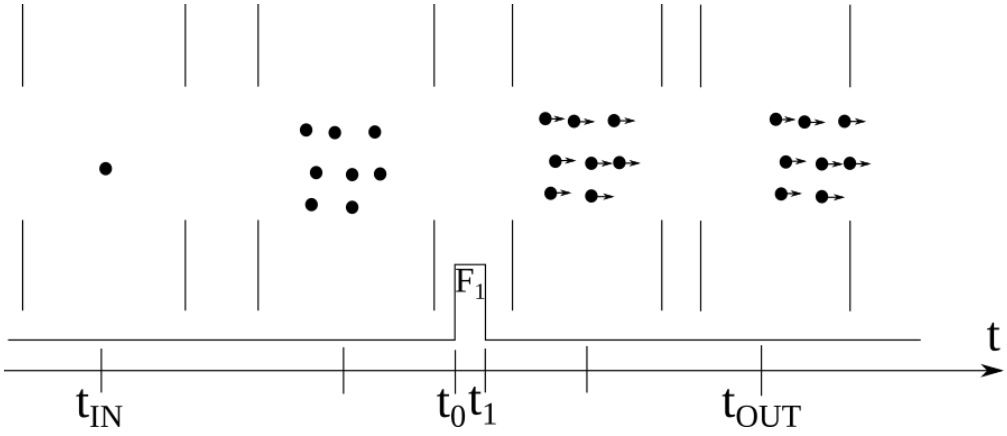

FIGURE 5.11: Schematic of pulsed extraction. Electrons are created at rest and are all given the same momentum-kick during the time window $t_1 - t_0$. t_{IN} is the time of the first electron and t_{OUT} is the time an electron exits the ionisation zone.

velocity in the z direction and Δv_0 its spread, $E_0 = \frac{1}{2} m_e v_0^2$ the mean kinetic energy of electrons before the extracting pulse, ΔE_0 its spread, and v_1, Δv_1, E_1, and ΔE_1 the same after the pulse. The differentiation of the kinetic energy formula gives:

$$\Delta v = \frac{\Delta E}{m_e v} \tag{5.12}$$

The action of the field can be expressed by:

$$\int_{t=t_0}^{t=t_1} eF dt = (\Delta t) e F_1 = \delta p \tag{5.13}$$

which is equivalent to a "velocity kick" (or "momentum kick" of amplitude δp)[30]. The consequence is that Δv is conserved during the acceleration, and we have:

$$\Delta v_1 = \Delta v_0 \tag{5.14}$$

$$v_1 = v_0 + \frac{(\Delta t) e F_1}{m_e} \tag{5.15}$$

$$E_1 = \frac{1}{2} m_e v_1^2 = E_0 + v_0 (\Delta t) e F_1 + \frac{((\Delta t) e F_1)^2}{2 m_e} \tag{5.16}$$

$$\Delta E_1 = m_e v_1 \Delta v_1 = \Delta E_0 + m_e \Delta v_0 (\Delta t) e F_1 \tag{5.17}$$

For electrons created at rest we have $\Delta v_0 = 0$, which gives $\Delta E_1 = 0$. However, any initial energy spread ΔE_0 will be amplified by the pulsed extraction. GPT-Simulations starting

from electrons at rest with an isotropic initial kinetic energy spread of 0.01 meV accelerated to 10 eV during 10 ns give an extracted electron bunch with an energy spread of 1.5 eV. Pulsed extraction effectively removes the energy spread linked to initial position spread, but exacerbates any initial small energy spread linked to atomic temperature or excess ionisation energy. In the case of threshold ionisation of laser cooled atoms, this pulsed extraction could still be viable, because there is virtually no initial energy spread that can be amplified. To be effectively used however, this extraction has to be followed by a static acceleration of the bunch, because it would be very difficult to bring electrons at energies around 1 keV with only pulsed acceleration.

A potential useful usage of this effect could be that it gives us access to the initial temperature of the electrons solely due to the ionisation process, by amplifying it so that it can be measured with reasonable accuracy.

Delayed extraction

Another version of time-dependent extraction is called delayed extraction[4], where the extracting field is turned on with a delay after the ionisation but is kept on after electrons leave the zone. A schematic of this situation is shown on figure 5.12. This does not

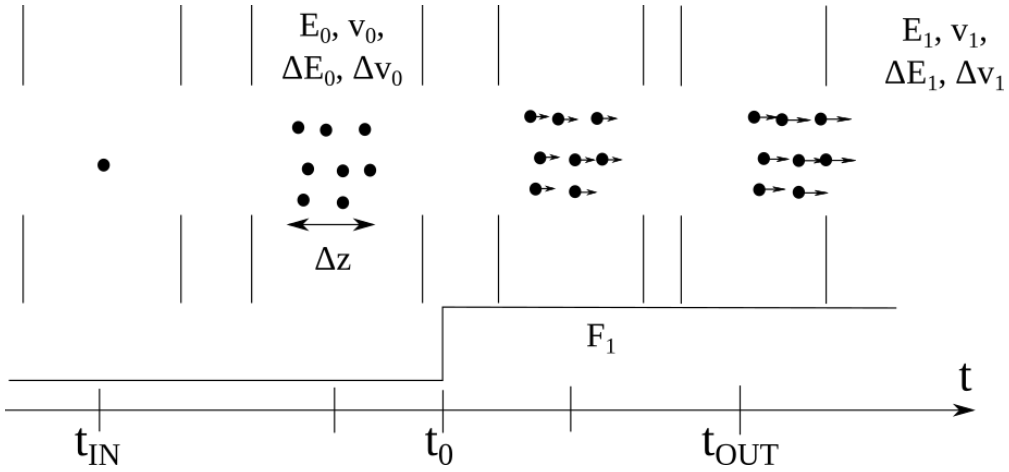

FIGURE 5.12: Schematic of delayed extraction. Electrons are created with a mean distance z_0 from the exit of the extraction zone, over a spatial spread Δz. All electrons leave the extraction zone before the field is shut off. t_{IN} is the time of the first electron and t_{OUT} is the time an electron exits the ionisation zone.

suppress the position related energy spread, as all electrons are given the energy corresponding to their distance to the end of the extraction zone z_0. We can thus write the relation:

$$E_1 = E_0 + z_0 e F_1 \tag{5.18}$$

This procedure is used in ToF-MS to increase the precision of the ToF measurement. The idea is that if the ionisation process is long, the resulting bunch length can be lowered by delaying the extraction after the end of the ionisation process. This means that electrons with non-zero velocities will move in the ionisation zone before the extraction pulse, or

that the ionisation volume will increase with the initial velocity of the electrons, amplifying the position-induced energy spread[10]. Thus we won't consider this kind of delayed extraction as a promising tool for our electron source, because of high electron initial velocities that will create large energy spread if we wait before applying the extracting field.

Interrupted extraction

Another version of time-dependent extraction for the reduction of energy spread can also be considered: when the field is already present at the creation of electrons but is cut off before they leave the ionisation zone. I call it "interrupted extraction". A schematic of the sequence can be seen on the following figure:

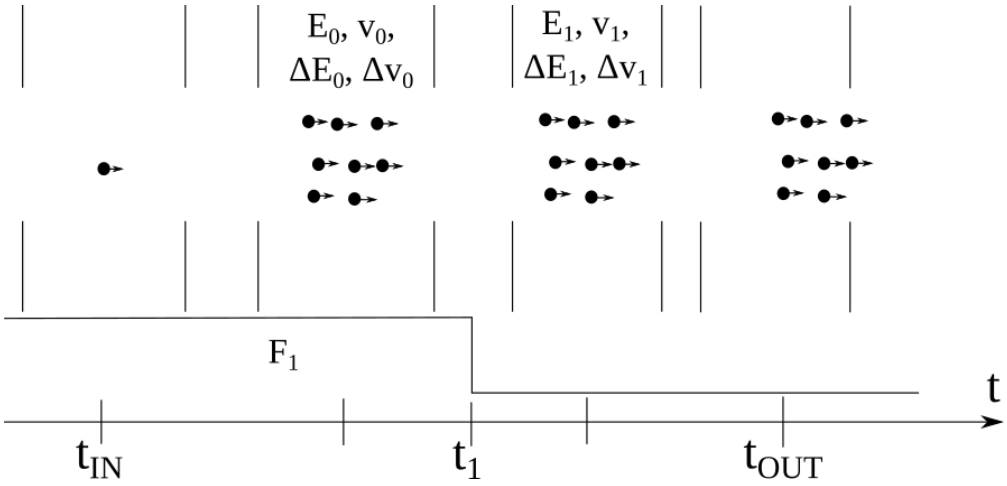

FIGURE 5.13: Schematic of interrupted extraction. Electrons are created with the electric field applied, and acquire all the same energy because the field is cut off before they leave the extraction zone.

The fact that the field is cut off before t_{OUT} effectively suppress the position-induced energy spread, but also conserves the velocity spread. Indeed, as for pulsed extraction I can write:

$$\Delta v_1 = \Delta v_0 \tag{5.19}$$
$$v_1 = v_0 + (t_1 - t_{IN})eF_1 \tag{5.20}$$
$$E_1 = \frac{1}{2}m_e v_1^2 = E_0 + v_0(\Delta t)eF_1 + \frac{((\Delta t)eF_1)^2}{2m_e} \tag{5.21}$$
$$\Delta E_1 = m_e v_1 \Delta v_1 = \Delta E_0 + m_e \Delta v_0 (\Delta t)eF_1 \tag{5.22}$$
$$\tag{5.23}$$

The high velocity of electrons means that the field pulse must be very short (to be off before electrons leave the ionisation zone), so this kind of acceleration can only bring

[10] A version of this extraction is used in zero-electron kinetic energy (ZEKE) spectroscopy to increase the precision of measurement, because electrons with initial velocity will crash into the walls of the ionisation chamber while electrons created with near-zero kinetic energy will still be present and extracted. This ensures that the ionising radiation is tuned precisely at the value of the ionisation threshold of the ionised atom/molecule[31].

electrons to a very small value of energy. Thus a static zone of acceleration is required after the pulsed extraction zone. The final energy spread is now totally dominated by the initial velocity spread Δv_0 and the length $(t_1 - t_{IN})$/amplitude (F_1) of the extracting pulse, and the size of the ionisation zone Δz plays no role. As an illustration of the possibilities of this version of time-dependent extraction, I simulated the extraction and acceleration of an electron bunch with very large initial extension (a square box of side 1 mm). The extraction is done in a 1 mm box centred at 0 by a -1 V/cm field turned on before $t = 0$ and shut off at $t = 5$ ns. From $z = 1$ mm there is an acceleration zone extending to $z = 11$ mm with a static field of -1000 V/cm. An initial isotropic velocity spread of 2600 m/s gives a final energy spread of 3.4 meV at an energy of 1 keV, comparable with values obtained with pulsed extraction in this case. In a static extracting field the same configuration would give an energy spread of $\Delta E = 1\,\text{mm} \times 1\,\text{V/cm} = 100$ meV.

In terms of energy spread, pulsed extraction and interrupted extraction are equivalent. One advantage of interrupted extraction over pulsed extraction however is that the ionisation is done under an electric field, which means that the very efficient ionisation and directional emission of Rydberg field-ionisation (see section 4.1.2) can be used.

We have seen the three different ways one can use time-dependent electric fields to extract electrons from the ionisation zone and create an electron bunch. The properties of this bunch depend strongly on the kind of extraction used, either time-dependent or static. Once this bunch is created and propagates, its properties can still be modified by static or time-dependent electric fields. This is what we explore in the following sections.

5.3.2 Velocity and energy conservation when manipulating bunches

In this sub-section I insist on an interesting aspect of the behaviour of electron bunches under static or time-dependent acceleration: *the conservation of their energy spread for static action, and the conservation of their velocity spread in the case of pulsed action*. This is important to have in mind if we want to understand how time-dependent manipulation can improve the properties of electron bunches. As an illustration of the static case first (not

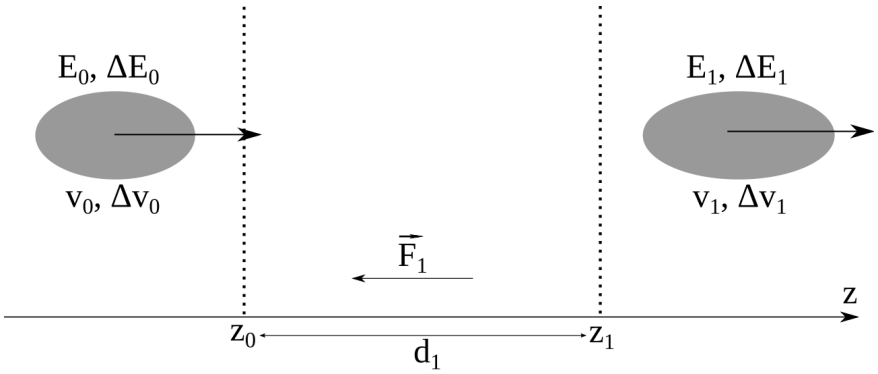

to be confused with static *extraction*) I consider an electron bunch with a given mean energy E_0 (with the mean velocity v_0), a kinetic energy spread ΔE_0 (that corresponds to a velocity spread of Δv_0) that enters (cf. top panel of figure 5.14) a spatial region of width d_1 (starting in $z = z_0$ and finishing at $z = z_1$) where a static electric field F_1 is oriented along its velocity.

The important point is that the bunch is formed before the acceleration zone, so that all electrons acquire the same amount of additional energy. The total action of the electric

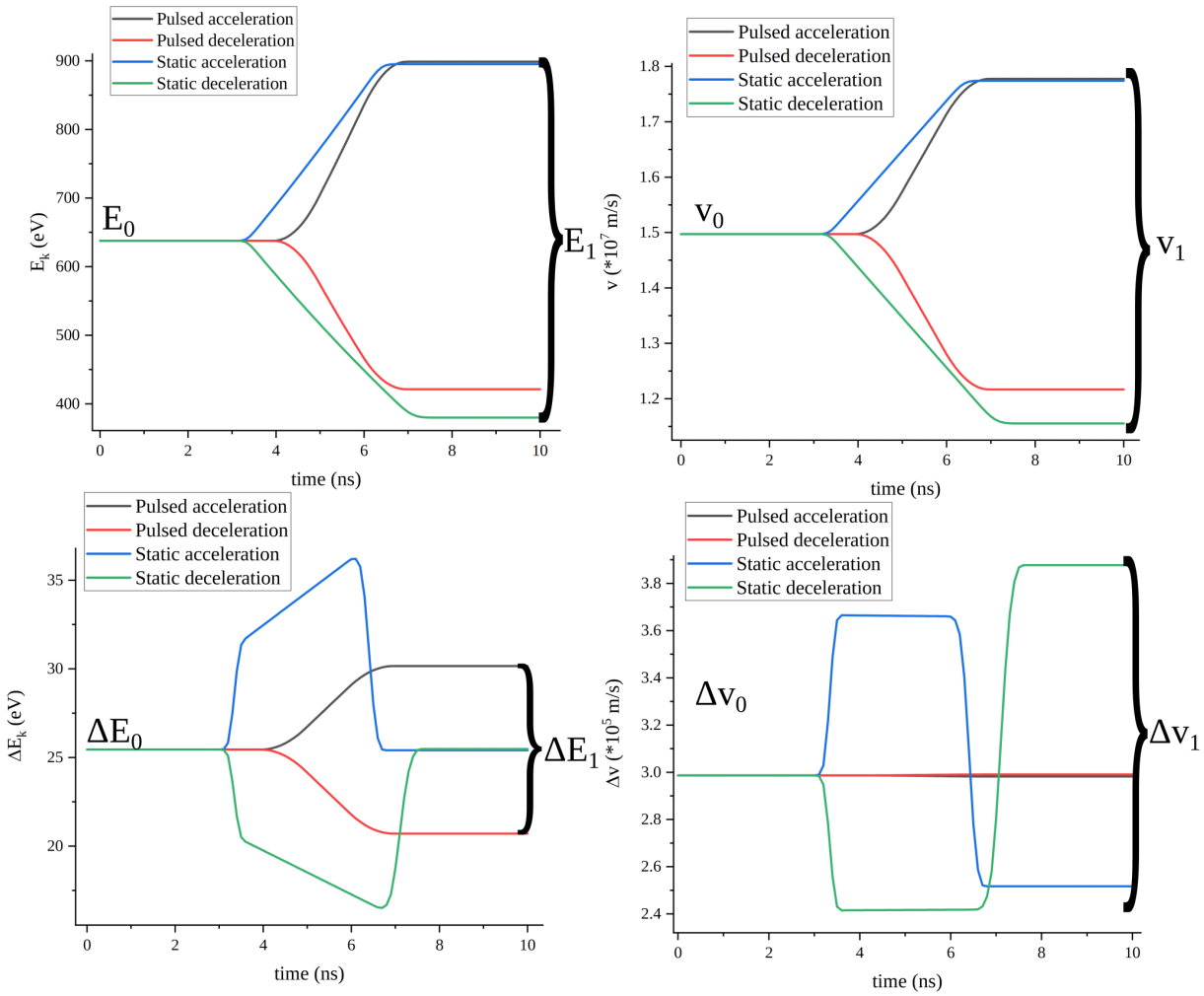

FIGURE 5.14: Simulations results of GPT showing the conservations and changes in velocity and energy spread of an electron bunch with Gaussian energy spread during static/pulsed acceleration/deceleration. Note the linear/parabolic evolution of speed and energy in static/pulsed action, respectively. Particles are created with a velocity along the $+z$ axis and enter a zone of static electric field (blue and green) or experience a homogeneous pulsed electric field along z (black and red). Pulsed action conserves the velocity spread, static action conserves the energy spread (once out of the acting zone). Static fields' amplitude are $\pm 51.7\,\mathrm{V/cm}$ for $d_1 = 5\,\mathrm{cm}$ and pulsed fields' amplitudes are equal to $\pm 80\,\mathrm{V/cm}$ with 1 ns rise, up and fall time.

field is then equal to $\int_{z=z_0}^{z=z_1} eF_1 dz = eF_1 d_1$, that is a constant energy addition, i.e. $E_1 = E_0 + eF_1 d_1$ and $\Delta E_0 = \Delta E_1$. We can then compute:

$$v_1 = v_0 \times \sqrt{\frac{2}{m_e}\left(1 + \frac{eF_1 d_1}{E_0}\right)} \tag{5.24}$$

$$\Delta v_0 = \frac{\Delta E_0}{m v_0} = \frac{\Delta E_0}{\sqrt{2 m_e E_0}} \tag{5.25}$$

$$\Delta v_1 = \frac{\Delta E_1}{m v_1} = \frac{\Delta E_0}{\sqrt{2m\left(1 + \frac{eF_1 d_1}{E_0}\right)}} \tag{5.26}$$

This means that before and after the acceleration zone, ΔE is constant, but E, v or Δv are not. We can thus consider that an electron bunch entering and leaving a region of constant electric field will experience an "energy kick"[30]. In the same conditions, if the field is pulsed during the presence of the bunch in the field region, the bunch experiences a velocity kick instead, exactly like in pulsed extraction presented in section 5.3.1.

In order to confirm the conservation laws in the two cases (static vs pulsed field), I performed realistic simulations of an electron bunch inside GPT[32]. I had first to write a custom element for GPT, allowing the definition of time-dependent electric fields with control of the rise time, pulse length and amplitude. The results of these simulations are shown on figure 5.14. An electron bunch is started with a velocity oriented along the $+z$ direction at $E_0 \approx 640\,\text{eV}$ (v_0 is the corresponding electron velocity) with a relatively large energy spread of $\Delta E_0 \approx 25.3\,\text{eV}$ (Δv_0 is the corresponding velocity spread) and either enters a region with an accelerating/decelerating field, or experiences a homogeneous pulsed electric field. These simulations clearly confirm the conservation of velocity spread in the case of pulsed action, and the conservation of energy spread in the case of static action (provided the electron bunch is created *outside* of the field region).

This is a very interesting result, because this means that in a pulsed deceleration, the energy spread of the electron bunch is reduced. We can thus imagine a sequence of constant acceleration and time-dependent deceleration, that realises the monochromation of the electron bunches. To show how this could be used to decrease the energy spread of an electron bunch, I performed the GPT simulation of such a process with a static acceleration for 5 cm followed by a pulse deceleration with amplitude 1530 V/cm for 10 ns (with 1 ns rise and fall time) to confirm this behaviour, the results are presented on figure 5.15 and show an energy spread divided by 3.

This represent a form of lossless cooling without any radiation or evaporation (loss of particles), very similar to adiabatic expansion cooling. The volume in phase space is constant, but the spread in momenta is transferred to spatial spread. The factor 3 is modest but the field amplitudes are easily accessible in laboratory and no precise timing of the field is required[11]. Further investigation is required to study if this process could be applied to decrease the energy spread of our electron bunches, but this simple way of cooling electron bunches is interesting in itself.

The manipulations described here are based on the fact that all electrons in the bunch experience the same field. We can go further into the manipulation of electron bunches

[11] A very recent publication proposes a more efficient lossless monochromation method for electron microscopes, that requires precise timing of two cavity excitations[33]

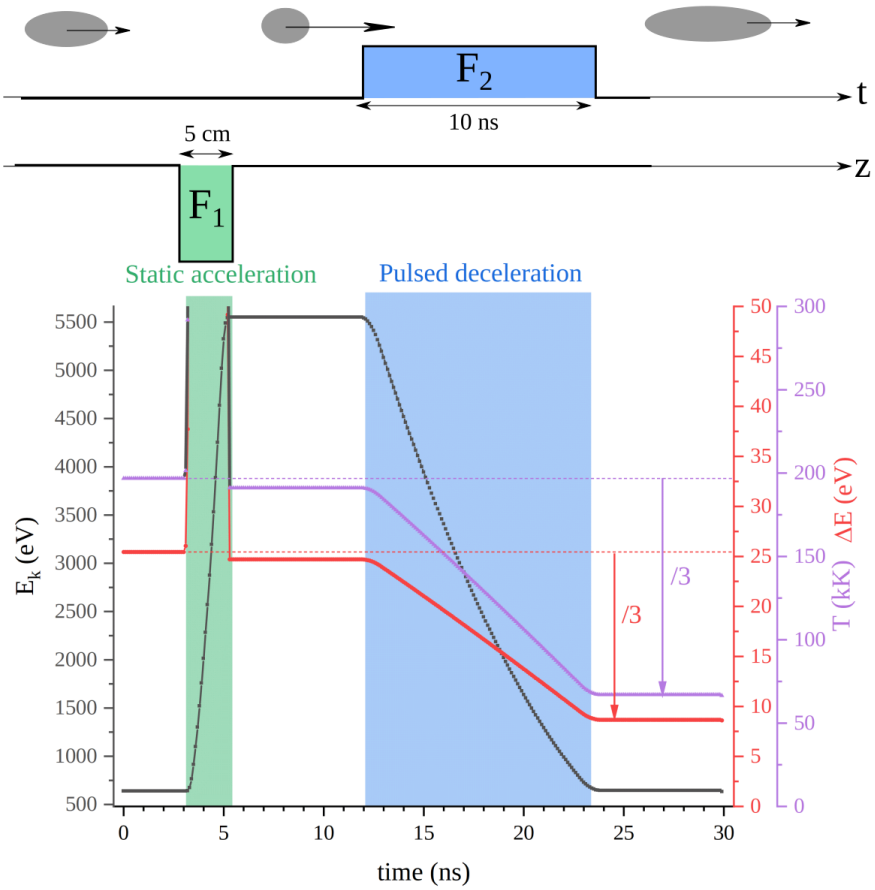

FIGURE 5.15: Evolution of the energy (left axis, in black), the energy spread (right axis, in red) and the associated temperature (right axis, in pink) (from the formula $T = \frac{2e\Delta E}{3k_B}$) for an electron bunch experiencing a sequence of static acceleration (in green, $F_1 = -1\,\mathrm{kV/cm}$ for 5 cm) and pulsed deceleration (in blue, $F_2 = 1530\,\mathrm{V/cm}$ for 10 ns with 1 ns rise time). Field amplitudes are tuned to keep the energy constant before and after the sequence (around 640 eV). The energy spread and temperature are divided by a factor 3, but the beam energy is not modified by the process (before and after).

by acting differently on different portions of the bunch, to correct its properties. This is what we explore in the following section.

5.3.3 Active bunching: velocity spread cancelling and velocity focusing

In the case where the temporal spread of a pulse is completely dominated by its energy spread (see section 5.1.2), it should be possible to decrease its pulse length by actively accelerate only the slower electrons[34]. Indeed, a "real" electron bunch with a non-negligible energy spread rapidly evolves into a cigar-like bunch, with the fastest electrons in the front and the slowest in the back. The velocity gradient of the electron bunch is thus linear along the bunch:

$$v[z] = v_0 + k \times (z - z_0) \tag{5.27}$$

with $k = \frac{dv}{dz}$ the velocity gradient along the propagation axis of the bunch. This is represented on figure 5.16.

Two "active-bunching" solutions are possible: the first is to accelerate the slowest electrons to the same velocity as the fastest electrons to reduce the energy spread and keep the pulse length constant. This is achieved best by a momentum-kick with the same spatial gradient as the velocity spread, i.e. a pulsed acceleration with an electric field gradient k. As the initial spatial spread is linear in velocity (and not in energy), the time-dependent field allows full compensation. Using equation 5.13, and in the hypothesis that $\Delta z \gg v_0 \Delta t$[12], the shape of the electric field pulse must be taken as:

$$F_1(z) = -\frac{m_e(z - z_0)k'}{e\Delta t} \tag{5.28}$$

with $k' = k$. This field pulse is odd around $z = z0$ so that it does not change the mean velocity of the beam v_0. I call this the velocity spread cancelling. This is quite demanding in terms of electrodes because a large number of them are needed to create a long, constant field gradient.

A slight variation of this technique is to take $k' > k$. Thus the slowest electrons will be accelerated a bit more, and the fastest will be decelerated a bit more than what is required to cancel the energy spread. This creates another point of temporal focusing down the column, on the sample for example. I call this variant velocity focusing. The position of the focus z_f is simply given by:

$$z_f = z_0 + \frac{v_0}{k' - k} \tag{5.29}$$

To summarize, the effect of the active bunching can be classified simply from the value of the gradient of the applied field k':

- $k' < k$, this reduces the velocity spread but keeps the bunch growing afterwards.
- $k' = k$, this cancels the velocity spread and freezes the bunch at its initial length.

[12] This is to make sure that electrons don't travel too much during the application of the correcting pulse. For a beam of $\Delta z = 1$ cm at 100 eV, this gives $\Delta t < 150$ ps to be safe

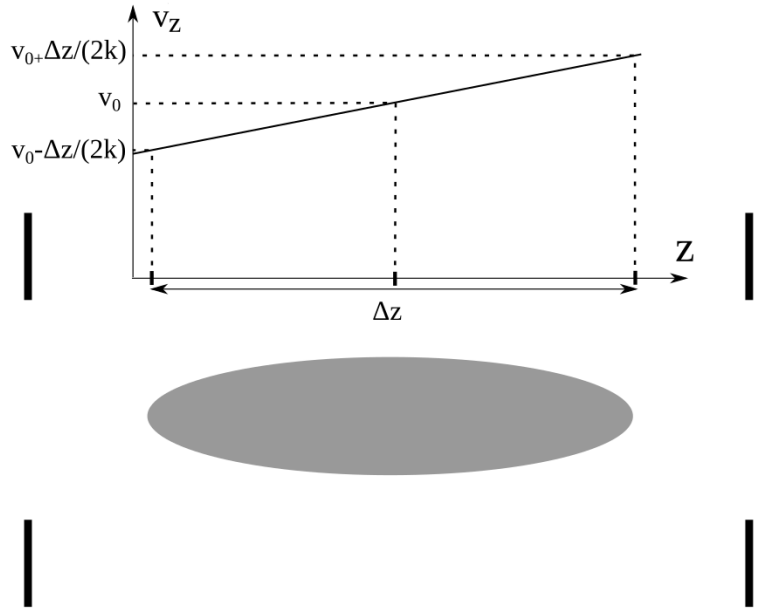

FIGURE 5.16: Schematic of a cigar-like bunch, whose velocity's v_z spatial spread is linear, with a gradient k along z, with a mean velocity v_0 and an extension in z of Δz.

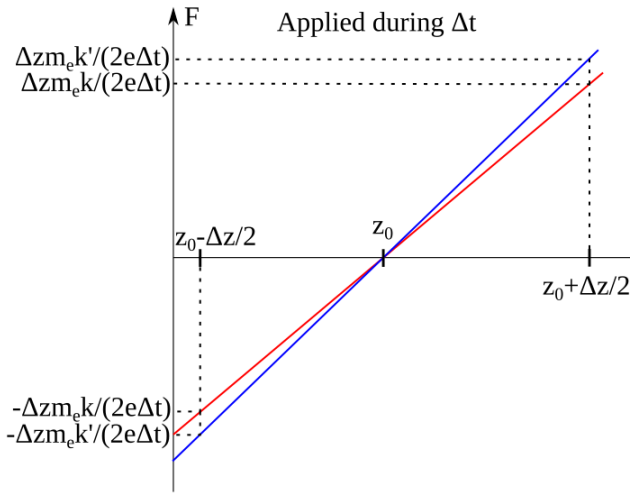

FIGURE 5.17: Spatial profile of the pulsed electric field (applied for Δt) for velocity spread cancelling (in red) and velocity focusing (in blue). k is the velocity gradient of the electron bunch, and k' is the pulsed electric field gradient in the case of velocity focusing

- $k < k' < 2k$, this reduces the energy spread and reverses it, meaning that the electrons at the back of the bunch will be slightly faster than the one at the center, and even more than the ones at the front of the bunch. This creates a velocity focal point at $z_f = z_0 + \frac{v_0}{k'-k}$ so it can also reduce the temporal spread.
- $k' = 2k$, this keeps the same velocity spread but reverses it, inducing a velocity focusing at $z = z_0 + \frac{v_0}{k}$.
- $2k \leq k'$, this increases the energy spread but can be used to strongly focus the bunch in time, at $z_f = z_0 + \frac{v_0}{k'-k}$, and hence drastically decrease the temporal spread. It has already been used to go from ps-range electron pulses to fs-range electron pulses to study very fast process in ultrafast electron diffraction[35], but at the expense of a much larger energy spread than before bunching.

A crucial aspect of this method is the quality of the initial velocity spread, i.e. the correlation between the electron's position is space and their velocity. This requires a drift length, like in ToF measurements (for the same reason) and the longer the drift length, the lowest the attainable corrected energy spread. In the simulations shown in figure 5.18, the initial beam energy is 100 eV with a large energy spread of 30 eV and a large spatial spread of $\Delta z_0 = 4$ mm. It requires around 50 cm to take a cigar-like shape, sufficiently spread out to allow strong cooling by active bunching. For simulations at lower energy, after 160 ns of free propagation, the electron bunch is at $z = 30$ cm, and its distribution is sufficiently spread out for a correct monochromation.

For us both the energy spread and the temporal spread are very important, so careful study of the effect of bunching on both these figure of merit is needed, and only gentle focusing are worth considering. To show the potential of this technique I simulated these two solutions in GPT ($k' = k$ and $k' = 1.5k$), in two cases: large and low initial energy spread. The results of these simulations are shown on figure 5.18 and 5.19. It shows that, in large energy spread conditions ($E_0 = 100$ eV, $\Delta E_0 = 30$ eV), putting $k' = k$ divides the electron energy spread by 32, and stops its temporal spread. If the temporal spread is more important, but that the energy spread must not increase, the velocity-focusing bunching ($k' = 1.5k$) is also useful, and figure 5.18 shows that the temporal spread can be divided by 17 (at the focal point), while halving the energy spread.

The simulations with a smaller energy spread of 50 meV (corresponding to the electron bunch presented in section 5.2.4) are shown on figure 5.19. The lower drift energy relaxes a bit the condition for the small Δt of the electric field pulse, so I take it with 200 ps pulse length. The results are very similar to the one at higher energy spread, because the energy spread is divided by 36 (final energy spread of 1.4 meV) for velocity spread cancelling, and the temporal spread is divided by 18.5 at the focal point for the velocity focusing case, down to 7.3 ps.

This shows that with reasonable electric fields, precise timing and careful tuning of the field gradient, it should be possible to greatly improve the properties of the pulsed electron bunches, in terms of energy spread and/or time spread. This requires however a dedicated drift length (and thus careful magnetic shielding because of low energy electrons) for the electron bunch to have a linear velocity gradient. Some experimental results of active bunching to reduce the energy spread have been obtained on Rubidium ions[30], but such results on electrons are still non-existent, particularly because of their high velocity. The realistic simulations I have presented confirm that this technique could very

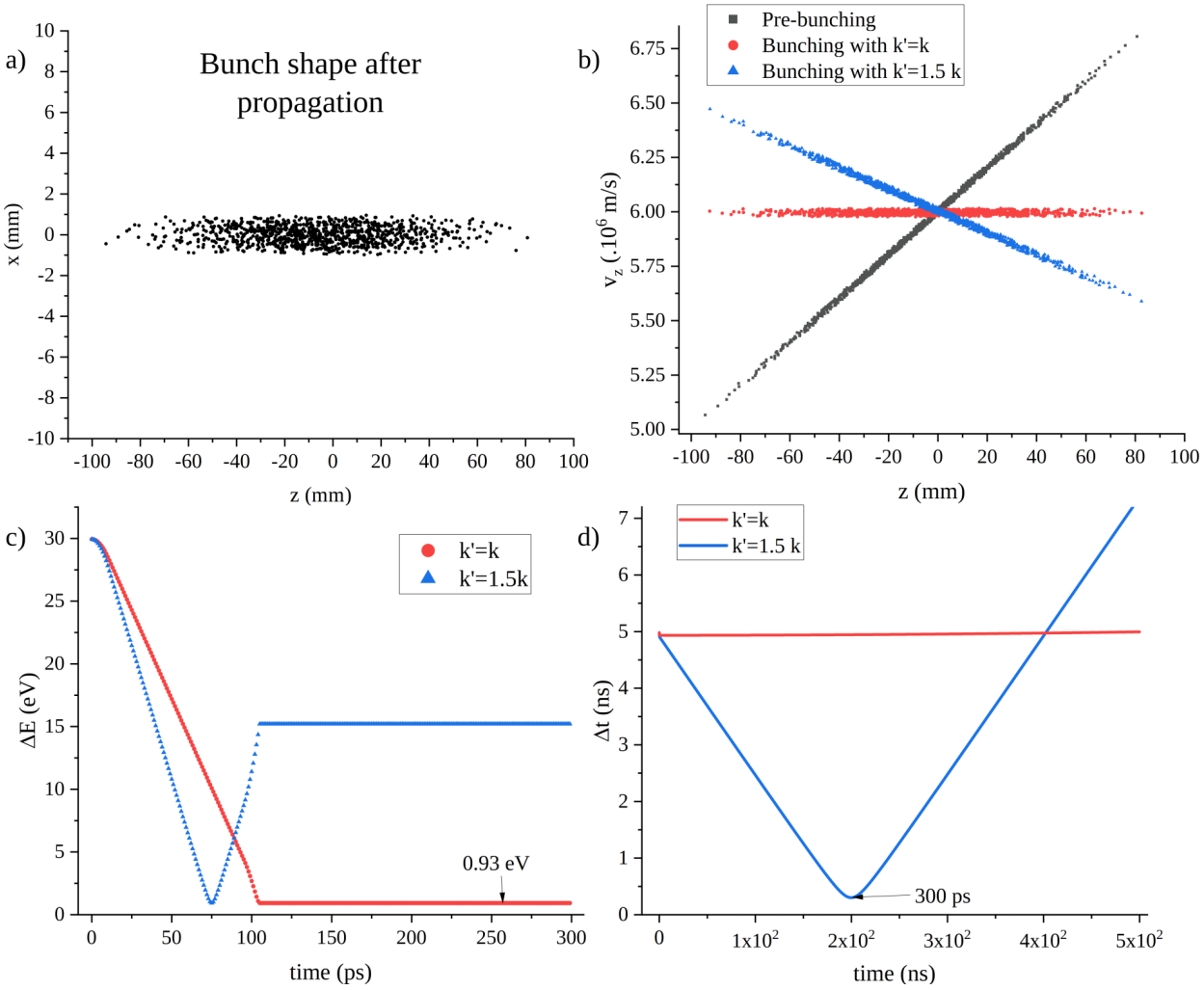

FIGURE 5.18: Results of the GPT simulations of the velocity spread cancelling ($k' = k$) and velocity focusing ($k' = 1.5k$) an electron bunch of mean kinetic energy 100 eV and energy spread of 30 eV propagate along z, and after 100 ns it has the shape presented on panel a). The correlations between z position and v_z are shown on panel b) for the bunch before (in black) and after a linearly increasing correcting electric field pulse (with $k' = k$ in red, it cancels the velocity spread, and $k' = 1.5k$ in blue, it halves and reverses it). The pulse is applied at $t = 100$ ns on the total bunch extension for 85 ps with a rise and fall time of 10 ps. The effect on the energy spread of the beam is shown on panel c). It is halved for $k' = 1.5k$ (in blue) and divided by 32 for $k' = k$ (in red). The effect on the temporal spread is shown on panel d), where the temporal spread (due to velocity spread) is stopped for $k' = k$ (in red) and the temporal spread is divided by 17 for $k' = 1.5k$ (in blue) at the velocity focal point.

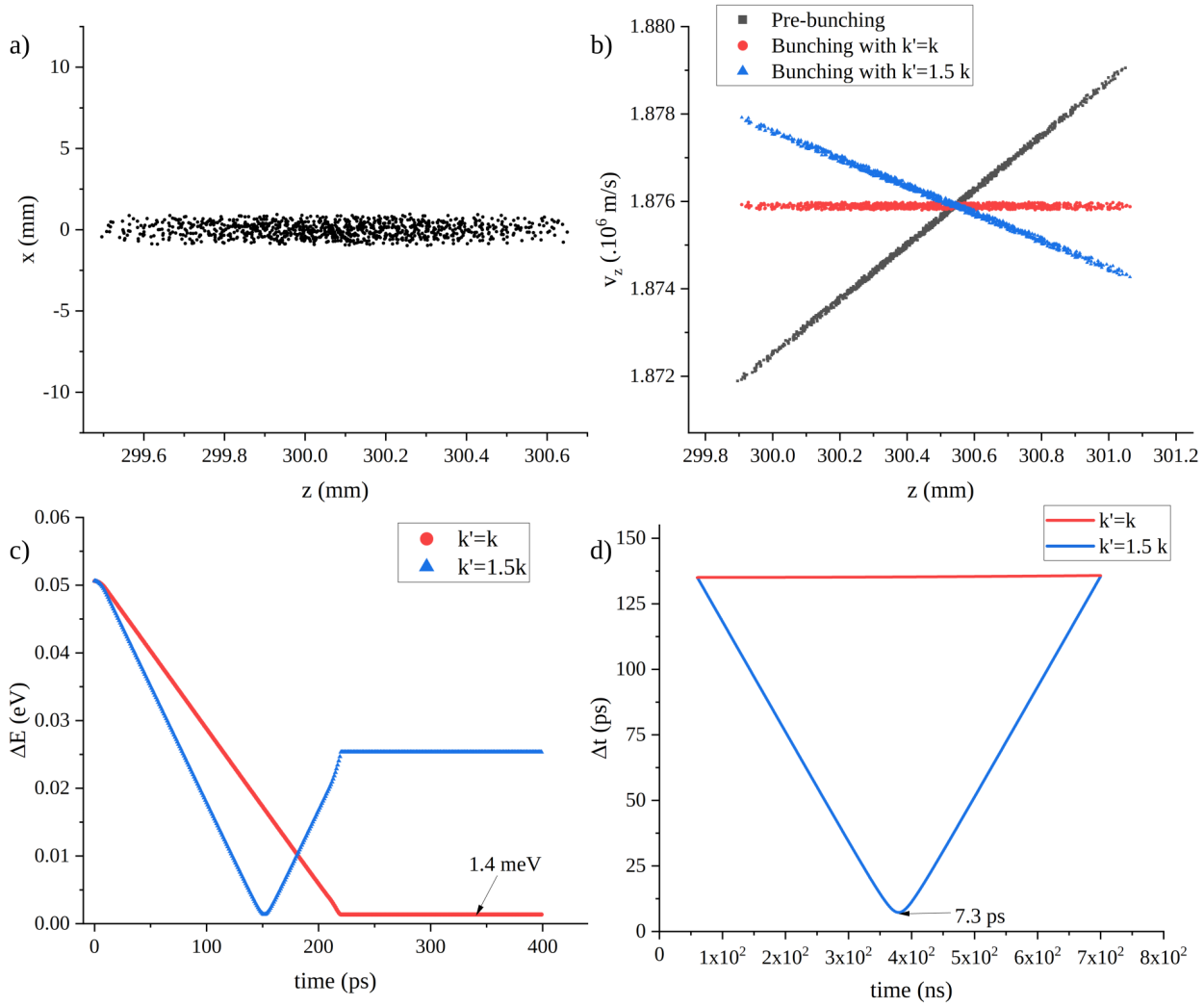

FIGURE 5.19: Results of the GPT simulations of the velocity spread cancelling ($k' = k$) and velocity focusing ($k' = 1.5k$) for an electron bunch of mean kinetic energy 10 eV and energy spread of 50 meV propagate along z, and after 160 ns (propagation of 30 cm) it has the shape presented on panel a). The correlations between z position and v_z are shown on panel b) for the bunch before (in black) and after a linearly increasing correcting electric field pulse (with $k' = k$ in red, it cancels the velocity spread, and $k' = 1.5k$ in blue, it halves and reverses it). The pulse is applied at $t = 160$ ps on the total bunch extension for 200 ps with a rise and fall time of 10 ps. The effect on the energy spread of the beam is shown on panel c). It is halved for $k' = 1.5k$ (in blue) and divided by 35.7 for $k' = k$ (in red), attaining an energy spread of 1.4 meV. The effect on the temporal spread is shown on panel d), where the temporal spread (due to velocity spread) is stopped for $k' = k$ (in red) and the temporal spread is divided by 18.8 for $k' = 1.5k$ (in blue) at the velocity focal point, attaining 7.3 ps.

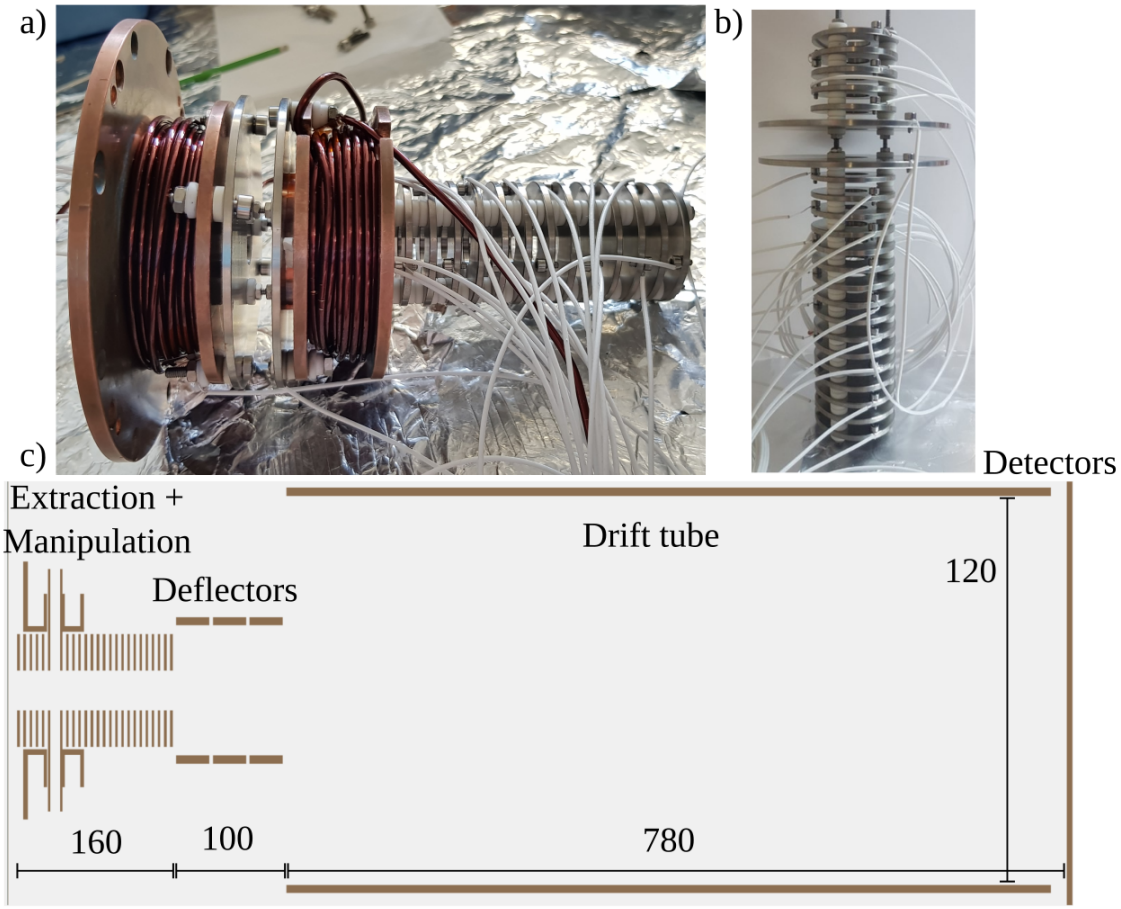

FIGURE 5.20: Details of the experimental set-up in Mainz: a) Picture of the stack of electrodes enclosed in the copper housing that also holds the coils of the 3D-MOT b) Electrodes stack alone c) Simion simulation of the new electrode configuration, with the extraction electrodes, deflectors, drift tube and detectors

well be used in a real pulsed electron source, to greatly improve its properties. A simpler version of this concept, requiring only a pulsed field (and not a constant gradient) could be used to correct chromatic aberrations in an electron microscope[34,36]. In the next section I will present some attempts to demonstrate active bunching on the electron source in Mainz.

5.3.4 Modification of the electrodes in the Mainz set-up

In order to experimentally test the ideas of time-dependent electron manipulation, the experimental set-up presented in section 5.2.3 had to be modified. This was started by Olena Fedchenko, Serguey Chernov and Daniel Comparat before I was involved in the project, and I helped finishing the experimental work. This consisted in the insertion of many electrodes around the ionisation zone and along the electron path. This stack of electrodes can be seen on figure 5.20 along with a Simion modelling of the new electron path.

This internal electrode configuration was completed by an external resistive voltage divider to allow the production of a pulsed electric field with controllable gradient. One

voltage pulse is applied to all electrodes and divided at each electrode by a known value of resistance, so this allows the production of a gradient-free electric field, or with a specific gradient, all depending only on the resistances. These experiment were done with a constant value of the resistances, creating the same voltage drop at each electrode, so that the field is of spatially constant amplitude. The pulser provides pulsed voltage of 15 V for 10 ns, and is synchronised with the pulsed laser at 40 MHz, corresponding to a period of 25 ns on the DLD.

The rest of the set-up in unchanged, so we start with a 3D-MOT of caesium, excite the atoms with two cw-laser and ionise them with a fs-TiSa, and measure the resulting time-dependent signals after around 0.8 m of free propagation.

5.3.5 Experiments on time-dependent manipulation of electron bunches

Simulations

Experimental data was acquired with this set-up for just one week before it had to be dismantled, and I tried to rationalise the observations, with the help of Simion simulations. On figure 5.21 I show one example of experimental data, corresponding to p-polarised photoionisation with a laser bandwidth of 24 meV and a mean excess energy of $E_\lambda = 16$ meV. The simulations showed that in the case of s-polarisation, the orthogonal emission and the absence of constant extraction field implied that a large numbers of these electrons would crash into the electrodes. Experimentally this was confirmed as signal level for p-polarisation is orders of magnitude bigger than with s-polarisation.

A crucial point to understand the experimental data is to know the delay between the electron creation and the electric field pulses. Indeed we are not certain that the delay between the electron creation and the electric field pulses is the same that the delay between the voltage pulse and the laser pulse (that we control via the pulser). The propagation of the voltage pulse through the cables to the electrodes could indeed introduce a delay. As the field pulser was synchronised with the laser, the delay between the laser and the pulse is not known but is always the same.

In order to retrieve this delay from the experimental data shown on figure 5.21 I performed a series of simulations in this electrode geometry with $\Delta E = 24$ meV (due to the spectral linewidth of the fs-laser) tuned at $E_\lambda = 16$ meV (thus in photoionisation), with a varying delay between the electrons creation and the electric field pulse. These can be seen on figure 5.22. As the laser/pulser are pulsed at 40 MHz, the maximum delay is 25 ns, so I performed the simulations for delays going from 0 ns to 22.5 ns, with 2.5 ns steps. Indicated on the figure is also the time window corresponding to the common time period (period of the laser shots, of the electric field pulses and time window of the DLD). The simulations show first that, as there is no constant extracting field, and that the pulsed voltage is quite low (15 V), the electrons spend a lot of time in the accelerator section, and experience many field pulses (7-8) before they enter the ToF tube. This means that no matter what the ionisation/pulsed-field delay is, the electrons will experience the same mean acceleration, plus or minus one pulse. The simulations (almost) all feature two peaks in the temporal structure, which is expected since I try to simulate p-polarised photo-ionisation and thus, as demonstrated in section 5.2.3, the electron emission is composed of two distinct electron bunches with opposite starting momentum distribution.

To illustrate the electron behaviour let's choose a time delay of 7.5 ns. Electrons in the first bunch (ejected forwards) arrive in one peak, 25 ns before electrons ejected backwards,

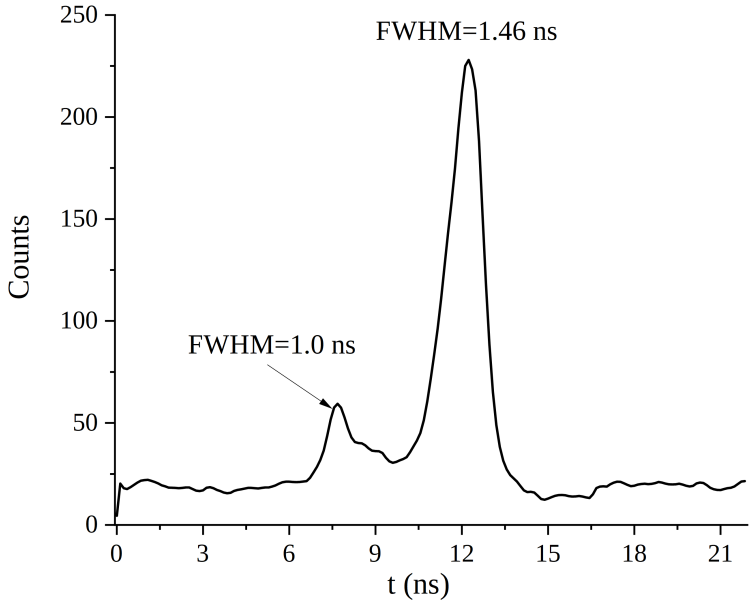

FIGURE 5.21: Time-dependent electron signal, acquired with a laser bandwidth of 24 meV and a mean excess energy of $E_\lambda = 16$ meV, with an electric-field pulsed at 40 (MHz (as described in section 5.3.4). Two peaks are visible, a large with 1.4 ns FWHM and a smaller one with a FWHM of 1.0 ns.

that also form a well-defined peak. To simplify the analysis I plot the time evolution of the velocity of one electron of each group on figure 5.23.

This figure shows that electrons ejected forwards experience 7 full electric field pulses before exiting the accelerator, and that electrons emitted backwards experience 8 full pulses. The particular choice of pulse amplitude, pulse duration and emission kinetic energy is, by chance, perfectly tuned so that this extra pulse cancels the initial energy difference, so that both electrons leave the accelerator with the same kinetic energy, regardless of the orientation of their emission. The delay between these two electron bunches is thus constant in the rest of the set-up and the "measurement" gives two well defined peaks with a delay of 25 ns. In other time delays, the situation is more complicated.

Comparing the time delays with the panel k of figure 5.22, it clearly shows that time delays of 0 ns-2.5 ns and 12.5 ns-25 ns result in a temporal spread of the electrons on the detector, and thus a substantial overlap between time windows of the DLD. This would mean, experimentally, that no matter the central point chosen for the DLD, the background signal would be very large. On the contrary, time delays of 5 ns to 10 ns show two clear peaks, with close to 0 background. The special case of 7.5 ns delay shows 25 ns between the two well isolated peaks, meaning that the appropriate choice for the center of the DLD window would make these two peaks appear as only one peak. This is easily explained by the fact that all these time delays correspond to electron bunches created as the electric field is on, meaning that they are well extracted from the ionisation region. On the contrary, for all other delays the electrons propagate freely before being extracted, which increases the temporal spread of these bunches and makes the signals overlap.

Another effect of the time delay plays a role into the observed time-dependent structures: if an electron bunch exits the accelerator while the field is changing (during a rise or fall time), all electrons of the bunch won't be accelerated the same way, and this will affect the temporal distribution. This explains why the peaks in figure 5.22 (e) (delay of

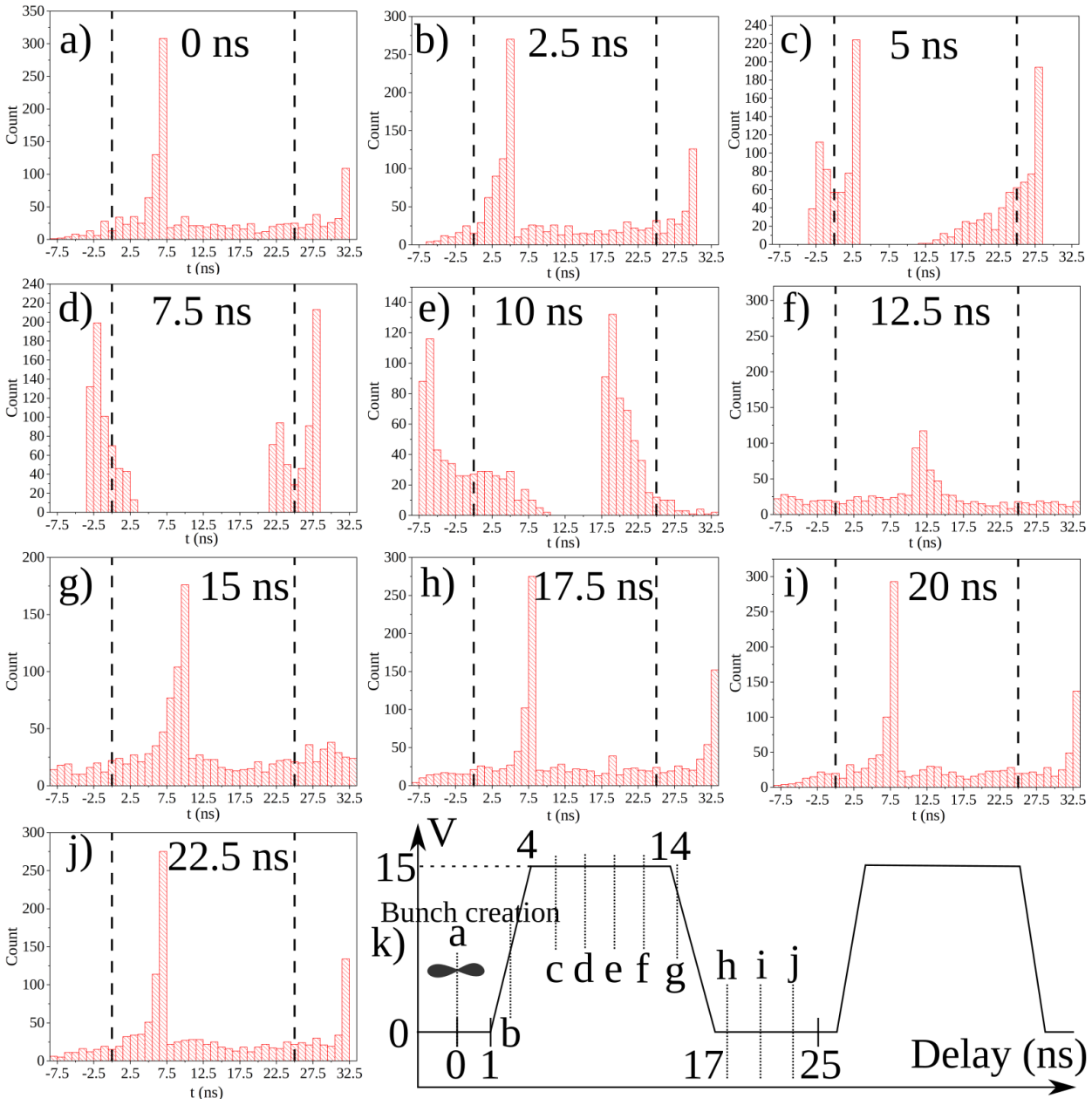

FIGURE 5.22: a)-j) Simion simulations of the arrival time of an electron bunch created by photoionisation with p-polarisation (taking into account the emission cone) with $\Delta E = 24\,\text{meV}$ tuned at $E_\lambda = 16\,\text{meV}$, with various delay to the voltage pulse, from 0 ns (a) to 22.5 ns (j). The vertical dash lines at 0 ns and 25 ns indicate the size of the DLD window and the period of the laser shots and the field pulses. k) Time evolution of the voltage pulse from 0 V to 15 V, with a period of 25 ns and rise/fall time of 3 ns. The binning is 1 ns.

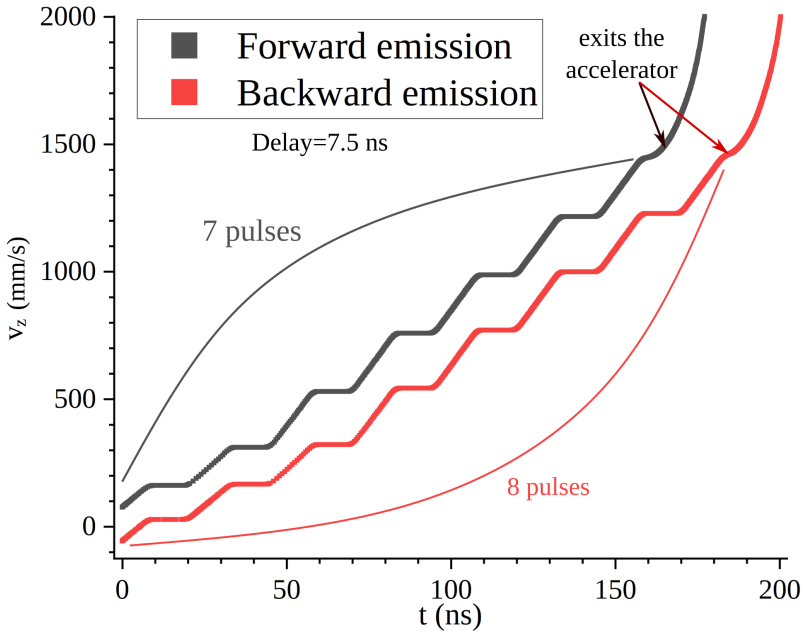

FIGURE 5.23: Temporal evolution of the velocity along z of photo-electrons emitted with a time delay of 7.5 ns, one forward (in black) and one backward (in red). This corresponds to electron emission when the field is on. The electron ejected forward experiences 7 field pulses before it exits the accelerator, the electron ejected backward experiences exactly one pulse more, and both leaves between pulses.

10 ns) are spread out even though they are created when the field is on. The two peaks have a tail towards the long ToF, which is due to the fact that most of the electron bunch is accelerated by the last electric pulse, but a small part of the bunch is not, and arrives a bit later.

Interestingly the data at a delay of 5 ns (c) shows that one peak is fine while the other is spread out, with its tail towards the lower ToF. This indicates, by contrast, that the first electron bunch exits while the field is off, and that the tip of the second bunch is partially accelerated by the falling electric field pulse. For time delays of 12.5 ns and 15 ns (5.22 f), g)) there is only one peak, and a strong background. This happens because the bunches exit the accelerator during the fall and rise period, so that the temporal distribution is completely scrambled.

Comparison with experiment

As already mentioned, the first comparison between experiments and theory is in the relative intensity of p-polarisation against s-polarisation photo-ionisation. Both in the simulations and in the experiments, only p-polarisation yielded enough signal. As the electrode train is placed at the start of the electron path, it allows testing time-dependent extraction, but not active bunching. The time structure shown on figure 5.21, featuring moderate levels of background and only one well resolved peak indicates that the experimental delay between the electric field pulse and the laser pulses is around 0 ns, or between 17.5 ns and 22.5 ns. This is further indicated by the relatively small FWHM of

the main peak (1.4 ns), to compare to the large temporal width of the peaks presented on figure 5.22 for time delays of 5 ns to 15 ns.

There were no data acquired with a varied time delay, so it is hard to make sure the determined value of the delay is correct. Furthermore the amplitude of the voltage pulse is too small to completely extract electrons from the accelerator in one pulse, which means that a voltage pulse can occur while the bunch is exiting the accelerator. This blurs the temporal distribution of the bunch and makes the interpretation difficult. Providing more voltage at this rate, with this timing precision is not trivial however. One solution could probably have been to use a pulse picker on the laser, to reduce the frequency down to a few kHz, so that the pulse could be higher and more spaced in time, to suppress all overlap between bunches. Furthermore, having a real, absolute ToF measurement (and not modulo 25 ns) would greatly facilitate the comparison with the simulations, and is not very difficult to implement. Sadly, the experimental set-up had to be dismantled before we managed to improve the acquisition set-up and acquire more meaningful data.

Section summary

Time-dependent manipulation of electron bunches

This section involved the formation and manipulation of electron bunch with the help of time-dependent voltages. Several different concepts are presented, that could intervene in the construction of a high-performance electron source. First the time-dependent extraction (i.e. formation of the electron bunch), that can take three different forms:

- Pulsed extraction: the electron energy spread coming from their different initial potential is suppressed, meaning that even a large ionisation zone in z direction won't induce large energy spread. However, the pulsed acceleration amplifies any initial energy spread by orders of magnitude (at low energy).
- Delayed extraction: can be used to compensate for a longer τ_{ion} than the bunch length required, but any initial electron velocity will induce large energy spread as the field is kept constant after they leave the ionisation zone.
- Interrupted extraction: the field is on during the ionisation but is off before electron leave the ionisation zone. This suppresses the energy spread due to Δz but as the electrons are not free to expand before the extraction (like in the other two time-dependent extractions), the initial velocity spread has far less influence on the final energy spread. This is the most promising time-dependent extraction for our purposes.

I then presented the conservation relations for the static acceleration of a an already formed bunch, that conserves the energy spread of the bunch, and the pulsed acceleration that conserves the velocity spread of the bunch. I presented simulations showing how this could be used to divide the energy spread of a bunch by three. Then I presented another aspect of time-dependent action on electrons, that is active bunching, to reduce the time or the energy spread of electron bunches. Strategies for each of these cases were presented, with simulations showing that energy spread can be divided by ≈ 30 with a constant time spread, or the energy spread could be halved by dividing the time spread by ≈ 18. Efforts to show this experimentally in Mainz are also presented, with detailed simulations that show the importance of the time delay between the electron bunch and the electric field pulse.

5.4 Pulsed ionisation: pulsing the electric field

This section deals with the formation of electron bunch with the help of electric field pulses and continuous lasers. This is different from the concepts described in section 5.3.3 because here the ionisation itself relies on a pulsed electric field. The first way to ionise atoms with a pulsed electric field is pulsed-field ionisation.The term pulsed field-ionisation (PFI) has a precise meaning in ZEKE spectroscopy, as a way to improve the resolution. For us, PFI is the excitation of an atom in its Rydberg state followed by an

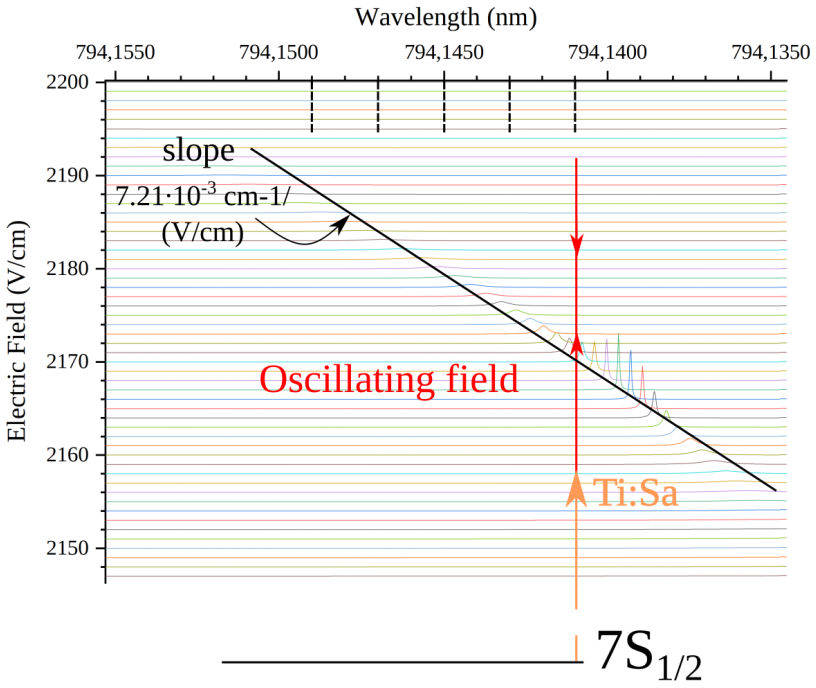

FIGURE 5.24: Stark-map showing an appropriate state for Rydberg pulsed-resonance field ionisation. It is well-isolated from other states so that a 30 V/cm pulse amplitude leads to only one resonance. Its Stark slope is $\frac{dv}{dF} = 7.21 \times 10^{-3}\,\mathrm{cm}^{-1}/(\mathrm{V/cm}$. Its linewidth strongly depends on the field/wavelength so that we can study the link between the linewidth and the observed ionisation duration. The laser is tuned out of resonant from the $7S$ and an oscillating field brings it in and out of resonance. The top dashed black lines corresponds to values of Ti:Sa wavelength where we took experimental data.

electric field pulse that ionises the Rydberg state. This was used to produce electron pulses of length 250 ps in Ref. [37], where the authors excited Rydberg states of rubidium atoms under no electric field, and pulsed a large electric field in a very short time. The main issue of this method is that the amplitude of the electric field to pulse is large (up to 1.4 kV/cm[37]) to ensure complete ionisation in a short time. This creates experimental difficulties and a large energy spread. In the next section I present another approach to the ionisation of Rydberg atoms with the aid of pulsed electric field, that has the advantage of using small voltage pulses, that can easier be pulsed at a higher repetition rate. I introduce the concept of Rydberg pulsed-resonance field-ionisation (RPRFI) with experimental results that confirm its appeal for the production of a pulsed electron source for HREELM, and its potential applications to the production of very low energy spread, very short electron bunches.

5.4.1 Rydberg pulsed-resonance field-ionisation (RPRFI): an innovative pulsed ionisation scheme

Pulsed-field ionisation is the ionisation of a stable Rydberg state by a pulsed electric field. The state is excited by a pulsed or continuous laser, and the electric field pulse lowers the

ionisation threshold for the duration of the pulse. It is widely used in laboratories in this form to detect Rydberg atoms for example.

In this section I introduce a new ionisation scheme that I call Rydberg pulsed-resonance field-ionisation. The idea is to have atoms in a static electric field and a continuous laser with a very low linewidth tuned very close to a Rydberg Stark shifted-resonance, as presented on figure 5.24. The electric field is applied by two electrodes, one at high negative[13] voltage and the other at ground. On the electrode at ground we apply a time-dependent voltage that will induced a time-dependent electric field at the atoms. Under the right circumstances (of laser detuning, Stark shift and pulsed-potential amplitude) the varying electric field (of small amplitude against the static electric field) will bring the laser frequency at resonance only during a very short time, enhancing the excitation and ionisation of the Rydberg states by several orders of magnitude, thus creating a pulsed-electron source. This has the big advantage of having to pulse only a few volts to ionise the atoms via the Rydberg states, so that it is a lot less demanding in terms of electronics. Furthermore, the use of a continuous wave laser allows very small spectral linewidth (as opposed to pulsed lasers) and thus allows the selection of a specific Stark-shifted Rydberg state.

If the target state is sufficiently isolated in the Stark map, we can safely model the situation with an open lossy two-state system interacting with a monochromatic laser of frequency ω_L featuring a time-dependent detuning $\Delta(t)$. Describing an open quantum system can be really involved but we will simplify the theoretical treatment by using an *effective* lossy Hamiltonian[14]. The ground state $|g\rangle$ is taken as the $|7S\rangle$ state, and we neglect the effects of its 50 ns lifetime (because it is connected to a reservoir or lower lying atoms via a saturated transition).

The excited state $|e\rangle$ is the Stark shifted Rydberg state. Its transition angular frequency from the "ground" state is ω_0, and its coupling to the ground state is characterised by the rate Γ_{SE}, to which we add a general loss term $i\Gamma_{Loss}$. The term Γ_{SE} is calculated from d_0 the dipole moment of the $|g\rangle \longleftrightarrow |e\rangle$ transition as:

$$\Gamma_{SE} = \frac{\omega_0^3 d_0^2}{3\pi\epsilon_0\hbar c^3} \tag{5.30}$$

The time-dependency of the detuning comes from the combination of the fixed laser wavelength, the pulsed electric field and the Stark shift of the Rydberg state. We suppose it has a linear temporal dependency as:

$$\Delta(t) = \Delta(0) + \Delta a * t = \Delta_0 + \Delta a * t \tag{5.31}$$

In this definition the term Δ_0 is the detuning's initial (at $t = 0$) value, and Δa is its temporal slope. Δa is given by the ratio of the state's Stark slope ($\frac{d\nu}{dF}$) and the electric field temporal variation ($\frac{dF}{dt}$) as:

$$\Delta_a = \left(\frac{d\nu}{dF} * \frac{dF}{dt}\right) = \frac{d\nu}{dt} \tag{5.32}$$

I use the formalism of the optical Bloch equation, because I consider both coherent and incoherent processes, and I am interested in the dynamics of the population evolution.

[13] or positive

[14] the "right" way to treat a dynamical open-quantum system is to formulate it in terms of Lindblad equation[38] in the Born-Markov approximation[39]

This starts by considering the density-of-state matrix $\hat{\rho}$ in the $\{|g\rangle, |e\rangle\}$ basis:

$$\hat{\rho} = \begin{pmatrix} \rho_{gg} & \rho_{ge} \\ \rho_{eg} & \rho_{ee} \end{pmatrix} \tag{5.33}$$

As the intensity of our laser is moderate (the Rabi frequency Ω and the detuning $\Delta(t)$ are small against ω_L), the time-evolution of the density of state matrix can be decomposed in two main components[39]:

$$\frac{d\hat{\rho}}{dt} = \left.\frac{d\hat{\rho}}{dt}\right|_{coherent} + \left.\frac{d\hat{\rho}}{dt}\right|_{incoherent} \tag{5.34}$$

This separation means conceptually that the incoherent processes are not directly influenced by the laser radiation. The first term of this separation, the coherent term, is given by the interaction of the two-level system with the laser light, whose amplitude is given by:

$$E(t) = E_0 \cos(\omega_L t - \phi) \tag{5.35}$$

The corresponding Rabi frequency (in the rotating field approximation, which removes rapidly oscillating terms) is:

$$\Omega = \frac{dE_0 \exp(i\phi)}{\hbar} \tag{5.36}$$

with d the reduced electric dipole of the $|g\rangle \longleftrightarrow |e\rangle$ transition. The interaction Hamiltonian $\hat{H}$ (in the dipole-electric approximation, including the loss term in the excited state population) can thus be written:

$$\hat{H} = \frac{\hbar}{2} \begin{pmatrix} \Delta(t) & \Omega^* \\ \Omega & -\Delta(t) - i\Gamma_{Loss} \end{pmatrix} \tag{5.37}$$

with "*" denoting the complex conjugate. I neglect the direct coupling of the ground state to the continuum via the laser radiation, based on the fact that the signature of such a coupling is a Butler-Fano profile (pronounced asymmetry in the peaks[40]), that we have not observed in all our experimental data.

The term Γ_{Loss} will group all the possible leaks of the excited state outside of the two-level system, including ionisation and spontaneous emission towards other states than $|g\rangle$. This makes the Hamiltonian no longer hermitian and the population is no longer conserved (or $\hat{H}^\dagger \neq \hat{H}$ and $\mathrm{Tr}(\hat{\rho}) \leq 1$).

The incoherent evolutions (the second term of equation 5.34) are given by the Fermi golden rule for the spontaneous emission process[39]:

$$\left.\begin{cases} \frac{d\rho_{gg}}{dt} &= \rho_{ee}\Gamma_{SE} \\ \frac{d\rho_{eg}}{dt} &= -\rho_{eg}\frac{\Gamma_{SE}}{2} \\ \frac{d\rho_{ge}}{dt} &= -\rho_{ge}\frac{\Gamma_{SE}}{2} \\ \frac{d\rho_{ee}}{dt} &= -\rho_{ee}\Gamma_{SE} \end{cases}\right|_{incoh.} \tag{5.38}$$

It is completed by the coherent evolution[15] to give:

$$\begin{cases} \frac{d\rho_{gg}}{dt} = \frac{i}{2}\Omega^* \left(\rho_{ge} - \rho_{eg}\right) + \rho_{ee}\Gamma_{SE} \\ \frac{d\rho_{eg}}{dt} = \frac{i}{2}\left(\rho_{ee}\Omega^* - \rho_{gg}\Omega\right) + i\Delta(t)\rho_{eg} - \frac{\rho_{eg}\Gamma_{Loss}}{2} - \frac{\Gamma_{SE}}{2} \\ \frac{d\rho_{ge}}{dt} = \frac{i}{2}\left(\rho_{gg}\Omega - \rho_{ee}\Omega^*\right) - i\Delta(t)\rho_{ge} - \frac{\rho_{ge}\Gamma_{Loss}}{2} - \frac{\Gamma_{SE}}{2} \\ \frac{d\rho_{ee}}{dt} = \frac{i}{2}\Omega\left(\rho_{eg} - \rho_{ge}\right) - \rho_{ee}\Gamma_{Loss} + \Gamma_{SE} \end{cases} \tag{5.41}$$

In total there are five independent parameters in our model: Ω, Γ_{SE}, Γ_{Loss}, Δ_0 and Δa. As we will compare the calculations with experimental data, we plug in the specific corresponding values of Δ_0 and Γ_{Loss} (see 5.24) that are reported in table 5.2.

λ (nm)	794.141	794.143	794.145	794.147	794.149
Γ_{Loss} ($10^9 s^{-1}$)	0.601	1.644	2.728	3.767	4.447
Δ_0 (GHz)	10	11.949	13.569	14.982	16.229

TABLE 5.2: Values of the parameters in the experiments, obtained from the LFT-Stark map shown on figure 5.24

The value for Δ_0 ($\lambda = 794.141$ nm) is arbitrary as it is just a delay, so I choose 10 GHz, and the rest are derived in relation to this value. Δa is an experimentally tunable parameter. There is still the value of Ω and Γ_{SE} to be determined. From there we recall that Γ_{SE} represents the spontaneous emission rate from a Rydberg state towards a low-n state, that is negligible against black-body-induced transitions towards other states[41] or ionisation rate in our case. I then numerically solved these equations in Mathematica with different values of Ω.

Equation 4.13 gives a way to estimate the value for Ω in our case, that I find equal to $\Omega = 8.9 \cdot 10^7 rad.s^{-1}$[16]

With this value of the Rabi frequency I plot on figure 5.25 the evolution of the different populations described in the model for different value of Δa.

We can see clearly that the parameter Δa has, as expected, a strong influence both on the final electron population (i.e. the ionisation efficiency) and on the ionisation dynamics. With the given experimental parameters, the model predicts an ionisation efficiency

[15] from the definition of the density matrix and the time-dependent Schrödinger equation for wavefunctions:

$$\rho_{ij} = |\Psi_i\rangle\langle\Psi_j| \tag{5.39}$$

$$i\hbar\frac{d|\Psi_i\rangle}{dt} = \hat{H}|\Psi_i\rangle \tag{5.40}$$

[16]

$$\Omega = \frac{\mu F_{Laser}}{\hbar} \tag{5.42}$$

with:

$$F_{Laser} = \sqrt{\frac{4P_{Laser}}{\epsilon_0 c \pi w_{Laser}^2}} \tag{5.43}$$

and $P_{Laser} = 1$ W, $w_{Laser} = 30\,\mu$m. For $F = 2170$ V/cm the ionised Rydberg states have $n = 20$, ARC gives $\mu^{F=0}_{7S\to 20P} = 0.031\, e\, a_0$, and LFT-Stark maps give for this state a field-free/2170 V/cm intensity ratio of $r_{n=20}(2170\,\text{V/cm}) = 4.88\%$).

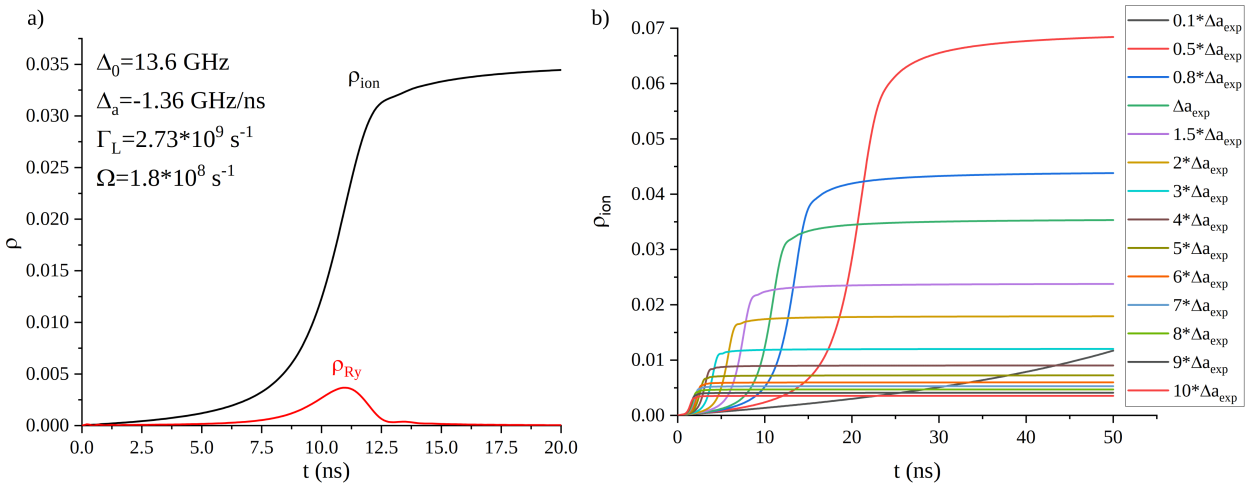

FIGURE 5.25: a) Population of electrons over time (in black) and in the Rydberg state (in red) given by eqs. 5.41 for the experimental conditions indicated on the panel. b) Influence of the parameter Δa (temporal slope of the detuning) on the time evolution of the electron population. It has a clear influence both on the final electron population (ionisation efficiency) and on the dynamics of ionisation. Differents values for Δa are given as multiple of Δa_{exp}, which is $-1.36\,\mathrm{GHz/ns}$.

of 3.5%. From these curves we can obtain the value of τ_{ion} by deriving against time and taking the FWHM of the obtained peak. For the plot shown on figure 5.25 a) I obtain $\tau_{ion} = 2.44\,\mathrm{ns}$.

5.4.2 Adaptation of our set-up to pulse ionisation

Experiments on RPRFI were performed in LAC, on the experimental set-up presented in section 3.1. The detection part had to be adapted to be able to measure precise timing on the electrons, as well as the voltage supply of electrode 1 (V1). In order to test this innovative ionisation scheme in the electric field range we are familiar with, I kept the electric field around $-2170\,\mathrm{V/cm}$, so $V_5 = -870\,\mathrm{V}$ and $V_1 = 0\,\mathrm{V}$, and connected V1 to a pulse generator. The measured voltage pulses can be seen on figure 5.26. The cable used to connect the pulse generator to V1 was a very short, non-shielded cable to minimize its capacitance, to minimize pulse lengthening due to propagation in the cable. The fact that electrodes 0 and 1 are separated by 0.4 cm means that pulsing 6 V on electrode 1 induces an electric field pulse of amplitude 15 V/cm, for example. The potentials applied to electrode V5 and V1 produces a potential around $-435\,\mathrm{V}$ where the electrons are created. They are thus accelerated to 435 eV at the end of electrode 4 (that is kept at 0 V) and fly to the detector through the spectrometer, for a distance of approximately 55 cm.

A very important aspect of theses experiments is the duration of the produced electron bunches. The acquisition thus needs to be adapted to measure this time spread. To this end we added a complete coincidence acquisition set-up. The electrons are detected by the usual detectors (MCPs), and the signal is amplified and digitised by a constant threshold discriminator. It is then transferred directly to a time-to-digital converter (TDC), that also records trigger pulses from the pulser providing the potential to electrode 1. A schematic of these measurements is presented on figure 5.27. As the TDC

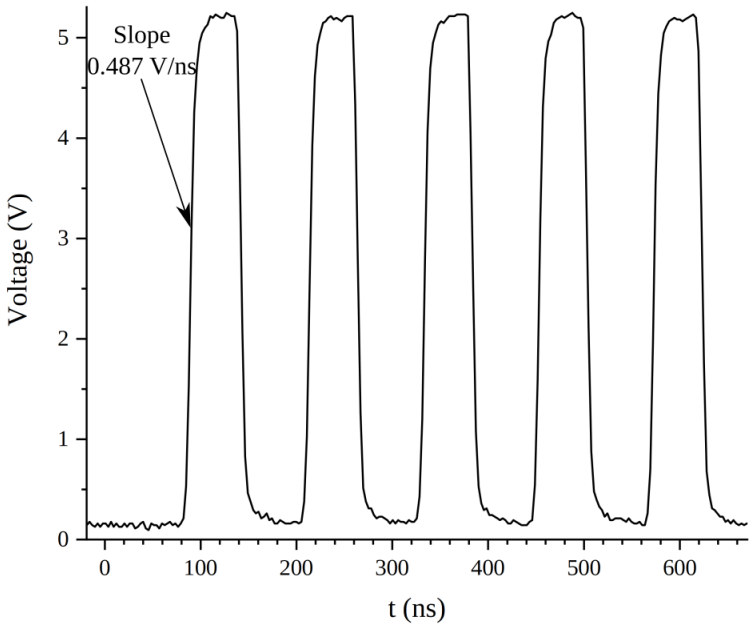

FIGURE 5.26: Voltage pulses from the burst pulser recorded by an oscilloscope. The slope measured here is 5 times smaller than the slope obtained from the analysis of experimental data.

triggers only on NIM signals the main pulses are transformed into NIM signals for every rising front. The TDC is "opened" independently for 50 µs during which it registers (with a binning time of 120 ps) the two kind of "stops" signals: pulses from the *main* pulser and electron hits from the MCPs. It sends it to a dedicated acquisition software. The acquisition software then stores the delay between each electron hits and the previous closest main pulse signal. This reconstructs a time-of-flight spectra from a lot of different and uncorrelated events.

5.4.3 Experimental demonstration of a short pulsed electron source

I conducted a study of the influence of a state linewidth on the observed bunch duration, to test the model presented in 5.4.1. We have taken data on the state presented on figure 5.24 under the same conditions except for the tuning of the Ti:Sa, that was changed from 794.141 000 nm to 794.149 000 nm by 0.002 nm steps (as indicated with dashed black lines on figure 5.24).

For all cases the spectra looked very similar (two examples are shown on figure 5.28) in terms of global structure. Electrons are created at each pulse, on the rising front as well as on the falling front. Indeed the electron signal shows doublet structures one of which is shown in more details in figure 5.29. Clearly the first peak of each doublet is more intense than the second while the separation between these two peaks corresponds to the voltage pulse length (i.e. the duration that the voltage pulse stays at its high level) chosen on the burst pulser. The reason for this intensity ratio remains unclear, but it could be explained by the fact that on the lower field region this state appears more intense than on higher field (see the Stark map on figure 5.24). This could induce a small population of Rydberg states while the field is low, that are then ionised by the pulse.

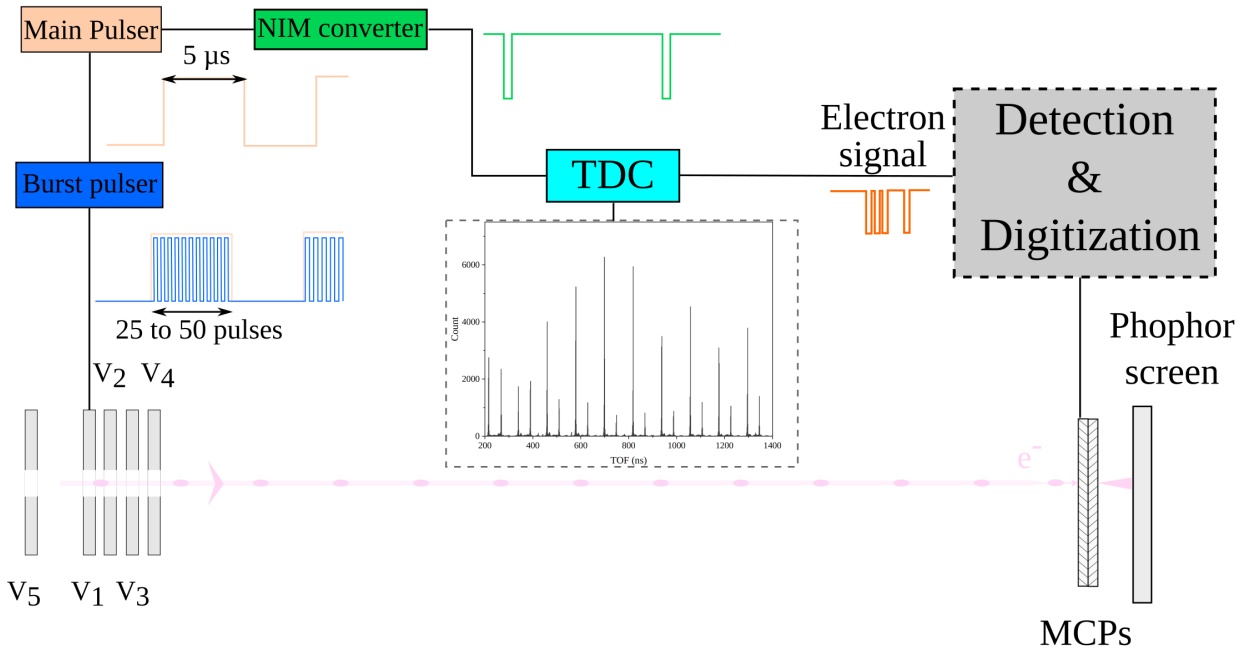

FIGURE 5.27: Schematic of the acquisition set-up for pulsed ionisation experiments, designed to acquire ToF spectra from MCPs signals. It builds up on figure 3.8. The main pulser constitutes the main clock, providing long pulses (5 µs) separated by 1.8 µs. Theses pulses trigger burst pulses from another pulser, of width 50 ns, rising times of 10 ns and amplitude 5 V that are directly linked to electrode 1. This separation allows easy variation of the ratio between TDC openings and electron signal, to optimise data acquisition and study amplitude variations over time.

Both spectra shown on figure 5.28 a) and b) show different levels of background electron emission, that is higher in the case of the laser tuned at 794.149 nm compared to the laser tuned at 794.141 nm. This is simply because as the pulsed potential is at its high level, the coupling with the Rydberg states is non-negligible, and some excitation/ionisation occurs. This background is a lot lower when the pulsed potential is at its low level.

In each spectrum I zoomed on the most intense peak (corresponding to a rising pulse) and extract its Gaussian FWHM[17]. The Stark map of figure 5.24 allows me to link the laser wavelength to the electric field and to the state linewidth. The ToF of the fitted (most intense) pulse at each wavelength are also shown on figure 5.28. They present a very clear time delay depending on the wavelength of the laser. As all the other experimental conditions are kept the same (pulsed voltage levels, pulsed delays...), and given the very good linearity with the wavelength (see inset in figure 5.28), I can safely consider that this time delay comes from the slightly different resonant electric field that is attained at different times, thus introducing a time delay for the electrons.

Using the link between electric-field and wavelength given by the Stark map, i.e. the Stark slope of the state $\frac{d\nu}{dF} = 7.21 \times 10^{-3}\,\mathrm{cm}^{-1}/(\mathrm{V/cm})$, I extract the experimental electric field temporal variation to be around $\frac{dF}{dt} = 6.30\,(\mathrm{V/cm})/\mathrm{ns}$. I note that this value of the experimental electric field temporal variation is quite different from the value I obtained by measuring the voltage pulses on an oscilloscope. The waveform of the voltage pulse directly from the pulser can be seen on figure 5.26, showing $\frac{dV}{dt} = 0.487\,\mathrm{V/ns}$. Taking into account the fact that this potential is applied between 0.4 cm, this gives $\frac{dF}{dt} = 1.22\,(\mathrm{V/cm})/\mathrm{ns}$. The factor 5 is probably due to a too small bandwidth of the oscilloscope that limits its accuracy in high frequencies.

The experimental value is plugged in the model of section 5.4.1, allowing a comparison with experimental results on figure 5.28 d). This comparison shows two surprising behaviours:

- The experimental pulse width are very similar for the five values of Γ_{Loss}, with less than 20% variation of τ_{ion} with 152% variation of Γ_{Loss}. On the contrary, the model shows a high sensitivity of τ_{ion} to the value of Γ_{Loss}, as τ_{ion} varies by 70%.
- The experiment shows a minimum for τ_{ion} at $\Gamma_{Loss} = 2.728 \times 10^9\,\mathrm{s}^{-1}$, which contradicts the monotonic relation of τ_{ion} and Γ_{Loss} given by the model.

A surprising (in a good way) thing is that all the measured temporal spread are a lot smaller than predicted, by a maximum ratio of 2.6 for $\Gamma_{Loss} = 4.447 \times 10^9\,\mathrm{s}^{-1}$. This measurements very probably overestimates the actual value of τ_{ion} (for various reasons detailed in section 5.4.4), so the ratio is very probably even higher than that. As we have verified in chapter 3 that the LFT Stark maps give very good predictions of the states' Γ and the Stark slopes, and as the field temporal variation is extracted from experimental data, we are confident about the values of the parameters fed to the model[18]. Furthermore, different parameters would not change the monotonic relations between the parameters and

[17] The experimental peaks are not perfectly described by a Gaussian peak, but as the detected shape is the convolution of several independent processes with different shapes (atomic rays are usually Lorentzian, the Doppler broadening is Gaussian, and the propagation blurs these shapes), it is a simple choice, that gives larger time spread than Lorentzian peaks

[18] Even thought we did not perform scans on this state to verify Γ in this case

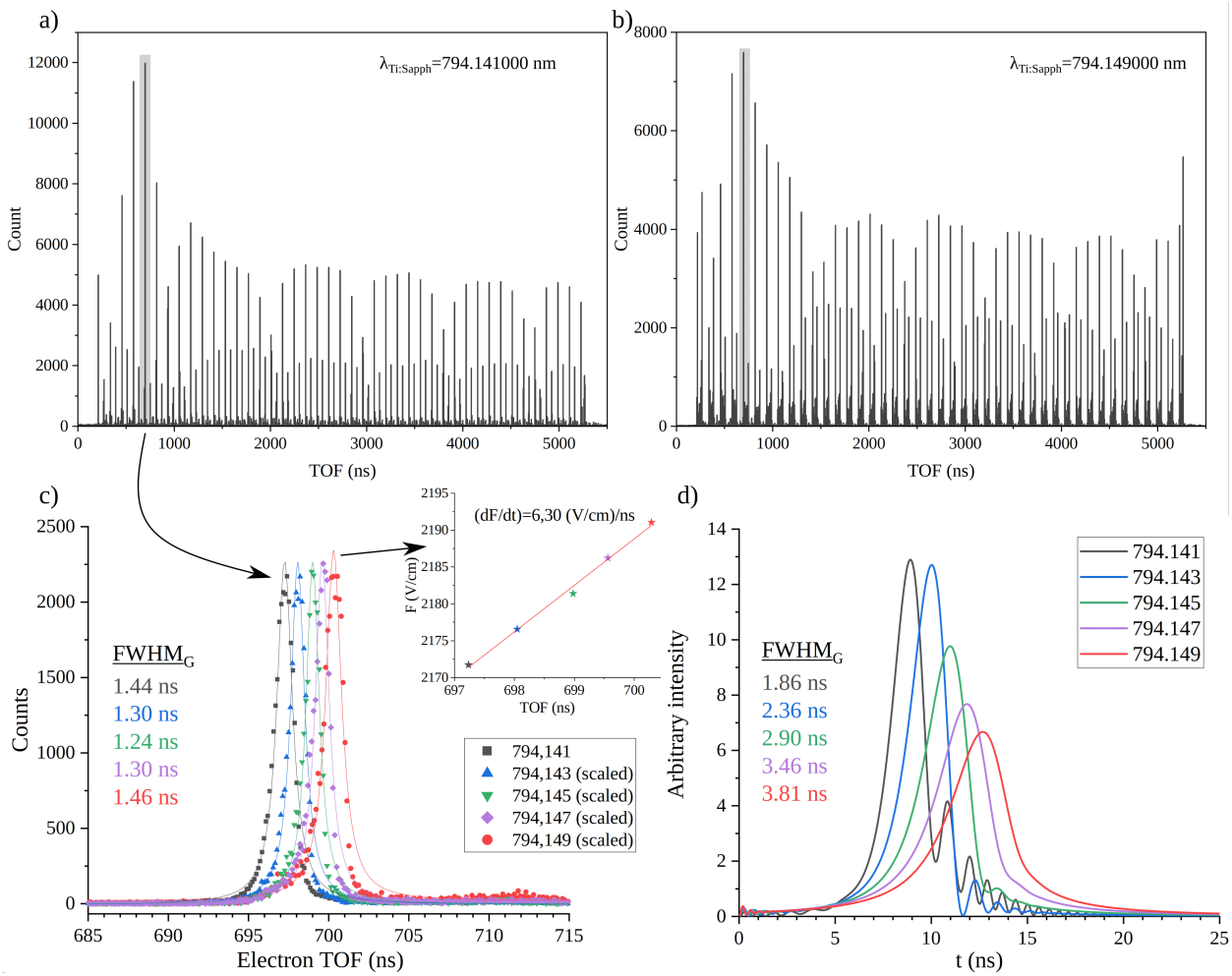

FIGURE 5.28: Complete ToF spectra reconstructed from several acquisitions with $\lambda_{Ti:Sa} = 794.141\,\text{nm}$ (a) and $\lambda_{Ti:Sa} = 794.149\,\text{nm}$ (b). The most intense peak is shown in gray, whose shape and position in fitted by Gaussian peak functions in c). c) Shape, positions of the most intense peak in scans taken at 5 different laser wavelength. The data at 794.141 nm is taken as intensity reference and all other data are normalised to it. The ToF feature a very clear time delay, depending on the wavelength. This gives us access to experimental electric field variation, fitted to $6.30\,(\text{V/cm})/\text{ns}$ in the inset of panel c). The FWHM of each peak is indicated. d) Time-dependent electron signal coming from the model presented in section 5.4.1, showing bigger FWHM as λ increases, i.e. as Γ_{Loss} increases (see table 5.2).

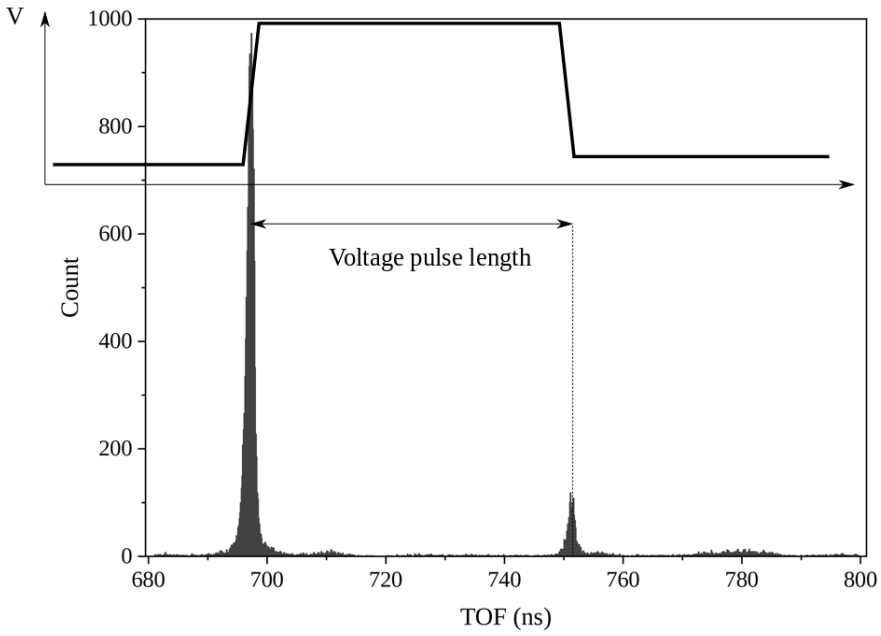

FIGURE 5.29: Zoom on two experimental peaks, showing the doublet structure, imposed by the fact that electrons are created at rising and falling resonant field. The intensity is strongest in the first, as in all the doublets in our experimental spectra.

τ_{ion} (a different value of Ω for example would simply change the population amplitude but not the dynamics).

This is why we can attribute these discrepancies to the two-level model that I presented in section 5.4.1. Modifying it by including the excitation dynamics of the $7S$ state would probably improve its predictions. The Coulombic interaction between the escaping electron and the ion can also play a dominant role in the extraction dynamics, as explained in section 4.1.2, but this can not fully explain the discrepancy observed here because this interaction would increase τ_{ion} instead of decreasing it (we observe shorter pulses than expected). Another possible source of errors comes from that fact that the electric field changes rapidly, while LFT-Stark maps (and the values of Γ that we extract from them) assume static fields. Even if the AC-part of the field is less than 1% of the DC-field, the coupling to the continuum could very well be different than in the static case (i.e. in the LFT-Stark maps). Introducing dynamic Stark effect in the LFT theory could be another approach to improve the model, but is really beyond the course of this work. Reflecting on the conclusions of chapter 2, the LFT method could be advantageously replaced by numerically solving the time-dependent Schrödinger equation to obtain more correct energies and ionisation rates of these states).

Not having a trustworthy model to predict the value of τ_{ion} complicates the optimisation of experimental parameters to improve the properties of the produced electron beam. The reported measurements seem to indicate an optimal value (to decrease τ_{ion}) of Γ_{Loss} at $2.728 \times 10^9\ s^{-1}$. Further experiments are needed, with other states and other experimental parameters (Stark slope, electric field temporal variation, DC-electric field...) to confirm that it is effectively optimal, and how the other parameters could modify the optimal value for Γ_{Loss}.

Sadly (again) the experiments had to be shut down and deconstructed as the LAC was moving to another building.

Nevertheless, this technique (RPRFI) allows the formation of ns time scale electron bunches at high repetition rate (>10 MHz) from individual Rydberg states, with a continuous wave ionising laser. A very useful aspect of replacing the pulsed laser by a pulsed electric field is that the repetition rate of the ionisation and the delay between pulses can be adjusted freely by adjusting the delays in voltage pulses, that is much easier than adjusting repetition rates in an optical system. Using a continuous laser also gives the great advantage of being able to selectively ionise one particular Rydberg state. Combining this to LFT-Stark maps, it gives not only a way to produce electron bunches for a pulsed electron source, but also to study in details the dynamics of ionisation of a strongly shifted-Rydberg state under an AC-Stark effect.

5.4.4 Improving the experimental set-up

Limitations to the time resolution

I must insist on the fact that these experiments were done as proof-of-concept experiments, on the set-up presented in section 3.1, i.e. on a non-optimal set-up for these experiments. The distance from the ionisation to the detector is quite long (estimated to 55 cm) and the energy spread is large (around 6 eV for the presented results, but it could be lowered with a smaller electric field), so that the measured time spread Δt is a convolution of τ_{ion} and $\tau_{\Delta E}$, where τ_{ion} is the intrinsic duration of the ionisation process and $\tau_{\Delta E}$ is the temporal spread due to the energy spread.

To evaluate the impact of this energy spread to the measured time spread, I performed simulations in Simion, comparing the arrival time spread Δt for electrons bunches with the same ΔE but with different τ_{ion}: electrons of the first bunch are all started at the exact same time ($\tau_{ion} = 0$ ns), electrons in the second bunch are started within a 0.75 ns time window ($\tau_{ion} = 0.75$ ns) and a third bunch has a time spread of 1 ns. The results can be seen on figure 5.30. It clearly shows than even with an infinitely small time delay at start (in green), we could not have measured a bunch time under 0.41 ns. With $\tau_{ion} = 0.75$ ns (in orange), the energy spread increases the time spread by 0.09 ns. For the third bunch with $\tau_{ion} = 1$ ns, the energy-spread-induced time-spread is negligible (at our value of the flight energy). In the presented results this probably has a negligible effect because the presented peaks are all longer than 1 ns. If we manage to decrease this time-spread, the energy spread could very well become a problem. An obvious direction of improvement is thus to lower the electric field, to decrease the energy spread and remove this temporal broadening.

The measured values of τ_{ion} are probably overestimated due to the effects of jitter between the main pulses (that serves as clocks) and the ionising pulses (coming from the burst pulser), that would need to be measured. Broadening of the time-dependent signal can also come from the acquisition system. Indeed the transformation of raw MCPs signal to NIM pulses requires the action of a discriminator, that triggers a numerical signal when the analogue signal crosses a certain threshold. In the acquisition set-up used for these measurements a simple threshold discriminator was used, which can induce non-negligible broadening of the arrival time deduced from the signal of the MCPs. Indeed the MCPs raw signal can have a range of different amplitudes, meaning that the signal will cross a certain threshold at a time that depends on the signal timing but also on

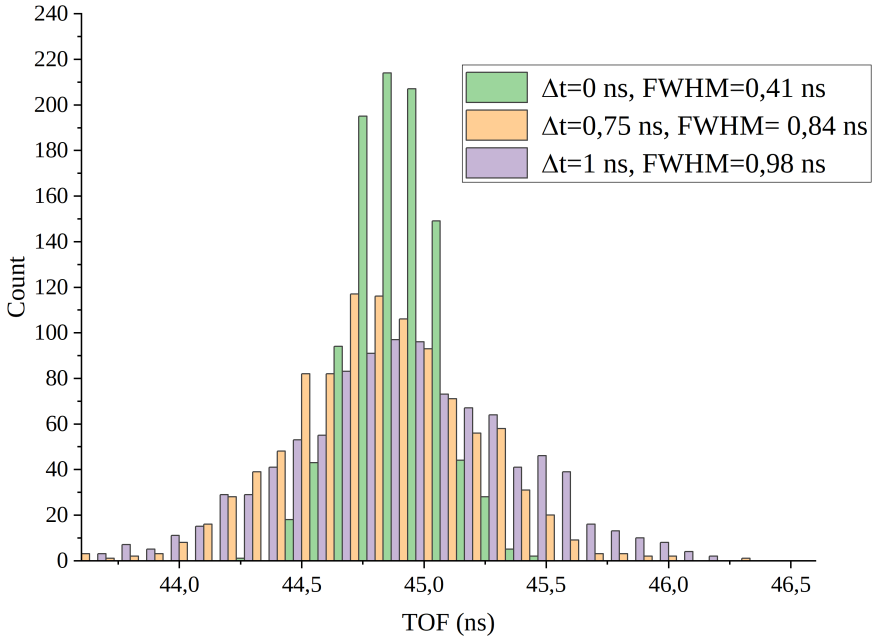

FIGURE 5.30: Simion simulations showing the impact of initial energy spread ($\Delta E \approx 6$ eV) on the resulting time spread. The same energy spread is given to electron bunch with different τ_{ion}, and I plot the resulting Δt on the detector after a 55 cm propagation at 435 eV. $\tau_{ion} = 0$ ns gives $\Delta t = 0.41$ ns, a 0.75 ns bunch is spread out to 0.84 ns and a 1 ns bunch has no additional time spread due to the energy spread.

its amplitude. A perfectly timed signal with double the amplitude will cross a certain threshold at a different time, thus introducing jitter. A more robust constant fraction discriminator should be enough to limit this jitter to negligible values.

Overall the main drawback of RPRFI is that the total resonant interaction time is very short so the ionisation efficiency is low and it is hard to get enough current. A potentially interesting twist on this method would be to introduce the pulsed behaviour to the ionisation part. Indeed here the electric field oscillations bring the continuous beam into resonance with an ionising state, creating a pulsed ionisation. But the oscillating electric field can also drive a continuously excited Rydberg stable state to an ionising field condition (something close to standard PFI), using the kind of states presented in figure 4.33. This would require a detailed control of the state evolution in the field (including during crossings with other states, which involve a description in terms of diabatic/adiabatic evolution), that would be inspired by the developments in highly-selective field ionisation Rydberg spectroscopy[42–46]. This would hopefully increase the population transfer to the Rydberg state and increase the electron flux.

Adding radio-frequency to the mix

Another very promising development pathway to improve the RPRFI ionisation scheme is the addition of radio-frequency (RF) radiations. The main interest of using RF radiations with Rydberg is their huge excitation cross-sections, so a very low power is required to fully saturate Rydberg-Rydberg transitions. The ionisation of an atom with

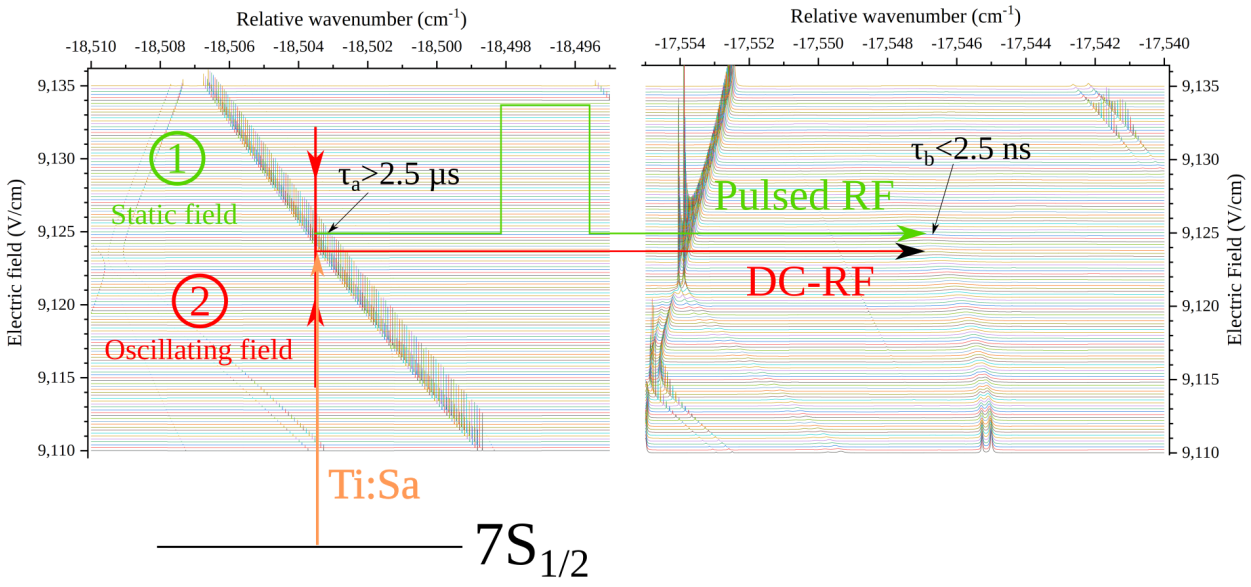

FIGURE 5.31: Illustration of the two proposed ionisation scheme for RPRFI with the addition of RF radiations (3 GHz). It takes advantage of large states lifetime change in small energy range (three orders of magnitude between in the lifetimes τ_a and τ_b in less than 1 cm^{-1}) and of the very-high transition dipoles between Rydberg states. Low electric field and high cross section should provide low energy spread and high current. The first scheme (in green) uses a static field to saturate the slowly ionising Rydberg state and a pulsed RF radiation to bring it to ionisation. The second scheme (in red) uses a constant RF radiation to couple the stable state to the rapidly ionising one and a pulsed electric field to pulse the excitation of the stable state.

these radiations can be either thought of as a microwave multi-photon ionisation, or as field-ionisation due to a time-dependent electric field.

RF waves can be incorporated in two different ways to the pulsed excitation/ionisation process. A summary sketch of these ionisation pathways can be found on figure 5.31, using a typical 3 GHz radiation:

1. in a static electric field with a continuous beam laser coupling a low-lying state (like the 7*S* state) to a stable Rydberg state. The laser is tuned to an intense transition and saturates it. The RF waves couples this stable state to a particular unstable state, that ionise due to Rydberg field-induced ionisation. This radiation is pulsed, creating electron bunches whose length can be varied by choosing another state with different ionisation rate. The fact that the pulsed RF radiation is coupling two Rydberg states (that have high transition dipolar moments) should allow a very good transfer of population and acceptable current.

2. in a time-dependent electric field with a continuous laser and continuous RF radiation. The laser is tuned exactly as in the previous case, but this time the pulsed behaviour is imposed by the electric field. It is very similar to RPRFI but instead of a pulsed-resonance of a rapidly ionising state it relies on the pulsed-resonant excitation of a stable state that is continuously driven towards an unstable stae by DC-RF radiation. This could enable a more efficient excitation by allowing the excitation of

an intense state, regardless of its ionisation rate (and thus give a little more freedom in the choice of the state).

Using the states presented on figure 5.31, we should be able to achieve a pulsed (<1 ns), low energy spread ($\Delta E < 10\,\text{meV}$ from $F < 10\,\text{V/cm}$ and $\Delta z < 10\,\mu\text{m}$) electron source with high-enough current to achieve ToF electron spectroscopy. We are currently setting-up RF irradiation in our experimental set-up to test these ideas and show how much of a current increase they allow.

Section summary

Pulsed ionisation: pulsing the electric field

In this section I presented concepts and preliminary results to construct a pulsed electron source from the ionisation of Rydberg atoms in an innovative way. I coined this ionisation process Rydberg pulsed-resonance field-ionisation, because the pulsed behaviour is introduced by the Rydberg resonance via an oscillating electric field, and the ionisation is due to the state's intrinsic coupling to the continuum. The set-up that we used was not optimal but we nevertheless proved the production of electron bunches in the ns range, probably below 1 ns, with an energy spread around 6 eV (because of the high extracting field of 2170 V/cm). On the three requirements for the electron source HREELM ($\leq 5\,\text{meV}$ energy spread, a temporal spread $\Delta t \leq 150\,\text{ps}$ and a current $I \geq 10\,\text{pA}$), this technique provides almost an adequate pulse length. Decreasing the energy spread will require a lower electric-field (less than 10 V/cm), that will allow even faster field sweeps (pulsing a few tens of millivolts instead of several volts), thus potentially improving also the time spread. Introducing RF-fields to increase the ionisation efficiency is another very promising improvement path to establish this new kind of pulsed electron source as usable in future experiments and ultimately in the HREELM project.

5.5 Conclusion on pulsed electron sources

In this chapter I have presented our experimental efforts to produce and study a monochromatic pulsed electron source. This pulsed source will be essential to the ToF version of the energy analysis in HREELM. It adds a new requirement in the specifications of our electron source, that requires a new approach to the ionisation of atoms. The first step to construct an adapted pulsed electron source is to establish the requirements for the electron source from the ambition of the HREELM project. Indeed, the target energy resolution of 5 meV measured by a ToF implies that the electron pulses are at least shorter than the time spread induced by a 5 meV difference. To make the link between the spectral resolution and the required pulse length, other parameters had to be considered. In particular I spent some time explaining how usual ToF experiments are conducted, and how we could conduct this kind of energy analysis in HREELM while keeping the ability to image the surface at high resolution.

I proposed a detailed ToF measurement sequence based on existing detectors (MCPs combined with TimePix3 chips) and acquisition tools. The details of the measurement

sequence showed that a total current of 10 pA, composed of bunches of at least 6 aC at a rate of 3.5 MHz is enough to fulfil the goals of HREELM. This proposition is based on an electron temporal spread of 150 ps. This gives a new dimension to this work, because no electron source to this day provides this kind of electron bunches while also fulfilling the requirements in term of energy spread and current. Analogously with the energy spread sources at the end of chapter 1, I introduce five terms that play an independent role in the final time spread of an electron bunch: τ_L, τ_{ion}, $\tau_{\Delta E}$, τ_{SC} and τ_{mom}. The rest of the chapter deals with experimental ways to minimise these terms.

The first exploration towards this kind of source consisted in the study of an electron source from the fs-photoionisation of cold caesium atoms. This showed the importance of the polarisation of the ionising laser in photoionisation in the emission directionality, but also that a fs laser pulse does not produce fs electron pulses, but rather ns pulses. In particular, when ionising Rydberg states, the very poor spectral resolution given by a fs laser beam does not allow the selection of particular Rydberg states and gives a ns electron pulse.

I then explored one way to obtain these very good properties in electron bunches: time-dependent manipulation. The pulsed aspect of the electron pulse indeed gives new opportunities to decrease the energy spread of the created electrons, from time-dependent extraction to manipulations during the propagation of the electron bunch. I showed, with the help of many simulations, how these techniques could be implemented in our electron source either to decrease the energy spread or the time spread, or both. In particular, interrupted extraction removes the starting potential difference and could be very useful in our source. These kind of manipulations are still uncommon for electrons as they are too fast, making experiments particularly delicate, something that we also verified.

Finally I introduced Rydberg pulsed-resonance field-ionisation, a technique that has the advantage of ionising a single, highly-shifted Rydberg state. I studied the impact of the state's linewidth (as given by the LFT method) on the resulting ionisation time and found that it was small, and it even contradicts the conclusion of the lossy, time-dependent-detuning two-level model that I presented. The reason for this discrepancy is still unclear, and more theoretical and experimental work is needed to optimize the length of the created pulse, that is already around 1 ns.

Future work will involve further development of this technique, by decreasing the electric field and measuring more precisely the temporal spread while changing parameters. Increasing the current obtained by this method will probably require the addition of RF fields, a possibility that we are currently exploring.

References

[1] S. Karkare, G. Adhikari, W. A. Schroeder, J. K. Nangoi, T. Arias, J. Maxson, and H. Padmore. "Ultracold Electrons via Near-Threshold Photoemission from Single-Crystal Cu(100)". In: *Physical Review Letters* 125.5 (2020). ISSN: 0031-9007. DOI: 10.1103/PhysRevLett.125.054801.

[2] D. Price and G. J. Milnes. "The renaissance of time-of-flight mass spectrometry". In: *International Journal of Mass Spectrometry and Ion Processes* 99.1-2 (1990), pp. 1–39. ISSN: 01681176. DOI: 10.1016/0168-1176(90)85019-X.

[3] U. Even and B. Dick. "Optimization of a one-dimensional time-of-flight mass spectrometer". In: *Review of Scientific Instruments* 71.12 (2000), p. 4421. ISSN: 0022-3654. DOI: 10.1063/1.1322584.

[4] W. C. Wiley and I. H. McLaren. "Time–of–Flight Mass Spectrometer with Improved Resolution". In: *Review of Scientific Instruments* 26.12 (1955), pp. 1150–1157. ISSN: 0034-6748. DOI: 10.1063/1.1715212.

[5] K. Medjanik et al. "Progress in HAXPES performance combining full field k-imaging with time of flight recording". In: *Journal of synchrotron radiation* 26.Pt 6 (2019), pp. 1996–2012. DOI: 10.1107/S1600577519012773.

[6] W. Verhoeven, J. F. M. van Rens, M. A. W. van Ninhuijs, W. F. Toonen, E. R. Kieft, P. H. A. Mutsaers, and O. J. Luiten. "Time-of-flight electron energy loss spectroscopy using TM110 deflection cavities". In: *Structural dynamics (Melville, N.Y.)* 3.5 (2016), p. 054303. ISSN: 2329-7778. DOI: 10.1063/1.4962698.

[7] RoentDek Handels GmbH. *The TDC4HM multi-stop Time-to-digital converter*. URL: http://www.roentdek.com/products/electronics_description/TDC4HM%20description.pdf.

[8] X. Llopart on behalf of the Medipix4 Collaboration. *Timepix4 detectors*. URL: https://indico.cern.ch/event/876275/contributions/3729426/attachments/1986038/3309319/Xavi_Timepix4_Muon.pdf.

[9] J. Long, F. J. Furch, J. Durá, A. S. Tremsin, J. Vallerga, C. P. Schulz, A. Rouzée, and M. J. J. Vrakking. "Ion-ion coincidence imaging at high event rate using an in-vacuum pixel detector". In: *The Journal of chemical physics* 147.1 (2017), p. 013919. DOI: 10.1063/1.4981126.

[10] R. Ballabriga, M. Campbell, and X. Llopart. "Asic developments for radiation imaging applications: The medipix and timepix family". In: *Nuclear Instruments and Methods in Physics Research Section A: Accelerators, Spectrometers, Detectors and Associated Equipment* 878 (2018), pp. 10–23. ISSN: 01689002. DOI: 10.1016/j.nima.2017.07.029.

[11] J. H. Jungmann, D. F. Smith, A. Kiss, L. MacAleese, R. Buijs, and R. M.A. Heeren. "An in-vacuum, pixelated detection system for mass spectrometric analysis and imaging of macromolecules". In: *International Journal of Mass Spectrometry* 341-342 (2013), pp. 34–44. ISSN: 13873806. DOI: 10.1016/j.ijms.2013.02.010.

[12] Gary W. Paterson, Raymond J. Lamb, Rafael Ballabriga, Dima Maneuski, Val O'Shea, and Damien McGrouther. "Sub-100 nanosecond temporally resolved imaging with the Medipix3 direct electron detector". In: *Ultramicroscopy* 210 (2019), p. 112917. ISSN: 03043991. DOI: 10.1016/j.ultramic.2019.112917.

[13] R. van Gastel, I. Sikharulidze, S. Schramm, J. P. Abrahams, B. Poelsema, R. M. Tromp, and S. J. van der Molen. "Medipix 2 detector applied to low energy electron microscopy". In: *Ultramicroscopy* 110.1 (2009), pp. 33–35. ISSN: 03043991. DOI: 10.1016/j.ultramic.2009.09.002.

[14] I. Sikharulidze, R. van Gastel, S. Schramm, J. P. Abrahams, B. Poelsema, R. M. Tromp, and S. J. van der Molen. "Low energy electron microscopy imaging using Medipix2 detector". In: *Nuclear Instruments and Methods in Physics Research Section A: Accelerators, Spectrometers, Detectors and Associated Equipment* 633 (2011), S239–S242. ISSN: 01689002. DOI: 10.1016/j.nima.2010.06.177.

[15] C. Lopez, A. Trimeche, D. Comparat, and Y.J. Picard. "Real-Time Trajectory Control of Deterministically Produced Ions". In: *Phys. Rev. Applied* 11 (6 2019), p. 064049. DOI: 10.1103/PhysRevApplied.11.064049.

[16] J. G. H. Franssen, T. L. I. Frankort, E. J. D. Vredenbregt, and O. J. Luiten. "Pulse length of ultracold electron bunches extracted from a laser cooled gas". In: *Structural Dynamics* 4.4 (2017), p. 044010. ISSN: 2329-7778. DOI: 10.1063/1.4978996.

[17] A. J. McCulloch, D. V. Sheludko, M. Junker, and R. E. Scholten. "High-coherence picosecond electron bunches from cold atoms". In: *Nature communications* 4 (2013), p. 1692. DOI: 10.1038/ncomms2699.

[18] W. J. Engelen, M. A. van der Heijden, D. J. Bakker, E. J. D. Vredenbregt, and O. J. Luiten. "High-coherence electron bunches produced by femtosecond photoionization". In: *Nature Communications* 4 (2013), p. 1693. ISSN: 2041-1723. DOI: 10.1038/ncomms2700.

[19] J. G. H. Franssen, J. M. Kromwijk, E. J. D. Vredenbregt, and O. J. Luiten. "Energy spread of ultracold electron bunches extracted from a laser cooled gas". In: *Journal of Physics B: Atomic, Molecular and Optical Physics* 51.3 (2018), p. 035007. ISSN: 0953-4075. DOI: 10.1088/1361-6455/aa9954.

[20] A. J. McCulloch, R. W. Speirs, J. Grimmel, B. M. Sparkes, D. Comparat, and R. E. Scholten. "Field ionization of Rydberg atoms for high-brightness electron and ion beams". In: *Physical Review A* 95.6 (2017), p. 101. ISSN: 1050-2947. DOI: 10.1103/PhysRevA.95.063845.

[21] G. M. Lankhuijzen and L. D. Noordam. "Frequency- and time-resolved study of the dynamics of rubidium Rydberg wave packets in an electric field". In: *Physical Review A* 52.3 (1995), pp. 2016–2028. ISSN: 1050-2947. DOI: 10.1103/PhysRevA.52.2016.

[22] G. M. Lankhuijzen and L. D. Noordam. "Streak-camera probing of rubidium Rydberg wave packet decay in an electric field". In: *Physical review letters* 76.11 (1996), pp. 1784–1787. ISSN: 1079-7114. DOI: 10.1103/PhysRevLett.76.1784.

[23] Ch. Bordas, F. Lépine, C. Nicole, and M. J. J. Vrakking. "Semiclassical description of photoionization microscopy". In: *Physical Review A* 68.1 (2003), p. 1463. ISSN: 2469-9926. DOI: 10.1103/PhysRevA.68.012709.

[24] O. Fedchenko, S. Chernov, G. Schönhense, R. Hahn, and D. Comparat. "Narrow-band pulsed electron source based on near-threshold photoionization of Cs in a magneto-optical trap". In: *Physical Review A* 101.1 (2020). ISSN: 1050-2947. DOI: 10.1103/PhysRevA.101.013424.

[25] O. Fedchenko, S. Chernov, A. McCulloch, M. Vielle-Grosjean, D. Comparat, and G. Schönhense. "Extraction dynamics of electrons from magneto-optically trapped atoms". In: *Applied Physics Letters* 111.2 (2017), p. 021104. ISSN: 0003-6951. DOI: 10.1063/1.4991366.

[26] Anthony Starace. "Photoionization of Atoms". In: *Springer Handbook of Atomic, Molecular, and Optical Physics*. Ed. by Gordon Drake. Vol. 102. New York, NY: Springer New York, 2006, pp. 379–390. ISBN: 0142196355. DOI: 10.1007/978-0-387-26308-3_24.

[27] Pindzola. "Photoelectron angular distributions for excited ns subshells of cesium". In: *Physical review. A, General physics* 32.3 (1985), pp. 1883–1884. ISSN: 0556-2791. DOI: 10.1103/PhysRevA.32.1883.

[28] R. W. Speirs, A. J. McCulloch, B. M. Sparkes, and R. E. Scholten. "Identification of competing ionization processes in the generation of ultrafast electron bunches from cold-atom electron sources". In: *Physical Review A* 95.5 (2017). ISSN: 1050-2947. DOI: 10.1103/PhysRevA.95.053408.

[29] BA Mamyrin, VI Karataev, DV Shmikk, and VA Zagulin. "The mass-reflectron, a new nonmagnetic time-of-flight mass spectrometer with high resolution". In: *Zh. Eksp. Teor. Fiz* 64.1 (1973), pp. 82–89.

[30] M. P. Reijnders, N. Debernardi, S. B. van der Geer, P. H. A. Mutsaers, E. J. D. Vredenbregt, and O. J. Luiten. "Time-dependent manipulation of ultracold ion bunches". In: *Journal of Applied Physics* 109.3 (2011), p. 033302. ISSN: 0021-8979. DOI: 10.1063/1.3544009.

[31] R. Lindner, H.-J. Dietrich, and K. Müller-Dethlefs. "Basic principles of ZEKE spectroscopy. Optimized resolution and accurate ionization energy". In: *Chemical Physics Letters* 228.4-5 (1994), pp. 417–425. ISSN: 00092614. DOI: 10.1016/0009-2614(94)00959-7. (Visited on 06/20/2018).

[32] S.B. van der Geer and M.J. de Loos. *Pulsar Physics and the General Particle Tracer (GPT) code*. 2018. URL: http://www.pulsar.nl/gpt/.

[33] C.J.R. Duncan, D. A. Muller, and J. M. Maxson. "Lossless Monochromation for Electron Microscopy with Pulsed Photoemission Sources and Radio-Frequency Cavities". In: *Physical Review Applied* 14.1 (2020). DOI: 10.1103/PhysRevApplied.14.014060.

[34] G. Schöhense and Spiecker H. "Array for achromatic imaging of a pulsed particle beam". US Patent US006737647B2. May 18, 2004. URL: https://patentimages.storage.googleapis.com/68/26/7d/358dc1678e2fda/US6737647.pdf.

[35] T. van Oudheusden, P. L. E. M. Pasmans, S. B. van der Geer, M. J. de Loos, M. J. van der Wiel, and O. J. Luiten. "Compression of subrelativistic space-charge-dominated electron bunches for single-shot femtosecond electron diffraction". In: *Phys. Rev. Lett.* 105 (26 Dec. 2010), p. 264801. DOI: 10.1103/PhysRevLett.105.264801.

[36] Anjam Khursheed. "Dynamic chromatic aberration correction in low energy electron microscopes". In: *Journal of Vacuum Science & Technology B: Microelectronics and Nanometer Structures* 23.6 (2005), p. 2749. DOI: 10.1116/1.2062432.

[37] B. M. Sparkes, D. Murphy, R. J. Taylor, R. W. Speirs, A. J. McCulloch, and R. E. Scholten. "Stimulated Raman adiabatic passage for improved performance of a cold-atom electron and ion source". In: *Physical Review A* 94.2 (2016). ISSN: 1050-2947. DOI: 10.1103/PhysRevA.94.023404.

[38] G. Lindblad. "On the generators of quantum dynamical semigroups". In: *Communications in Mathematical Physics* 48.2 (1976), pp. 119–130. ISSN: 0010-3616. DOI: 10.1007/BF01608499.

[39] Claude Cohen-Tannoudji, Jacques. Dupont-Roc, and Gilbert Grynberg. *Processus d'interaction entre photons et atomes*. Savoirs actuels. Physique. Les Ulis and Paris: EDP Sciences and CNRS Editions, 20012001. ISBN: 9782868833587.

[40] U. Fano. "Effects of Configuration Interaction on Intensities and Phase Shifts". In: *Physical Review* 124.6 (1961), pp. 1866–1878. ISSN: 0031-899X. DOI: 10.1103/PhysRev.124.1866.

[41] Thomas F. Gallagher. *Rydberg atoms*. Cambridge monographs on atomic, molecular and chemical physics. Cambridge University press, 1994. ISBN: 0521021669.

[42] U. Hollenstein, R. Seiler, H. Schmutz, M. Andrist, and F. Merkt. "Selective field ionization of high Rydberg states: Application to zero-kinetic-energy photoelectron spectroscopy". In: *The Journal of Chemical Physics* 115.12 (2001), pp. 5461–5469. ISSN: 0021-9606. DOI: 10.1063/1.1396856. (Visited on 05/07/2018).

[43] M Tada, Y Kishimoto, M Shibata, K Kominato, S Yamada, T Haseyama, I Ogawa, H Funahashi, K Yamamoto, and S Matsuki. "Manipulating ionization path in a Stark map: Stringent schemes for the selective field ionization in highly excited Rb Rydberg". In: *Physics Letters A* 303.4 (2002), pp. 285–291. ISSN: 0375-9601. DOI: 10.1016/S0375-9601(02)01263-X. URL: http://www.sciencedirect.com/science/article/pii/S037596010201263X.

[44] Vincent C. Gregoric, Xinyue Kang, Zhimin Cheryl Liu, Zoe A. Rowley, Thomas J. Carroll, and Michael W. Noel. "Quantum control via a genetic algorithm of the field ionization pathway of a Rydberg electron". In: *Physical Review A* 96.2 (2017), p. 28. ISSN: 1050-2947. DOI: 10.1103/PhysRevA.96.023403.

[45] Vincent C. Gregoric, Jason J. Bennett, Bianca R. Gualtieri, Ankitha Kannad, Zhimin Cheryl Liu, Zoe A. Rowley, Thomas J. Carroll, and Michael W. Noel. "Improving the state selectivity of field ionization with quantum control". In: *Physical Review A* 98.6 (2018). ISSN: 1050-2947. DOI: 10.1103/PhysRevA.98.063404. (Visited on 09/10/2019).

[46] Markus Stecker, Raphael Nold, Lea-Marina Steinert, Jens Grimmel, David Petrosyan, József Fortágh, and Andreas Günther. "Controlling the Dipole Blockade and Ionization Rate of Rydberg Atoms in Strong Electric Fields". In: *Physical Review Letters* 125.10 (2020). ISSN: 0031-9007. DOI: 10.1103/PhysRevLett.125.103602.

Chapter 6

Conclusion, on-going work and perspectives

This thesis covers a wide range of different concepts, techniques and experimental set-up. Each of the 5 chapters are dedicated to one aspect of the work done during these 3 years. Even if this constructs a coherent ensemble, they are self-contained, and largely independent. At the end of each section, and at the end of each chapter, the important results, the limits and the perspectives are given. This is why, to avoid redundancy in this already long document, I won't repeat these elements here but simply give an overview of what has been presented.

The first chapter introduced the HREELM project as a new kind of instrument for the surface science community. I showed how it relies on a particular, high-performance electron source that still does not exist, but that could be constructed from the improvement of existing sources based on the photo-ionisation of free atoms for example by using Rydberg atoms. This demands a way to predict the position and ionisation rates of strongly Stark-shifted Rydberg states. Such a theory (the local-frame transformation theory) is presented in some details in chapter 2, together with some details about Rydberg states. This theory is experimentally tested in caesium in chapter 3, with good agreement overall. It is then used to explore two different realisations of the Rydberg-based electron source, the continuous electron source in chapter 4 and the pulsed electron source in chapter 5.

In this last chapter, I will present the on-going work at Laboratoire Aimé Cotton. This work revolves around the design and build up of a novel experimental set-up, from scratch, that I conducted during this last year. I thus start with the description of this set-up as I intended it. It should allow us to perform a series of new studies, that I detail next. Finally I give the status of the construction of this new set-up.

6.1 A new set-up for new electron source studies

6.1.1 Improved electrodes for an improved control of the field lines

Building on the conclusion of section 4.3.4, 4.3.5 and the electrode configuration proposed in section 4.4.1, I drew a new set of electrodes that allow 4-degrees-of-freedom control of the electric field lines. It should allow, for example, to realise close-to-flat electric field lines in aperture electrodes. This set of electrodes follows the recommendation of section 4.4.1 to increase the inner bore of the central aperture electrodes, to give new degrees of freedom to determine the field lines at the center. A great deal of attention was drawn

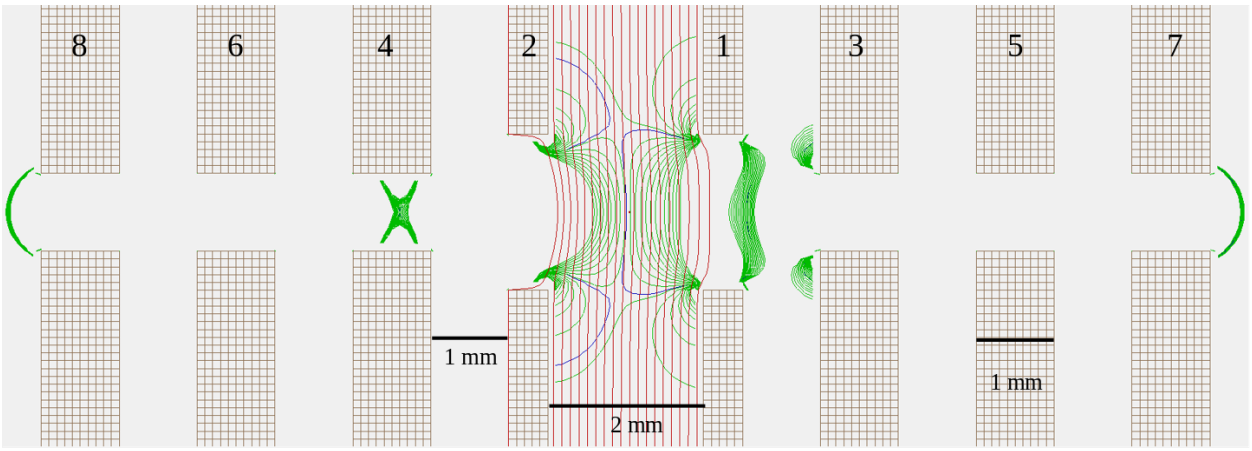

FIGURE 6.1: Planar-cut of the cylindrically symmetric electrodes in Simion. The field and potential lines correspond to the flat line configuration of figure 4.31 There are 8 electrodes, 1 and 2 are 0.5 mm thick and all the others are 1 mm thick. Both ends of the optical axis are open, to allow the extraction of the electrons and the ions.

to the mechanical structure of the electron gun, particularly concerning the concentricity and coplanarity of electrodes. Figure 6.1 shows a planar-cut of this new electro design.

Figure 6.2 shows an *écorché* 3D-drawing of the electrode mounting. To have the best concentricity and coplanarity of electrodes we[1] decided to use circular electrodes, all fixed on a single holding piece. Provided the holding piece is at numerical machining precision, and that the circular electrodes (which are very simple shapes) are correctly centred on this piece, then the concentricity and coplanarity of electrodes should be close to optimal.

The holding piece must obviously be made of an insulating, machinable and mechanically sturdy material. We considered both ceramics like Macor or high-quality plastics like PEEK, but chose the latter because of the difficulty to machine fine structures in ceramics. Indeed, with ceramics these small features can easily break and, as the piece should hold all the electrodes, it is not easily replaceable. The mechanical realisation was done at the mechanic's workshop of *Institut des Sciences Moléculaires d'Orsay*[2], on a 5-axis numerical machine, providing very high precision on the surfaces, angles and distances in the holding piece.

To effectively center the electrodes, the holding piece is in a amphitheatre-like shape, with a series of concentric, increasingly bigger openings. A total of 13 steps go from a smallest diameter of 26 mm to the largest diameter of 68 mm, holding 8 electrodes. Additional steps are inserted between electrode-resting steps, to increase the isolator distance between electrodes to decrease the risk of electric breakdown.

The eight electrodes, consisting in flat stainless-steal disks with increasing diameter (from 26 mm to 68 mm with 6 mm steps) were glued on the holding piece with ThorSeal, and connected electrically through a metal sheet welded to the disk. The welded sheet is folded downwards (relatively to the concentric axis) and fixed on a PEEK ring where it is connected to an isolated cable that goes out of the contraption.

[1] with the great help of Bruno Vivan from our design office, who provided all the 3D-drawings presented in this chapter

[2] as the LAC was moving to another building during the conception of this new experiment

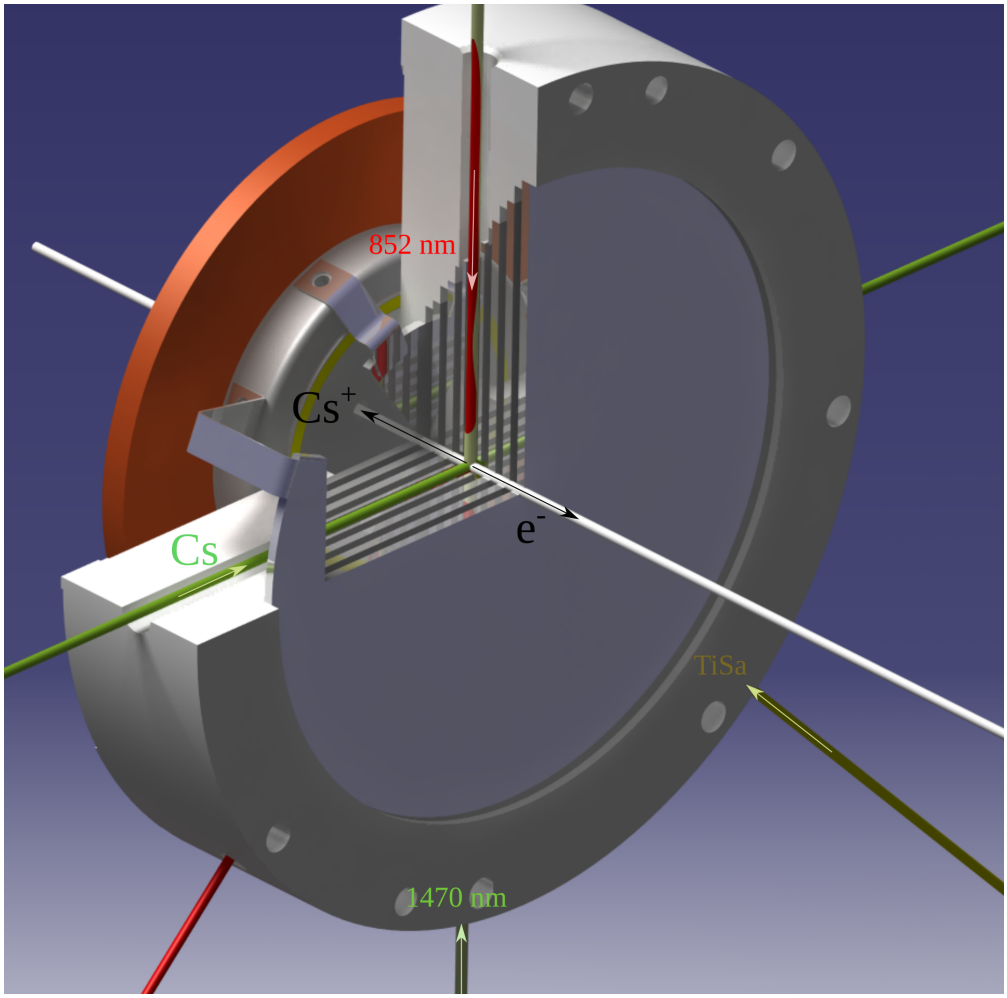

FIGURE 6.2: 3-D *écorché* of the piece that holds the electrodes in the new experimental set-up. Lasers axis (as well as the neutral caesium beam axis) are represented by coloured cylinder and arrows. The electron axis (i.e. principal field direction) is the white cylinder. The 8 electrodes rest on the steps of the white piece, that is in insulating material. The amphitheatre-like shape centers the electrodes and guaranties coplanarity at machine-precision. Oblong apertures in the centring piece hold the electrode-welded metal sheet that are used for electrical contacts at the base of the holding piece.

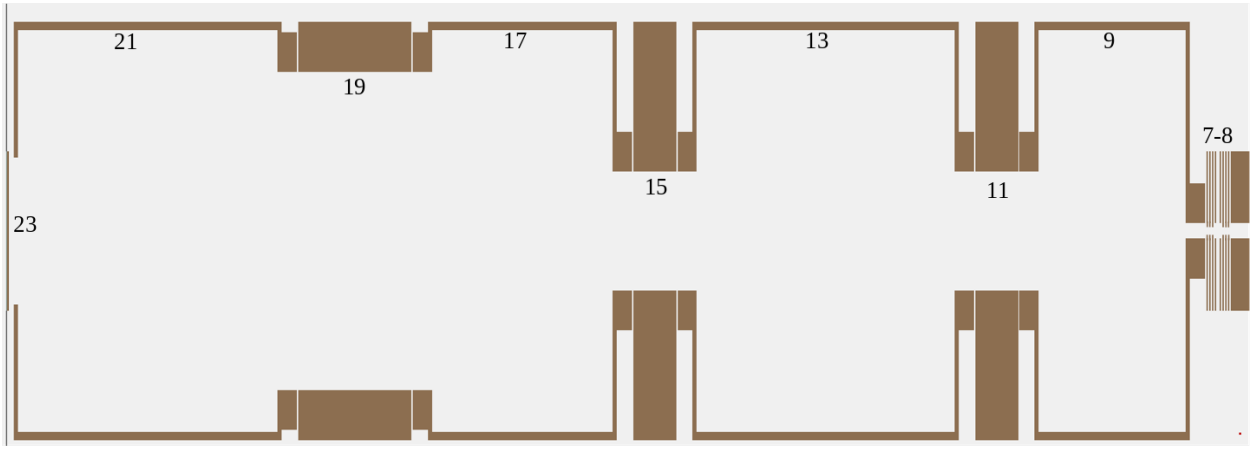

FIGURE 6.3: Simion planar cut of the ion spectrometer that should allow imaging the ionisation zone with a magnification $\times 1000$. It features three consecutive cylinder Einzel lenses, each of them with a $\times 10$ magnification. Electrodes 7 to 8 are the ones shown on figure 6.1, electrodes 9, 13, 17 and 21 are kept at the same potential, that determines the flying energy of the ions. Electrode 11, 15 and 19 are the active part of the Einzel electrodes. Electrode 23 is the detector, kept at the same potential as 21 or slightly lower, to attract ions.

An important feature of this electrode assembly is, beyond the very good concentricity and coplanarity of the electrodes, that both ends of the optical axis are free, so that the caesium ions can also be extracted and detected. The next section deals with this side of the set-up.

6.1.2 An ion spectrometer

On the ion side of the set-up (from electrode 8), I drew an ion spectrometer to be able to image the ionisation zone with a magnification of $\times 1000$. It is strongly inspired by the work of Ref. [1] and is presented on figure 6.3. It is based on three cylindrical Einzel lenses, each of them allowing a $\times 10$ magnification with less aberrations than aperture lenses. The potential required for this $\times 1000$ magnification are under $-1000\,\mathrm{V}$.

A position-sensitive detector would thus allow imagery of the x and y positions of the starting ion cloud. With a time sensitive detection we could also obtain information about the starting z position of the ions, with a resolution depending on the flight energy and the temporal resolution of the detector. Simulations in the presented geometry (with an extracting field of $5\,\mathrm{V/cm}$) shown on figure 6.4 show that 150 ps temporal resolution at a flight energy of 230 eV gives a resolution of 3.3 µm on the starting z position (in the case of negligible initial time spread). This spectrometer should thus allow the 3D-imagery of the starting ions, with applications described in section 6.3.2.

6.1.3 µ-metal chamber

This assembly (the ionisation electrodes and the ion spectroscope) will take place in a newly constructed vacuum chamber, that has the peculiarity of being made in 5 mm-thick

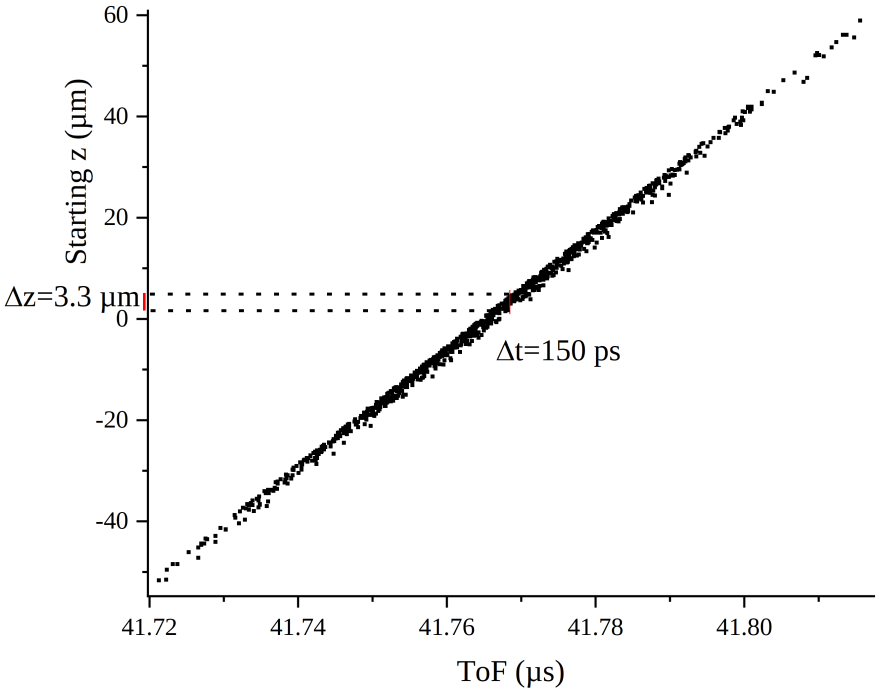

FIGURE 6.4: Simulations in the presented geometry, showing that the initial z positions of ions created at random with $\Delta z = 25\,\mu$m and flying at 230 eV can be determined with 3.3 µm resolution with a precision of 150 ps. Here clearly the limiting point to the spatial resolution is not the temporal resolution but the poor correlation between arrival time and starting position, that can be improved by decreasing the flight energy.

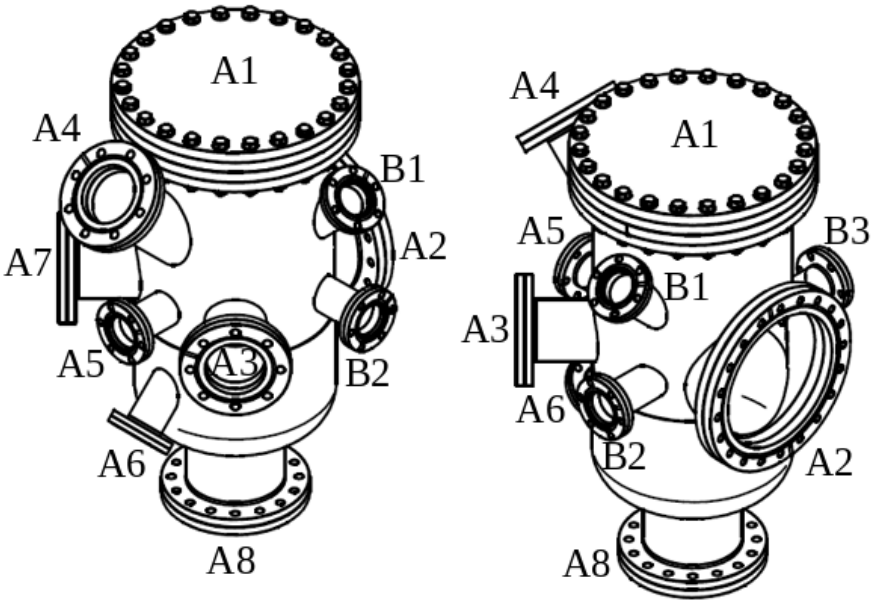

FIGURE 6.5: 3D-Schematic of the mu-metal chamber represented twice with 90° rotation. All the flanges are explicitly numbered and their use is given in table 6.1.

µ-metal. I designed it completely and it was constructed by the Kurt Lesker Company at the beginning of the 2020 year. 3D-drawing of this chamber can be seen on figure 6.5.

This chamber has many flanges, that will have different uses depending on the configuration of the experiment. Indeed this set-up will serve two purposes:

1. It will host studies on the electron source, to test our ideas to improve it. This will require the set-up to work in the "ToF electron source" configuration.

2. Once the electron source will have appropriate properties in terms of energy spread, temporal spread and current, the chamber will enable the first realisation of a HREELM prototype. It will then be used in the "HREELM 0.0" configuration.

Each of these configurations uses the flanges of the chamber in a different way, which are summed-up in table 6.1.

The "ToF electron source" configuration uses the CF150 flange(A2) to plug the electron source to the chamber, that will be used to hold the sample manipulator in the "HREELM 0.0" configuration. The excellent shielding provided by the chamber should allow very low ToF electron energy measurement to be performed. The ToF distance, and thus the energy resolution, can be increased by an additional shielded drift-tube on flange A5.

The flanges B1, B2 and B3 are not centred towards the center of the main cylinder of the chamber, but on a point in the same plane but closer to the flange A2. These flanges will be used (as viewports and holding sample transfer tools) in the "HREELM 0.0" configuration to manipulate the sample and fix it on the sample manipulator plugged in flange A2.

Some flanges still don't have definitive uses, but could be used to incorporate additional elements in the future.

N°	Size	"ToF electron source" configuration	"HREELM 0.0" configuration
A1	CF200	Access to the chamber during assembly, blanked afterwards	
A2	CF150	Electron source	Sample manipulator
A3	CF63	Viewport	Imaging optics, drift tube and PTSD
A4	CF63	Viewport	Viewport
A5	CF40	Drift-tube and TSD	Viewport or mass spectrometer
A6	CF40	Viewport	Viewport
A7	CF63	Viewport	Electron source
A8	CF100	Pumping	Pumping
B1	CF40	Viewport	Viewport
B2	CF40	Viewport	Sample manipulation
B3	CF40	Viewport	Sample manipulation

TABLE 6.1: Summary of the flanges available on the mu-metal chamber, and their usage in both the "ToF electron source" and the "HREELM 0.0" configurations. TSD: time-sensitive detector, PTSD: position-and-time-sensitive detector.

6.2 On-going work: improving the electron source

As I mentioned in the conclusion of chapter 5, this new set-up will be used first to pursue our studies on RPRFI, at lower fields. A photograph of the current state of the set-up is shown on figure 6.6. A decisive advantage of this set-up is that it allows low-energy ToF energy analysis of our electron source, so we will be able to directly measure low energy spread, in the "ToF electron source" configuration. We could for example ionise the state presented in section 4.4.2 and optimise the experimental parameters to obtain the required electron bunch properties. Attaining very low energy spread ($\approx$ 5 meV) requires to decrease the electric field down to 10 V/cm or even lower. A first objective of this set-up is thus to confirm that RPRFI is indeed also valuable at low field, and that we will be able to create electron bunch with less than 1 ns duration and very low energy spread.

Elucidating the influence of the ionisation rate of the state Γ on the ionisation dynamics in a pulsed field will require some theoretical developments beyond a lossy two-level system. Indeed having a model that could predict the resulting ionisation time would be really useful.

6.3 Perspectives: realising the first HREELM prototype

6.3.1 HREELM 0.0

The set-up also has, in a longer time scale, the purpose of realising the first functioning prototype of the HREELM instrument. Once the electron source will have had demonstrated good enough properties, we swill switch to the "HREELM 0.0" configuration. This allows the introduction of a sample in the way of the electrons, that will travel from the electron source (on flange A7) and impinge on the sample at a 45° angle, then travel towards a ToF dedicated-analyser fixed in flange A3 (that is provided by the team of Prof. Schoenehense, together with the collection optics) where we will image the sample. The

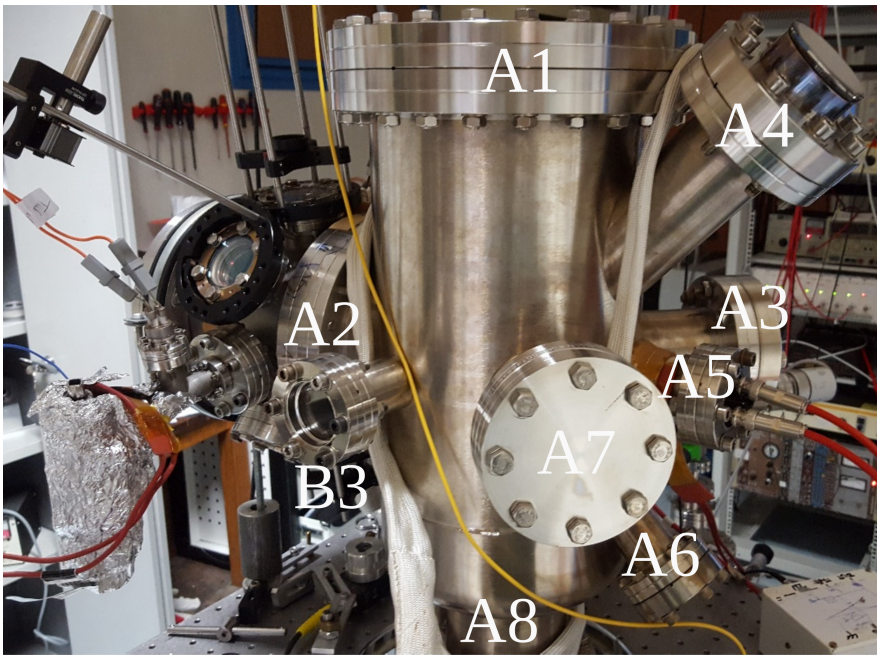

FIGURE 6.6: Photograph of the current state of the experiment, with the mu-metal chamber in the "ToF electron source" configuration. Flange A2 holds the electron source and the detector is fixed at the flange A5. A longer drift tube will be fixed on A5 once an stable electron signal is obtained.

45° angle is far from optimal for the imagery, but it does not require the expensive beam separation of the actual HREELM design. This should be enough to acquire the first spectroscopy-correlated images of samples thanks to our electron source.

This will also be a very good platform to test the proposed detection based on the correlation of MCPs signals and TimePix signals. We started a scientific discussion with the group of Vincent Schoepff at CEA/LIST to lay the basis of a collaboration around the TimePix detectors. Indeed they are expert users of this kind of detectors, and could provide us with TimePix3 chips, together with their expertise.

6.3.2 Using ions to improve the resolution

One final note about this set-up and the future studies is the importance of the ions. Recent experiments in our lab have shown that when ionising Rydberg states under an electric field, detecting the position of an electron on a detector in front of the ionisation zone gives the starting position of the ion and even allows controlling its trajectory in real time[2]. The key ingredient is that the ionisation of highly Stark shifted Rydberg states is gentle enough to guaranty good correlation between the detected positions of the two charged particles. Here I propose to use this correlations in the other way, i.e. to detect the ions and use the information they provide on the electrons.

I envision two ways this can be used effectively in the context of HREELM:

- Improving the energy resolution on energy losses in a pulsed electron source. In section 6.1.2 I have detailed how this set-up would allow 3D-imagery of the starting positions of the ions, the z direction being measured by the arrival time of the ion of the detector. The idea is simple and illustrated on figure 6.7: at t_0 some atoms

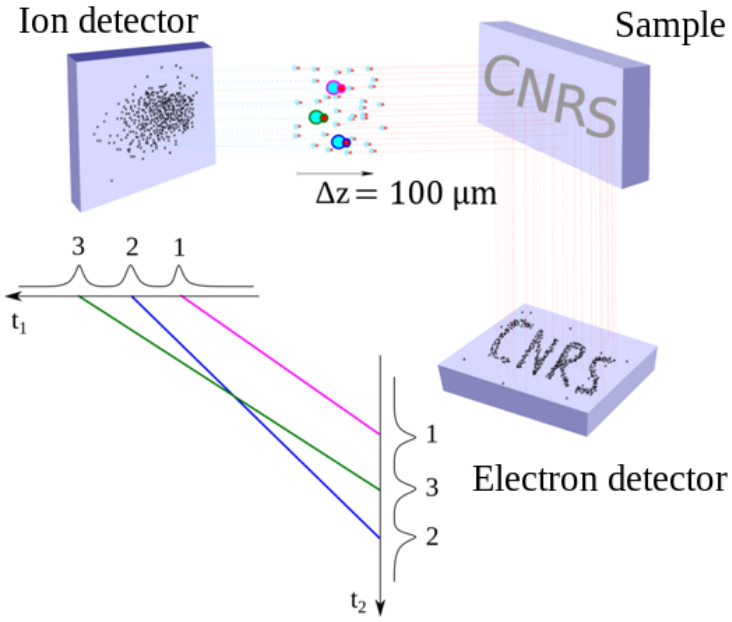

FIGURE 6.7: Schematic of the principle of using ions detected in correlation with electrons to improve the spectroscopic resolution.

are ionised in the ionisation region, in a box of say 50 µm × 50 µm × 50 µm under an electric field that separates the charges and the $3D$ coordinates of the ions are measured. The electrons travel in the chamber, hit the sample at t_1, possibly lose energy, and then fly towards the detector. It records the position of the electrons as well as their arrival time t_2. The x and y coordinates of electrons represent the image of the sample, and the x and y coordinates of the ions can be used to correlate them with the detected electrons. The advantage of this correlation is that we can also correlate the arrival time of the ion, i.e. its starting z position. This means that we know the starting position of the electron to the precision of the timing arrival of the ion. This circumvents the need for a low electron energy spread, as long as the dominant electron energy comes from the z position. The spectroscopic resolution then comes from the precision on t_1 and the correlation between the arrival times of the ions and their initial z position, and *not from the electron energy spread*. This allows large ionisation zone, thus removing the impact of ion space charge and electron-electron interactions in the ionisation zone.

- Allowing the unprecedented *continuous ToF energy analysis*. This would require a small ionisation zone in the z direction, and a continuous electron production. A schematic is shown on figure 6.8. The principle is that even if the ionisation is continuous, the moment of ionisation of the electron t'_0 is given by the measured ion arrival time and the known time it takes an ion to travel from the ionisation zone to the detector. When an ion is detected, we check if an electron has been measured in the time window compatible with the known travel time and possible energy losses. If such an electron was detected (in the same detector area of the ion) in the time window, we can deduce the energy loss at the sample from the difference between t_2 and t'_0.

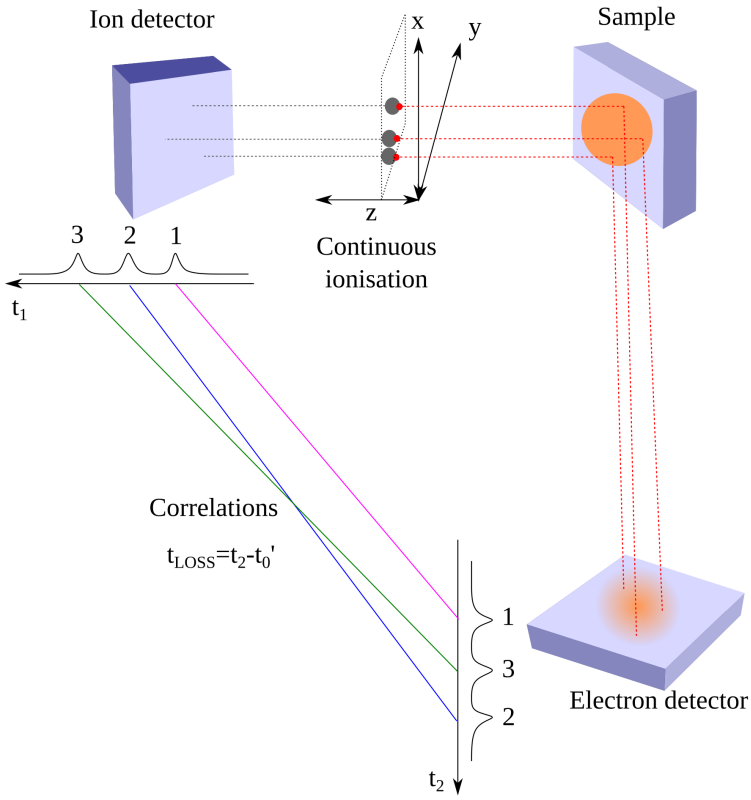

FIGURE 6.8: Schematic of the principle of using ions detected in correlation with electrons to implement continuous ToF measurements.

As these techniques are quite involved in terms of detection and data analysis, they are not priorities, but could really serve as last resort to allow the functioning of HREELM.

These long-term perspectives conclude this thesis devoted to the use of Rydberg atoms to improve current electron sources.

References

[1] M. Stecker, H. Schefzyk, József Fortágh, and Andreas Günther. "A high resolution ion microscope for cold atoms". In: *New Journal of Physics* 19.4 (2017), p. 043020. ISSN: 1367-2630. DOI: 10.1088/1367-2630/aa6741.

[2] C. Lopez, A. Trimeche, D. Comparat, and Y.J. Picard. "Real-Time Trajectory Control of Deterministically Produced Ions". In: *Phys. Rev. Applied* 11 (6 2019), p. 064049. DOI: 10.1103/PhysRevApplied.11.064049.

Appendices

Appendix A: Aligning the electron beam in the spectrometer: a procedure

A common issue in electron optical system is the misalignment of the electron beam inside the different elements. Indeed, to obtain the best performances with such instruments, one must minimize the misalignment between the electron axis and the instrument's optical axis.

This is achieved in our set-up by three sets of deflectors. The first set (see "Deflectors" on figure 9) is composed of three electrostatic dipoles, placed after the electron source and before the diaphragm. The procedure for this alignment starts with shutting off the magnetic field in the magnetic sector and monitoring the electronic current on the inner tube. Then the diaphragm is closed to its first position and the potentials on deflectors is tuned to maximize the current reading. We then close the diaphragm to its second step, optimize the potentials, and close it to its third and final step.

If we open the diaphragm completely at this point, the current should increase by no more than a factor 2. If there is more than a factor 2 between the current reading with a fully-open and a fully-closed diaphragm, then the electron beam is too divergent. Indeed the ionisation zone is not more than 500 µm, and the fully-closed diaphragm has an aperture of 1 mm, so the main part of the beam should pass easily through the diaphragm, even fully closed. The potential on the Einzel lens (i.e. the potential on electrode 3) can then be tuned to modify the collimation decrease the ratio between the two extreme cases.

The second set of deflectors is placed after the diaphragm and before the magnetic sector (see $dipole2$ and DMX on figure 9). It is composed of two magnetic dipoles that act on the X and Y axis independently. From now on we tune the current in the magnetic sector to have the electron beam centred on the detectors. If there is a misalignment in the Y axis, then changing the current in the magnetic sector shifts the electron spot along a line that is not perfectly horizontal (the X direction). We tune the current inside DMX to correct the angle between the spot travel line and the horizontal axis.

The third set of deflectors is placed just after the magnetic sector and before the first post-sector quadrupole $Q1$. It is again a pair of magnetic dipole, called DX and DY. DY is adjusted so that the electron beam pass at the center of $Q4$ (the last quadrupole before the detector). We check that it also passes at the center of the other quadrupoles. If not, DMX is slightly modified and DY is tuned to pass through $Q4$.

The $dipole2$ deflector acts on the X direction and is adjusted together with the current in the sector, and with DX. They are tuned until the electron beam is at the center of $Q1$, $Q2$,$Q3$ and $Q4$.

To determine if the electron beam passes through the center of any quadrupole, the simplest way is to activate the quadrupole, and check if the electron spot shifts on the detector due to the effect of the quadrupole in question. A proper alignment makes any quadrupole focus the spot in one direction and defocus it in the other direction, without any shifts. If the center of the electron spot moves, this means that the electron beam is

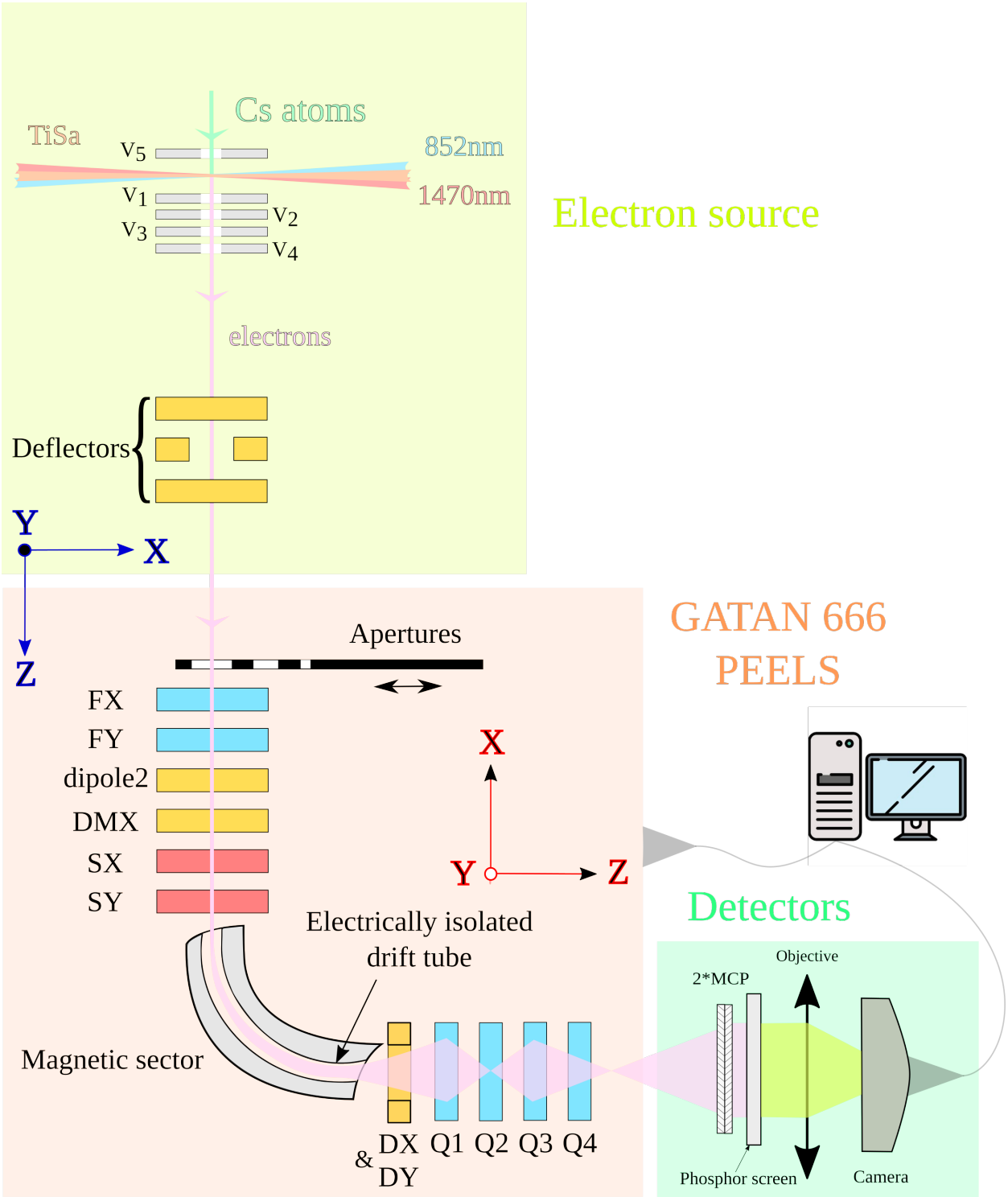

FIGURE 9: Schematic of the experimental set-up, containing the electron source, the Gatan 666 photo electron energy loss spectrometer and the detectors. The blue frame of reference is for elements before the magnetic sector, while elements after the sector are referenced in the red frame. See text for detailed explanation of specific parts.

not at the center of the quadrupole. Indeed the quadrupole magnetic potential (see figure 4.13) only acts as a lens on a centred beam, meaning that if there is a shift, it is due to a dipolar behaviour caused by a misalignment. Tuning the alignment of an electron beam on a quadrupole is thus done most efficiently when the excitation of the quadrupole is changed automatically and rapidly (wobbled), this way one only has to tune the deflector while observing the effect of the quadrupole's changing excitation. This wobble is best done via a script, instead of the tedious job of wobbling by hand between each modification of the adjusted parameter.

That is why I wrote a script in Dm for each quadrupole, that wobbles the quadrupole excitation on demand. As stated before, this is very useful to align the electron beam in the instrument. When the electron beam is correctly aligned, the next step towards an energy spread measurement is the tuning of the pre- and post-sector quadrupoles and hexapoles.

université PARIS-SACLAY

ÉCOLE DOCTORALE
Ondes et matière
(EDOM)

Titre: Source d'électrons monochromatique par l'ionisation d'atomes de Rydberg de césium pour des applications en spectroscopie et en microscopie électronique

Mots clés: source d'électrons, atomes de Rydberg, césium, jet atomique, monochromaticité

Résumé: Les sources d'électrons utilisées en microscopie électronique ont une haute brillance mais une haute dispersion en énergie (>250 meV). D'autres types de sources existent, basées sur la photo-ionisation de jets atomiques, remarquables par leur finesse énergétique (quelques meV), mais à faible courant (quelques dizaines de pA au mieux) ce qui interdit leur usage en microscopie. Une source d'électrons générant un courant de 1 nA tout en gardant une faible dispersion en énergie permettrait d'améliorer grandement certaines techniques de microscopie en se débarrassant des aberrations chromatiques dans la colonne, mais aussi de construire un nouvel instrument : HREELM. Cet instrument permettrait, pour la première fois, de coupler des mesures de microscopie électronique à basse énergie (de surface, type LEEM) avec des mesures de spectroscopie de perte d'énergie d'électrons de haute résolution (de type HREELS). Cette thèse explore comment une connaissance fine des états de Rydberg et de leur ionisation permet d'améliorer les sources actuelles d'électrons. Ceci repose sur la prédiction de leur position et taux d'ionisation en champ électrique, possible notamment par la théorie de changement de repère local (LFT). Cette théorie est présentée en chapitre 2 et comparée à l'expérience en chapitre 3. L'utilisation d'atomes de Rydberg pour une source continue d'électrons est détaillée en chapitre 4, dans lequel je montre des résultats de mesure de dispersion en énergie par un spectromètre magnétique, ainsi que deux propositions détaillées de sources permettant de réaliser HREELM. L'apport des atomes de Rydberg pour une source pulsée est présenté en chapitre 5, dans lequel je montre des résultats de l'ionisation d'un MOT de césium ainsi qu'un processus d'ionisation pulsé appelé ionisation par champ par résonance Rydberg pulsée (RPRFI).

Title: Ionisation of caesium Rydberg atoms for a monochromatic electron source for applications in electron microscopy and spectroscopy

Keywords: electron source, Rydberg atoms, caesium, atomic beam, monochromatic

Abstract: Electron sources used in electron microscopy have high brightness but high energy spread (>250 meV). Other types of sources exist, based on the photo-ionisation of an atomic beam, remarkable for their low energy spread (a few meV), but low current (a few tens of pA at best) which prohibits their use in microscopy. An electron source generating a current of 1 nA while keeping a low energy spread would greatly improve certain microscopy techniques by getting rid of chromatic aberrations in the column, but would also make it possible to build a new instrument: HREELM. This instrument would allow, for the first time, to couple surface low energy electron microscopy measurements (LEEM) with high-resolution electron energy loss spectroscopy measurements (HREELS). This thesis explores how a detailed knowledge of Rydberg state and their ionization can improve current electron sources and move towards this goal. This is based on the prediction of their position and ionisation rate in electric fields, possible with the local frame transformation theory (LFT). This theory is presented in chapter 2 and compared to experiment in chapter 3. The use of Rydberg atoms for a continuous source of electrons is detailed in chapter 4, in which I show results of energy dispersion measurements by a magnetic spectrometer, as well as two detailed electron source proposals for the realisation of HREELM. The contribution of Rydberg atoms for a pulsed electron source is presented in chapter 5, in which I show results of the ionisation of a caesium MOT as well as an experimental demonstration of a pulsed ionisation process called Rydberg pulsed resonance field ionisation (RPRFI).

Université Paris-Saclay
Espace Technologique / Immeuble Discovery
Route de l'Orme aux Merisiers RD 128 / 91190 Saint-Aubin, France